Tritium Transport, Corrosion, and Fuel Performance Modeling in the Fluoride Salt-Cooled High-Temperature Reactor (FHR)

by

John Dennis Stempien

S.M., Nuclear Science and Engineering, 2011
Massachusetts Institute of Technology

B.S., Chemistry, 2008
University of Vermont

SUBMITTED TO THE DEPARTMENT OF NUCLEAR SCIENCE AND ENGINEERING IN PARTIAL FULFILLMENT OF THE REQUIREMENTS FOR THE DEGREE OF

DOCTOR OF PHILOSOPHY IN NUCLEAR SCIENCE AND ENGINEERING
AT THE
MASSACHUSETTS INSTITUTE OF TECHNOLOGY
JUNE 2015

Signature of Author: Signature redacted
Department of Nuclear Science and Engineering
May 12, 2015

Certified by: Signature redacted
Ronald G. Ballinger, Ph.D.
Professor of Nuclear Science and Engineering, and Materials Science and Engineering
Thesis Supervisor

Certified by: Signature redacted
Charles W. Forsberg, Ph.D.
Senior Research Scientist, Nuclear Science and Engineering
Thesis Reader

Accepted by: Signature redacted
Mujid S. Kazimi, Ph.D.
TEPCO Professor of Nuclear Engineering
Chair, Department Committee on Graduate Students

THIS PAGE LEFT INTENTIONALLY BLANK

Tritium Transport, Corrosion, and Fuel Performance Modeling in the Fluoride Salt-Cooled High-Temperature Reactor (FHR)

by

JOHN DENNIS STEMPIEN

SUBMITTED TO THE DEPARTMENT OF NUCLEAR SCIENCE AND ENGINEERING
ON MAY 12, 2015 IN PARTIAL FULFILLMENT OF THE
REQUIREMENTS FOR THE DEGREE OF DOCTOR OF PHILOSOPHY IN
NUCLEAR SCIENCE AND ENGINEERING

Abstract

The Fluoride Salt-Cooled High-Temperature Reactor (FHR) is a pebble bed nuclear reactor concept fueled by tristructural isotropic (TRISO) fuel particles embedded in graphite spheres and cooled by a liquid fluoride salt known as "flibe" (^7LiF-BeF_2). A system of models was developed which enabled analyses of the performance of a prototypical pebble bed FHR (PB-FHR) with respect to tritium production and transport, corrosion, TRISO fuel performance, and materials stability during both normal and beyond design-basis accident (BDBA) conditions.

A model of TRITium Diffusion EvolutioN and Transport (TRIDENT) was developed and benchmarked with experimental data. TRIDENT integrates the effects of the chemical redox potential, tritium mass transfer, tritium diffusion through pipe walls, and selective Cr attack by tritium fluoride. Systems for capturing tritium from the coolant were proposed and simulated with TRIDENT. A large nickel permeation window reduced the tritium release rate from 2410 to 800 Ci/EFPD. A large gas stripping system reduced tritium release rates from 2410 to 439 Ci/EFPD. A packed bed of graphite located between the reactor core and the heat exchanger reduced peak tritium release rates from 2410 to 7.5 Ci/EFPD. Increasing the Li-7 enrichment in flibe from 99.995 to 99.999 wt% reduced both the tritium production rate and the necessary sizes of tritium capture systems by a factor of 4.

An existing TRISO fuel performance model called TIMCOAT was modified for use with PB-FHRs. Low failure rates are predicted for modern uranium oxycarbide (UCO) TRISO fuels in a PB-FHR environment. Post-irradiation examinations of surrogate TRISO particles determined that the outer pyrolytic carbon layer is susceptible to cracking if flibe were to freeze around the particles.

Chemical thermodynamics calculations demonstrated that common constituents of concrete will not be stable in the event they contact liquid flibe. The chemical stability of fission products in reference to the coolant redox potential was determined in the event the TRISO UCO kernel is exposed to flibe during a BDBA. Noble gases (Kr and Xe) will escape the coolant. Cesium, strontium, and iodine are retained in the salt. All other important radionuclides are retained in the kernel or within the coolant system.

Thesis Supervisor: Ronald G. Ballinger

Title: Professor of Nuclear Science and Engineering, and Materials Science and Engineering

THIS PAGE LEFT INTENTIONALLY BLANK

Acknowledgments

This work was made possible by the Department of Energy (DOE) Nuclear Energy University Program (NEUP), which awarded a 3-year Integrated Research Project (IRP) to MIT and its partners at the University of California-Berkeley and the University of Wisconsin-Madison for research and development of the fluoride-salt-cooled high-temperature reactor (FHR).

I am grateful for the guidance and support I received from my advisor Professor Ronald Ballinger (MIT) and my thesis reader Dr. Charles Forsberg (MIT). It was great to experience their genuine interest in not only my work, but also my professional and personal development and well-being. Thank you both very much!

I would like to thank Professor Jacopo Buongiorno (MIT) and Dr. Paul Humrickhouse (INL) for their assistance with the tritium transport calculations that I developed in my model. I would like to acknowledge the research engineers and research scientists (Dr. David Carpenter, Dr. Gordon Kohse, Dr. Michael Ames, and Yakov Ostrovsky) at the MIT Nuclear Reactor Laboratory. Without your work in installing and retrieving the sample capsules from the MIT research reactor, my post-irradiation examinations (PIE) of the TRISO particles would not have been possible. I would also like to thank Dr. John Hunn and Dr. Tyler Gerczak of ORNL for their technical support in establishing a procedure for the TRISO particle PIE. I would also like to thank Dr. Hunn for performing PIE on some of the irradiated TRISO particles from MIT in order to help determine the cause of layer cracking in the irradiated particles.

To my dear wife Amber, thank you for your faithful, undying encouragement, constant prayers, and patience throughout my time at MIT. You have been an unwavering support for me. I am looking forward to the next step in the rest of our lives together. Thank you Mom, Dad, Natalie, and Emily. You all mean the world to me and I have been blessed to have you as my family. Finally, most people who know me know that I profess that Jesus Christ is my Lord and Savior. Only by God's grace and faithfulness have these studies have been completed.

Table of Contents

List of Figures

List of Tables

1 Introduction

Forsberg, *et. al.* have proposed a new type of reactor: one which combines the graphite-matrix, coated-particle fuel developed for gas-cooled reactors with the fluoride salt coolant used in the Molten Salt Reactor Experiment [1]. Originally called the Advanced High-Temperature Reactor (AHTR), this concept is now known as the fluoride salt-cooled high-temperature reactor (FHR). Interest from the U.S. Department of Energy (DOE) has enabled both universities and national laboratories to engage in research and development related to the FHR [2,3]. While the FHR has numerous potential capabilities, configurations, and applications, in order to commercialize it, FHR proponents must make a compelling economic and technical case if it is to become a viable candidate for next-generation power systems. The current commercial case for the FHR is that it enables a nuclear and renewable electric grid and increases revenue by 50% or more compared to base-loaded, light water reactor (LWR) nuclear plants [3,4].

The FHR possesses a number of appealing characteristics including coolant outlet temperatures of at least 700 °C and a number of inherent and engineered passive safety features. Major inherent safety features are due to the design of the coated particle fuel, which is stable to greater than 1600 °C, and the high boiling point of the coolant, which exceeds 1400 °C. These properties would enable the FHR to operate at atmospheric pressure with hundreds of degrees of margin to fuel damage and coolant boiling [5]. Major engineered passive safety features include the use of a pool-type vessel and a natural circulation decay heat removal system passively activated by a fluidic diode. By virtue of its high outlet temperature, the FHR can couple to an open-air Brayton combined-cycle, provide high quality steam, and enable efficient hydrogen production.

1.1 Thesis Motivation

No FHR has ever been built, and uncertainties will need to be addressed before either a test or commercial reactor can be built. The Molten Salt Reactor Experiment (MSRE) operated at Oak Ridge National Laboratory (ORNL) in the 1960s using uranium fuel dissolved in the $LiF\text{-}BeF_2$ coolant [6]. The issue of tritium production in this coolant was only realized at the end of the MSRE program. Tritium production rates, tritium release rates, and tritium distribution throughout an FHR are currently unknown. Corrosion rates are uncertain because they are sensitive to the presence of impurities within the coolant [7]. The accident response of FHRs is unclear. One reason for this uncertainty is that the FHR is the first reactor to use a TRISO coated particle fuel with a fluoride salt coolant. Another uncertainty is the response of concrete and pipe insulation in the event of a coolant leak. Finally, TRISO fuels have been used in gas-cooled reactors, but the FHR temperature range, power density, and fuel pebble characteristics are different from the existing experience base. Thus fuel performance in an FHR is also of interest.

In order to address these uncertainties, a model integrating tritium transport, coolant chemistry, and corrosion was developed and benchmarked. An existing TRISO fuel performance model was adapted for use with the FHR in order to simulate TRISO fuel behavior and predict failure rates. During a beyond design basis accident (BDBA), fuel may be damaged and coolant leaks may occur. The chemical stability of fission products in the TRISO fuel/flibe system was analyzed. A chemical thermodynamic analysis was performed in order to determine the chemical stability of common concrete and insulation constituents in the event they are exposed to flibe. Under normal circumstances, TRISO particles should never come into contact with salt because they are embedded in fuel pebbles. If severe fuel damage were to occur during a BDBA, salt-TRISO contact might occur. Post-irradiation examination (PIE) was performed for TRISO particles after irradiation in flibe in order to characterize their behavior. The results of this work help build a technical basis for constructing and operating an FHR.

This chapter will provide important background for FHR technology. Section 1.2 will introduce the FHR and its major systems. Section 1.3 will introduce the baseline fuel form selected for the FHR. A brief history of molten salt reactors is given in Section 1.4 in order to describe the various factors which shaped the early molten-salt reactor concepts and continue to influence modern FHR design. Section 1.5 will enumerate the desirable properties of a fluoride salt coolant.

1.2 FHR Systems-Level Overview

This thesis addresses FHR fuel, coolant chemistry, tritium transport, and materials compatibility issues. These topics span many of the FHR systems, and different options may exist within each system. For example, there are several fuel options: pebble fuel, pin-type fuel, prismatic block fuel, etc. In this section (Section 1.2), the baseline options selected for the commercial FHR design will be discussed. The option space for fuels, coolants, and materials selection will be discussed in later sections.

1.2.1 Reactor Core

In September 2014, UC-Berkeley reported on their initial commercial FHR design, the Mark 1 Pebble-Bed FHR, known as the Mk1 PB-FHR [8]. There are a number of potential core configurations and fuel types that might be compatible with an FHR, but the Mk1 PB-FHR utilizes a pebble bed core with online refueling. The fuel pebbles consist of sub-millimeter-scale tristructural-isotropic (TRISO) coated particle fuel embedded in the graphite matrix of the pebble. In this application, the baseline fuel pebble is 3 cm in diameter. The Mk1 PB-FHR design specifies low-enriched uranium at 19.90 wt. % U-235. A more detailed introduction to TRISO fuel is provided in Section 1.3. As depicted in Figure 1.1, the reactor core is an annular core featuring a fixed, graphite central reflector and a fixed, outer graphite reflector. Since fuel pebbles are buoyant in the coolant,

the pebbles are inserted at the bottom of the core and removed from the top of the core. A group of un-fueled graphite "blanket" pebbles are located between the fuel pebbles and the outer graphite reflector in order to reduce neutron dose to the reflector graphite, metal downcomer, and metal reactor vessel.

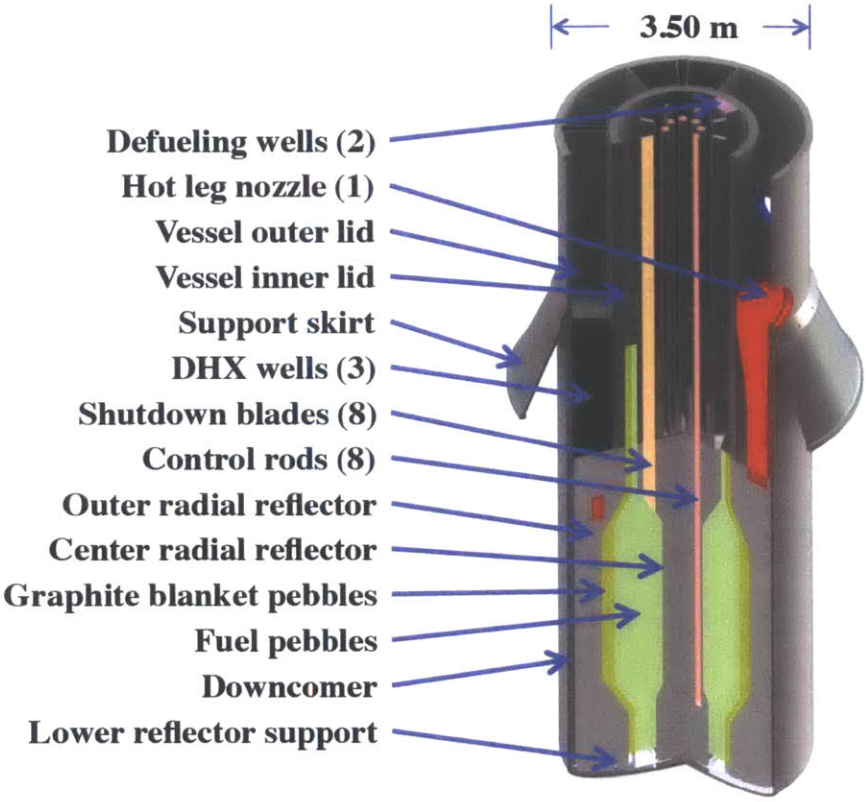

Figure 1.1: Mk1 PB-FHR reactor vessel. From [8].

1.2.2 Power Cycle

As depicted in Figure 1.2, the Mk1 PB-FHR will operate with a nuclear air-Brayton combined cycle (NACC). This power cycle couples the nuclear reactor to a gas-turbine and a heat recovery steam generator. The reactor heats a fluoride salt coolant from an inlet temperature of 600 °C to an outlet temperature of 700 °C. Ambient air is drawn through a filter and into the compressor side of the gas turbine. The compression step alone raises the air temperature to greater than 400 °C [8]. This is one reason why only high-temperature reactors can effectively couple to Brayton power cycles: the nuclear heat added to the working fluid in the Brayton cycle must be at a temperature greater than that of the fluid at the compressor outlet. Two coiled-tube air heaters (CTAH) transfer heat from the reactor coolant to the air. The heated air turns the turbines to produce electricity. The air exiting the turbine can then proceed to a steam Rankine cycle in order to produce additional electricity and increase overall plant efficiency.

One unique feature of the FHR is the ability to inject natural gas to the air stream just prior to the low pressure stage of the turbine. This further increases electricity output which can be used to

provide peak-power during times of high grid demand, or for purposes of stabilizing the electrical grid [3]. Ongoing studies have shown that, utilizing natural gas co-firing, the FHR can boost its revenue by greater than 40 % over simple baseload operations [9]. A commercial FHR may have three or more operating modes in which it provides steam, dry air, electricity, or some combination of the three depending on which product can be sold for the greatest profit at any given point in time [4,9,10].

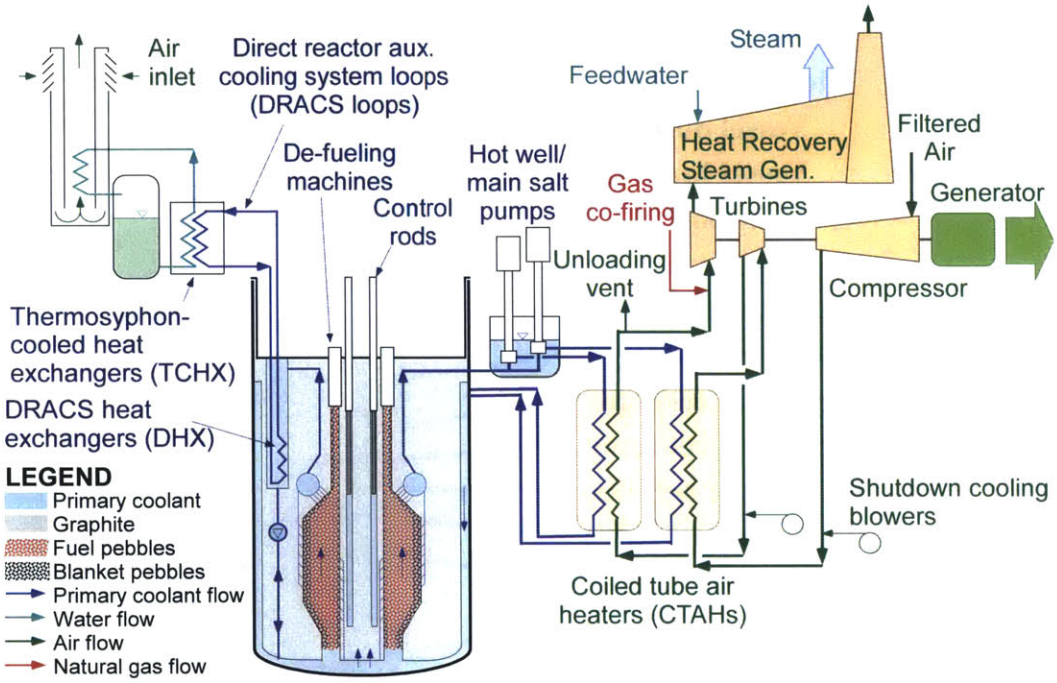

Figure 1.2: FHR systems and flow schematic. From [8].

1.2.3 Core Cooling Systems

All reactors must effectively remove decay heat upon shut down. If decay heat is not removed, temperatures in the system will rise and may damage reactor structures and/or the fuel. If fuel failure occurs, radionuclides may be released. As shown in Eq (1.1), the total reactor fission product decay power (P) can be related to the reactor operating thermal power (P_o) prior to shutdown, the time after shutdown (t_s in units of seconds), and the time of reactor operation (τ_s in units of seconds) [11]. If the time after shutdown is much smaller than the operating time ($t_s << \tau_s$), then Eq (1.1) can be simplified to Eq (1.2). Using Eq (1.2), Figure 1.3 shows the percentage of reactor decay power (100 x P/P_o) as a function of time after shutdown. After 1 second, decay power has dropped to about 6.5%, and after 1 day, decay power has dropped to about 0.7%. While 0.7% may seem small, it represents 1.4 MWt for a reactor which was initially operating at 200 MWt.

$$P = 0.066 \times P_o \times \left[t_s^{-0.2} - (t_s + \tau_s)^{-0.2} \right] \quad (1.1)$$

$$P \cong 0.066 \times P_o \times t_s^{-0.2} \tag{1.2}$$

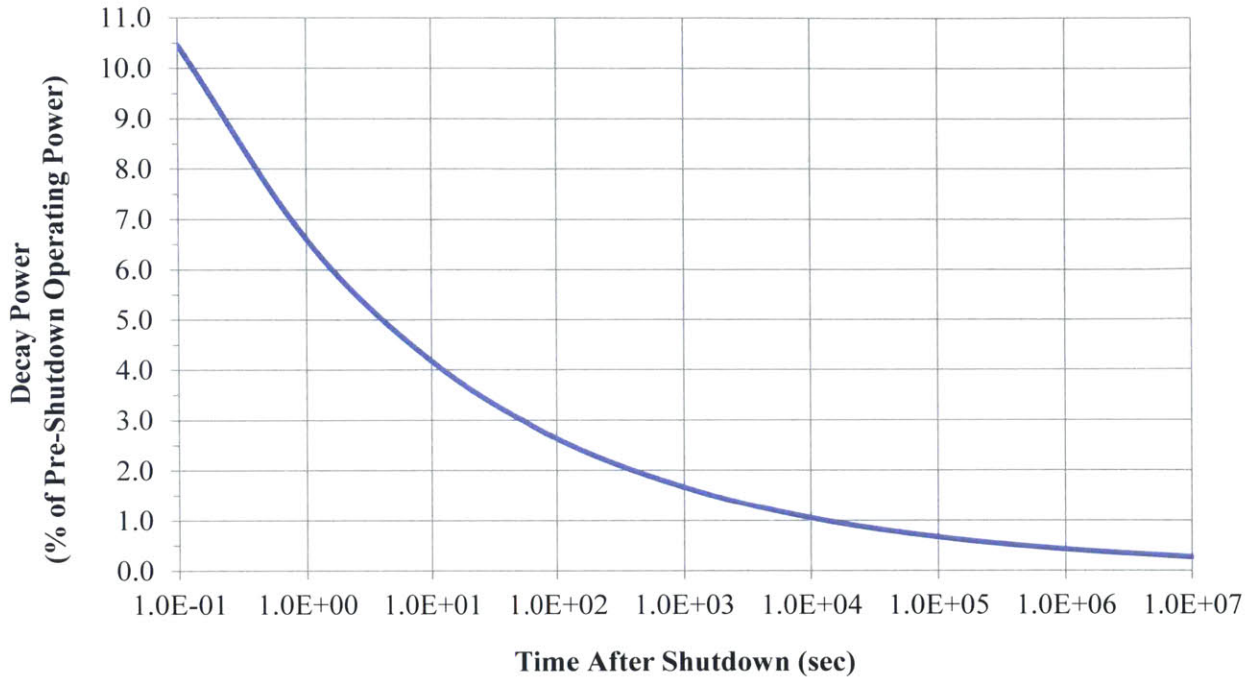

Figure 1.3: Percentage decay power versus time after shutdown. Calculated with Eq (1.2).

As depicted in Figure 1.2, when the coolant pumps are running, salt flows from the bottom of the reactor to the top. During normal shutdowns, one or both main coolant pumps will operate at reduced speed, and air will circulate through one or both CTAHs in such a fashion as to maintain cold leg temperatures at 600 °C [8]. The FHR will use several passive, engineered systems for rejecting heat during both design basis accidents, and beyond-design-basis accidents. Additionally, the FHR takes advantage of inherent properties of the fuel, coolant, and construction materials in order to ensure adequate margins to fuel failure temperatures.

If forced convection is lost, the direct reactor auxiliary coolant system (DRACS) activates automatically and operates passively via natural circulation in order to remove decay heat [8]. This is made possible by use of a fluidic diode which has no moving parts and which has high resistance to liquid flow in the upward direction with low resistance to fluid flow in the downward direction. During a loss of forced circulation (LOFC), *i.e.* the primary pumps fail or are shut down, hot lower-density coolant leaves the top of the reactor core, flows down through DRACS, is cooled in the DRACS heat exchanger (DHX), and circulates back to the bottom of the reactor core. As the DRACS fluid is heated by reactor coolant in the DHX, it becomes less dense and flows upward to the thermosiphon-cooled heat exchangers (TCHX). Water in the TCHX loop flows to an air-cooled heat exchanger where heat is rejected via a combination condenser/chimney. This system is able to provide passive long-term cooling of the reactor core.

In a beyond-design-basis-accident (BDBA) where all coolant heat rejection has been lost (i.e. neither the coolant pumps nor the DRACS are working) the FHR uses a BDBA decay heat removal system which transfers heat from the reactor core into the silo housing the core where heat can then escape to the environment [12]. The BDBA system is activated only at the higher temperatures characteristic of a BDBA. A frozen BDBA salt is incorporated between the reactor vessel and the silo surrounding the reactor vessel. In the event of a BDBA, the increase in vessel temperature melts the frozen salt and thermally couples the reactor vessel to the silo wall. Heat can be transferred to the environment via conduction and radiation to the ground. This is possible due to the large temperature difference between the reactor coolant (> 700 °C) and the environment (~20 °C). Additionally, any salt that contacts colder parts of the system may freeze due to its high freezing point of ~350 °C. By allowing the BDBA salt to freeze, it will plug any cracks or holes that may have developed in the silo wall during the accident.

1.3 FHR Fuel

FHR fuel will be the tristructural-isotropic (TRISO) coated particle fuel originally developed for high-temperature gas-cooled reactors (HTGRs) [5]. This fuel has been proven to retain fission products at temperatures in excess of 1600 °C [13]. Additionally, TRISO fuels have a high degree of proliferation resistance. Due to the high volume fraction of refractory materials (silicon carbide and graphite) used in TRISO fuel construction, it is very difficult to separate fissile material from the fuel [14].

1.3.1 TRISO Coated Particle Fuel

Coated particle fuel has been under development since the 1960s in countries including the United States, Germany, Japan, the United Kingdom, China, and South Africa [13]. In the earlier stages of development, both bistructural isotropic (BISO) and TRISO constructions were being evaluated, but the two-layer BISO designs have ultimately been abandoned in favor of the three-layer TRISO designs which demonstrate better fission product retention [13,14]. As depicted in Figure 1.4, TRISO fuel consists of multiple layers: the outer pyrolytic carbon layer (OPyC), the silicon carbide layer (SiC), the inner pyrolytic carbon layer (IPyC), the graphite buffer layer, and the central fuel kernel. Each layer serves a specific purpose, and depending on the design (fuel enrichment, kernel stoichiometry, etc.), the dimensions of these layers may vary.

In the center of a TRISO particle is the fuel kernel. Historically, kernels have been made of UO_2 (uranium-dioxide), UCO (uranium oxycarbide), a mixed-oxide of fissile/fertile U/ThO_2, or a carbide-oxide mixture of UCO/ThO_2 [13]. The FHR will use the UCO fuel being qualified in the AGR program [8]. It has been shown that UCO fuel reduces the oxygen chemical potential in the kernel and prevents kernel thermal migration (the "amoeba effect") [15]. A typical UCO kernel has a density greater than 10.4 g/cm^3. The buffer is a porous graphite layer which surrounds the fuel

kernel. The buffer is intended to contain fission recoils, allow for the volumetric swelling of the kernel, and provide porosity which can contain fission gases. Typically, the buffer density is about 1.10 g/cm^3. The IPyC layer is a dense (1.90 g/cm^3) pyrolytic carbon layer which protects the kernel from reactive chemicals used during the chemical vapor deposition (CVD) of the SiC layer. The SiC layer is the primary structural layer in the TRISO particle. It acts as a pressure vessel, providing hermeticity and serving as the primary barrier to fission product migration. The OPyC layer is another dense pyrolytic carbon layer which protects the underlying layers during fuel compacting.

Table 1.1 lists TRISO fuel dimensions for two types of TRISO particles. The EU 2309 TRISO particle was fabricated between 1981 and 1990 in Germany, and the AGR-1 particle was irradiated from late 2006 through late 2009 in the first of eight irradiations as part of the advanced gas reactor (AGR) fuel development and qualification program at the Idaho National Laboratory (INL).

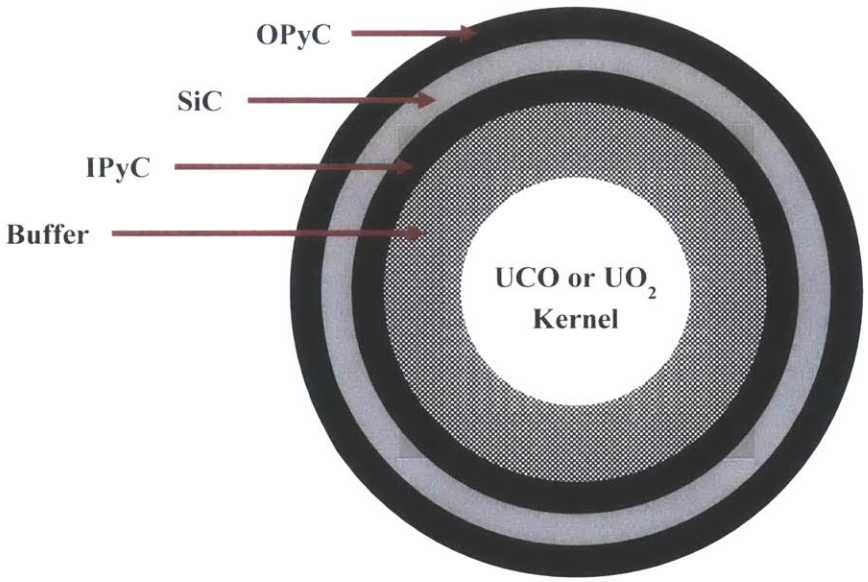

Figure 1.4: Generalized TRISO fuel schematic.

Table 1.1: Selected TRISO particle dimensions.

	EUO 2309 from ref [13]	AGR-1 Baseline from ref [16]
Kernel Type	UO_2	$UC_{0.5}O_{1.5}$
Kernel Diameter (μm)	497	350
Buffer Thickness (μm)	93	104
IPyC Thickness (μm)	37	39
SiC Thickness (μm)	51	36
OPyC Thickness (μm)	38	41
Particle Overall Diameter (μm)	922	800

1.3.2 TRISO Manufacturing

A brief overview of TRISO production will be given below. A detailed review of TRISO fuel fabrication is available from both Sawa and Wang [17,18]. TRISO fuel manufacture begins with the fabrication of the kernel using either external or internal gelation sol-gel techniques. In external gelation, U_3O_8 powder is processed with aqueous nitric acid (HNO_3) in order to yield an aqueous solution of $UO_2(NO_3)_2$. After adding polyvinyl-alcohol or tetra-hydro-furfuryl alcohol, this nitric acid solution is then treated with ammonium hydroxide (NH_4OH) in order to form drops of a gel-like precipitate called ammonium di-uranate (ADU) which has a generalized stoichiometry of $(NH_4)_2U_2O_7$. In progressively higher temperature processes, the particles are then aged, washed, dried (200 °C), and calcined (800 °C) [17,19,20]. In order to produce UO_2 kernels, ADU particles are sintered in hydrogen gas (1600 °C) after calcining. In order to produce UCO kernels, carbon is added to the nitric acid solution prior to particle gelation, and the sintering process is carried out under $CO_{(g)}$ in order to achieve the desired C/O stoichiometry [17].

Once the kernel has been fabricated, the buffer, IPyC, SiC, and OPyC layers can be progressively deposited on the surface of the kernel using a fluidized-bed chemical vapor deposition process [17,20]. The coating processes are summarized below in Figure 1.5. The porous carbon buffer layer is deposited from the decomposition of ethene. The high-density pyrocarbon IPyC layer is deposited from a mixture of ethene and propene. The SiC layer is deposited from the decomposition of methyl-trichloro-silane (MTS), CH_3SiCl_3. The OPyC layer is deposited in the same fashion as the IPyC layer. By varying the temperatures, reactant gas flow rates, and reactant gas compositions, the physical properties of the coating can be altered.

Once the coating has been completed, thousands of TRISO particles are then incorporated into a larger graphite matrix. Two common graphite matrix geometries are spheres (for pebble bed reactors) or right-circular cylinders (for prismatic block reactors). (See Section 1.3.3 for a discussion of possible fuel forms for TRISO particles). A powder of matrix graphite is prepared by blending a binder with graphite powder. The TRISO particles are then overcoated with this mixture. The matrix-overcoated particles are then pressed into spheres or cylindrical compacts by pressing in a die at elevated temperature. In order to minimize the chance of damaging the TRISO particles during the pressing/compacting step, the particle packing fraction in the matrix graphite, the temperature, and the applied force must be carefully controlled. The newly-formed spheres or compacts are then carbonized at 800 °C in a nitrogen atmosphere in order to remove volatile impurities from the binder [17,20]. After carbonization, the sphere or cylinder is sintered at 1800 °C in a vacuum.

With the implementation of the AGR TRISO fuel development and qualification program at INL, pilot-scale production facilities have been constructed at Babcock & Wilcox, and production-scale facilities have been constructed at General Atomics [20].

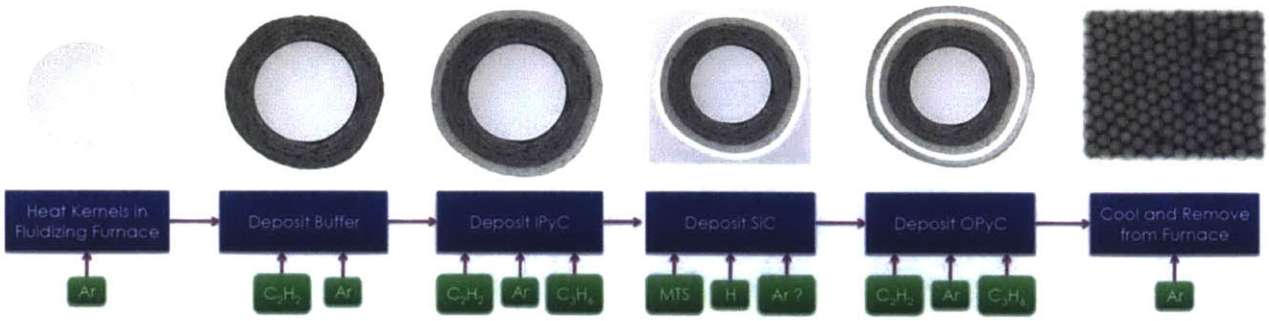

Figure 1.5: TRISO coating deposition processes. From [20].

1.3.3 Fuel Geometry

There are several possible fuel geometries for arranging TRISO particles in a reactor. One option, as mentioned above, is to embed TRISO particles in a spherical graphite matrix in order to make a fuel pebble such as that in Figure 1.6. Typical gas-cooled pebble-bed reactor designs utilize a pebble that is 6 cm in diameter [21]. In comparison, the baseline geometry for the Mk1-PB-FHR is a fuel pebble of 3 cm diameter with a central graphite annulus as depicted in Figure 1.7. This annular fuel reduces peak fuel temperatures for a given power density. A major advantage to the use of pebble fuel is the ability to refuel the reactor online.

Compacts are another common fuel form for TRISO-based fuels. Compacts consist of a right circular-cylindrical graphite matrix into which TRISO particles are embedded. A typical compact is about 2.5 cm long and 1.25 cm in diameter [13]. There are two options for fuel compact arrangements. Compacts can be loaded into a long stack with a central spine (as in the original American Peach Bottom reactor application) or they can be loaded into fuel holes in a prismatic block of graphite (as in the Japanese HTTR reactor) [14]. Figure 1.8 shows the relative size of TRISO particles, compacts, and a graphite prismatic block fuel element. Since fuel compacts are generally smaller than fuel pebbles, many TRISO fuel irradiations use fuel compacts.

A third type of TRISO fuel geometry is the plate-type fuel element which has been proposed by Oak Ridge National Laboratory (ORNL) for use in FHRs [22]. Figure 1.9 shows one possible configuration of a plate-type fuel element. TRISO particles are housed in a plate-shaped graphite matrix. Several of these plates are aligned parallel to one another and at an angle to other sets of plates in the same hexagonal-shaped elements. Plate-type fuel has never been constructed or demonstrated.

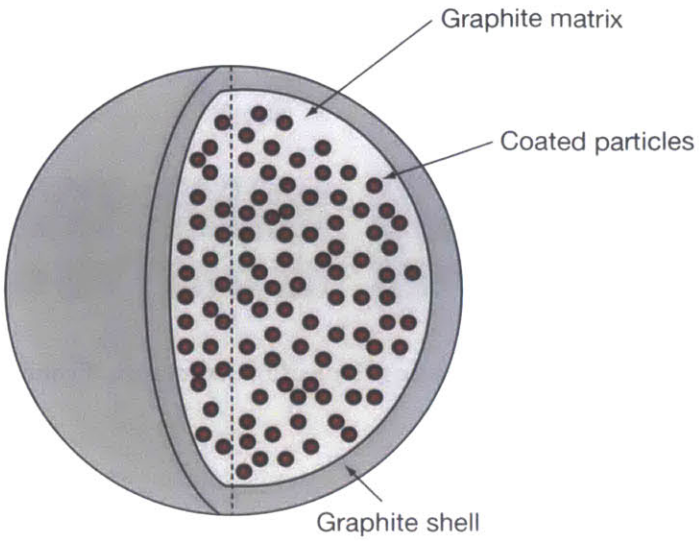

Figure 1.6: Schematic of fuel pebble with graphite matrix and TRISO coated particles. From [17].

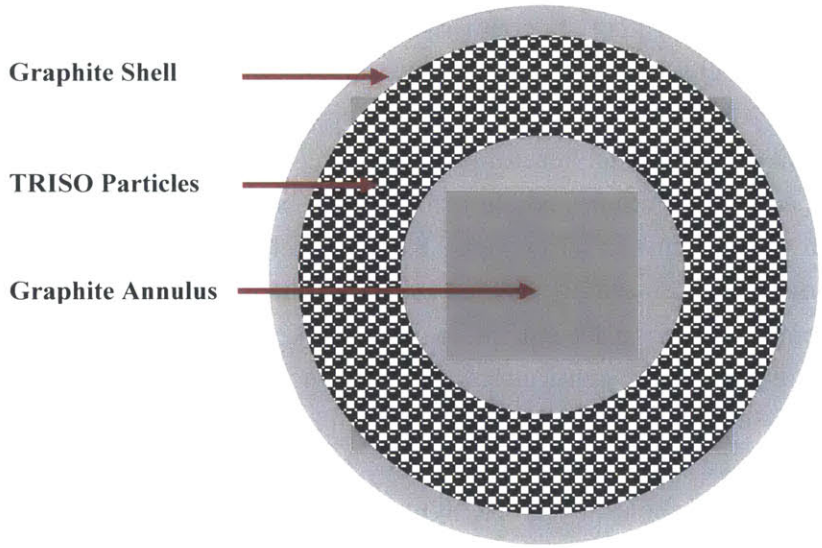

Figure 1.7: Schematic of annular fuel pebble for Mk1-PB-FHR.

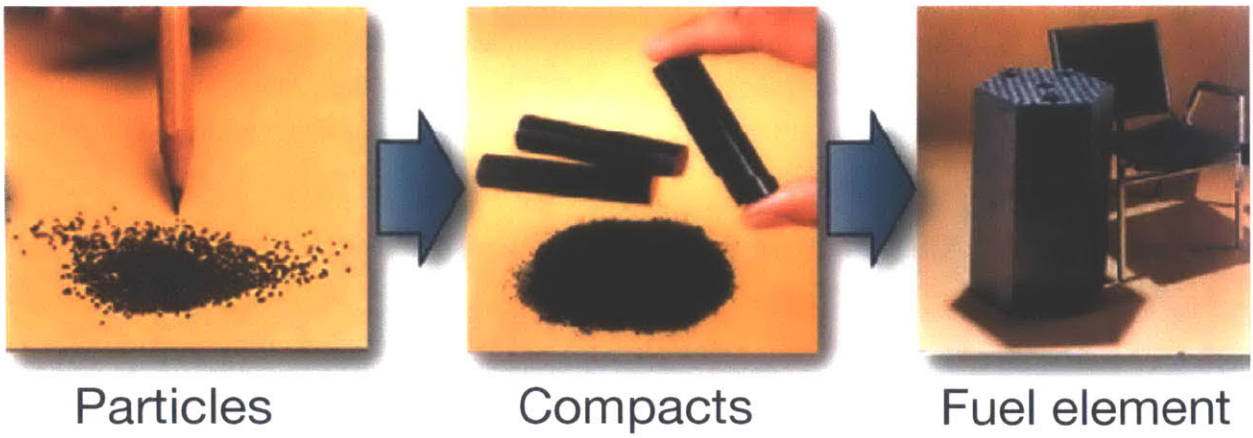

Figure 1.8: Fuel compacts are composed of TRISO particles. Compacts may be used in graphite prismatic-type fuel elements. From [13].

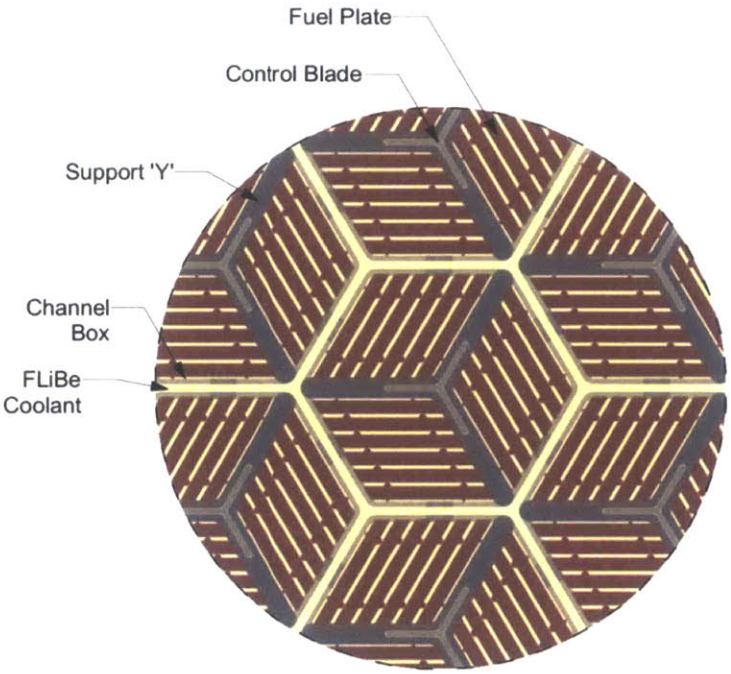

Figure 1.9: Plate-type fuel element proposed by ORNL for use with FHRs. From [22].

1.4 A Brief History of Molten Salt Reactors

The original molten salt reactor (MSR) was a reactor in which the fuel was dissolved in the coolant and circulated throughout the reactor primary circuit. With the advent of the FHR, came the need to distinguish a reactor with solid fuel and a molten salt coolant (such as the FHR) from a reactor with fuel dissolved in the molten salt coolant (an MSR). More recently the term "molten salt reactor" has been used to refer to a reactor in which the fuel is dissolved in a molten salt. The term "molten salt-cooled reactor" is used to refer to a reactor with solid fuel which is cooled by a molten

salt. To date, most of the experience with molten salts in nuclear reactors is derived from the Molten Salt Reactor Experiment (MSRE) at Oak Ridge National Laboratory in the 1960s. This work is well documented (in the ORNL-XXX and ORNL-TM-XXX series of reports) and is an important resource for FHR development [23,24].

1.4.1 The Aircraft Nuclear Propulsion Project and the Birth of the Molten Salt Reactor

World War II saw nuclear power demonstrated in its most fearsome application, the atomic bomb. Immediately after the war, the U.S. military explored additional uses for nuclear power and civilian uses for nuclear power were in their nascent stages. In an age before nuclear-powered submarines and intercontinental ballistic missiles (ICBMs), the U.S. Air Force sought long-range, supersonic and/or high-subsonic bombers. In 1946, the U.S. Army Air Force (the predecessor to the U.S. Air Force) initiated a series of feasibility studies in the Nuclear Energy for Propulsion of Aircraft (NEPA) program [25,26]. Initial aircraft reactor designs focused on the use of solid fuel and directly or indirectly heating air for use in a jet turbine [25]. In late 1949, about one year before the NEPA phase of the nuclear aircraft project ended, Oak Ridge National Laboratory (ORNL) was directed by the U.S. Atomic Energy Commission (AEC) to develop the indirect air heating cycle in the new Aircraft Nuclear Propulsion (ANP) project [25,26]. NEPA officially ended in January of 1951 and the focus was placed on hardware development through the ANP. In the spring of 1951, General Electric (GE) replaced the Fairchild Engine and Airplane Corporation in the development of the direct-air heating cycle option for the ANP. Thus, both the direct and indirect heating of air were studied in parallel.

In order to power an aircraft, air drawn in through a compressor would be heated either by passing directly through the reactor core or via a heat exchanger in which liquid sodium transferred nuclear heat to the air. Once heated, the air would pass through the turbine and produce thrust. Three direct-air systems called the Heat Transfer Reactor Experiment (HTRE) were constructed by GE and tested in Idaho. Figure 1.10 shows a schematic for the HTRE-1 GE direct-air heating cycle which operated a J-47 turbojet at powers up to 18.5 MWt for greater than 100 hours and U-Cr-UO_2 fuel temperatures up to 1010 °C [27]. Notice that the HTRE-1 incorporates a fuel burner section capable of burning jet fuel with or without the addition of nuclear heat. This same feature appears in the FHR power cycle in Figure 1.2.

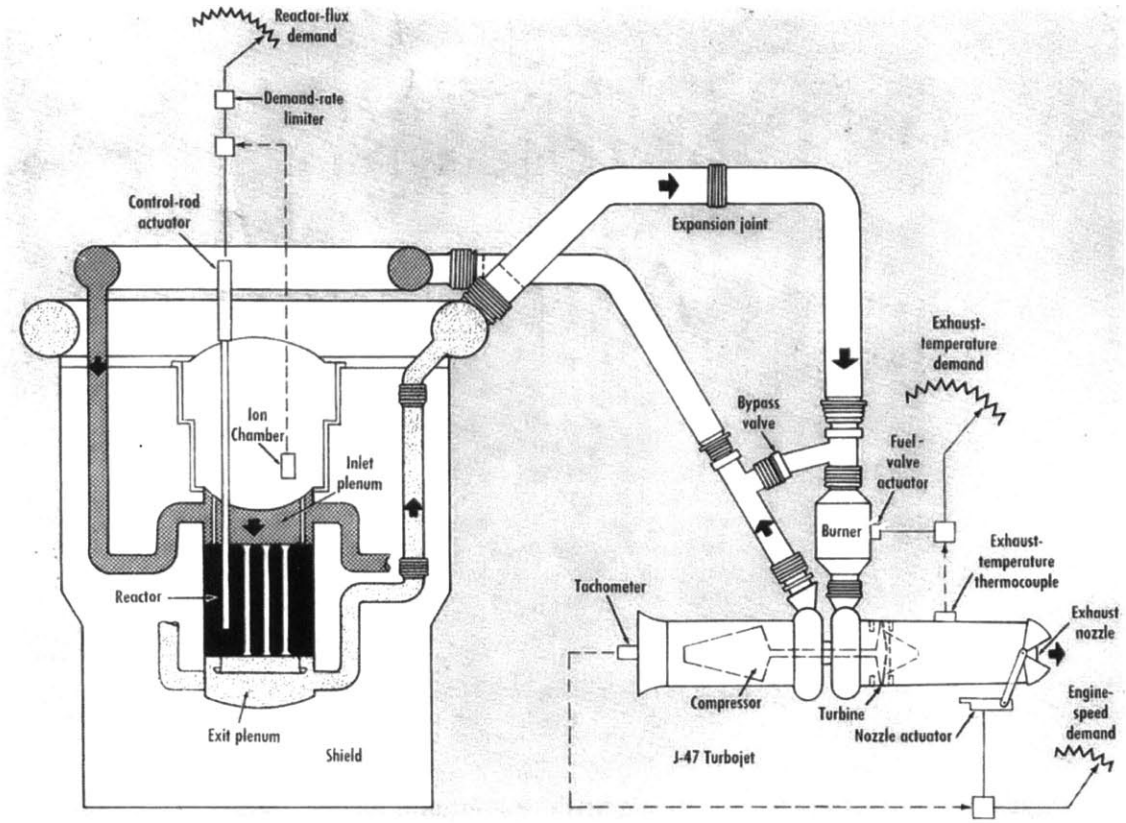

Figure 1.10: Schematic for aircraft nuclear propulsion system HTRE-1. From [27].

The branch of the ANP project at ORNL was referred to internally as the Aircraft Reactor Experiment (ARE), and the initial ARE design differed substantially from the design which was ultimately constructed and operated [28]. At the outset of the ARE, ORNL pursued a thermal spectrum reactor using solid fuel and a liquid sodium coolant. The fuel was to be UO_2 in a stainless steel cladding, and hexagonal blocks of BeO (see Figure 1.11) were to function as the moderator. The design was changed after calculations showed that a significant xenon instability due to fission product Xe-135 (a potent neutron poison) could exist at the ARE temperature and power levels, thus causing a positive temperature coefficient of reactivity [25,28].

In order to circumvent this problem, the ARE switched to the use of a liquid fuel. The initial concept called for replacing the solid fuel in the BeO moderator with a stagnant molten fluoride salt containing dissolved uranium [28]. The logic behind this is that a rise in temperature would decrease the density of the fuel-salt, causing volumetric expansion which would force some of the salt out of the moderator region, thus reducing reactor power with an increase in temperature. The design was changed yet again when it was determined that the radial temperature profile in the stagnant, fuel-salt was so high that the margin to the salt boiling point was not sufficient. In order to maintain suitable fuel-salt temperatures while achieving the desired power output, a design which used a circulating fuel-salt and a fixed, solid moderator was adopted [28]. The molten salt reactor (MSR) was born!

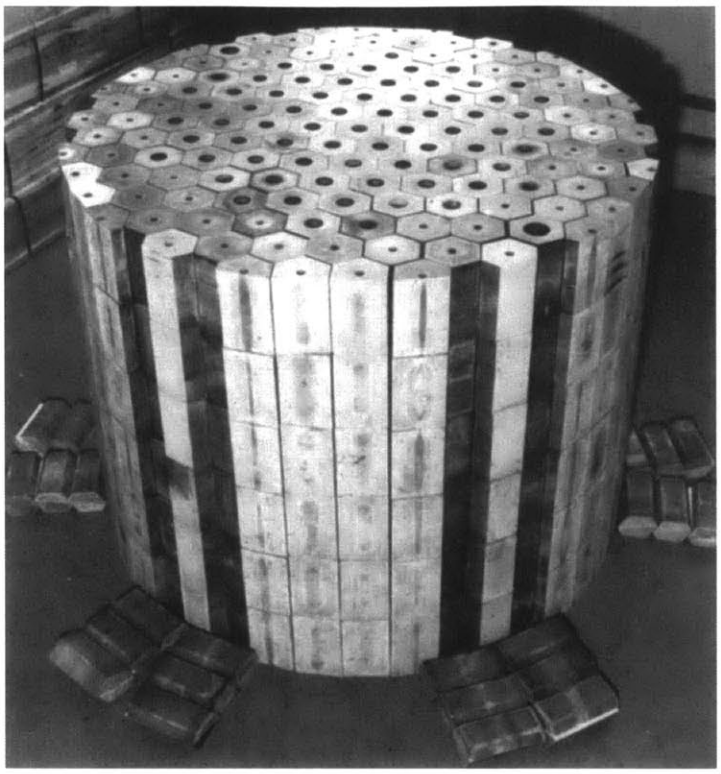

Figure 1.11: BeO moderator blocks with coolant and fuel channels. From [28].

A schematic drawing of the 3 MW molten-salt-fueled ARE that was constructed at ORNL is shown in Figure 1.12. The ARE first went critical on November 3 and was shut down for the last time on November 12, 1954 [29]. The fuel-salt in the ARE was comprised of NaF-ZrF_4-UF_4 in 53, 41, and 6 mole percent, respectively. Due in part to the desire to use the BeO moderator blocks ordered before the design had been completed, the ARE utilized several cooling loops. The fuel-salt was cooled by transferring heat to helium in an intermediate heat exchanger. This helium was then cooled by water. The BeO reflector was cooled by liquid sodium which rejected heat first to a helium loop and then to a water circuit. The final experiment conducted with the ARE was the measurement of xenon in the salt after a 25 hour run at full power which indicated that fission product xenon was not appreciably retained by the salt [29].

Designs for a flyable reactor which could couple to jet turbines proceeded in parallel with the design and construction of the ARE reactor [30]. After the completion of the ARE, focus shifted toward constructing a new, larger (60 MW) reactor that would determine the feasibility and challenges of a circulating-fuel aircraft reactor system [31]. This new phase of the project at ORNL was called the Aircraft Reactor Test (ART). The ART core design is depicted in Figure 1.13 where the NaF-ZrF_4-UF_4 fuel circulates through the core annulus/reflectors and transfers heat to a sodium-potassium (NaK) salt via a heat exchanger integral with the reactor vessel. In the concept pictured in Figure 1.14, the NaK heated by the circulating fuel transfers heat to air after the air passes through the compressor stage of a turbojet engine [30].

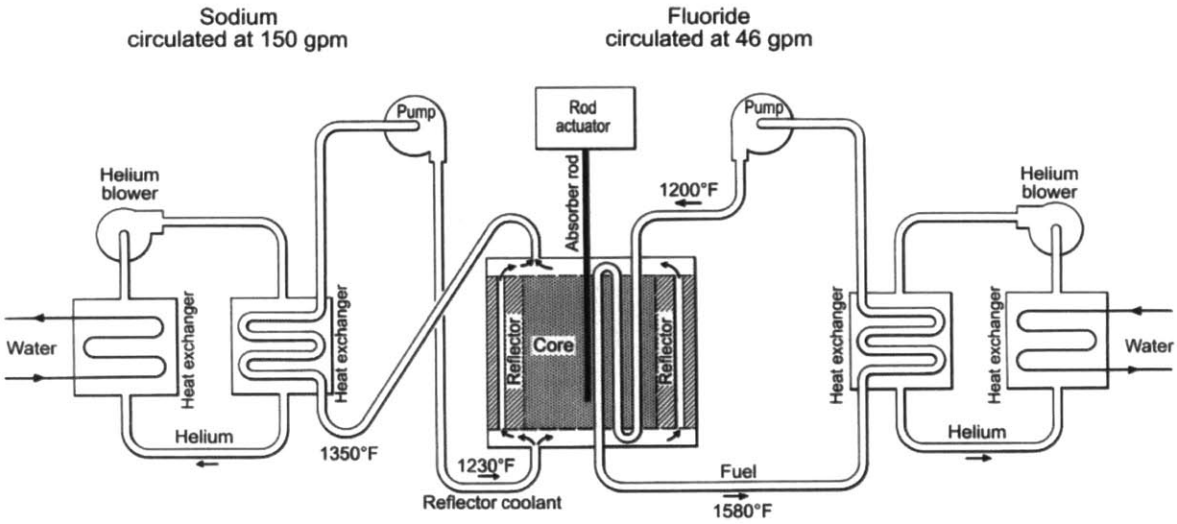

Figure 1.12: Schematic of ARE molten-salt reactor operated at ORNL in 1954. From [28].

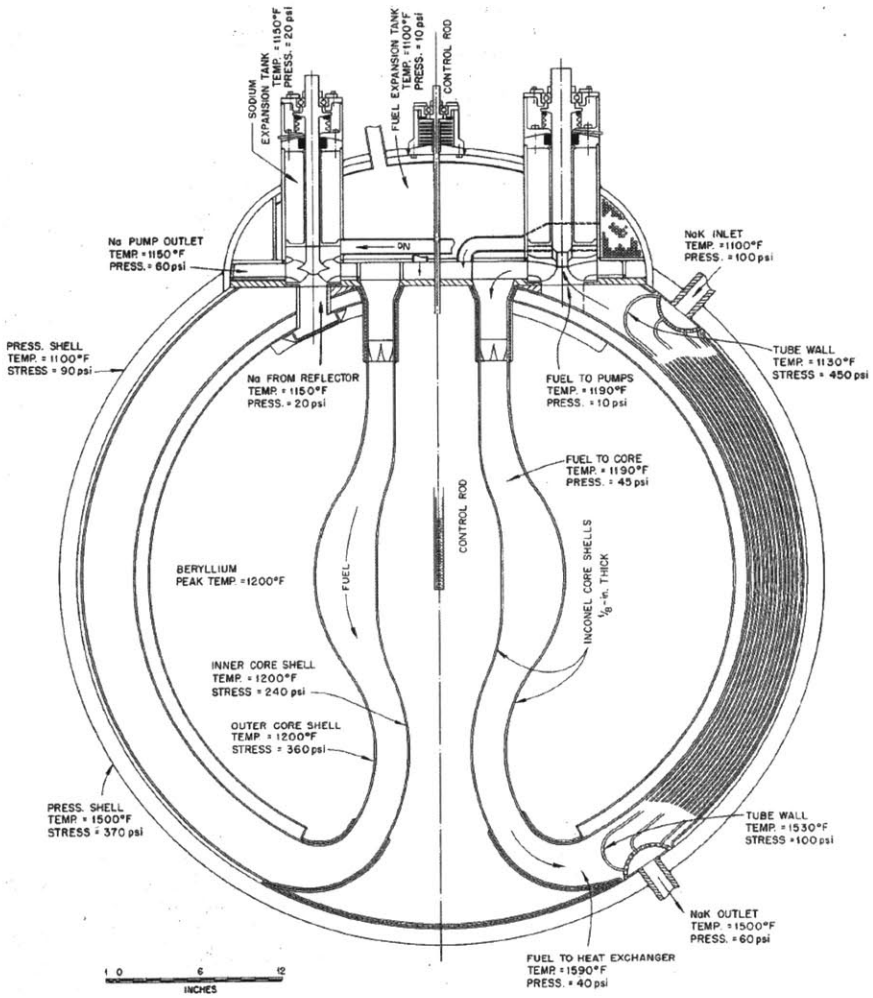

Figure 1.13: Core layout for ART reactor. From [30]. See also [31].

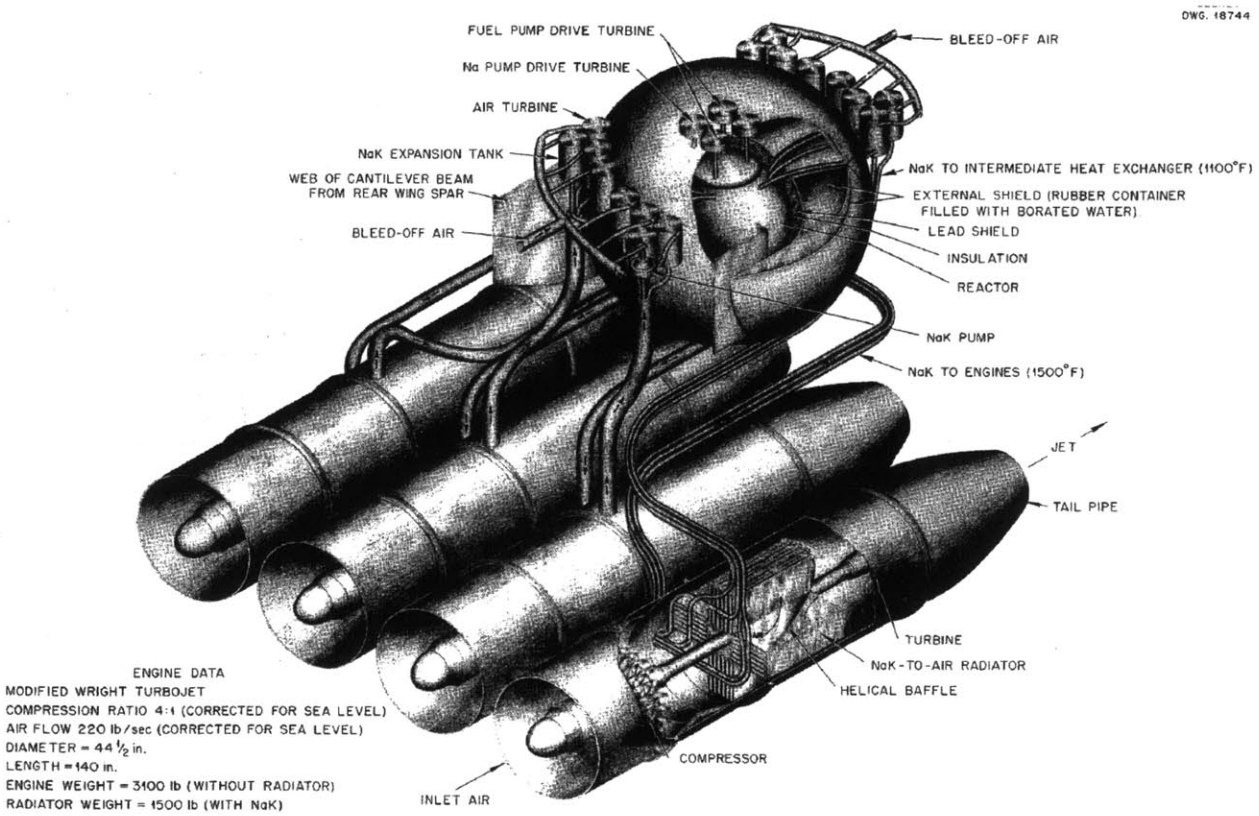

Figure 1.14: Aircraft power plant. Molten salt reactor with NaF-ZrF_4-UF_4 circulating fuel and NaK secondary coolant coupled to jet turbines. From [30].

1.4.2 The Molten Salt Reactor Experiment (MSRE)

During the ANP project, the potential of molten salt reactors to produce power in civilian applications was recognized. In 1956, H.G. MacPherson's group studied both burner (conversion ratio < 1) and breeder (conversion ratio > 1) molten salt reactors because of their promising resource utilization and potentially low electricity costs [32]. A molten salt reactor would be capable of online refueling and continuous processing of fission products and/or bred fuel. Two graphite moderated concepts were identified. In one concept, the fluoride salt contained a mixture of uranium-233 and thorium. The second concept utilized a two-fluid system in which a graphite barrier physically separated the uranium-bearing fuel salt from a fertile blanket comprised of a thorium-bearing fertile salt [25,32]. In 1959, the U.S. AEC compared several of the liquid fuel reactors and concluded that the molten salt reactor had the greatest chance of success [25]. ORNL proposed that a molten salt reactor be constructed in order to study the features that such a reactor must have in order to produce commercial power. In 1960, following approval by the AEC, the Molten Salt Reactor Experiment (MSRE) at ORNL began design of a single-fluid molten salt reactor. The single-fluid design was selected for construction in order to simplify the design and produce conditions similar to those

expected in the fuel-salt of a two-fluid molten salt breeder reactor [32]. MSRE construction began in 1962, and first criticality was achieved in 1965. From June 1965 through March 1968, the MSRE operated on U-235. After this period of operation, the U-235 was removed from the salt via fluorination and volatilization of the UF_6 produced from the fluorination. In October 1968, the MSRE went critical on U-233 produced from thorium in a production reactor, making it the first reactor to use U-233 as a fuel [6,25]. The MSRE was shut down for the last time in December, 1969.

Figure 1.15 shows the MSRE and much of its piping and pumps installed in a pit originally built to house the ARE and ART reactors at ORNL [6,24]. The MSRE was a graphite moderated, molten salt reactor with a design power of 10 MW. The fuel salt was chosen for its good fluid properties, high actinide solubility, chemical compatibility, and low neutron absorption [24]. For operation with 33% enriched U-235, the fuel-salt composition was initially ^7LiF-BeF_2-ZrF_4-UF_4 (65.0-29.1-5.0-0.9 mole %) [6,24]. Figure 1.16 shows the generalized MSRE facility layout. The fuel-salt flowed through the critical geometry of the MSRE core, allowing fission to occur. Figure 1.17 shows the MSRE core and reactor vessel and Figure 1.18 shows the geometry of the MSRE moderator graphite with its integrated fuel channels. After exiting the core, the fuel-salt flowed up to the heat exchanger and fuel pump. One novel feature of MSRs is that at least some fraction of the delayed neutrons (which are an essential part of controlling the nuclear chain reaction) are born outside of the core. By changing the fuel-salt flow rate, the fraction of delayed neutrons born in the core could be altered. In the heat exchanger, the fuel-salt transferred heat to a clean coolant-salt comprised only of ^7LiF-BeF_2 (66.7-33.3 mole %). This coolant-salt then transferred heat to air-cooled radiators for ultimate heat rejection.

The development of several specialized materials and components were critical in the design of the MSRE. First, the moderator graphite was low-permeability grade CGB graphite produced by Union Carbide. Since the moderator graphite was unclad and in direct contact with the fuel-salt, low permeability was a requirement in order to prevent fuel-salt, soluble fission products, and fission product gases from penetrating the graphite and affecting core reactivity [33]. It was reported that CGB graphite was produced from petroleum coke bonded with coal-tar pitch which underwent a series of impregnations and heat treatments at temperatures of 2800 °C minimum [34]. The average density of CGB graphite was 1.86 g/cm^3, accessible porosity was 9.6% and 96% of the accessible porosity had pore entrance diameters smaller than 0.2 μm. With these properties, it was determined that a pressure of 4.1 MPa (600 psi) would be required in order to force the coolant salt (which does not wet the graphite under normal circumstances) into 0.5% of the graphite bulk volume [34].

Next, the core vessel and all of the piping was fabricated from Hastelloy-N (originally called INOR-8, sometimes called Alloy-N). Hastelloy-N is a nickel-base alloy with a basic composition of 72 wt % Ni, 16 wt % Mo, 7 wt % Cr, and 5 wt % Fe. Coolant chemistry, materials compatibility, and corrosion will be discussed in greater detail Chapter 3, but for the purposes of introduction, it can be said that Hastelloy-N showed good corrosion resistance in molten salts with average corrosion rates of less than 25.4 μm (1 mil) per year [6,35]. Some embrittlement of Hastelloy-N was found to

occur due to fission product tellurium. It was found that the addition of roughly 2 wt % niobium to Hastelloy-N helped to prevent this embrittlement [36].

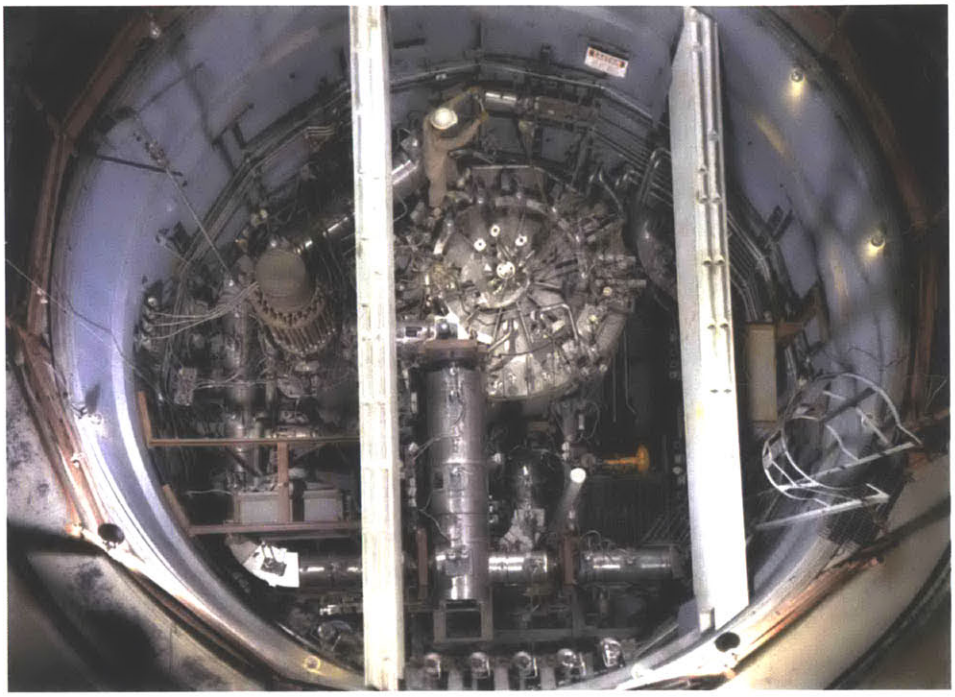

Figure 1.15: MSRE reactor vessel fuel pump and primary heat exchanger. ORNL Photo 67051-64 from [25]. For high-resolution image see [37].

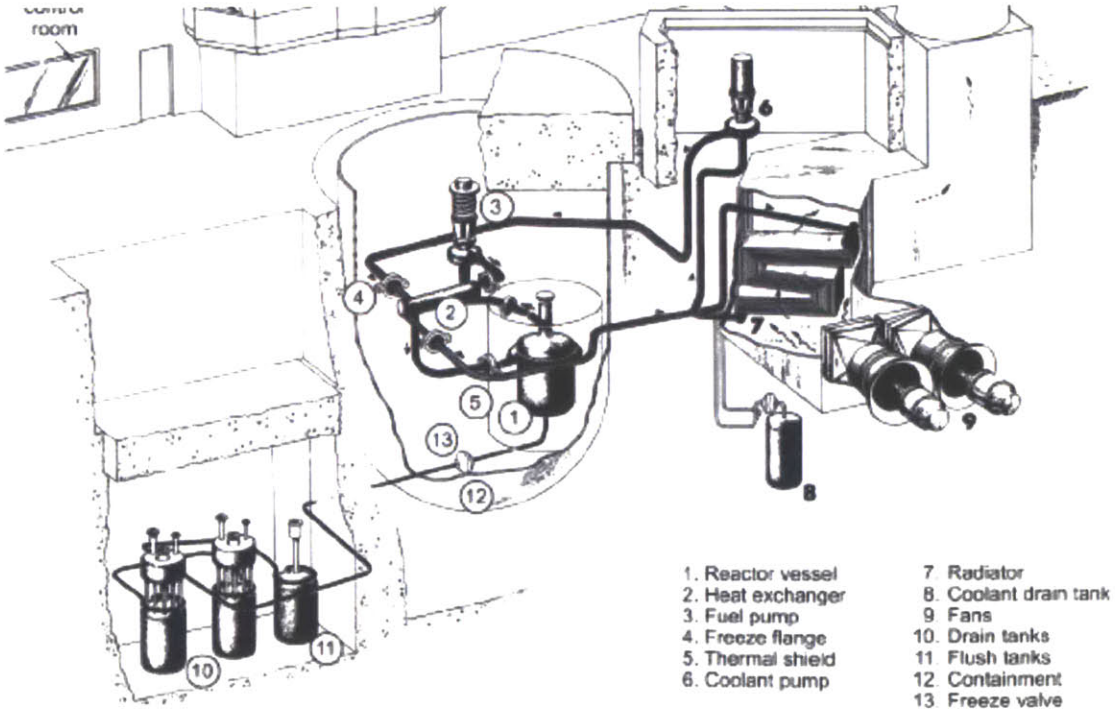

Figure 1.16: MSRE schematic. From [25].

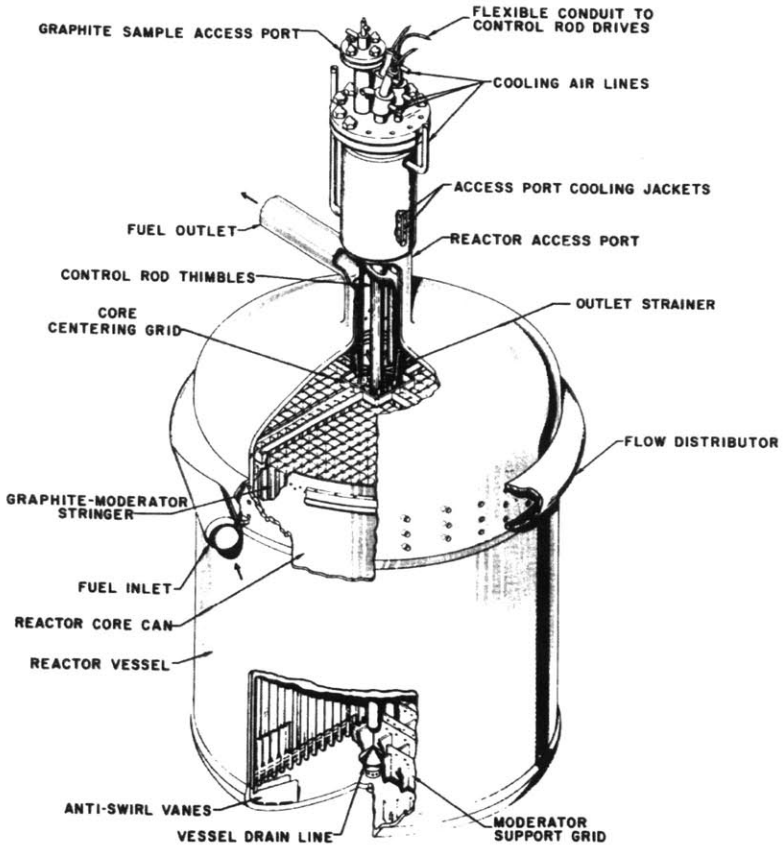

Figure 1.17: MSRE core and reactor vessel. From [6].

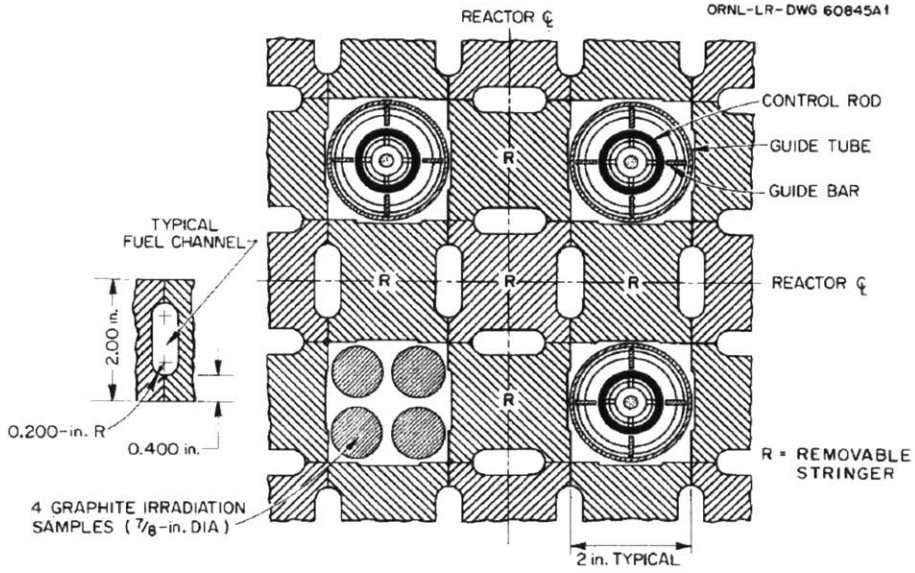

Figure 1.18: Top-down view of MSRE graphite moderator with fuel channels for fuel-salt flow, sample irradiation positions, and control rods. From [38].

The fuel pump was another important development for the MSRE. Figure 1.19 shows the centrifugal, sump-type fuel pump used in the MSRE. Not only did the pump have to reliably circulate the fuel-salt without allowing salt to freeze in its many ports and orifices, it performed several other important functions. Some of the fuel was sprayed into the gas space in the pump bowl so that a helium sparge gas could remove fission product xenon and krypton into an off-gas system [6]. This helium cover gas also helped to prevent air ingress. The chemical potential of the fuel-salt was periodically adjusted via insertion of a Be metal rod in order to help control corrosion [6]. Samples of the salt could be removed via the sampler-enricher, and additional fuel in the form of a eutectic compound of UF_4-LiF could be added to the fuel salt through the sampler-enricher [6].

Other seemingly simple, yet crucial components to the successful operation of the MSRE were valves and flanges. In order to connect piping in the primary system such that the pipes or components could be replaced by remotely operated tools, freeze flanges were used. Freeze flanges consisted of an O-ring joint and a frozen salt seal [24]. No mechanical valves were used in MSRE salt piping. Instead freeze valves were used which were activated by heating or cooling the salt in flattened sections of the piping in order to open or close the flow. One such freeze valve was located between the primary system and the fuel-salt dump tanks as depicted in Figure 1.16.

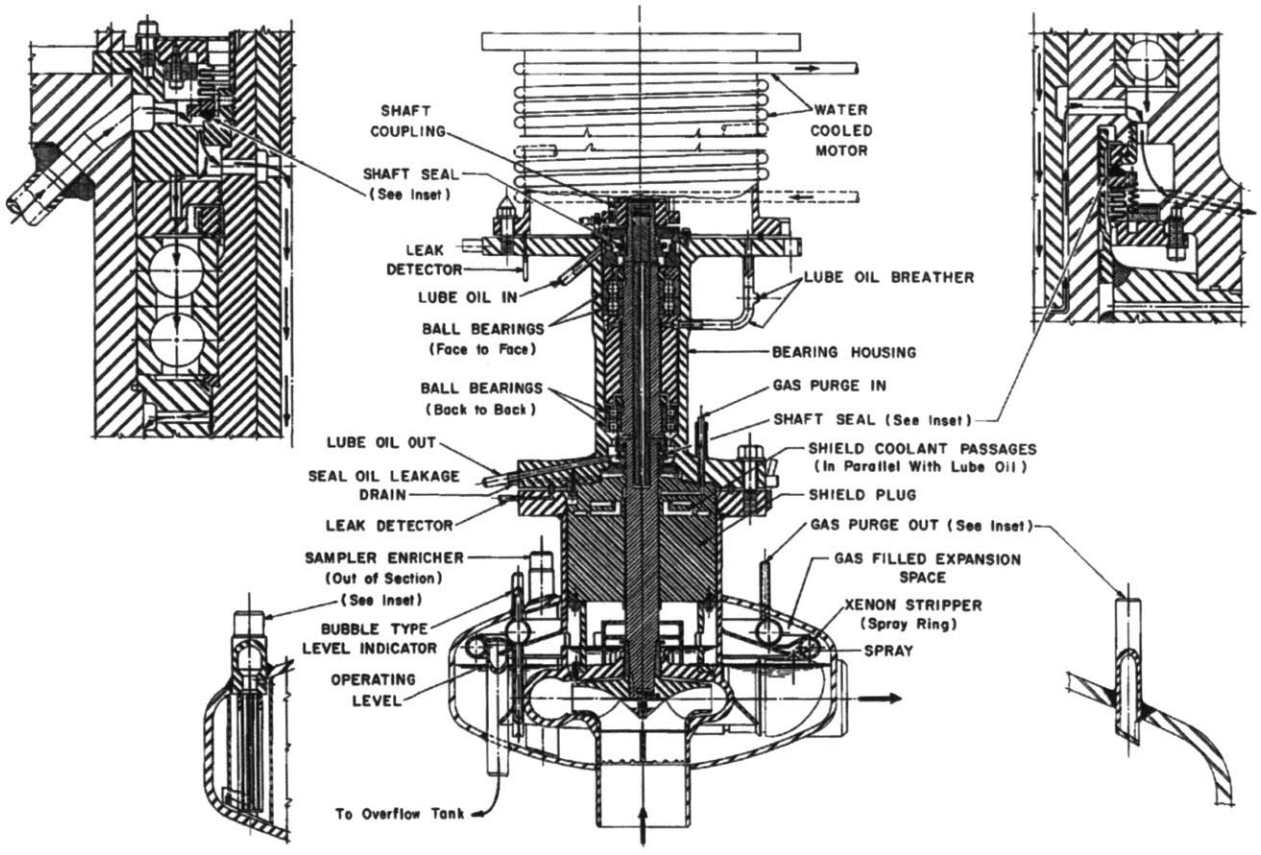

Figure 1.19: MSRE fuel pump. From [24].

1.5 FHR Fluoride-Salt Coolant

The FHR will use a fluoride-salt primary coolant. Prolific research from the MSRE provides a sound basis for selecting "flibe", $^{7}LiF\text{-}BeF_2$ (66.7-33.3 mole %), as the baseline coolant in the FHR. Other fluoride salts may also be attractive for different reasons. This section will enumerate the key criteria for selecting a fluoride salt for use in an FHR or MSR. The reasoning behind selecting flibe will be discussed in light of its thermophysical properties and experimental experience. Alternative candidate salt coolants will also be briefly discussed.

1.5.1 Criteria for selecting a salt coolant

In 1967, Grimes summarized much of the research and development on molten salt coolants and fuel-salts since the early 1950s [39]. The following is a list of criteria for selecting a suitable molten salt. Much of this list is derived from Grimes' discussion. Certain criteria have been grouped according to their applicability to FHRs or MSRs. The FHR uses solid fuel and a clean (un-fueled) fluoride-salt coolant. MSRs (such as the MSRE), on the other hand, utilize a fuel-salt where the primary coolant is a liquid salt in which the fuel is dissolved.

General criteria applicable to both FHRs and MSRs:

- Salt constituents must have low neutron capture cross sections in the neutron energy spectrum of the reactor.
- Salt must have low vapor pressure.
- Salt must possess suitable heat transfer and fluid properties appropriate for a reactor coolant.
- The ideal salt would have a low melting point and a high boiling point in order to enable high core outlet temperatures while allowing operation at atmospheric pressure.
- Salt must be chemically compatible with other system materials used in the piping, moderator, etc.
- The ideal salt should not react violently with air or water.
- Salt must be chemically stable (resistant to radiolysis) in a neutron field.
- The ideal salt should not be expensive or difficult to obtain.

Criteria applicable to MSRs only:

- Salt must have good solubility for fissionable material.
- Salt must be able to accommodate fission products without appreciable degradation of other properties.
- The ability to apply certain chemical processes to the fuel-salt may also apply. For example if the reactor is to be a molten-salt breeder reactor (MSBR), the ability to recover fissile isotopes from the salt may be a requirement.

1.5.2 Flibe as the FHR baseline coolant

Recall from Section 1.4.2 that the fuel-salt from the MSRE was ^{7}LiF-BeF_2-ZrF_4-UF_4 (65.0-29.1-5.0-0.9 mole %). The MSRE used this particular fuel-salt composition because it fulfilled most of the criteria listed in Section 1.5.1. Because the fuel, UF_4, melts at 1035 °C, diluent salts are required in order to attain a salt with a suitably low melting point (< 500 °C). In order to help determine suitable diluent salts, Grimes compiled a list (annotated by Williams, and reproduced in Table 1.2) of elements that might be suitable for use as a fuel salt. In Table 1.2, all salts listed as "OK" in bold-type form fluoride salts and are ranked according to their thermal neutron capture cross sections. A salt comprised of LiF and BeF_2 makes the most neutronically favorable salt. LiF and BeF_2 are two of the most chemically stable fluorides. As shown in Table 1.3, LiF-BeF_2 salts have favorable thermophysical properties compared to other candidate salts. (Table 1.4 lists the compositions and formula weights for the salts listed in Table 1.3.) Furthermore, this salt has a suitably low melting point. Thus, it was determined that ^{7}LiF and BeF_2 were the preferred diluent fluorides. The LiF/BeF_2 portion of this fuel-salt acted as the solvent in which UF_4 was dissolved and comprised roughly 94 mole % of the total fuel-salt composition. ZrF_4 acted as an oxygen getter. In the event moisture or oxygen infiltrated the system, the ZrF_4 would react to form ZrO_2 before any UO_2 could form. Although the solubility limit for UO_2 is 1000 ppm, the ZrF_4 getter would protect against UO_2 precipitation and possible criticality accidents [6].

The secondary coolant for the MSRE was a clean (un-fueled) salt consisting of 0.667 mole fraction ^{7}LiF and 0.333 mole fraction BeF_2. This specific mixture of LiF and BeF_2 is called "flibe" and represents the baseline coolant choice for the FHR. There a several ways in which flibe having this molar composition is represented in the literature. The first way is to write flibe as 0.667 LiF-0.333 BeF_2. If the reader were to calculate the molar mass from this representation, the correct value of 32.96 g/mol would be obtained. The second common way to represent flibe with this molar composition is to write 2LiF-BeF_2. A third common representation is to write Li_2BeF_4. If the molar mass of is calculated from the second and third representations, an incorrect value of 98.89 g/mol is obtained. Thus, in this thesis, the term "flibe" is used to refer specifically to salt that is 0.667 mole fraction in LiF and 0.333 mole in fraction BeF_2. The shorthand notation of 2LiF-BeF_2 and Li_2BeF_4 will not be used here.

Flibe possesses a number of appealing characteristics. Besides being the most neutronically favorable salt, flibe is chemically compatible with graphite and structural metals, is optically transparent, has the best coolant properties of all candidate salts (see Table 1.3), and possesses a relatively low melting point. Table 1.3 lists the boiling points for several salts for which boiling points are available. Williams lists the boiling point for flibe at about 1400 °C based on extrapolations from lower temperature data; however, Ingersoll et. al. list flibe's boiling point at 1430 °C [40,41]. Despite the volume of research completed on molten salts, there are still significant uncertainties in some measurements of thermophysical properties such as the thermal conductivity.

In Figure 1.21, the phase diagram for LiF-BeF_2 salts shows two eutectic points: one at 32.8 mole % BeF_2 and T_{melt} = 456 °C, and one at 51.7 mole % BeF_2 and T_{melt} = 363 °C [42]. Pure LiF, on the other hand, has a melting point of 845 °C [43]. Thus, adding BeF_2 to LiF reduces the melting point of the salt. However, one must be mindful of the BeF_2 fraction in the salt because increasing the BeF_2 fraction increases the viscosity of LiF-BeF_2 melts [40,42]. This is due to the fact that BeF_2 is a Lewis acid which readily accepts an electron pair from a Lewis base, such as F^-. When BeF_2 melts, it retains some molecular order. Solid BeF_2 has a molecular structure like that of SiO_2 where Be^{2+} ions are surrounded by four F^- ions to form a tetrahedral structure which forms a larger 3D network. Liquid BeF_2 is believed to have a similar polymeric structure [44]. LiF is a typical ionic salt which melts into Li^+ and F^- ions. Generally, alkali metal fluorides (such as LiF) readily give up their fluoride (F^-) ions. F^- ions act as Lewis bases by donating an electron pair to a Lewis acid such as BeF_2 [40]. As LiF is added to BeF_2, the viscosity is reduced because the fluoride linkages between neighboring Be^{2+} ions are disrupted, as illustrated in Figure 1.20.

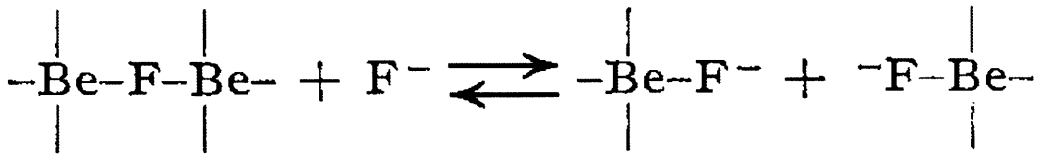

Figure 1.20: Polymeric structure of BeF_2 melts. As LiF is added, F^- linkages are disrupted. From [44].

It is interesting to note that the thermodynamically optimized phase diagram of Benes and Konings (Figure 1.21) differs slightly from the original phase diagram reported by ORNL in Figure 1.22. Both report a eutectic phase at about 52 mole % BeF_2 with a melting point of about 360 °C. However, they report slightly different phase equilibria around the mole composition of flibe in the FHR (66.7 LiF-33.3 BeF_2). Figure 1.22 shows a peritectic point at 33.3 mole % BeF_2 and T_{melt} = 458 C. At this peritectic point, Figure 1.22 shows that 66.7 LiF-33.3 BeF_2 melts incongruently to a liquid mixture plus LiF. Figure 1.21, on the other hand, reports a eutectic point at 32.8 mole % BeF_2 where 67.2 LiF-32.8 BeF_2 will melt congruently into a homogenous liquid at 456 °C. Despite this apparent discrepancy, it is generally held that flibe has a eutectic composition of 66.7 LiF-33.3 BeF_2 with a melting point of 460 °C [40,45].

As with any technology, one must confront engineering trade-offs. The choice of a primary coolant for the FHR is no different. The main disadvantage of flibe is that neutron transmutation in flibe produces tritium (^3H), a radioactive isotope of hydrogen. This tritium is a radiological concern because tritium can readily diffuse through and escape from most metals at FHR temperatures. Tritium is also a corrosion concern because the tritium generated is initially in the form of tritium fluoride. Like hydrogen fluoride, tritium fluoride is a strong oxidant and represents the principle corrosion concern in the FHR. The use of a salt enriched in ^7Li reduces parasitic neutron absorption from ^6Li, but having to enrich the salt in ^7Li makes the salt more expensive. Another drawback to the use of flibe is that beryllium poses health risks due to the toxicity of beryllium metal.

Table 1.2 List of suitable salt constituent elements (bold) for use in a nuclear reactor. All suitable salts in bold below make fluoride salts. From [40].

Element or Isotope	Neutron Capture Cross Section (barns, at 0.025 eV)	Reason for Exclusion from Consideration
Nitrogen-15	0.000024	Stability and compatibility
Oxygen	0.0002	Stability and compatibility
Deuterium	0.00057	Stability and compatibility
Hydrogen	0.33	
Carbon	0.0033	No thermo-stable liquids
Fluorine	**0.009**	**OK – suitable salts exist**
Beryllium	**0.010**	**OK – suitable salts exist**
Bismuth	0.032	Not compatible with alloys
Lithium-7	**0.033**	**OK – suitable salts exist**
Boron-11	**0.05**	**OK – suitable salts exist**
Magnesium	0.063	No low-melting salts exist
Silicon	0.13	Not compatible with alloys
Lead	0.17	Not compatible with alloys
Zirconium	**0.18**	**OK – suitable salts exist**
Phosphorus	0.21	Stability and compatibility
Aluminum	0.23	No low-melting nonvolatile salts
Rubidium	**0.37**	**OK – suitable salts exist**
Calcium	0.43	No low-melting salts exist
Sulfur	0.49	Stability and compatibility
Sodium	**0.53**	**OK – suitable salts exist**
Chlorine-37	0.56	Less attractive than F; requires ^{7}Li
Tin	0.6	Not compatible with alloys
Cerium	0.7	No low-melting salts exist

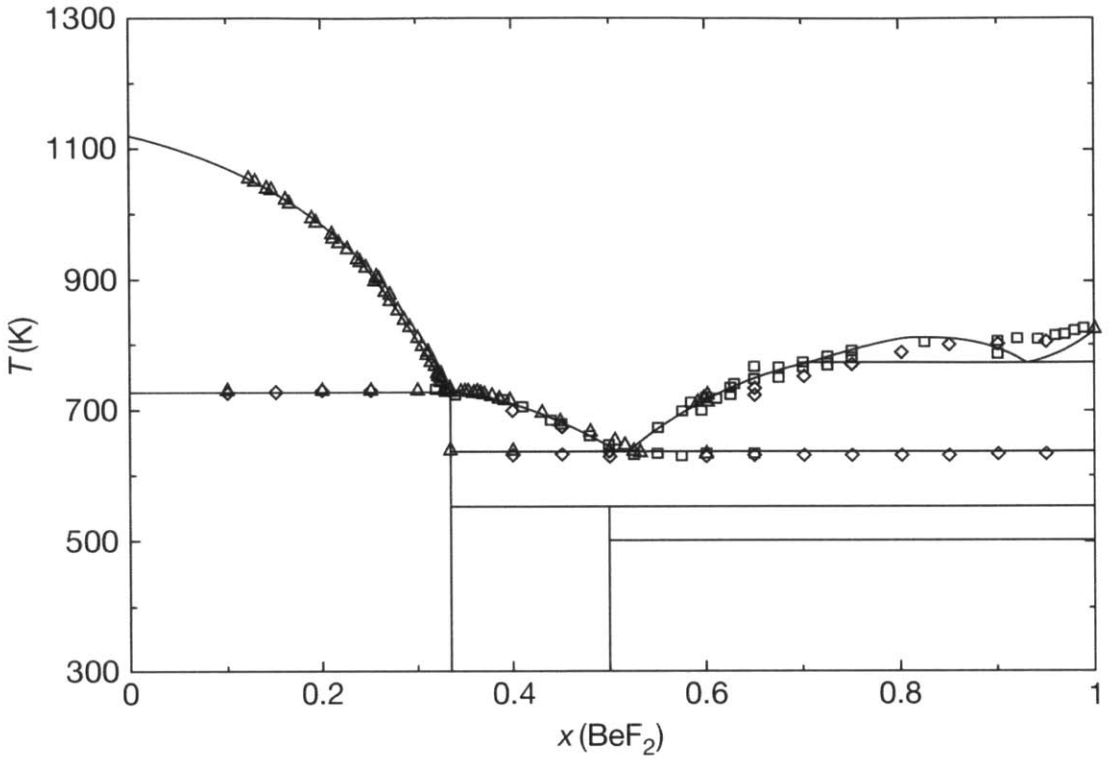

Figure 1.21: Calculated phase diagram for LiF-BeF_2. From [42].

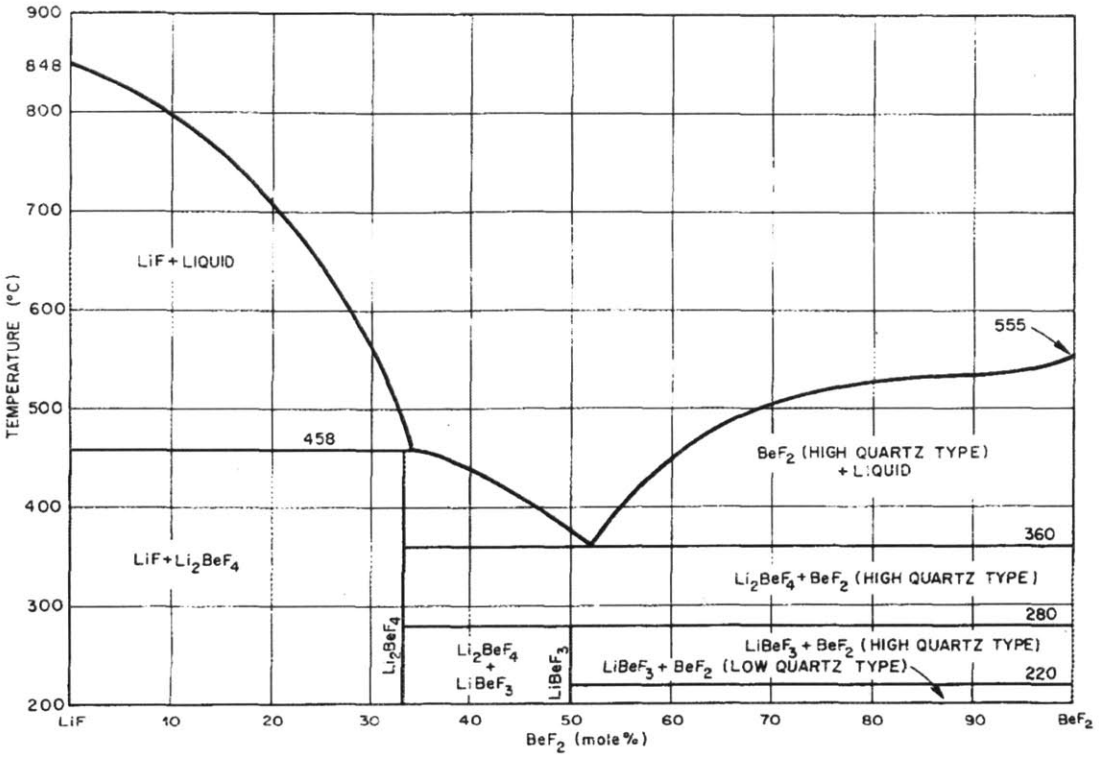

Figure 1.22: LiF-BeF_2 phase diagram. From [46]

Table 1.3: Summary of properties for flibe and other candidate salts at 700 °C. Modified from Williams, 2006.

Salt[a]	Melting Point (°C)	Boiling Point[b] (°C)	Vapor Pressure at 900 C (Pa)	ρ Density (g/cm^3)	$\rho*C_p$ Volumetric Heat Capacity (J/cm^3-°C)	Viscosity (10^{-3} Pa-s)	Thermal Conductivity (W/m-K)	Neutron Capture Relative to Graphite	Moderating Ratio[c]
LiF-BeF2	460	1459	160	1.94	4.68	5.6	1.0	8	60
NaF-BeF2	340	~1400	187	2.01	4.39	7	0.87	28	15
LiF-ZrF4	509	--	10265	3.09	3.76	> 5.1	0.48	9	29
NaF-ZrF4	500	~1350	667	3.14	3.68	5.1	0.49	24	10
KF-ZrF4	390	--	--	2.80	2.93	< 5.1	0.45	67	3
RbF-ZrF4	410	~1450	173	3.22	2.68	5.1	0.39	14	13
LiF-NaF-KF	454	1570	93	2.02	3.80	2.9	0.92	90	2

[a] Salt compositions listed below in Table 1.4

[b] The boiling point for some salts is not well known. The boiling point for flibe ($LiF-BeF_2$) is 1430 °C according to Ingersoll, 2004.

[c] A figure-of-merit for relating the effectiveness of moderation versus parasitic neutron capture. Higher values are better.

Table 1.4: Compositions for salts listed in Table 1.3. From Williams, 2006.

	mole % LiF	mole % BeF_2	mole % NaF	mole % ZrF_4	mole % KF	mole % RbF	Formula Weight (g/mol)
$LiF-BeF_2$ ("flibe")	67	33	-	-	-	-	33.0
$NaF-BeF_2$	-	43	57	-	-	-	44.1
$LiF-ZrF_4$	51	-	-	49	-	-	95.2
$NaF-ZrF_4$	-	-	59.5	40.5	-	-	92.7
$KF-ZrF_4$	-	-	-	42	58	-	103.9
$RbF-ZrF_4$	-	-	-	42	-	58	132.9
LiF-NaF-KF ("flinak")	46.5	-	11.5	-	42	-	41.3

2 Tritium production, diffusion, and absorption

In order to develop a model of tritium transport in an FHR, tritium production rates, tritium behavior in the salt, tritium behavior on graphite, and tritium diffusion in structural metals must be considered. This chapter reviews, collects, processes, and selects data for use in the tritium transport model developed in Chapter 5.

Tritium (^{3}H, also referred to as T) is a radioactive isotope of hydrogen. It can be produced due to human activity and reactions of cosmic rays in the atmosphere and in the ocean [47]. It has been estimated that between 4 and 8 megacuries of tritium are produced naturally per year on earth [47]. Chemically, tritium behaves like protium (^{1}H) but the kinetics of T diffusion and certain chemical reactions may be reduced compared to ^{1}H due to the kinetic isotope effect which arises from T's higher molar mass (3.016 g/mol) [47]. Tritium decays with a half-life of 12.3 years to ^{3}He via the emission of a beta particle having an average energy of 5.69 keV and a maximum energy of 18.6 keV [48]. The specific activity of tritium is 3.59×10^{14} Bq/g or 9703 Ci/g or 29263.8 Ci/mol T [49].

Any fluoride salt reactor coolant will generate tritium due to neutron transmutation. Tritium is an important issue for FHRs for two reasons. First, tritium is a corrosion concern because tritium generated in the salt is initially in the form of tritium fluoride (TF). Like hydrogen fluoride (HF), tritium fluoride is a strong oxidant and represents the principle corrosion concern in the FHR. Tritium may also exist in the reactor as T_2 depending on the chemical redox potential in the salt and/or the occurrence of chemical reactions. Second, tritium is a radiological concern. Both TF and T_2 can be absorbed on graphite, which represents a significant sink for tritium [50]. Tritium in the form of TF does not diffuse through metals [51]. However, tritium can present an off-site concern even under normal operating conditions because tritium in the form of T_2 can readily diffuse through and escape from most metals at FHR temperatures (~700 °C) [51,52]. Since the FHR will operate with an open-air Brayton power cycle, tritium diffusion through heat-exchangers must be limited. The use of a salt enriched in ^{7}Li reduces parasitic neutron absorption and tritium production from ^{6}Li, but this does not eliminate tritium production.

2.1 Tritium production reactions

Eqs (2.1) through (2.5) show the major production pathways for tritium in flibe. Figure 2.1 shows the neutron cross sections for the neutron transmutation reactions in Eqs (2.1) through (2.4). Although the FHR intends to use flibe enriched to 99.995 wt % in Li-7, the remaining 0.005 wt % Li-6 poses a significant problem because it produces tritium via an n,α reaction with thermal neutrons. The Li-6 cross section for this reaction follows a $1/v$ dependence and reaches nearly 5,000 barns at low neutron energies. The Li-7 *n,n'* reaction is a fast neutron reaction occurring only with neutron energies above 0.546 MeV. The reaction in F-19 only occurs for neutron energies greater than 9.5 MeV; thus the contribution from this reaction is minimal in MSRs and especially minimal in FHRs [41,50]. The n,α reaction in Be-9 does not generate T directly; however, it does generate He-6,

which decays with a 0.8 second half-life into new Li-6. Thus, the initial 0.005 wt % of Li-6 in flibe can be consumed by neutron transmutation, but additional Li-6 is continually produced by neutron transmutation in Be-9. This means that the rate of tritium production will vary through the reactor life (assuming the coolant is not replaced with fresh flibe).

As Eqs (2.1) and (2.2) show, tritium is produced in flibe as tritium fluoride [53–56]. TF can dissolve in flibe as T^+ and F^- ions. The solubility of TF in flibe goes according to Henry's law of solubility for gases [57]. See Figure 2.21, Eq (2.12), and the associated discussion in Section 2.5 for information about TF solubility and its Henry's law constant in flibe. As discussed in Section 3.1, TF is chemically oxidizing toward structural metals and represents the principle oxidative species and corrosion concern in FHRs. If TF undergoes a chemical reaction, it can be converted to $T_{2(g)}$. This type of reaction occurs when TF oxidizes metal or if it is reduced to T_2 by any redox control methods used in the FHR coolant. Tritium as $T_{2(g)}$ also follows Henry's law for solubility in flibe (see Figure 2.22 and Eq (2.13) for the Henry's law constant for H_2) and represents a radiological concern because of its high permeability through structural metals.

$$^{6}\mathrm{LiF} + n \rightarrow {}^{4}_{2}\mathrm{He} + {}^{3}_{1}\mathrm{HF} \tag{2.1}$$

$$^{7}\mathrm{LiF} + n \rightarrow {}^{4}_{2}\mathrm{He} + {}^{3}_{1}\mathrm{HF} + n' \tag{2.2}$$

$${}^{19}_{9}\mathrm{F} + n \rightarrow {}^{17}_{8}\mathrm{O} + {}^{3}_{1}\mathrm{H} \tag{2.3}$$

$${}^{9}_{4}\mathrm{BeF_2} + n \rightarrow {}^{4}_{2}\mathrm{He} + {}^{6}_{2}\mathrm{He} + 2\mathrm{F} \tag{2.4}$$

$${}^{6}_{2}\mathrm{He} \rightarrow {}^{6}_{3}\mathrm{Li} + e^{+} + \overline{\nu}_e \quad \left(t_{1/2} = 0.8\,\mathrm{sec}\right) \tag{2.5}$$

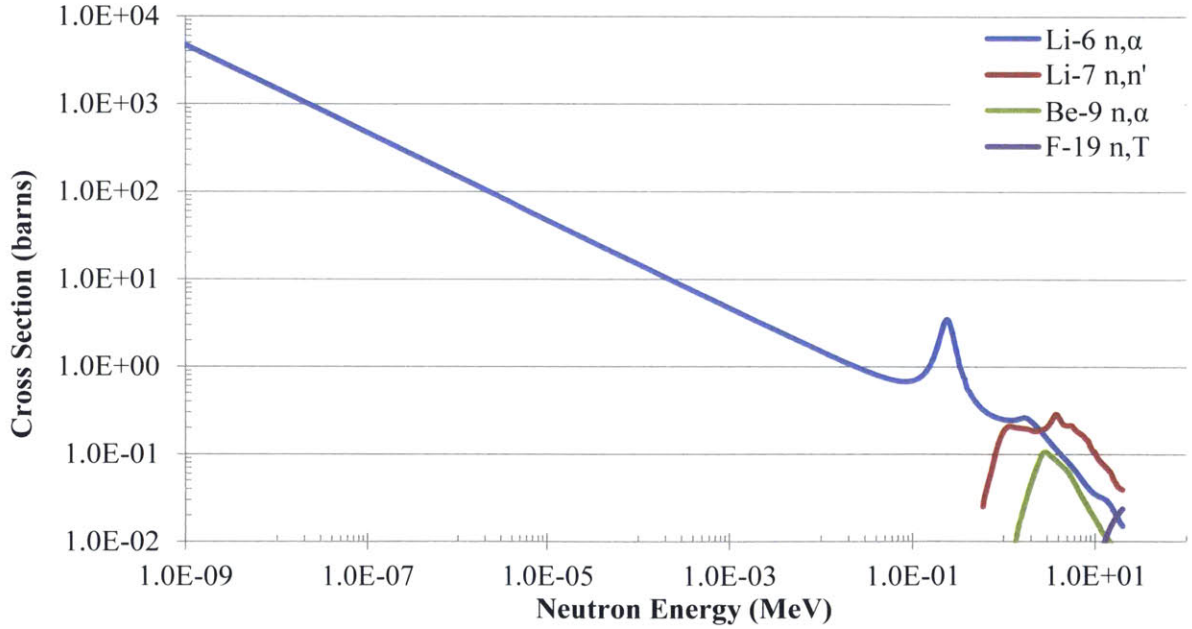

Figure 2.1: Nuclear cross sections for major tritium-producing reactions. Data for Li-6 from CENDL-3.1. Data for Li-7 from ENDF/B-VIII.0. Data for Be-9 and F-19 from ENDF/B-VII.1.

2.2 Tritium production rate comparison

All reactors produce tritium from ternary fission and reactions in the coolant and/or neutron poisons. Light-water reactors produce tritium in B-10 and the lithium used for water chemistry control. Graphite moderated reactors produce tritium due to impurities in the graphite [58]. Gas-cooled reactors produce tritium from He-3. Tritium produced from ternary fission in TRISO fuel is well retained in the fuel [59,60]. The tritium production rate in flibe depends on several factors: neutron spectrum, neutron flux, total salt inventory, core salt inventory, and Li-7 enrichment. Several estimates of tritium production rates in salt-cooled reactors have been made over the years, but only 1 set of measurements have been made. In 1969, during planning for the molten-salt breeder reactor (MSBR), shortly before the MSRE was shut down for the last time, the importance of tritium production and distribution in large salt-cooled reactors was realized [61]. At full power, the MSRE (a molten-salt reactor where the fuel is dissolved in the coolant) produced about 7.3 MWt and the total tritium production rate was 54 Ci/d [50]. In 2004, it was estimated that a 2400 MWt FHR (known at the time as an Advanced High Temperature Reactor, or AHTR) would produce 5000 Ci of T per day at the beginning of life and 500 Ci of T per day at equilibrium [41]. If this estimate is normalized by reactor power, it predicts that an FHR should produce 2083 Ci T/GWt/d.

Another way to calculate the tritium production rate in an FHR as a function of time is by use of Eq (2.6) from ref [62]. The first term accounts for tritium production from Li-7, assuming the number density of Li-7 remains constant. The second term accounts for the production of tritium due to transmutation in Li-6 while accounting for Li-6 burnup. The third term accounts for production of Li-6 from transmutation in Be-9 and the subsequent destruction of this Li-6 by either tritium production or neutron absorption. The symbols in Eq (2.6) are defined below. Table 2.1 shows the flux and cross sections required for calculating tritium production using Eq (2.6) for a PB-FHR. From the specifications for the 236 MWt Mk1 PB-FHR, V_{core} = 7.2 m^3 and V_{loop}= 46.82 m^3. Using these volumes and the values in Table 2.1, the tritium production rate can be calculated as a function of reactor operating time (effective full power years, EFPY) normalized by the reactor thermal output, as shown in Figure 2.2. Initially, when the flibe coolant is fresh, the tritium production rate is 10,000 Ci/GWt/d. Once the initial 0.005 wt % Li-6 has been reduced and the rate of Li-6 destruction is balanced by the rate of Li-6 production from Be-9, the tritium production rate is about 3000 Ci/GWt/d after 15 EFPD. Table 2.2 summarizes the BOL and equilibrium rates of tritium production in a prototypical PB-FHR and compares them with the tritium generation rates in different reactor types.

$\dot{T}(t)$ = tritium production rate at time t of reactor operation (atoms T/cm^3-s)
t = cumulative reactor operating time (s)
ϕ = neutron flux (n/cm^2-s)
$\sigma^T_{Li\text{-}7}$ = microscopic cross section for tritium production in Li-7 (barn)
$N_{Li\text{-}7}$ = number density of Li-7 in flibe at a given temperature (atoms/cm^3)

$\sigma^{T}_{Li\text{-}6}$ = microscopic cross section for tritium production in Li-6 (barn)
$N^{\circ}_{Li\text{-}7}$ = initial number density of Li-6 in flibe at a given temperature (atoms/cm^3)
V_{core} = volume of flibe in reactor core (m^3)
V_{loop} = total volume of flibe in reactor primary system (m^3)
$\sigma^{abs}_{Li\text{-}6}$ = microscopic absorption cross section in Li-6 (barn)
$\sigma^{\alpha}_{Be\text{-}9}$ = microscopic cross section for He-6 production from n,α reaction in in Be-9 (barn)
$N_{Be\text{-}9}$ = number density of Be-9 in flibe at a given temperature (atoms/cm^3)

$$\dot{T}(t) = \phi\sigma^{T}_{Li-7}N_{Li-7} + \phi\sigma^{T}_{Li-6}\left(N^{o}_{Li-6}e^{-\frac{V_{core}}{V_{loop}}\phi\sigma^{abs}_{Li-6}t} + \frac{\phi\sigma^{\alpha}_{Be-9}N_{Be-9}}{\phi\sigma^{abs}_{Li-6}}\left(1-e^{-\frac{V_{core}}{V_{loop}}\phi\sigma^{abs}_{Li-6}t}\right)\right) \quad (2.6)$$

Table 2.1: PB-FHR energy and volume-averaged flux in the coolant. One-group cross sections. From [62].

ϕ (n/cm^2-s)	$3.41\text{x}10^{14}$
$\sigma^{T}_{Li\text{-}6}$ (b)	148.026
$\sigma^{abs}_{Li\text{-}6}$ (b)	148.032
$\sigma^{\alpha}_{Be\text{-}9}$ (b)	$3.63\text{x}10^{-3}$
$\sigma^{T}_{Li\text{-}7}$ (b)	$1.00\text{x}10^{-3}$

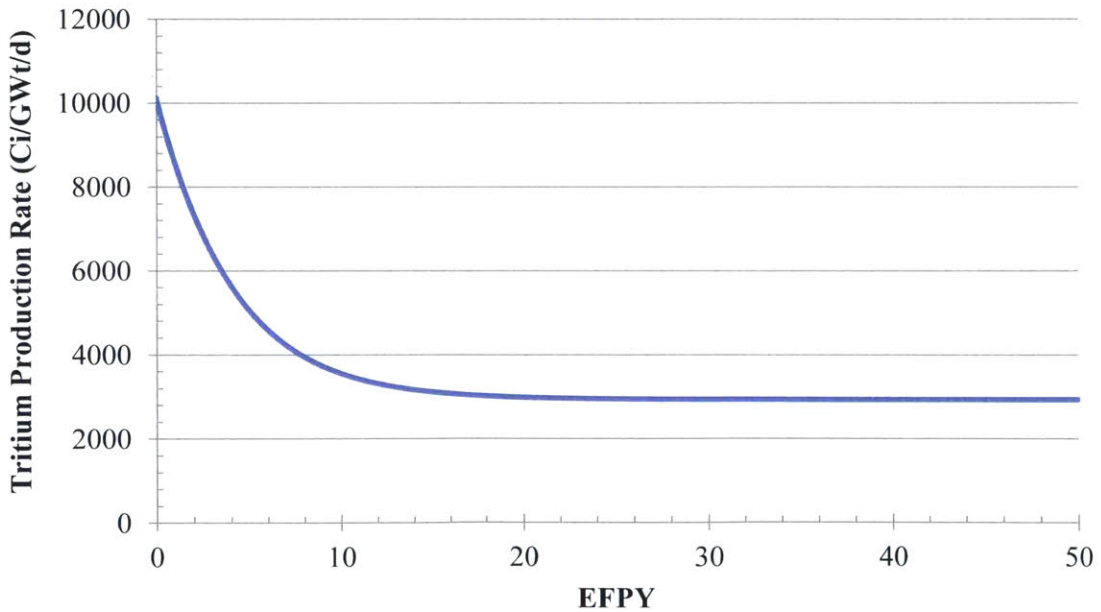

Figure 2.2: Tritium production rate (Ci/GWt/d) for Mk1 PB-FHR using flibe enriched to 99.995 weight % Li-7 as a function of EFPY.

Table 2.2: Tritium production rates in various reactors compared to FHRs. *Calculated from data in ref [63]. FHR values calculated from Eq (2.6) and Table 2.1.

	Total Tritium Production Rates [Ci/GWt/d]
BWR*	12.3
PWR*	13.9
GCR*	18.0
HTGR*	18.5
FBR*	24.9
HWR*	1176
FHR	BOL: 10129 EQ: 2931

Among other things, Eq (2.6) depends on the ratio of the core coolant volume to the total loop coolant volume. In a PB-FHR, the pebble packing fraction is 0.60. This means that 40 % of the core volume is occupied by the coolant. In an MSR, the volume of fuel-salt existing in the core is a much smaller fraction of the core volume. Figure 1.18 shows the relatively small fuel-salt channels in the graphite moderator of the MSRE. Thus, it may be possible to reduce the tritium production rate in an FHR by altering the core layout (fuel form, geometry, *etc.*) in order to have a smaller fraction of salt in the core.

2.3 Tritium release rate comparison

Table 2.3 summarizes typical tritium release rates (Ci/GWt/d) for various reactor types. Because no FHR has been built, no data exist for FHR tritium release rates. In order to address this uncertainty, a model has been developed in order to predict tritium release rates from FHRs. The development of this model and the simulations performed with it will be discussed in detail in Chapters 5 and 6. Tritium release rates depend on several main factors: tritium production rate, system temperature, tritium chemical form, materials used for system boundaries, location of tritium production within the system, and the power cycle. The higher the temperature, the higher the rate of tritium diffusion in a given material. In an LWR or heavy water reactor (HWR), coolant temperatures are generally between 260 and 330 °C. Gas cooled reactors have inlet temperatures of about 300 °C and outlet temperatures of about 700 °C. Sodium-cooled fast reactors have coolant temperatures between about 400 and 550 °C [11]. In an FHR, coolant temperature varies between 600 and 700 °C.

The tritium chemical form plays a large role in the mobility of tritium within a system. In an FHR, tritium exists either as T_2 or TF. T_2 can diffuse through metals and has a low solubility in the salt. TF cannot diffuse through metals, and has a higher salt-solubility than T_2 [64]. If H_2 is added to the FHR system, tritium may exist as HT when isotopic exchange occurs [55]. This HT would

behave in much the same way as T_2 or H_2. In heavy water reactors (HWRs), tritium is formed from neutron capture in deuterium and exists as T_2O, DTO, or HTO, which are simply forms of water and do not diffuse through metals. HTO may be an attractive chemical form for storing tritium [52]. If hydrocarbon grease (such as would be used for pump lubrication) were to contaminate the primary coolant, tritium may also replace protium in those compounds.

Most, if not all, primary system boundaries in any reactor are made of metal. Different metals have different permeabilities for tritium. For example, Pd has a permeability roughly 1000 times higher than austenitic stainless steel. The presence of an oxide layer on the metal can reduce the permeability of the tritium by up to several orders of magnitude. Other coolant-facing materials such as the fuel and moderator may also play an important role. Graphite, for example, is an effective sink for tritium in various chemical forms. The location of tritium production within the system determines how many barriers it must pass through before it can escape the system. Tritium produced in the fuel kernel of a TRISO particle must first diffuse out of the particle, then out of the graphite matrix and into the coolant. From the coolant it must then diffuse through a metal vessel.

The type of power cycle is also an important factor influencing the escape of tritium from a reactor system. A closed-power cycle never exhausts the working fluid into the environment. The FHR intends to use an open-air Brayton power cycle in which air is heated by salt in a heat exchanger. This air is then exhausted either directly to the environment or exhausted to the environment after passing through a Rankine bottoming cycle. Fluoride salts tend to dissolve metal oxides, thus a metal oxide layer on a salt-facing surface will not be stable; however, an oxide layer on the side of an air-facing pipe would be stable and would be able to reduce tritium permeation.

Table 2.3: Tritium release rates for different reactor types. ‡Calculated from data in ref [63].

	Gaseous Effluent*	Liquid Effluent*	**Total Tritium Escape***
BWR‡	0.04	0.09	**0.13**
PWR‡	0.09	0.65	**0.74**
GCR‡	0.22	0.33	**0.56**
HWR‡	16.05	4.01	**20.07**
*Units: Ci/GWt/EFPD			

A summary of regulatory limits for tritium emissions is given in Table 2.4. A concise discussion of the meaning and significance of these limits is given by Sherman and Adams [65]. In the context of a conceptual reactor, Sherman and Adams suggest the use of the ALARA limits outlined in Table 2.4. The ALARA annual radiation dose limits are for whole-body exposure to the general public due to air or water contaminated with tritium. The calculated effluent concentration limits do not limit the amount of tritium that can be released, but only limit the concentration of the

effluent. Thus some benefit may be gained by sufficiently diluting any tritium releases. One should also be aware of the social component to managing tritium in a new reactor such as the FHR. This most likely means that the FHR should not release a higher absolute amount of tritium than other reactor types, regardless of how well it is diluted.

Table 2.4: Regulatory limits for tritium emissions in the United States. From reference [65].

		Annual Radiation Dose		Effluent Concentration			
				Air		Water	
	Regulation	(mrem)	(mSv)	(μCi/ml)	(Bq/ml)	(μCi/ml)	(Bq/ml)
Limit	10 CFR 20.1301(a)1	100	1	-	-	-	-
	Table 2 of Appendix B to 10 CFR 20	50	0.5	1E-7	3.7E-3	1E-3	37
Standard	10 CFR 20.1301(e)	25	0.25	(5E-8)[a]	(1.85E-3)[a]	(5E-4)[a]	(18.5)[a]
ALARA	Appendix I to 10 CFR 50	20 (β,air)	0.20	(4E-8)[a]	(1.48E-3)[a]	-	-
		3 (water)	0.03	-	-	1.5E-5	0.56
Drinking Water	EPA standard	4	0.04	-	-	2E-5	0.74

a. Calculated by assuming the linear relationship between the annual dose of 50 mrem and the values in Table 2 of Appendix B of 10 CFR 20.
ALARA = as low as reasonably achievable
CFR = Code of Federal Regulations

2.4 Tritium sorption/desorption from graphite

Near the close of MSRE operations, it was found that the moderator graphite was a significant sink for tritium [50]. Since the FHR uses pebble bed fuel, the graphite surface area per unit reactor power in the FHR will be larger than that in the MSRE, and the effect of tritium sorption on graphite will be important for determining tritium transport.

2.4.1 Tritium behavior on MSRE graphite

A 64.5 inch long graphite moderator "stringer" from the MSRE was analyzed for its tritium content after the MSRE had been shut down [66]. It was found that the tritium surface concentration was $1x10^{11}$ disintegrations/minute/gram, and at a depth of 1/16 inches, the concentration was about

$1x10^9$ dis/min-g. Based on the tritium content of this stringer, it was determined that about 15% of the total tritium produced during the lifetime of MSRE operations had been captured on the graphite moderator. Several specimens of POCO graphite having large, uniform pores which had been exposed to the MSRE salt for the final 1786 hours of operation were also analyzed. The exterior tritium concentrations were about $4.5x10^{10}$ dis/min-g and the interior concentrations were below $1x10^8$ dis/min-g.[1] This suggested that the graphite surface saturates relatively quickly compared to the time it takes for tritium to diffuse into the graphite bulk [66].

The major forms of tritium in the MSRE were T_2 and TF, with the relative amounts of T_2 and TF being affected by the chemical redox potential in the salt [67]. Measurements and observations from the MSRE indicate both TF and T_2 are absorbed on graphite [50,61,64]. Given that such a substantial amount of tritium was found on the MSRE graphite, ORNL calculations from that era assumed that any T_2 or TF reaching the graphite surface was retained by the graphite [50]. This has implications for capturing tritium and possibly controlling coolant chemistry in an FHR where, if no redox control is applied, TF and T_2 are the two species dictating the chemical potential. (See Section 3.2 for a discussion of redox control, corrosion, etc.)

2.4.2 Experimental data for hydrogen sorption on graphite

The importance of obtaining data about the solubility of hydrogen, permeability of hydrogen in metals, the capacity of graphite for hydrogen, and the reaction rates of hydrogen fluoride dissolved in salt with metals was recognized in a 1974 report [68], but it would seem that the MSBR program (which came after the MSRE) was terminated (in 1976) before the data could be obtained [69]. Thus, most of the available data for hydrogen behavior on graphite come from more recent work of a variety of researchers. The data are still limited in several ways. Experimental temperatures are often near room temperature (for studying carbon as a storage medium for hydrogen) or at high temperatures (for understanding hydrogen behavior on graphite for nuclear fusion applications). For the development of a tritium transport model for FHRs, the mechanisms and rates of tritium sorption on graphite, the graphite capacity for tritium, and the temperature and pressure dependence of the capacity will be important.

2.4.2.1 Mechanistic behavior of hydrogen in graphite

Generally speaking, the higher the Brunauer-Emmett-Teller (BET) surface of a material (also known as specific surface area), the higher the specific hydrogen capacity (atoms/cm^2 or atoms/g) [70]. A direct, linear dependence of specific hydrogen capacity with specific surface area has been observed [70,71]. Typical nuclear-grade graphites have specific surface areas between 0.25 and 1.0

[1] This unit is tritium disintegrations per gram graphite per minute. $4.5x10^{10}$ dis/g-min = $2.09x10^{-6}$ g T/g graphite. $1x10^8$ dis/g-m = $4.6x10^{-9}$ g T/g graphite

m^2/g [71,72]. However, numerous other types of graphite have much higher BET surface areas. Activated graphite such as AX-21, GX-31, and Maxsorb have BET surface areas up to about 4000 m^2/g [70]. The generally held mechanism of hydrogen adsorption is by chemisorption where hydrogen is adsorbed on the surface of graphite and a weak chemical bond (of strength ~ 0.5 eV) between the hydrogen and the carbon is established [59,73–77]. A preference for adsorption on graphite crystallite (subgrain) edge-sites (on the graphite prism plane rather than on the basal plane) has been noted [74,76]. Depending on the temperature of the chemisorption, it may either be molecular chemisorption or dissociative chemisorption. There is some discrepancy as to when molecular or dissociative chemisorption occurs on graphite. For pressures between 0.5 and 100 Pa and temperatures between 293 and 983 K, it has been shown that hydrogen can pass through graphite in molecular form [78]. At a graphite surface, molecular hydrogen does not dissociate into atomic hydrogen unless temperatures are above approximately 1000 K [71]. However, catalytic hydrogen dissociation has been observed on graphene, which also demonstrates higher specific hydrogen capacity than its BET surface area would predict [70]. At 1023 K and a $T_{2(g)}$ pressure of 0.14 Pa, Strehlow measured the specific capacity of three types of graphite (A681, CGB, and POCO AXF-5QBG) [79]. He proposed dissociative chemisorption as the adsorption mechanism under these conditions. Strehlow notes that the specific capacity follows a square root dependence on the tritium pressure, which is said to indicate a dissociative adsorption mechanism [79]. In support of the dissociative chemisorption mechanism, Stehlow cites work by Yang et. al. who suggested dissociative H_2 chemisorption at temperatures as low as 973 K [80,81]. However, this work was done in the presence of H_2O and CO_2, and oxygen can help promote hydrogen dissociation at carbon surfaces [74]. On the other hand, Atsumi et. al. noticed that data obtained for the hydrogen sorption on ISO-88 graphite at 973 K do not exactly follow a square root dependence on the pressure [82]. Because of this deviation, they propose a sorption mechanism involving molecular hydrogen [82].

Since higher temperatures are required for hydrogen dissociation on graphite, this implies that molecular hydrogen can be retained on carbon at lower temperatures. At lower temperatures, hydrogen may diffuse and adsorb along and on graphite surfaces. At higher temperatures (> 1000 K), hydrogen solubility, diffusion, and trapping processes in carbon grains is significant [71]. At these higher temperatures, the atomic hydrogen can adsorb at chemically active sites on the surface-facing grain boundaries of graphite grains or along the edges of subgrains [71]. Atomic hydrogen may migrate along subgrain boundaries and enter the interior of a grain. In another high-temperature process separate from hydrogen "solubility" in graphite, hydrogen may also be trapped at active sites with a measureable binding energy [71].

2.4.2.2 Graphite specific capacity for hydrogen

A number of studies have collected data on the hydrogen capacity of graphite for various grades of graphite, at different pressures and at different temperatures. As far as the data relevance to FHR conditions, few experimental data cover the temperature and low hydrogen pressure regimes

expected in the FHR. In some cases, it may be possible to extrapolate existing data; however, besides the limited data collected at the end of MSRE operations, no data have ever been collected for graphite in contact with fluoride salt containing hydrogen or hydrogen fluoride. In this section, a brief summary of relevant data on graphite hydrogen capacity will be given, and the most useful set of data for FHR purposes will be highlighted.

Progressing chronologically, in 1960, Redmond and Walker measured hydrogen sorption on TSP nuclear graphite as shown in Figure 2.3. The TSP graphite samples had measured density and BET surface area of 1.70 g/cm^3 and 0.3 m^2/g, respectively. For a fixed pressure, the hydrogen capacity appears to increase, reach a maximum, and then decrease as the temperature is increased. This is likely due to the temperature dependence of trapping effects. At lower temperatures, traps are not activated or the hydrogen takes a long time to diffuse to the traps, but at high temperatures, the hydrogen is more mobile, allowing it to migrate to and escape from traps [71]. The data were converted into more contemporary units for reporting in Figure 2.4. By representing the data as isotherms in Figure 2.4, one can see that the capacity begins to reach saturation at higher pressures. This is due to the fact that a finite trap density and/or available surface area exists in the graphite [71].

In 1979, Causey et. al. measured deuterium solubility in laminar pyrolytic carbon over the temperature range from 900 to 1500 °C [83]. In this type of carbon, over this temperature range, the deuterium solubility decreased with increasing temperature. The solubility data were originally reported in units of atoms D/atom C-atm$^{0.5}$. Using the density of the laminar pyrolytic carbon (1.89 g/cm^3), the units reported in Figure 9 of ref [83] were converted to the units reported in Figure 2.5.

The 1986 experiments by Strehlow reported specific tritium capacities and BET surface areas for several different grades of graphite at several temperatures and two pressures [79]. Some samples were oxidized with T_2O prior to exposure to $T_{2(g)}$. Interestingly, the tritium capacity of oxidized graphite was higher than that of un-oxidized graphite by up to an order of magnitude. Several different samples of each type of graphite were used for the measurements. The measured BET surface areas differed somewhat within each sample set. For example, for the measurement at 0.14 Pa, the BET surface of A681 was 0.203 m^2/g, but the sample used for the measurement at 0.04 Pa had a BET of 0.506 m^2/g. The BET for CGB graphite varied from 0.218 to 0.319, and the BET for AFX-5QBG varied from 0.205 to 0.280 m^2/g. The results for the un-oxidized samples are reported in Figure 2.6.

In two separate 1986 reports, Causey and co-workers reported the retention of deuterium in Papyex and POCO graphites [84,85]. Some data were reported for graphite exposed to deuterium gas only, and other data were reported for graphite exposed to 100 eV deuterium ions. Figure 2.7 summarizes data converted into the current units from Figure 4 in ref [84]. Here, Papyex graphite of density 1.1 g/cm^3 and BET surface area 20 m^2/g was exposed to deuterium gas at 0.66 Pa for 1.5 hours. At temperatures below 973 K, it is reported that hydrogen isotopes can migrate into graphite only by surface diffusion along internal porosity [84]. A set of data for graphite exposed to both deuterium ion implantation and deuterium gas (Figure 1 in ref [84]) shows a reduction in capacity as

temperature increases from 373 to 900 K. As Figure 2.7 shows, at 973 K, the capacity begins to increase again. Above 1000 K, it is theorized that processes other than surface adsorption and surface diffusion take place and account for the peak near 1250 K. These processes are transgranular diffusion of deuterium in the bulk graphite and the occupation of trapping sites in the bulk graphite [84]. Above 1250 K, the traps begin to "thermally depopulate" and the total capacity is reduced.

The same experiment described in the preceding paragraph was also carried out on POCO AXF-5Q graphite (BET: 1 m^2/g, density: 1.84 g/cm^3) where the same temperature-dependent behavior was observed and attributed to the same mechanistic behavior [85]. Figure 2.8 summarizes data from this experiment.

For the temperature and pressure-dependent specific capacity of hydrogen on graphite, the set of data that will be used in this thesis comes from an article published in 1988 by Atsumi et. al [86]. These data were also used by Causey in formulating a best estimate for hydrogen diffusivity in graphite [71]. The graphite investigated by Atsumi was Toyo Tanso ISO-88 having a density of 1.90 g/cm^3. Figure 2.9 shows the deuterium solubility in ISO-88 as a function of the square root of the deuterium pressure for temperatures from 850 to 1050 °C. As shown in Eq (2.7), Atsumi et. al. provided an equation for the solubility of deuterium in ISO-88 in units of cm^3 D_2/g carbon at STP. Here P is the pressure in Pa, R is the universal gas constant in units of kJ/mol-K, and T is temperature in K. Using the ideal gas law, this equation can be converted into units of moles D/g carbon according to Eq (2.8). Figure 2.10 plots Eq (2.8) over a range of pressures for temperatures from 700 to 1050 °C.

Although the data from ref [86] will serve as the baseline data for tritium uptake in FHRs, ISO-88 is not an exact match for the IG-110U graphite used in the central and radial reflectors in the Mk1 PB-FHR. Limited reviews of hydrogen solubility in graphite are available. First, Tanabe and Atsumi summarized hydrogen solubility in a number of types of graphite (see Figure 2.11), and noticed that the hydrogen solubility decreases with increasing degree of graphitization (crystallinity) [87]. Second, Atsumi et. al. measured the hydrogen capacity of many types of graphite at 1000 °C and 101 kPa (see Figure 2.12). For data specific to IG-110U, refer to ref [88] where the hydrogen retention in Toyo Tanso IG-110U and other nuclear-grade graphites was analyzed. Assuming a density of 1.77 g/cm^3 for IG-110U (from ref [89]), the data extracted from ref [88] were converted from units of atom ppm to units of atoms H/g IG-110U. The results are plotted in Figure 2.13. At 1273 K, they found that the hydrogen capacity obeyed a square root of pressure dependence below 10 kPa. Beyond 10 kPa, the graphite capacity saturated. Note that the hydrogen capacity of IG-110U in Figure 2.13 is comparable to the hydrogen capacity of ISO-88 in Figure 2.10.

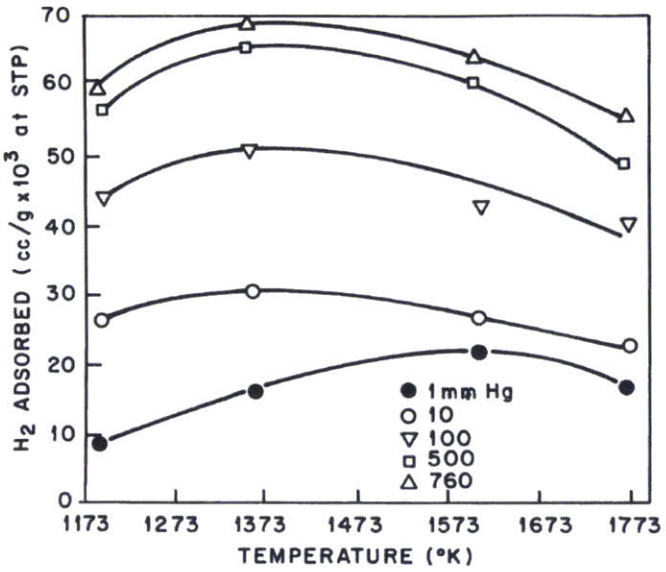

Figure 2.3: Isobars for the adsorption of hydrogen on TSP nuclear-grade graphite. Work reported in ref [74], figure from ref [58].

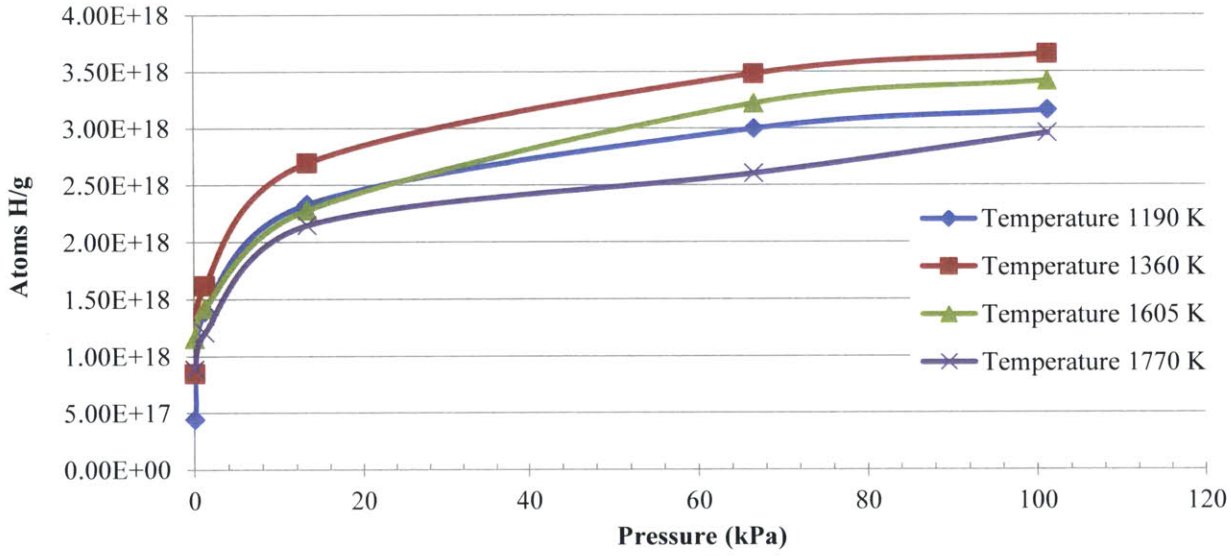

Figure 2.4: Data from Figure 2.3 converted to new units. Pressure ranges from 0.13 to 101.3 kPa.

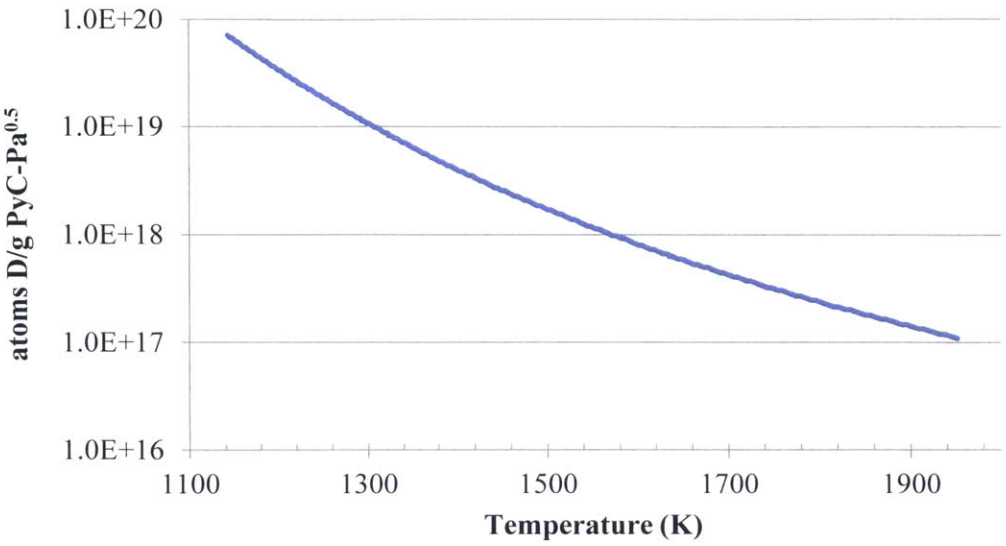

Figure 2.5: Solubility of deuterium in pyrolytic carbon (PyC). Converted to current units from data in ref [83].

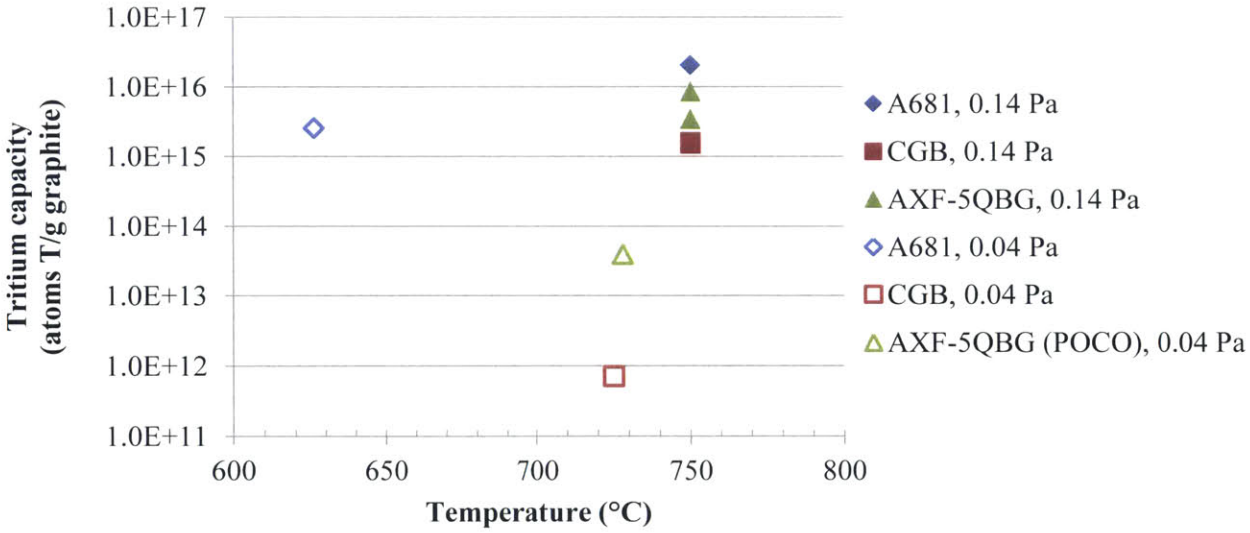

Figure 2.6: Specific capacity for tritium on three grades of un-oxidized graphite. Data converted to current units from original data in [79].

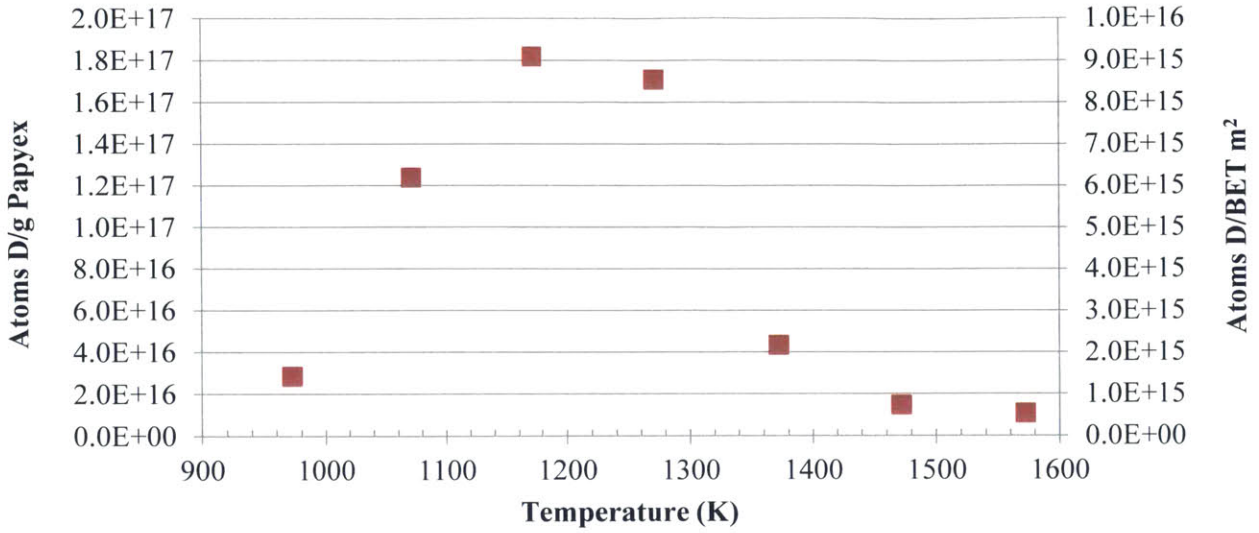

Figure 2.7: Specific capacity of Papyex graphite under deuterium gas only at 0.66 Pa. Original data from Figure 4 of ref [84] converted to current units using sample dimensions, density, and BET surface area from ref [84].

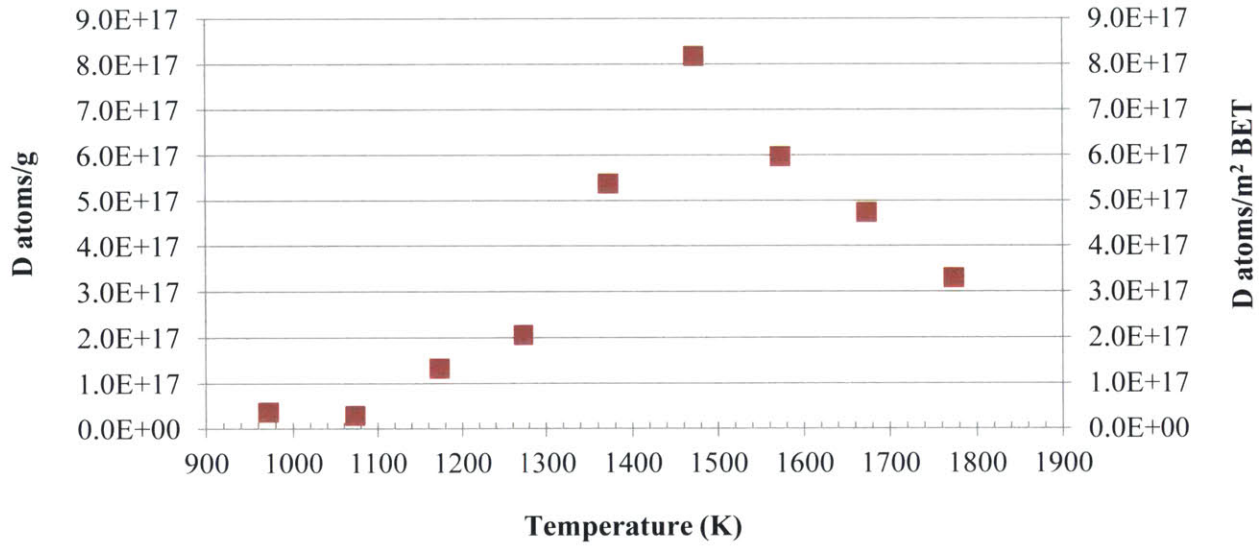

Figure 2.8: Deuterium capacity on POCO AXF-5Q graphite under deuterium gas only at 0.66 Pa. Original data from Figure 4 of ref [85] converted to current units using sample dimensions, density, and BET surface area from ref [85].

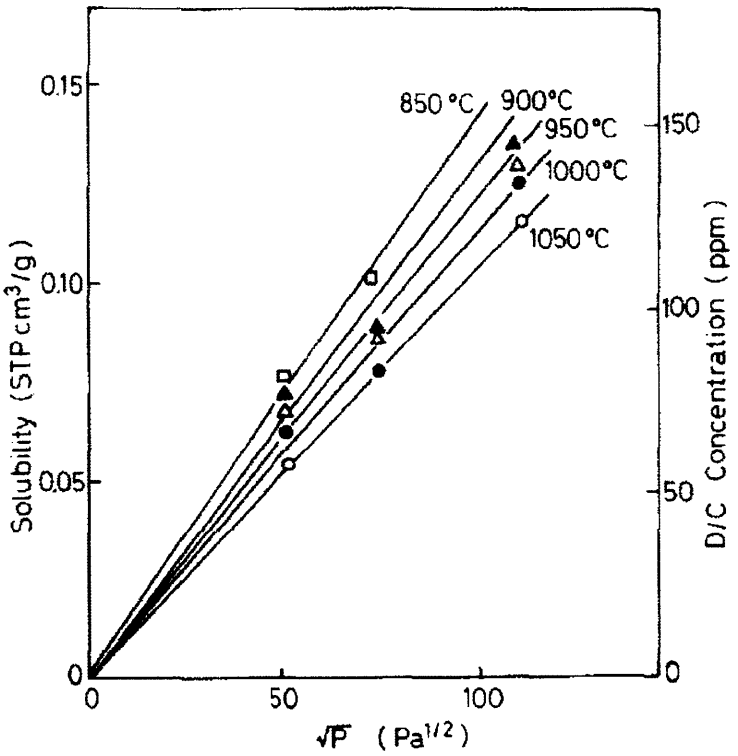

Figure 2.9: Solubility isotherms for deuterium adsorption on ISO-88 graphite. From ref [86].

$$S\,[\mathrm{cm^3 D_2/g\,graphite}] = 1.9\times10^{-4}\sqrt{\mathrm{P[Pa]}}\exp\left(19[\mathrm{kJ/mol}]/\mathrm{RT}\right) \tag{2.7}$$

$$S\,[\mathrm{mol\,D/g\,graphite}] = \left\{1.9\times10^{-4}\sqrt{\mathrm{P[Pa]}}\exp\left(19[\mathrm{kJ/mol}]/\mathrm{RT}\right)\right\}\times\left(\frac{\mathrm{P}}{\mathrm{RT}}\right)\times 2 \tag{2.8}$$

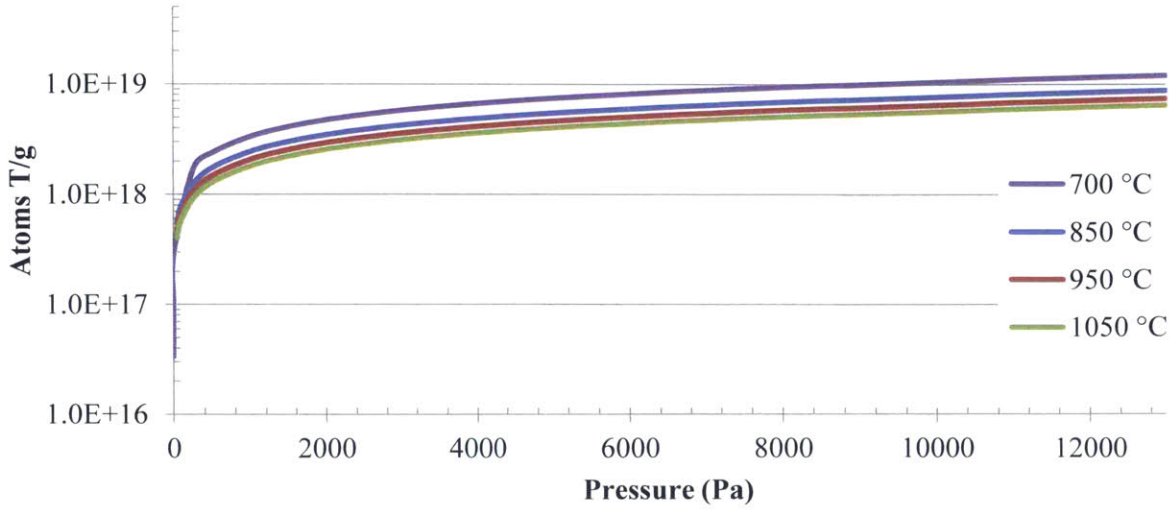

Figure 2.10: Specific capacity/solubility of $D_{2(g)}$ on ISO-88 graphite. Plot of Eq (2.8) converted from Eq (2.7) from ref [86].

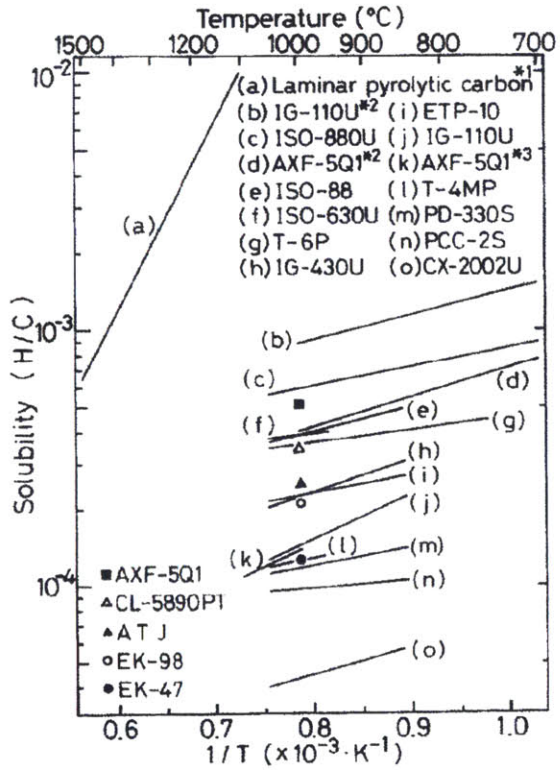

Figure 2.11: Comparison of hydrogen solubility in various grades of graphite. Pressure unknown. From ref [87].

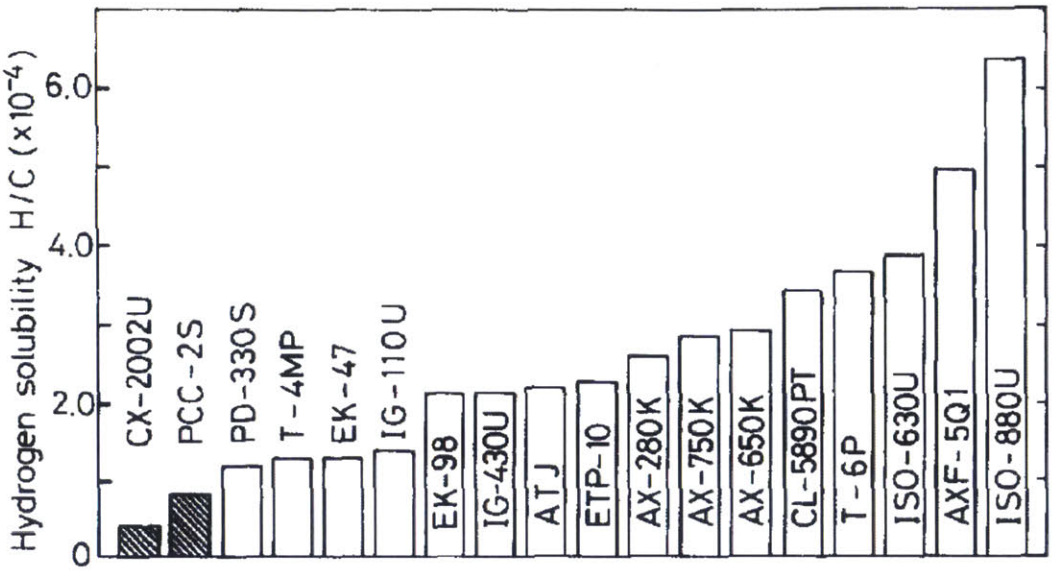

Figure 2.12: Hydrogen retention in graphite and carbon fiber composites at 1000 °C and 101 kPa. From ref [82].

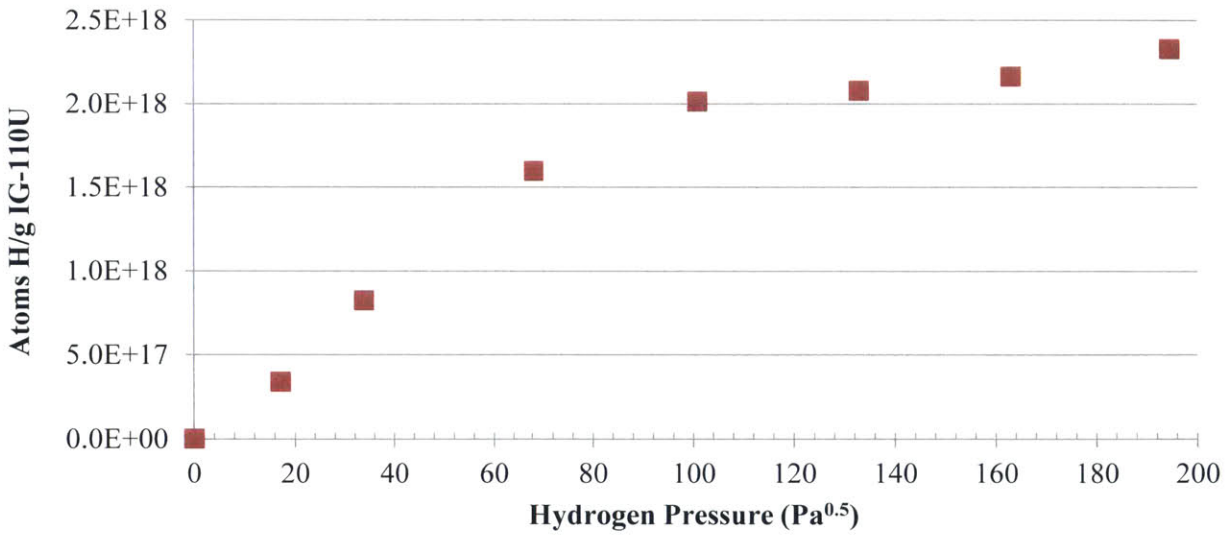

Figure 2.13: IG-110U hydrogen capacity versus the square root of applied hydrogen pressure at 1273 K. Units converted to Atoms H/g graphite from atomic ppm. Original data from ref [88].

2.4.2.3 Radiation effect on graphite hydrogen capacity

The graphite capacity for hydrogen can vary with a number of variables. The preceding section focused mainly on variations with pressure and temperature, but other factors are also important. Graphite specific hydrogen capacity increases with increasing BET surface area [70]. Capacity decreases with increasing degree of graphitization [87]. Capacity can decrease with increasing

crystallite size, but increase with increasing grain size [88,90]. In some cases the difference may be two orders of magnitude.

Radiation damage can also affect the hydrogen capacity in graphite [87,90–93]. Causey et. al. reported on the effects of neutron and ion irradiation on the concentration of tritium trapping sites in Great Lakes H-451 and Graphnol N3M graphite [91]. The original plot from this work is shown in Figure 2.14. The initial trap concentration for un-irradiated N3M is about 2 atom ppm (appm). After neutron irradiation at 600 °C to 10 displacements per atoms (dpa), the trap concentration in N3M increased to about 2000 appm. The trap concentration in N3M after irradiation at 875 °C and 10 dpa was about 400 appm. Comparing the measured trap concentrations at 875 °C with that at 600 °C indicates an annealing effect which reduces the number of traps generated from radiation damage [91].

The data from Figure 2.14 were extracted using the DataThief program and a fit was applied to the data from the ion irradiation only. The equation for the fit is given as a function of dpa in Eq (2.9) and is plotted in Figure 2.15 in order to provide some predictive information.

Atsumi et. al. measured the effect of irradiation on hydrogen capacity in IG-430U and ISO-880U graphites [92]. They observed two types of hydrogen trapping sites: "trap 1" and "trap 2". Trap 1 sites are clusters of interstitial loops with a binding energy of 4.4 eV, and trap 2 sites are dangling carbon bonds at the edge of crystallites with a binding energy of 2.6 eV. Atsumi et. al. found that at low neutron fluences, trap 2 sites are created, but at higher fluences, trap 1 sites are created. Some of the new trapping sites (particularly the trap 2 sites) can be subsequently annealed, resulting in a substantial decrease (by about 50%) in peak hydrogen retention when compared to the same irradiated graphite prior to the anneal [93]. Additionally, the temperature range over which peak retention is achieved is reduced by annealing effects.

After converting the original data from Atsumi et. al. into units of atoms H/g IG-430U, the hydrogen capacity due to each trap type as a function of dpa is plotted in Figure 2.16. This plot illustrates not only the increase in hydrogen capacity with dpa, but also the fact that trap 1 sites are generated more at higher fluences before saturating after about 0.2 dpa. At 0.65 dpa, the hydrogen retention is 140 times higher than in the un-irradiated case. This graphite had been irradiated at 1273 K and the hydrogen capacity was measured by exposing the samples to a saturating hydrogen pressure of 10 kPa. Figure 2.17 shows the hydrogen retention of both IG-430U and ISO-880U irradiated at 1273 K to 0.047 dpa. To construct Figure 2.17, data were extracted from Fig 2 in ref [92]. Then, using the densities of IG-430U and ISO-880U (1.82 g/cm^3 and 1.9 g/cm^3 respectively), the extracted data were converted into units of atoms H/g graphite. The increase in the hydrogen capacity after irradiation to 0.047 dpa is about a factor of 25 in the case of IG-430U and a factor of 20 for ISO-880U.

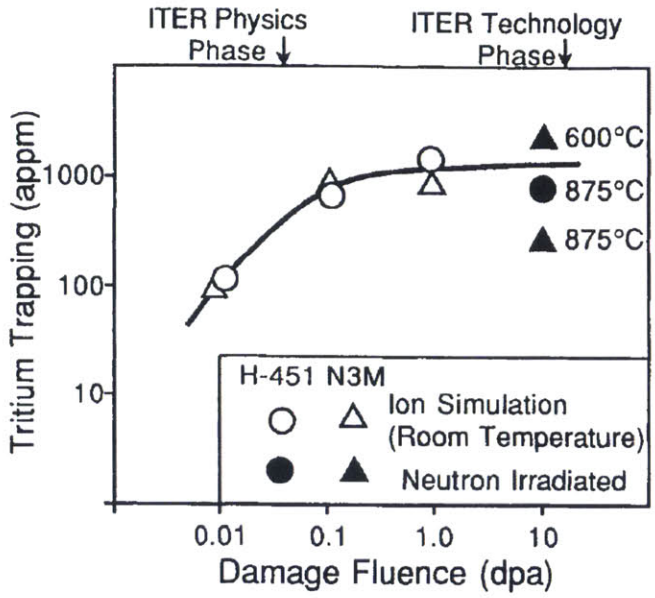

Figure 2.14: Tritium trap concentration (atom ppm) for H-451 and N3M graphite after irradiation at different temperatures. From ref [91].

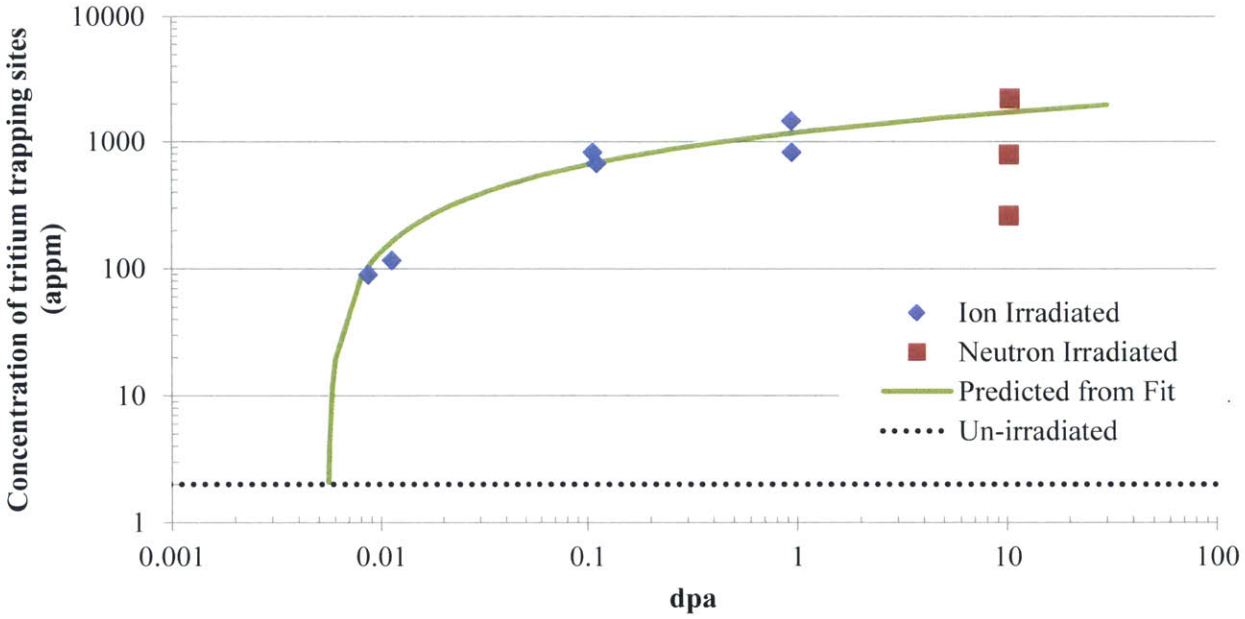

Figure 2.15: Tritium tapping sites in N2M and H-451 after irradiation. Original data points extracted from Figure 3 of ref [91]. A fit (plotted in green) was applied to the original data from the ion irradiation.

$$\text{Number of Tritium Trapping Sites (appm)} = 230.9\ln(dpa) + 1201 \quad (2.9)$$

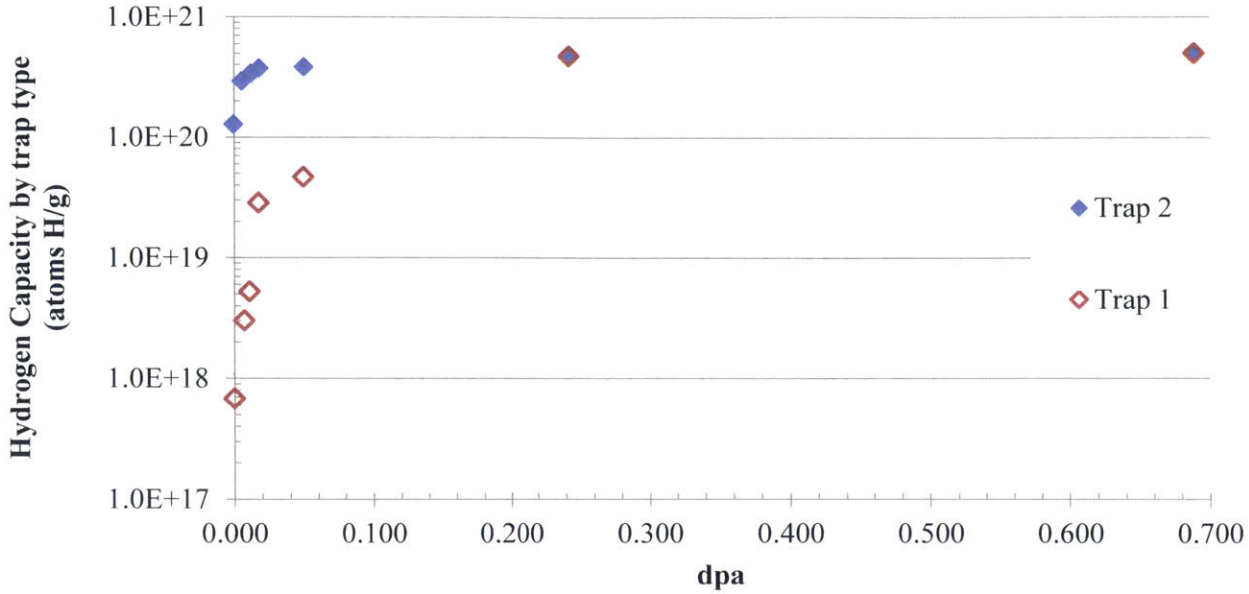

Figure 2.16: Hydrogen capacity on IG-430U converted to units of atoms H/g graphite after data extraction from Figure 1 in ref [92]. Irradiation was at 1273 K and H_2 pressure was 10 kPa.

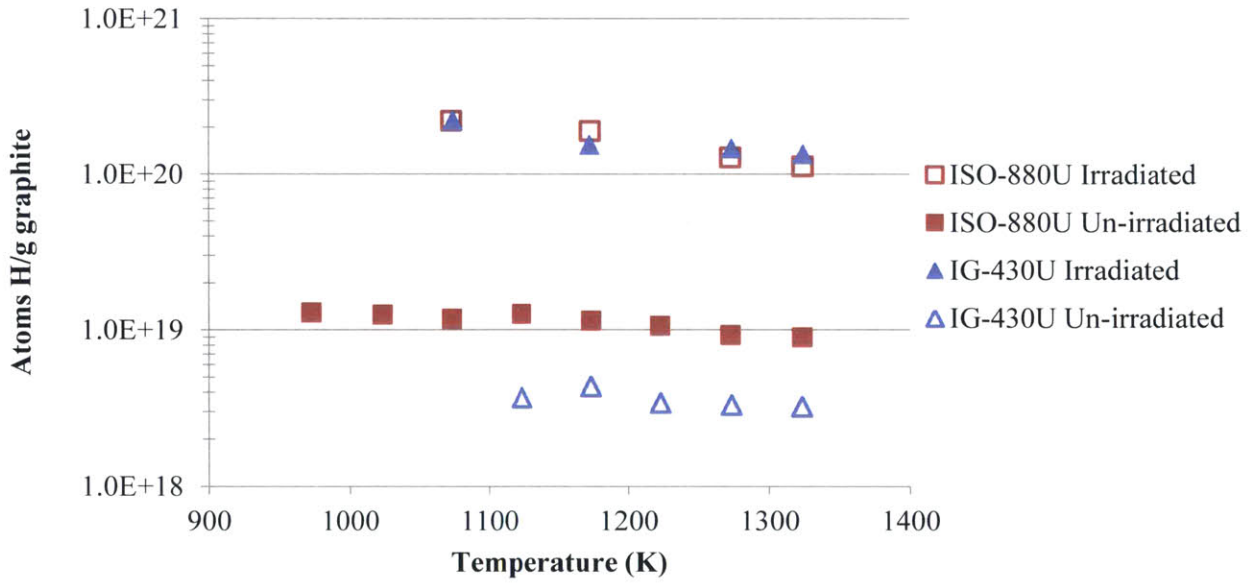

Figure 2.17: Hydrogen retention in ISO-880U and IG-430U. Data converted into current units after extraction from Fig 2 of ref [92]. Irradiation was to 0.047 dpa.

2.4.2.4 Graphite hydrogen uptake kinetics

The rate at which graphite adsorbs hydrogen is also an important factor and is affected by a number of different variables such as pressure, temperature, graphite microstructure, and irradiation.

For example, the absorption rate can decrease with increasing grain size. The hydrogen absorption rates in 8 types of graphite and 1 carbon fiber composite (CFC) were measured at 1273 K and 10 kPa [88]. The reported absorption rate "D/r^2" has units of inverse seconds where D is the hydrogen diffusion coefficient in graphite and r is the grain radius [92]. Although this rate metric is not well explained in the article, the results allow for relative comparisons in the plot reproduced in Figure 2.18. Here, the absorption rates decrease with increasing grain size as the reported grain size is 5 μm for ISO-880U, 14 μm for IG-110U and 40 μm for ETP-10. In the same article, a plot of the hydrogen absorption rate in IG-110U is shown to increase with increasing hydrogen pressure until leveling off at about 30 kPa.

Figure 2.19 reproduces absorption rates in graphite as a function of temperature and pressure. The author shows that the slope of the adsorption rate plots remains virtually constant with temperature and pressure. This indicates that the diffusion process controlling hydrogen absorption is the same at both high and low pressures [94].

The hydrogen diffusion coefficient in graphite increases with temperature, but it also varies with irradiation, and this has implications for the rates of hydrogen uptake on graphite [90,92,93,95]. In the previous section, it was explained that radiation damage can *increase the capacity* of graphite for hydrogen; however, radiation damage *reduces the rate* at which this hydrogen is absorbed. An example of the impact of neutron irradiation on the hydrogen diffusion coefficient in graphite is shown in Figure 2.20. The authors observed an increase in the time it took to reach saturation, and attributed this to the reduction of the diffusion coefficient with irradiation [93].

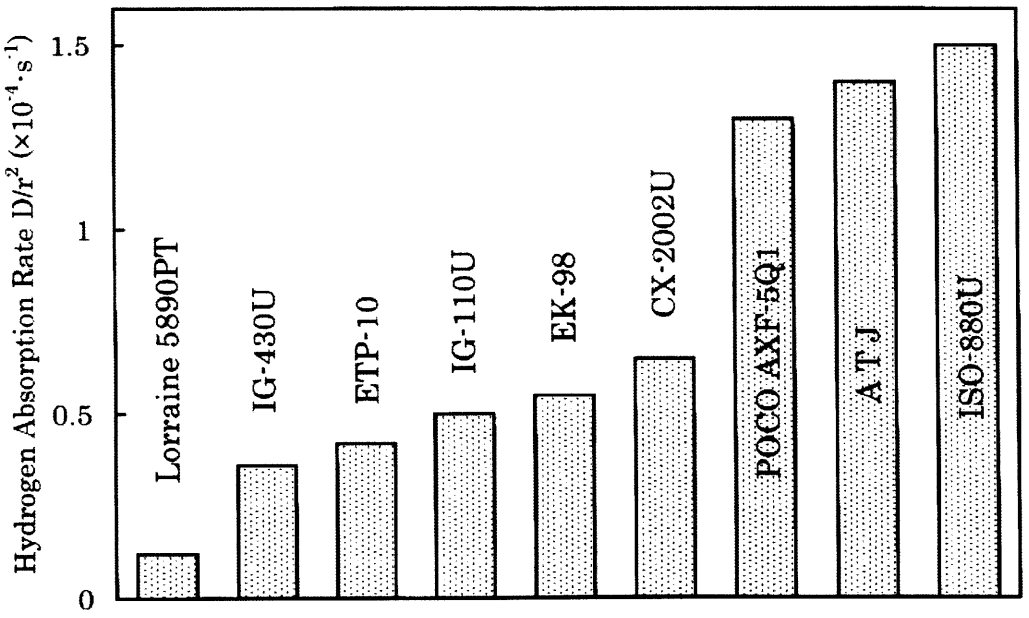

Figure 2.18: Hydrogen absorption rates in graphite and the CFC CX-2002U. T = 1273 K and P = 10 kPa. From [88].

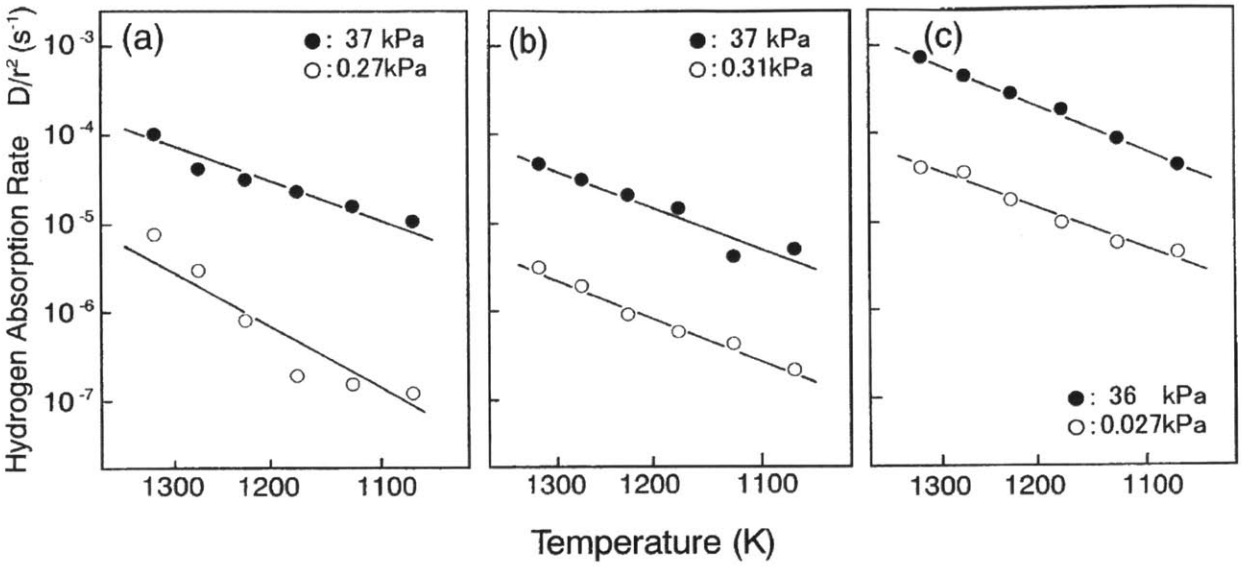

Figure 2.19: Hydrogen absorption rate in (a.) IG-110U, (b.) IG-430U, and (c.) ISO-880U. From [94].

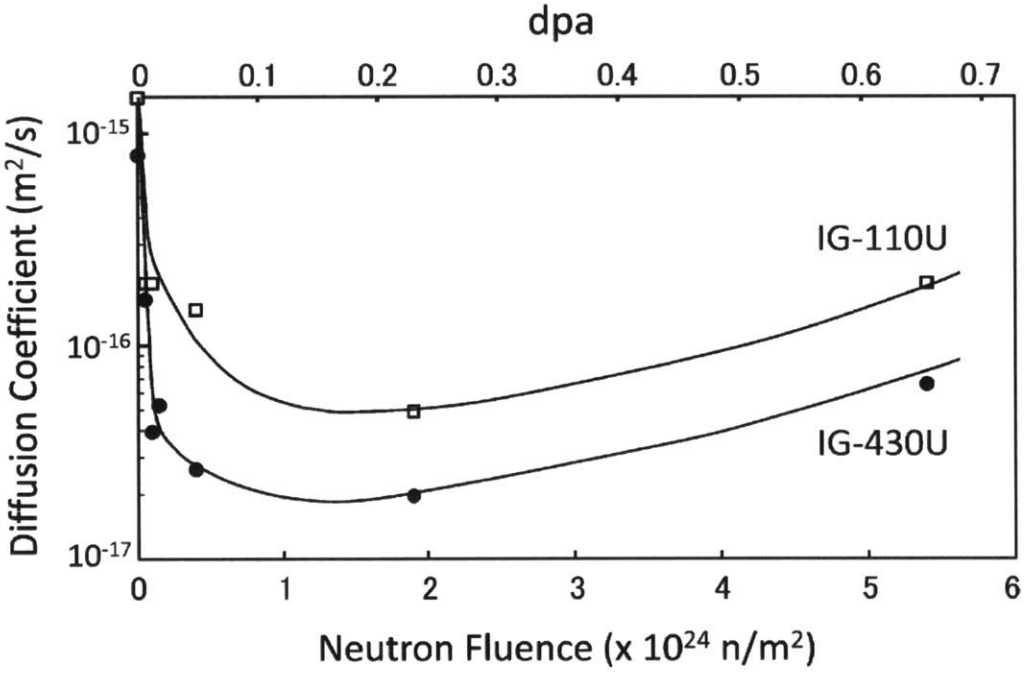

Figure 2.20: Hydrogen diffusion coefficient in irradiated IG-110U and IG-430U at 1273 K and 10 kPa as a function of neutron fluence. From [93].

2.5 Tritium solubility and diffusion in fluoride salts

As Section 3.2 discusses, the chemical redox potential in molten salt mixtures determines the chemical state in which tritium will exist. Whether tritium exists in the fluoride salt as TF or T_2 will impact its behavior in terms of its solubility, diffusivity, permeability, and corrosivity [54,96,97]. This can make interpreting experimental H_2 diffusivity and solubility data from the literature somewhat difficult because some tests employ redox control (in order to ensure that most hydrogen exists as H_2 in flibe) and others do not (which means that some hydrogen will exist as HF and some will exist as H_2). As will be discussed, the experimental apparatus used for the measurements may also affect the results. Relatively little data are available for the diffusivity and mass-transfer of hydrogen isotopes in flibe from the MSRE experiments. Most recent studies for hydrogen behavior in molten fluoride salts were undertaken mainly from a perspective of the use of fluoride salts as a breeder blanket in fusion reactors.

All literature sources agree that the solubility of TF and T_2 in fluoride salts is according to Henry's law [57,98–101]. Henry's law, expressed in Eq (2.10), states that the concentration c of a gas in a liquid solution is proportional to the product of the partial pressure p of that gas over the solution with the Henry's law constant k_{Henry} at a given temperature. Where some of these reports differ is on the chemical form in which the hydrogen is dissolved in the salts in the experiments. All reports indicate that H_2 dissolves as the H_2 molecule in flinak [54,99,102]. It has also been suggested that flinak (LiF-NaF-KF) is more easily maintained in a reducing condition than flibe (LiF-BeF_2) [54]. However, other sources explain that salts (such as flinak) which lack a Lewis acid component (such as BeF_2) will be more corrosive because they do not have a Lewis acid to capture free F^- ions [103]. This might account for the strong redox effects in experiments with flibe. Most reports contend that H_2 dissolves in flibe as molecular hydrogen (H_2), but insufficiently reducing conditions can cause H_2 to react and become HF [51,53,54,98,99,101,102,104–106]. One report contends that, in flibe, H_2 dissolves in the salt as ionic hydrogen (H^+) even under reducing redox control [100]. This assertion may be due to either incomplete redox control or an effect having to do with the measurement apparatus. If the argon cover gas in the experiment was not dry, moisture will generate HF in flibe. Also, the experimental apparatus used in ref [100] was different than that used by Malinauskas et. al. [98,106] in that it required hydrogen recombination at a Ni/flibe interface prior to its diffusion in flibe.

Virtually the only data for HF solubility in flibe come from Field and Shaffer [57]. The Henry's law constant from Field and Shaffer was converted to units of [mol HF/m^3 flibe-Pa] using the molar mass (32.89 g/mol) and density of flibe. Eq (2.11) shows the correlation for the density of flibe versus temperature used in this conversion [45]. Here ρ_{flibe} is in units of kg/m^3 and T is units of Kelvin. Figure 2.21 shows the three data points from Field and Shaffer after conversion to the current units. An exponential fit was applied to these data points in order to yield Eq (2.12), the Henry's law constant (in units of mol HF/m^3 flibe-Pa) for HF in flibe as a function of temperature

(°C) from 500 to 700 °C. Here, it is approximated that the Henry's law constant for TF, $k_{Henry,TF}$, should be nearly the same as that for HF, $k_{Henry,HF}$.

The most reliable data for true H_2 solubility (not influenced by HF production) is that from Malinauskas and co-workers [98,106]. Others have reported the solubility for H_2 in flibe, but they acknowledge that their data more closely reflect the solubility for HF in flibe rather than for H_2 [53,100,104]. The Ostwald constant for the solubility of H_2 in flibe from Malinauskas and Richardson (ref [98]) was converted to a Henry's law constant in units of [mol H_2/m^3 flibe-Pa] and these points are plotted in Figure 2.22. An exponential best-fit for these data produced the expression in Eq (2.13) for the Henry's law constant of H_2 in flibe from 500 to 800 °C. In this equation $k_{Henry,H2}$ has units of mol H_2/m^3 flibe-Pa and T is in degrees Celsius. Here, it is assumed that the solubility of T_2 in flibe should be roughly the same as that for H_2 such that $k_{Henry,T2} = k_{Henry,H2}$. Figure 2.21 and Figure 2.22 show that the solubility of HF in flibe is about 1000 times greater than the solubility of H_2. Additionally, the solubility of HF decreases with increasing temperature, but the solubility of H_2 increases with increasing temperature. In flinak, the Henry's law constant for H_2 is given by Eq (2.14) in units of mol H_2/m^3 flinak-Pa [99]. The activation energy in the exponent was corrected from the erroneous value of 34.4 J/mol to 34400 J/mol. In this equation, R is the universal gas constant (J/mol-K) and T is in Celsius. The H_2 solubility in flinak is 1000 + times higher than the H_2 solubility in flibe, and decreases with increasing temperature. The HF solubility in flibe is up to 1000 times higher than the H_2 solubility in flibe.

$$c = p \times k_{Henry} \tag{2.10}$$

$$\rho_{flibe} = 2415.6 - 0.49072 \times T \tag{2.11}$$

$$k_{\text{Henry, flibe, HF}} = 1.707 \times 10^{-3} e^{-4.260 \times 10^{-3} T} \tag{2.12}$$

$$k_{\text{Henry, flibe, H}_2} = 2.714 \times 10^{-8} e^{4.235 \times 10^{-3} T} \tag{2.13}$$

$$k_{\text{Henry, flinak, H}_2} = 3.98 \times 10^{-7} \exp\left(\frac{34.4 \times 10^3}{RT}\right) \tag{2.14}$$

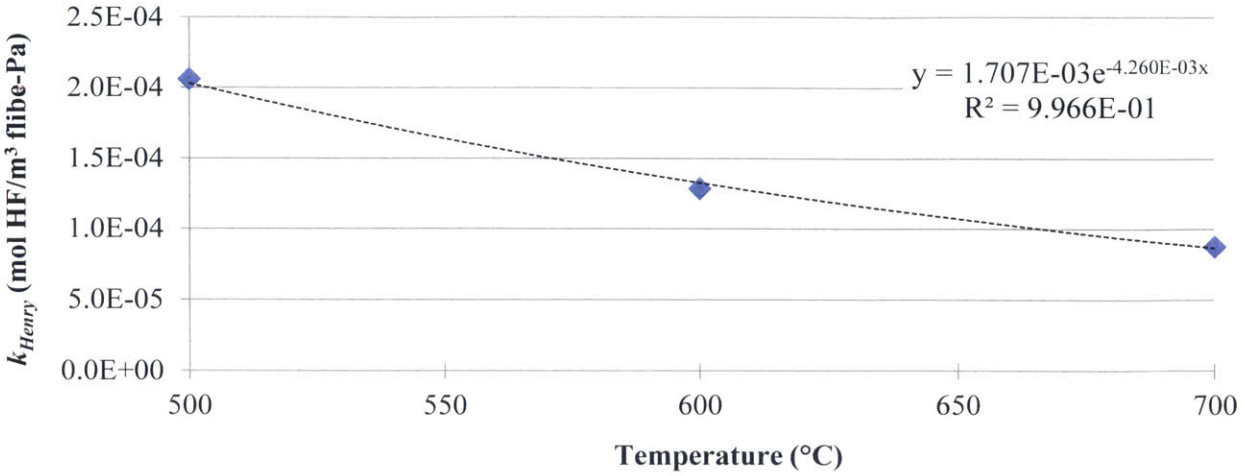

Figure 2.21: Henry's law constant for HF in flibe. Data points are from ref [57]. Exponential fit was applied.

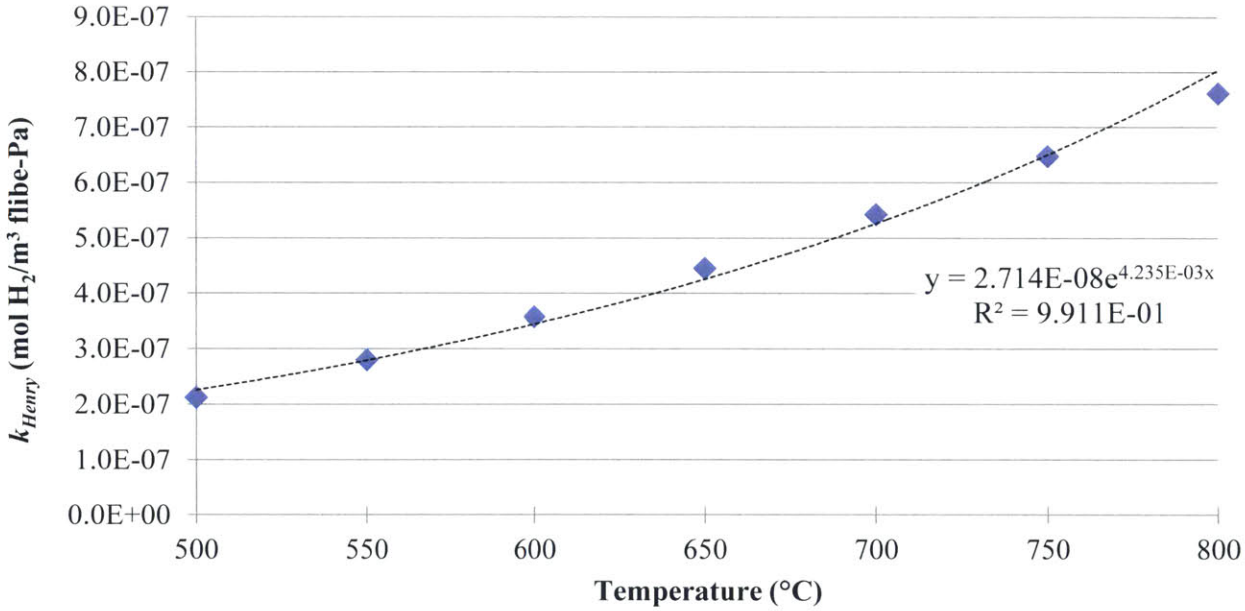

Figure 2.22: Henry's law constant for H_2 in flibe. Data points are from ref [98]. Exponential fit was applied.

The diffusivity of T_2 in flibe was measured by Calderoni et. al. and the diffusivity of H_2 in flinak was measured by Fukada and Morisaki [99,100]. Oishi et. al. measured the diffusivity of TF in flibe, and the diffusivity of D_2 in flibe was measured by Anderl et. al. [53,105]. The empirical equation determined by Calderoni and co-workers for T_2 diffusivity (m^2/s) in flibe is given in Eq (2.15). Here, T is in K and R is the universal gas constant in J/mol-K. The equation given by Fukada and Morisaki for the diffusivity of H_2 in flinak is not correct. It does not match the correct data plotted in Figure 5 of reference [99]. A program was used to extract the values of the original fit from Fukada and

Morisaki's Figure 5. A power fit was then applied to these extracted data in order to arrive at Eq (2.16), where $D_{H2,\,flinak}$ is in units of m^2/s and T is temperature in K. A program was used to extract the data published by Oishi et. al. for TF diffusivity in flibe [105]. These data were then fit with a power function given in Eq (2.17) where T is temperature in Kelvin and the diffusivity is in units of m^2/s. Typical forms for the temperature dependence of the diffusivity are given by Arrhenius-type equations. A power fit was used here simply because it fits the extracted data more exactly.

$$D_{T_2,\,flibe} = 9.3\times10^{-7}\exp\left(\frac{-42\times10^{3}}{RT}\right) \tag{2.15}$$

$$D_{H_2,\,flinak} = 2.4537\times10^{-29}T^{6.9888} \tag{2.16}$$

$$D_{TF,\,flibe} = 6.4854\times10^{-26}T^{5.7227} \tag{2.17}$$

For comparison purposes, the equations above are plotted in Figure 2.23. It is evident that the diffusivity in flinak is higher than the diffusivity in flibe, even when the isotope effect is accounted for. The cause of this stems from the fact that flibe maintains some structure even when molten. As was discussed in Section 1.5.2, when molten, the BeF_2 component of flibe arranges in a polymeric type structure amounting to tetrahedra of BeF_4^{2-} [101]. This structure may inhibit the free movement of dissolved species in flibe. Flinak lacks any long-range ordering. Assuming the difference between the TF diffusivity from Oishi and the T_2 diffusivity from Calderoni is larger than the experimental uncertainty, TF might display a higher diffusivity than T_2 because TF dissolves in flibe as the T^+ and F^- ions. A T^+ ion would be roughly half the size of a T_2 molecule, enabling it to move more easily through flibe.

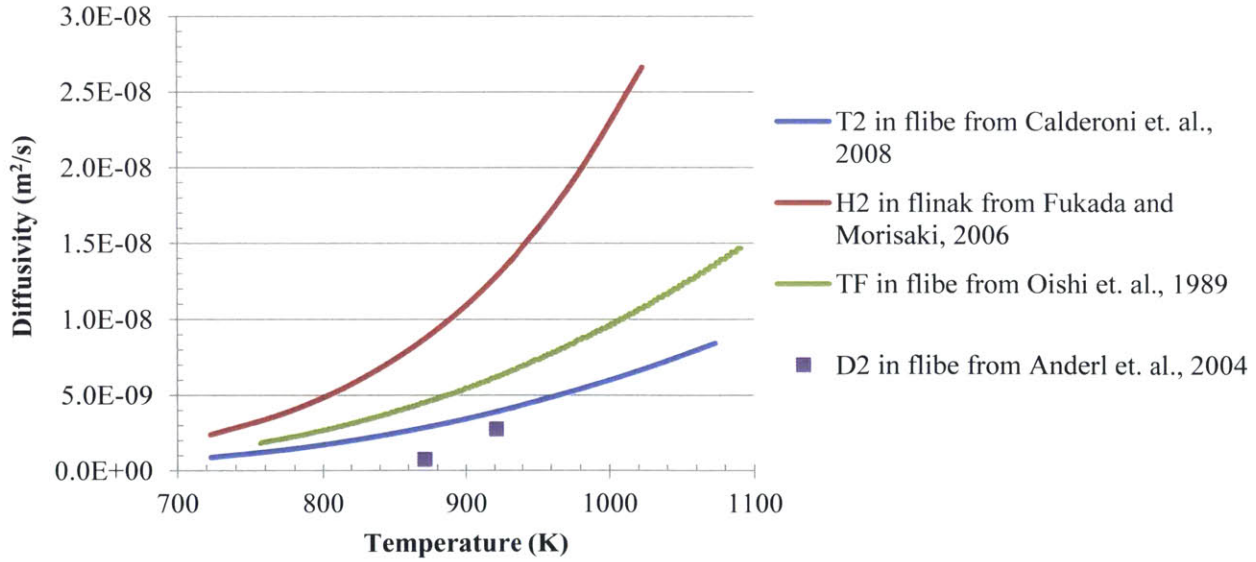

Figure 2.23: Diffusivity of T_2, D_2, and TF in flibe. Diffusivity of H_2 in flinak. Plotted from Equations (2.15), (2.16), and (2.17).

2.6 Tritium solubility and diffusion in metals and metal oxides

Much of the data for hydrogen (especially tritium) diffusion in metals originates with nuclear fusion programs which use tritium and/or deuterium as fuel, and several good data reviews are available in the literature. Hydrogen diffusion through metals begins with dissociation on the metal surface and subsequent dissolution of the atomic hydrogen in the metal [71]. In the presence of a concentration gradient, the atomic hydrogen diffuses down the concentration gradient and through the metal lattice to the opposite face of the metal. After passing through the metal, atomic hydrogen can recombine into molecular form on the free surface of the metal.

The diffusion coefficient (denoted as D with common units of m^2/s) generally adheres to an Arrhenius dependence on temperature as depicted in Eq (2.18) where D_o is the constant pre-exponential factor, E_D is the diffusion activation energy, R is the universal gas constant, and T is the temperature. For hydrogen in metals, the solubility (also called the Sievert's law constant) follows an Arrhenius dependence as in Eq (2.19). Here, K_o is constant and ΔH_s is the heat of solution. The Sievert's law constant K_s (commonly in units of mol H_2/m^3 metal-$MPa^{0.5}$) can be used to determine the concentration (c_{H2}) at equilibrium of hydrogen in metal at a given temperature for an applied partial pressure of hydrogen (p_{H2}) above the metal according to Eq (2.20). The permeability of hydrogen through metal is defined as the steady-state diffusional transport of hydrogen through a material which has a hydrogen partial pressure gradient across its thickness [71]. Mathematically, permeability (Φ) is the product of solubility K_s with the diffusion coefficient D as expressed in Eq (2.21). At equilibrium, the steady-state flux of hydrogen across a metal membrane is a function of the partial pressure of hydrogen on each side of the membrane according to Eq (2.22). In this equation, D and K_s are the diffusion coefficient and solubility of hydrogen in metal, respectively. The partial pressure of hydrogen at side "a" of the metal membrane is given by $p_{H2,a}$. The partial pressure of hydrogen at side "b" of the metal membrane is given by $p_{H2,b}$, and x is the thickness of the metal membrane. With the partial pressures in units of MPa, x in units of meters, and D and K_s with the units prescribe above, j_{H2} has units of moles H_2/m^2-s. Classical rate theory predicts an isotope effect such that the ratio of the diffusivities of hydrogen isotopes is related according to Eq (2.23). For T compared to H, the tritium diffusivity should be about 60% of the protium diffusivity.

$$D = D_o \exp\left(-E_D / RT\right) \tag{2.18}$$

$$K_s = K_o \exp\left(-\Delta H_s / RT\right) \tag{2.19}$$

$$c_{H_2} = K_s \sqrt{p_{H_2}} \tag{2.20}$$

$$\Phi = K_o D_o \exp\left(-\left(\Delta H_s + E_D\right) / RT\right) \tag{2.21}$$

$$j_{H_2,a\to b} = \frac{D \times K_s}{x}\left(\sqrt{p_{H_2,a}} - \sqrt{p_{H_2,b}}\right) \tag{2.22}$$

$$\frac{D_T}{D_H} = \sqrt{\frac{m_H}{m_T}} \tag{2.23}$$

A number of studies have measured and compared the available data for the solubility, diffusion and permeation of hydrogen through various metals. The data compiled in four such studies are given in Table 2.5 through Table 2.8. Additional data are available from other journal articles [107,108]. In each case, the pre-exponential constants and the exponential constants are given such that the Arrhenius equations can be used to calculate the permeability, diffusivity, or solubility as a function of temperature. In Table 2.5, the units for "D^*" and the Arrhenius equation for diffusivity were corrected from mistakes in ref [109].

Between these studies, the diffusion coefficient for Type 316 SS, for example, may vary by a factor of two or three, and the isotope effect lies within the data scatter. After comparing data from different reports, the data from Tanabe (ref [110]) will be used for Type 316 SS in the tritium transport model developed in this thesis.

Certain metals, such as tungsten and beryllium, have much lower hydrogen permeabilities than austenitic stainless steels. From the data in Table 2.8, at 700 °C, W and Be have hydrogen permeabilities of 1.0E-11 and 7.4E-12 mol H_2/m-s-$MPa^{0.5}$, respectively. From the data in Table 2.6, at 700 °C, Type 316 SS and Ni have permeabilities of 1.3E-7 and 8.1E-7 mol H_2/m-s-$MPa^{0.5}$, respectively. Palladium has one of the highest hydrogen permeabilities among metals. At 700 °C, Pd has a hydrogen permeability of 3.2E-5 mol H_2/m-s-$MPa^{0.5}$ [111]. This suggests that if the goal is to contain tritium, metals with a low permeability (W, stainless steel, etc.) are better for this purpose. On the other hand, if the goal is to remove tritium from a specific part of the system, metals with a high-permeability (such as Pd) could be used as permeation windows such that the tritium preferentially exits the system through the window. The effect of permeation windows on tritium transport in FHRs will be investigated using the model developed herein.

If using permeation windows in order to deliberately remove tritium from specified parts of an FHR might be desirable, using permeation barriers to prevent un-wanted tritium escape through FHR piping would also be desirable. In the preceding paragraph it was shown that W and Be have hydrogen permeabilities 4 or 5 orders of magnitude lower than Type 316 SS. While Be metal is not thermodynamically stable in flibe, W would be. Metal oxides are also renowned for their low hydrogen permeabilities [71]. A term called the permeation reduction factor (PRF) is used as a metric for comparing the effectiveness of permeation barriers. The PRF is the ratio of the permeability of a material without a permeation barrier to the permeability of a material with a permeation barrier according to Eq (2.24) [71]. Hollenberg et. al. provide a review of PRFs for permeation barrier coatings applied to steel and stainless steel base metals [112]. A summary of this review is reproduced in Table 2.9. For stainless steels, the natural oxide layer is mainly chromium oxide (Cr_2O_3) which affords a PRF of 10 to 20 on austenitic stainless steels [112,113]. Specially applied coatings may offer higher PRFs of 1000 or higher. The Space Nuclear Auxiliary Power (SNAP) program utilized a uranium-zirconium-hydride fuel/moderator clad in Hastelloy-N [114–

116]. In order to retain the hydrogen moderator within the fuel, the inside of the Hastelloy-N was coated in a hydrogen permeation barrier comprised of various metal oxides (see Table 1 of ref [114] and Table 2 of [115]) having permeation reduction factors of 1000 or higher compared to the base metal [115]. While metal oxides make effective hydrogen permeation barriers, they are not stable when facing fluoride salts. Thus the use of a metal oxide hydrogen permeation barrier in FHRs would have to be restricted to application on air or vacuum-facing surfaces of pipes and vessels. Section 6.6.1 investigates the effects on tritium transport of varying the PRF and materials selection (such as using W in place of Type 316 SS) in FHR heat exchangers.

$$PRF = \frac{\Phi_{\text{bare material}}}{\Phi_{\text{material with permeation barrier}}} \tag{2.24}$$

Table 2.5: Constants to calculate permeability (Φ) and diffusion coefficients (D) from Arrhenius equations given in the table for isotopes of hydrogen in various grades of stainless steel [109].

Materials	Isotope	Temperature range (K)	Input pressure (MPa)	$\Phi=\Phi^{\circ}\exp(-H_{\Phi}/RT)$		$D=D^{*}\exp(-H_{D}/RT)$		Ref.
				Φ° (mol H_2/m·s$\sqrt{\text{MPa}}$)	H_{Φ} (kJ/mol)	D° (m^2/s)	H_D (kJ/mol)	
304L	D	573~1,073	1.33×10^{-7}~0.1					(6)
304, 304L	D	650~1,050	10^{-10}~10^{-7}	1.18×10^{-5}	64.04	3.5×10^{-8}	42.42	(7)
304	H	403~673	0.1		54.3			(9)
304	H	523~873	1.3×10^{-4}~0.54		74.4			(10)
304	T	373~573				1.24×10^{-6}	56.8	(11)
304	H	373~873	0.01~3.0	1.06×10^{-3}	64	2.72×10^{-6}	54.3	(12)(8)
304	T	298~498	5×10^{-4}~7×10^{-3}			1.8×10^{-6}	58.5	(13)
304, 304L, 304N, 309, 309S, 310	D	385~713	0.10~0.3	8.4×10^{-5}	59.8	4.7×10^{-7}	53.9	(14)(15)
304	H	673~1,073	1.33×10^{-3}~7.98×10^{-2}	8.78×10^{-4}	72.06			(16)
304	H	910~982	2.66×10^{-6}~2.13×10^{-6}					(17)
304	T	573~723	1.3×10^{-14}~11.3×10^{-9}		57.76			(18)
304	H	648~871	0.1					(19)
309S	H	423~873	1.3×10^{-4}~0.13	6.0×10^{-6}	58.9	1.2×10^{-6}	54.8	(20)(8)
309S	D	〃	〃	4.8×10^{-6}	59.8	1.2×10^{-6}	55.6	(20)(8)
309	D	523~723	1.32×10^{-3}~0.1	1.2×10^{-4}	62.3			(21)
310	H	472~779	4.4×10^{-4}~4.4×10^{-3}	2.84×10^{-4}	56.56	5.15×10^{-7}	48.82	(8)
310	D	〃	〃	2.49×10^{-4}	55.84	3.20×10^{-7}	48.07	(8)
316	H	673~1,073	1.33×10^{-3}~7.98×10^{-2}	4.46×10^{-4}	65.29			(16)
316	T	500~1,000	4.65×10^{-3}~0.104	3.43×10^{-4}	68.06			(22)
316	H		10^{-7}~10^{-6}	1.41×10^{-3}	63.51			(23)
321	H	573~1,073	0.01~3.0	3.31×10^{-3}	64.80	7.33×10^{-7}	52.30	(24)(8)
446	H	977~1,481	0.107					(25)
21-6-9	D	523~723	1.32×10^{-3}~0.1	3.6×10^{-4}	66.0			(21)
A-286	D			1.4×10-4	62.1			(21)

Table 2.6: Permeability, diffusivity, solubility of hydrogen ($^1H_2$) in different alloys and metals. From ref [110].

	Permeability		Diffusivity		Solubility	
	mol/m s $MPa^{1/2}$	kJ/mol	m^2/s	kJ/mol	$mol/m^3MPa^{1/2}$	kJ/mol
304 SS	6.25×10^{-4}	65.4	8.25×10^{-7}	49.7	7.58×10^{2}	15.7
316 SS	2.70×10^{-4}	61.7	6.32×10^{-7}	47.8	4.27×10^{2}	13.9
YUS 170	1.29×10^{-4}	64.3	1.70×10^{-7}	37.6	7.59×10^{3}	26.7
Inconel 600	9.50×10^{-4}	66.2	1.36×10^{-7}	37.7	1.98×10^{3}	28.5
Inconel X	2.39×10^{-5}	54.1	4.62×10^{-8}	36.6	5.17×10^{2}	17.5
Nichrom	2.20×10^{-4}	60.3	1.11×10^{-7}	37.2	1.98×10^{3}	23.1
Monel	2.63×10^{-4}	51.6	1.43×10^{-7}	34.4	1.84×10^{3}	17.2
Cu	3.66×10^{-5}	60.5	2.26×10^{-7}	29.3	1.37×10^{2}	31.2
Ni	7.08×10^{-4}	54.8	7.43×10^{-7}	44.1	9.53×10^{2}	10.7
γFe	6.34×10^{-4}	71.6*	6.63×10^{-7}	44.9**	9.55×10^{2}	26.7

*: ref. 15 **: ref. 16

Table 2.7: Permeability (Φ), diffusivity (D), and solubility (K) constants for hydrogen ($^1H_2$). Data converted into current units from original data in ref [117].

	E_Φ (kJ/mol)	Φ_o (mol H_2/m-s-$MPa^{0.5}$)	E_D (kJ/mol)	D_o (m^2/sec)	ΔH (kJ/mol)	K_o (mol H_2/m^3-$MPa^{0.5}$)
SUS 316 L	66.6	8.17E-04	54.0	1.30E-06	12.5	662.9
Inconel 600	63.7	7.37E-04	42.5	4.90E-07	21.2	1491.5
Inconel 750	64.6	9.32E-04	53.1	1.60E-06	11.6	580.0
Nimonic 80A	64.6	9.32E-04	53.1	1.40E-06	11.6	704.3
Hastelloy X	64.6	8.29E-04	43.4	4.90E-07	21.2	1698.6

Table 2.8: Diffusivity (D) and solubility (K) constants for hydrogen ($^1H_2$). From ref [71].

Alloy	*Diffusivity*		*Solubility, Φ/D*	
	$D = D_0 \exp(-E_D/RT)$		$K = K_0 \exp(-\Delta H_s/RT)$	
	D_0 ($m^2\ s^{-1}$)	E_D ($kJ\ mol^{-1}$)	K_0 ($mol\ H_2\ m^{-3}\ MPa^{-1/2}$)	ΔH_s ($kJ\ mol^{-1}$)
Beryllium	3×10^{-11}	18.3	18.9[a]	16.8[a]
			5.9×10^{6}[a]	96.6[a]
Graphite	9×10^{-5}	270	19	−19.2
Aluminum	2×10^{-8}	16	46	39.7
Vanadium	3×10^{-8}[b]	4.3[b]	138	−29
RAFM steels[c]	1×10^{-7}	13.2	436	28.6
Austenitic stainless steel	2×10^{-7}	49.3	266	6.9
Nickel	7×10^{-7}	39.5	564	15.8
Copper	1×10^{-6}	38.5	792	38.9
Zirconium	8×10^{-7}	45.3	3.4×10^{7}	35.8
Molybdenum	4×10^{-8}	22.3	3300	37.4
Silver	9×10^{-7}	30.1	258	56.7
Tungsten	6×10^{-4}	103.1	1490	100.8
Platinum	6×10^{-7}	24.7	207	46.0
Gold	5.6×10^{-8}	23.6	77 900[d]	99.4[d]

Table 2.9: Summary of PRFs for various hydrogen/tritium barriers on base metals. From ref [112].

Barrier coating	Base metals	Permeation reduction
Aluminide (or Al_2O_3)	SS316, MANET, TZM, Hastelloy-X, Ni	10 to above 10000
TiC, TiN, TiO_2	SS316, MANET, TZM, Ti	Less than 10 to above 10000
Cr (or Cr_2O_3)	SS316	10
Si	Steels	10
BN	304SS	100
Sn	Ferritic steel	Rapidly degraded
H_3PO_4 glass	304SS	100 (unstable)
N	Iron	10–20

2.7 Chapter summary of tritium behavior in FHR reactor materials

In order to develop a model of tritium transport in an FHR, tritium production rates, tritium behavior in the salt, tritium behavior on graphite, and tritium diffusion in structural metals must be considered. This chapter reviewed, collected, processed, and selected data for use in the tritium transport model developed in Chapter 5. It was shown that FHRs produce more tritium per MWt than other power reactors. Additionally, because this tritium can exist as T_2, it will permeate through structural metals. Tritium in LWRs and HWRs is often in the form of T_2O which is not diffusive in metals and is more easily contained. Experience from the MSRE showed that graphite is a significant sink for tritium, and a comprehensive review of tritium sorption/desorption from graphite was given. These data are necessary for building a reactor system-level model of tritium transport in the FHR.

3 Fluoride Salt Coolant Chemistry and Material Compatibility

The baseline FHR salt selection is flibe, a lithium-beryllium-fluoride salt. Other salt candidates exist; however, all of them are fluoride-based salts which have similar chemical behavior. Chloride salts are generally neutronically and chemically inferior to their fluoride counterparts. Some neutronic and thermo-physical properties of flibe were discussed in Section 1.5.2. This chapter will discuss the chemical behavior of flibe and how it pertains to FHRs. Relationships for the chemical redox potential will be derived which will be used in a number of following sections, including: the analysis of fission product behavior in FHRs (Section 4.1), an evaluation of the compatibility of Type 316 stainless steel in the FHR, tritium production and transport (Chapter 5), and corrosion modeling in the FHR (Section 5.8). Plots of the equilibrium Cr corrosion product concentration in the salt as a function of temperature and redox potential will be presented. Using Henry's law, the concentrations of TF and T_2 in the salt are linked to the chemical redox potential of the salt.

3.1 Chemical stability and corrosion in flibe

Much of chemistry involves determining which reactions are energetically favorable and which reactions are not. This provides a relative comparison of which compounds are chemically stable in a given chemical environment and which compounds are not. Due to extensive research on fluoride-based salts in the MSRE program, equilibrium constants for important reactions, Gibbs free energies of formation for important compounds, and other chemical thermodynamic data are available in several reports from the MSRE [61,118,119].

Perfectly clean flibe will not corrode structural metals. Rather, corrosion in flibe is due to impurities present in the flibe. For a metal or alloy to be compatible with a molten salt, the salt constituents must not be chemically reduced (accept electrons) upon contact with the metal. Conversely, the structural metals must not be oxidized (lose electrons) upon contact with the salt [120]. A good way to visualize the relative stability of salt constituents and structural metals is with the help of an Ellingham diagram which plots the Gibbs free energy of formation as a function of temperature for various fluorides of interest. The Gibbs free energy indicates the chemical potential energy of a system, and reactions proceed in directions which minimize this energy. A reaction is spontaneous if its Gibbs reaction free energy is negative. On the other hand, a Gibbs free energy of formation denotes the energy change in a system due to the formation of 1 mole of a substance in its standard state from its constituent elements in their standard states. The Gibbs free energy of formation can be used to compare chemical stabilities of different compounds. The more negative the Gibbs free energy of formation, the more stable that compound will be. Figure 3.1 shows an Ellingham diagram for various fluorides of structural metals and flibe constituents. In order to construct Figure 3.1, the formation free energies for the compounds listed were calculated from empirical relations compiled by Baes [118]. These calculated formation free energies were then normalized by the number of moles of fluorine atoms in the compound of interest.

The more negative the Gibbs free energy of formation for a given fluoride, the more stable that fluoride will be. Figure 3.1 shows that LiF and BeF_2 have two of the most negative formation free energies, making them two of the most stable fluorides. Fluorides of major structural metals (Cr, Ni, Fe) have formation free energies more positive than LiF and BeF_2. This means that in pure flibe, structural metal fluorides will not form and metallic Cr, Ni, and Fe will be stable. Any element or compound which can form a fluoride having a formation free energy more positive than that of structural metal fluorides is capable of corroding structural metals. Of the structural metals, Cr makes the most stable metal fluoride. This means that most corrosion in the FHR will be through selective oxidation of Cr.

Oxidation can occur if Cr metal reacts with oxidizing impurities in the coolant. Figure 3.1 shows that HF has a Gibbs formation free energy more positive than that of the fluorides of structural metals. This means that HF can corrode structural metals and could pose a significant corrosion problem [121]. Tritium (in the form of ^3HF, also written as TF) is an impurity generated in the salt from neutron transmutation. In flibe, this TF dissolves as the ions T^+ and F^-. It is also possible for moisture to react with flibe to produce HF according to Eq (3.1) [122]. Eq (3.2) shows that this dissolved TF (or HF) will oxidize Cr to CrF_2, and a byproduct of this reaction is $T_{2(g)}$ which is highly mobile through heat exchangers.

Although they can be reduced during salt purification, it is common for impurity Fe and Ni fluorides to exist in as-prepared flibe [123]. Fe and Ni fluorides can actually corrode metallic Cr. Figure 3.1 shows that NiF_2, and FeF_2 are less stable fluorides than CrF_2. Eq (3.3) and Eq (3.4) show how solid Cr will react to replace less-stable impurity iron and nickel fluorides in solution.

In light water reactors, corrosion products are metal oxides which are insoluble in water. Often, this means that a stable oxide layer can form on the surface of the metal, protecting the underlying metal through passivation. In fluoride salt-cooled reactors, corrosion products are metal fluorides. Metal fluorides are soluble in fluoride salts. This means that corroded metal fluorides dissolve into the salt, and material is lost from the underlying metal. Thus, protecting metals in the FHR by passivation on the metal surface is not possible. The best means to protect the metal in an FHR is to keep the salt clean from impurities and/or impose a chemically reducing condition in the salt. Effective structural materials in fluoride salt systems are ones which exist in near thermodynamic equilibrium with the salt [40].

$$H_2O + BeF_{2(l)} \rightarrow BeO + 2HF_{(l)} \quad (3.1)$$

$$2TF_{(d)} + Cr_{(s)} \rightarrow CrF_{2(d)} + T_{2(g)} \quad (3.2)$$

$$NiF_{2(d)} + Cr_{(s)} \rightarrow CrF_{2(d)} + Ni_{(s)} \quad (3.3)$$

$$FeF_{2(d)} + Cr_{(s)} \rightarrow CrF_{2(d)} + Fe_{(s)} \quad (3.4)$$

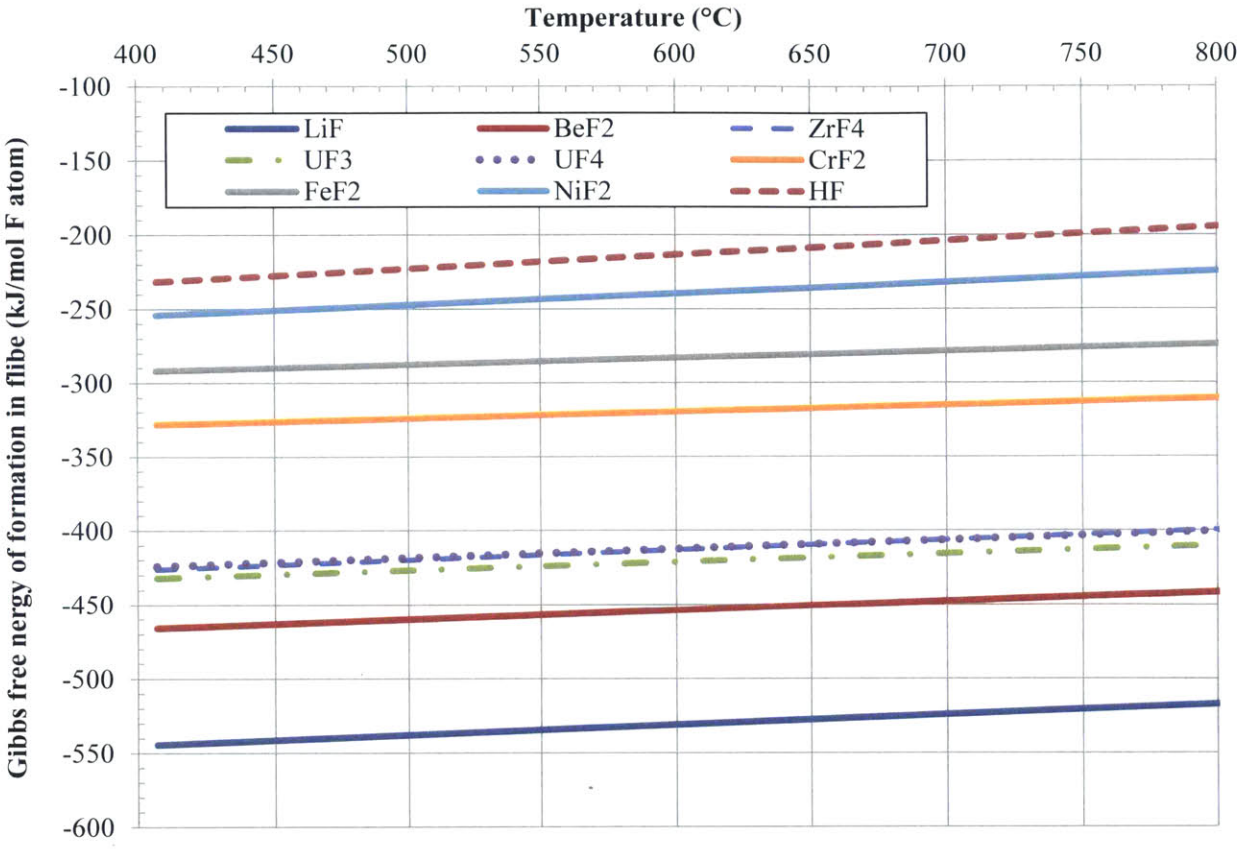

Figure 3.1: Ellingham diagram (Gibbs free energy of formation) for compounds dissolved in flibe. Calculated from data in [118].

3.1.1 Mechanisms of corrosion

In the preceding section, it was established that in structural alloys comprised of Fe, Ni, and Cr, Cr is the most vulnerable element for corrosion by impurities in flibe. In fact, an analysis of corrosion in fluoride salts can focus on Cr (the least noble structural metal) because appreciable Fe and Ni corrosion does not occur [35,40,124]. A similar phenomenon occurs in sodium-cooled reactors where Ni and Cr are selectively dissolved [125].

In a coolant system in which temperature varies throughout the loop, there are several mechanisms which affect the location and rates of corrosion. From a rate perspective, corrosion rates are initially high (compared to steady-state rates) as surface Cr is corroded and impurities in the salt are consumed through reactions such as those in Eqs (3.3) and (3.4) [7,35,126]. For salts containing UF_4 or ThF_4 (such as in the MSRE or in a Molten Salt Breeder Reactor) or salts in which TF is continually produced from neutron transmutation (such as MSRs and FHRs), long-term corrosion can occur at lower rates [35,127]. Long-term corrosion rates are governed by the rate of Cr diffusion to the metal surface [35,40,127,128]. More specifically, experimental findings suggest that the

corrosion rate is governed by grain boundary diffusion of Cr, rather than bulk diffusion. This is true in both the nickel-base alloy Hastelloy-N (introduced in Section 1.4.2), but is especially evident in austenitic stainless steels such as types 304 and 316 [126,129,130]. Additionally, experiments have shown that selective Cr corrosion can produce subsurface voids in the metal due to the Kirkendall effect where Cr diffuses out of the metal (by a vacancy process) faster than Fe, Ni and other alloying elements can diffuse in to fill the Cr vacancies [35].

Figure 3.2 shows the diffusion coefficient for bulk Cr diffusion in Type 316 stainless steel [131]. Using the program DataThief, the data from the closed circles were extracted and an exponential fit was applied in order to yield Eq (3.5). Here $D_{Cr,bulk\ 316}$ has units of m^2/s and T is temperature in K. Figure 3.3 shows grain boundary diffusion coefficients for Cr in types 316 and 316L stainless steel [131]. Mizouchi et. al. provided an Arrhenius equation for Cr grain boundary diffusion in solution-treated Type 316L stainless steel. This equation is given in Eq (3.6) where $D_{Cr,gb\ 316}$ has units of m^2/s, R is the universal gas constant (kJ/mol-K), and T is temperature (K). The grain boundary Cr diffusion coefficient is up to 10 orders of magnitude higher than the bulk Cr diffusion coefficient. Additionally, the bulk Cr diffusion coefficients in Hastelloy-X and Inconel have been measured to be similar to the bulk Cr diffusion coefficients in Type 316 SS [127,132]. Chromium grain boundary diffusion coefficients for Hastelloy-N do not seem to have been measured. However, the bulk Cr diffusion coefficient in Hastelloy-N has been measured [127]. Using DataThief, the data plotted in Figure 2 of reference [127] were extracted and an exponential fit was applied in order to arrive at Eq (3.7), the temperature-dependent bulk Cr diffusion coefficient in Hastelloy-N. Again, $D_{Cr,bulk\ N}$ is in units of m^2/s and T is in Kelvin.

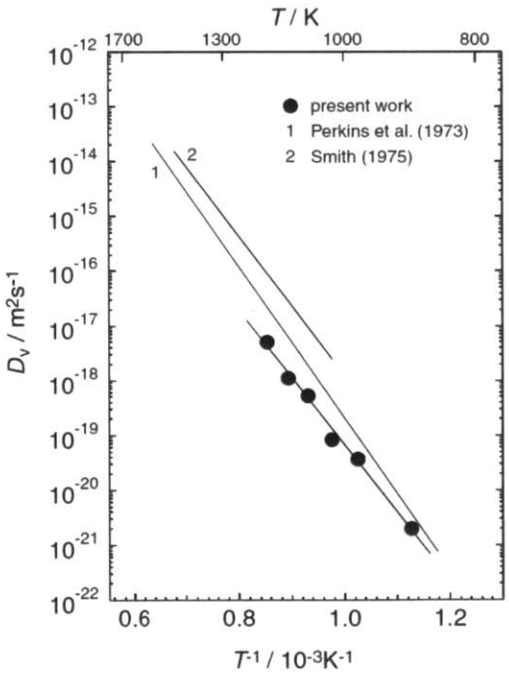

Figure 3.2: Bulk Cr diffusion coefficient in Type 316 stainless steel. From Mizouchi et. al. [131].

$$D_{Cr,bulk316} = 2.9080\times10^{-32} e^{2.8343\times10^{-2}T} \tag{3.5}$$

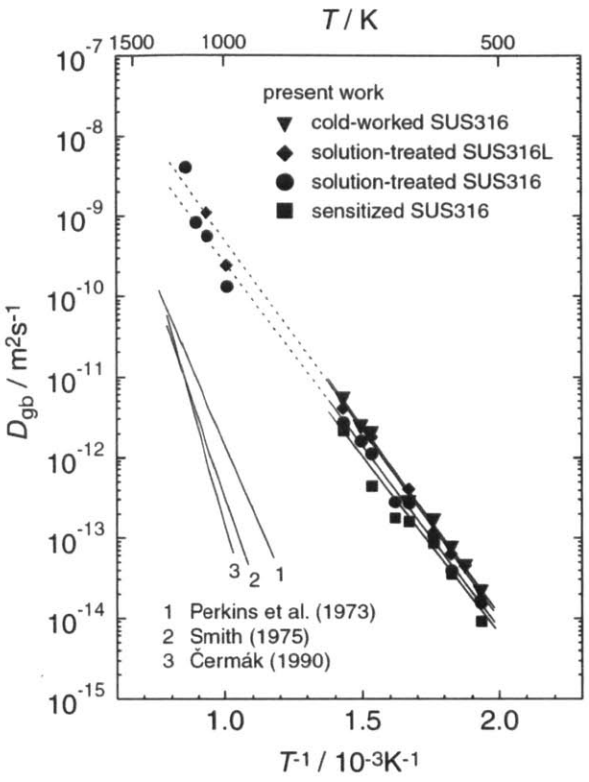

Figure 3.3: Grain boundary diffusion coefficients for different heats of types 316 and 316L stainless steel. From Mizouchi et. al. [131].

$$D_{Cr,gb316} = 2.84\times10^{-5} e^{-90.6/RT} \tag{3.6}$$

$$D_{Cr,bulkN} = 1.745\times10^{-30} e^{2.863\times10^{-2}T} \tag{3.7}$$

While the corrosion rate in fluoride salts is limited by the solid-state diffusion of the least noble element in the base metal, the location of corrosion depends on mass transfer and temperature conditions along the loop. Below, an expression will be developed which shows the temperature dependence of the reaction between UF_4 and Cr observed in the MSRE. This temperature dependence results in the loss of Cr from the hot parts of a coolant circuit and the deposition of Cr in the cool parts of the circuit. Later on, Sections 3.1.2.1 and 3.1.2.2 provide experimental examples of impurity and temperature gradient effects on corrosion.

The principle corrosion reaction in the MSRE was between UF_4 and Cr. In order to help control this and other reactions, the MSRE maintained a ratio of UF_4:UF_3 at 100:1 in the MSRE fuel-salt. Thus, the uranium in an MSR can be used for both fuel and corrosion control. The use of UF_4/UF_3 for corrosion control in the MSRE is discussed in detail in Section 3.2. For the MSRE, the reaction

of concern is shown by Eq (3.8). Here the subscript *d* denotes a species dissolved in the salt, and the subscript *s.s.* denotes that the Cr is in a solid solution in an alloy and not in pure, metallic form. Now the equilibrium constant, K_1, for the reaction in Eq (3.8) can be written as Eq (3.9). Assuming the activity coefficients to be 1, K_1 is a unitless value made up of the concentrations of each species in brackets. The concentrations of CrF_2, UF_4, and UF_3 are their concentrations in the salt and the concentration of $Cr_{(s.s)}$ is its concentration in the alloy in contact with the salt. Common concentration units may be mole fraction or moles/cm^3.

$$Cr_{(s.s.)} + 2UF_{4(d)} \rightleftharpoons CrF_{2(d)} + 2UF_{3(d)} \tag{3.8}$$

$$K_1 = \frac{[CrF_2][UF_3]^2}{[UF_4]^2[Cr_{(s.s.)}]} \tag{3.9}$$

Next, equilibrium constants obtained from direct measurements can be employed. The equilibrium constants have been reported for two reactions related to Eq (3.8) by Baes [118]. The chemical reactions and the Log_{10} of their associated equilibrium constants (K_2 and K_3) are written below in Eqs (3.10) through (3.13) where T is temperature in Kelvin. The equilibrium constant for the reaction in Eq (3.10) is given by Eq (3.11). The equilibrium constant for the reaction in Eq (3.12) is given by Eq 3.13. In order to arrive at Eq (3.8), Eq (3.10) is reversed, Eq (3.12) is multiplied by 2 and then they are added together. In order to arrive at a temperature dependent expression for K_1, the same operations are performed on the expressions for K_2 and K_3 in Eqs (3.11) and (3.13). The result is Eq (3.14). Equating Eqs (3.9) and (3.14) gives Eq (3.15). Solving for $[CrF_2]$ gives Eq (3.16): the equilibrium concentration of CrF_2 in the salt when an alloy containing Cr at a specified concentration is in contact with flibe containing a specified concentration of UF_4 and UF_3 at a specified temperature. With a ratio of $[UF_4]$ to $[UF_3]$ of 100:1 and the chromium concentration in Hastelloy-N of 0.08 mole fraction and the chromium content of 0.1915 mole fraction in Type 316 L, the equilibrium concentration of CrF_2 in flibe contacting Hastelloy-N and Type 316 L stainless steel over a range of temperatures is plotted in Figure 3.4. The solubilities of CrF_2 in both flibe and flinak are also plotted in order to show the temperature dependence of solubility which also plays a role in mass transfer of CrF_2. The calculation from Eq (3.16) does not account for the effects of the solubility limit, and predicts that near 800 °C, the calculated equilibrium concentration of CrF_2 can exceed the solubility. This is impossible, and the solubility limit will force precipitation of CrF_2 corrosion products, if necessary. The higher Cr content in Type 316 L stainless steel means that it will result in a higher equilibrium concentration of CrF_2 in flibe than will Hastelloy-N. It should also be noted that this equilibrium calculation will not give any information about the kinetics of the reaction (*i.e.* how fast the reaction occurs and how fast equilibrium is reached). Experiments and/or knowledge of the rate-limiting step for corrosion are required in order to calculate reaction rates. As was discussed above, the rate limiting step for corrosion in flowing salt is the grain boundary diffusion rate of Cr in the metal.

$$H_{2(g)} + CrF_{2(d)} \rightleftharpoons Cr + 2HF_{(g)} \tag{3.10}$$

$$Log(K_2) = 5.12 - \frac{9060}{T} \tag{3.11}$$

$$\tfrac{1}{2}H_{2(g)} + UF_{4(d)} \rightleftharpoons UF_{3(d)} + HF_{(g)} \tag{3.12}$$

$$Log(K_3) = 4.07 - \frac{9330}{T} \tag{3.13}$$

$$Log(K_1) = 3.02 - \frac{9600}{T} \tag{3.14}$$

$$Log(K_1) = Log\left(\frac{[CrF_2][UF_3]^2}{[UF_4]^2[Cr_{(s.s.)}]}\right) = 3.02 - \frac{9600}{T} \tag{3.15}$$

$$[CrF_2] = 10\,\wedge\left\{3.02 - 9600/T + Log([Cr_{(s.s.)}]) + 2Log\left([UF_4]/[UF_3]\right)\right\} \tag{3.16}$$

A similar analysis can be done for Cr corrosion by HF dissolved in flibe. To begin with, the corrosion reaction is written as Eq (3.17) and the equilibrium constant for this reaction is written as Eq (3.18). Here, $[CrF_2]$ is the equilibrium concentration of CrF_2 in flibe contacting a given alloy, and $[Cr_{(s.s.)}]$ is the concentration of Cr in that alloy. Here, P_{HF} and P_{H2} are the fractional partial pressures of HF (p_{HF}) and H_2 (p_{H2}) divided by the total pressure p_{total}. The work of Baes provides an empirical relationship for this equilibrium constant from Eq (3.19) [118]. Setting Eq (3.18) equal to Eq (3.19) and solving for $[CrF_2]$ gives Eq (3.20). Note that Eq (3.20) features the fraction $[P_{HF}]^2/[P_{H2}]$. The value of this fraction is related to the corrosive chemical potential in the salt: the higher the value of the fraction, the more corrosive is the salt. This will be discussed in detail in Section 3.2.3. For the time-being, a value of 8.46×10^{-9} is assumed for this fraction because it is representative of the typical chemical potential in the fuel-salt of the MSRE. The calculation of this value will be discussed in Section 3.2.3. Plotting Eq (3.20) versus temperature in Figure 3.5 shows how the equilibrium concentration of CrF_2 in flibe contacting Type 316 L stainless steel and Hastelloy-N varies due to corrosion by HF over a range of temperatures. Compared to the behavior in Figure 3.4, Figure 3.5 shows a temperature dependence where the equilibrium concentration of CrF_2 decreases with temperature. This is due to the fact that the reaction in Eq (3.17) is exothermic whereas the reaction in Eq (3.8) is endothermic. Since heat is generated from the reaction in Eq (3.17), the reaction proceeds more strongly to the right at lower temperatures. The opposite effect occurs for the reaction in Eq (3.8). This implies that in a system, such as the FHR, where TF is the principle oxidant, mass transfer could occur from an area of low temperature to an area of high temperature [133]. This implication for corrosion mass transfer is discussed in Section 3.1.2.2 and in Chapter 5 where a corrosion model for the FHR is developed.

$$Cr_{(s.s.)} + 2HF_{(g)} \rightleftharpoons CrF_{2(d)} + H_{2(g)} \tag{3.17}$$

$$K = \frac{[CrF_2][P_{H_2}]}{[Cr_{(s.s.)}][P_{HF}]^2} \tag{3.18}$$

$$Log(K) = -5.12 + \frac{9060}{T} \tag{3.19}$$

$$[CrF_2] = 10\,\wedge\left\{-5.12 + \frac{9060}{T} + \text{Log}([Cr_{(s.s.)}]) + \text{Log}\left(\frac{[P_{HF}]^2}{[P_{H_2}]}\right)\right\} \tag{3.20}$$

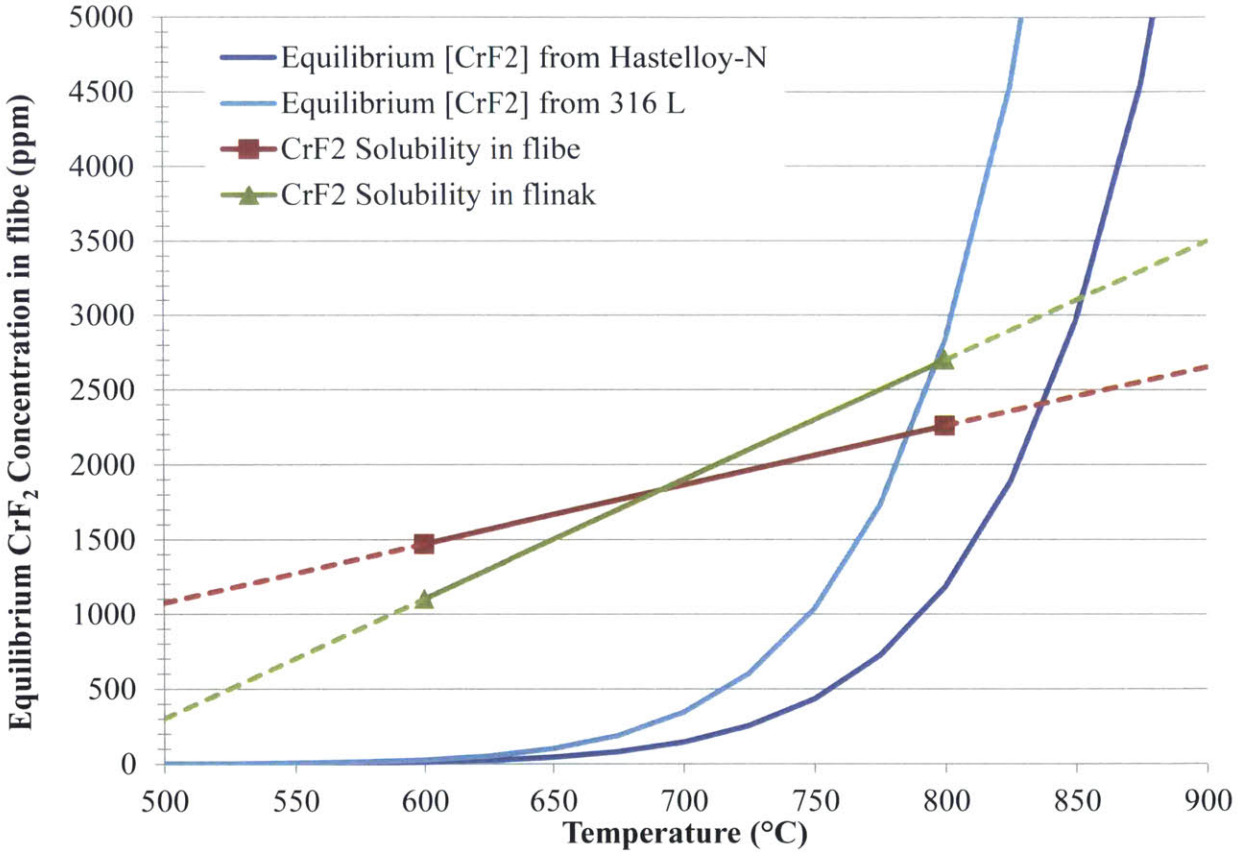

Figure 3.4: Equilibrium concentration of CrF_2 in flibe with UF_4:UF_3 = 100:1 if Hastelloy-N or Type 316L is in contact with flibe. Calculated using Eq (3.16). Solubility points in flibe and flinak are from ref [45]. Dashed line segments denote extrapolation.

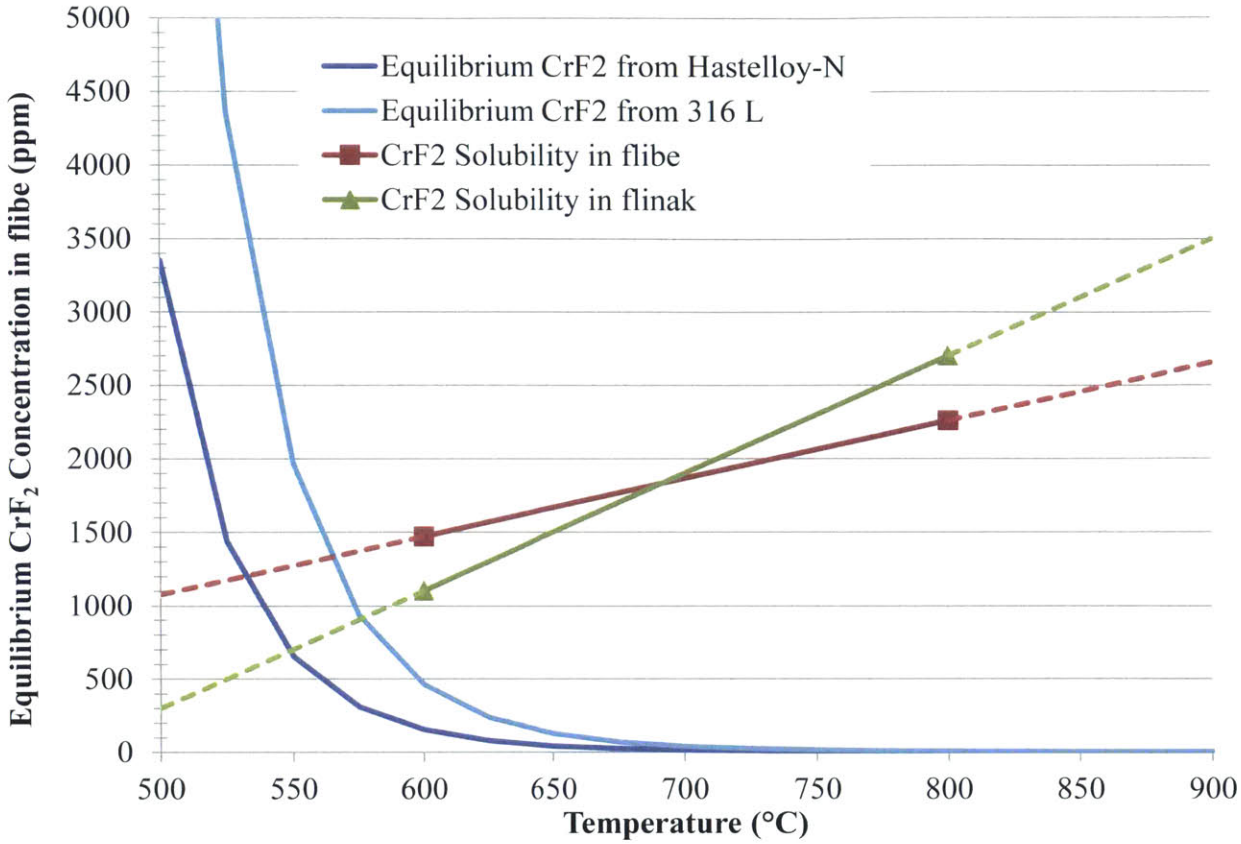

Figure 3.5: Equilibrium concentration of CrF_2 in flibe if $[p_{HF}]^2/[p_{H2}] = 8.46x10^{-9}$ for Hastelloy-N and Type 316L in contact with flibe. Calculated with Eq (3.20). Solubility points in flibe and flinak are from ref [45]. Dashed line segments denote extrapolation.

3.1.2 Alloy chemical compatibility for the FHR

This section further discusses concepts of corrosion and mass transport applicable to FHRs. Construction of a commercial FHR must utilize qualified materials. Type 316L stainless steel has been selected for the piping, reactor vessel, and heat exchangers for the Mk1 PB-FHR. Other alloys such as alloy 800H and Hastelloy-N may be attractive materials in the future, but Type 316L offers the best near-term solution. It is attractive for the FHR reactor vessel, piping, and heat exchanger for several reasons. First, as shall be discussed, Type 316 SS has a demonstrated chemical compatibility in clean, high-purity flibe in the absence of a neutron field [7,134]. This is important because oxide layers are not stable in fluoride melts and metal fluoride corrosion products are soluble in the melt. Thus, one cannot rely on a passivating layer to protect the stainless steel from corrosion in the FHR. Second, there is significant experience with Type 316 SS in the temperature and fluence regime of LWRs as fuel support structures, core barrels, and flow baffle plates [135]. Third, Type 316 SS is considerably less expensive than the nickel-base alloy Hastelloy-N. Fourth, there is an existing

ASME Section III code case for Type 316 SS. This code qualification does not exist for Hastelloy-N. ASME section II defines the allowable stresses as a function of temperature for Type 316 SS.

The current ASME code temperature limits for Type 316 SS are enumerated in Table 3.1, and a description of the code sections is provided in Table 3.2. The chemical compositions of four grades of Type 316 stainless steel are listed in Table 3.3. The low-carbon Type 316L is commonly used in LWRs, and Type 316H is a candidate for very high temperature operations [135]. Some key physical and mechanical properties for Type 316 SS are listed in Table 3.4.

Table 3.1: Current ASME code operating temperature limits for 316 stainless steel. From [8]

Applicable AMSE Code Sections	Temperature Limits (°Celsius)
Section III: Subsection NH	816
Section III: Subsection NB, NC, ND	427
Section III: Subsection NG with Code Case N-201-5	816

Table 3.2: Description of relevant ASME code sections and subsections. From [136].

Code Sections and Subsections	Description
Section III	Rules for construction of nuclear facility components
Subsection NB	Components that are part of the primary core cooling system
Subsection NC	Components that are part of safety grade emergency core cooling systems
Subsection ND	Components that are part of various systems needed for plant operation
Subsection NG	Core support structures
Subsection NH	Components from subsection NB and NC that are used in elevated temperature service

Table 3.3: Chemical composition of 316 stainless steel. Units are wt %. Data from [137].

	C	Mn	Si	P	S	Cr	Mo	Ni	Ti	Fe
316	0-0.08	0-2.0	0-1	0-0.05	0-0.02	16.5-18.5	2-2.5	10-13	-	Bal
316L	0-0.3	0-2.0	0-1	0-0.05	0-0.01	16.5-18.5	2-2.5	10-13	-	Bal
316H	0.04-0.1	0-2.0	0-0.75	0-0.05	0-0.02	16.5-18.5	2-2.6	11-14	-	Bal
316Ti	0-0.08	-	0-0.75	0-0.05	0-0.03	16.0-18.0	2-3	10-14	0-0.7	Bal

Table 3.4: Mechanical and physical properties of 316 stainless steel. Data from [138].

Ultimate Tensile Strength (MPa)	0.2% Yield Strength (MPa)	Elastic Modulus (MPa)	Density (g/cm^3)	Melting Range (°C)	Thermal Conductivity (W/m-K)	Electrical Resistivity (μΩ-cm)	C_p from 0-100°C (kJ/kg-K)
579	290	1.93 E5	7.99	1370 - 1400	16.2 @ 100 °C 21.4 @ 500 °C	74 @ 20 °C	0.50

3.1.2.1 Salt impurity effects on corrosion

In a natural convection flow loop experiment, it was found that flibe in the "as-received" condition (containing significant concentrations of FeF_2 and NiF_2 which are oxidizing toward Cr metal)[2] was oxidizing toward Type 316 SS, and weight loss was observed as elements from the stainless steel reacted with impurities in the flibe to make flibe-soluble metal fluorides [134]. Figure 3.6 shows the weight loss as a function of flibe exposure time for Type 316 SS samples. It was concluded that weight loss was due to selective Cr attack [134]. Between 3000 and 9000 hours of exposure at 650 °C, the average material loss was 15 μm/yr in the "as-received" case. Because beryllium forms such a stable fluoride (BeF_2), it was found that the addition of Be metal to the salt reduced the corrosion of the SS to a rate less than 2 μm/yr [134]. In this instance, beryllium metal was sacrificially oxidized to BeF_2, preventing structural elements (particularly Cr) from being oxidized to metal fluorides.

A dramatic example of the corrosion effects of impurities on metals in molten salts is given by Manly *et. al.* for Inconel (15 wt % Cr, 7 % Fe, ~77 % Ni) in an unirradiated natural convection loop with NaF-ZrF_4-UF_4 molten salt at 815 °C [139]. The report does not specify the type of Inconel used; however, given the year of the report (1957) and the chemical composition, this Inconel was most likely Inconel-600. From here on, it is assumed that the Inconel referred to in ref [139] is Inconel-600. Figure 3.7 shows void formation due to Cr leaching from the surface of Inconel-600 exposed to salt with varying degrees of impurities. This shows that dissolved Fe, Ni, and HF in the salt can result in the oxidation of Cr to soluble CrF_2. Unfortunately, the meanings of "high", "moderate", and "low" concentrations were not defined in the report.

[2] As-received means that the flibe was not purified after it was mixed from the two component salts, LiF and BeF_2.

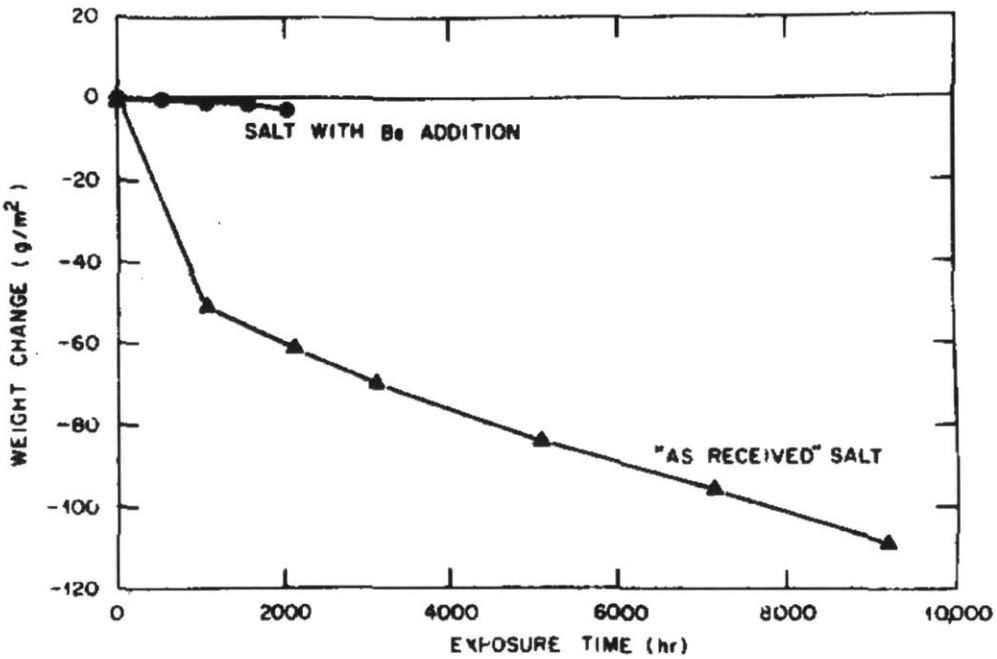

Figure 3.6: Weight change for Type 316 SS exposed to "as-received" flibe and flibe with Be metal addition. From [134].

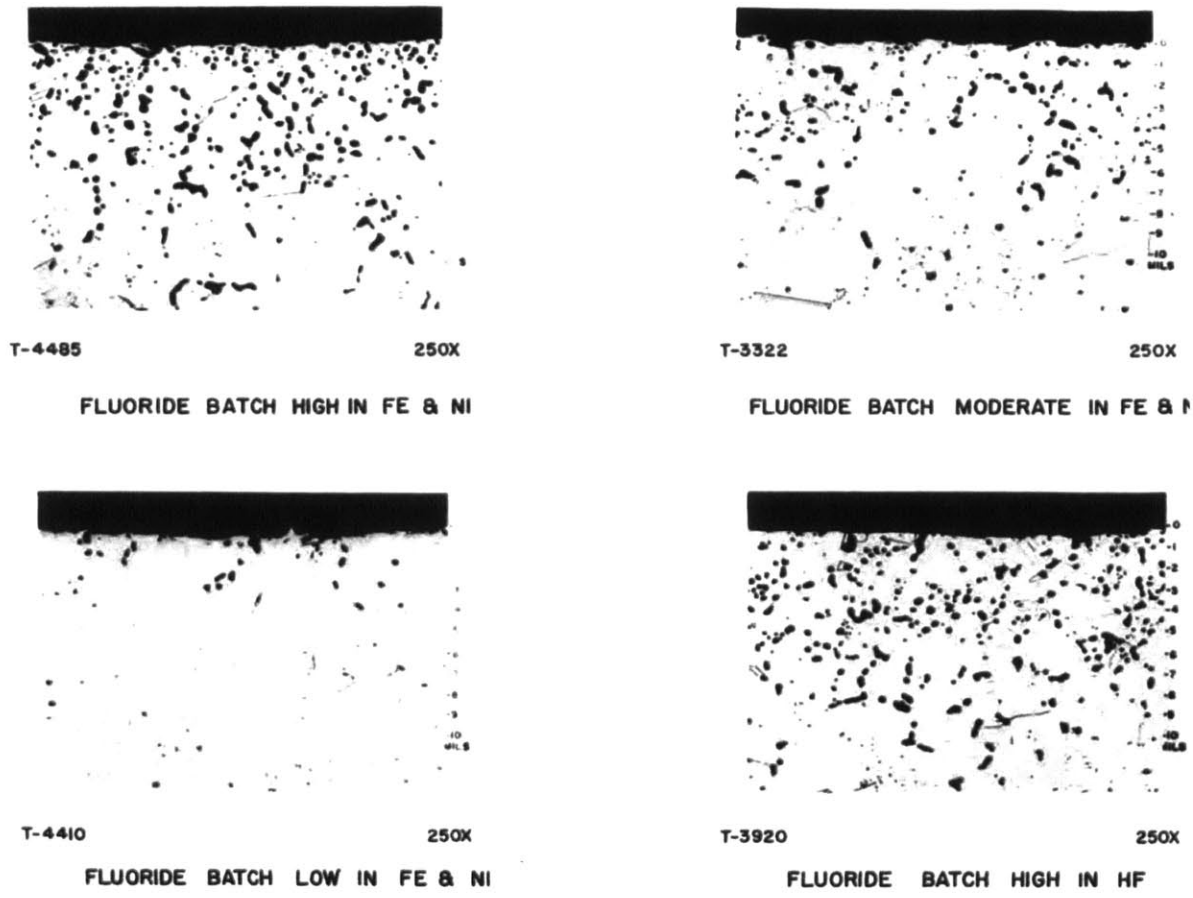

Figure 3.7: Impurity corrosion of Cr from Inconel-600 in molten NaF-ZrF_4-UF_4 salt. From ref [139].

3.1.2.2 Mass transfer effects on corrosion

In tests with Type 316 SS (17 wt% Cr), Kesier *et. al.* observed mass transfer of Cr from the hot section of their loop to the cold section; however, they did not discuss the process in greater detail [134]. As depicted in Figure 3.8, Koger observed substantial mass transfer effects in corrosive attack of Cr during a 9.2 year test of Hastelloy-N (7.4 wt% Cr) in flibe containing UF_4 and ThF_4 [35]. The maximum temperature in the loop was 700 °C and the minimum temperature of the loop was 560 °C. Going from micrograph G to micrograph A, one can see surface void formation as Cr is corroded from the samples. Micrograph G was taken on a pipe section at the entrance to the first heated region, and exhibited minimal corrosion. However, the depth and concentration of the voids increase with temperature, and micrographs taken from hotter sections F-A show substantial voids. The Corrosion depth was 76 to 102 μm deep in the worst sections, corresponding to a loss rate of 8.3 to 11.0 μm/year. In the cold leg of the loop, beginning with micrograph I and moving to micrograph H, Koger observed Cr deposition. Most of the Cr, it would appear, was deposited in these cold sections prior to reaching section G. Additional loop tests exist for Hastelloy-N variants and Inconels, but the

only data on flow loop corrosion tests for Type 316 SS are from Keiser *et. al.* (refs. [7,134]). The rate of corrosion product mass transfer in the FHR will need to be determined, and a means for either verifying that this rate is acceptable or mitigating it is required.

It is interesting to note that in salts with UF_4 and/or NiF_2 and FeF_2 impurities, the mass transfer effect is to remove Cr from the hot part of the loop and deposit it in the cold part of the loop. In a clean salt where HF is the principle oxidant, however, chemical thermodynamics (see Section 3.1.1) suggest that mass transfer will occur from the cold part of the loop to the hot part of the loop [133]. This is a phenomenon that appears not to have been investigated experimentally [133]. Since the principle oxidant in the FHR will be HF due to tritium fluoride production in the salt, the specifics of this mass transfer must be understood. This issue will be explored in greater detail during the discussion of the corrosion model developed for the FHR in Section 5.8.

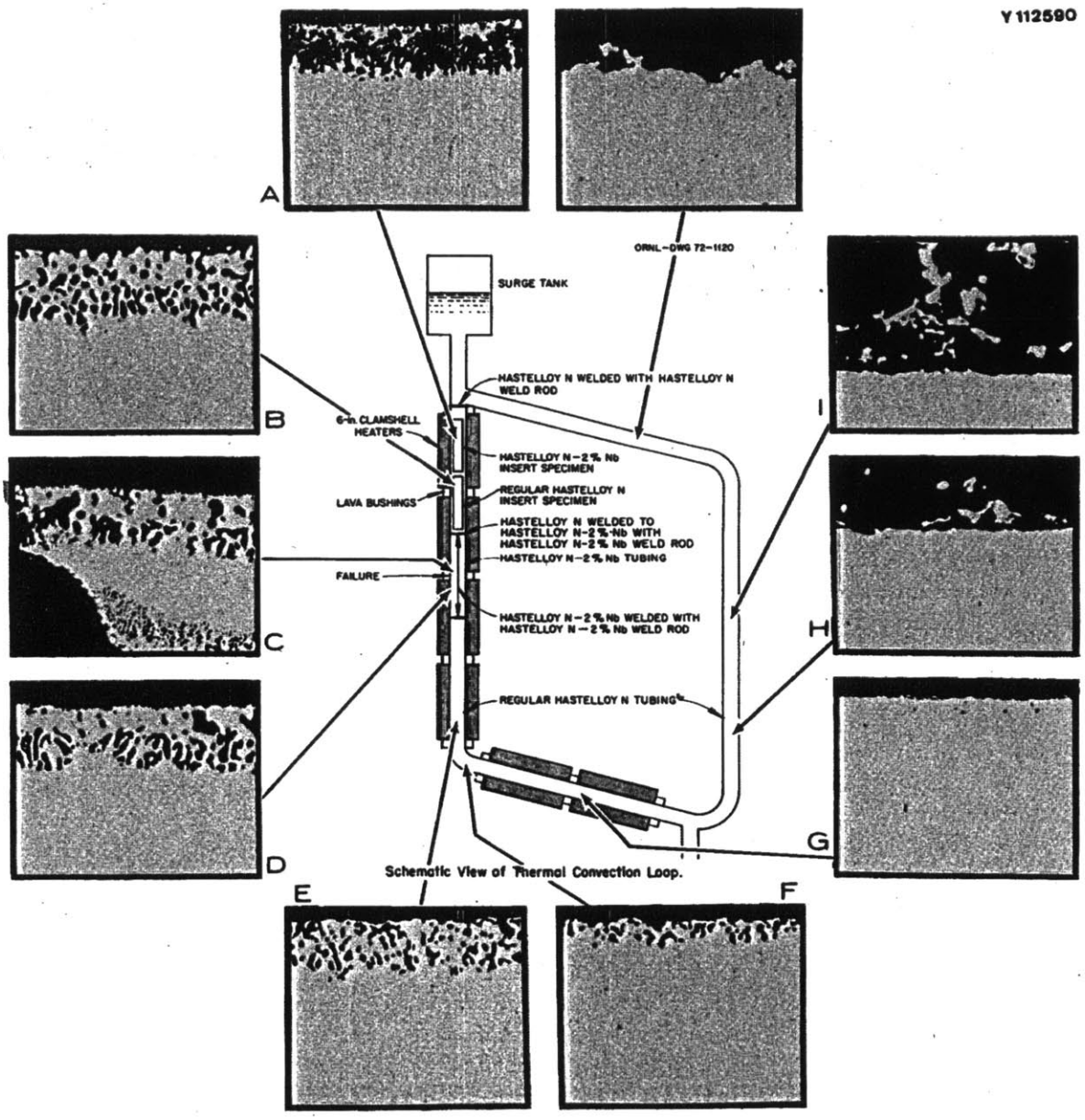

Figure 3.8: SEM micrographs of Hastelloy-N tube sections from various parts of thermal convection loop. 500x magnification. From ref [35].

3.2 Definition and control of chemical redox potential

Chemical redox potential is a term used to describe whether the coolant is oxidizing or reducing with respect to structural metals (*e.g.* Cr, Fe, Mo, Ni, etc.). It is a useful quantity for discussing both tritium behavior and corrosion reactions. As will become evident, in a clean fluoride salt reactor coolant, tritium behavior and corrosion are coupled phenomena which can be described with help of

the redox potential. "Redox" refers to a reaction where one reactive species is reduced ("red") and the other is oxidized ("ox"). For example, Eq (3.21) shows a reaction where dissolved tritium fluoride (TF) oxidizes metallic Cr to CrF_2, which then dissolves in the coolant as Cr^{2+} and $2F^-$. In this case, tritium (T) is reduced and Cr is oxidized. "Potential" describes the thermodynamic propensity for this reaction to occur and dictates the ratios of Cr^{2+}:Cr and T^+:T_2 which would exist at equilibrium.

$$2TF_{(d)} + Cr_{(s)} \rightarrow CrF_{2(d)} + T_{2(g)} \tag{3.21}$$

In the coolant, the chemical redox potential is dictated by the prevailing electron-transfer reactions. In aqueous systems, the chemical redox potential is oxidizing (corrosive) with respect to a metal if hydrogen is reduced, and the chemical potential is reducing (non-corrosive) with respect to a metal if hydrogen is oxidized. In aqueous solutions, the chemical potential for these reactions can be shifted to be more or less thermodynamically favorable by altering the partial pressure of oxygen over the solution and/or by varying the concentration of dissolved H^+ in solution. Similarly, the redox potential in fluoride salts can also be described by the tendency to reduce or oxidize hydrogen existing in the system [118]. This hydrogen may exist in an FHR due to tritium production via neutron transmutation or by deliberate protium addition for purposes of active redox control. Analogous to the effect of oxygen partial pressure in aqueous systems, the partial pressure of fluorine, F_2, over the molten salt can also be used to describe the redox potential in the salt [140].

A useful convention is to refer to the redox potential in the FHR coolant as defined by the fluorine potential method suggested by Olander [140]. Mathematically, the fluorine potential, ΔG_{F2}, has units of kJ/mol F_2 and is given by Eq (3.22) where R is the universal gas constant (8.314E-3 kJ/mol-K), T is temperature (Kelvin), and P_{F2} is the fractional partial pressure of F_2 (p_{F2}) over the total system pressure (p_{total}) shown in Eq (3.23).

$$\Delta G_{F_2} \equiv RT \ln(P_{F_2}) \tag{3.22}$$

$$P_{F_2} = \frac{p_{F_2}}{p_{total}} \tag{3.23}$$

The fluorine potential can be used to describe the overall redox potential in any fluoride salt coolant. The fluorine potential can also be dictated by a controlling reaction occurring in the salt. Recall that the MSRE used a fuel-salt where the uranium fuel was dissolved directly in the coolant as uranium fluoride (UF_4). The coolant chemistry concerns for the MSRE were TF production, buildup of fission products in the fuel salt, and slow oxidation of Cr by reaction with the dissolved UF_4 fuel according to Eq (3.24).

$$2UF_4 + Cr \rightleftharpoons CrF_2 + 2UF_3 \tag{3.24}$$

Even though UF_4 is a more stable fluoride than CrF_2, some reaction of Cr with UF_4 does occur, and thanks to the temperature dependent equilibrium constant for this reaction, Cr can be transported within a polythermal loop containing dissolved UF_4 [124]. Figure 3.1 shows that the Gibbs formation free energy for UF_4 and UF_3 are nearly identical. Since UF_3 is more negative than the formation free energy for CrF_2, UF_3 acts as a reductant in the salt. (UF_5 does not form in flibe; thus, UF_4 will not act as a reductant.) In order to maintain a reducing potential in the coolant, the MSRE maintained a 100:1 ratio of dissolved UF_4:UF_3. Thus, in addition to fueling the reactor, UF_4 and UF_3 acted as a redox buffer for maintaining the desired redox potential. Engel *et. al.* noted that if the ratio of UF_4/UF_3 were reduced to about 6:1 or lower, uranium carbide (UC_2) would form via a reaction between UF_3 and carbon which would damage the graphite [141]. A 100:1 ratio was chosen for the MSRE because it was reducing enough to minimize corrosion of Cr, but not so reducing that the moderator graphite was degraded by uranium carbide formation via reaction with dissolved UF_3 [124,142].

If buildup of TF and/or fission products occurred, the result was that some UF_3 was oxidized to UF_4 and the coolant redox potential remained virtually constant [6]. For example, TF could be consumed by UF_3 according to Eq (3.25). If the ratio of UF_4:UF_3 increased to greater than 100:1, the 100:1 ratio was re-established in the MSRE by periodically inserting a Be rod which reacted to convert excess UF_4 into UF_3 [6,42]. The mixture of UF_4 and UF_3 not only fueled the reactor, it also acted as a redox buffer in the coolant.

$$2UF_{3(d)} + 2TF_{(d)} \rightleftharpoons 2UF_{4(d)} + T_{2(g)} \tag{3.25}$$

3.2.1 Comparison of redox agents and suggestion of new agent

Fission products (which can raise the redox potential) are not produced in the FHR coolant; however, tritium fluoride (TF) is produced in the FHR coolant and will raise the redox potential unless a redox control method is employed.[3] Since the FHR operates with an un-fueled coolant, the use of a UF_4/UF_3 buffer is not possible. However, other options exist for controlling the redox potential in the FHR. A gaseous mixture of H_2/He (or H_2/Ar) could be bubbled through the coolant in order to remove any dissolved $T_{2(g)}$ and some TF. A gaseous mixture of H_2/HF could also be used to enforce a reducing potential on the coolant [143]. Section 3.2.2 will show that maintaining the appropriate ratio of H_2 to HF can achieve the same redox potential that was used in the MSRE. However, while H_2 is sufficiently reducing to remove NiF_2 and FeF_2, it was found to be difficult to remove CrF_2 from solution using H_2 alone [123]. The use of H_2/HF for redox control is currently being investigated at the University of Wisconsin-Madison.

[3] An average fission event in UF_4 generates fission products with a net oxidation state of less than 4+; however, four fluorine atoms are released. The result is that UF_4 fission creates an oxidizing effect. On the contrary, fission in PuF_3 may generate a somewhat reducing effect [143].

Another option is the use of a dissolved redox buffer analogous to the use of UF_4/UF_3 in the MSRE. Possible dissolved buffers include CeF_4/CeF_3, SmF_3/SmF_2, YbF_3/YbF_2, VF_3/VF_2, and EuF_3/EuF_2 [143,144]. Several of these may incur a neutronic penalty depending on the required concentration in the salt. Another issue to consider is that the presence of certain dissolved metal-fluorides may alter the solubility of other metal fluorides. For example, it was found that ThF_4, BaF_2, and CeF_3 reduce the solubility of PuF_3 in flibe [145]. While an FHR should never have Pu in the coolant, this effect would be important in MSRs. Next, since Zr is known to make ZrF_4, it has been postulated that ZrF_3 might also exist in the coolant such that a ZrF_4/ZrF_3 buffer could also be a possibility. However, previous investigations in lithium-sodium-potassium-fluoride salts did not observe lower oxidation states of Zr [146]. Another option is the use of major-metal redox control by inserting a sacrificial anode such as Be or Zr into the salt [147]. Beryllium has been investigated for this purpose because it reacts strongly with HF/TF and is already a component of flibe [56]. In Section 3.1.2.1, an example of the use of Be metal to reduce corrosion of Type 316 SS in flibe was discussed. However, the findings cited by Engel *et. al.* (ref. [141]), Cantor and Grimes [121], and the assertions from Williams *et. al.* (ref. [148]) indicate that the use of Be or a high concentrations of other strong reducing agents will result in the formation of carbides and the degradation of graphite. This would be unacceptable in a graphite-moderated pebble-bed reactor. Thus major-metal control might be suitable for systems with no graphite (such as fusion reactors), but in the FHR, Be or Zr major-metal control could degrade graphite through formation of beryllium or zirconium carbides *unless* their use can be kept to an absolute minimum. It may also be possible to have electrodes in the salt which would use impressed current to enforce a reducing chemical potential in the coolant.

The different dissolved redox buffers and major-metal agents proposed for redox control were compared based on their free energies of formation. Figure 3.9 is an Ellingham diagram plotting the Gibbs free energy of formation for metal fluorides which have been proposed for redox control in flibe. This diagram was constructed using HSC Chemistry. Two metal fluorides (YbF_2 and EuF_2) were not available in the database. More stable metal fluorides appear on the plot with more negative free energies of formation. In order for chromium to be stable as a metal, and for the constituents of flibe (LiF and BeF_2) to be stable, the redox potential in the coolant (in terms of the Gibbs formation free energy) must be more negative than the free energy of formation for CrF_2, but more positive than the free energy of formation for BeF_2. This redox potential region where both Cr and BeF_2 are stable is shaded in green in Figure 3.9. If the redox potential is too oxidizing, Cr can be oxidized and preferentially attacked in structural alloys. If the redox potential is too reducing, beryllium fluoride (BeF_2) could be reduced to beryllium metal (Be).

Because Zr and Be have only one oxidation state in flibe (4^+ and 2^+), they represent major-metal redox control agents where the redox couples are Zr/ZrF_4 and Be/BeF_2, which set a very reducing potential in the salt. The other metal fluorides (CeF_4/CeF_3, SmF_3/SmF_2, YbF_3/YbF_2, VF_3/VF_2, UF_3/UF_4, and EuF_3/EuF_2) can dissolve in flibe in two oxidation states. This allows them to buffer the redox potential in flibe. For example, for the UF_3/UF_4 couple, UF_3 sets a more reducing potential than UF_4. If UF_3 is oxidized to UF_4, the redox potential is then set by UF_4 which is only a little more

oxidizing than UF_3. According to the relative stabilities plotted in Figure 3.9, in order to ensure that BeF_2 is stable, the SmF_3/SmF_2, YbF_3/YbF_2, CeF_4/CeF_3, and EuF_3/EuF_2 couples should not be used. Both samarium fluorides have formation free energies more negative than that of BeF_2. Both the EuF_3 and YbF_3 species have formation free energies slightly more negative than BeF_2. (Data for the formation free energies of EuF_2 and YbF_2 were not available.) The CeF_3 species has a more negative Gibbs free energy of formation than BeF_2, but the CeF_4 species has a more positive Gibbs free energy of formation than BeF_2. The CeF_4/CeF_3 couple could be used for redox control as long as the CeF_3 content is kept very low. One problem with the CeF_4/CeF_3 couple is that the oxidation of CeF_3 to CeF_4 results in a considerable increase in the redox potential [140]. The VF_3/VF_2 couple might work for redox control as long as the VF_3 content is always kept low. Oxidation of VF_2 to VF_3 also results in a considerable increase in the redox potential, and the redox potential enforced by VF_3 is not considerably less than the Gibbs formation free energy of CrF_2. Thus VF_3/VF_2 is likely not strong enough as redox control agent.

One metal that is absent from mention in the literature as a possibility for major-metal redox control is aluminum. Beryllium metal has been shown to dissolve in flibe after reaction with HF in order to create a reducing potential in flibe, and some beryllium dissolves in flibe in the metallic form Be^o [7,56,149]. Analogous to the use of Be, aluminum metal immersed in flibe would react with TF to produce T_2 and maintain a reducing potential in the salt. Galvanic coupling of the aluminum to the container metal would enhance this reaction [149]. In this case, the redox couple would be metallic Al and dissolved AlF_3. Figure 3.9 shows that AlF_3 has a formation free energy more positive than BeF_2 (and UF_3) but more negative than ZrF_4 (and UF_4). Thus, aluminum major-metal control would produce a more reducing environment than control by Zr metal, but less reducing than control by Be metal. A drawback to the use of Zr and Be for major-metal redox control is the possibility of zirconium carbide or beryllium carbide formation. Figure 3.10 shows the formation free energies for relevant metal carbides.[4] Compared to carbides formed by the two other major-metal redox agents, Be and Zr (which form Be_2C and ZrC, respectively), the stability of aluminum carbide (Al_4C_3) is considerably less. This indicates that the risk of carbide formation in a salt controlled by Al major-metal should be less than that for Be and Zr major-metal control.

The vapor pressure of AlF_3 is low. At 1511 K, the vapor pressure of pure AlF_3 is 0.12 kPa [151]. In comparison, at 1420 K, the vapor pressure of pure BeF_2 is 79.9 kPa [152]. AlF_3 also has good solubility in flibe [153]. Flibe, and other mixtures of LiF and BeF_2, have previously been evaluated as a solvent for reprocessing nuclear fuel from aluminum-uranium alloys clad in aluminum [153,154]. Solubility of AlF_3 in LiF-BeF_2 was observed up to 31 weight % AlF_3 [154]. A ternary phase diagram for AlF_3-LiF-BeF_2 showed that even at high AlF_3 loadings, the liquidus point in the AlF_3-flibe system (AlF_3-0.67LiF-0.33BeF_2) was less than 600 °C [154]. Given that less than 1/3 of a gram of T is produced per GWD in FHRs, little dissolved AlF_3 would be generated, and any

[4] Note that both UC and UC_2 are plotted. Although the data show that UC is a more stable fluoride, experiments have determined that UC_2 is the primary carbide formed from reaction of dilute UF_3/UF_4 mixtures with graphite [150].

alteration of the melting point of flibe by AlF_3 should be negligible. Additionally, in flibe, AlF_3 can compete for unassociated fluoride ions in order to form AlF_6^{3-} [154]. This was undesirable for fuel reprocessing, but might be advantageous in FHRs where free F^- ions contribute an oxidizing influence.

The neutronic impact of any redox agent may also be of concern. Figure 3.11 shows the total cross section for possible redox agents. In Figure 3.11, elements Ce, Eu, Sm, Zr, V, and Yb all have more than one significant isotope. The isotope with the smallest cross section is plotted in Figure 3.11. Natural aluminum and beryllium exist with only one significant isotope. Figure 3.11 indicates that the neutronic effect of dissolved AlF_3 in the salt should be the smallest of all possible redox agents. If a strong redox agent is required, redox control using Al major-metal control may be a reasonable option. Experimental studies would be required in order to determine the rate of reaction between Al and TF and/or free fluoride and for determining the amount of Al that could be used without excessive carbide formation.

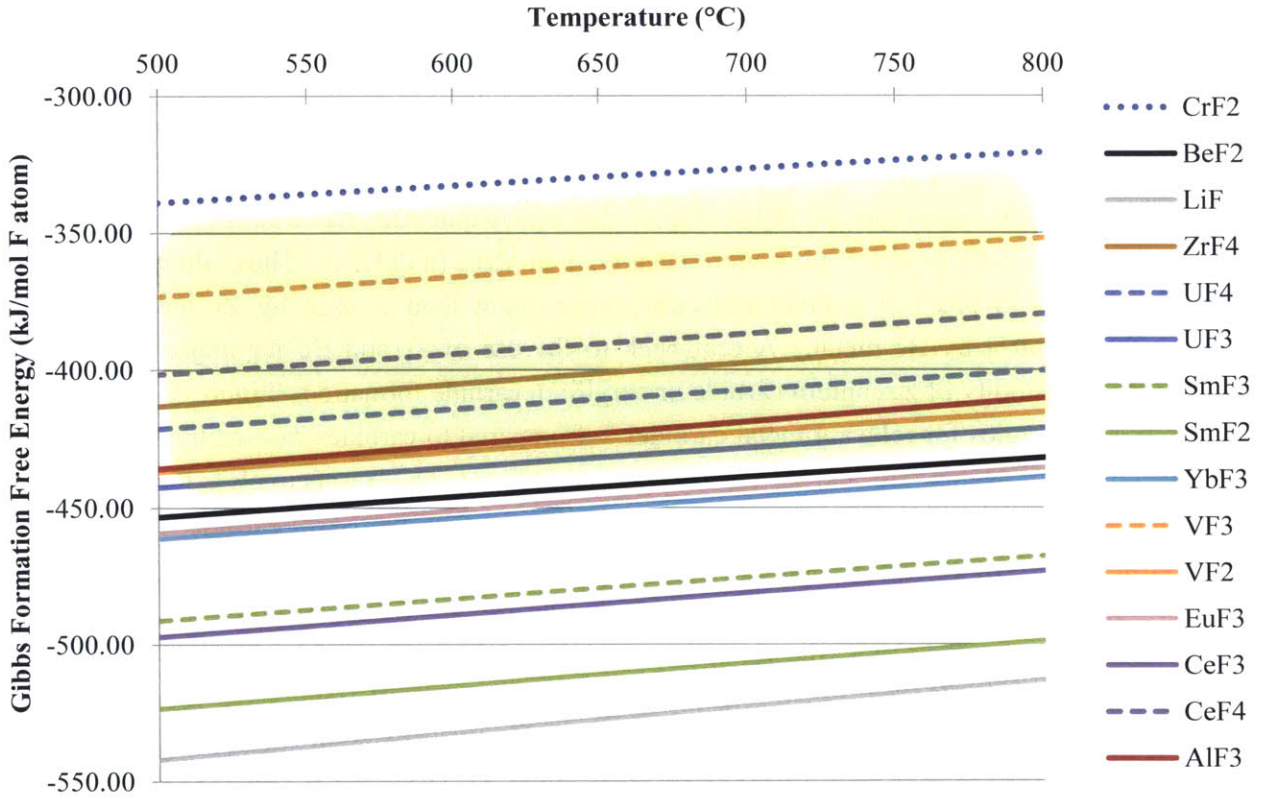

Figure 3.9: Ellingham diagram comparing relative stabilities of metal fluorides proposed for redox potential control in flibe. Region for FHR shaded in green. Calculated with HSC.

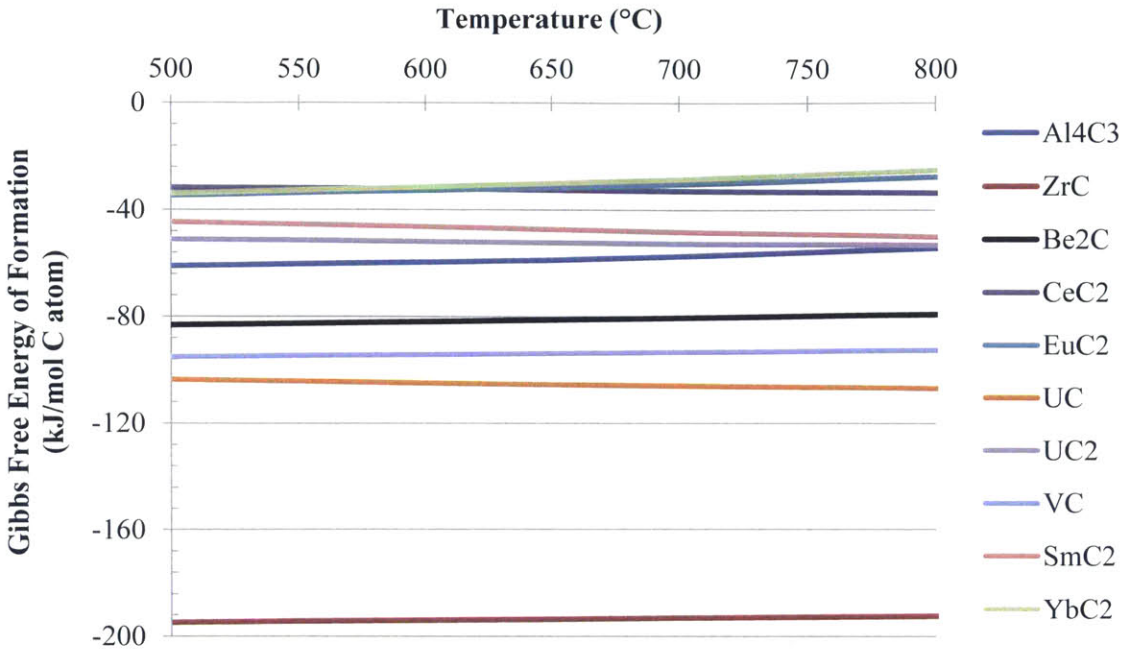

Figure 3.10: Ellingham diagram comparing relative stabilities of metal carbides formed by metals of potential redox agents. Calculated with HSC.

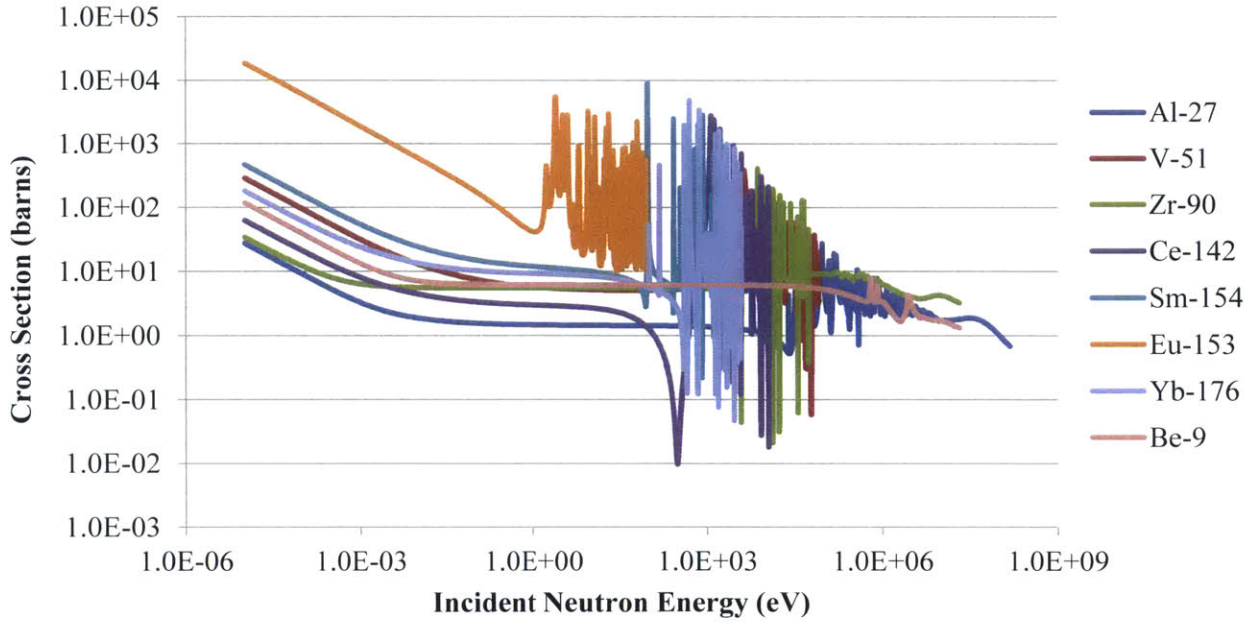

Figure 3.11: Total neutron cross sections. For elements with multiple isotopes, the least absorbing isotope is plotted. All data from ENDF/B-VII.1 except for Yb-176 which is from JENDL-4.0.

3.2.2 Derivation of fluorine potential

Olander provides a brief presentation of an equation for fluorine potential based on control by the redox couple of dissolved CeF_3/CeF_4 [140]. Below, an equation for fluorine potential as a function of the ratio of the dissolved redox couple UF_4/UF_3 will be developed. Then, a unique formulation for the fluorine potential for use in a system controlled by the ratio of HF/H_2 will be developed.

3.2.2.1 Fluorine potential for dissolved-salt redox control

As was discussed earlier in Section 3.2, the MSRE used a 100:1 ratio of UF_4 to UF_3 in order to maintain the desired redox potential in the coolant. The MSRE proved that a 100:1 ratio of dissolved UF_4:UF_3 in flibe created a suitable potential: oxidizing enough to prevent production of uranium carbides from UF_3, but reducing enough to prevent excessive Cr corrosion. In this case, the fluorine potential is fixed by the ratio UF_4:UF_3, and the controlling reaction is given by Eq (3.26) where UF_3 and UF_4 interact with hydrogen and hydrogen fluoride present in the system. Unless hydrogen and/or hydrogen fluoride is deliberately added to the system (this might be done in order to help control the redox potential in the salt), the only hydrogen in the system will be from tritium produced due to neutron transmutation in the salt. Thus, in the equations which follow, hydrogen is denoted as T for the tritium isotope of hydrogen. In order to write the controlling reaction in terms of moles of F_2, Eq (3.27) is added to Eq (3.26) in order to obtain Eq (3.28). Next, the equilibrium constant for Eq (3.28) is written in Eq (3.29), where P_{F2} is the fraction of the partial pressure of F_2 (p_{F2}) over the total system pressure (p_{total}), and a_{UF3} and a_{UF4} are the activities of UF_3 and UF_4 in solution, respectively. The Gibbs reaction free energy for the reaction in Eq (3.28) is written as $\Delta G^{\circ}_{3.28}$ in Eq (3.30). Again, R is the universal gas constant (8.314E-3 kJ/mol) and T is temperature (Kelvin). Substituting Eq (3.29) into Eq (3.30) and re-arranging results in the usual form for a law of mass action depicted in Eq (3.31). Solving Eq (3.31) for P_{F2}, and substituting this into the definition of fluorine potential from Eq (3.22) gives the fluorine potential in the salt (ΔG_{F2}) in Eq (3.32) with units of kJ/mol-F_2.

$$UF_{3(d)} + TF_{(d)} \rightleftharpoons UF_{4(d)} + \tfrac{1}{2}T_{2(g)} \tag{3.26}$$

$$\tfrac{1}{2}T_2 + \tfrac{1}{2}F_2 \rightleftharpoons TF \tag{3.27}$$

$$UF_3 + \tfrac{1}{2}F_2 \rightleftharpoons UF_4 \tag{3.28}$$

$$K_{3.28} = \frac{\sqrt{P_{F_2}}\, a_{UF_3}}{a_{UF_4}} \tag{3.29}$$

$$\Delta G^{\circ}_{3.28} = -RT \ln(K_{3.28}) \tag{3.30}$$

$$K_{3.28} = \frac{\sqrt{P_{F_2}}\, a_{UF_3}}{a_{UF_4}} = \exp\left(\frac{-\Delta G^{\circ}_{3.28}}{RT}\right) \tag{3.31}$$

$$\Delta G_{F_2} = 2RT \ln\left(\frac{a_{UF_4}}{a_{UF_3}}\right) + 2\Delta G^{\circ}_{3.28} \tag{3.32}$$

Experimental data specifically for $\Delta G^{\circ}_{3.28}$ do not exist; however, since Eq (3.28) was found by adding Eq (3.26) to Eq (3.27), $\Delta G^{\circ}_{3.28}$ can be calculated by adding the known reaction free energies of Eq (3.26) and Eq (3.27). In Eq (3.33), Baes has reported the equilibrium constant for the reaction in Eq (3.26). Solving Eq (3.33) for $K_{3.26}$ and using it in Eq (3.34) results in a value for $\Delta G^{\circ}_{3.26}$ in units of kJ/mol. Reaction free energy data for the reaction of Eq (3.27) in flibe are not available. In order to find $\Delta G^{\circ}_{3.27}$, a thermodynamics program called HSC Chemistry v.7.1 was used to calculate $\Delta G^{\circ}_{3.27}$ from a vast database of reaction enthalpies and entropies with respect to temperature. HSC cannot account for solvent effects; however, the error associated with ignoring solvent effects was generally found to be no more than 5-10 %. The temperature dependence of the reaction free energy ($\Delta G^{\circ}_{3.27}$) is plotted in Figure 3.12. A polynomial fit to the HSC calculation from 500 to 1600 °C is shown on Figure 3.12 and in Eq (3.35) where T is in Kelvin. At 650 °C, $\Delta G^{\circ}_{3.26}$ = -106.7 kJ/mol and $\Delta G^{\circ}_{3.27}$ = -278.9 kJ/mol. With $\Delta G^{\circ}_{3.26}$ and $\Delta G^{\circ}_{3.27}$, $\Delta G^{\circ}_{3.28}$ in kJ/mol is calculated from Eq (3.36). At 650 °C, $\Delta G^{\circ}_{3.28}$ = -385.6 kJ/mol. Assuming activity coefficients of unity, a_{UF4}/a_{UF3} becomes simply the mole ratio x_{UF4}/x_{UF3}. With the MSRE mole ratio of x_{UF4}/x_{UF3} = 100 and the value for $\Delta G^{\circ}_{3.28}$ in Eq (3.32), taken at 650 °C, the fluorine potential of the MSRE salt is -700.5 kJ/mol F_2 at 650 °C. Thus, in Eq (3.32) a means has been established for expressing the chemical potential of the MSRE salt in terms of the fluorine potential if the temperature and mole fraction x_{UF4}/x_{UF3} is known.

$$\mathrm{Log}(K_{3.26}) = -4.07 + 9.33\left(1000/T\right) \tag{3.33}$$

$$\Delta G^{\circ}_{3.26} = -RT \ln(K_{3.26}) \tag{3.34}$$

$$\Delta G^{o}_{3.27} = \Delta G^{o}_{TF} = -4.6976\times10^{-10}T^3 + 3.1425\times10^{-6}T^2 - 8.8612\times10^{-3}T - 2.7305\times10^{2} \tag{3.35}$$

$$\Delta G^{\circ}_{3.28} = \Delta G^{\circ}_{3.26} + \Delta G^{\circ}_{3.27} \tag{3.36}$$

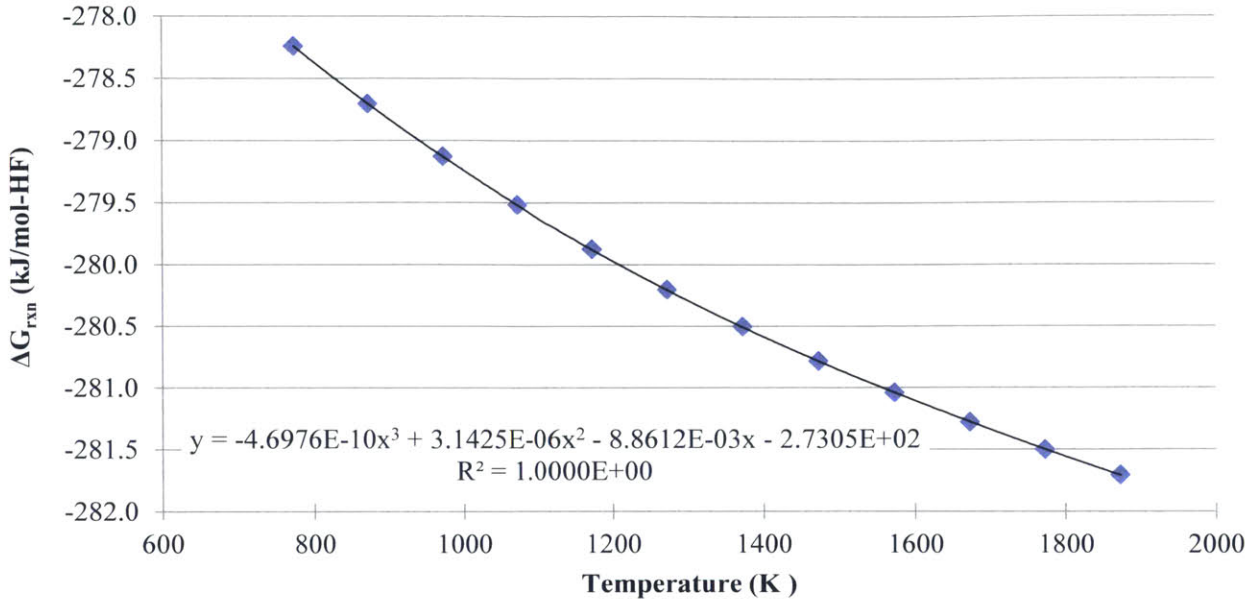

Figure 3.12: Reaction free energy ($\Delta G^{o}_{3.27}$) for Eq (3.27). Points calculated with HSC Chemistry. Polynomial fit applied to yield Eq (3.35).

3.2.2.2 Fluorine potential for gas-phase redox control

In the previous section, an equation was developed for expressing the fluorine potential (a measure of the chemical redox potential) in the MSRE due to redox control by dissolved uranium fluoride (UF_4/UF_3) at 650 °C. In the FHR, TF is generated in the salt due to neutron transmutation and T_2 is produced due to metal corrosion by TF. Additionally, HF/H_2 may be deliberately added for redox control. In either case, the relative equilibrium amounts of TF and T_2 (or HF and H_2) in the FHR coolant can be related to the fluorine potential (ΔG_{F2}) in the salt. If HF and H_2 are used to actively control the redox potential, then the fluorine potential will be dictated by the ratio of $HF:H_2$ injected into the system. Alternatively, if some other means of applying redox control is assumed (such as impressed current or a dissolved redox buffer), this will enforce a particular ΔG_{F2} fluorine (redox) potential on the coolant, and this redox potential will determine the relative amounts of TF and T_2 in the system. Thus, depending on the specific arrangement of the system, a specific ΔG_{F2} could be enforced (and from this fluorine potential, the ratio of $TF:T_2$ could be calculated) or one could specify a particular $TF:T_2$ (and from this, calculate the corresponding ΔG_{F2}).

In Eqs (3.37) and (3.38), P_{TF} and P_{T2} are the fractional partial pressures of TF (p_{TF}) and T_2 (p_{T2}) divided by the total pressure p_{total}. Eq (3.39) (borrowed from ref [140]) can be used to calculate the relative amount of TF versus T_2 in the coolant given a specific fluorine potential ΔG_{F2}. In this equation, ΔG^{o}_{TF} is the Gibbs formation free energy for Eq (3.27), which can be calculated as a function of temperature from Eq (3.35) in units of kJ/mol-F_2. Solving Eq (3.39) for $P_{TF}/(P_{T2})^{1/2}$ gives Eq (3.40).

$$P_{TF} = \frac{p_{TF}}{p_{total}} \tag{3.37}$$

$$P_{T_2} = \frac{p_{T_2}}{p_{total}} \tag{3.38}$$

$$\Delta G_{F_2} = 2RT \ln\left(\frac{P_{TF}}{\sqrt{P_{T_2}}}\right) + 2\Delta G^{\circ}_{TF} \tag{3.39}$$

$$\frac{P_{TF}}{\sqrt{P_{T_2}}} = \exp\left(\frac{\Delta G_{F_2} - 2\Delta G^{\circ}_{TF}}{2RT}\right) \tag{3.40}$$

Next, a means for determining the absolute values for P_{TF} and P_{T2} from the ratio $P_{TF}/(P_{T2})^{1/2}$ is needed. In order to do this, Henry's law from Eq (2.10) for the solubility of gases in liquid fluoride salts and a mass balance for the total amount of tritium in the salt in order to arrive at a set of 2 equations and 2 unknowns will be employed. The Henry's law constant (k_{HF}) from Field and Shaffer (ref [57]) was converted to units of [mol HF/m^3 flibe-Pa] using the molar mass (32.89 g/mol) and density of flibe. An exponential fit was applied to these data points in order to yield Eq (2.12): the Henry's law constant (in units of mol HF/m^3 flibe-Pa) for HF in flibe as a function of temperature (°C) from 500 to 700 °C. Here, it is approximated that the Henry's law constant for TF, $k_{Henry,TF}$, should be nearly the same as that for HF, $k_{Henry,HF}$.

The Ostwald constant for the solubility of H_2 in flibe from Malinauskas and Richardson (ref [98]) was converted to a Henry's law constant in units of [mol H_2/m^3 flibe-Pa]. An exponential best-fit for these data produced the expression in Eq (2.13) for the Henry's law constant of H_2 in flibe from 500 to 800 °C. In this equation $k_{Henry,H2}$ has units of mol H_2/m^3 flibe-Pa and T is in degrees Celsius. Here, it is assumed that the solubility of T_2 in flibe should be roughly the same as that for H_2 such that $k_{Henry,T2} = k_{Henry,H2}$.

Now that suitable Henry's law constants for TF and T_2 have been attained, these can be used in Henry's law, and the results from Henry's law can be used in Eq (3.40). First, Henry's law is written for TF and T_2 as Eq (3.41) and Eq (3.42), respectively. Here, c_{TF} and c_{T2} are the concentrations of TF and T_2 in flibe in units of mol/m^3 flibe. The partial pressures of TF and T_2 are written as p_{TF} and p_{T2} in units of Pa. The Henry's law constants in units of mol/m^3 flibe-Pa are $k_{Henry,TF}$ and $k_{Henry,T2}$. Eqs (3.37) and (3.38) are solved for p_{TF} and p_{T2} and then substituted into Eqs (3.41) and (3.42) in order to give Eqs (3.43) and (3.44). Solving Eqs (3.43) and (3.44) for P_{TF} and P_{T2} and substituting these into Eq (3.40), results in Eq (3.45). In a given volume of flibe, the total amount of tritium in that volume of flibe can be expressed by summing the two chemical forms of tritium according to Eq (3.46). Solving Eq (3.46) for c_{TF} and substituting this into Eq (3.45) gives Eq (3.47).

Eq (3.47) can be used in a number of different ways. If the total system pressure is known, then p_{total} is known. In the case of the FHR, the total system pressure is 1 atm or 101325 Pa. If the redox potential in terms of the fluorine potential (kJ/mol-F_2) of the salt is known, then ΔG_{F2} is known.

ΔG^{o}_{TF} is known from Eq (3.35). R is the universal gas constant (8.314E-3 kJ/mol-K), and T is temperature in Kelvin. The Henry's law constants for TF and T_2 are known. If c_{total} is also known, then Eq (3.47) can be solved for c_{T2}. Once both c_{total} and c_{T2} are known, c_{TF} can be calculated using Eq (3.46). If the right-hand side of Eq (3.47) is known, $P_{TF}/(P_{T2})^{0.5}$ can be solved for. Alternatively, if the relative amounts of TF and T_2 in the system are known (*i.e.* $P_{TF}/(P_{T2})^{0.5}$ is known) Eq (3.47) can be solved for the redox (fluorine) potential in the coolant.

$$c_{TF} = k_{Henry,TF} p_{TF} \tag{3.41}$$

$$c_{T_2} = k_{Henry,T_2} p_{T_2} \tag{3.42}$$

$$c_{TF} = k_{Henry,TF} P_{TF} p_{total} \tag{3.43}$$

$$c_{T_2} = k_{Henry,T_2} P_{T_2} p_{total} \tag{3.44}$$

$$\frac{P_{TF}}{\sqrt{P_{T_2}}} = \frac{c_{TF} \Big/ k_{Henry,TF} p_{total}}{\sqrt{c_{T_2} \Big/ k_{Henry,T_2} p_{total}}} = \exp\left(\frac{\Delta G_{F_2} - 2\Delta G^{o}_{TF}}{2RT}\right) \tag{3.45}$$

$$c_{total} = 2c_{T_2} + c_{TF} \tag{3.46}$$

$$\frac{P_{TF}}{\sqrt{P_{T_2}}} = \frac{\left(c_{total} - 2c_{T_2}\right) \Big/ k_{Henry,TF} p_{total}}{\sqrt{c_{T_2} \Big/ k_{Henry,T_2} p_{total}}} = \exp\left(\frac{\Delta G_{F_2} - 2\Delta G^{o}_{TF}}{2RT}\right) \tag{3.47}$$

3.2.3 Use of MSRE redox potential as a reference for FHR

The MSRE proved that a 100:1 ratio of dissolved UF_4:UF_3 in flibe created a suitable redox potential: oxidizing enough to prevent production of uranium carbides from UF_3, but reducing enough to prevent excessive Cr corrosion. Since both the FHR and MSRE have a fluoride salt in contact with graphite and metal containing chromium, the chemical redox potential in the MSRE can serve as a suitable baseline redox potential for the FHR. Since the FHR uses a clean, unfueled salt, UF_4/UF_3 cannot be used as a redox agent in the FHR, but other methods (such as those mentioned at the beginning of Section 3.2 and discussed in Section 3.2.1) could be used in the FHR in order to attain the same (or similar) redox potential as in the MSRE.

Mathematically, the redox potential generated by a ratio of UF_4:UF_3 can be expressed in a number of conventions. Two such conventions will be discussed here. One is using the Gibbs free energy of formation such that the redox potential from UF_4:UF_3 can be plotted in an Ellingham diagram. The other, is to express the UF_4:UF_3 ratio in terms of the fluorine potential derived earlier. In order to calculate the equivalent Gibbs formation free energy for a mixture of UF_4 and UF_3, the

Gibbs-Duhem relationship will be used. The Gibbs-Duhem relationship for a binary mixture at constant pressure and temperature says that the chemical potential of such a system is essentially the mole-fraction-weighted average of the chemical potential of the two components in the mixture [155]. Using the Gibbs-Duhem relationship, the redox potential in terms of the Gibbs free energy of formation for a 100:1 mixture of UF_4 to UF_3 in flibe was calculated and plotted as function of temperature in Figure 3.13. The green region in Figure 3.13 indicates the potential (in terms of a Gibbs free energy of formation) that must exist in flibe for both the salt and structural metals to be chemically stable. Again, anything that exists above the MSRE redox potential dotted line will not be a stable fluoride, and anything that exists below the dotted line will be a stable fluoride.

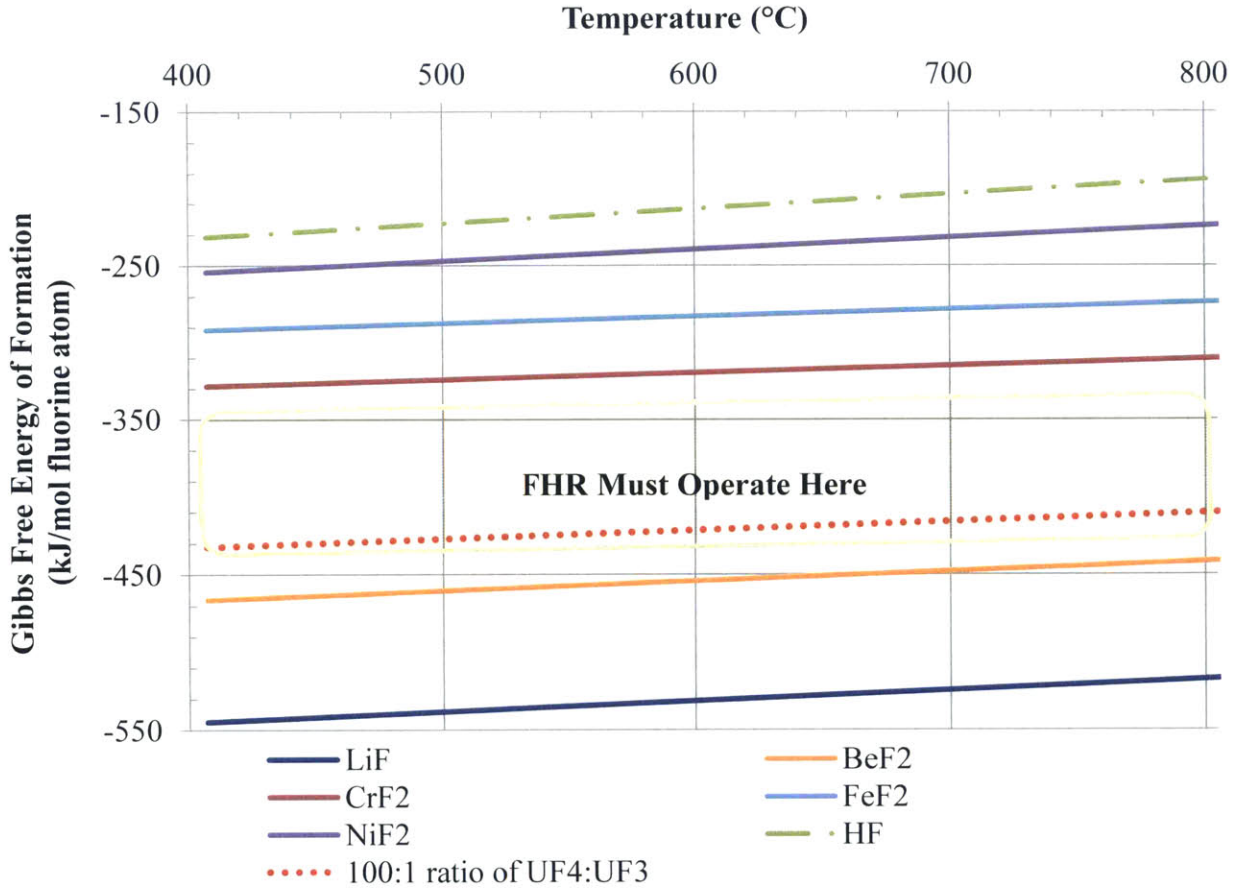

Figure 3.13: Ellingham diagram showing calculated Gibbs free energy of formation for a mixture containing 100:1 UF_4:UF_3 in flibe.

Putting the redox potential in terms of the Gibbs formation free energy, as was done for Figure 3.13, is useful for visually representing the relative stabilities of various compounds and predicting the compounds which will be stable under a given redox regime. In order to calculate how much of a certain species exists in a particular chemical state, the fluorine potential is a more useful representation. In section 3.2.2.1, Eq (3.32) was developed, which can be used to convert a UF_4:UF_3 ratio of 100:1 into a fluorine potential in kJ/mol-F_2. Assuming the activity coefficients for UF_4 and

UF_3 are 1, then the fraction a_{UF4}/a_{UF3} in Eq (3.32) reduces to the mole fraction. At 650 °C, a UF_4:UF_3 ratio of 100:1 equates to a fluorine potential of -700.5 kJ/mol-F_2. Figure 3.14, made with Eq (3.32), illustrates how the fluorine potential changes with varying UF_4:UF_3 ratio and temperature. In a system, such as the FHR, whose redox state is controlled by the HF/H_2 (or TF/T_2) couple, the MSRE fluorine potential can be converted into the ratio $[P_{HF}]^2/[P_{H2}]$ using Eq (3.47). In this case, a fluorine potential of -700.5 kJ/mol-F_2 equates to a ratio of $[P_{HF}]^2/[P_{H2}]$ = 8.46E-9. This value for $[P_{HF}]^2/[P_{H2}]$ was used in Section 3.1.1 to generated Figure 3.5.

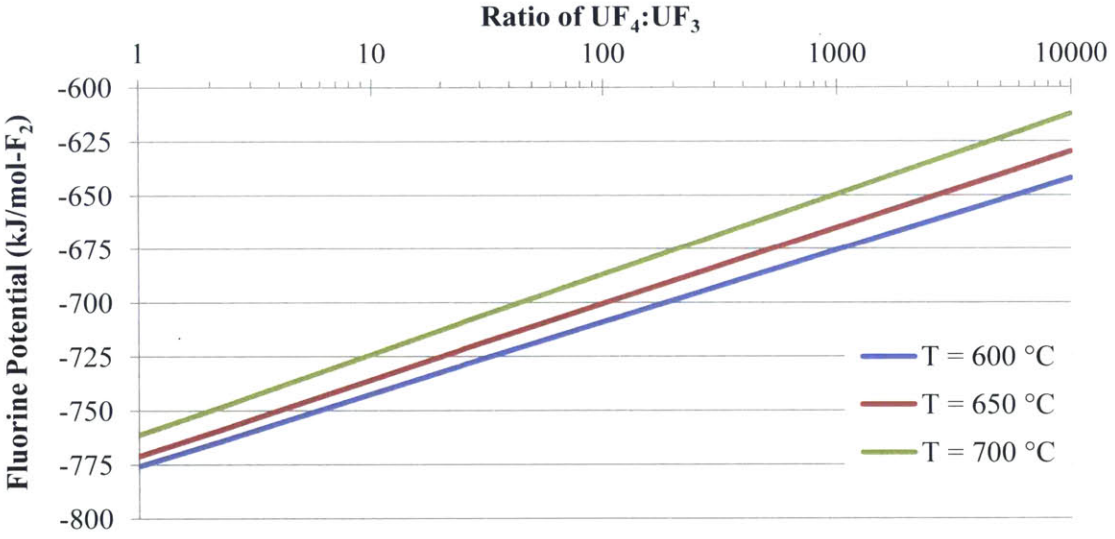

Figure 3.14: Plot of fluorine potential as a function of the UF_4:UF_3 ratio and temperature. Calculated with Eq (3.32).

Using Eq (3.47), the ratio of TF and T_2 in flibe versus the fluorine potential can be plotted. If TF and T_2 are not the agents controlling the redox potential, then the fluorine potential is determined by whatever means is used to control redox (such as impressed current, a dissolve redox buffer, etc.), and the ratio of TF to T_2 is dependent this redox potential. Figure 3.15 shows that as the fluorine potential increases, the ratio of TF to T_2 increases. If the fluorine potential is decreased (made more reducing) the ratio of TF to T_2 decreases. Conversely, if TF and T_2 are the main redox agents in the salt (as would be the case if no redox control methods are applied to the FHR or if HF/H_2 are used for redox control), then it is the fluorine potential which is dependent on the ratio of TF to T_2.

Now that the use of the fluorine potential has been established, Figure 3.5 can be re-plotted in terms of the fluorine potential and the ratio $[P_{HF}]^2$:$[P_{H2}]$. Figure 3.16 shows the equilibrium concentration of Cr^{2+} dissolved in flibe contacting Type 316 L stainless steel at 650 °C. The top horizontal axis shows the fluorine potential and the bottom horizontal axis shows the corresponding ratio of $[P_{HF}]^2$:$[P_{H2}]$. As the fraction of TF increases, the redox fluorine potential increases, the salt becomes more oxidizing, and a greater amount of Cr^{2+} is corroded.

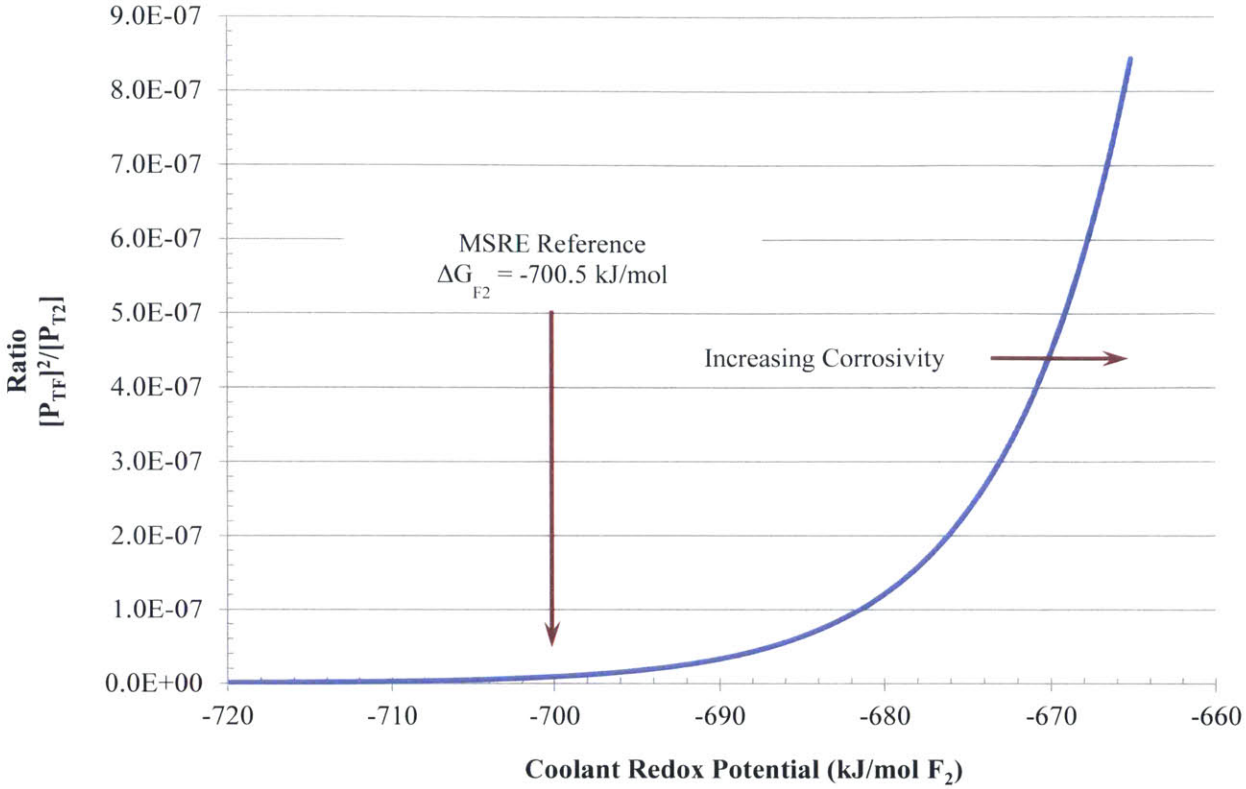

Figure 3.15: $[P_{TF}]^2$:$[P_{T2}]$ versus fluorine potential at 650 °C. Calculated with Eq (3.47).

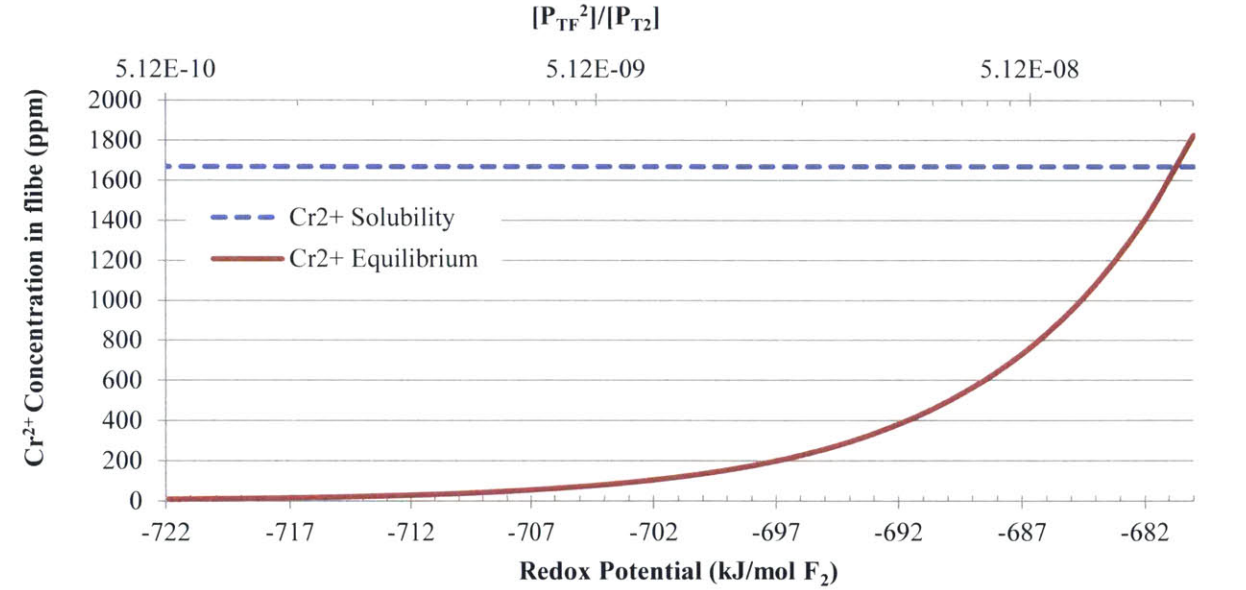

Figure 3.16: Equilibrium concentration of CrF_2 in flibe if Type 316 SS is exposed to flibe at 650 °C over a range of redox (fluorine) potentials determined by $[P_{TF}]^2$:$[P_{T2}]$. Calculated with Eq (3.20).

3.3 Chapter summary of fluoride salt chemistry

The FHR is a fluoride salt cooled reactor. In order to model tritium transport and corrosion reactions (as is done in Chapter 5 and Chapter 6), an understanding of fluoride salt chemistry is required. It was shown that the redox potential determines the extent of corrosion and the chemical form of tritium in the salt. Methods of redox control were compared based on their range of redox potentials, propensity for carbide formation, and nuclear cross section. If experiments determine that a strong redox agent is required, the use of aluminum was suggested as an alternative to major-metal control by Be or Zr. The concept of a redox potential, as defined by the fluorine potential in the salt, was introduced. A reference redox potential was chosen for the FHR based on the potential maintained in the MSRE. This potential maintains the chemical stability of flibe while simultaneously maintaining the chemical stability of structural metals.

The mechanisms of corrosion were reviewed based on experiments from the MSRE which show that Cr is selectively attacked by corrosive impurities in the salt. The ultimate rate of corrosion is limited by solid-state grain boundary diffusion of Cr in the base metal. A corrosive impurity is any fluoride in the salt which is less stable than CrF_2. NiF_2 and FeF_2 can corrode Cr, but these reactions go to completion and will not persist once the Ni and Fe fluorides have been consumed. Tritium fluoride (TF) is a strong oxidant which will preferentially corrode Cr. Because tritium is produced as TF in flibe, corrosion of Cr by TF is a concern in FHRs.

An equation linking the redox potential with the amounts of TF and T_2 dissolved in the salt was derived in Eq (3.47). This is an important realization because TF and T_2 will dictate the redox potential in the FHR unless a redox control method is implemented. With an increasing redox potential, the fraction of tritium existing in the salt as TF increases, the relative amount of T_2 decreases, and the thermodynamic driving force for Cr corrosion increases. Tritium as T_2 has a low solubility in flibe and can diffuse through structural metals. Thus the selection of a redox potential presents a compromise between limiting corrosion by TF and limiting tritium diffusion out of the system as T_2.

Equations were derived which show the temperature and redox dependence of corrosion reactions in Type 316 stainless steel and Hastelloy-N. Eq (3.16) shows the temperature and redox dependence for the corrosion of Cr by UF_4 (which occurred in the MSRE). Eq (3.20) shows the temperature and redox dependence for the corrosion of Cr by TF (which is the principle corrosion reaction in FHRs). As shown in Figure 3.15, an increasing redox potential means an increase in the ratio of TF to T_2 and an increase in the equilibrium concentration of Cr dissolved in the salt from corrosion. Figure 3.5 shows the temperature dependence of the reaction of Cr with TF (for a fixed redox potential). Because of the negative reaction enthalpy for this reaction, corrosion of Cr by TF is exothermic and proceeds more strongly at lower temperatures. By contrast, the corrosion of Cr by UF_4 is an endothermic reaction occurring more readily at higher temperatures. This has implications for mass transfer of Cr due to corrosion by TF. The tritium transport and corrosion model developed

in Chapter 5 accounts for the temperature and redox potential effects on the TF to T_2 ratio and the extent of corrosion in the system.

4 Chemical stabilities and TRISO fuel PIE in support of BDBA analysis

The previous section introduced basic elements of fluoride salt chemistry and derived relationships that will be useful for further analysis. This chapter analyzes the chemical stability of fission products and concrete in FHRs. This is the first fission product analysis to consider TRISO fuels in a liquid fluoride salt environment. This section presents the first look at the stability of concrete in contact with a fluoride salt under severe accident conditions. This section also presents the results of post-irradiation examinations (PIE) of TRISO particles after irradiation in flibe.

4.1 BDBA analysis of fission product behavior in FHRs

The preceding sections provided a background in the chemistry of fluoride salts. With that, the fission product behavior during beyond-design-basis-accidents (BDBAs) in FHRs can be analyzed. Recall that the TRISO fuel in FHRs will utilize a UCO kernel. TRISO particles are characterized by their low failure rates and stable high-temperature operation, and the flibe coolant has the ability to dissolve many fission products as stable fluorides. However, because the FHR is the first concept to pair TRISO fuel with a salt coolant, an analysis of fission product behavior is required in order to prove that the FHR can effectively contain fission products during both normal and accident conditions.

As a preliminary look at the fission product behavior in the FHR, fission product release data from TRISO fuel irradiations for gas-cooled reactors were combined with data from fission product behavior observed in the MSRE. A series of plots of Gibbs free energies of formation for fission product fluorides, carbides, and oxides were constructed in order to help predict the chemical form of certain fission products with varying coolant chemical (redox) potential. Plots of Gibbs reaction free energies were also made in order to determine the likelihood of key reactions occurring.

4.1.1 Connecting fission product behavior to coolant chemistry

If fission products are released from the fuel pebble, they will encounter the flibe coolant in the FHR. The chemical redox potential of the coolant will determine whether these fission products will be stable fluorides dissolved in the coolant, or volatile forms liable to escape the coolant. Figure 3.1 and Figure 3.13 show how the stability of certain fluorides can vary with the redox potential in the coolant. Flibe has excellent solubility for fission product fluorides, but in a highly reducing environment, it might be possible to reduce soluble fission product fluorides (such as cesium fluoride) such that they exist in the more volatile metallic state.

The MSRE employed a redox buffer by setting the ratio of UF_4:UF_3 in the fuel salt at 100:1. TF and fission product build-up in the MSRE salt caused this ratio to increase above 100:1. The ratio was re-established by periodically inserting a Be rod in order to convert excess UF_4 back into UF_3. It

was found that this ratio was sufficiently reducing to keep Cr corrosion to a minimum while not so reducing as to generate uranium carbides. In Section 3.2.3 the case was made that the MSRE potential provides a suitable reference potential for what a real FHR may see. Thus, fission product behavior in this section will be described in the context of a dominant coolant redox potential equivalent to that for the UF_4/UF_3 couple existing in a 100:1 ratio from the MSRE.

4.1.2 Fission product behavior in TRISO fuel

Since the FHR combines TRISO fuel with a salt coolant, an analysis of fission product behavior in FHRs must begin with an understanding of fission product behavior in the fuel. Numerous reviews on fission product release from TRISO particles exist in the open literature [156]. Table 4.1 summarizes the key radionuclides for accident and normal operation and their release behavior from TRISO fuel. Except for Ag-110m and noble gases, nominal releases from a single fuel compact or fuel pebble are only a small fraction of the inventory of a single TRISO particle.

Table 4.1: Summary of fission product release from TRISO fuel in high temperature gas-cooled reactors (HTGRs).

Element	Important Nuclide(s)	Importance	Hold-up/Release Behavior	Refs
Ag	Ag-110m	Normal operation; plant maintenance	Release through intact SiC; little/no hold-up in graphite	[13,157–159]
Cs	Cs-134/137	Severe Accident Release; main indicator of SiC failure	Release through broken SiC, some hold-up in matrix graphite	[159–161]
Ce	Ce-144	Normal Operation	Release through broken SiC, hold-up by forming Ce carbide	[158,159]
Eu	Eu-154	Normal Operation	Release through intact coatings; hold-up in matrix graphite via formation of Eu carbide	[158,159]
I	I-131	Severe accident release and licensing	Release through broken SiC; intact OPyC delays release	[159,160]
Kr	Kr-85/90	Indicates defect; Kr-85 gives same release as I-131 and Xe-133; Kr-90 is Sr-90 precursor	Release through broken SiC; intact OPyC delays release	[159–161]
Pd	Pd-105	Normal operation; may corrode SiC	Release through intact coatings	[158,159]
Sr	Sr-90	Severe Accident Release, indicates SiC failure	Similar to Cs but with greater hold-up in matrix graphite via Sr carbide formation	[159–161]
Xe	Xe-133/137	Indicates defect; use to estimate upper limit for iodine release; Xe-137 is Cs-137 precursor	Release through broken SiC; intact OPyC delays release	[159,160]

4.1.3 Fission product behavior in the MSRE

Recall that the MSRE was a molten salt reactor with the fuel dissolved in the coolant. This means that fission products are produced directly in the coolant. Fission products in the MSRE can be divided into three categories: noble gases, salt-seeking elements, and noble-metal elements. Noble gases are Xe and Kr which have a small solubility in the salt but are readily stripped into the off-gas system by helium sparging of the salt [68]. Greater than 80% of the Xe-135 was removed from the salt in this manner. Some of the noble gas inventory diffused into the moderator graphite [66].

Salt-seeking elements are those which form stable fluorides which are soluble in the salt. Salt-seeking elements include Ba, Ce, Cs, Rb, Sr, Y, Zr, rare-earth elements, and the lanthanides. An aerosol salt mist produced in the pump bowl allowed small amounts of these elements to be collected in the off-gas [66]. Barium, Cs, Rb, Sr, and Y have noble-gas precursors with half-lives long enough for some of the gas to be stripped from the salt before decaying.

Noble-metal fission products include Ag, Mo, Nb, Pd, Rh, Ru, Sb, Tc, and Te. These do not form stable fluorides and deposit on system surfaces such as metal, graphite, or at the salt/cover-gas interface [66]. However, under higher than normal redox conditions, Nb can be oxidized to a fluoride. Tellurium has a vapor pressure of 1.7 kPa at 650 °C which allowed some of it to be captured in the off-gas, whereupon Te-131 decayed to I-131 [66]. Iodine could be considered to be in a category of its own. Iodine was often found to remain in the salt with no evidence of deposition on metal or graphite surfaces. At the redox potential of the MSRE, iodine existed in the salt as the iodide ion or as iodides (*e.g.* CsI), and less than 0.1% was stripped from the salt as I_2 gas [66]. If the salt were to be increasingly oxidizing, a greater portion of the iodine would be in the I_2 gas form.

4.1.4 Fission product behavior in FHRs

Under normal operating conditions, only those elements listed in Table 4.1 are a concern for the FHR. MSRE experience indicates that Ce, Cs, Eu, and Sr will form stable fluorides which are soluble in the salt at the intended redox potential and operating temperatures. Figure 4.1 shows an Ellingham diagram for key fission product metals, calculated using the HSC Chemistry v7.1 software. HSC comes with libraries of temperature-dependent thermodynamic data (*e.g.* enthalpies and entropies of formation) tabulated from the open literature. It uses linear interpolation to fill in temperature ranges for which data are not explicitly available. HSC is not capable of accounting for solvent effects; however, HSC showed only a 5-10% difference when comparisons were made to experimental data. Additional nuclides, not expected to be released from the TRISO fuel in significant quantities, are also included in Figure 4.1. With the redox potential set equivalent to that used in the MSRE, the metal fluorides below the "Reference Redox" line (Ce, Cs, Sr) will be stable in the salt. Metal fluorides above the "Reference Redox" line will exist in the reduced metallic state

and will not be soluble in the salt. For example, silver (Ag-110m) will deposit on metal, graphite, and at the salt-cover gas interface. Iodine will largely stay in the salt as the iodide ion or as an iodide compound. Noble gases Kr and Xe will mostly exit the salt in the off-gas stream.

Figure 4.1 shows that when the coolant temperature approaches the boiling point of flibe (1430 °C), CsF is less stable. At extreme temperatures, CsF will have reduced stability and some Cs may be volatilized from the metallic state. Additionally, if the redox potential is significantly more reducing than that used in the MSRE, CsF stability will be reduced. Strontium appears to form a stable fluoride under any possible coolant state.

Under normal reactor conditions, the liquid salt does not wet the graphite and is not expected to enter the graphite pores [162]. Thus, under normal conditions, the salt will not enter the fuel pebble graphite and will not come into direct contact with the TRISO particles. This means that only the fission products listed in Table 4.1 should be a concern for release to the salt as long as salt/TRISO separation is maintained.

Under certain conditions, however, the MSRE program observed salt wetting of the graphite [162]. This was observed in smaller loop experiments when a graphite surface was contacted by flibe under an atmosphere of helium gas containing moisture of about 10 ppm or higher [162]. Wetting of fuel pebbles by the salt might present additional challenges. It might enhance fission product transport out of the pebble. This is not a major concern for salt-soluble fission products, but might be a concern for gaseous fission products. Another possibility that will need investigation is the possibility of damaging the graphite if the salt were to wet it and then the reactor were to cool below the freezing point of flibe (459 °C).

If an accident were to severely damage the fuel, such that the fuel kernel is directly exposed to the salt, the fission product analysis becomes more complicated. Part of the virtue of the TRISO particle is that it can retain many fission products and actinides as stable oxides or carbides [15]. In an intact UCO kernel (not exposed to salt), the metal oxide versus metal carbide stability is determined by the chemical redox potential in the kernel. In the context of an intact kernel, the redox potential is best expressed as the oxygen potential, which is governed by the reaction $UC_2 + O_2 = UO_2 + 2C$ [15].

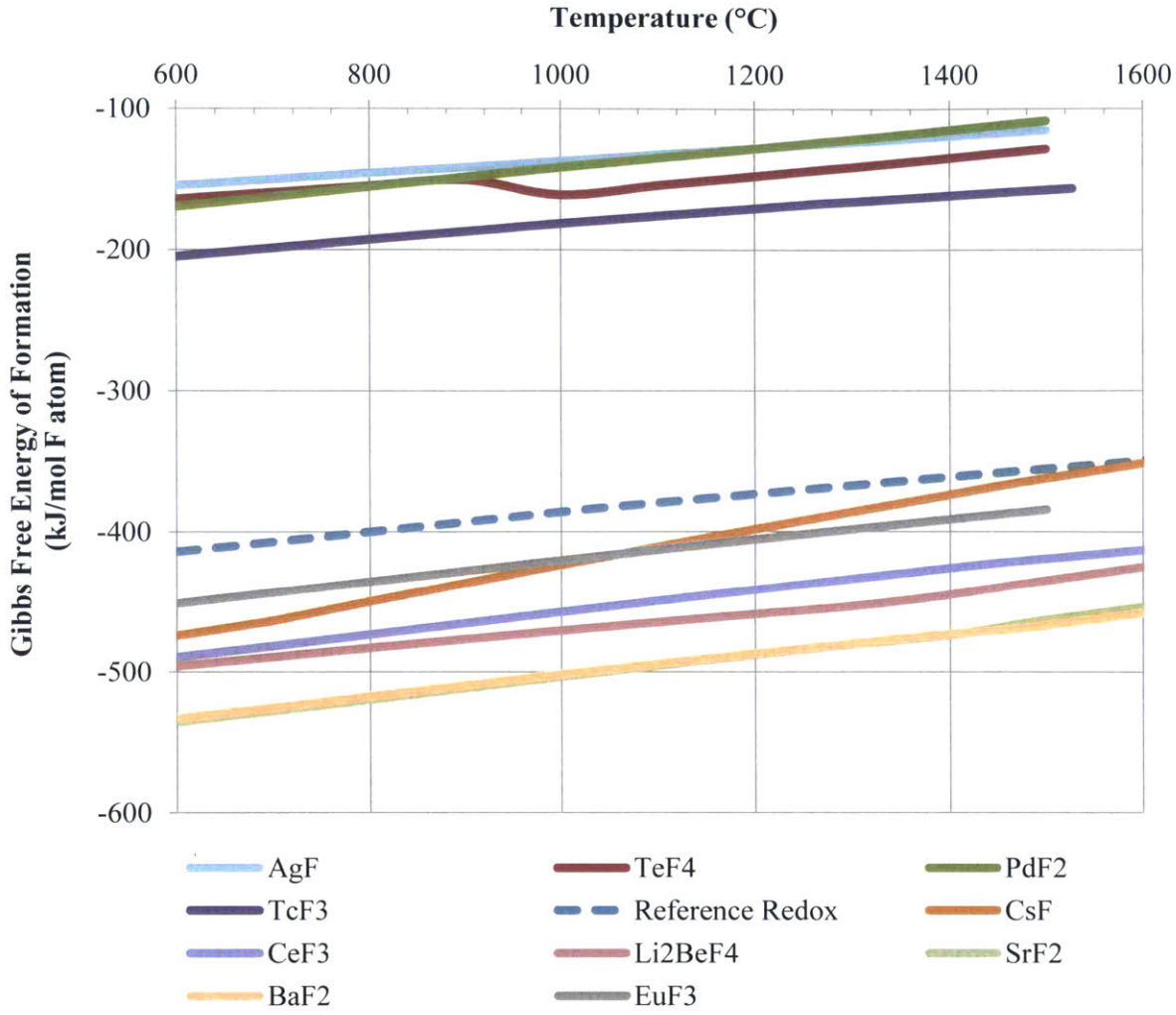

Figure 4.1: Ellingham diagram (Gibbs free energy of formation) for select fission product metal fluorides. Calculated with HSC. Reference redox potential is set equivalent to MSRE redox potential and expressed in terms of a formation free energy.

If a damaged UCO fuel kernel is exposed to salt, the relative stabilities of metal fluorides compared to metal carbides and metal oxides must be known. These stabilities are determined, in part, by the dominant chemical redox potential in the coolant. In this case, the chemical redox potential is determined by the fluorine potential in the coolant in contact with the exposed kernel. As was discussed earlier, the FHR will operate with a chemical redox potential similar to that used in the MSRE. This MSRE redox potential can be used as a reference potential for the FHR by converting it into a fluorine potential as was done in Section 3.2.3. This reference fluorine potential can then be used to determine the relative stability of metal oxides *vs* metal fluorides *vs* metal carbides.

Figure 4.2 and Figure 4.3 depict the relative stability of fluorides compared to carbides, and fluorides compared to oxides, respectively. This comparison is made by plotting the Gibbs reaction free energy for relevant reactions. A negative Gibbs reaction free energy indicates that a reaction

will proceed spontaneously to the right, subject to the dominant redox potential in the media in which the reaction occurs. The reaction free energies ($\Delta G_{rxn} = \Sigma G_{products} - \Sigma G_{reactants}$) were calculated with HSC and normalized with respect to the moles of F_2 required to balance equations of the type $xMC + nF_2 \rightarrow yMF_z + zC$ or $xMO + nF_2 = yMF_z + zO_{2(g)}$. A more accurate formulation of the equations would have BeF_2 reacting with the metal oxides and LiF reacting with the metal carbides; however, these reactions cannot be related to the fluorine potential. Using F_2 as the reactant allows comparison with the fluorine potential and is not expected to alter the qualitative order of stabilities of the compounds in question. The reference redox potential (in terms of the fluorine potential) is plotted as a dashed line. Figure 4.2 shows that elements below the dashed redox line will be fluorides and elements above the line will be carbides. Analogously, Figure 4.3 shows that elements below the dashed redox line will be fluorides and elements above the line will be oxides. For an element like Pu, which has oxides and carbides above the redox line in Figure 4.2 and Figure 4.3, one can refer to the oxygen potential in the fuel kernel in order to determine whether a carbide or an oxide would be favored [15]. It should be mentioned that the plots indicate thermodynamic stabilities. The plots contain no kinetic information and cannot indicate how quickly, for example, a metal carbide might react in the coolant to form a metal fluoride. The significance of Figure 4.2 and Figure 4.3 is that if the kernel were to be exposed to the salt, most elements of interest should remain as immobile oxides or carbides in the kernel or as soluble fluorides in the melt. This helps contain radioactivity in the event of a severe accident.

The key message that this analysis conveys is that the FHR benefits from the use of the highly retentive TRISO fuel particle and a coolant salt (flibe) which is capable of dissolving many fission products and actinides (Cs, Sr, U, Am, etc.) as well as holding up iodine. Under normal conditions, fission product releases to the FHR coolant should be limited to those observed in HTGRs. In severe cases where fuel kernels are exposed to coolant, the system should inherently act to retain other key nuclides.

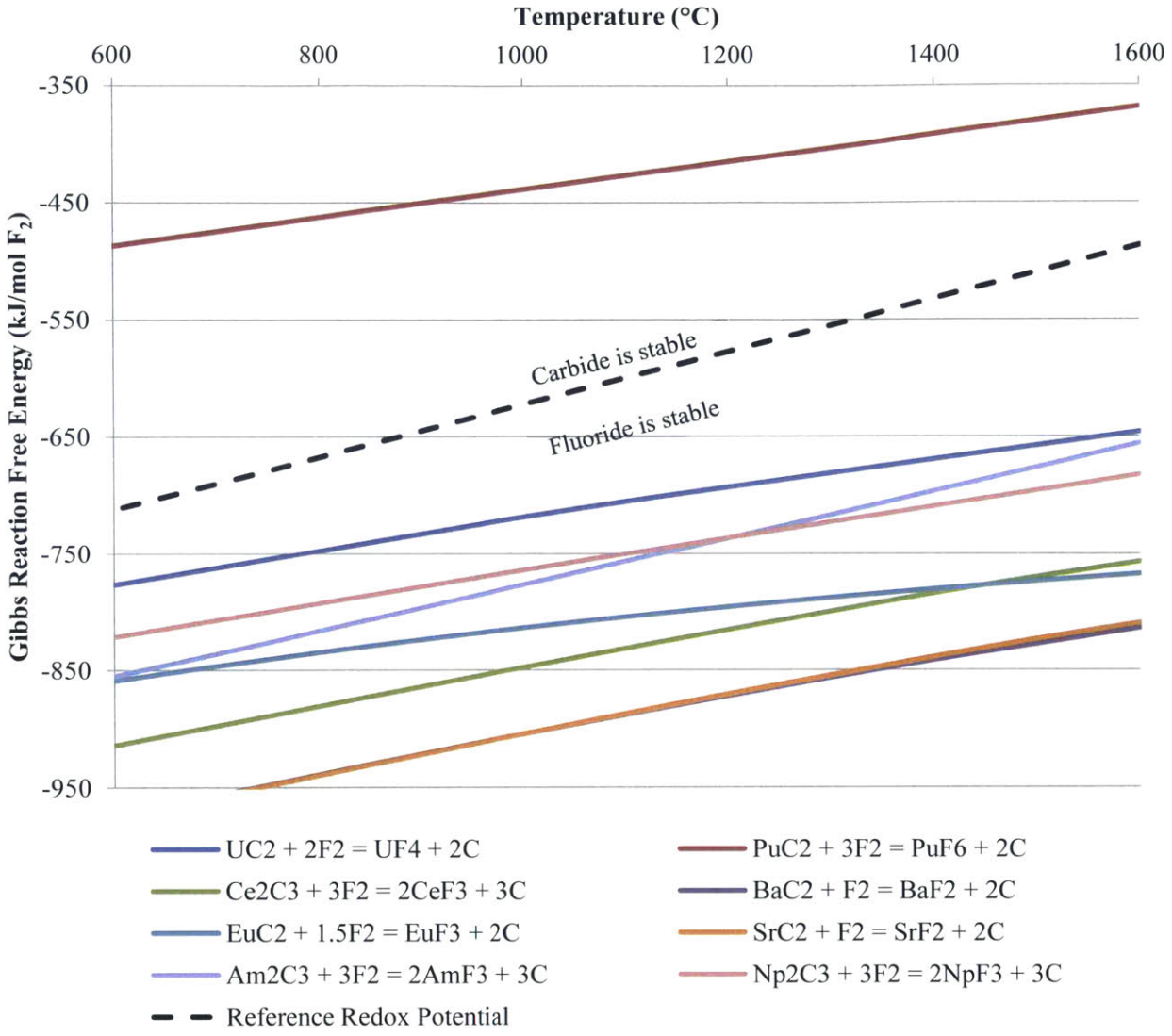

Figure 4.2: Fluoride vs carbide stability represented as the Gibbs reaction free energy for reactions between metal carbides and oxides. Calculated with HSC.

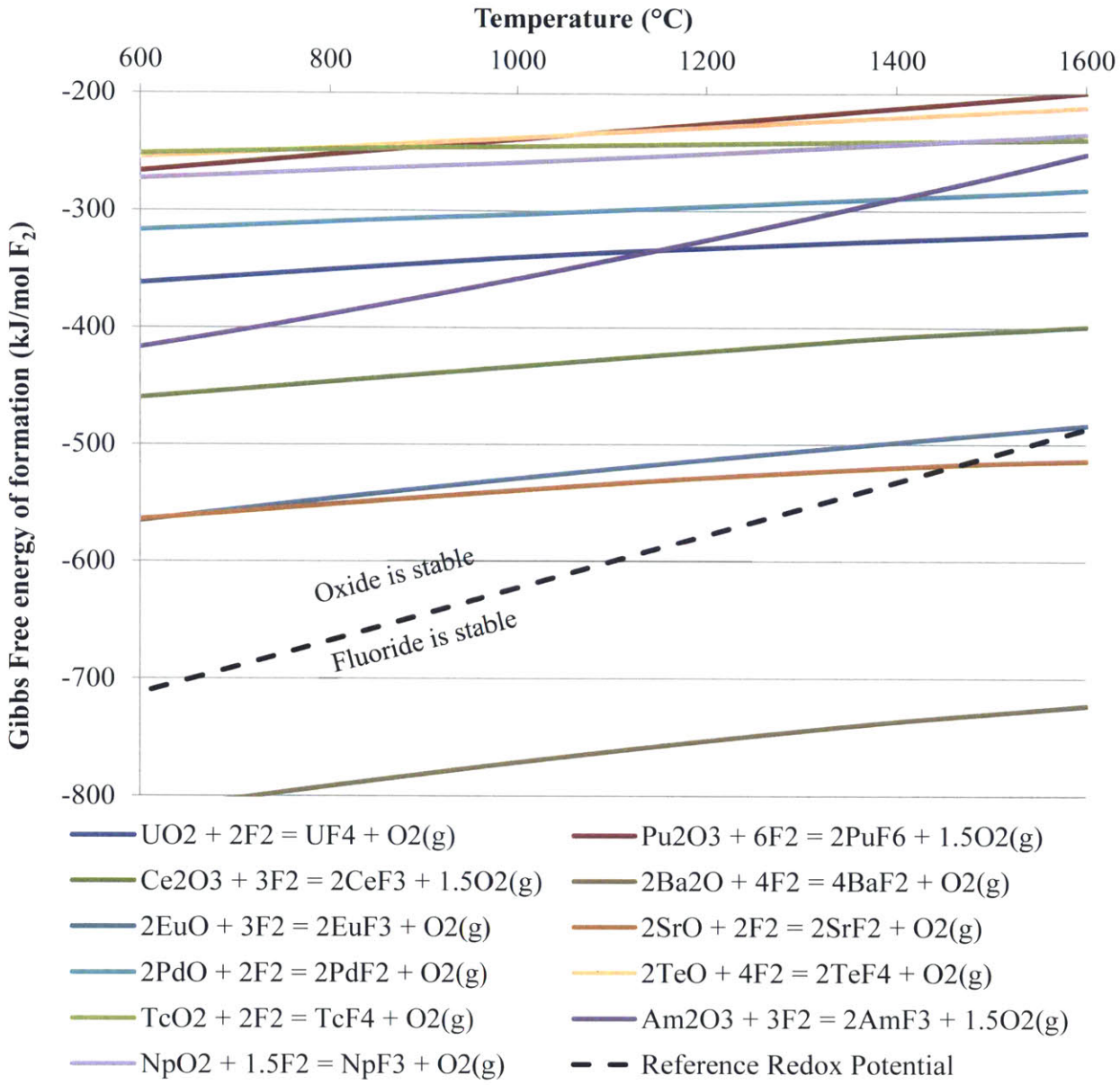

Figure 4.3: Fluoride vs oxide stability represented as the Gibbs reaction free energy for reactions between metal fluorides and oxides. Calculated with HSC

4.2 Concrete and insulation stability during BDBA in FHRs

A challenge all reactor types must face is how the coolant interacts with the rest of the plant in the event of a coolant leak. This could be a small pipe leak or a large leak associated with an accident. Experience with LWRs, sodium fast reactors (SFRs) and HTGRs shows that heat and gas generation from chemical reactions from such an event can be minimized by choosing appropriate materials. What follows is a basic examination of the chemical compatibility of salt coolants and

common materials that might be found in insulation, concrete aggregate, and other materials of construction. Possible interactions of the salt coolants with other fluids (air, water, etc.) are also examined.

Current materials limit FHR core exit temperatures of to about 700°C. Under normal operations a pipe break or leak would release salt no hotter than the core exit temperature. In a severe accident, however, the temperatures would be higher. The physical properties (flibe melts at 459 °C, and fluoride salts in general melt between 350 and 500 °C) of the coolant imply that only high-temperature materials will be located near the primary system. It also implies that such salts will quickly freeze and self-seal in the event of a leak. In the event of a coolant leak, the high temperatures could damage out-of-core materials. This must be considered in the context of plant design. The goal of materials selection is to limit exothermic chemical reactions and gas generation which could cause additional damage. Eliminating all coolant-material chemical interactions is not a licensing requirement, but predictability and limited consequences are required.

4.2.1 Concrete and cement composition

The most common type of cement is portland cement which is composed of tricalcium silicate, dicalcium silicate, tricalcium aluminate, and tetracalcium aluminoferrite. This is summarized in Table 4.2 along with a range of compositions based on concrete of Type I through Type V from the ASTM C150 standard [163]. Other types of concrete found in nuclear systems include basaltic concrete, limestone concrete, and limestone/ common-sand concrete [164]. Typical compositions for these types of concrete are summarized in Table 4.3. Basaltic concrete is often used in LWR systems [164].

Table 4.2: Composition of portland cement. Summarized from [163].

	Formula	Wt %
Tricalcium Silicate	$3CaO\text{-}SiO_2$	28-55
Dicalcium Silicate	$2CaO\text{-}SiO_2$	19-49
Tricalcium Aluminate	$3CaO\text{-}Al_2O_3$	4-10
Tetracalcium alumninoferrite	$4CaO\text{-}Al_2O_3\text{-}Fe_2O_3$	7-12
Other	MgO, TiO_2, etc.	6-9

Table 4.3: Compositions of nuclear-type concrete. Summarized from [164].

	Basaltic Concrete	Limestone Concrete	Limestone/Common Sand
SiO_2	54.7	3.6	35.7
CaO	8.8	45.4	31.2
Al_2O_3	8.3	1.6	3.6
MgO	6.2	5.7	0.5
Fe_2O_3	6.3	1.2	1.4
K_2O	5.4	0.7	1.2
TiO_2	1.1	0.12	0.2
Na_2O	1.8	0.1	0.8
MnO	-	0.01	0.03
Cr_2O_3	-	0.004	0.014
H_2O	5	4.1	4.8
CO_2	1.5	35.7	22

4.2.2 Relevant fluoride salt-concrete chemical reactions

The major constituents of concrete are metal oxides. Experience from the Molten Salt Reactor Experiment (MSRE) at Oak Ridge National Laboratory (ORNL) in the 1960s has shown that BeF_2 in flibe reacts with structural metal oxides (Cr_2O_3, NiO, FeO, etc.) to make structural metal fluorides (CrF_2, NiF_2, FeF_2, *etc.*) [119,123]. Metal fluorides are soluble in flibe and will dissolve in it. A generalized reaction of a metal oxide (MO) with BeF_2 is shown in Eq (4.1). Subscript *s* indicates a solid, *l* indicates a liquid, and *d* indicates a dissolved species. The dissolution of the metal fluoride is depicted in Eq (4.2). In order to determine the set of reactions of concern and help verify that in clean flibe, BeF_2 will react with metal oxides before LiF, the chemical stability of lithium and beryllium fluorides and oxides was compared using the program HSC Chemistry v7.1. HSC comes with libraries of temperature-dependent thermodynamic data (e.g. enthalpies and entropies of formation, phase transition temperatures, etc.) tabulated from the open literature. The Gibbs reaction free energy for Eq (4.3), is -212.4 kJ/mol-BeO at 700 °C, indicating that the reaction goes spontaneously to the right as-written in Eq (4.3). Thus, our analysis is limited to the reaction of BeF_2 with metal oxides commonly found in concrete.

$$MO_{(s)} + BeF_{2(l)} \rightarrow MF_{2(d)} + BeO_{(s)} \quad (4.1)$$

$$MF_2 \rightarrow M^{2+} + 2F^- \quad (4.2)$$

$$Li_2O_{(s)} + BeF_{2(d)} \rightarrow 2LiF_{(d)} + BeO_{(s)} \quad (4.3)$$

The Gibbs reaction free energies for the reactions of metal oxides with BeF_2, the type of reaction illustrated by Eq (4.1), were evaluated for all of the major metal oxide constituents of the various types of concrete. The results were normalized by the number of moles of BeF_2 required to balance the equations. The final results are displayed in Figure 4.4 along with the full equations list. Since the results are normalized to the moles of BeF_2, the reaction free energies must be compared against the BeF_2 potential in flibe which is plotted as a dashed line in Figure 4.4. At equilibrium, the chemical potential of a substance in a liquid is equal to the chemical potential of that substance in the vapor above the liquid. Thus, the BeF_2 chemical potential can be written as follows in Eq (4.4). Here, R is the universal gas constant (0.008314 kJ/mol-K), T is the temperature in K, p_{BeF2} is the partial pressure of BeF_2 over flibe, and p^o is the total pressure over flibe (assumed to be 1 atm or 101325 Pa). Following after Olander, Eq (4.5) gives the partial pressure of BeF_2 in flibe (p_{BeF2}) from the activity coefficient of BeF_2 in flibe (γ_{BeF2}), the mole fraction of BeF_2 in flibe (x_{BeF2}), and the vapor pressure of pure BeF_2 (p^o_{BeF2}) [152]. In flibe (0.67LiF-0.33BeF_2), the mole fraction of BeF_2 is 0.33. The activity coefficient of BeF_2 in flibe (γ_{BeF2}) is about 0.33 [152]. The vapor pressure of pure BeF_2 (p^o_{BeF2}) in units of atm is given by Eq (4.6) [152].

A Gibbs reaction free energy which is more positive than the BeF_2 potential means that the reaction will tend toward the left as written. A Gibbs reaction free energy which is more negative than the BeF_2 potential means that the reaction will tend toward the right as written. A Gibbs reaction free energy which is at or near the BeF_2 potential means that the products and reactants exist at or near thermodynamic equilibrium.

It has been suggested that a general rule for determining the nobility of a material in the salt is that the difference in Gibbs formation free energies between the material and the salt should be greater than 80 kJ/mol-K [128]. If this logic is applied to the Gibbs reaction free energies and the BeF_2 potential, then this suggests that none of the metal oxides are truly stable in the salt. This is an assertion that is well supported by experiments which show that fluoride salts dissolve metal oxides, leaving a clean metal surface [165,166]. For a reaction such as that in Eq (4.7), the equilibrium constant (K) is written as Eq (4.8), and the reported value for this equilibrium constant is 1.06E-4 at 650 °C [118]. Thus, even metal oxides with Gibbs reaction free energies slightly more positive than the BeF_2 potential will react to some extent to make metal fluorides with BeF_2. Since the BeF_2 potential increases with temperature, none of the listed metal oxides are stable at higher temperatures in flibe. SiO_2 appears to be somewhat stable at lower temperatures; however, its reaction in an experiment with LiF-NaF-KF at 850 °C resulted in the failure of a Type 316L stainless steel capsule [165]. Additionally, any HF, TF, or free fluorine will react quantitatively with any metal fluoride. HF is used for removing oxide from the salt during preparation and will convert metal oxides to metal fluorides.

Transition metal oxides are generally not stable in flibe. If metal oxides must be used in locations where they may come into contact with salt, then the most stable of the metal oxides should be chosen. This may require new formulations of concrete or it may require that critical concrete structures can never come in contact with salt even during an accident. Based on their reaction free

energies being near the BeF_2 potential, nickel, chromium, iron and aluminum oxides are more stable compared to other metal oxides. Calcium, magnesium, potassium, and titanium oxides are least stable in flibe.

$$\Delta G_{BeF_2} = RT \ln\left(\frac{p_{BeF_2}}{p^o}\right) \tag{4.4}$$

$$p_{BeF_2} = \gamma_{BeF_2} x_{BeF_2} p^o_{BeF_2} \tag{4.5}$$

$$\log\left(p^o_{BeF_2}\right) = 10.491 - \frac{10953}{T} \tag{4.6}$$

$$NiO_{(s)} + BeF_{2(l)} = NiF_{2(d)} + BeO_{(s)} \tag{4.7}$$

$$K = \left[\mathrm{NiF}_{2(d)}\right] \tag{4.8}$$

Besides looking at the chemical stability of metal oxides versus metal fluorides in flibe, it is important to know whether these reactions are exothermic (generate heat) or endothermic (absorb heat). HSC was used to compute the reaction enthalpy (ΔH) for the reactions considered in Figure 4.4. Since these reactions will occur at the interface between the flibe coolant and a solid, this reaction enthalpy can be used to calculate the increase (from exothermic reactions) or decrease (from endothermic reactions) in the coolant temperature due to the chemical reaction. For a chemical reaction occurring at constant pressure, Eq (4.9) is used. Here, ΔH is the reaction enthalpy (kJ/mole metal oxide), c_p is the specific heat of the coolant (kJ/kg flibe-K), m is the mass of coolant in which the reaction occurs (kg), and $\Delta T_{coolant}$ is the change in temperature. In order to get an idea of the consequence of each reaction, $\Delta T_{coolant}$ for each reaction was calculated assuming one gram of metal oxide reacted in 1 gram of flibe. The specific heat for flibe has little or no temperature dependence and is reported as 2.39 kJ/kg-K [42].

$$-\Delta H = c_p m \Delta T_{coolant} \tag{4.9}$$

Figure 4.5 shows the temperature change in 1 g of flibe if 1 g of the specified metal oxide reacts according to the equations in Figure 4.4. The sharp jumps in the curves are due to phase changes in the oxide with temperature. The reaction of K_2O is the most exothermic, causing a 15 °C increase in 1 g of flibe. The reaction of SiO_2 is the most endothermic from 500 to 800 °C. Above 800 C, a phase change in Cr_2O_3 results in a more endothermic reaction. Whether an exothermic or endothermic reaction is desirable depends on the situation. If the salt is cooled by an endothermic reaction, this cooling may aid the freezing of the salt, which could plug leaks. On the other hand, freezing might block desirable salt coolant flow. Exothermic reactions might heat the salt further, weakening structural materials and changing the chemical stability of any dissolved fission products.

While this analysis discusses chemical stabilities and reaction enthalpies, it does not discuss reaction kinetics. Experimental observations indicate that reactions of fluoride salts with metal oxides are relatively fast [165]. If metal oxides must be used for insulation and/or concrete where a

severe accident could result in exposure to flibe, the information in Figure 4.4 and Figure 4.5 can be used to suggest suitable concrete and insulating materials as well as determine which materials should be avoided. In locations where a salt leak is possible, aluminum (Al_2O_3), iron (FeO), and nickel (NiO) oxides have better stability than some metal oxides and have small effects on coolant temperature when they do react. For example, Figure 4.4 shows that NiO and FeO have reaction free energies near the BeF_2 line. Figure 4.5 shows that when NiO and FeO react, they have relatively small effects on coolant temperature. Chromium oxide may also be a reasonable choice if metal oxides must be used.

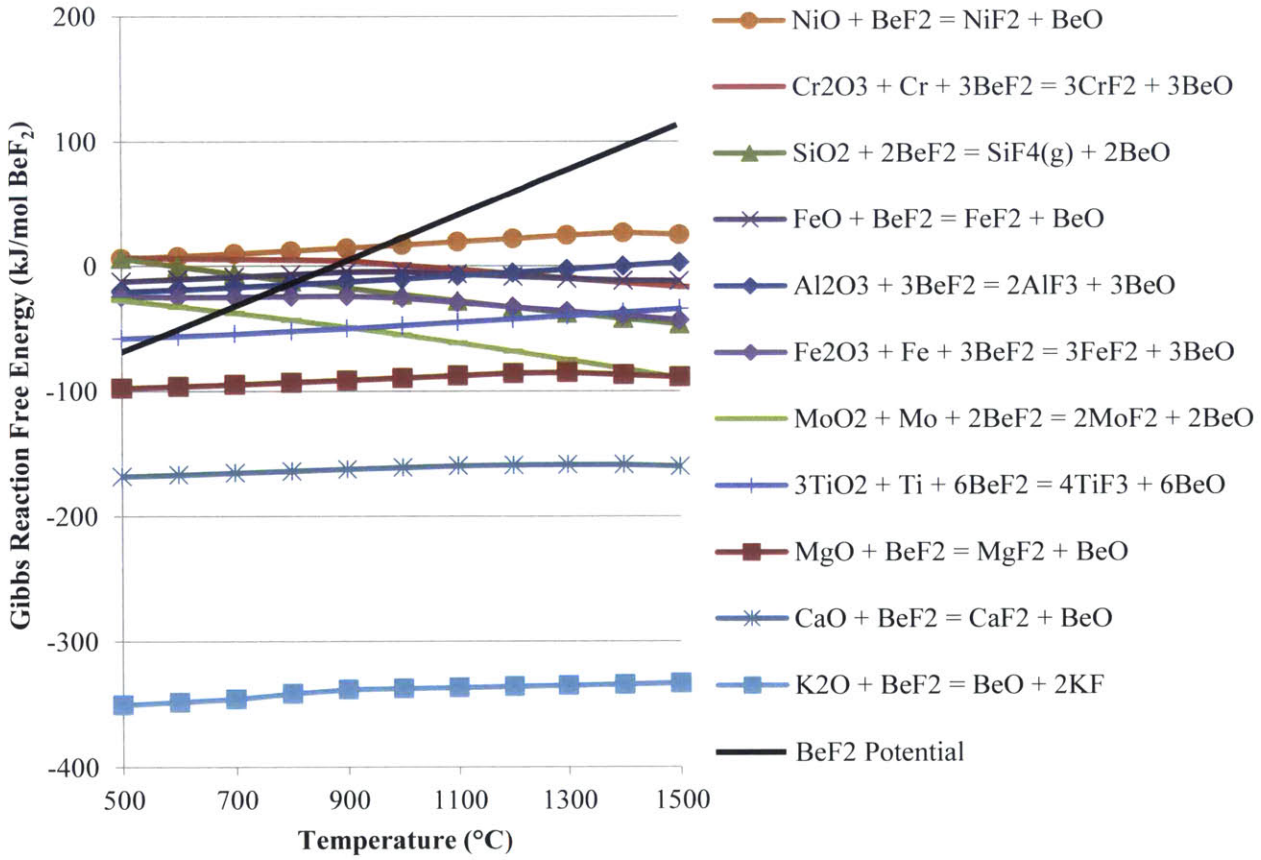

Figure 4.4: Gibbs reaction free energies for reaction of metal oxides with BeF_2. Calculated with HSC. Calculation of BeF_2 potential described in preceding paragraphs.

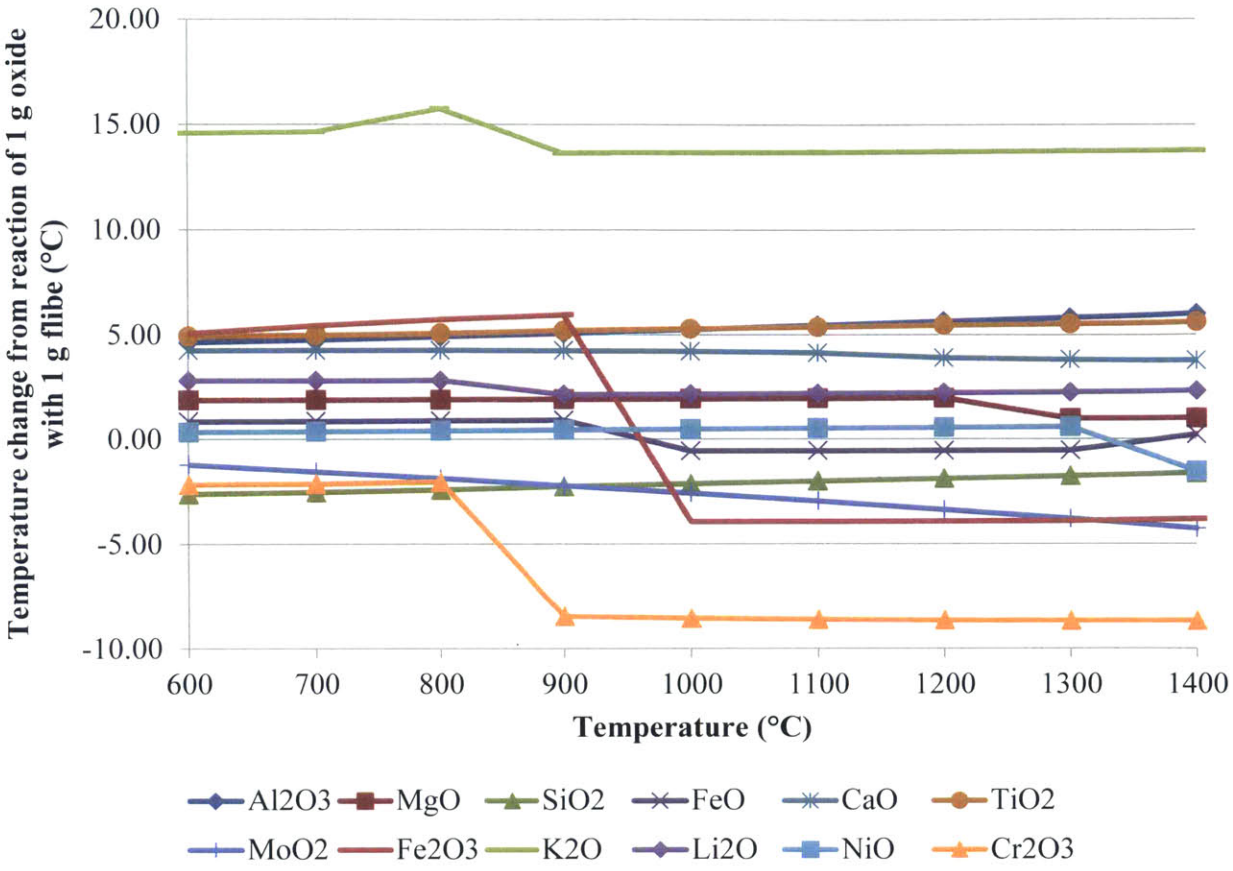

Figure 4.5: Temperature change if 1 gram of metal oxide reacts with BeF_2 in 1 g of flibe according to reactions listed in legend of Figure 4.4. Calculated with HSC. Sharp jumps due to phase change.

4.2.3 Other important reactions with fluoride salts

Reactions between flibe, H_2O, and CO_2 were evaluated as well. At high temperatures, CO_2 can come out of concrete as $CO_{2(g)}$, but thermodynamic analysis with HSC indicates that it will not react with flibe. At high temperatures, H_2O can come out of concrete as $H_2O_{(g)}$. Pressurization of shield buildings by $CO_{(g)}$ and $H_2O_{(g)}$ should be avoided. Water vapor can also react with flibe to make HF according to the reaction in Eq (4.10). Metal oxides are generally not stable with respect to HF. $HF_{(g)}$ is used to remove oxides from flibe during processing [123]. HF (both gaseous and dissolved in flibe) can react with metal oxides according to Eq (4.11). Thus, the net reaction between Eq (4.10) and Eq (4.11) is the conversion of BeF_2 and MO into BeO and MF_2. Besides degrading concrete and insulation, HF is also poisonous. Thus, minimizing the moisture content in concrete is desirable.

$$H_2O_{(g)} + BeF_2 \rightarrow BeO + 2HF_{(g)} \quad (4.10)$$

$$2HF + MO \rightarrow MF_2 + H_2O \quad (4.11)$$

4.3 PIE of surrogate TRISO particles after irradiation in flibe

Under normal circumstances, TRISO particles will never come into contact with flibe in an FHR because they will be embedded in graphite fuel pebbles, the salt is not expected to enter the graphite pores to any significant extent, and the salt does not usually wet the graphite [162]. However, during a BDBA, if the fuel pebbles were damage and TRISO particles were to come into contact with the salt, irradiations of TRISO particles in flibe will help predict possible effects. A batch of surrogate TRISO fuel particles (containing a ZrO_2 kernel in place of a UCO or UO_2 kernel) were irradiated in the MIT research reactor in a helium atmosphere and in molten flibe. While irradiations were carried out at MIT, parallel tests were carried out at UW-Madison which matched the MIT irradiation conditions except that the UW tests did not have any neutron exposure. TRISO particles irradiated in a helium atmosphere were also analyzed. Thus TRISO particles from the same batch with four different histories could be compared:

- As-fabricated
- Exposed to molten salt only (no neutron exposure)
- Simultaneously exposed to neutron flux and molten salt
- Simultaneously exposed to neutron flux and inert helium gas

Comparing as-fabricated particles to particles irradiated in a helium atmosphere to particles irradiated in flibe to particles exposed to flibe in the absence of neutrons allows for the determination of irradiation effects, combined radiation/chemical effects, and chemical effects. A detailed discussion of the irradiations and the procedures for the PIE is provided in Appendix A. In this section, only results pertinent to the behavior of TRISO particles during irradiation in flibe are presented.

The surrogate particles used for these experiments were fabricated as batch "ZrO2-500-AK2" during early development of TRISO fabrication procedures at ORNL [167]. One group of these particles was irradiated for 2200 hours at 1000 °C in a $He_{(g)}$ atmosphere to a fast fluence $3.7x10^{20}$ n/cm^2 (E > 0.1MeV) [168]. Another group of particles was irradiated in liquid flibe for 3000 hours at 700 °C to a fast fluence of $1.25x10^{21}$ n/cm^2 (E > 0.1 MeV). In a parallel test without irradiation, several hundred TRISO particles from batch ZrO2-500-AK2 were also exposed to flibe in a capsule at 700 °C for 3000 hours at the University of Wisconsin-Madison. This test was designed to mirror the conditions of the flibe irradiations at MIT except that the UW test would not have any neutron exposure. Prior to irradiation in flibe, the exterior of these particles was in the as-fabricated condition depicted in Figure 4.6.

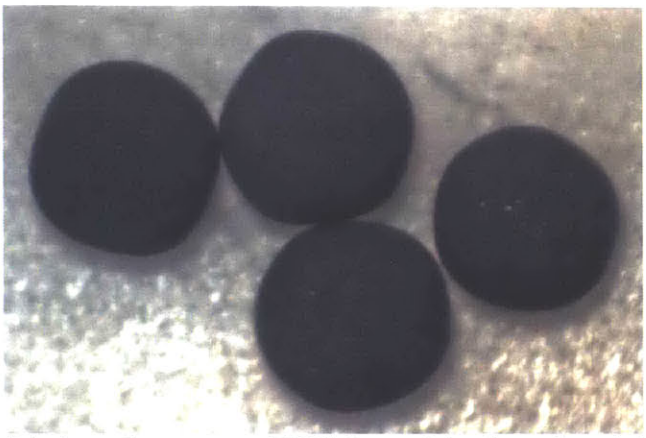

Figure 4.6: As-fabricated surrogate TRISO particles from batch ZrO2-500-AK2.

After irradiation, the sample capsule containing flibe and the TRISO particles was moved to a glove box at the MIT nuclear reactor laboratory. Because the flibe was frozen at this point, the capsule was heated in an oven to 600 °C in order to melt the flibe. Then the flibe was poured over a mesh in order to filter out the TRISO particles. In most cases, due to the non-wetting nature of the salt, the filtered particles did not appear to have any residual salt on their surfaces. However, these extracted particles all featured cracked OPyC layers. Figure 4.7 shows OPYC cracks on four different particles after extraction from flibe following the end of the 3000 hour irradiation in flibe at the MITR. Some particles were soaked in deionized (DI) water for 24 hours or more in order to dissolve any residual flibe. Figure 4.8 shows one particle after soaking in DI water. A large section of the OPyC came loose from the particle during soaking. This is evidence that liquid flibe had entered the cracks in the OPyC layer. Soaking the particle in water dissolved the frozen flibe from the crack and allowed the OPyC layer to come loose from the particle.

The four particles from Figure 4.7 were mounted and polished using the procedure outlined in Appendix A.1.5. Figure 4.9 shows optical micrographs (at 100x magnification) of four particles from the irradiation in flibe after mounting and polishing. The same types of tangential and circumferential cracks observed in the SiC layers of the particles irradiated in helium (see Appendix A.1.6) are observed here as well. The particle at the bottoms left in Figure 4.9 also exhibits a pair of buffer and IPyC cracks similar to those observed in some of the particles irradiated in helium. As discussed in Appendix A.1.6.3, it was determined that the layer cracks in the particles irradiated in helium were due to mounting and polishing and that the cracks did not occur during the irradiation itself. Irradiation embrittlement of the layers made them susceptible to cracking during mechanical polishing. The most obvious difference between the particles irradiated in flibe and the particles irradiated in helium is that the particles from the irradiation in flibe have large (wide) radial OPyC cracks and large OPyC-SiC gaps. There is one other difference between the SiC cracking in the helium-irradiated particles and the SiC cracking in the flibe-irradiated particles, however. Because of the large OPyC-SiC gap in the particles irradiated in flibe, the circumferential cracks in the SiC layers progress radially outward before terminating on the outside of the SiC layer. The SiC cracks

in the case of the helium-irradiated particles terminated within the SiC layer. For the particles from the irradiation in flibe, in places where there is no longer OPyC-SiC contact, any compressive influence that the OPyC would have had on the outside of the SiC layer during grinding and polishing is now gone.

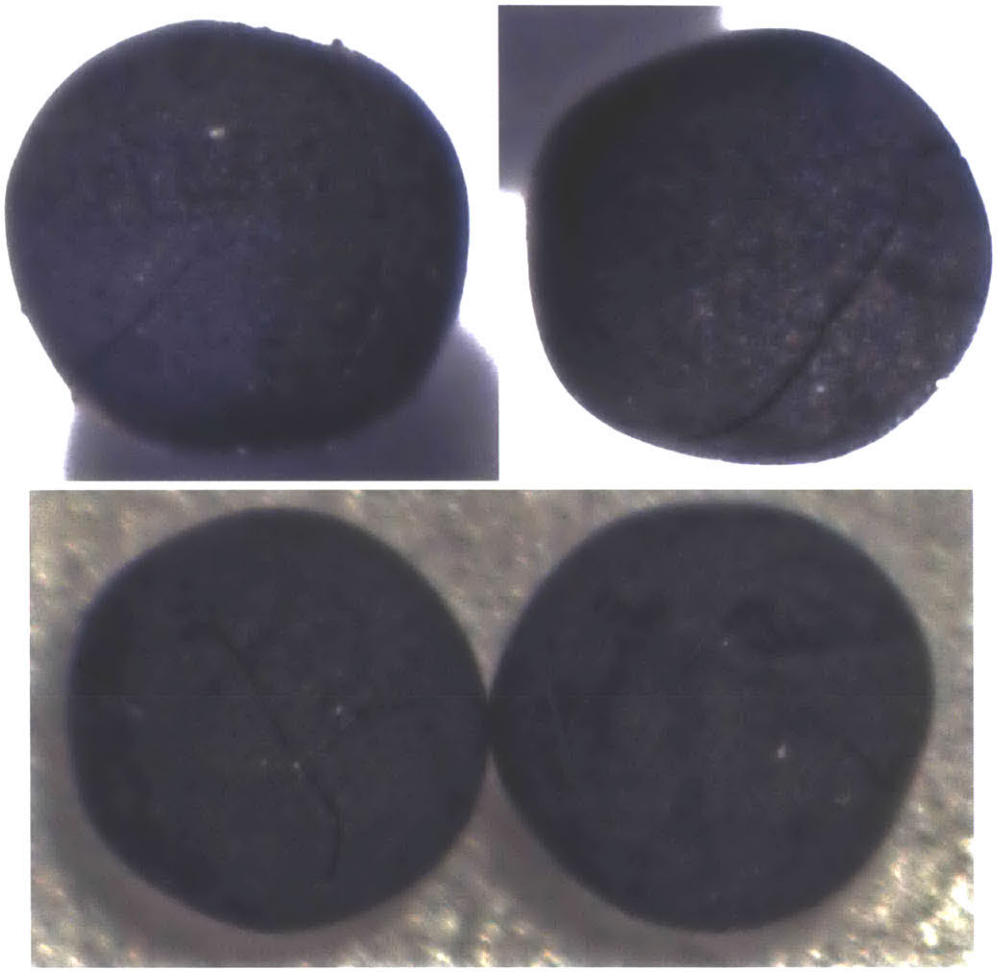

Figure 4.7: Outer surfaces of four different TRISO particles after irradiation in flibe shows significant OPyC cracks.

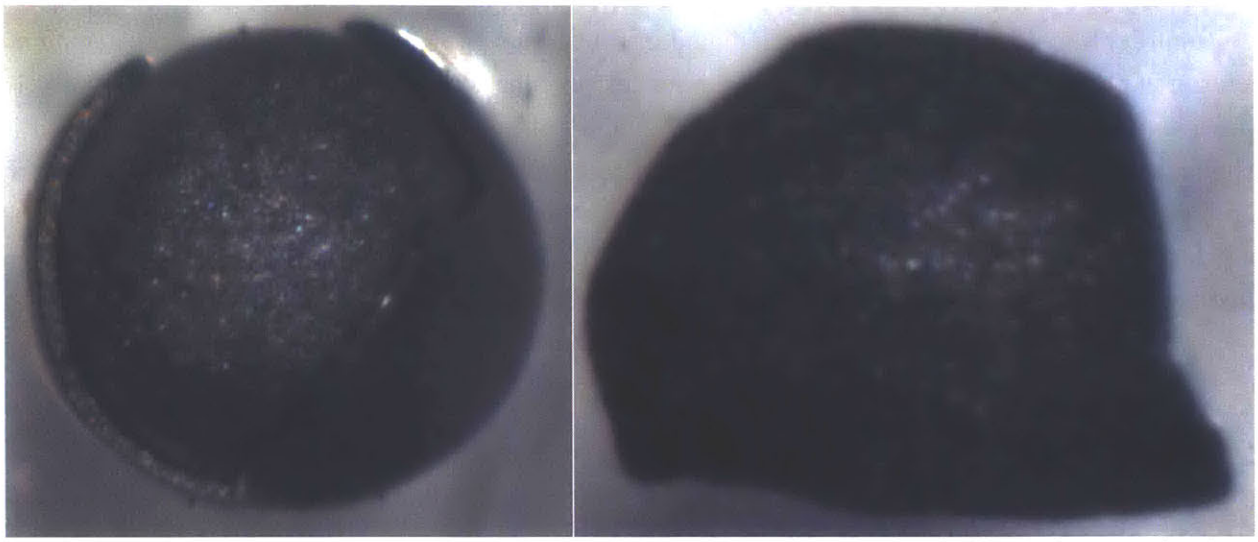

Figure 4.8: TRISO particle and loosened OPyC shard from irradiation in flibe after soaking in deionized water for 24 hours.

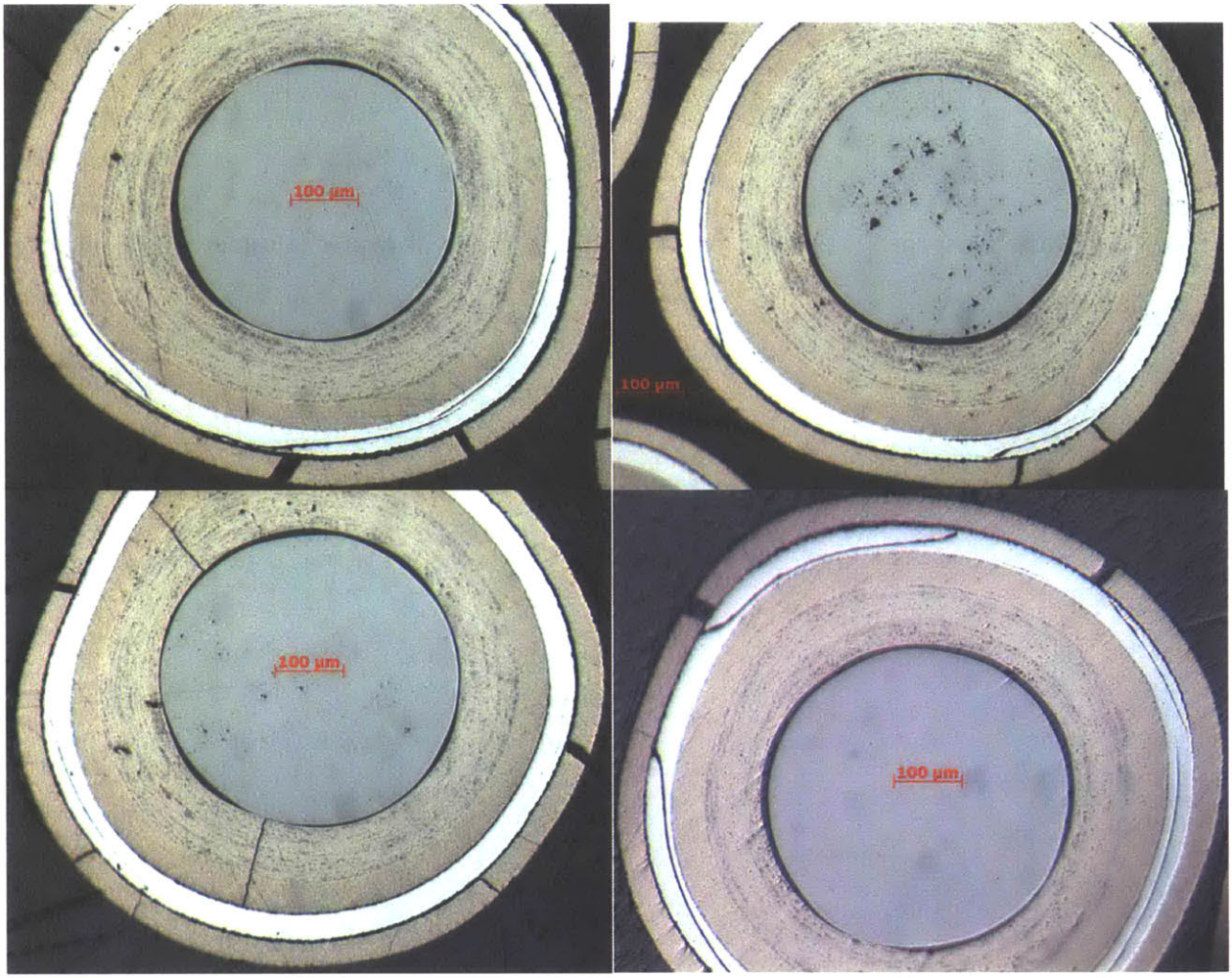

Figure 4.9: Four different TRISO particles from the irradiation in flibe after mounting and polishing. Magnification is 100x.

In order to compare the particles irradiated in flibe to the particles exposed to flibe only (with no neutron exposure), particles from the 3000 hour test in flibe were obtained from UW. Figure 4.10 shows two of the UW particles prior to mounting and polishing following the procedure outlined in Appendix A.1.5. All of the particles exhibited pristine outer surfaces which matched those in the as-fabricated condition. Figure 4.11 shows optical micrographs of these particles after mounting and polishing. No layer cracks or defects of any kind were observed. Thus, in the absence of a neutron flux, the TRISO particles exposed to flibe for 3000 hours show no signs of degradation.

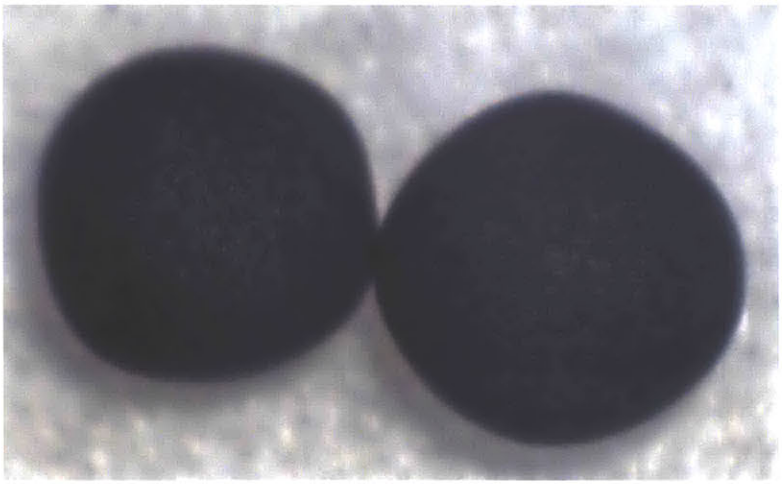

Figure 4.10: Particles from 3000 hour exposure to flibe (with no neutron exposure) at UW prior to mounting.

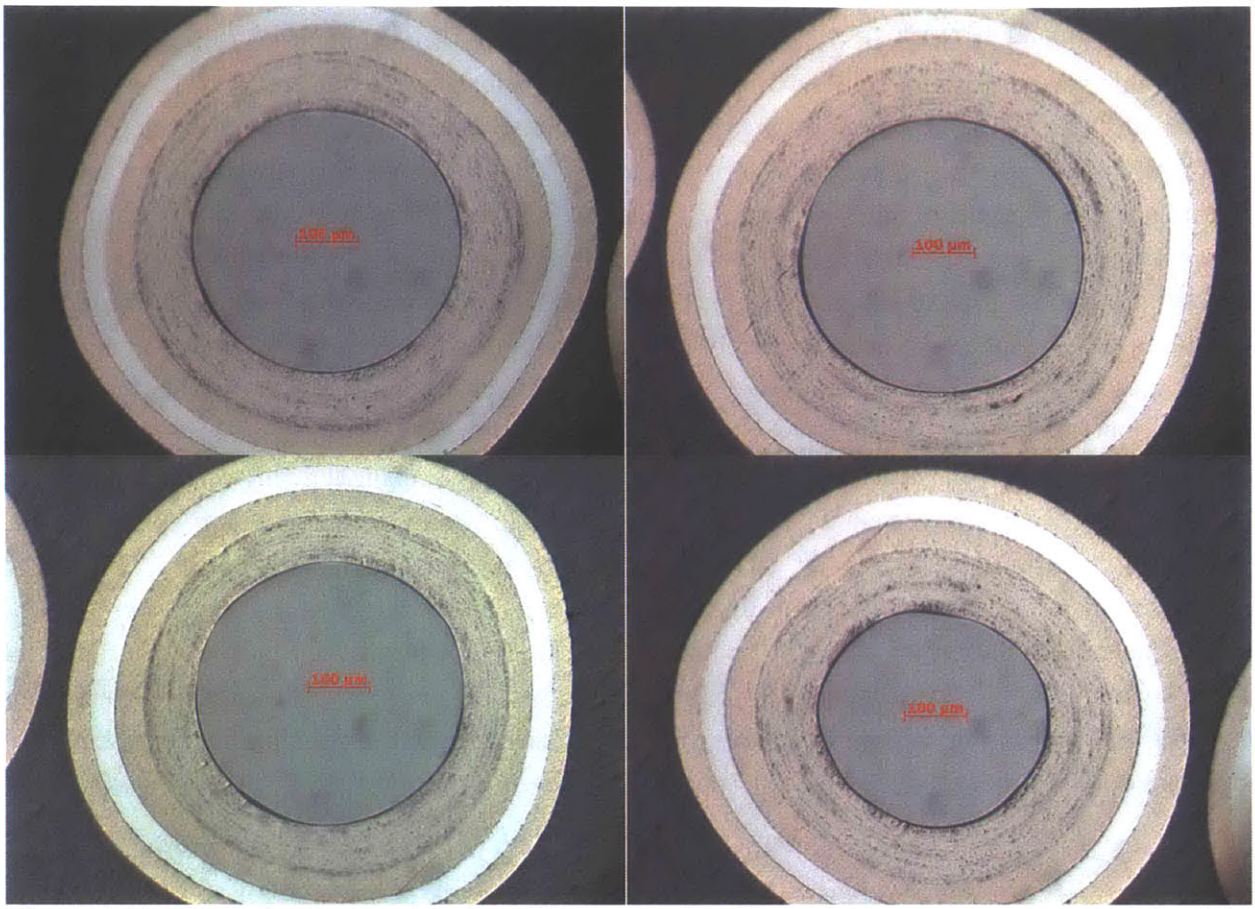

Figure 4.11: Optical micrographs of particles exposed to flibe only (no neutron exposure) for 3000 hours at UW.

As described in Appendix A.1.6.3, it was determined that all of the cracking in the OPyC, SiC, IPyC, and buffer layers of the particles irradiated in helium was due to grinding and polishing of the particles (for metallography) and the particular susceptibility of the irradiation-embrittled layers to cracking. For the particles irradiated in flibe, it is believed that the buffer, IPyC, and SiC cracking are due to this same mechanism. For the OPyC layer of the particles irradiated in flibe however, cracking was observed before the particles were even mounted in epoxy (see Figure 4.7). In comparison, Figure 4.10 and Figure 4.11 show that TRISO particles exposed to flibe in the absence of a neutron field experience no degradation of any kind. In order to determine the cause of OPyC cracking in the particles irradiated in flibe, as-fabricated particles, particles irradiated in helium, and particles exposed to flibe in the absence of neutrons were put in flibe and the flibe was allowed to free and thaw. After the freezing and thawing cycles, the particles were compared.

Figure 4.12 shows a set of as-fabricated particles prior to the freezing and thawing tests in flibe. Figure 4.13 shows the same set of as-fabricated particles after several cycles of freezing and thawing in flibe. No cracking or degradation of the OPyC layer was observed in these as-fabricated particles after exposure in flibe. Figure 4.10 shows a couple of flawless particles obtained after exposure in

flibe for 3000 hours at UW. In order to extract these particles from flibe at UW, they had already been through several freezing and thawing cycles in flibe before they were sent to MIT. Figure 4.14 shows that these particles remain pristine after additional freezing and thawing cycles in flibe. Figure 4.15 shows that the outer surface of the OPyC layer on the particles irradiated in helium is pristine prior to the freezing and thawing tests in flibe. Figure 4.16 shows the results of exposing helium-irradiated particles to freezing and thawing cycles in flibe. Four different particles are depicted in Figure 4.16. All of these particles experienced OPyC cracking as a result of freezing and thawing in flibe. In the case of the top right and middle left particles, the OPyC fractured and came apart from the particle. The middle right image is the OPyC shard that broke away from the particle in the middle left image. This test proves conclusively that irradiation embrittles the OPyC layer of these surrogate TRISO particles and that the surface tension and freezing/thawing forces imparted on the OPyC layer from flibe are enough to rupture the layer and separate it from the rest of the particle. Table 4.4 summarizes the findings of TRISO exposures to freezing and thawing in flibe. This set of experiments has shown that irradiation degradation of the TRISO particles can occur such that the forces imparted on the OPyC layer of the particles during flibe freezing and thawing can crack the OPyC layer. The SiC layer appears to withstand this without cracking. This set of experiments indicates that preventing the salt from freezing around any low-density graphite structures will be important during accidents.

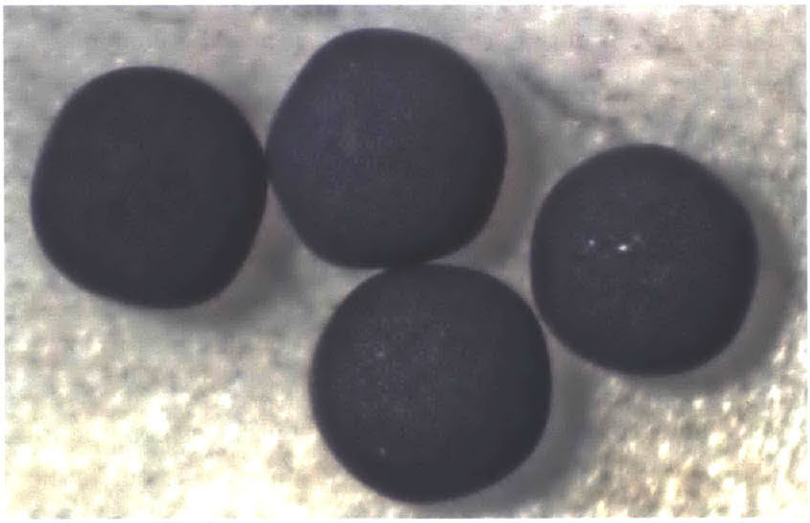

Figure 4.12: As-fabricated particles prior to freezing and thawing in flibe.

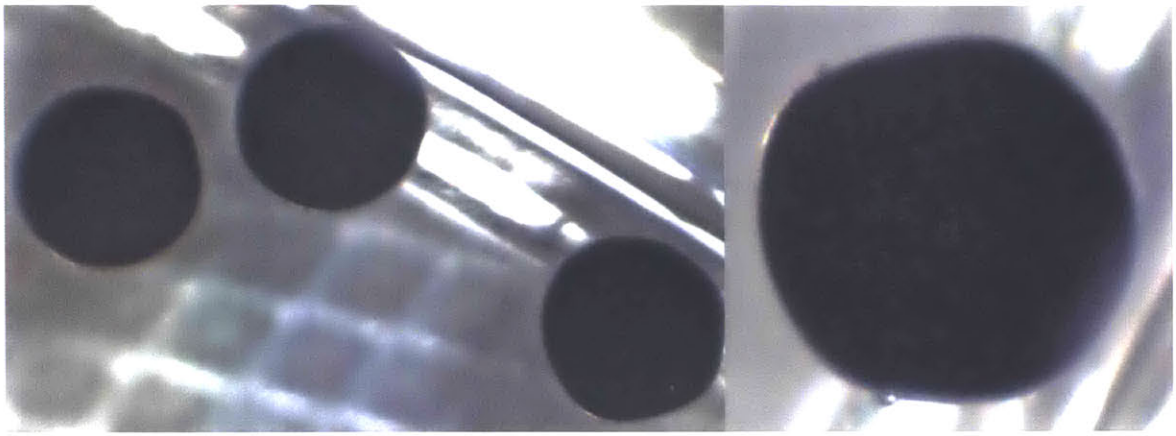

Figure 4.13: As-fabricated particles after several freeze-thaw cycles in flibe.

Figure 4.14: Particles from UW test in flibe after additional freezing and thawing cycles in flibe at MIT.

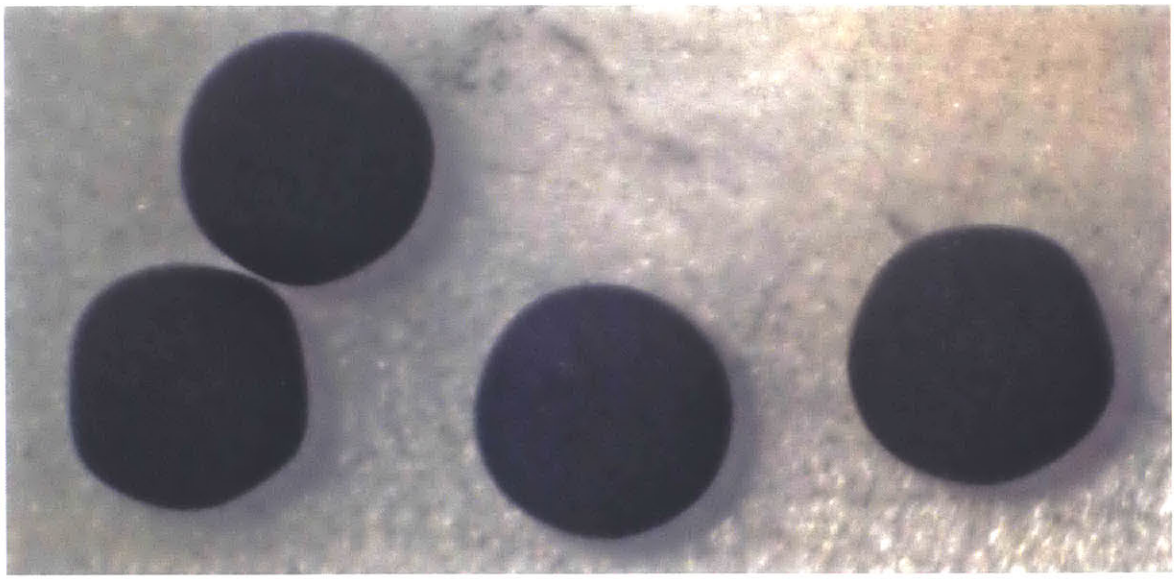

Figure 4.15: Particles from the 3000 hour irradiation in helium prior to freezing and thawing in flibe.

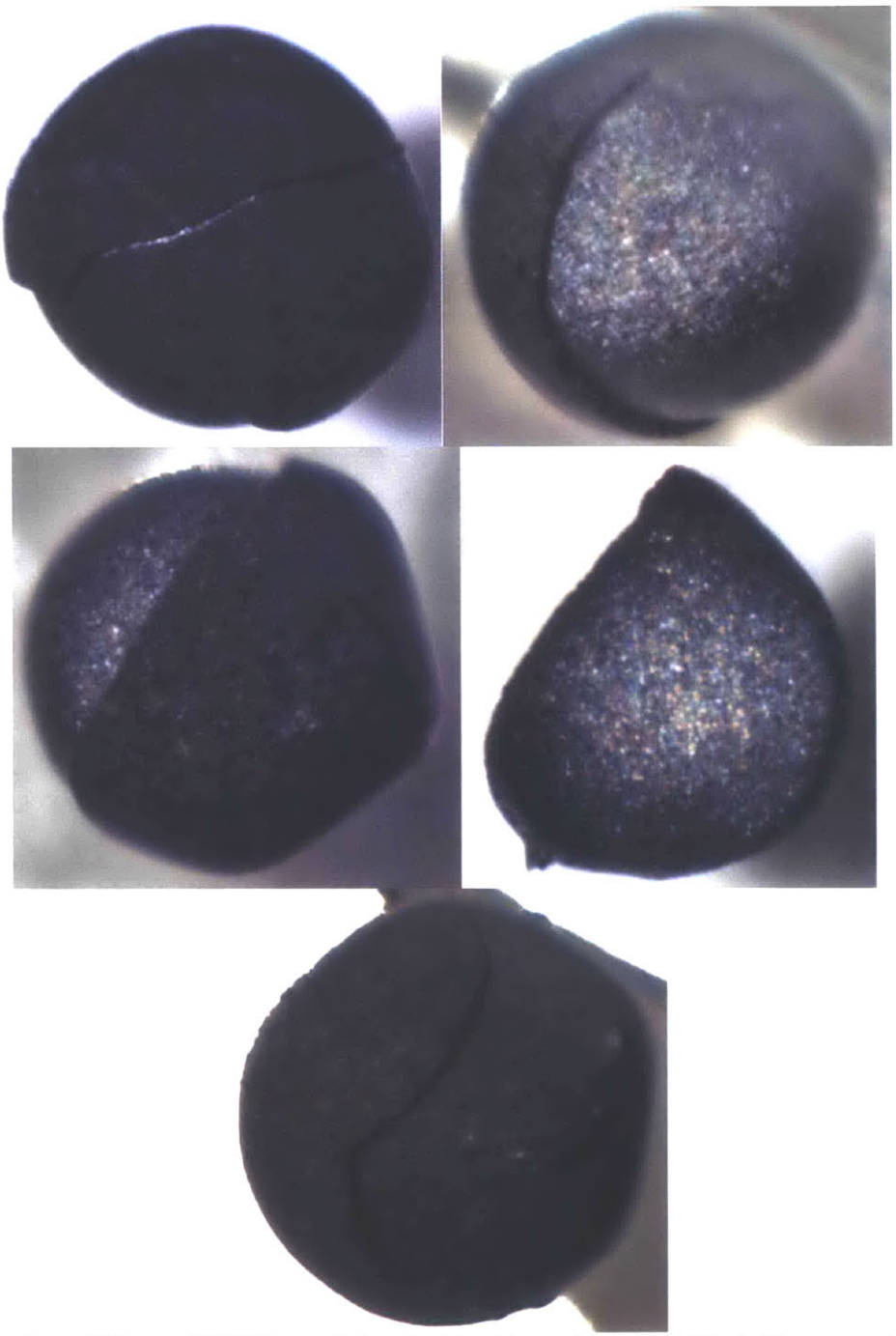

Figure 4.16: Four different TRISO particles that had been irradiated in helium are pictured after going through several freeze-thaw cycles in flibe. One OPyC shard belonging to the middle left particle is also shown.

Table 4.4: Summary of OPyC after exposure to flibe for TRISO particles with different histories.

TRISO History	Fast Neutron Fluence (n/cm^2, E > 0.1 MeV)	OPyC cracking after exposure to flibe?
As-fabricated	0	No
Exposed to flibe for 3000 hours	0	No
Irradiated in $He_{(g)}$ for 2200 hours	$3.7x10^{20}$	Yes
Irradiated in flibe for 3000 hours	$1.25x10^{21}$	Yes

4.4 Chapter summary of concrete and fission product stability in flibe and TRISO particle PIE after irradiation in flibe

The chemical stability of fission products has been analyzed in MSRs (where the fuel is dissolved in the coolant and all of the fission products are generated in the coolant) and in TRISO fuels separately, but the fission product stability as a function of redox potential in a system utilizing both a fluoride salt and TRISO fuel has never been performed until now. The available data for fission product behavior in the MSRE and in TRISO fuels were combined in order to help establish a general framework for fission product stability in the FHR. Calculations were performed in order to determine the stability of fission products in reference to the redox potential in the coolant for a severe case where the TRISO kernel is exposed to the salt.

If fission products are released from an intact fuel pebble, they will encounter the flibe coolant in the FHR. The chemical redox potential of the coolant will determine whether these fission products will be stable fluorides dissolved in the coolant, or volatile forms liable to escape the coolant. For TRISO particles with intact SiC layers, only Ag, Eu, and Pd are able to escape, and the Gibbs formation free energies plotted in Figure 4.1 show that at the reference redox potential, Ag and Pd will form metals, but Eu will form a salt-soluble fluoride. If TRISO layers are damaged (such as at high temperatures > 1600 °C), Cs, Ce, I, Kr, Sr, and Xe may escape the particles. Figure 4.1 shows that at the reference redox potential, Cs, Ce, and Sr will form stable fluorides. The noble gases (Kr and Xe) will be released to the off-gas system. At extreme temperatures, CsF will have reduced stability and some Cs may be volatilized from the metallic state. Additionally, if the redox potential is significantly more reducing than that used in the MSRE, CsF stability will be reduced and some Cs may exist in metallic form. Strontium appears to form a stable fluoride under any possible coolant temperature. In the MSRE, iodine was often found to remain in the salt with no evidence of deposition on metal or graphite surfaces. At the reference redox potential of the MSRE, iodine existed in the salt as the iodide ion or as iodides (e.g. CsI), and less than 0.1% was stripped from the salt as I_2 gas [66]. If the salt were to be increasingly oxidizing, a greater portion of the iodine would be in the I_2 gas form.

The stability of fission product carbides, oxides, and fluorides was analyzed by comparing a set of Gibbs reaction free energies. The significance of these results in Figure 4.2 and Figure 4.3 is that if the kernel were to be exposed to the salt, most elements of interest should remain as immobile oxides or carbides in the kernel or as soluble fluorides in the melt. This helps contain radioactivity in the event of a severe accident.

In the event of a coolant leak where liquid salt contacts concrete, concrete chemical stability is important. Most concretes are composed of metal oxides. The Gibbs reaction free energies for the reactions of metal oxides with BeF_2 were evaluated for all of the major metal oxide constituents of the various types of concrete. Many types of thermal insulation are composed of metal oxides. Thus, this analysis is applicable in both cases. The results were normalized by the number of moles of BeF_2 required to balance the equations. The reaction free energies were compared against the BeF_2 potential in flibe in Figure 4.4 which shows that none of the metal oxides are truly stable in the salt. This is an assertion that is well supported by experiments from other researchers which show that liquid fluoride salts dissolve metal oxides. While this analysis determined chemical stabilities, it did not discuss reaction kinetics. Experimental observations by other researchers indicate that reactions of fluoride salts with metal oxides are relatively fast. If metal oxides must be used in locations where they may come into contact with salt, then the most stable of the metal oxides should be chosen. This may require new formulations of concrete or it may require that critical concrete structures can never come in contact with liquid salt even during an accident. Based on their reaction free energies being near the BeF_2 potential, nickel, chromium, iron and aluminum oxides (though still unstable) are more stable compared to other metal oxides. Calcium, magnesium, potassium, and titanium oxides are the least stable metal oxides in flibe.

It is also important to know whether these reactions are exothermic (generate heat) or endothermic (absorb heat). The reaction enthalpy for each reaction was calculated and used to determine the increase (from exothermic reactions) or decrease (from endothermic reactions) in the coolant temperature due to a chemical reaction between BeF_2 and metal oxides. The results were given in Figure 4.5. Whether an exothermic or endothermic reaction is desirable depends on the situation. If the salt is cooled by an endothermic reaction, this cooling may aid the freezing of the salt, which could plug leaks. If the salt were to freeze on contact with the concrete, this would reduce or eliminate salt-concrete chemical reactions. On the other hand, freezing might block desirable salt coolant flow. Exothermic reactions might heat the salt further, weakening structural materials and changing the chemical stability of any dissolved fission products. Thus, it may be beneficial to select materials with the smallest absolute value of reaction enthalpy. In locations where a salt leak is possible, aluminum, iron, and nickel oxides have better stability than some metal oxides and have small effects on coolant temperature when they do react.

TRISO particles from batch ZrO2-500-AK2 having different exposure histories were examined. Particles in the as-fabricated condition showed no defects of any of the layers. Particles which had been exposed for 3000 hours to flibe at 700 °C in the absence of a neutron field showed no signs of outer degradation and no signs of inner degradation after mounting and polishing. Under normal

circumstances, TRISO particles should never come into contact with salt because they are embedded in fuel pebbles. If severe fuel damage were to occur during a BDBA, salt-TRISO contact might occur. By performing a series of freeze-thaw tests in flibe, it was determined that the OPyC layer of irradiated particles is susceptible to cracking in flibe if the salt is allowed to freeze around the particles. This indicates that preventing the salt from freezing around any low-density graphite structures will be important.

5 TRIDENT model development

Since no FHR has ever been constructed and only limited data on tritium mobility in MSRs is available from the MSRE, a model called TRItium Diffusion EvolutioN and Transport (TRIDENT) was developed in order to track tritium movement and chemical reactions throughout the FHR. A high-level flow chart for the model is given in Figure 5.1. Tritium is born in the coolant as dissolved TF. Depending on the chemical redox condition of the coolant (defined by the fluorine potential described in Section 3.2) tritium will speciate into both TF and T_2 via chemical reactions. The fluorine potential in the coolant determines the thermodynamic driving force for corrosion and the relative amounts of TF and T_2 in the system. Both TF and T_2 can be adsorbed on graphite in the core depending on the mass transport parameters and graphite capacity for tritium. In FHRs, tritium is intimately linked with corrosion. Tritium born in the coolant as TF can corrode structural metals, and a byproduct of these reactions is $T_{2(g)}$. If corrosion products are deposited/precipitated in the system, the reaction is the reverse of the corrosion reaction, and TF is generated as T_2 is consumed. Corrosion control is based on mitigating selective Cr attack by TF, and the radiological management of tritium is based on preventing unwanted diffusion of T_2. TRIDENT couples the redox potential to TF/T_2 speciation, allowing it to realistically predict tritium buildup in the reactor, relevant corrosion reactions, tritium trapping on graphite, and tritium diffusion through system barriers. If desired, TRIDENT can simulate different engineered mechanisms for TF and T_2 removal from the coolant (such as gas-stripping and permeation windows). Only T_2 can diffuse through metal. Thus, only T_2 is allowed to diffuse out of the primary system through the heat exchangers. TRIDENT is capable of simulating single loop reactors or two-loop reactors having both a primary and secondary system. Any tritium not escaping through the heat exchangers or not removed by engineered systems is then returned to the core through the core coolant inlet.

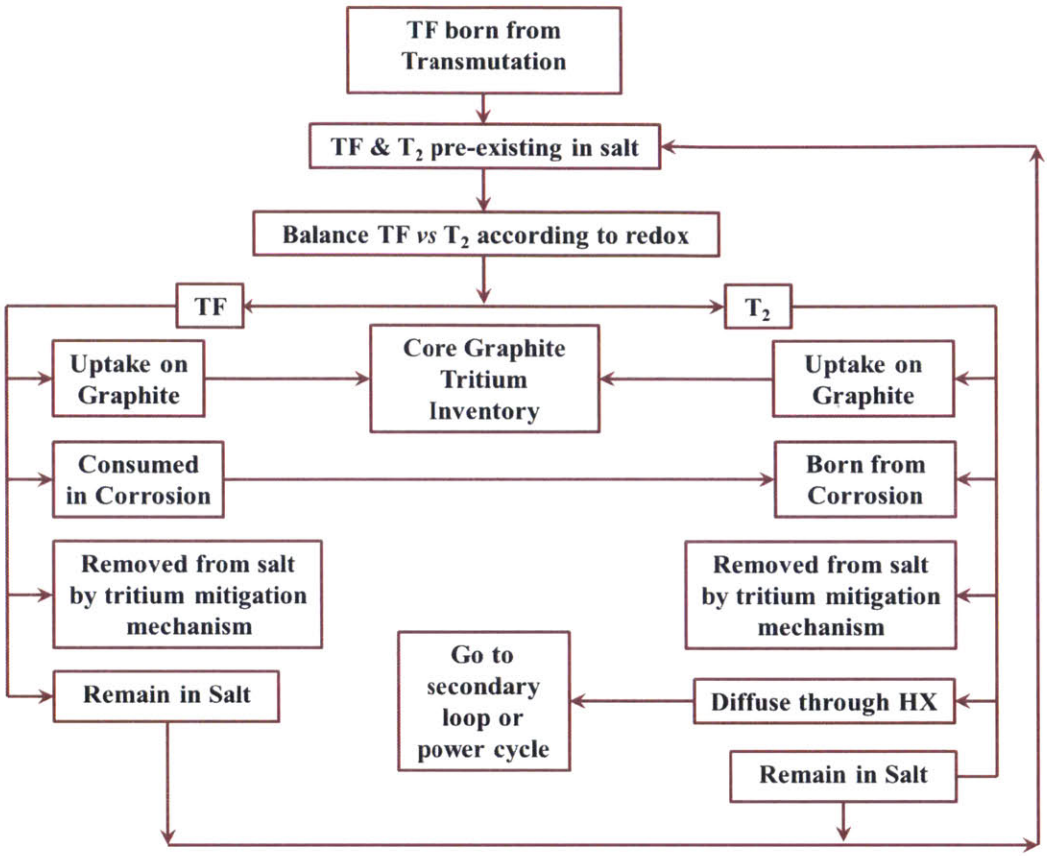

Figure 5.1: TRIDENT model flow chart.

5.1 Tritium Production in TRIDENT

The significant tritium production pathways were introduced in Section 2.1. TRIDENT does not account for tritium produced from impurities in graphite, neutron poisons, burnable absorbers, or ternary fission. Compared to the tritium production from transmutation in flibe, these other sources are negligible. Most of the tritium from these sources is not mobile and is not released to the coolant. As described in Section 2.2, tritium production from neutron transmutation is modeled in TRIDENT using Eq (2.6) and the neutronic parameters listed in Table 2.1. A plot of Eq (2.6) normalized to reactor power was given in Figure 2.2. This model accounts for the variation in the tritium production rate with reactor operating time. It is assumed that tritium is produced uniformly throughout the core.

5.2 Tritium speciation in TRIDENT

Tritium produced using the model from Eq (2.6) is initially in the form of TF dissolved in the coolant as T^+ and F^- ions. Through chemical reactions, this TF can be converted to T_2 in two ways. The first way is via a redox reaction driven by the dominant redox (fluorine) potential in the coolant.

As discussed in the beginning of Section 3.2, there are numerous ways to intentionally control the redox potential. Under redox control, the TF produced will speciate into T_2 in accordance with the chosen fluorine potential. For a given fluorine potential, the relative amounts of TF and T_2 present in any fluoride salt can be calculated using Eq (3.40)

The second means of tritium speciation is via a corrosion reaction between TF and the least noble structural metal in contact with the salt. Between Cr, Fe, and Ni, Cr is the least noble and will be corroded by TF to produce CrF_2 and T_2 according to the reaction in Eq (3.17). If the redox potential is not actively controlled, reactions between TF and the structural metals in the reactor will dictate the redox potential and produce T_2. In this case, if the amounts of T_2 and TF in the system are known, the fluorine potential can be calculated using Eq (3.47). Figure 3.15 showed that as the fluorine potential increases, the amount of tritium existing as TF increases (the ratio of TF to T_2 increases). If the fluorine potential is decreased (made more reducing), the ratio of TF to T_2 decreases, and the amount of tritium in the system existing as T_2 increases.

TRIDENT uses Eq (3.47) to account for the effects of the fluorine potential. One option in TRIDENT allows the user to specify a fluorine potential (ΔG_{F2}). In this mode, the fluorine potential in the system is fixed, and Eq (3.47) is used to balance the relative amounts of TF and T_2 in the system in accordance with the specified fluorine potential. Another option in TRIDENT allows the simulation of a system without redox control. In this mode, the fluorine potential is allowed to drift, and the relative amounts of TF and T_2 are allowed to drift as well. Redox drift occurs for several reasons: corrosion reactions consume TF and generate T_2, T_2 diffuses out of the system while TF cannot, and TF and/or T_2 are removed from the system (such as via sorption on graphite) in varying amounts.

5.3 Control volumes for primary coolant transport in TRIDENT

The level of detail of an FHR modeled in TRIDENT is given in Figure 5.2. Additional systems such as gas stripping columns and permeation windows are optional within TRIDENT and will be discussed in Chapter 6. Within the primary system, the major zones modeled in TRIDENT are the reactor core, primary hot leg, primary heat exchanger, and the primary cold leg. Different phenomena occur and are modeled within each axial zone. TRIDENT considers tritium production in the coolant in the core and tritium interactions with the pebble fuel and the central/radial graphite reflectors. TRIDENT considers the flow of the coolant through the hot leg and into the primary heat exchanger (PHX). In the PHX, tritium can diffuse into the next system. If the FHR being modeled has only a primary loop, tritium diffusion is from the primary coolant into the air in the Brayton power cycle. If the FHR being modeled has two loops, then the tritium diffusion is from the primary coolant into the secondary coolant. Primary coolant exiting the PHX flows through the cold leg before returning to the reactor core. A basic schematic of the detail of an FHR secondary loop modeled in TRIDENT is given in Figure 5.3. In the secondary loop, the major zones modeled in TRIDENT are the primary heat exchanger, hot and cold secondary legs, and the secondary heat

exchanger. Chromium corrosion and deposition reactions are analyzed within each segment of the primary system. Since the oxidant tritium fluoride from neutron transmutation is only produced in the primary system, corrosion and deposition reactions are not modeled in the secondary system.

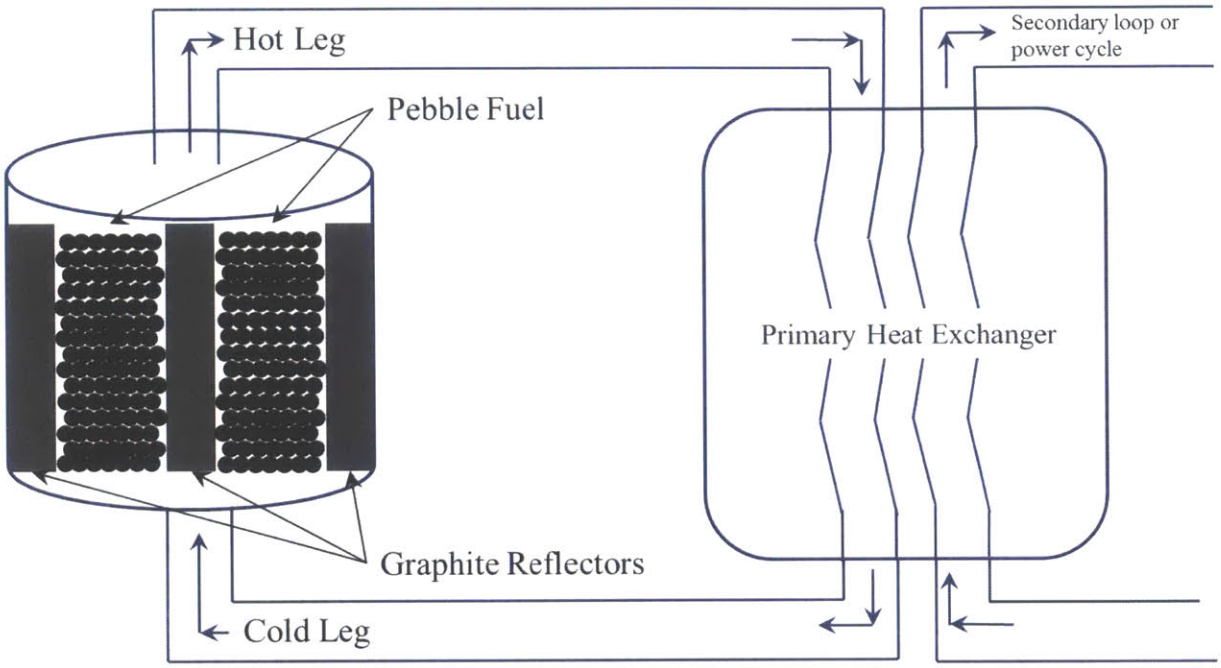

Figure 5.2: Schematic of FHR primary coolant system modeled in TRIDENT.

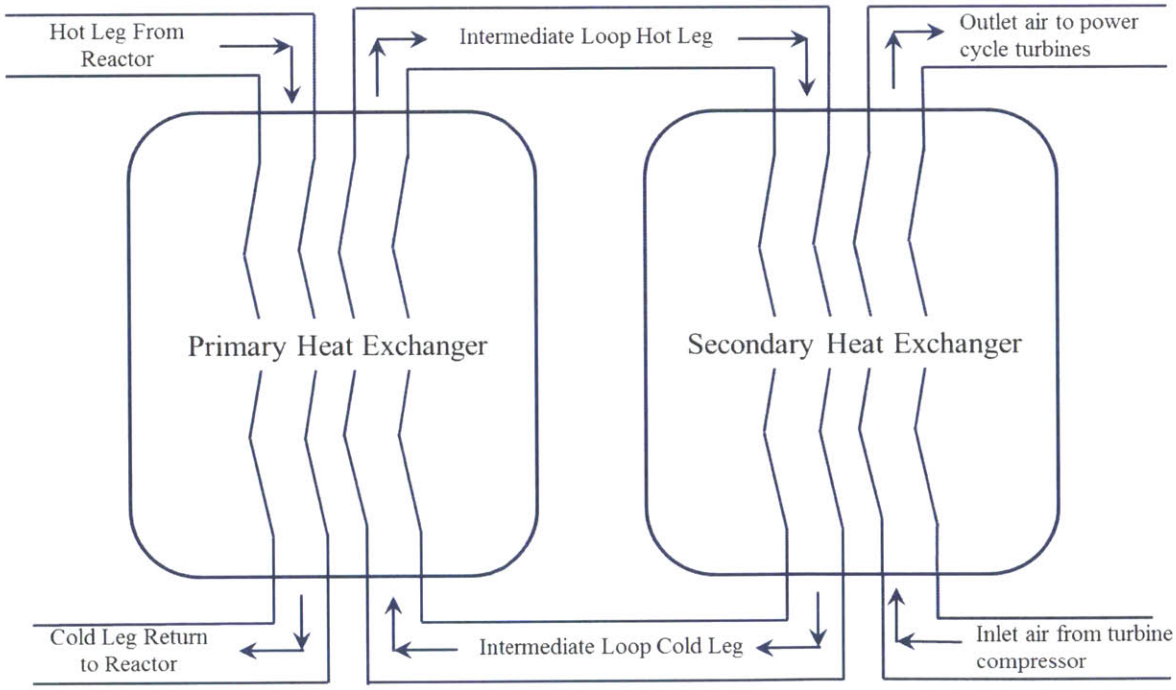

Figure 5.3: Schematic of FHR optional secondary coolant system modeled in TRIDENT.

5.3.1 Reactor core control volumes

Each zone modeled in TRIDENT (core, hot leg, PHX, etc.) is further divided into axial segments. One reason for doing this is so that a temperature profile can be applied within the model such that the temperature can vary from segment to segment. Section 5.4 discusses the method used for building a temperature profile for use in TRIDENT. Figure 5.4 shows the reactor core divided into n axial segments, each of which makes a control volume with its own temperature. The reactor core in TRIDENT is modeled in 1D where only axial coolant flow from forced convection is considered. Mass transfer to surfaces in each segment is also modeled.

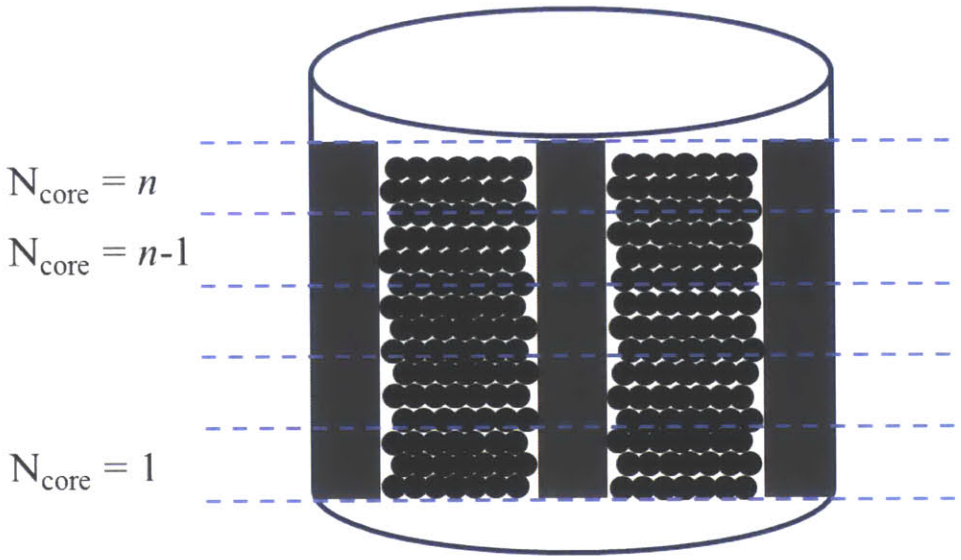

Figure 5.4: Axial segments defining control volumes in the reactor core.

In order to speed the calculations, the coolant is considered to be 0D in the hot and cold leg pipes and 1D in the core and heat exchanger. This approximation is made due to an assumption of turbulent mixing in the pipes and pumps where the Reynolds number exceeds $1x10^5$. Depending on the core design, the flow regime may be laminar or transitional in the pebble-bed core. In a given core control volume N, the mass balance for T_2 is given by Eq (5.1), the mass balance for TF is given by Eq (5.2), and the mass balance for the Cr^{2+} corrosion product is given by Eq (5.3).[5] The tritium production rate is held constant throughout the core so that $\dot{T}(t)$ in segment N = n is equal to $\dot{T}(t)$ in segment N = 1. As a conservative approximation, tritium radioactive decay is not accounted for. The symbols are defined below. The dotted values describe rates whose calculation will be discussed in Section 5.6.1. $\dot{A}^N_{graphite,T_2}$ is defined in Eq (5.33). $\dot{A}^N_{graphite,TF}$ is defined in Eq (5.34). $\dot{D}^N_{deposition,Cr}$ is defined in Eq (5.35). $\dot{D}^N_{deposition,T2}$ is defined in Eq (5.38). $\dot{D}^N_{deposition,TF}$ is defined in Eq (5.39).

[5] Current PB-FHR designs do not have metal facing the coolant in the core. Thus, $\dot{C}_{corrosion,Cr}$ in the core is always 0; however, $\dot{D}_{deposition,Cr}$ is accounted for in the core.

$$\frac{dm_{T_2}^{\ N}}{dt} = \dot{v} \times c_{T_2}^{\ N-1} + \sigma \dot{T}(t) - \dot{A}^N_{graphite,T_2} - \dot{D}^N_{deposition,T_2} + \dot{C}^N_{corrosion,T_2} \quad (5.1)$$

$$\frac{dm_{TF}^{\ N}}{dt} = \dot{v} \times c_{TF}^{\ N-1} + \sigma \dot{T}(t) - \dot{A}^N_{graphite,TF} + \dot{D}^N_{deposition,TF} - \dot{C}^N_{corrosion,TF} \quad (5.2)$$

$$\frac{dm_{Cr^{2+}}^{\ N}}{dt} = \dot{v} \times c_{Cr^{2+}}^{\ N-1} - \dot{D}^N_{deposition,Cr} + \dot{C}^N_{corrosion,Cr} \quad (5.3)$$

t = reactor operating time [s]

$m_{T2}^{\ N}$ and $m_{TF}^{\ N}$ = moles of T_2 and moles of TF in control volume N, respectively

$\dot{v}$ = coolant volumetric flow rate [m^3/s]

$m_{Cr2+}^{\ N}$ = moles of Cr^{2+} in control volume N

$c_{T2}^{\ N-1}$ and $c_{TF}^{\ N-1}$ = concentration of T_2 and TF in the coolant exiting the previous control volume N-1 [mol/m^3]

$c_{Cr}^{\ N-1}$ = concentration of Cr^{2+} in the coolant exiting the previous control volume N-1 [mol/m^3]

σ_{TF} and σ_{T2} = tritium speciation factor for TF and T_2 determined by solving Eq (3.47) if c_{total} and the specified fluorine potential is known. c_{TF} can then be calculated from Eq (3.46). This determines how much new tritium from transmutation will become T_2 and how much will remain as TF.

$\dot{T}(t)$ = Calculated from Eq (2.6), tritium atom production rate from neutron transmutation in control volume N [moles T atoms/s]

$\dot{A}^N_{graphite,T_2}$ and $\dot{A}^N_{graphite,TF}$ = T_2 and TF adsorption rate on core graphite [mol/s]

$\dot{D}^N_{deposition,T2}$ = Rate of T_2 consumption accompanying metal corrosion product deposition in volume N [mol/s]

$\dot{D}^N_{deposition,TF}$ = Rate of TF generation accompanying metal corrosion product deposition in volume N [mol/s]

$\dot{C}^N_{corrosion,T_2}$ = Rate of T_2 generation due to corrosion of metals by TF in volume N [mol/s]

$\dot{C}^N_{corrosion,TF}$ = Rate of TF consumption due to corrosion of metals by TF in volume N [mol/s]

$\dot{D}^N_{deposition,Cr}$ = Rate of Cr deposition on core surfaces in control volume N [mol/s]

$\dot{C}^N_{corrosion,Cr}$ = Rate of Cr dissolution from coolant-facing metal into the coolant in control volume N [mol/s]

5.3.2 Hot and cold leg control volumes

The hot and cold leg pipes are divided into n control volume as well. No production of tritium occurs in these pipes, and tritium diffusion through the pipe wall is neglected. Since the pipe wall is orders of magnitude thicker than the walls of the HX tubing and the HX tubing surface area is orders of magnitude higher than that of the main coolant pipes, it is assumed that no tritium diffuses through the hot or cold leg pipe walls. This is a conservative assumption which will result in some over prediction of the losses of tritium through the heat exchanger. Because the flow through the pipes is turbulent and coolant pumps will cause mixing, the coolant in the hot and cold leg pipes is modeled in 0D and any processes occurring here are homogenized over the entire coolant inventory in order to provide a first-order approximation of mixing. The mass balances for the these pipes are given in Eqs (5.4), (5.5), and (5.6). The new symbols are defined below. In the hot and cold leg pipes, the values for m_{Cr2+}, m_{TF}, and m_{T2} change as the coolant passes through each segment N, but the changes are normalized over the entire coolant volume. The dotted parameters are rates of deposition, corrosion, production, and consumption defined in Equations (5.48) through (5.50).

m_{Cr2+} = total moles of Cr^{2+} in the primary coolant [moles Cr^{2+}]

m_{TF} and m_{T2} = total moles of TF and T_2 in the primary coolant, respectively [moles TF or moles T_2]

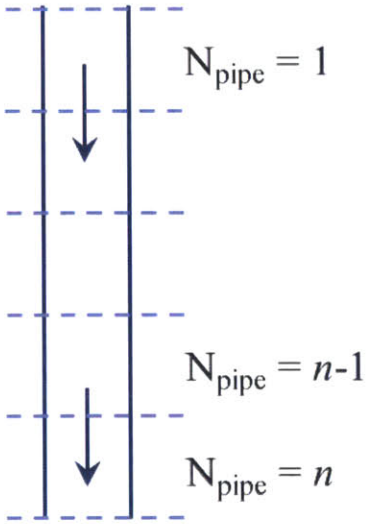

Figure 5.5: Axial control volume divisions in hot and cold leg pipes.

$$\frac{dm_{T_2}^{N_{pipe}}}{dt} = \dot{D}_{deposition,T_2}^{N_{pipe}} + \dot{C}_{corrosion,T_2}^{N_{pipe}} \tag{5.4}$$

$$\frac{dm_{TF}^{N_{pipe}}}{dt} = \dot{D}_{deposition,TF}^{N_{pipe}} - \dot{C}_{corrosion,TF}^{N_{pipe}} \tag{5.5}$$

$$\frac{dm_{Cr^{2+}}^{N_{pipe}}}{dt} = \dot{D}_{deposition,Cr}^{N_{pipe}} + \dot{C}_{corrosion,Cr}^{N_{pipe}} \tag{5.6}$$

5.3.3 Heat exchanger control volumes

Figure 5.6 shows the primary heat exchanger divided into n axial segments, each of which makes a control volume with its own temperature. The primary heat exchanger in TRIDENT is modeled in 1D where only axial coolant flow from forced convection is considered. In a given control volume N, the mass balance for T_2, TF, and Cr^{2+} are given by Eqs (5.7), (5.8), and (5.9). The $\dot{C}$ and $\dot{D}$ symbols are rates of corrosion and deposition related reactions defined in Equations (5.48) through (5.50). $\dot{P}^N$ is the rate of T_2 permeation into the HX tube-wall within control volume N (in units of moles T_2/s). A mathematical definition of $\dot{P}^N$ is given in Eq (5.52). Other symbols are as defined in Section 5.3.1.

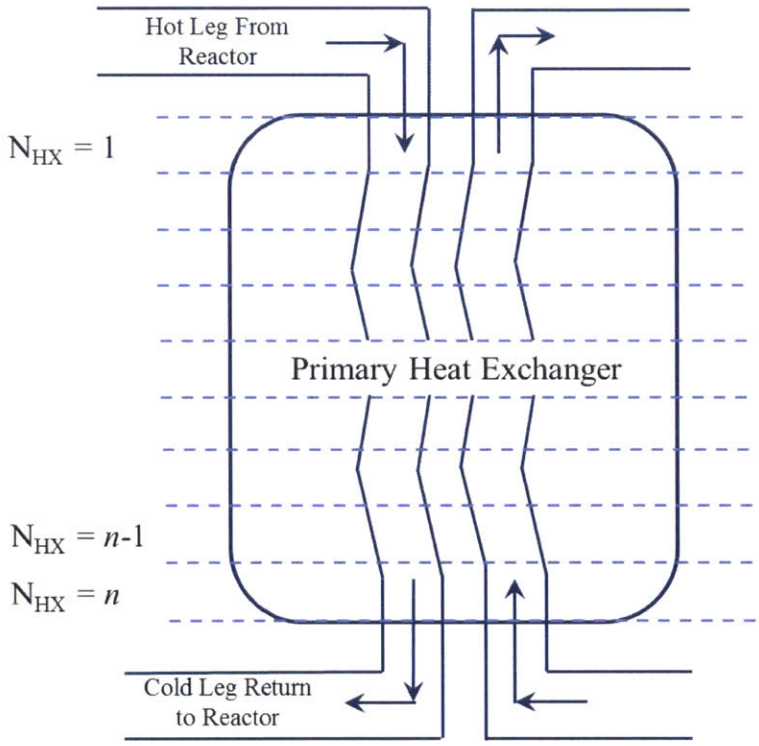

Figure 5.6: Axial segments defining control volumes in the primary heat exchanger.

$$\frac{dm_{T_2}^{N_{HX}}}{dt} = \dot{v} \times c_{T_2}^{N_{HX}-1} - \dot{P}^{N_{HX}} - \dot{D}_{deposition,T_2}^{N_{HX}} + \dot{C}_{corrosion,T_2}^{N_{HX}} \tag{5.7}$$

$$\frac{dm_{TF}^{N_{HX}}}{dt} = \dot{v} \times c_{TF}^{N_{HX}-1} + \dot{D}_{deposition,TF}^{N_{HX}} - \dot{C}_{corrosion,TF}^{N_{HX}} \tag{5.8}$$

$$\frac{dm_{Cr^{2+}}^{N_{HX}}}{dt} = \dot{v} \times c_{Cr^{2+}}^{N_{HX}-1} - \dot{D}_{deposition,Cr}^{N_{HX}} + \dot{C}_{corrosion,Cr}^{N_{HX}} \tag{5.9}$$

5.4 System temperature profile

Because properties such as solubility, mass transport, diffusion, and chemical reaction rates are temperature dependent, a coolant temperature profile is applied to the primary system model in TRIDENT. Temperature-dependent processes occurring in a specific part of the system are then calculated using the coolant temperature associated with that location in the primary loop. Unlike the primary system, the secondary system is assumed to be isothermal throughout at a specified average temperature. If a basic temperature profile is not available for the primary coolant, TRIDENT calculates one from specific input parameters including: core thermal power, core height, coolant mass flow rate, coolant heat capacity, core coolant inlet temperature, and core coolant outlet temperature. First, if the primary and/or secondary coolant mass flow rates are not known, TRIDENT calculates them from the specified inlet and outlet temperatures and the reactor power according to Eq (5.10) where q is reactor power in watts, $\dot{m}$ is the coolant mass flow (kg/s), c_p is the coolant heat capacity, T_{out} is the core (or heat exchanger) outlet temperature, and T_{in} is the (core or heat exchanger) inlet temperature in Kelvin. The heat capacity for flibe has little or no temperature dependence and is reported as 2390 J/kg-K [42]. The heat capacity for flinak (in units of J/kg-K) has been published with a temperature dependence according to Eq (5.11), where T is in Kelvin [45]. Flinak has been proposed as a secondary coolant in some FHR concepts.

$$q = \dot{m} c_p (T_{out} - T_{in}) \tag{5.10}$$

$$c_{p,flinak} = 976.78 + 1.0634 \times T \tag{5.11}$$

Once the mass flow rates have been obtained, in order to calculate a core coolant temperature profile, it is assumed that the neutronic extrapolation length (L_e) can be approximated by the physical height of the core (L). Next, a sinusoidal variation in the core axial linear power is assumed according to Eq (5.12) [11]. In this equation, L is the height of the reactor core, z is the location in the core ($0 \leq z \geq L$), q'_o is the axial peak linear heat generation rate in units of W/m, and q'(z) is the axial linear heat generation rate (in units of W/m) at location z. In order to calculate q'_o, total reactor thermal power is divided by the integral of Eq (5.12) from -L/2 to L/2. For a 900 MWt reactor with a core height of 3.2 m (such as the older PB-FHR [169,170]), q'_o is 441.8 MW/m. For a 236 MWt reactor with a core height of 4.65 m (such as the Mk1 PB-FHR [8]), q'_o is 79.7 MW/m. Now, Eq (5.13) can be used to calculate the core coolant temperature as a function of z. Again, it is assumed that the neutronic extrapolation length (L_e) can be approximated by the physical height of the core (L). Thus $L_e = L$.

$$q'(z) = q'_o \cos\left(\pi z / L\right) \tag{5.12}$$

$$T_{coolant}(z) = T_{in} + \frac{q'_o}{\dot{m}c_p}\frac{L_e}{\pi}\left(\sin\left(\frac{\pi z}{L_e}\right) + \sin\left(\frac{\pi L}{2L_e}\right)\right) \tag{5.13}$$

The primary hot leg temperature is set equal to $T_{core,out}$ for the length of the hot leg pipe. A linear temperature profile is assumed for the primary heat exchanger, and the primary cold leg temperature is set equal to $T_{core,in}$ for the length of the cold leg pipe. If a secondary system is modeled, a primary heat exchanger efficiency of 100% is assumed and the temperature throughout the entire secondary loop is simply set to $T_{avg} = (T_{core,in} + T_{core,out})/2$. A coolant temperature profile for the 236 MWt PB-FHR with each of the four major zones divided into 10 segments is given in Figure 5.7.

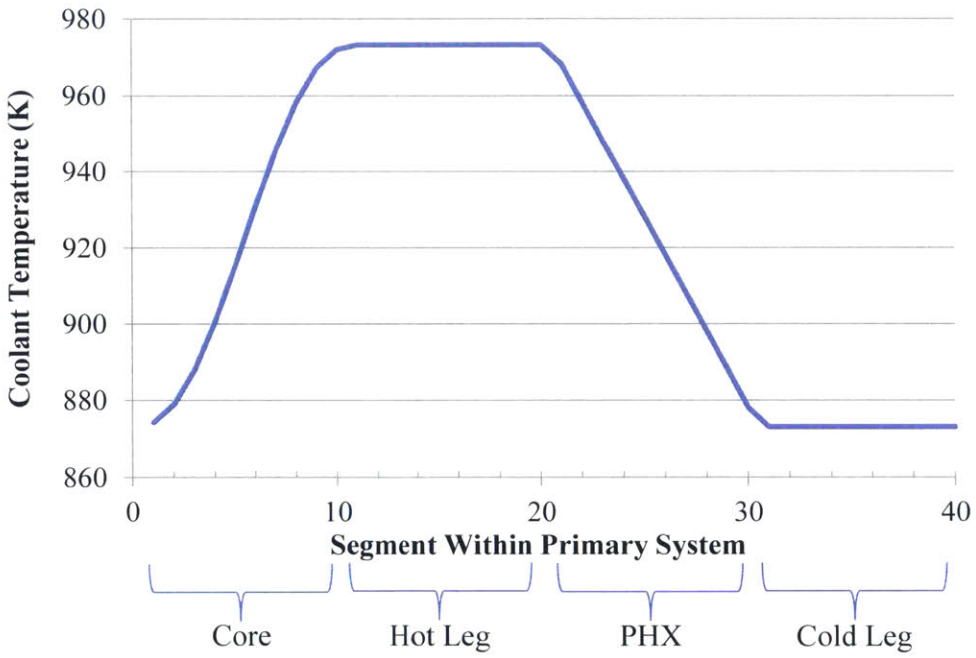

Figure 5.7: Primary system coolant temperature profile for 236 MWt Mk1 PB-FHR. Each zone was divided into 10 segments, but the number of segments can be varied as desired.

5.5 Control volumes for secondary coolant in TRIDENT

If a secondary coolant loop is modeled in TRIDENT, the system is modeled in much the same way as in the primary coolant loop which was discussed above. However, because TF cannot diffuse through metal, only T_2 will exist in the secondary system unless oxide contaminants are present to generate TF. Thus, TRIDENT models only the transport of T_2 in the secondary system. In terms of tritium releases, this is a conservative consumption. The presence of TF and the possibility of corrosion reactions are not considered in the secondary loop by TRIDENT. Because no corrosion reactions are modeled in the secondary loop, corrosion product mass transfer reactions do not occur

and the secondary loop temperature is set to a fixed averaged temperature ($T_{avg} = (T_{core,in} + T_{core,out})/2$) as described above in Section 5.4. As is done in the primary system, the secondary coolant is modeled in 1D in each heat exchanger, but is 0D in each main coolant leg. Figure 5.8 illustrates the volume element divisions made in the secondary system. Since corrosion reactions are not modeled in the secondary loop and tritium transport only occurs in the PHX and SHX, no mass balances are required in either hot or cold legs in the secondary loop.

In the secondary coolant flowing through the primary heat exchanger (PHX), the rate of change of T_2 within a given volume element N is given by Eq (5.14). In the secondary coolant flowing through the secondary heat exchanger (SHX), the rate of change of T_2 within a given volume element N is given by Eq (5.15). The secondary coolant volumetric flow rate is given by $\dot{v}_2$ in units of m^3/s. The rate of T_2 permeation from the PHX tube wall into the secondary coolant in volume element N_{PHX} is given by $\dot{P}^{N}_{HX1}$. Within volume element N_{SHX}, the rate of T_2 permeation out of the secondary coolant into the tube wall separating the secondary coolant from the power cycle in the SHX is given by $\dot{P}^{N}_{HX2}$. $\dot{P}^{N}_{HX1}$ is defined mathematically by Eq (5.55) and $\dot{P}^{N}_{HX2}$ is defined mathematically by Eq (5.56).

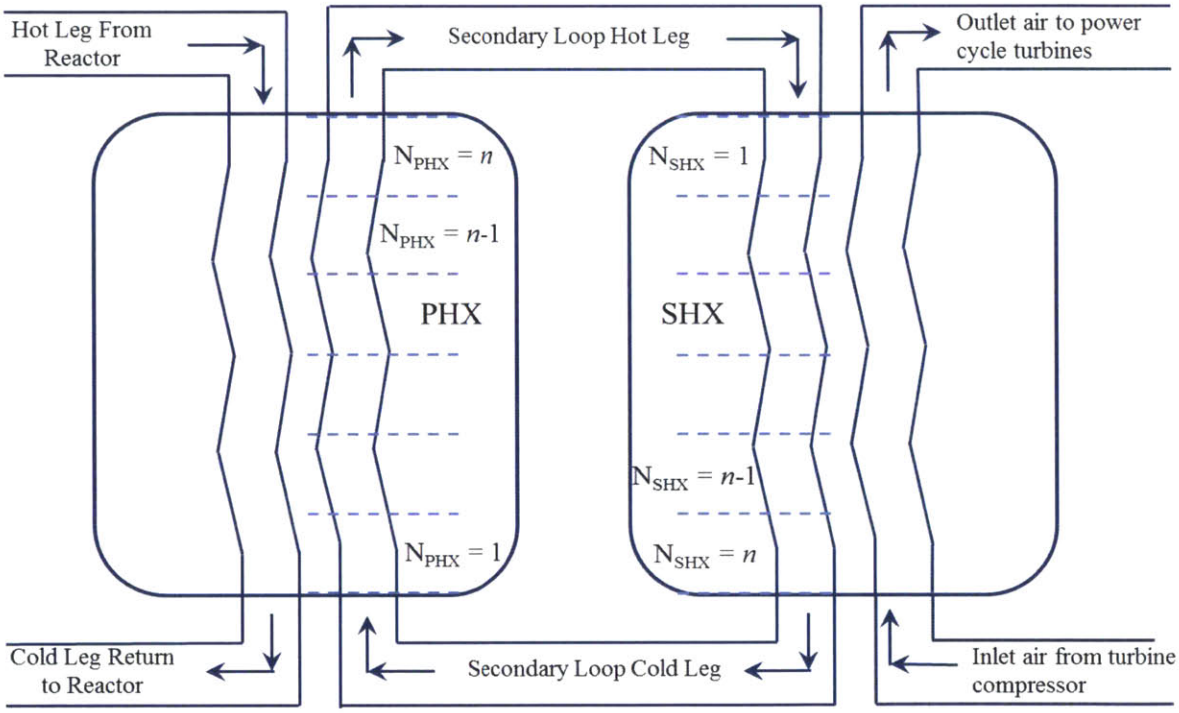

Figure 5.8: Control volumes within the secondary coolant system. PHX = primary heat exchanger. SHX = secondary heat exchanger.

$$\frac{dm_{T_2}^{\ N}}{dt} = \dot{v}_2 \times c_{T_2}^{\ N-1} + \dot{P}_{HX1}^{\ N} \tag{5.14}$$

$$\frac{dm_{T_2}^{\ N}}{dt} = \dot{v}_2 \times c_{T_2}^{\ N-1} - \dot{P}_{HX2}^{\ N} \tag{5.15}$$

5.6 Surface mass transport models in TRIDENT

Within the coolant, tritium is transported by bulk forced convection with mass balances given by the equations in the preceding Sections 5.3.1 through 5.3.3. In order to model corrosion/deposition, tritium adsorption on graphite, and tritium permeation through metal membranes, tritium and corrosion product mass transport to various surfaces must be calculated.

5.6.1 Mass transport to graphite surfaces

Figure 5.9 illustrates the mass transport phenomena modeled in the reactor core. Tritium adsorption on graphite pebbles and reflector graphite is modeled in TRIDENT, and these calculations begin with determining the mass transfer coefficients for T_2 and TF. It is assumed that the rate of tritium uptake on graphite is determined by the rate at which tritium is transported to the graphite surface and not on the rate of tritium diffusion on the graphite surface or within the graphite bulk. This assumption has been made in previous studies based on experimental observations, and is reasonable given that the vast majority of tritium will remain at or near the graphite surface [50,66]. For adsorption on the pebbles, the Reynolds analogy is used to modify a heat transfer correlation for packed beds into a mass transfer correlation [171]. The result is the Sherwood number ($Sh_{x,pebble}$) which is given by equation (5.16) where Sc_x is the Schmidt number given by Eq (5.17), and Re is the Reynolds number given by Eq (5.18). The Sherwood number is the mass transfer analog of the Nusselt number. This equation is valid for Reynolds numbers from 22 to 8000. Typical Reynolds numbers in a salt-cooled pebble bed core range from about 500 to about 2000, depending on core design. $Sh_{x,pebble}$ and Sc_x are calculated separately for each species being transported ($x = Cr^{2+}$, T_2, or TF). The superficial velocity (v_S) of coolant in a packed bed is given by Eq (5.19). The mass transfer coefficient for species x in flibe to the pebble surface is given by Eq (5.20). Definitions of each symbol in these equations are given below. An alternative equation, which results in a $Sh_{x,pebble}$ twice as large as that calculated from Eq (5.16), is given in Eq (5.21) for Reynolds numbers from 250 to 500,000 [172,173]. Eq (5.16) will be used in TRIDENT because it is a conservative calculation of the rate of mass transfer of T_2 and TF to the pebble surfaces.

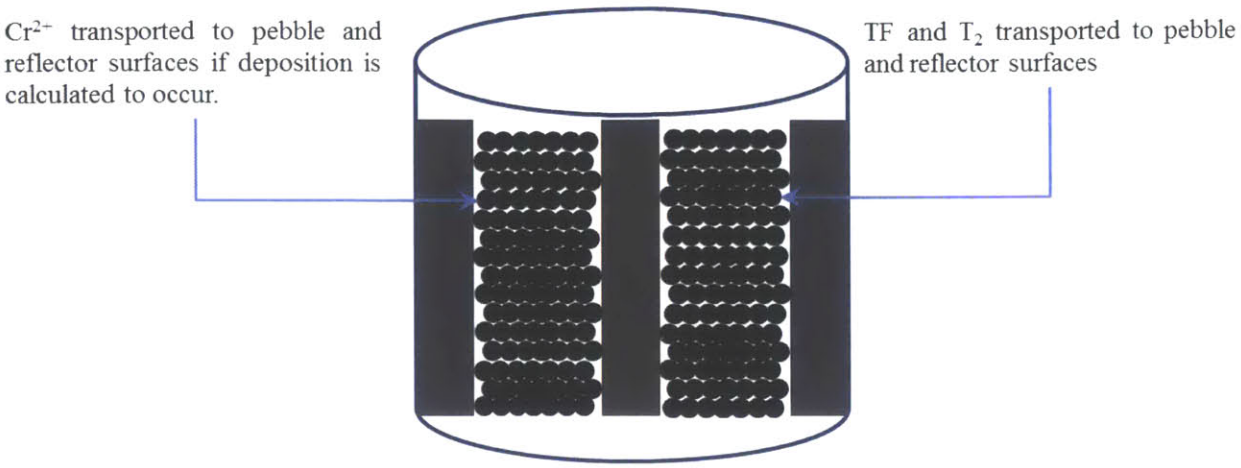

Figure 5.9: Mass transport to surfaces in the reactor core.

$$\mathrm{Sh}_{x,pebble} = (0.5\,\mathrm{Re}^{1/2} + 0.2\,\mathrm{Re}^{2/3})\mathrm{Sc}_x^{\,1/3} \tag{5.16}$$

$$\mathrm{Sc}_x = \frac{\mu}{\rho D_{x,flibe}} \tag{5.17}$$

$$\mathrm{Re} = \frac{\rho v_S d_{pebble}}{\mu P_f} \tag{5.18}$$

$$v_S = \frac{\dot{\mathrm{v}}}{A} \tag{5.19}$$

$$k_{x,pebble} = \frac{\mathrm{Sh}_{x,pebble} D_{x,flibe}}{D_{pebble}} \tag{5.20}$$

$$\mathrm{Sh}_{x,pebble} = \mathrm{Sc}_x^{1/3}\left[\left(1.18\,\mathrm{Re}^{0.58}\right)^4 + \left(0.23\,\mathrm{Re}^{0.75}\right)^4\right]^{0.25} \tag{5.21}$$

$\mathrm{Sh}_{x,pebble}$	=	Sherwood number for transport of species x (Cr^{2+}, TF, or T_2) from the coolant to the pebble surface. Mass transfer equivalent of Nusselt number
Re	=	Reynolds number in coolant
Sc_x	=	Schmidt number for species x (Cr^{2+}, TF, or T_2). Mass transfer equivalent of Prandtl number
μ	=	coolant viscosity [Pa/s]. Flibe and flinak viscosities are given in Eqs (5.24) and (5.25), respectively.
ρ	=	coolant density [kg/m^3]. Flibe and flinak densities are given in Eqs (2.11) and (5.26), respectively
$D_{x,flibe}$	=	diffusivity of species x (Cr^{2+}, TF, or T_2) in flibe [m^2/s]. The diffusivities for each species are given in Eqs (5.27) through (5.30)
v_S	=	Superficial velocity of coolant in core [m/s]
P_f	=	pebble packing fraction in the core
d_{pebble}	=	pebble diameter [m]

$\dot{v}$	=	coolant volumetric flow rate [m^3/s]
A	=	free-flow core cross sectional area [m^2]
$k_{x,pebble}$	=	mass transfer coefficient for species x (Cr^{2+}, TF, or T_2) to the pebble surface [m/s]

Tritium and Cr^{2+} mass transport to the graphite reflector surfaces are also modeled in TRIDENT. This begins with the calculation of mass transfer coefficients to the reflector surfaces adjacent to the packed bed of fuel pebbles. First, the Reynolds number for the packed bed is calculated using Eq (5.18). Next, the Schmidt number for each species x (TF, T_2, or Cr^{2+}) is calculated according to Eq (5.17). Then, the Sherwood number for mass transfer to the reflector surfaces is calculated using Eq (5.22) borrowed from Dixon and Labua [174]. Here, $d_{core,eff}$ is the effective diameter of the core. Finally, the mass transfer coefficient $k_{x,wall}$ (m/s) is calculated from Eq (5.23).

$$\mathrm{Sh}_{x,\mathrm{reflector}} = \left(1 - d_{pebble} / d_{core,eff}\right) \times \mathrm{Sc}_x^{1/3} \times \mathrm{Re}^{0.61} \tag{5.22}$$

$$k_{x,wall} = \mathrm{Sh}_{x,\mathrm{reflector}} \times \left(D_{x,flibe} / d_{core,eff}\right) \tag{5.23}$$

Several of the quantities required in the equations above are available from the literature and possess a temperature dependence. The viscosities for flibe and flinak come from references [42] and [45], respectively, and are given below in Eqs (5.24) and (5.25). Here the viscosity is in units of Pa-s and T is temperature in Kelvin. The temperature dependence of the density of flibe was given in Eq (2.11). The temperature dependence of the density of flinak (in units of kg/m^3) is given in Eq (5.26) where T is temperature in Kelvin [45]. A number of studies have measured the diffusivity of T_2 and TF in fluoride salts. Eqs (5.27) through (5.29) show the diffusivities for T_2 and TF in flibe and flinak in units of m^2/s. In each case, T is the temperature in Kelvin, and R is the universal gas constant in units of J/mol-K. T_2 diffusivity in flibe was measured by Calderoni et. al. [100]. TF diffusivity in flibe was measured by Oishi et. al. [105]. H_2 diffusivity in flinak was measured by Fukada and Morisaki [99]. The equation for H_2 diffusivity in flinak from Fukada and Morisaki is incorrect, but the data plotted in Figure 5 of Fukada and Morisaki are correct. Eq (5.29) was generated by first extracting the data from Figure 5 in Fukada and Morisaki and then applying a power fit. Since the diffusivity of T_2 in flinak has not been measured, it is approximated that the diffusivity of T_2 in flinak is the same as the diffusivity of H_2 in flinak. The data could be adjusted according to the kinetic isotope effect (see Eq (2.23)), but the scatter in experimental data are larger than the difference this adjustment would make. Eq (5.28) was generated by extracting the data from Figure 3 in Oishi et. al. and applying a power fit. Eqs (5.27) through (5.29) were plotted for comparison purposes in Figure 2.23. The diffusivity of Cr^{2+} in flibe has not been measured, but it can be estimated using the Stokes-Einstein equation shown in Eq (5.30). Here, k_B is the Boltzmann constant (in units of J/K), T is temperature (in Kelvin), μ_{flibe} is the viscosity of flibe, and R_{Cr2+} is the effective radius of the Cr^{2+} ion (8×10^{-11} m).

$$\mu_{flibe} = 1.16\times10^{-4}\exp\left(3755/T\right) \tag{5.24}$$

$$\mu_{flinak} = 2.487\times10^{-5}\exp\left(4478.62/T\right) \tag{5.25}$$

$$\rho_{flinak} = 2579.3 - 0.624T \tag{5.26}$$

$$D_{T_2,flibe} = 9.3\times10^{-7}\exp\left(-42000/RT\right) \tag{5.27}$$

$$D_{TF,flibe} = 6.4854\times10^{-26}T^{5.7227} \tag{5.28}$$

$$D_{H_2,flinak} = 2.4537\times10^{-29}T^{6.9888} \tag{5.29}$$

$$D_{Cr^{2+},flibe} = \frac{k_B T}{6\pi\mu_{flibe}R_{Cr^{2+}}} \tag{5.30}$$

After determining the mass transfer coefficients, the flux of a given species to the graphite pebble surface (in units of moles x/m^2-s) during a given time step i can be calculated from Eq (5.31). The flux of a given species to the graphite reflector surfaces (in units of moles x/m^2-s) can be calculated from Eq (5.32). Here, $c_{x,bulk}{}^i$ and $c_{x,graph}{}^i$ are the concentrations (in units of moles/m^3) of x in the bulk of the coolant and at the flibe-graphite interface for time step i, respectively. The MSRE program assumed that any tritium (both TF and T_2) reaching the graphite surface was adsorbed on that surface [50]. This is the same as saying that tritium absorption on graphite is instantaneous. This assumption is adopted here as well. This means that the concentration of T_2 or TF in flibe at the graphite surface can be assumed to be zero. Tritium uptake by graphite is a case of mass transfer from a liquid to a solid surface. Analogous approximations are made in calculations of mass transfer from a solid surface into a liquid. For example, in cases where metal is corroded by liquid lead-bismuth eutectic (LBE), it is often assumed that the corrosion kinetics are dictated by the mass transfer rate of the corrosion product away from the liquid-interface [175,176]. In the case of tritium sorption on graphite, it can be assumed that the tritium sorption rate is limited by the mass transfer rate of tritium to the graphite surface. In the LBE case, it is assumed that the corrosion product is removed into continuously refreshed LBE such that the bulk concentration in the liquid can be set to zero [175,176]. For the sake of conservativeness, in the case of tritium transport to the graphite surface, the tritium concentration in the salt at the graphite-salt interface ($c_{x,graph}{}^i$) is assumed to be 1 % (rather than zero) of the concentration in the bulk coolant ($c_{x,bulk}{}^i$).

The rate of graphite T_2 adsorption in a specific core segment N at a specific time step i is given by Eq (5.33). Similarly, the rate of graphite TF adsorption in a specific core segment N at a specific time step i is given by Eq (5.34). If TRIDENT determines that corrosion product Cr^{2+} is to be deposited in the core, the rate of deposition on graphite in a specific core segment N at a specific time step i is given by Eq (5.35). Section 5.8 describes the Cr deposition reactions in greater detail. The total amount of tritium adsorbed on the core graphite is calculated for each time step in each core segment according to Eq (5.36). The total amount of Cr deposited on the core graphite is calculated

for each time step in each core segment according to Eq (5.37). The symbols not previously defined are summarized below.

$$j^{i}_{x,pebble} = k^{i}_{x,pebble}\left(c^{i}_{x,bulk} - c^{i}_{x,\text{graph}}\right) \tag{5.31}$$

$$j^{i}_{x,wall} = k^{i}_{x,\text{wall}}\left(c^{i}_{x,bulk} - c^{i}_{x,\text{graph}}\right) \tag{5.32}$$

$$\dot{A}^{N,i}_{graphite,\text{T}_2} = A^{N}_{g,pebble} j^{i}_{\text{T}_2,pebble} + A^{N}_{g,\text{wall}} j^{i}_{\text{T}_2,\text{wall}} \tag{5.33}$$

$$\dot{A}^{N,i}_{graphite,\text{TF}} = A^{N}_{g,pebble} j^{i}_{\text{TF},pebble} + A^{N}_{g,\text{wall}} j^{i}_{\text{TF},\text{wall}} \tag{5.34}$$

$$\dot{D}^{N,i}_{deposition,Cr} = A^{N}_{g,pebble} j^{i}_{\text{Cr},pebble} + A^{N}_{g,\text{wall}} j^{i}_{\text{Cr},\text{wall}} \tag{5.35}$$

$$mg^{N,\text{i}}_{\text{T}} = mg^{\text{N,i}-1}_{\text{T}} + \left(2 \times \dot{A}^{N,i}_{graphite,\text{T}_2} + \dot{A}^{N,i}_{graphite,\text{TF}}\right) \Delta t / N_{core} \tag{5.36}$$

$$mg^{N,\text{i}}_{Cr} = mg^{\text{N,i}-1}_{Cr} + \dot{D}^{N,i}_{deposition,Cr} \, \Delta t / N_{core} \tag{5.37}$$

$j_{x,pebble}{}^{i}$ = flux of species x to the graphite pebble surface during time step i [moles x/m^2-s]

$j_{x,wall}{}^{i}$ = flux of species x to the graphite reflector surfaces during time step i [moles x/m^2-s]

$A_{g,pebble}{}^{N}$ = pebble graphite surface area within core segment N [m^2]

$A_{g,wall}{}^{N}$ = reflector graphite surface area within core segment N [m^2]

$\dot{A}^{N}_{graphite,T_2}$ = rate of T_2 adsorption on graphite in core segment N at time step i [moles T_2/s]

$\dot{A}^{N}_{graphite,TF}$ = rate of TF adsorption on graphite in core segment N at time step i [moles TF/s]

$\dot{D}^{N,i}_{deposition,Cr}$ = rate of Cr deposition on graphite in core segment N at time step i [moles Cr/s]

$mg_x{}^{N,i}$ = total moles of species x adsorbed on graphite surface in core segment N up through the current time step i

$mg_x{}^{N,i-1}$ = total moles of species x adsorbed on graphite in core segment N up through the previous time step i-1

Δt = size of time step [s]. For calculations in regions of the reactor coolant loop that have been divided into segments (this is done in the core and the heat exchanger) the size of the time step must be divided by the number of regions in the segment in question.

N_{core} = number of specified divisions in the reactor core

N = specific core segment (varies from 1 to N_{core})

Tritium adsorption on graphite is allowed until the graphite capacity for tritium is reached. This is determined by employing Eq (2.8). Using Henry's law (Eq (2.10)) and the Henry's law constants for TF and T_2 (see Eqs (2.12) and (2.13)), the partial pressure of TF and T_2 above the graphite is

determined.[6] These partial pressures are used in Eq (2.8) to specify the graphite capacity for T_2 and TF in units of mole T/g graphite. Once $mg_x^{N,i}$, normalized by the grams of graphite in core segment N, is equal to this capacity, further adsorption is not allowed. If the partial pressure were to increase again, then the graphite capacity will also increase, and adsorption would be allowed again until the new capacity is filled. Additionally, Eq (2.8) includes the temperature dependence for graphite capacity; thus, the hotter parts of the core will have a lower tritium capacity than the cooler parts.

TRIDENT does not account for radiation effects on tritium or hydrogen uptake, but it could be modified to do so in the future. With respect to the effects of neutron irradiation on the graphite capacity for hydrogen, three effects are in competition. First, irradiation may increase hydrogen retention on graphite by introducing new bulk trapping sites in graphite. Second, the rate of hydrogen uptake into these new bulk trapping sites may be reduced with irradiation due to a reduction in the hydrogen diffusion coefficient in graphite. Third, the number of trapping sites generated due to radiation may be reduced with annealing. In Section 2.4.2.3 the effects of radiation damage on the graphite capacity for hydrogen were discussed. Experiments have shown that radiation damage (up to about 0.6 dpa) increases graphite's capacity for hydrogen by generating new hydrogen trapping sites within the graphite. The capacity for tritium (in terms of atoms T/g graphite) may increase by a factor of 10 to 25 (after 0.05 dpa) or up to a factor of 140 (after 0.65 dpa) [92,93]. (A correlation between dpa and the number of trapping sites was proposed in Eq (2.9).) On the other hand, experiments discussed in Section 2.4.2.4 show that the rate of hydrogen uptake on graphite decreases with irradiation and that about 50% of the new trapping sites can be subsequently annealed at temperatures above the irradiation temperature.

Because most of the tritium in the FHR will be absorbed on the pebble graphite in the core, in order to accurately model these effects, the pebble irradiation and temperature histories must be known. The path a pebble takes through the core will determine these histories. The rate at which the graphite hydrogen capacity increases as a function of irradiation dose and irradiation temperature must be known. The rate of trapping site annealing must be known because the temperature of the pebble varies with its location in the core, and trapping sites generated by radiation damage at lower temperatures (toward the core inlet) may be annealed at higher temperatures (toward the core outlet). Considering that radiation damage reduces the rate of tritium uptake into the new trapping sites and that some of these new trapping sites can be annealed, the effect of irradiation on hydrogen uptake on graphite in the FHR is likely to be small.[7] Some additional trapping may occur as a result of irradiation in graphite, but neglecting this effect provides more conservative results from the TRIDENT model.

If the chemical thermodynamics calculations in TRIDENT determine that Cr^{2+} corrosion product deposition occurs, then Cr^{2+} is also transported to pebble graphite in the core. Experiments have shown that Cr^{2+} deposits via the inverse of the corrosion reaction given in Eq (3.17), and it is

[6] It is assumed that the solubilities for T_2 and TF are the same as those for H_2 and HF, respectively.

[7] Because the FHR is refueled online, tritium absorbed on fuel pebbles could be desorbed from the pebbles by deliberately heating them after removal from the core. This would cause some annealing of radiation damage.

deposited on surfaces as Cr metal [35,120,124]. This is not an adsorption reaction; thus, the chemical fluorine potential controlling redox reactions is the only limit to the amount of Cr that could be deposited on a given surface. The methodology for determining whether corrosion or deposition occurs is discussed in Section 5.8.1. Eq (5.35) and Eq (5.37) are used for determining the mass transfer of Cr^{2+} to the graphite surface and the amount of Cr deposited at the graphite surface, respectively. Under conditions of deposition, Eq (5.35) is the definition of the rate of Cr deposition on graphite, $\dot{D}^N_{deposition,Cr}$, used in Eq (5.3). The inverse of Eq (3.17) shows that for each mole of Cr deposited, 1 mole of H_2 or (T_2) is consumed and 2 moles of HF or (TF) are produced. Thus, the rate of T_2 *consumption* due to Cr^{2+} deposition is $\dot{D}^N_{deposition,T2} = \dot{D}^N_{deposition,Cr}$. Conversely, the rate of TF *production* due to Cr^{2+} deposition is $\dot{D}^N_{deposition,TF} = 2 \times \dot{D}^N_{deposition,Cr}$. A summary of these definitions is provided below.

$$\dot{D}^N_{deposition,T_2} = \dot{D}^N_{deposition,\mathrm{Cr}} \tag{5.38}$$

$$\dot{D}^N_{deposition,TF} = 2 \times \dot{D}^N_{deposition,\mathrm{Cr}} \tag{5.39}$$

5.6.2 Mass transport to pipe surfaces

Mass transfer to pipe surfaces is important for both corrosion phenomena and tritium transport/diffusion. Because the kinetics of the corrosion reactions are unknown, it is assumed that the reaction rates are determined initially by the rate at which the reactant (TF) can be transported to the metal surface. Long-term corrosion rates are controlled by the rate of Cr diffusion in the base metal. Figure 5.10 illustrates the mass transport phenomena modeled in major coolant pipes and the heat exchangers. Once again, the mass transfer coefficients are required. The coolant velocity (v) is given by Eq (5.40) where d_{pipe} is the inner diameter of the pipe. The Reynolds number in a circular pipe is given in Eq (5.41). The Schmidt number for species x (where x can be TF, T_2, or Cr^{2+}) is given by Eq (5.42). Next, the Sherwood number, which is the mass transfer equivalent of the Nusselt number, is required. Because the flow regimes in FHR piping may be laminar, transitional, or turbulent at different locations in the loop, a specific correlation is employed for each flow regime. In the heat exchanger pipes, the Reynolds number may be less than 2000 (as is the case for the heat exchangers in the Mk1 PB-FHR). However, in the main coolant legs, the Reynolds number in these large pipes may be > 10000. For a flow with 13 < Re < 2030, a correlation developed by Graetz, modified by Sieder and Tate, and presented by Whitaker is used [171]. This correlation is given in Eq (5.43) where L is the length of the pipe and d_{pipe} is the pipe's inner diameter. For a flow with 2030 < Re < 10000, the Sherwood number is given by the correlation in Eq (5.44) presented by Whitaker [171]. For a case where Re > 10000, the Sherwood number for species x is given by Eq (5.45). This equation is the Dittus-Boelter correlation (as presented by reference [11]) modified for use in mass transfer using the Reynolds analogy. Finally, the mass transfer coefficient for the transport of species x to a circular pipe surface is given by Eq (5.46). Each of these parameters is

calculated at a given segment N where the specific temperature at that location is used to update the coolant density, viscosity, species diffusion coefficient, etc.

Once the mass transfer coefficients have been specified, the fluxes of species x, the rates of corrosion, the rates of deposition, and the rates of permeation can be specified in the pipes and heat exchangers. In a hot leg or a cold leg or in a heat exchanger, the flux of TF or Cr^{2+} to a pipe surface in a given loop segment N at time step i is given by Eq (5.47) in units of mole/m^2-s. For the case of a reactant in a liquid phase being transported to the surface of a solid phase for reaction, the concentration of the reactant at the surface is unknown and the concentration of the reactant in the bulk of the fluid (together with the mass transfer coefficient) determines the rate of mass transfer [177]. If the reaction rate constant is known (or if it is a limiting factor) an effective reaction rate can be written which combines the mass transfer coefficient and the reaction rate constant [177]. In Eq (5.47), for x = TF, it is assumed that $c^i_{x,wall}$ is zero. This is based on the assumption that at the high temperatures of the FHR (600 °C minimum) the corrosion reaction between Cr and TF occurs instantly such that the concentration of TF in the coolant at the metal surface can be approximated as zero, the rate of mass transfer is determined by the bulk concentration of TF in the salt ($c^i_{TF,bulk}$) and the mass transfer coefficient, and the reaction rate constant can be ignored.

If the actual bulk concentration of CrF_2 in the salt entering a given segment ($c^i_{Cr,bulk}$) is greater than the local equilibrium concentration of CrF_2 in that segment ($c^i_{Cr,eq}$ in units of mole/m^3), then deposition of Cr onto surfaces in that region is allowed. Eq (3.20) is used to calculate the local equilibrium concentration of CrF_2 dissolved in the salt according to the local temperature and redox conditions. Then, the rate of Cr deposition on surfaces in the loop segment is determined from Eq (5.47) where the bulk CrF_2 concentration is given by $c^i_{Cr,bulk}$ and the surface concentration $c^i_{Cr,wall}$ is set equal to $c^i_{Cr,eq}$ (which is determined from Eq (3.20)). The surface concentration is specified in this way so that deposition would occur until the concentration of Cr in the salt is equal to the local equilibrium concentration. The rate of Cr deposition in a pipe or heat exchanger is given by Eq (5.48) in units of mol/s. The symbol A^N_{pipe} represents the pipe surface area facing the coolant within volume element N in the pipe. The rate of T_2 consumption accompanying Cr deposition is given by Eq (5.49) in units of mol/s. The rate of TF production accompanying Cr deposition is given by Eq (5.50) in units of mole/s.

The flux of T_2 from the salt to the salt-metal interface at the heat exchanger tube wall is given by Eq (5.51) in units of mol/m^2-s. Here, $c^*_{T2,coolant\ wall}$ is the concentration of T_2 in the salt at the salt-heat exchanger tube interface. This concentration is calculated through solving a system of equations described in Section 5.7. The rate of T_2 permeation into the heat exchanger tube wall is given by Eq (5.52) in units of mol/s. The symbol $A^{N_{HX}}_{HX}$ is the surface area facing the primary coolant within volume element N_{HX} in the primary heat exchanger.

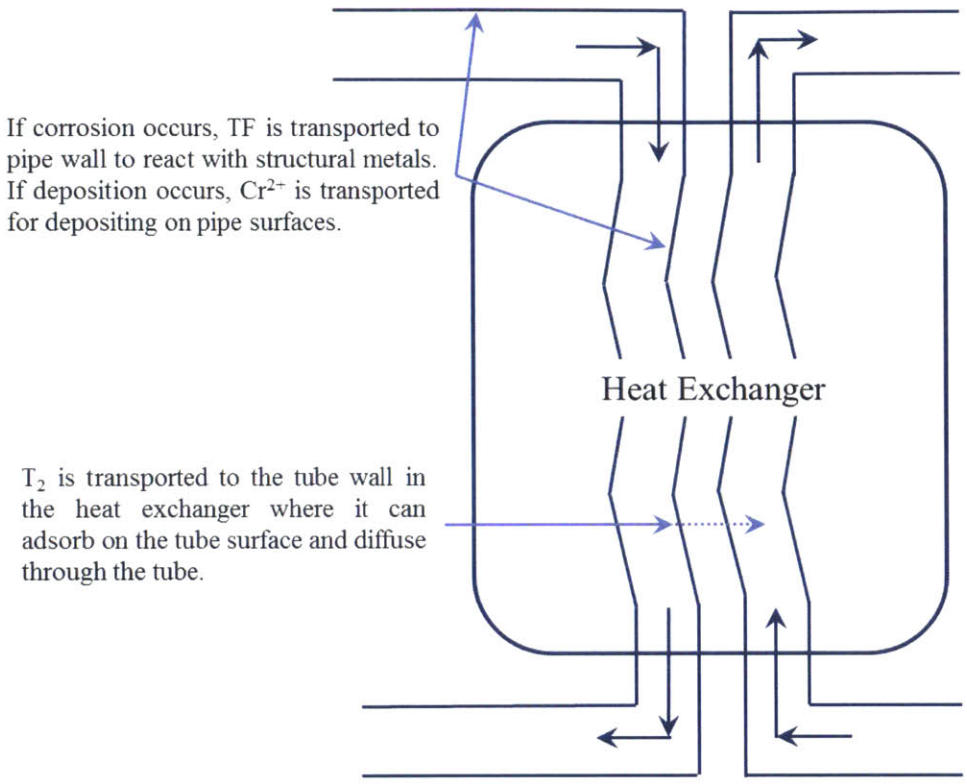

Figure 5.10: Major mass transfer phenomena to pipe surfaces in TRIDENT.

$$v = \frac{\dot{v}}{\pi\left(d_{pipe}/2\right)^2} \tag{5.40}$$

$$\mathrm{Re}_{pipe} = \frac{\rho v d_{pipe}}{\mu} \tag{5.41}$$

$$Sc_{x,pipe} = \frac{\mu}{\rho D_{x,flibe}} \tag{5.42}$$

$$Sh_{x,pipe} = 1.86\,\mathrm{Re}^{1/3}\, Sc_{x,pipe}^{1/3}\left(L/d_{pipe}\right)^{-1/3} \tag{5.43}$$

$$Sh_{x,pipe} = 0.015\,\mathrm{Re}^{0.83}\, Sc_{x,pipe}^{0.42} \tag{5.44}$$

$$Sh_{x,pipe} = 0.023\,\mathrm{Re}_{pipe}^{0.8}\, Sc_{x,pipe}^{0.4} \tag{5.45}$$

$$k_{x,pipe} = \frac{Sh_{x,pipe} D_{x,flibe}}{d_{pipe}} \tag{5.46}$$

$$j^{N,i}_{\mathrm{TF\,or\,Cr}^{2+},pipe} = k^{N,i}_{\mathrm{TF\,or\,Cr}^{2+},pipe}\left(c^{N,i}_{\mathrm{TF\,or\,Cr},^{2+}bulk} - c^{N,i}_{\mathrm{TF\,or\,Cr}^{2+},wall}\right) \tag{5.47}$$

$$\dot{D}^{N,i}_{deposition,Cr} = A^{N}_{pipe} j^{N,i}_{\mathrm{Cr}^{2+},pipe} \tag{5.48}$$

$$\dot{D}^{N,i}_{deposition,T_2} = \dot{D}^{N,i}_{deposition,\mathrm{Cr}} \tag{5.49}$$

$$\dot{D}^{N,i}_{deposition,TF} = 2 \times \dot{D}^{N,i}_{deposition,\mathrm{Cr}} \tag{5.50}$$

$$j^{N_{HX},i}_{T_2,\mathrm{HX}} = k^{i}_{T_2,pipe}\left(c^{N_{HX},i}_{T_2,bulk} - c^{*}_{T_2,coolant\ wall}\right) \tag{5.51}$$

$$\dot{P}^{N_{HX},i} = A^{N_{HX}}_{HX}\, j^{N_{HX},i}_{T_2,\mathrm{HX}} \tag{5.52}$$

5.6.3 Mass transport in the secondary coolant

Mass transport in the secondary coolant is virtually the same as mass transport in the primary coolant. One major difference is that the secondary coolant may be a different salt (such as flinak). It is approximated that the same equations used for the primary coolant mass transfer coefficient in the PHX (see Section 5.6.2) can be used for the secondary coolant passing through the PHX and in the SHX. The appropriate secondary coolant properties and fixed temperature are used in these equations in order to make them applicable to the secondary coolant. The flux of T_2 out of the PHX tube wall into the secondary coolant in volume element N_{PHX} at time step i is given by Eq (5.53). In Eq (5.53), $c^{*}_{T2,coolant\ wall}$ is the concentration of the coolant at the interface between the PHX tube wall and the secondary coolant in volume element N_{PHX} at time step i, and $c^{NPHX,i}_{T2,bulk}$ is the concentration of T_2 in the bulk of the secondary coolant. Next, the flux of T_2 out of the secondary coolant and into the tube wall of the SHX (in volume element N_{SHX} at time step i) is given by Eq (5.54). In Eq (5.54) $c^{*}_{T2,coolant\ wall}$ is now the T_2 concentration at the interface between the secondary coolant and the SHX tube wall. In Eqs (5.53) and (5.54), $c^{*}_{T2,coolant\ wall}$ is calculated by solving a system of equations described in Section 5.7. The rate of T_2 permeation (at volume element N and time step i) from the PHX into the secondary coolant is given by Eq (5.55), and the rate of T_2 permeation from the secondary coolant into the SHX tube wall is given by Eq (5.56). As usual, A^{N}_{PHX} and A^{N}_{SHX} are the surface areas facing the secondary coolant in a given volume element N in the secondary sides of the primary and secondary heat exchangers, respectively.

$$j^{N_{PHX},i}_{T_2,\mathrm{PHX}} = k^{i}_{T_2,pipe}\left(c^{*}_{T_2,\mathrm{coolant\ wall}} - c^{N_{PHX},i}_{T_2,bulk}\right) \tag{5.53}$$

$$j^{N_{SHX},i}_{T_2,\mathrm{SHX}} = k^{i}_{T_2,pipe}\left(c^{N_{SHX},i}_{T_2,bulk} - c^{*}_{T_2,\mathrm{coolant\ wall}}\right) \tag{5.54}$$

$$\dot{P}_{HX1}{}^{N,i} = A_{PHX}{}^{N}\, j^{N_{PHX},i}_{T_2,\mathrm{PHX}} \tag{5.55}$$

$$\dot{P}_{HX2}{}^{N,i} = A_{SHX}{}^{N}\, j^{N_{SHX},i}_{T_2,\mathrm{SHX}} \tag{5.56}$$

5.7 Model of tritium diffusion in metal

Tritium reaching the surface of a metal membrane may permeate through the membrane from the side of high concentration to the side of low concentration. The rate at which tritium reaches the metal surface and the relevant solubility laws applicable to the coolant and the metal on the upstream surface provide boundary conditions. Within the metal, the rate of tritium diffusion must be modeled and the amount of tritium conserved. On the downstream surface of the metal, the rate of tritium transport from the surface and the prevailing solubility laws provide boundary conditions similar to those on the upstream surface.

Previous sections discussed the coolant volume elements and the mass balances and reaction rates within them. The diffusion of T_2 through the heat exchangers is treated as 1D diffusion through the metal tube wall. Only radial diffusion through the metal is considered. Axial diffusion within the metal is neglected. Figure 5.11 shows the axial and radial zoning within the tube wall of the primary heat exchanger. The tube wall is treated as a planar geometry, but the cross-sectional area of the tube perpendicular to the radial direction is allowed to change throughout the tube's thickness.

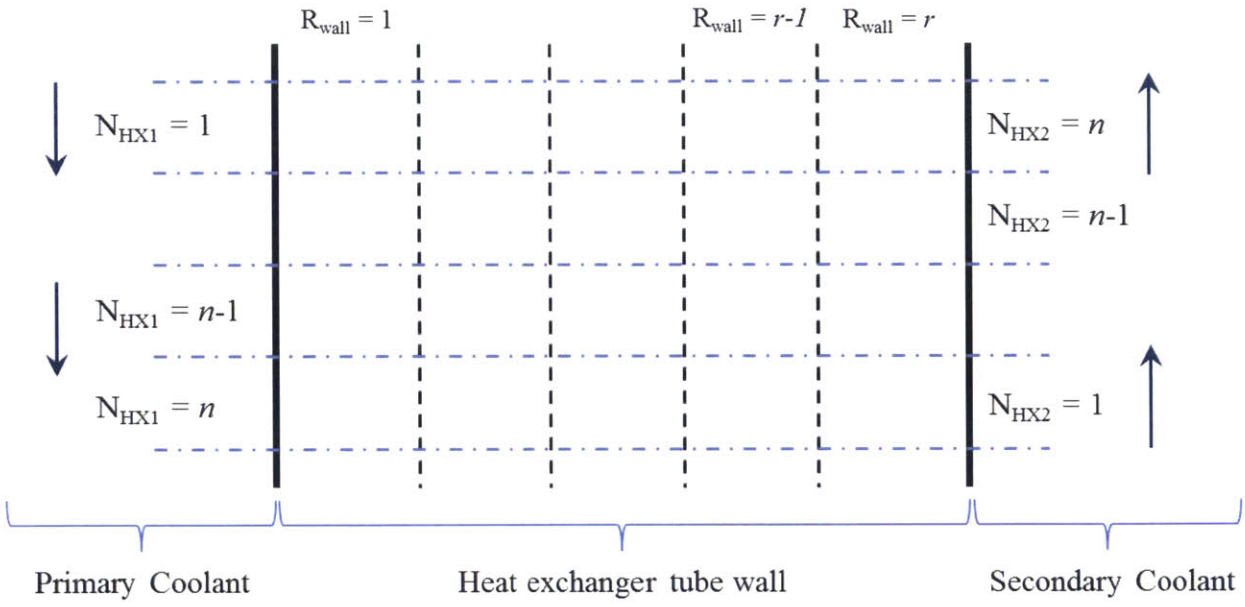

Figure 5.11: Radial and axial elements in the heat exchanger tube separating the primary and secondary coolant.

5.7.1 Tritium diffusion boundary conditions

As the mass transport equations developed in Section 5.6 show, there is a rate at which T_2 can be transported to the surface of a metal membrane, such as the tube wall in a heat exchanger. What those equations do not show is that the rate of T_2 transport into and through the HX wall is dependent not only on the rate at which the coolant can supply T_2 to the metal surface, but also on the T_2 solubility and diffusivity within the metal. This section will define a system of equations which will

link these phenomena and help determine the rate of T_2 permeation through a metal membrane contacting molten salt bearing T_2. Experiments have determined that the permeation rate is limited by mass transport/diffusion and not by the rate of T_2 dissociation/recombination on the metal surface [54,178]. Thus, the assumption adopted here is that the permeation rate is limited by mass transport/diffusion and not by the rate of T_2 dissociation/recombination on the metal surface.

A set of boundary conditions are required at the interface between the primary coolant and the heat exchanger wall. Because the buildup and transport of tritium in the FHR is a transient problem, the numerical value of these boundary conditions changes with each axial segment (N_{HX}) in the heat exchanger and each time step i until equilibrium is achieved. The following two assumptions were adopted from Fukada et. al. [178]. First, it is assumed that tritium dissociation/recombination processes at the metal surface are instantaneous. Second, it is assumed that the tritium concentration at the metal side of the coolant-metal interface attains an instant equilibrium with the coolant side of the interface. Figure 5.12 illustrates the concentration profile of T_2 at the interface between the primary coolant and the heat exchanger metal. Note that in non-porous membranes (such as the metal tube wall) the solute concentration does not have to be continuous [179]. Using the concentration of T_2 in the coolant at the metal-coolant interface (given by $c^*_{T2,coolant\ wall}$), the partial pressure of T_2 over this solution is calculated from Henry's law according to Eq (5.57) where the Henry's law constant for T_2 in flibe comes from Eq (2.13). Using the concentration of T_2 in the heat exchanger metal at the metal-coolant interface (given by $c^*_{T2,metal\ wall}$), the partial pressure of T_2 over that metal surface is calculated according to Sievert's law in Eq (5.58). Here, the Sievert's law constant ($K_{S,T2,metal}$) comes from Eq (2.19) and the constants required in this Arrhenius equation can be chosen for a particular metal from data such as that in Table 2.5 through Table 2.8. The boundary condition specified here (borrowed from Fukada et. al. [178]) specifies that at the coolant-metal interface, these partial pressures must be equal to each other, as summarized in Eq (5.59).

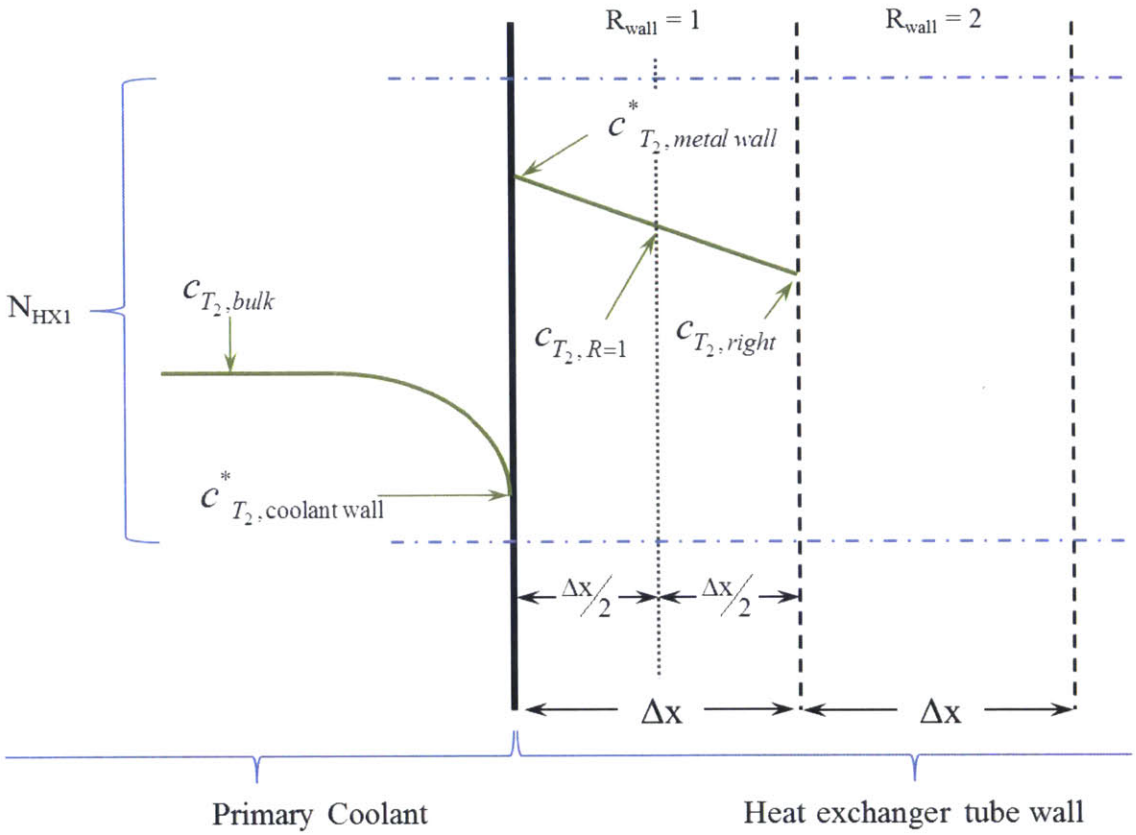

Figure 5.12: Schematic concentration profile of T_2 on the upstream side at the tube surface and within the first radial element of the tube.

$$p_{T_2,\text{coolant}} = \frac{c^*_{T_2,\text{coolant wall}}}{k_{Henry,T_2,flibe}} \tag{5.57}$$

$$p_{T_2,metal} = \left(\frac{c^*_{T_2,metal\,wall}}{K_{S,T_2,metal}} \right)^2 \tag{5.58}$$

$$p_{\text{interface}} = \frac{c^*_{T_2,\text{coolant wall}}}{k_{Henry,T_2,flibe}} = \left(\frac{c^*_{T_2,metal\,wall}}{K_{S,T_2,metal}} \right)^2 \tag{5.59}$$

A second boundary condition is specified at the coolant-metal interface: the flux of T_2 from the coolant to the coolant-metal interface (given by Eq (5.51)) must be equal to the flux from the interface into the metal (given by Eq (5.60)). In Eq (5.60), D is the diffusion coefficient of T_2 in the metal (in units of m^2/s) given by the Arrhenius relationship from Eq (2.18) and data such as that in Table 2.5 through Table 2.8. If data specifically for T_2 are not available, the diffusion coefficient for H_2 is used. The concentrations denoted by the letter "c" are in units of mole T_2/m^3. Fluxes of T_2 are denoted by the letter "j" in units of moles T_2/m^2-sec. Tritium diffuses through metal as T atoms, but the notation here uses T_2 throughout for easier accounting. Figure 5.11 and Figure 5.12 show that the

thickness of the HX tube wall is divided into a number of radial segments, each of thickness Δx. The segments containing the coolant-metal interfaces are subdivided into two smaller segments of thickness Δx/2. The T_2 concentration at the center of each segment ($c_{T2,R}$) is assumed to be the average concentration in that segment. The numerical values of each boundary condition will change with each time step i and axial segment of the heat exchanger (N_{HX}) until equilibrium is reached. Thus, each symbol in the equations below is calculated for each N_{HX} and i. The equality enforced by this flux boundary condition is summarized in Eq (5.61).

$$j_{T_2,HX\,in} = \frac{D}{\Delta x/2}\left(c^*_{T_2,metal\,wall} - c_{T_2,R=1}\right) \tag{5.60}$$

$$j^{N_{HX},i}_{T_2,\mathrm{HX}} = k_{T_2,pipe}\left(c_{T_2,bulk} - c^*_{T_2,coolant\,wall}\right) = j^{N_{HX},i}_{T_2,HX\,in} = \frac{D}{\Delta x/2}\left(c^*_{T_2,metal\,wall} - c_{T_2,R=1}\right) \tag{5.61}$$

Once the concentration and flux boundary conditions have been specified, two conservation equations are required: one for the coolant and one for the first radial segment of the heat exchanger. Once again, the superscript N_{HX} represents an axial element of the coolant or the metal in a heat exchanger. The superscript i represents a particular time step, and a superscript of i-1 denotes the value from the previous time step. The superscript R represents a radial segment of the heat exchanger tube wall. In Eqs (5.62) and (5.63), R =1. A^{NHX}_{HX} is the surface area (m^2) of the heat exchanger facing the primary coolant within axial segment N_{HX}, and Δt is the size of the time step in seconds. Because the heat exchanger is divided into $N_{HX,total}$ number of segments, the size of the time step must also be divided by $N_{HX,total}$ for calculations within the heat exchanger. $V_{HX}^{NHX,R}$ is the volume of heat exchanger metal in segment R in axial element N_{HX}. Eq (5.62) calculates a new average concentration of T_2 in axial segment N_{HX} and radial segment R in the heat exchanger metal. Eq (5.62) incorporates the flux from the coolant to the HX surface defined in Eq (5.51). Eq (5.63) calculates a new concentration of T_2 in the coolant volume segment passing through axial segment N_{HX}. Eq (5.63) incorporates the flux (defined by Eq (5.60)) from the metal surface to the center of the radial element R = 1 in the heat exchanger. Between Eqs (5.59), (5.61), (5.62), and (5.63) there is a system of 4 equations and 4 unknowns. The unknowns are $c_{T_2,R}^{N_{HX},i}$, $c_{T_2,\mathrm{bulk}}^{N_{HX},i}$, $c^*_{T_2,coolant\,wall}$, and $c^*_{T_2,metal\,wall}$. TRIDENT solves this non-linear system using the `fsolve` function in MatLab.

$$c_{T_2,R}^{N_{HX},i} = \frac{c_{T_2,R}^{N_{HX},i-1} \times V_{HX}^{N_{HX},R} + k^i_{T_2,pipe}\left(c^{N_{HX},i}_{T_2,bulk} - c^*_{T_2,coolant\,wall}\right) \times A^{N_{HX}}_{HX} \times \Delta t / N_{HX,total}}{V_{HX}^{N_{HX},R}} \tag{5.62}$$

$$c_{T_2,\mathrm{bulk}}^{N_{HX},i} = \frac{c_{T_2,\mathrm{bulk}}^{N_{HX},i-1} \times \dot{v} \times \Delta t - \frac{D}{\Delta x/2}\left(c^*_{T_2,metal\,wall} - c^{N_{HX},i}_{T_2,R_{1/2}}\right) \times A^{N_{HX}}_{HX} \times \Delta t / N_{HX,total}}{\dot{v} \times \Delta t} \tag{5.63}$$

Solving the above non-linear system using the `fsolve` function in MatLab will work for all coolants and metals. For the case of flibe, the diffusivity of T_2 in liquid flibe is actually less than the diffusivity for T in structural metals. This is somewhat counterintuitive, and may be attributed to the fact that flibe retains a tetrahedral BeF_4^- structure even when molten. Because the diffusivity of tritium in flibe is less than the diffusivity of tritium in the structural metals, this allows the use of a (10 times) faster iterative solving scheme. This scheme will not work if the salt is, for example, flinak. Certain other salt/metal combinations will also not work with the faster iterative scheme. For example, in Section 6.6.1, a tungsten HX is simulated. Tungsten has a diffusivity similar to that of Type 316 SS; however, the solubility of tritium in tungsten is 5000 times lower than in Type 316 SS. That simulation required the use of the `fsolve` function. TRIDENT has the ability to use either the `fsolve` scheme described above or the iterative scheme described below. The number of moles of T_2 entering the heat exchanger in a single time step of size Δt is given by $m_{T2,in}$. The concentration of T_2 in the coolant at the coolant/metal interface is given by $c^*_{T_2,coolant\,wall}$ which is guessed initially and calculated as the iteration runs its course. The number of moles of T_2 remaining in the coolant exiting a segment of the heat exchanger is given by $m_{T2,out}$. The iterations end when the flux to the HX tube wall has converged according the criteria in the "if" statement below. Currently, this iterative solution is employed in TRIDENT for the transport of tritium from the coolant into the primary HX tube wall or from the coolant into the tube wall of a permeation window (described in Section 6.6.2). If the use of the `fsolve` function is desired, the user can go into the TRIDENT function called `polythermal.m`, comment-out the section titled "Primary HX iteration block", and un-comment the section titled "Primary HX fsolve block". Similarly, if the use of the `fsolve` function is desired for the permeation window model, the user can go into the TRIDENT function called `polythermal.m`, comment-out the section titled "Primary permeation window iteration block" and un-comment the section titled "Primary permeation window fsolve block". This is only necessary if the type of primary coolant is a salt other than flibe. If a secondary (or intermediate) loop is modeled, by default, TRIDENT uses the `fsolve` scheme to handle the boundary conditions for the case of tritium exiting the primary heat exchanger into a flinak secondary salt and for the case of tritium transport into the tube wall of the secondary heat exchanger from the flinak secondary salt.

Definition of $m_{T_2,in}$:

$$m_{T_2,in} = c_{T_2,bulk} \times \dot{v} \times \Delta t$$

Guesses prior to entering iterations:

$$j_{old} = 0$$

$$j^{N_{HX,i}}_{T_2,\mathrm{HX}} = 1$$

$$c^{*}_{T_2,coolant\,wall} = 0.001 \times c_{T_2,bulk}$$

Iterations:

$$\texttt{if} \left| \frac{j_{old} - j^{N_{HX,i}}_{T_2,\mathrm{HX}}}{j^{N_{HX,i}}_{T_2,\mathrm{HX}}} \right| < 1 \times 10^{-15}$$

`break`

`else`

$$j_{old} = j^{N_{HX,i}}_{T_2,\mathrm{HX}}$$

$$j^{N_{HX,i}}_{T_2,\mathrm{HX}} = k_{T_2,pipe}\left(c_{T_2,bulk} - c^{*}_{T_2,coolant\,wall}\right)$$

$$c_{T_2,R=1}{}^{N_{HX},i} = \frac{j^{N_{HX,i}}_{T_2,\mathrm{HX}} \times A^{N_{HX}}_{HX} \times \Delta t / N_{HX,total}}{V_{HX}{}^{N_{HX},R=1}} + c_{T_2,R=1}{}^{N_{HX},i-1}$$

$$c^{*}_{T_2,metal\,wall} = c_{T_2,R=1}{}^{N_{HX},i} + \frac{\Delta x \times k_{T_2,pipe}}{2D}\left(c_{T_2,bulk} - c^{*}_{T_2,coolant\,wall}\right)$$

$$c^{*}_{T_2,coolant\,wall} = k_{Henry,T_2,flibe}\left(\frac{c^{*}_{T_2,metal\,wall}}{K_{S,T_2,metal}}\right)^2$$

$$c_{T_2,bulk} = \frac{m_{T_2,in} - j^{N_{HX,i}}_{T_2,\mathrm{HX}} \times A^{N_{HX}}_{HX} \times \Delta t / N_{HX,total}}{\dot{v} \times \Delta t}$$

$$m_{T_2,\mathrm{out}} = m_{T_2,in} - j^{N_{HX,i}}_{T_2,\mathrm{HX}} \times A^{N_{HX}}_{HX} \times \Delta t / N_{HX,total}$$

`end`

The same equations can be used for tritium diffusing out of the primary heat exchanger and into the secondary coolant or for tritium diffusing from the secondary coolant into the secondary heat cxchanger metal. For use on the secondary side, the appropriate mass transfer coefficients and coolant properties for the secondary coolant can be used in place of those from the primary coolant. For the case of tritium diffusing out of the primary heat exchanger metal and into the secondary coolant, the symbols are re-defined in Figure 5.13. For tritium diffusing out into the power cycle, the concentration of T_2 at the metal-power cycle interface is held at 0. Additionally, if the air-facing

surface of the salt-to-air heat exchanger in the power cycle has an oxide layer, this layer is accounted for in TRIDENT by use of the permeation reduction factor (PRF) described in Section 2.6. As discussed in Section 2.6, and shown schematically in Figure 5.14, oxide layers have a low permeability for hydrogen and reduce a hydrogen permeation flux compared to bare metal. With an oxide layer on the air-side of the salt-to-air heat exchanger, the rate of tritium permeation into the power cycle is reduced. This effect is implemented by dividing the diffusion coefficient (D) by the PRF at the surface node and at each point in the tube-wall thickness.

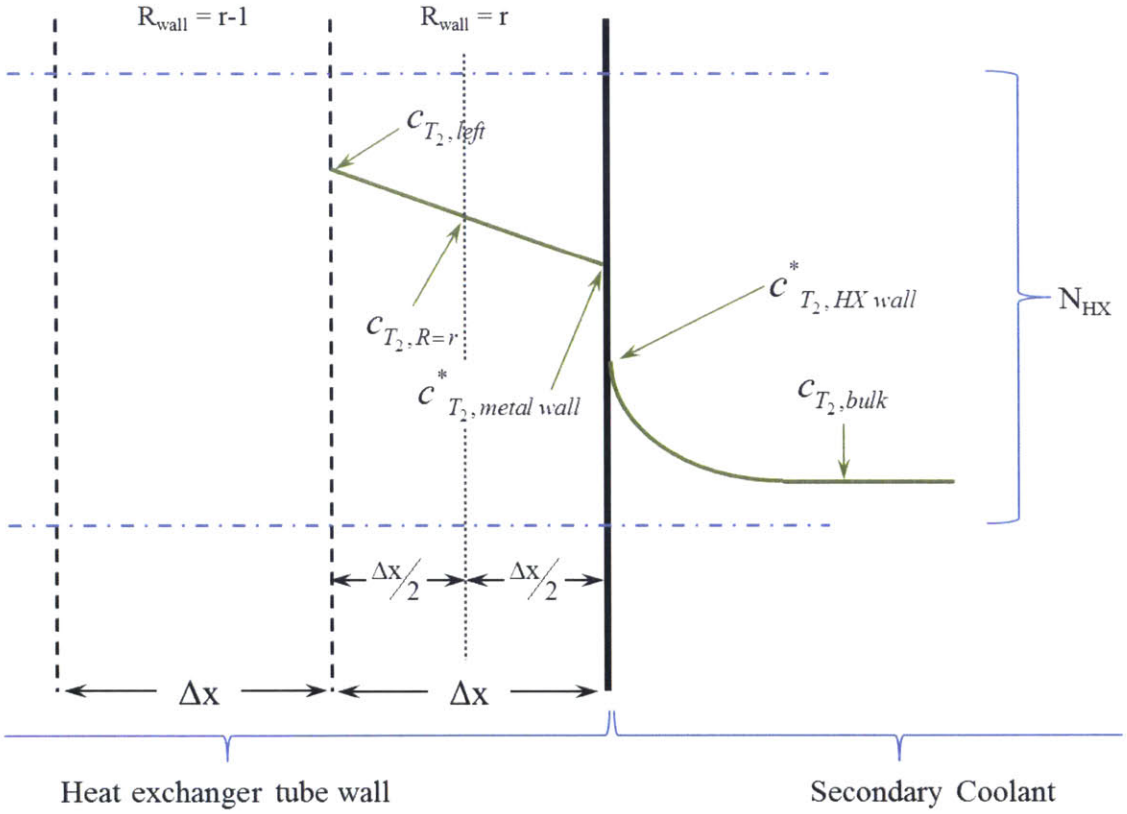

Figure 5.13: Schematic concentration profile of T_2 in the primary heat exchanger and the adjacent secondary coolant.

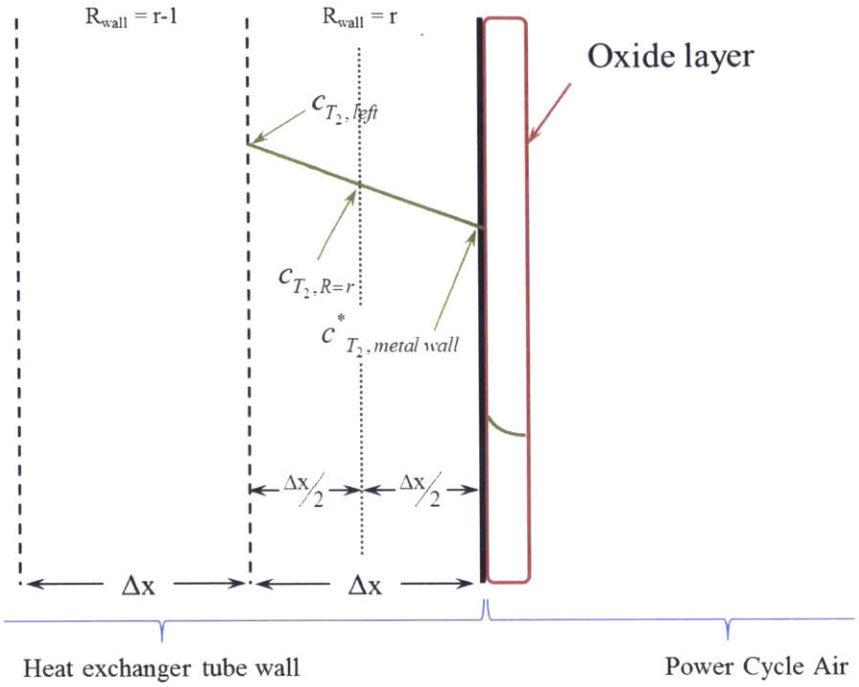

Figure 5.14: Schematic of hydrogen diffusion from the salt-to-air heat exchanger into the power cycle air through an oxide layer. Oxide layer reduces permeation by a factor of the PRF.

5.7.2 Tritium bulk diffusion in static media

The diffusion of T_2 through the heat exchangers is treated as 1D diffusion through the metal tube wall. Only radial diffusion through the metal is considered. Axial diffusion within the metal is neglected. The tube wall is treated as a planar geometry, but the cross-sectional area of the tube perpendicular to the radial direction is allowed to change throughout the tube's thickness. It is assumed that the tritium diffusion coefficient does not vary with the tritium concentration and that it is constant through the thickness of the diffusive medium. The temperature is assumed to be constant throughout the thickness of the tube wall. This is a conservative assumption because it keeps the diffusive medium at a temperature higher than it otherwise might be and the diffusion coefficient is evaluated at this temperature. Time-dependent tritium diffusion through metal requires a solution to the diffusion equation (Fick's second law) given for 1D in Eq (5.64). Here, c is the concentration of tritium (mol/m^3), D is the diffusion coefficient for tritium in the medium (m^2/s), x is the direction perpendicular to the metal surface (m), and t is time (s).

$$\frac{\partial c}{\partial t} = D\frac{\partial^2 c}{\partial x^2} \tag{5.64}$$

At steady state, the solution to Eq (5.64) for diffusion through metal is Eq (2.22). The tritium concentration profile through the metal and the concentrations at each surface of the metal vary with

time and are subject to the time-varying boundary conditions defined in Section 5.7.1. Thus Eq (2.22) cannot be used here. In order to find a solution, an explicit finite difference method which is central difference in space and forward difference in time is used. The nodalization for any internal (non-surface) segment of a diffusive medium using this scheme is depicted in Figure 5.15. The flux of T_2 from segment R-1 into segment R is given by Eq (5.65). The flux of T_2 out of segment R and into segment R+1 is given by Eq (5.66). In these equations, R represents a particular node, i represents a specific time step, Δx is the spacing between nodes (m), D is the diffusion coefficient for tritium in the medium (m^2/s), and c is the tritium concentration (moles T_2/m^3). For a planar geometry where the surface area separating each segment is constant, the recurrence relationship is given by Eq (5.67), where Δt is the size of the time step (sec). Because the HX tubes are cylindrical, Eq (5.67) is modified to make Eq (5.68) in order to account for the changing volume and area of each equally-spaced segment in the cylindrical tube wall. In Eq (5.68), Vol_R is the volume of segment R (m^3), and SA is the surface area between adjacent segments. The size of the time step is determined using Eq (5.69). Here F_o is the Fourier number set equal to 0.5, and the other symbols are as described above.

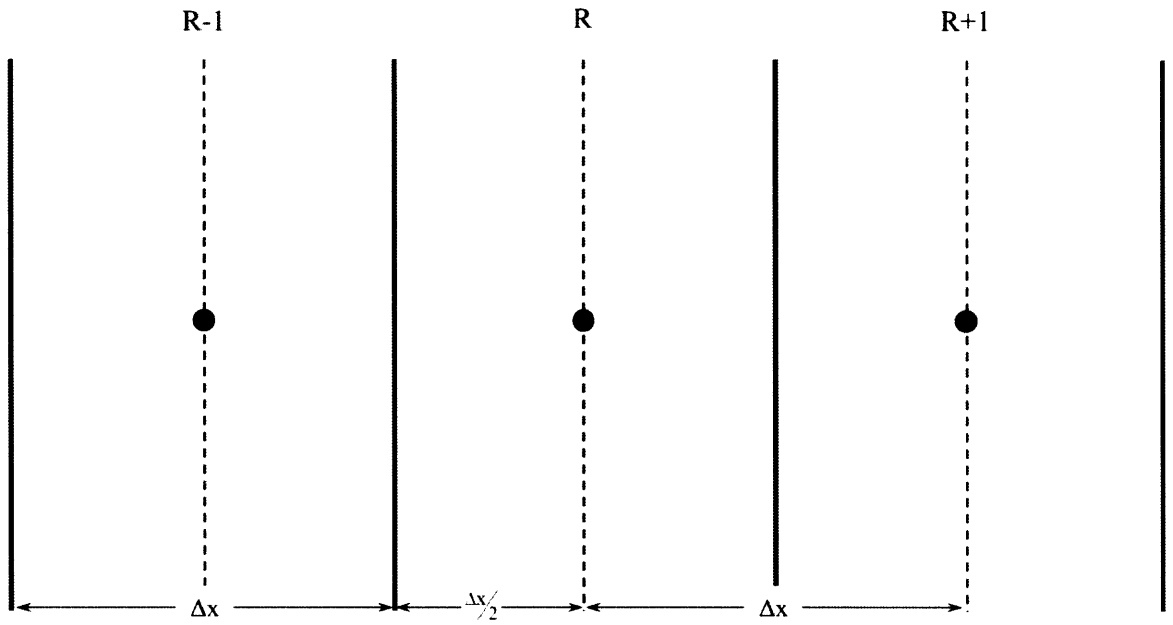

Figure 5.15: Nodalization for tritium diffusion through a static medium.

$$j^i_{R-1\to R} = \frac{D}{\Delta x}\left(c^i_{R-1} - c^i_R\right) \tag{5.65}$$

$$j^i_{R\to R+1} = \frac{D}{\Delta x}\left(c^i_R - c^i_{R+1}\right) \tag{5.66}$$

$$c^{i+1}_R = c^i_R + \frac{\Delta t}{\Delta x}\left(j^i_{R-1\to R} - j^i_{R\to R+1}\right) \tag{5.67}$$

$$c^{i+1}_R = c^i_R + \frac{\Delta t}{Vol_R}\left(j^i_{R-1\to R}\times SA_{R-1/R} - j^i_{R\to R+1}\times SA_{R/R+1}\right) \tag{5.68}$$

$$\Delta t = \frac{F_o \Delta x^2}{D} \tag{5.69}$$

5.8 Model of corrosion in TRIDENT

Section 3.1 introduced the major corrosion pathways in MSRs and FHRs. In MSRs, the higher-valence states of dissolved actinides (such as UF_4) are the principle oxidants. Thermodynamically, UF_4 is a weaker oxidant than TF, however, the concentration of UF_4 in the fuel-salt of an MSR is much higher than that of TF. In FHRs, TF will be the principle oxidant, but its concentration in the salt will be low compared to the concentration of UF_4 in the MSRE. In Fe-Cr-Ni alloys, Cr is attacked preferentially, and limited corrosion of Fe (with little or no corrosion of Ni) will occur. In fact, Fe and Ni fluorides are capable of attacking Cr via the corrosion reactions given in Eq (3.3) and Eq (3.4). Corrosion reactions of TF and UF_4 with Cr are given by Eq (3.2) and Eq (3.8), respectively. Equations to represent the equilibrium concentration of dissolved Cr in salts containing TF and UF_4 as the major oxidants were derived in Eq (3.20) and Eq (3.16) as a function of temperature and the $TF/T_2^{1/2}$ or UF_4/UF_3 ratios. The concept of redox potential, defined as the fluorine potential, was introduced based on previous work by Olander [140]. Following after Olander, Eq (3.32) was developed which defines a fluorine potential due to salt redox control by the UF_4/UF_3 ratio. Borrowing the form from Olander, Eq (3.40) was presented for the fluorine potential due to salt redox control by a mixture of TF and T_2 ($P_{TF}/(P_{T2})^{1/2}$). Using solubility laws, an equation was derived, Eq (3.47), which connects the fluorine potential from Eq (3.40) with the concentration of T_2 and TF in a salt mixture. The extent of corrosion is dependent on temperature, the fluorine potential in the salt, and the solid state diffusion of Cr within the metal. These mathematical relationships can be used to provide a simple model for the corrosion and mass transfer of Cr (or other probable corrosion products) within a reactor coolant loop.

5.8.1 Determination of corrosion versus deposition reactions

TRIDENT uses a simple logic for determining whether corrosion or deposition reactions occur in a particular part of the coolant loop. TRIDENT evaluates an equation such as Eq (3.20) (for corrosion of Cr by TF) or Eq (3.16) (for corrosion of Cr by UF_4 in an MSR) at each point along the primary coolant loop in order to determine the local equilibrium concentration of dissolved CrF_2. If the actual concentration of CrF_2 in the salt flowing into a given loop segment is less than the local equilibrium concentration of CrF_2, then corrosion is allowed. The corrosion model is discussed in detail in Section 5.8.3. On the other hand, if the actual concentration of CrF_2 in the salt entering a given segment is greater than the local equilibrium concentration of CrF_2 in that segment, then deposition/precipitation of Cr onto surfaces in that region is allowed.

In a system (such as the FHR) whose major corrosion reactions are determined by the TF/T_2 couple, the value of P_{TF}^2/P_{T2} is required for use in Eq (3.20). This value can be found using Eq (3.47) if the total system pressure is known, the total concentration of all tritium species (c_{total}) is known, and c_{T2} or c_{TF} is known. Alternatively, P_{TF}^2/P_{T2} can be found using Eq (3.47) if the fluorine potential (ΔG_{F2}) in the coolant is known or has been specified. With P_{TF}^2/P_{T2} and the temperature, Eq (3.20) is used to calculate the equilibrium CrF_2 concentration in the salt facing an alloy containing Cr. In an MSR-type system whose redox potential is determined by the UF_4/UF_3 couple for example, Eq (3.16) can be used with Eq (3.32).

5.8.2 Modeling deposition reactions

If the actual concentration of CrF_2 in the salt entering a given segment is greater than the local equilibrium concentration of CrF_2 in that segment, then deposition of Cr onto surfaces in that region is allowed. The mass transport equations were discussed in Section 5.6. The general equation for the flux of Cr from the salt to a surface for deposition is given by Eq (5.70). Here the deposition flux is given by $j_{deposition}$ in units of mol Cr/m^2-s. The mass transfer coefficient for dissolved Cr to a given surface is given by k_{Cr}. The actual concentration of Cr in the salt is given by $c_{Cr,actual}$ and the local equilibrium concentration of dissolved Cr is given by $c_{Cr,eq}$ (in units of $mole/m^3$). Eq (3.20) is used to calculate the equilibrium concentration of Cr dissolved in the salt according to the local temperature and redox conditions. Eq (5.70) was written so that deposition would occur until the concentration of Cr in the salt is equal to the local equilibrium concentration. The total amount of Cr deposited in a given time-step of size Δt (sec) in a region of the coolant loop having a surface area SA (m^2) is given by Eq (5.71). Since chemical reaction rate data for the deposition of Cr are not available, this treatment assumes that the rate of deposition is equal to the mass flux of Cr calculated in Eq (5.70). Benchmarking performed in Section 5.9.2 suggests that the chemical reaction rate may be the limiting step and not mass transport.

$$j_{deposition} = k_{Cr}\left(c_{Cr,actual} - c_{Cr,eq}\right) \tag{5.70}$$

$$\text{Moles Cr Deposited} = j_{deposition} \times \Delta t \times SA \tag{5.71}$$

5.8.3 Modeling of corrosion reactions

Two phases of corrosion are modeled. First, if Cr corrosion is allowed, initial corrosion rates are dictated by the mass transfer rate of a chemical oxidant to the metal surface [35]. Any pre-existing Ni fluoride and Fe fluoride impurities can also be consumed in this period, and this consumption generally goes to completion [35,124]. Since the contribution of NiF_2 and FeF_2 impurities to Cr corrosion is limited to early exposure times, these reactions are currently neglected in the model developed here. Next, once the surface Cr has been corroded, the second phase of corrosion begins

and the rate of Cr corrosion is determined by the Cr grain-boundary diffusion rate (see Section 3.1.1 for a detailed discussion). The corrosion model in TRIDENT accounts for these two phases of corrosion.

During the initial phase of corrosion, Cr is removed from the metal surface. In this phase, the rate of Cr corrosion is limited by the mass transfer rate of a chemical oxidant to the metal surface. In an MSR, the major oxidant is UF_4, but in an FHR, the major oxidant is TF. The mass transfer of the oxidant to the metal surface is calculated according to Eq (5.47). It is assumed that the oxidant reacts instantly at the surface such that the concentration of the oxidant at the metal surface can be set to zero in Eq (5.47). Cr is removed from the surface of the metal at a rate that matches the mass transfer flux of oxidant to the surface. For example, corrosion of Cr by TF goes according to Eq (3.17) where two moles of TF corrode one mole of Cr and produce one mole of T_2. In the initial corrosion phase, the flux of Cr into the coolant is equal to ½ of the flux of TF to the surface metal. This phase of corrosion is allowed until the surface has been depleted of Cr. At this point, the grain boundary corrosion mechanism takes over.

The metal surfaces facing the coolant are divided into radial and axial segments for the corrosion calculations. This is illustrated in Figure 5.16. For the purposes of this model, the metal surface over which initial corrosion occurs is defined as the thickness of metal from the metal/coolant interface down to a depth in the metal specified by the lattice parameter (δ) of that metal. Once all of the Cr has been corroded from this surface of thickness δ, the grain boundary corrosion mechanism is employed.

Grain boundaries are not explicitly modeled; however, the surface area available for corrosion is altered to correspond to the grain boundary surface area facing the coolant. A hexagonal grain shape is assumed. At left in Figure 5.17, the interface between three hexagonal grains is depicted. At right in Figure 5.17 the grain triple-point is highlighted. The width of the grain boundary (the space between adjoining grains) is symbolized as w_{gb}. The grain size (also called the grain diameter) is given by the distance between the flats (d) of the hexagonal grains. Based on the type of metal used for the piping, the grain boundary diameter d can be specified. The grain boundary diameter is used to calculate the length of the side of the grain s according to Eq (5.72). The radius (r) of the circle surrounding the triple-point is equal to the length of a side (s) of the hexagonal grain. The area of the circle (A_{circle}) is calculated by the familiar equation given in Eq (5.73). The grain boundary surface area (A_{gb}) within the circle is given by Eq (5.74). The ratio of the grain boundary surface area (A_{gb}) to the bulk metal surface (represented by A_{circle}) area is given by Eq (5.75).

The first phase of corrosion (limited by the rate of oxidant mass transport) leaves a metal surface that has a metallic Cr concentration of 0. This allows the use of a well-known analytical solution to the 1D time-dependent diffusion problem. For selective Cr corrosion without surface recession, the Cr concentration in the metal as a function of the depth in the metal (x) and the exposure time (t) is given by Eq (5.76) [180]. This equation assumes that the surface concentration is constant at 0, that the metal can be treated as having infinite thickness compared to the depth of corrosion losses, and that the Cr concentration deep within the metal ($c_{Cr,m}$) remains constant. The diffusion coefficient of

Cr in the metal is given by D_{Cr} in units of m^2/s and the Cr concentrations are given in units of mole Cr/m^3 metal. Once the first phase of corrosion (surface depletion of Cr) has ended according to the discussion above and the illustration in Figure 5.16, Eq (5.76) is used to calculate the Cr concentration profile in the metal as the time of the simulation progresses. In order to determine the flux of Cr from within the metal to the metal surface at a given time t, the Cr concentration gradient must be known. For this purpose, Eq (5.77) is used in order to calculate the depth in the metal ($x_{99\%}$) at which the Cr concentration is 99% of the bulk metal Cr concentration. Knowing the concentration at 99% of the bulk concentration ($c_{Cr,99\%} = 0.99c_{Cr,m}$) and $x_{99\%}$, the flux of Cr from the metal bulk to the metal surface ($j_{Cr,m}$) can be calculated according to Eq (5.78) where the concentration of Cr on the metal side of the metal-salt interface is equal to zero ($c_{Cr,surface} = 0$).

The scientific literature (see Section 3.1.1) suggests that the rate of Cr corrosion in metals exposed to fluoride salts is limited by solid state diffusion of Cr within the metal. More specifically, the corrosion rate is dominated by the rate of Cr grain boundary diffusion within the metal. In order to determine the flux of Cr to the metal-salt interface due to grain boundary diffusion, D_{Cr} in Eqs (5.76) through (5.78) is set to the Cr grain boundary diffusion coefficient. In order to determine the flux of Cr to the metal-salt interface due to bulk Cr diffusion, the bulk Cr diffusion coefficient in the base metal is used in Eqs (5.76) through (5.78).

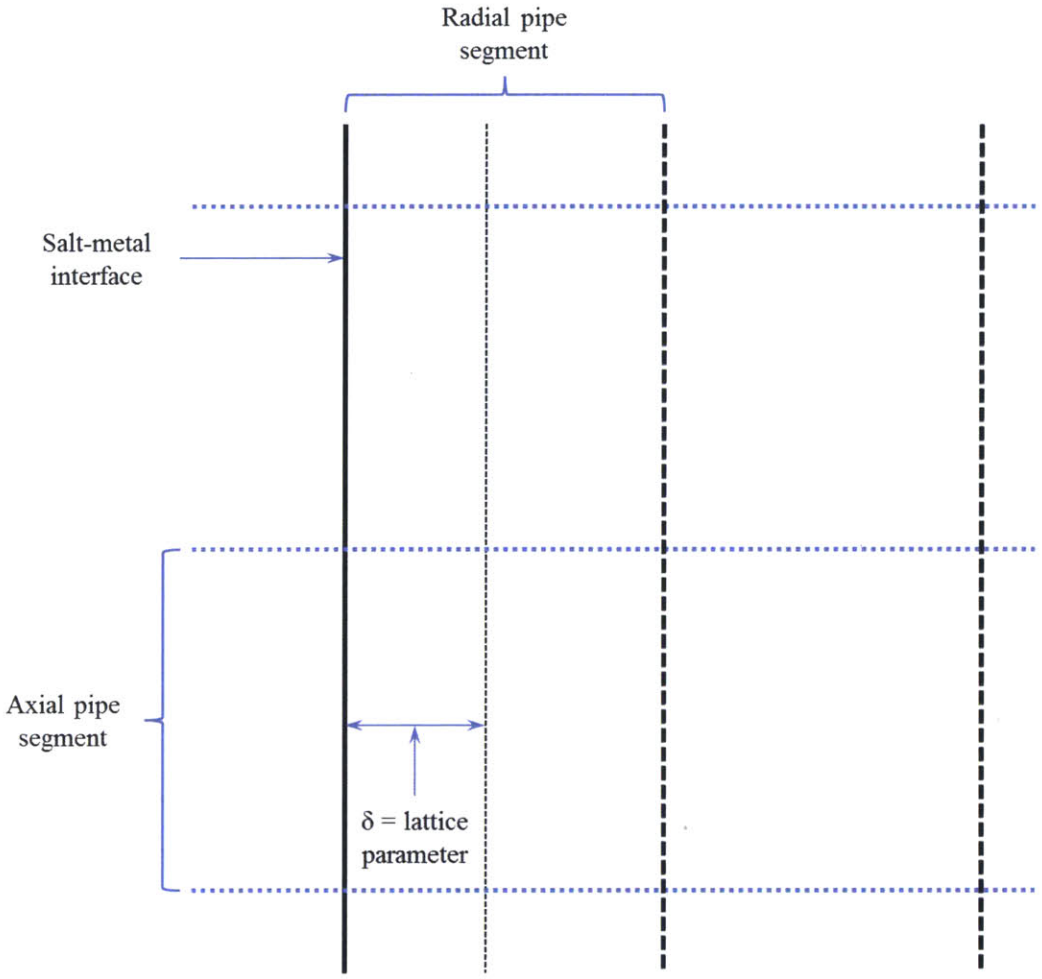

Figure 5.16: Radial and axial control volumes in metal surfaces facing the coolant used for corrosion calculations. (Not to scale).

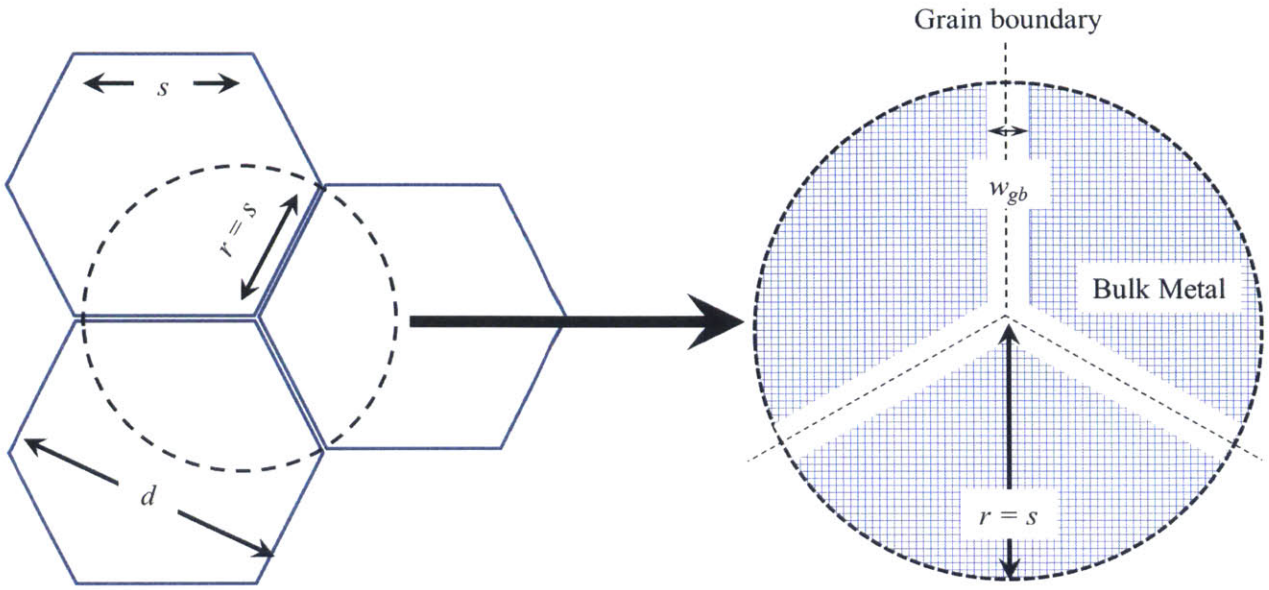

Figure 5.17: Grain boundary representation used to specify grain boundary surface area per unit surface area of bulk metal for use in TRIDENT corrosion model.

$$r = s = d + \frac{\sqrt{3} \times w_{gb}}{4} \tag{5.72}$$

$$A_{circle} = \pi r^2 \tag{5.73}$$

$$A_{gb} = 3dw_{gb} + \frac{\sqrt{3}}{4} w_{gb}^{\ 2} \tag{5.74}$$

$$\text{Area ratio}_{gb/\text{bulk}} = A_{gb} \Big/ A_{circle} \tag{5.75}$$

$$c_{Cr}(x,t) = c_{Cr,\text{m}} erf\left(\frac{x}{2\sqrt{D_{Cr}t}}\right) \tag{5.76}$$

$$x_{99\%} = 2\sqrt{D_{Cr}t}\, erf^{-1}(0.99) \tag{5.77}$$

$$j_{Cr,m} = \frac{D_{Cr}}{x_{99\%}}\left(c_{Cr,99\%} - c_{Cr,surface}\right) \tag{5.78}$$

The contributions from both bulk diffusion and grain boundary diffusion are calculated, although, as was mentioned above, grain boundary diffusion is the dominant rate-determining step of Cr loss from the metal to the salt. The moles of Cr lost due to corrosion limited by the bulk diffusion mechanism at a location in the loop having a surface area SA (m^2) during a time step of duration ΔT (sec) is given by Eq (5.79). To calculate $j_{Cr,m}$ for use in Eq (5.79), $D_{Cr,bulk}$ is used in Eqs (5.76) through (5.78) above. In order to determine the amount of Cr lost due to corrosion limited by the grain boundary diffusion mechanism, the effective surface area of the grain boundaries at the

coolant-metal interface must be accounted for. This is done by multiplying the geometric surface area presented by the metal (SA) with the ratio of the grain boundary surface area to the bulk metal surface area depicted in Figure 5.17 and given by Eq (5.75). Thus, the amount of Cr corroded from the grain boundaries in a segment of the coolant loop having a bulk surface area SA during a time step of duration Δt is given by Eq (5.80). To calculate $j_{Cr,m}$ for use in Eq (5.80), $D_{Cr,gb}$ is used in Eqs (5.76) through (5.78) above. At early times, the flux of Cr to the salt-metal interface via the grain boundary mechanism may be calculated to exceed the rate of TF mass transfer to the metal surface. In this instance then, the rate of Cr diffusion/corrosion is set equal to ½ the rate of TF mass transfer to the surface such that Eq (3.17) is satisfied.

$$\text{Cr Corroded via bulk diffusion mechanism} = j_{Cr,m} \times SA \times \Delta t \tag{5.79}$$

$$\text{Cr corroded via grain boundary diffusion} = j_{Cr,m} \times SA \times \text{Area Ratio}_{gb/bulk} \times \Delta t \tag{5.80}$$

5.9 TRIDENT Benchmarking

5.9.1 Tritium diffusion benchmarks

While data from a forced-convection polythermal loop of molten salt containing tritium do not exist for comparison, TRIDENT can be compared to data from static salt diffusion tests carried out within special test capsules. Two such tests will be used for benchmarking here. One test involves tritium diffusion through Ni and flibe, and the other test involves tritium diffusion through Ni and flinak. Fukada and Morisaki measured the permeability of hydrogen (^{1}H) through nickel and flinak using the apparatus in Figure 5.18 [99]. In the volume below the Ni membrane, a constant pressure and flow-rate of a mixture of H_2 and Ar gas was applied to the bottom surface of the Ni. The thickness of the Ni membrane was 2.0 mm. Hydrogen permeated through this Ni membrane into the flinak in contact with the upper surface of the Ni membrane. The standard thickness of flinak used in the measurements was 20.0 mm, but salt thicknesses up to 40.0 mm were also used. Because the TRIDENT model keeps a mass balance of tritium in every volume (including within the metal membrane), the volume of the Ni membrane must be known. Besides the thickness of the Ni membrane, Fukada and Morisaki do not provide any other dimensional data for the membrane in reference [99]. Despite this ambiguity, the area of the Ni membrane is confidently set to 20 cm^2. This is done for several reasons. The apparatus used by Calderoni et. al. was provided by Fukada, is the same apparatus used by Fukada in ref [99], and the membrane measures 2.52 cm in radius (19.95 cm^2) from Figure 1 in Calderoni et. al. [100]. Furthermore, the apparatus used by Fukada et. al. in measurements of hydrogen permeation in Li-Pb appears to be identical to that in Figure 5.18, and the listed cross-sectional area for the membrane is 20 cm^2 [181]. The input values required for TRIDENT to simulate the time dependent permeation of hydrogen in this system are listed in Table

5.1. The tritium transport and diffusion model from TRIDENT was isolated into a self-contained model called "TRIDENT_capsule" for these benchmarks.

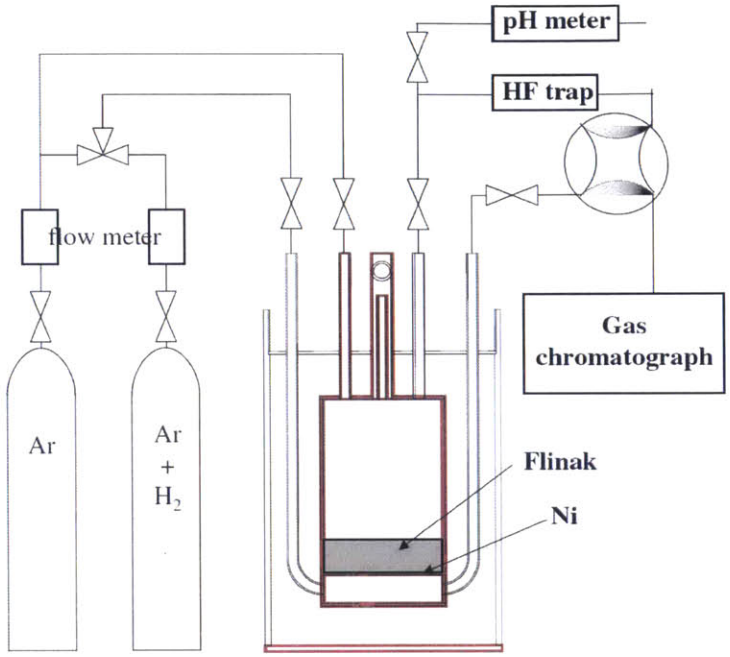

Figure 5.18: Apparatus used to measure permeability of hydrogen ($^1H_2$) through Ni and flinak. Image from ref [99].

Table 5.1: Input required to use TRIDENT to simulate experiments performed in reference [99] and generate Figure 5.19 through Figure 5.22.

	Input Units and Notes
Temperature	[K]
Ni membrane thickness	0.002 [m]
Ni membrane area	0.002 [m^2]
Flinak thickness	[m]
H_2 charge (input) pressure	[Pa]
H_2 upstream pressure above the salt	Set to 0 for all calculations. [Pa]
Henry's law constant for H_2 in flinak	See Eq (2.14). [mol/m^3-Pa]
Diffusivity of H_2 in flinak	See Eq (5.29). [m^2/s]
Diffusivity of hydrogen in Ni	See Eq (2.18) and data from Table 2.6. [m^2/s]
Sievert's law constant for H_2 in Ni	See Eq (2.19) and data from Table 2.6. [mol/m^3-$Pa^{0.5}$]

The time-dependent behavior was simulated in TRIDENT at 600, 650, and 700 °C for a flinak thickness of 20 mm and a fixed H_2 charge pressure of 1.01×10^5 Pa, the same conditions used by Fukada and Morisaki [99].[8] Fukada and Morisaki reported the time dependence of the downstream

[8] The label of L_{flinak}= 40 mm in Figure 2 of reference [99] is wrong. The correct label is L_{flinak} = 20 mm. This is verified by using equation (A.2) from reference [99] to reproduce this figure from this reference. A flinak thickness of 20 mm was used in TRIDENT for these time-dependent calculations.

hydrogen concentration in the sweep gas used in the volume above the flinak. TRIDENT does not calculate this value. So in order to compare this behavior, the time dependence of the tritium permeation flux calculated in TRIDENT was normalized against its steady state value. Likewise, the sweep gas hydrogen concentration from Fukada and Morisaki was normalized against its steady state value. These normalized time-dependent behaviors were then compared in Figure 5.19 through Figure 5.21 where good agreement is evident.

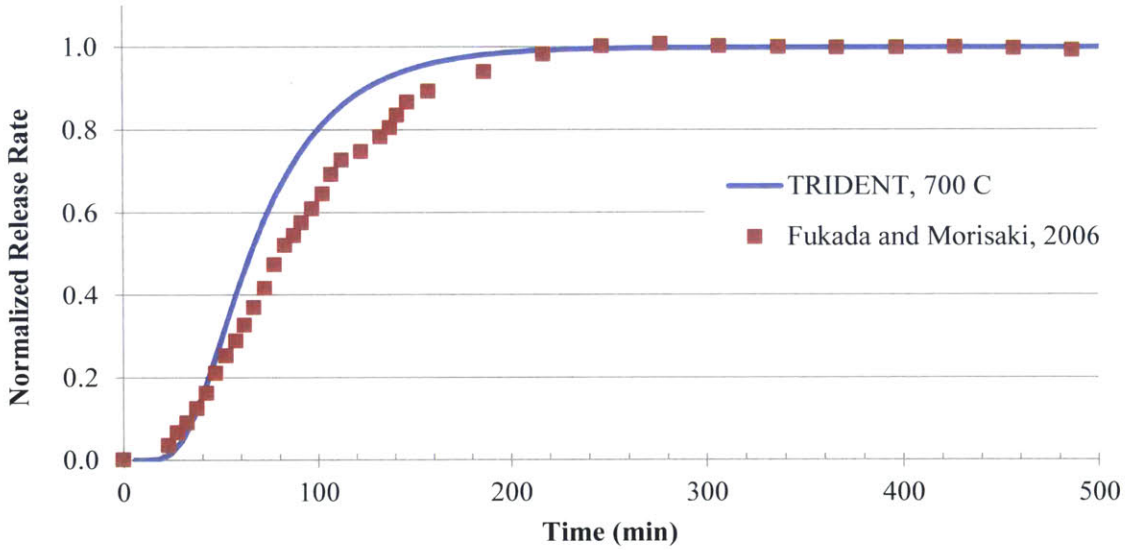

Figure 5.19: Normalized hydrogen permeation metrics for hydrogen permeation through the apparatus illustrated Figure 5.18. Temperature is 700 °C. Flinak thickness is 20 mm. H_2 charge pressure is 101 kPa. Solid line calculated with TRIDENT. Points are data from reference [99].

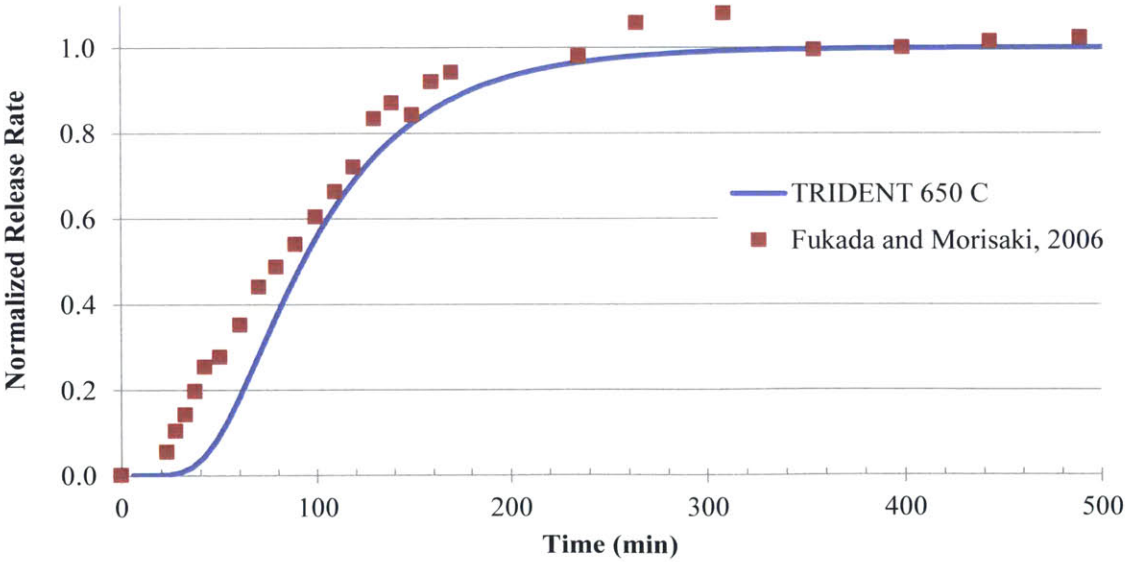

Figure 5.20: Normalized hydrogen permeation metrics for hydrogen permeation through the apparatus illustrated Figure 5.18. Temperature is 650 °C. Flinak thickness is 20 mm. H_2 charge pressure is 101 kPa. Solid line calculated with TRIDENT. Points are data from reference [99].

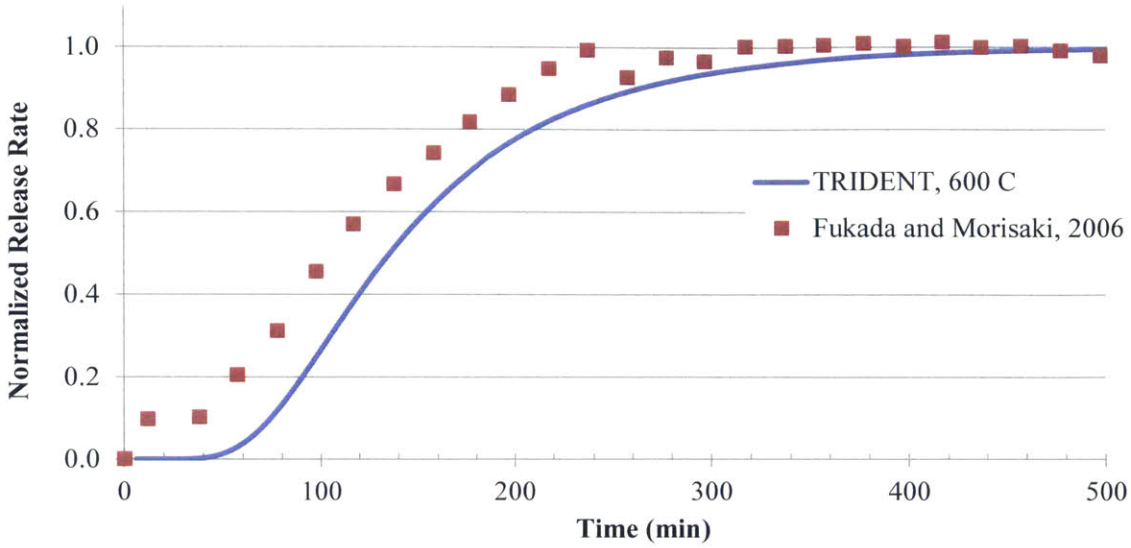

Figure 5.21: Normalized hydrogen permeation metrics for hydrogen permeation through the apparatus illustrated Figure 5.18. Temperature is 600 °C. Flinak thickness is 20 mm. H_2 charge pressure is 101 kPa. Solid line calculated with TRIDENT. Points are data from reference [99].

The figures above show that TRIDENT's modeling of transient behavior is in good agreement with experiment. The following figures show the consistency with which TRIDENT can match the steady-state hydrogen permeation fluxes determined from experiment. Good agreement is observed, especially at the higher temperatures (above 500 °C) and lower hydrogen pressures which will characterize FHR operation. Discrepancies between TRIDENT and the experimental values could exist due to experimental error and the choice of the diffusion coefficient and Sieverts law constant used in TRIDENT for the Ni membrane. Figure 5.22 shows the steady-state hydrogen permeation flux at three different temperatures for a system with a hydrogen input pressure of 101 kPa and salt thicknesses of 20 mm or 40 mm. The open symbols were extracted from the data in Figure 4 of reference [99]. The closed symbols were calculated with TRIDENT. Next, Figure 5.23 shows the stead-state hydrogen permeation flux for a flinak thickness of 20 mm, over a range of temperatures and input hydrogen pressures. The open symbols were extracted from the data in Figure 3 of reference [99]. The closed symbols were calculated with TRIDENT.

Calderoni et. al. measured the tritium permeation flux using the same apparatus as that pictured in Figure 5.18. In their experiment, they used T_2 gas and a layer of flibe on top of the Ni membrane. The diffusivity of T_2 in flibe and the Henry's law constant for T_2 in flibe were also measured. Table 5.2 summarizes the input parameters required for TRIDENT to simulate the experiments from Calderoni et. al. Figure 5.24 shows TRIDENT calculations compared to the data reported by Calderoni et. al. in Figure 2 of reference [100]. TRIDENT compares reasonably well with this experiment, although some deviation occurs at a couple points when higher hydrogen input pressures are used. Calderoni et. al. note that their Henry's law constant measured for T_2 in flibe more closely

matches the Henry's law constant for TF in flibe measured by Field and Shaffer [57,100]. This suggests that the redox condition in the flibe used by Calderoni et. al. may have been more oxidizing. This may also contribute to the difference because for these calculations, TRIDENT was operated under the assumption that the salt was 100% pure and all tritium existed in the system as T_2.

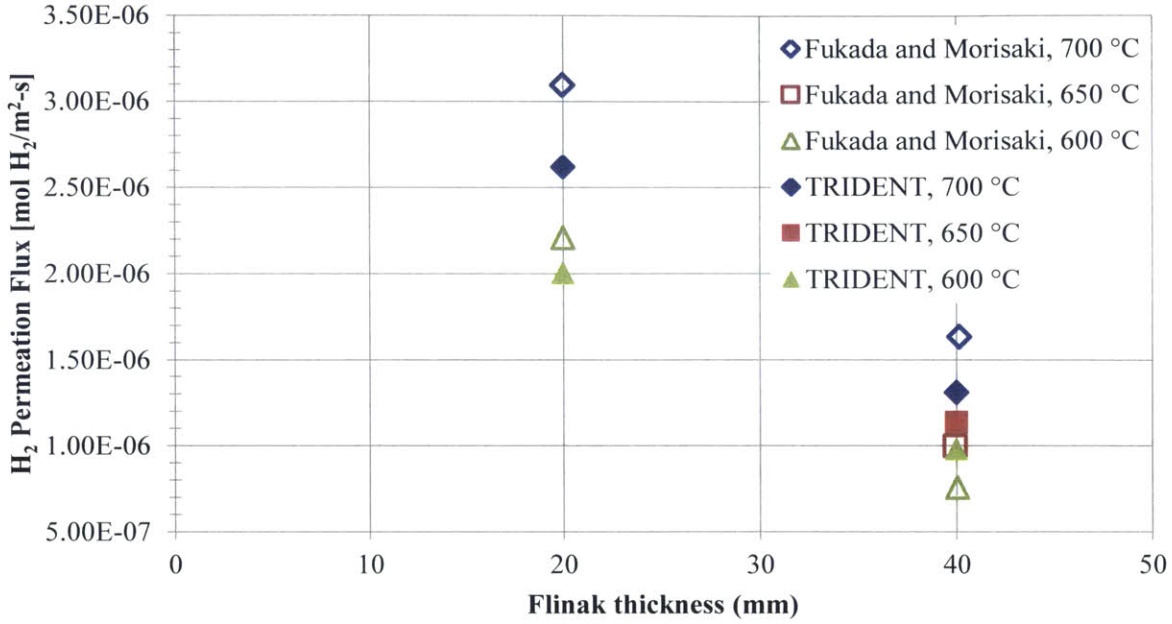

Figure 5.22: Solid symbols calculated with TRIDENT. Open symbols from reference [99]. Hydrogen input pressure was 101 kPa.

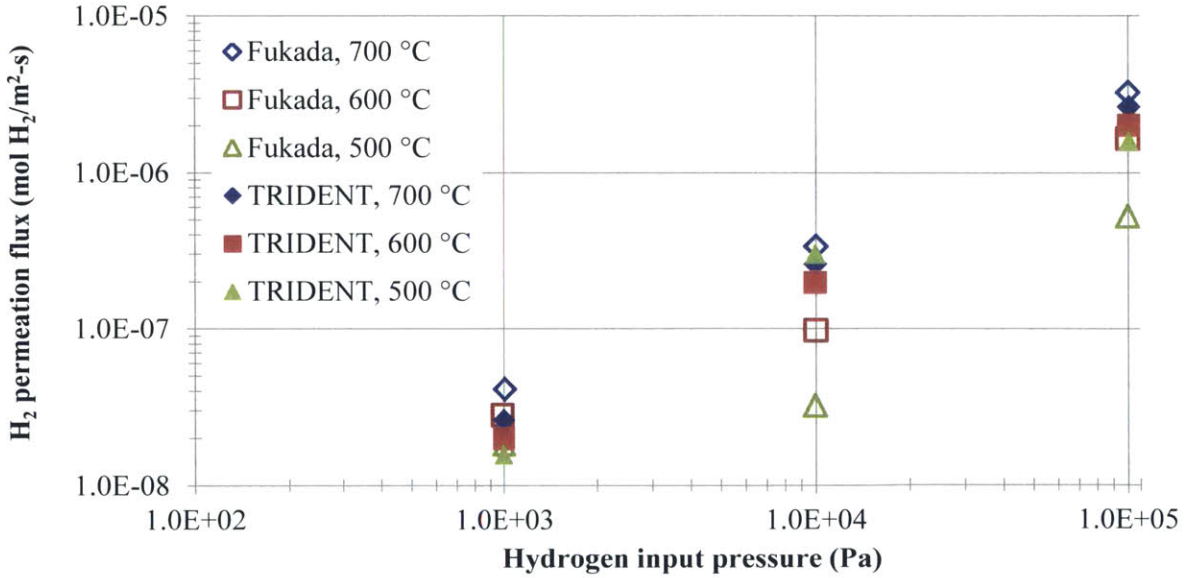

Figure 5.23: Solid symbols calculated with TRIDENT. Open symbols from reference [99]. Flinak thickness was 20 mm.

Table 5.2: Input required for TRIDENT to simulate experiments performed in reference [100] and generate Figure 5.24.

	Input Units and Notes
Temperature	[K]
Ni membrane thickness	0.002 [m]
Ni membrane area	0.002 [m^2]
Flibe thickness	[m]
T_2 charge (input) pressure	[Pa]
T_2 upstream pressure above the salt	Set to 0 for all calculations. [Pa]
Henry's law constant for T_2 in flibe from ref [100]	$k_{T_2,flibe} = 0.079\exp(-35000/(8.314\times T[\mathrm{K}]))$ [mol/m^3-Pa]
Diffusivity of T_2 in flibe from ref [100]	See Eq (2.15). [m^2/s]
Diffusivity of hydrogen in Ni	See Eq (2.18) and data from Table 2.6. [m^2/s]
Sievert's law constant for T_2 in Ni	See Eq (2.19) and data from Table 2.6. [mol/m^3-$Pa^{0.5}$]

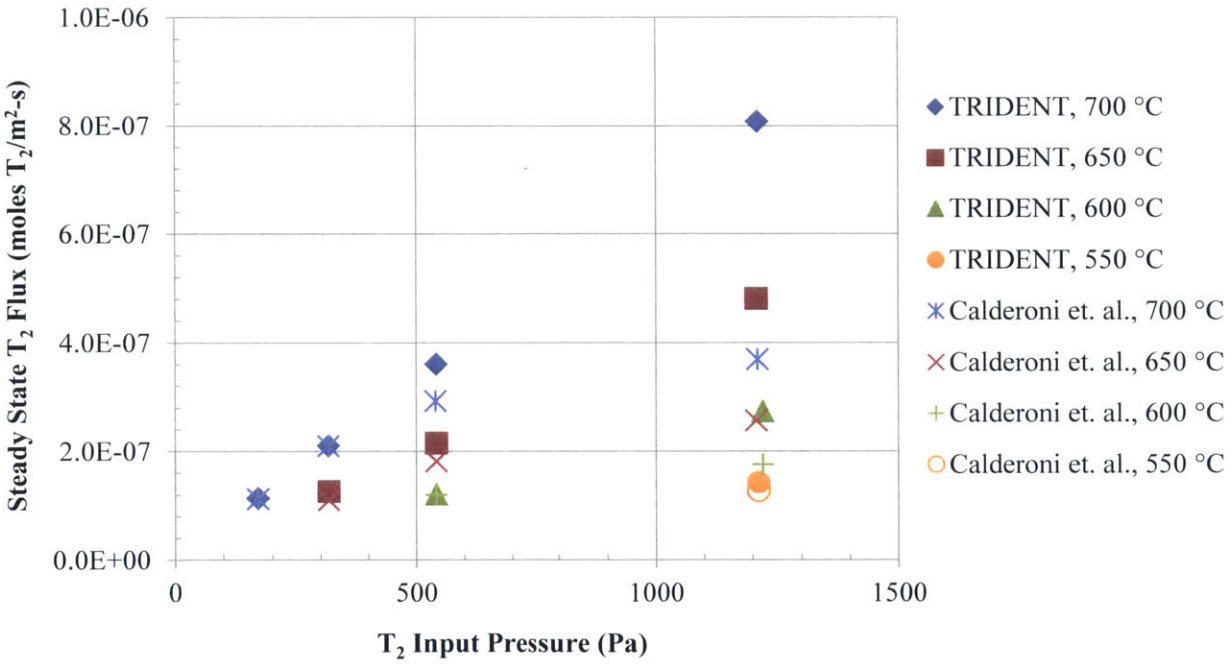

Figure 5.24: Tritium permeation flux through flibe. Solid symbols calculated with TRIDENT. Open and crossed symbols come from Figure 2 in reference [100]. Flibe thickness is 8.1 mm.

5.9.2 Corrosion benchmarks

A number of natural circulation and forced convection corrosion loops (sometimes referred to as "harps" due to their shape) were operated with different metals and fluoride salts during the 1960s and early 1970s at ORNL. The basic loop parameters for several tests are available in ORNL reports from that period [7,35,124,126]. Information such as the salt type, loop maximum and minimum salt temperature, loop metal, duration of test, and the weight change of samples during the test is available for several loops. Using input from the ORNL corrosion reports, a benchmark of the corrosion model in TRIDENT was performed. For this purpose, the corrosion and mass transfer models from TRIDENT were isolated in a version of TRIDENT called "TRIDEN_harp".

The first loop that was analyzed using the corrosion model in TRIDENT is the natural convection loop (NCL) 21A which operated at ORNL for 10,000 hours beginning in 1974 [124]. A schematic of NCL-21A is shown in Figure 5.25. The corrosion model in TRIDENT requires a number of input parameters, and no loop experiment at ORNL reports all of the required parameters. Thus some approximations and estimations were made in order to build a model for TRIDENT. Additionally, the loop treatment in TRIDENT is of lower fidelity than the actual experiments. For example, the surge tanks in Figure 5.25 were not modeled in TRIDENT. TRIDENT requires the length of piping in each section of the loop so that the length of the heated and un-heated sections is known. The lower and left vertical legs have heating elements, but the rest of the loop is un-heated and un-insulated. The length of each pipe segment was estimated based on Figure 5.25. The temperature profile around the loop is not known, but TRIDENT assumes a constant linear heating or cooling rate along each segment. The outer diameter of the Hastelloy-N tubing used to construct Loop 21A was 1.905 cm (0.75 inches) with a tube wall thickness of 0.18288 cm (0.072 inches) [126]. The average salt flow velocity in Loop 21A was 1 m/minute [124]. The chemical composition of the Hastelloy-N tubing is given in Table 5.3. The maximum and minimum loop temperatures were 704 °C and 566 °C, respectively [124]. A series of Hastelloy-N samples were placed throughout Loop 21A, and the weight change of the samples was measured periodically. Since the exact placement of these samples was not reported, this benchmark uses TRIDENT to calculate the weight change of the Hastelloy-N piping used to construct the loop. These weight changes were then compared to the weight changes for the samples reported in reference [124]. The salt used in Loop 21A was the molten salt breeder reactor fuel salt comprised of LiF-BeF_2-ThF_4-UF_4 (72-16-11.7-0.3 mole %) [124]. The temperature dependent density of this fuel salt was reported in Table 3.1 of reference [182]. This density was used in the simulation. Because relevant properties for fueled salts do not exist, all of the other coolant properties used in the simulation are those reported for clean flibe (0.67 LiF-0.33 BeF_2). In a fueled salt, the principle corrosion reaction of Cr is with UF_4 according to Eq (3.8), and the equilibrium concentration of dissolved Cr as a function of temperature and the UF_4:UF_3 ratio is given by Eq (3.16). The initial ratio of UF_4 to UF_3 in Loop 21A was 10,000:1. Compared to the typical MSRE ratio of 100:1, the salt in Loop 21A is more oxidizing. The initial concentration of Cr in the salt was not reported. A well-prepared salt generally has about 25 ppm Cr. Thus 25 ppm

Cr in the salt was specified as the initial concentration for the benchmark. The grain boundary diffusion coefficient for Cr in Hastelloy-N is not available, thus $D_{Cr,gb}$ from Eq (3.6) for 316 SS is used. The diffusion coefficient for bulk Cr diffusion in Hastelloy-N is from Eq (3.7). Finally, the grain size and grain boundary width of the Hastelloy-N piping are required for use in Eqs (5.72) through (5.80). Since these parameters were not reported, it is estimated that the grain boundary width is 10 nm. The grain size reported for Hastelloy-X (24 μm) was adopted here for Hastelloy-N [183]. A summary of the input parameters used for this benchmark is given in Table 5.4.

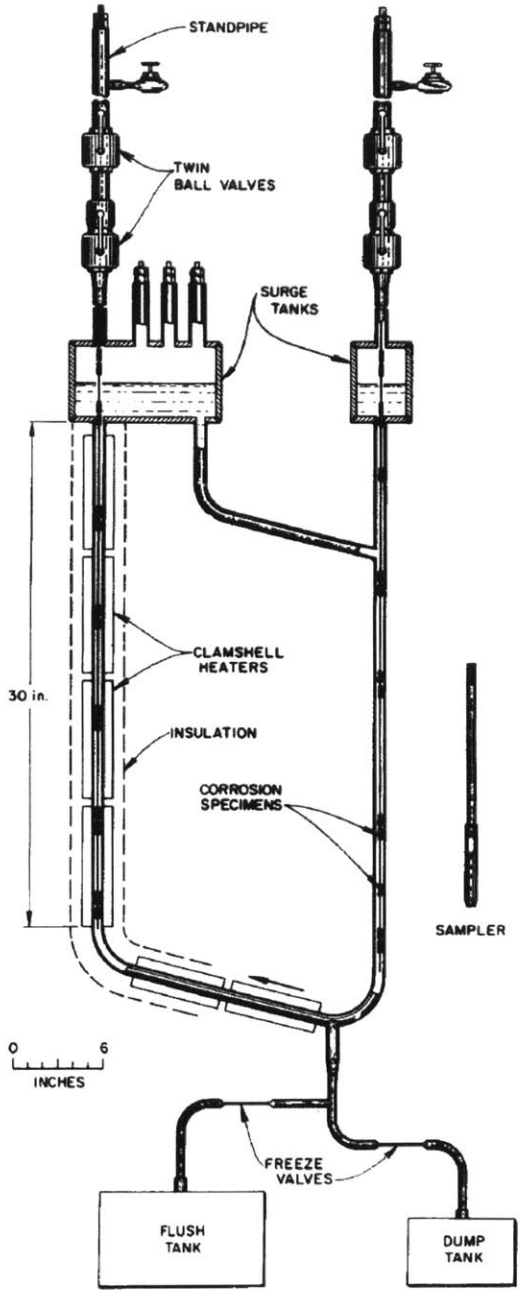

Figure 5.25: Schematic of Loop NCL-21A. Figure from [124].

Table 5.3: Composition of Hastelloy-N tubing used in Loop 21A. From [126].

Element	Weight Percent
Mo	16.5
Cr	6.9
Fe	4.5
Si	0.69
Mn	0.54
Ti	0.02
Ni	70.85

Table 5.4: Input parameters used for TRIDENT benchmark with ORNL Loop 21A.

Parameter	Value	Source
Left vertical leg length	0.762 m	Estimated from Figure 5.25
Upper horizontal leg length	0.476 m	Estimated from Figure 5.25
Right vertical leg length	0.729 m	Estimated from Figure 5.25
Bottom horizontal leg length	0.413 m	Estimated from Figure 5.25
Mesh points in each leg	10	-
Piping outer diameter	1.905 cm (0.75 inches)	Ref [126]
Piping wall thickness	0.18288 cm (0.072 inches)	Ref [126]
Salt flow velocity	1 m/min	Ref [124]
Chemical composition of Hastelloy-N piping	See Table 5.3	Ref [126]
Maximum loop temperature	704 °C	Ref [124]
Minimum loop temperature	566 °C	Ref [124]
Salt type and composition	LiF-BeF_2-ThF_4-UF_4 (72-16-11.7-0.3 mole %)	Ref [124]
Salt density (kg/m^3) (T in units of Kelvin)	$\rho_{fuel\,salt} = 3785.166 - 0.37323 \times (T \times (9/5) - 459.67)$	Table 3.1 of reference [182]
Initial UF_4:UF_3	10,000:1	Ref [124]
Initial concentration of Cr in salt	25 ppm	Estimated based on discussion in ref [123].
Hastelloy-N grain size	24 μm	Ref [183]
Hastelloy-N grain boundary width	10 nm	Estimated
Lattice Parameter	1.1 nm	[184]
Loop Temperature profile	Calculated in TRIDENT based on linear heating/cooling between maximum and minimum loop temperatures and pipe segment lengths	-

In Fig. 3 of reference [124], the weight changes of samples at 566 °C, 635 °C, and 704 °C in Loop 21A are plotted as a function of exposure time. The program DataThief was used to extract these data in order to compare with the results from a TRIDENT simulation of Loop 21A. These data along with the results from a TRIDENT simulation are plotted in Figure 5.26. After 10,000 hours, the weight change in the hottest section of the loop (704 °C) calculated by TRIDENT is about -2 mg/cm^2 compared to about -3.5 mg/cm^2 from experimental data of loop 21A. After 10,000 hours, ORNL/TM-5783 reported weight gain in samples at 653 °C and 566 °C of about 0.5 mg/cm^2 and 1.3 mg/cm^2. In comparison, the TRIDENT simulation calculated a weight change of about -1 mg/cm^2 at 653 °C. The weight gain calculated by TRIDENT at 573 °C has a similar value after 10,000 hours as that measured at 566 °C. After 10,000 hours, TRIDENT calculates a weight gain of about 60 mg/cm^2 at 566 °C (compared to 1.3 mg/cm^2 from experiment).

The difference between the weight change simulated with TRIDENT and the experimental data at 704 °C is reasonable given the estimations and approximations required to model Loop 21A in TRIDENT. The large difference between the simulated and experimental weight changes at 566 °C might be due to the overestimation of the deposition rate. TRIDENT calculates the equilibrium concentration of Cr in the salt at each point along the loop. If the salt entering that loop segment has a Cr concentration exceeding the equilibrium concentration, TRIDENT calculates deposition according to Eq (5.70) and Eq (5.71). The deposition rate, in this case, is assumed to be dependent on mass transfer of Cr to surfaces in that segment. In reality, the deposition rate may be dependent on the chemical rate of the inverse corrosion reaction (the inverse of Eq (3.8)). This rate is unknown. If the actual kinetics of the deposition reaction are slower than the rate of mass transfer, then compared to reality, the TRIDENT simulation will calculate higher rates of deposition. This would result in locally higher weight gain.

TRIDENT also simulates the Cr bulk concentration profile within the pipe beginning at the salt-pipe interface and extending into the bulk of the metal. Figure 5.27 shows the simulated bulk Cr concentration profile at the hot and cold sections of the loop after 10,000 hours of exposure. At 704 °C, Cr depletion extends to a depth of about 28 μm (1.1 mil). This corresponds to a loss rate of about 24 μm/yr (0.96 mil/yr) at this location. For such an oxidizing salt (UF_4:UF_3 = 10000:1), this is a high but not unreasonable loss rate when compared to other loop experiments [35,124,126].

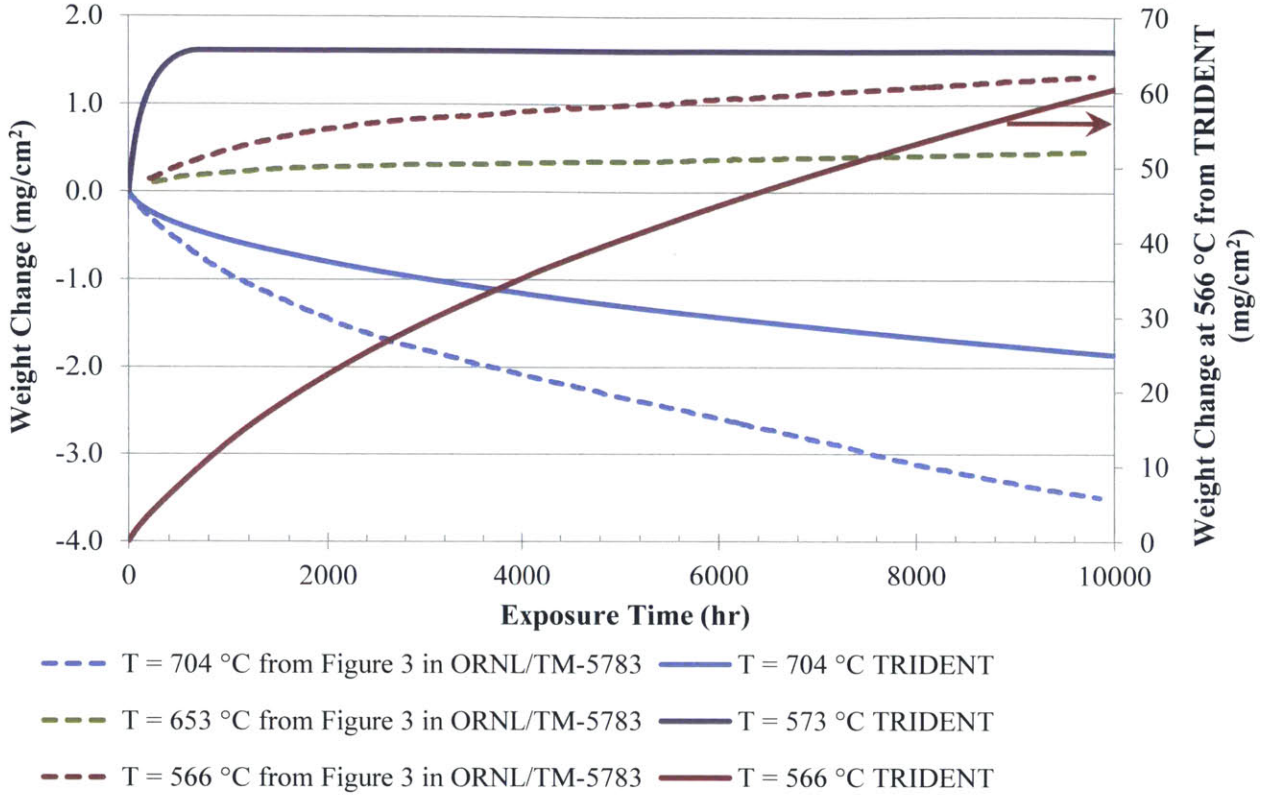

Figure 5.26: Weight change (mg/cm^2) at several temperatures throughout Loop 21A as a function of exposure time. Measurement data (from ORNL/TM-5783 [124]) are plotted in dashed lines. TRIDENT results are plotted as solid lines.

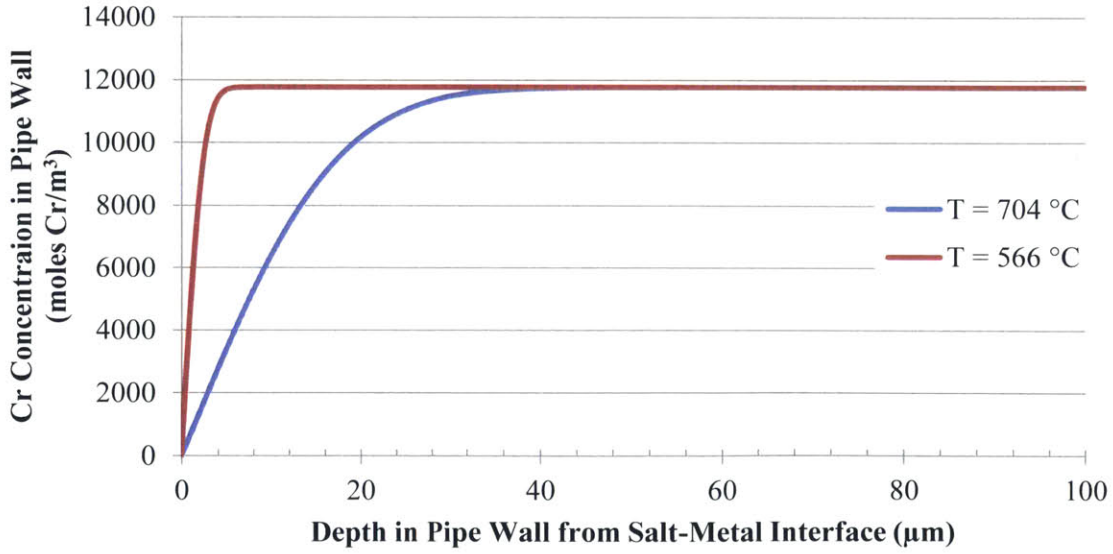

Figure 5.27: Chromium concentration profile within the Hastelloy-N tubing after 10,000 hours of exposure at the high (704 °C) and low (566 °C) temperatures of the loop. Simulated with TRIDENT.

One other comparison between TRIDENT and a corrosion loop from ORNL was performed. In this case the same types of approximations and estimations were required. Loop 1258 was a natural convection loop operated at ORNL for 82,500 hours [126]. The loop was constructed of Type 304L stainless steel and was filled with MSBR fuel salt. A series of Type 304L samples were placed in the hot leg of Loop 1258, and the weight change of the samples was measured periodically. Since the exact placement of these samples was not reported, this benchmark uses TRIDENT to calculate the weight change of the Type 304L SS piping used to construct the loop. These weight changes are then compared to the reported weight changes for the samples. The salt composition in Loop 1258 was LiF-BeF_4-ZrF_4-UF_4-ThF_4 (70-23-5-1-1 mole %) and the stainless steel composition is given in Table 5.5. The maximum salt temperature was 688 °C and the minimum salt temperature was 588 °C. The dimensions of Loop 1258 were not reported; thus the same loop dimensions used above for Loop 21A are used here. Additionally, the ratio of UF_4:UF_3 and the initial dissolved Cr concentration in the salt were not reported for Loop 1258. The grain boundary diffusion coefficient for Cr in Type 304 L was not available, thus the grain boundary diffusion coefficient for Cr in Type 316 stainless steel from Eq (3.6) is used here. The bulk Cr diffusion coefficient in Type 304 stainless steel from Daruvala and Bube [185] was converted into units of m^2/s and is given in Eq (5.81). Here, $D_{Cr,\ bulk\ 304}$ has units of m^2/s, R is the universal gas constant (0.008314 kJ/mol-K), and T is temperature (Kelvin). The input parameters used for this comparison are summarized in Table 5.6.

Table 5.5: Elemental composition of Type 304 L stainless steel used in Loop 1258. From [126].

Element	Weight %
Ni	11.07
Cr	18.31
C	0.028
Fe	Balance

$$D_{Cr,bulk\,304} = 3.06\times10^{-4}\exp\left(\frac{-282.58}{RT}\right) \tag{5.81}$$

Table 5.6: Input parameters used for TRIDENT comparison with ORNL Loop 1258.

Parameter	Value	Source
Left vertical leg length	0.762 m	Assumed to be same as Loop 21A
Upper horizontal leg length	0.476 m	Assumed to be same as Loop 21A
Right vertical leg length	0.729 m	Assumed to be same as Loop 21A
Bottom horizontal leg length	0.413 m	Assumed to be same as Loop 21A
Mesh points in each leg	15	-
Piping outer diameter	1.905 cm (0.75 inches)	Assumed to be same as Loop 21A

Table 5.6 continued from previous page		
Piping wall thickness	0.18288 cm (0.072 inches)	Assumed to be same as Loop 21A
Salt flow velocity	1 m/min	Assumed to be same as Loop 21A
Chemical composition of 304L piping	See Table 5.5	Ref [126]
Maximum loop temperature	688 °C	Ref [126]
Minimum loop temperature	588 °C	Ref [126]
Salt type and composition	LiF-BeF_2-ZrF_4-UF_4-ThF_4 (70-23-5-1-1 mole %)	Ref [126]
Salt density (kg/m^3) (T in units of Kelvin)	$\rho_{fuel\,salt} = 3785.166 - 0.37323 \times (T \times (9/5) - 459.67)$	Table 3.1 of reference [182]
Initial UF_4:UF_3	100:1	Estimated based on MSRE ratio
Initial concentration of Cr in salt	25 ppm	Estimated based on discussion in ref [123].
304L grain size	24 μm or 10 μm	Estimated from Ref [183]
304L grain boundary width	10 nm	Estimated
Lattice Parameter	0.369 nm	Estimated from Ref [186]
Loop Temperature profile	Calculated in TRIDENT based on linear heating/cooling between maximum and minimum loop temperatures and pipe segment lengths	-

Figure 5.28 shows the weight loss at four temperatures calculated with TRIDENT overlaid on Figure 28 from reference [126]. In this calculation a grain size in 304L of 24 μm was specified. Depending on the heat treatment, the grain size could be smaller or larger. The calculation was repeated after specifying a grain size of 10 μm, and the results are given in Figure 5.29. In this case the corrosion rate is increased, but after 24,000 hours, the calculated weight losses are about a factor of 4 less than what was measured in the experiment.

In this comparison, the TRIDENT simulation does not closely reflect the reported results for Loop 1258. Several differences between the experiment and the TRIDENT simulation are notable. The grain size of the Type 304L SS used in Loop 1258 was not known. The initial redox state of the salt in Loop 1258 was not known. The dimensions and flow velocity of Loop 1258 were not known. For the TRIDENT simulation, the dimensions and flow velocities for Loop 1258 were assumed to be the same as those for Loop 21A because both loops used the same salt with similar loop temperature gradients. The initial redox state in the salt in Loop 1258 was not known, but for the TRIDENT simulation, it was assumed that the redox state was determined by a UF_4:UF_3 ratio of 100:1 because this was the baseline ratio used for redox control in the MSRE. The wavy features in the experimental data are due to the fact that certain samples were replaced periodically and the weight loss from the new samples at a given location was added to the weight loss accrued from previous

samples at the same location in the loop. Replacing the samples would maintain a higher corrosion rates and explains some of the difference between the experiment and the simulation.

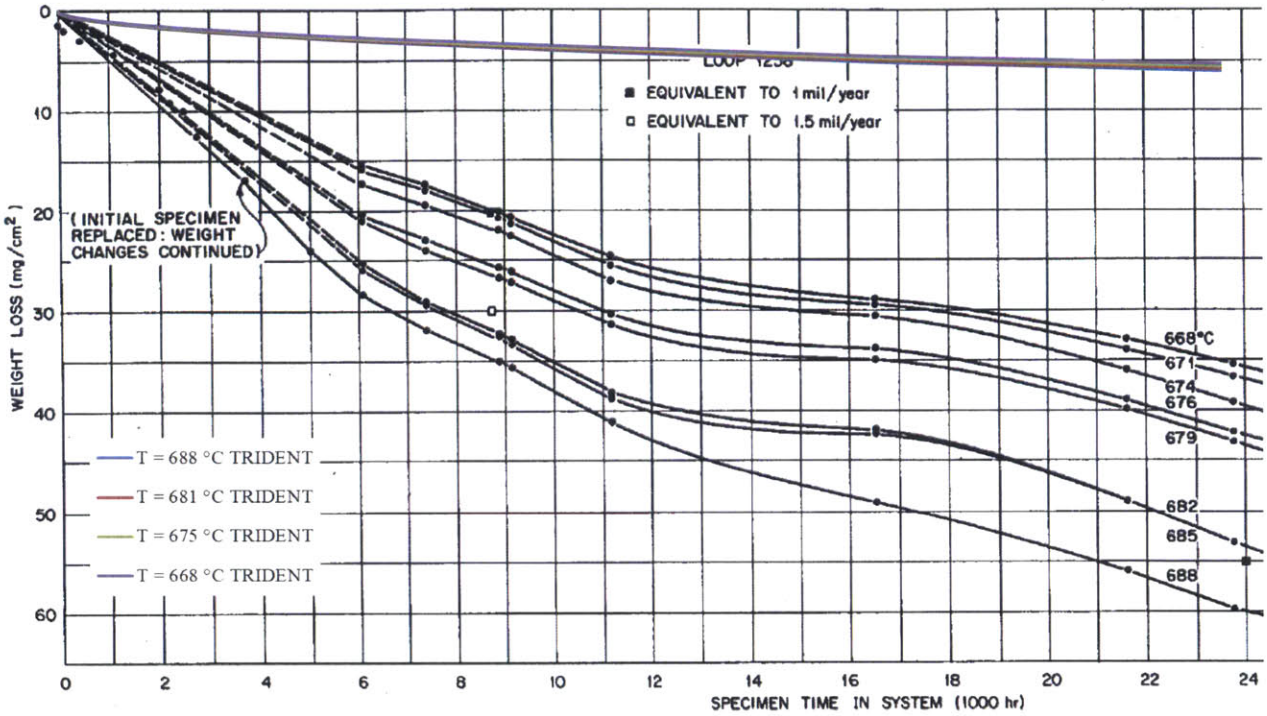

Figure 5.28: Weight loss (mg/cm^2) calculated by TRIDENT overlaid for comparison on measurements from Loop 1258 in reference [126]. 304L grain size set to 23 μm.

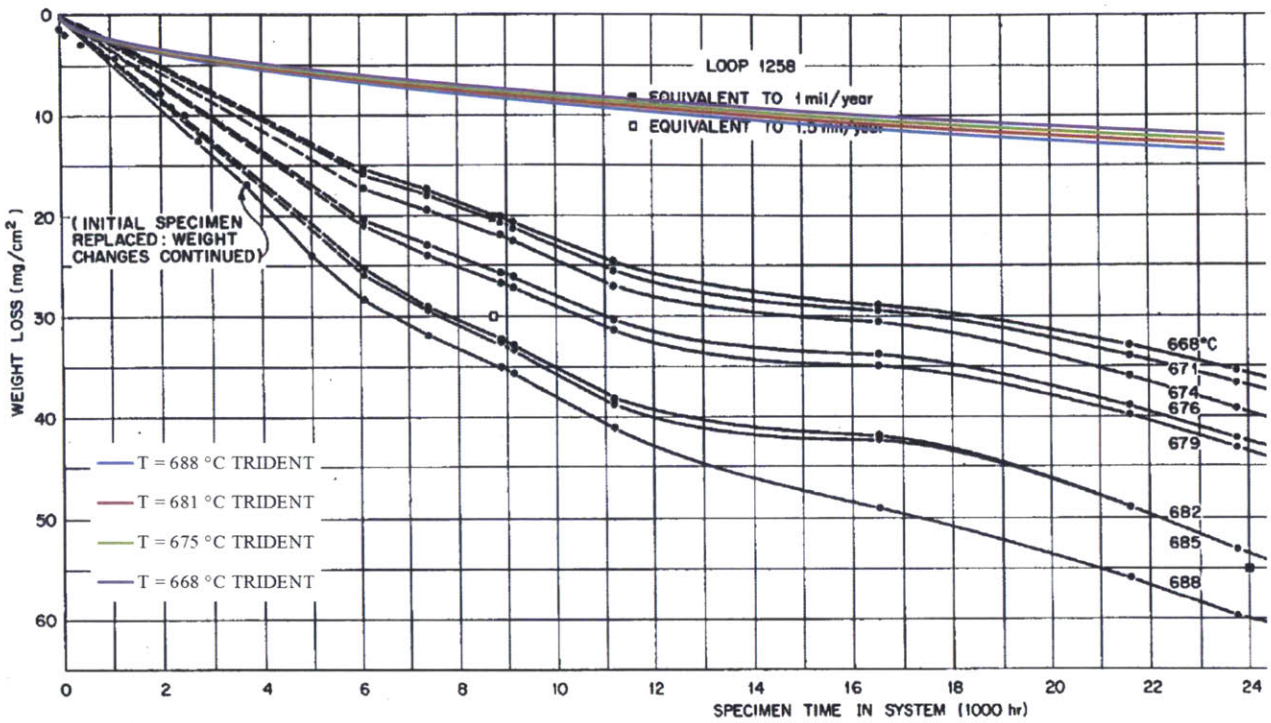

Figure 5.29: Weight loss (mg/cm^2) calculated by TRIDENT overlaid for comparison on measurements from Loop 1258 in reference [126]. 304L grain size set to 10 μm.

The experimental results between Loop 1258 and Loop 21A were compared. In loop 1258, the experimentally observed (and TRIDENT simulated) weight loss per cm^2 in Type 304L SS is much higher than the experimentally observed (and TRIDENT simulated) weight loss in Loop 21A with Hastelloy-N despite the use of a much more oxidizing salt in Loop 21A. This indicates the advantage of Hastelloy-N over Type 304 L SS with respect to corrosion. Additionally, experimental Type 304L SS samples exposed for 45,700 hours in Loop 1258 were laden with voids extending a minimum of 254 μm (10 mil) into the specimens. Average weight losses may seem reasonable, but localized losses (such as along grain boundaries) may be high. This void formation is not captured in the TRIDENT model. Grain boundaries are 3D networks which the current model treats in a 1D fashion where grain boundary diffusion is treated as a separate phenomenon which has no coupling to bulk diffusion. In reality, the grain boundaries can receive new Cr as Cr from the bulk of the metal diffuses into a grain boundary. This Cr can then diffuse down the grain boundary, which may have intersections with other grain boundaries. Thus improvements to the corrosion model must recognize that bulk diffusion and grain boundary diffusion of Cr can be related. Flow loop corrosion experiments may be required along with an investigation of the deposition kinetics (inverse of the corrosion reaction) in order to improve the corrosion model.

5.10 Chapter summary of TRIDENT model development and benchmarking

The model TRItium Diffusion EvolutioN and Transport (TRIDENT) was developed and benchmarked. The equations governing the tritium transport and diffusion phenomena were presented. TRIDENT considers one dimensional fluid transport and diffusion. The coolant is segmented into volume elements for applying the conservation equations, and the coolant loop is segmented into elements in order to apply a temperature profile and define specific locations in the loop where reactions such as corrosion, tritium absorption, or tritium diffusion may occur. Tritium diffusion through the heat exchanger walls is treated by a finite difference diffusion solution in the metal. The boundary conditions are specified by enforcing an equilibrium (determined by Henry's law in the salt and Sievert's law in the metal) at the salt-metal boundary and by conserving the mass flux to the metal surface with the mass flux into the metal surface. Both the tritium diffusion and corrosion models were benchmarked.

While data from a forced-convection polythermal loop of molten salt containing tritium do not exist for comparison, TRIDENT can be compared to data from static salt diffusion tests. Two such tests were used for benchmarking here. One test involves tritium diffusion through Ni and flibe, and the other test involves tritium diffusion through Ni and flinak. In each case, TRIDENT matched the transient and steady-state behavior of these tritium diffusion experiments.

The corrosion model in TRIDENT was compared against the natural convection flow-loop experiments at ORNL from the 1960s and early 1970s which used MSRE fuel salt containing UF_4. Despite the lack of data required by TRIDENT for modeling the loops, some reasonable results were obtained. The TRIDENT corrosion rates follow the experimentally observed dependence on the square root of the product of the Cr diffusion coefficient with time. Additionally the TRIDENT model shows mass transfer of corrosion products from the hot to the cold leg (as was observed in the experiments). Improvements to the corrosion model must recognize that bulk diffusion and grain boundary diffusion of Cr can be related due to the existence of 3D networks of grain boundaries in real materials. Flow loop corrosion experiments may be required along with an investigation of the deposition kinetics (inverse of the corrosion reaction) in order to improve the corrosion model.

6 Corrosion and Tritium transport simulations with TRIDENT

A recent FHR design comes from work at UC-Berkeley on the "Mk1 PB-FHR" [8]. TRIDENT can be used to simulate tritium transport and corrosion throughout this design. TRIDENT can also be used to simulate the effectiveness of various tritium mitigation measures such as permeation windows, gas strippers, and tritium capture on graphite. The goal here will be to emplace systems which mitigate tritium release rates such that they are comparable to the tritium release rates from heavy water reactors (HWRs).

6.1 TRIDENT reactor-specific input

First, TRIDENT requires various reactor parameters in order to simulate a PB-FHR. The parameters specific to the Mk1 PB-FHR are listed below in Table 6.1. Parameters denoted with a star (*) were estimated or calculated, but were not explicitly available in the Mk1 PB-FHR report. All other parameters were taken directly from the Mk1 PB-FHR report. The origins of parameters marked with a star (*) will be summarized in the paragraphs below.

The axial peak linear heat generation rate (q'_o) was calculated using Eq (5.12) from Section 5.4. The volume-averaged one-group flux was taken from a thesis completed on a larger, 900 MWt PB-FHR [62]. The core height was not explicitly given in the Mk1 PB-FHR report; however, it was estimated from a plot of the coolant temperature distribution, given as "Figure 2-17" in the Mk1 PB-FHR design report [8]. The Mk1 PB-FHR design report gives the outer diameter of the core vessel as 3.5 m. The vessel wall thickness was given as 6 cm. Thus the outer radius of the outer reflector was calculated as 1.69 m.

In the Mk1 PB-FHR, the flow of coolant exiting the core is split into two identical heat exchangers, called coiled tube air heaters (CTAH), which transfer heat from the salt coolant to the air in the power cycle. The Mk1 PB-FHR design specifies that a single CTAH has a surface area of 5041 m^2 and 13680 individual tubes. For simplicity, these two identical CTAHs are modeled as a single heat exchanger which is twice the size of an individual CTAH (2 x 5041 m^2) having twice the number of tubes (2 x 13680); however, the tube dimensions (diameter, length, etc.) are identical to those specified in the design report. The hot leg side of each CTAH consists of four manifold pipes which feed coolant into the CTAH tubes. For simplicity, these smaller manifold pipes are modeled as an equivalent single pipe by conserving the flow area within the pipe. The Mk1 PB-FHR design report specifies that each of the 4 hot leg manifold pipes in each of the two CTAHs has an outer diameter of 0.320 m and a wall thickness of 0.02 m. Thus, the total hot leg flow area is $8 \times \pi \times 0.14^2 = 0.4926 \text{m}^2$. A single hot leg pipe having this flow area has an inner diameter of 0.792 m. This is the diameter used in TRIDENT. The salt coolant exiting into the cold leg side of each of the two CTAHs does so into 4 cold leg manifold pipes in each CTAH. The specifications for these pipes are a wall thickness of 0.02 m and an outer diameter of 0.215 m. Thus, the total cold leg flow

area is $8 \times \pi \times 0.0875^2 = 0.4926 \text{m}^2$. An equivalent single cold leg pipe has an inner diameter of 0.495 m. This is the diameter used in TRIDENT for the cold leg pipe. The lengths of the hot and cold leg pipes are calculated in order to match the specified coolant volumes of the hot and cold legs in the Mk1 PB-FHR design. The Mk1 PB-FHR volume of the hot leg (11.13 m^3) plus the hot leg manifold pipes (3.52 m^3) 14.65 m^3. In order for a single hot leg pipe of inner diameter 0.792 m to contain this volume of salt, it must be 29.74 m long. Neglecting the drain tank, the cold leg coolant volume in the Mk1 PB-FHR is 5.44 m^3. The cold leg manifold pipes add an additional 1.38 m^3. Thus, the total cold leg salt volume is 6.82 m^2. In order for a single cold leg pipe of inner diameter 0.495 m to contain this volume of salt, it must be 35.44 m long.

One other simplification made in TRIDENT is that it can only model concentric cylindrical regions in the core. A schematic representation of the actual Mk1 PB-FHR core detail compared to the core detail modeled in TRIDENT is given in Figure 6.1. Since the narrowing of the core at the exit and entrance is not accounted for in TRIDENT, the TRIDENT core volume is a little larger than the actual Mk1 PB-FHR core volume. When filling the core will pebbles, TRIDENT calculates the volume of the fuel pebble region and the volume of the graphite pebble region. Then it fills each region so that the number of pebbles in each region corresponds with the core pebble packing fraction (`PF`). Then the relevant mass transport quantities are calculated for the core. Filling the core with pebbles in this fashion results in a larger number of pebbles than is specified by the Mk1 design. The only instance where this is a concern is when TRIDENT simulates mass transport and adsorption of tritium on the pebbles or mass transport and deposition of Cr corrosion products on the pebbles. In order to correct for this, the effective pebble surface area (for mass transport) and pebble mass (for tritium capture on graphite) is adjusted to correspond to the number of pebbles specified by the Mk1 design report.

Table 6.1: Baseline input parameters for TRIDENT simulation of Mk1 PB-FHR. *Indicates a parameter calculated or estimated. All others taken directly from the Mk1 PB-FHR report [8].

Parameter	Units (if applicable)	TRIDENT Variable Name	Value for Mk1 PB-FHR
Core inlet temperature	[K]	T_in	873.15
Core outlet temperature	[K]	T_out	973.15
Reactor power	[MWt]	Rx_power	236
Axial peak linear heat generation rate*	[MWt]	qo	79.72*
Number of separate coolant loops		Loops	1
Redox potential specified as the ratio $P_{TF}/(P_{T2}^{0.5})^*$		Ratio_TF_T2	$9.2\text{x}10^{-5}$
Li-7 enrichment in flibe	[wt %]	Li7_enrichment	99.995
Number of Fuel Pebbles in the Core		N_CoreFuelPebbles	$4.7\text{x}10^{5}$
Number of un-fueled graphite pebbles in the core		N_CoreGraphPebbles	$2.18\text{x}10^{5}$
Volume-averaged one-group flux* [62]	[n/cm^2-s]	flux	$3.41\text{x}10^{14}$*
TRISO fuel kernel diameter	[m]	Kernel_d	$400\text{x}10^{-6}$
TRISO fuel buffer thickness	[m]	Buffer_t	$100\text{x}10^{-6}$
TRISO fuel IPyC thickness	[m]	IPyC_t	$35\text{x}10^{-6}$
TRISO fuel SiC thickness	[m]	SiC_t	$35\text{x}10^{-6}$
TRISO fuel OPyC thickness	[m]	OPyC_t	$35\text{x}10^{-6}$
Number of TRISO particles per fuel pebble		TRISOperPebble	4730
Fuel pebble radius	[m]	Pebble_radius	0.015
Pebble packing fraction in the core		PF	0.60
Core height*	[m]	Core_height	4.65*
Radius of core central graphite reflector	[m]	CentralRef_radius	0.35
Outer reflector outer radius*	[m]	OuterRef_inradius	1.69*
Outer reflector inner radius	[m]	OuterRef_inradius	1.25
Inner radius of fuel pebble zone	[m]	Fuelzone_innerradius	0.35
Outer radius of fuel pebble zone	[m]	Fuelzone_outerradius	1.05
Hot leg pipe wall thickness	[m]	pipe_thick1	0.02
Hot leg pipe inner diameter*	[m]	pipe_d	0.792*
Hot leg pipe length*	[m]	pipe_l	29.74*
Cold leg pipe wall thickness	[m]	pipe_thick2	0.02
Cold leg pipe inner diameter*	[m]	pipe_d2	0.495*
Cold leg pipe length*	[m]	pipe_l2	35.44*
Number of tubes in primary heat exchanger*		Hx1tubes	$2.736\text{x}10^{4}$*
Heat exchanger tube outer diameter	[m]	Hx_tube_od	0.00635
Heat exchanger tube wall thickness	[m]	Thick	$8.89\text{x}10^{-4}$
Primary heat exchanger tube outer surface area*	[m^2]	A1	10082*

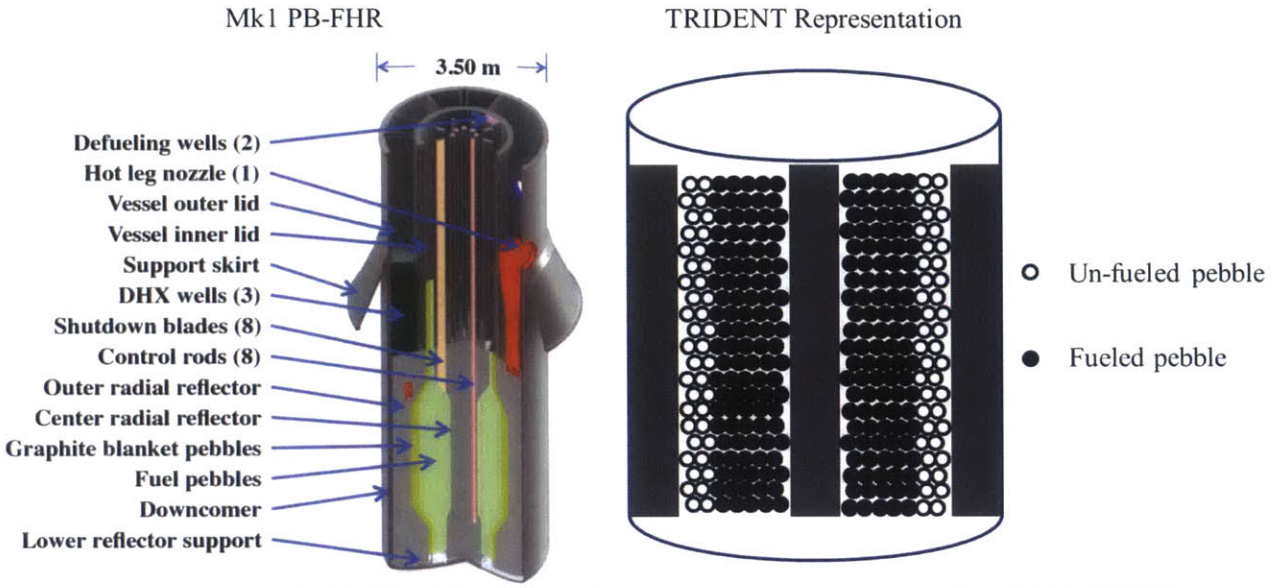

Figure 6.1: Actual Mk1 PB-FHR core detail compared to a representation of TRIDENT core detail.

6.2 TRIDENT material properties

The TRIDENT model requires a number of material properties such as the coolant viscosity, Henry's law constants, alloy compositions, and graphite specific capacity for tritium. All of the data and material properties required have been introduced in Chapters 2 and 3. In some cases, judgments were made in order to select the most reliable data when multiple choices were available. The summary of experimental data required for the model (excluding physical constants such as molar masses, the universal gas constant, etc.) are summarized in Table 6.2. Note that all piping and metal vessels in contact with salt in the reactor is Type 316L stainless steel, and all graphite is IG-110U.

Table 6.2: Baseline material properties used in TRIDENT.

Property	Value or Eq Number	Units	Reference
Baseline Redox Potential (specified as fluorine potential or ratio)	ΔG_{F2} = -700.5 kJ/mol-F_2 or $\frac{P_{TF}}{\sqrt{P_{T_2}}} = 9.2\times10^{-5}$		Section 3.2.3
Flibe specific heat	2.39	kJ/kg-K	[42]
Flibe density	Eq (2.11)	kg/m^3	[45]
Flibe viscosity	Eq (5.24)	Pa-s	[42]
Henry's law constant for T_2 in flibe	Eq (2.13)	mol T_2/m^3 flibe-Pa	[98]
Henry's law constant for TF in flibe	Eq (2.12)	mol TF/m^3 flibe-Pa	[57]
Diffusion coefficient for T_2 in flibe	Eq (2.15)	m^2/s	[100]
Diffusion coefficient for TF in flibe	Eq (2.17)	m^2/s	[105]
Diffusion coefficient for Cr^{2+} in flibe	Eq (5.30)	m^2/s	Section 5.6.1
Initial dissolved Cr concentration in the salt	25	ppm	[123]
Sieverts law constant for T_2 in 316 SS	Eq (2.19) with constants from Table 2.6	$\text{mol}\,T_2 / \text{m}^3\sqrt{\text{MPa}}$	[110]
Diffusivity of T_2 in 316 SS	Eq (2.18) with constants from Table 2.6	m^2/s	[110]
Baseline permeation reduction factor	10	-	[112]
Cr grain boundary diffusion coefficient in 316 SS	Eq (3.6)	m^2/s	[131]
316L SS elemental composition	Table 3.3	wt %	[137]
316L SS density	8.00	g/cm^3	[137]
316L SS lattice parameter	3.59x10^{-10}	m	[186]
316L SS grain diameter	31.8	μm	[137]
316 L grain boundary width	2.48	nm	Estimated in Section 5.8
Graphite capacity for tritium	Eq (2.8)	moles T atoms/g graphite	[86]
Graphite (IG-110) density	1.77	g/cm^3	[89]
Nuclear cross sections relevant to tritium production in flibe	Table 2.1	barn	[62]

6.3 TRIDENT simulation options

A variety of options are available for simulations with TRIDENT. The basic options are described below in Table 6.3. If tritium mitigation systems (permeation windows, gas stripping, or capture on a graphite bed outside of the core) are employed, additional options are available. These options are introduced in the following sections.

Table 6.3: Basic options for TRIDENT simulations. Additional options available if tritium mitigation systems (permeation windows, gas stripping, or capture on non-core graphite) are employed. Those options are discussed in later sections.

Input Option	Description
`Restart`	Option to restart a previously completed simulation. If `Restart` equals 1, the restart option is not used. If it equals 2, restart is used.
`Restartfilename`	Filename (with .mat suffix) of data for restarting a calculation if `Restart` equals 2
`Savefilename`	Filename for saving output from TRIDENT. TRIDENT will automatically save data after each simulation day. Simulations can be restarted from these files using the `Restart` option
`Loops`	Number of separate coolant loops to simulate. If `Loops` = 1, a single primary loop is simulated. If `Loops` = 2, a primary loop and a physically separate secondary loop are simulated.
`Days`	Number of reactor operating days to simulate
`Hour_Fraction`	Specify how many fractions of an hour pass in between storing calculations. If `Hour_Fraction` = 0.5, calculations are stored after every 30 minutes of reactor simulation time
`Elements`	Number of radial finite difference elements in the tritium diffusion calculation in the HX
`T_uptake`	Turn off/on tritium uptake on graphite: 1 = off; 2 = on
`CoreRefuelFrac`	Fraction of the core refueled per day for simulating pebble refueling. If *not* simulating refueling, set equal to 0.
`CoreGeometryAdjust`	Option to correct the pebble surface area in the core to account for the difference between TRIDENT's simplified core representation and more detailed specifications in which `N_CoreFuelPebbles` and `N_CoreGrapPebbles` are specified. 1 = off; 2 = on
`Redoxflag`	Turn off/on redox control: 1 = off, all tritium is treated as T_2 and there is no corrosion; 2 = TF and T_2 may exist subject to the redox option `Feedbackflag`
`Feedbackflag`	Redox control: 1 = TF and T_2 are produced at a constant rate based on the initially specified redox potential. The relative amounts of TF and T_2 are allowed to drift. 2 = Fixed redox potential. The ratio $\frac{P_{TF}}{\sqrt{P_{T_2}}}$ is held constant 3 = Redox is not controlled. All tritium is born as TF and corrosion reactions can generated T_2. The redox potential is calculated

	throughout the calculation, but it is not controlled. The relative amounts of TF and T_2 and the redox potential are allowed to drift.
	Table 6.3 continued from previous page
Oxideflag	Turn off/on effect of oxide layer on tritium permeation in HX: 1 = off; 2 = on
PRFinput	Permeation reduction factor due to oxide layer on air-side of HX
Corrosionflag	Turn off/on corrosion of structural metals: 1 = off; 2 = on
pipe_zone1	Pipe thickness over which corrosion calculations are performed for TF mass-transport limited regime. Only used if Corrosionflag = 2
pipe_zone2	Pipe thickness over which corrosion calculations are performed for Cr diffusion-limited regime. Only used if Corrosionflag = 2
slices1	Number of elements for Cr corrosion during mass-transport limited regime. Only used if Corrosionflag = 2
slices2	Number of elements for Cr diffusion calculations during Cr diffusion-limited regime. Only used if Corrosionflag = 2
Core_mesh	Number of axial divisions in the core for defining control volumes and a temperature profile
Hot_mesh	Number of axial divisions in the hot leg for defining control volumes and a temperature profile
HX_mesh	Number of axial divisions in the heat exchanger for defining control volumes and a temperature profile
Cold_mesh	Number of axial divisions in the cold leg for defining control volumes and a temperature profile
GBflag	Turn off/on metal surface area correction for grain boundaries 1 = off, corrosion may occur at any location on the metal surface; 2 = on, the active surface area for corrosion is only at the grain boundaries
C_Cr_initial_ppm	Initial concentration of Cr (ppm) in the salt. Only used if Corrosionflag = 2
Tritiumproductionflag	Specifies how the tritium production rate is calculated 1 = the BOL tritium generation rate is used through the calculation 2 = the equilibrium tritium generation rate is used throughout the calculation 3 = the tritium production rate varies with time according to Eq (2.6) 4 = the user can specify a tritium production rate

6.4 TRIDENT simulations of the baseline PB-FHR

The simulations in this section were carried out using the standard specifications of the baseline Mk1 PB-FHR defined in Table 6.1. The necessary material properties were summarized in Table 6.2, and the basic TRIDENT simulation options were summarized in Table 6.3. Certain options can be turned on or off in order to determine the effect of a particular phenomenon. For example, the model can be run with or without taking into account the effect of tritium capture on the graphite in the core. The model can be run with or without the effects of corrosion. As another example, the effect of an oxide layer on the air-facing side of the heat exchanger can be varied according to the

permeation reduction factor (PRF). The baseline PRF for Type 316 SS is set to 10 (as given by ref [112] and discussed in Section 2.6), but specially applied oxide layers can have PRFs of 1000 or higher. Each subsection below will highlight the effect of different phenomena such as the PRF and tritium capture on graphite.

6.4.1 Simulation with standard reactor configuration and no tritium capture

To begin, a simulation was carried out neglecting graphite capture of tritium and the effects of corrosion. The baseline oxide layer was accounted for with PRF = 10. The baseline, fixed redox potential of -700.5 kJ/mol-F_2 ($P_{TF}/(P_{T2})^{0.5} = 9.2x10^{-5}$) was used. In order to simulate tritium behavior in the Mk1 PB-FHR, TRIDENT requires a set of reactor-specific parameters, material properties, and simulation options. The baseline Mk1 PB-FHR reactor parameters were summarized in Table 6.1. A summary of the basic TRIDENT input options was given in Table 6.3, and the chosen options relevant to this particular simulation are summarized below in Table 6.4.

Table 6.4: Relevant TRIDENT simulation options for baseline calculations with no graphite capture of tritium, no corrosion, and a fixed redox potential.

Input Options	Value (and meaning)
Loops	1
Days	3
Hour_Fraction	0.1
Elements	6
T_uptake	1 (off, tritium uptake on graphite not simulated)
CoreRefuelFrac	Not used when T_uptake = 1
CoreGeometryAdjust	Not used when T_uptake = 1
Redoxflag	2 (TF and T_2 may exist subject to the redox option Feedbackflag)
Feedbackflag	2 (Redox potential is fixed at the baseline potential from Table 6.2)
Oxideflag	2 (oxide layer on air-side of HX is accounted for)
PRFinput	10 (permeation reduction factor)
Corrosionflag	1 (corrosion is not simulated)
Core_mesh	10
Hot_mesh	10
HX_mesh	10
Cold_mesh	10
GBflag	Not used. Meaningless when Corrosionflag = 1
C_Cr_initial_ppm	Not used. Meaningless when Corrosionflag = 1
Tritiumproductionflag	3 the tritium production rate varies with time according to Eq (2.6)

Figure 6.2 shows the buildup of tritium in the flibe coolant of the Mk1 PB-FHR as a function of reactor operating time beginning from time t = 0. The amount of tritium in the coolant is given in units of both moles and activity (Ci). The amount of tritium in the primary coolant quickly reaches a steady state about 2 hours from reactor start up. The amount of tritium retained in the coolant is

quite low: about 30 Ci. Figure 6.3 shows the buildup of tritium within the metal tube walls of the HX. Figure 6.3 shows that it takes about 5 hours for the amount of tritium dissolved in the HX metal to reach a steady state value. The total steady state amount of tritium in the HX metal is about 30 times greater than the amount of tritium remaining in the flibe coolant. This is because the tritium solubility in Type 316 SS is much higher than the solubility in flibe. The release rate of tritium is plotted versus reactor operating time in Figure 6.4. The release rate increases until reaching a steady state at about 2770 Ci/EFPD after about 5 hours. At this point, the rate of tritium production is equal to the tritium release rate. Although it is difficult to see in Figure 6.4, the tritium release rate is actually decreasing slightly with time after approximately 5 days. This is due to the consumption of the initial 0.005 wt% Li-6 in flibe and the production of new Li-6 from beryllium in flibe (at a lower rate) as discussed in Section 2.2. Finally, the total amount of tritium (Ci) released to the power cycle is shown as a function of effective full power days (EFPD) of reactor operation in Figure 6.5. There is a short period (less than 0.1 days) where little tritium is escaping into the power cycle. This lag period is due to the buildup of tritium in the coolant and HX metal tube walls through which the tritium is diffusing. Once the tritium levels have built up in the coolant and the HX metal tubing, the release rate is virtually constant (varying according to the tritium production rate described by Eq (2.6)).

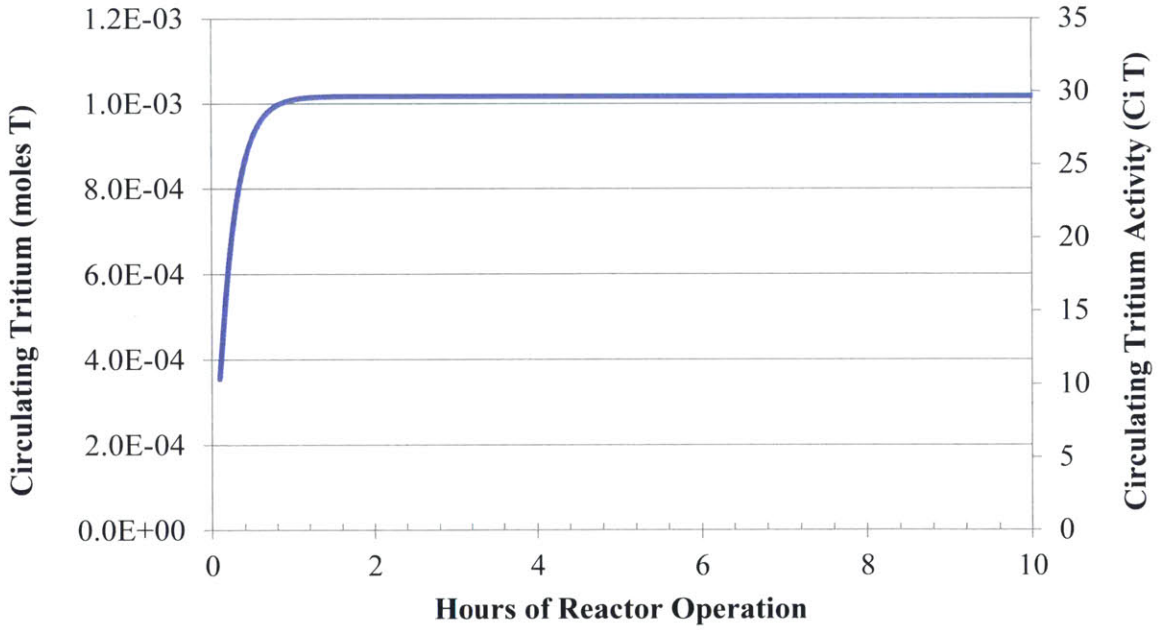

Figure 6.2: Tritium buildup in the flibe coolant of the Mk1 PB-FHR if tritium capture by graphite is neglected. Calculated with TRIDENT.

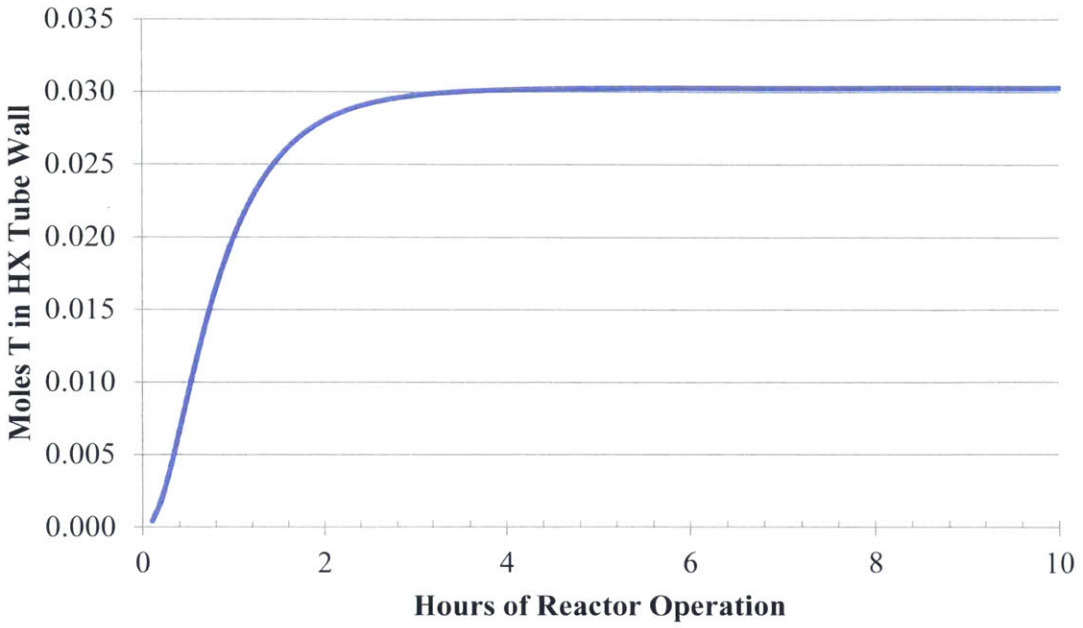

Figure 6.3: Buildup of tritium in the metal of the HX tube walls (total moles T) as a function of reactor operating hours. Calculated with TRIDENT.

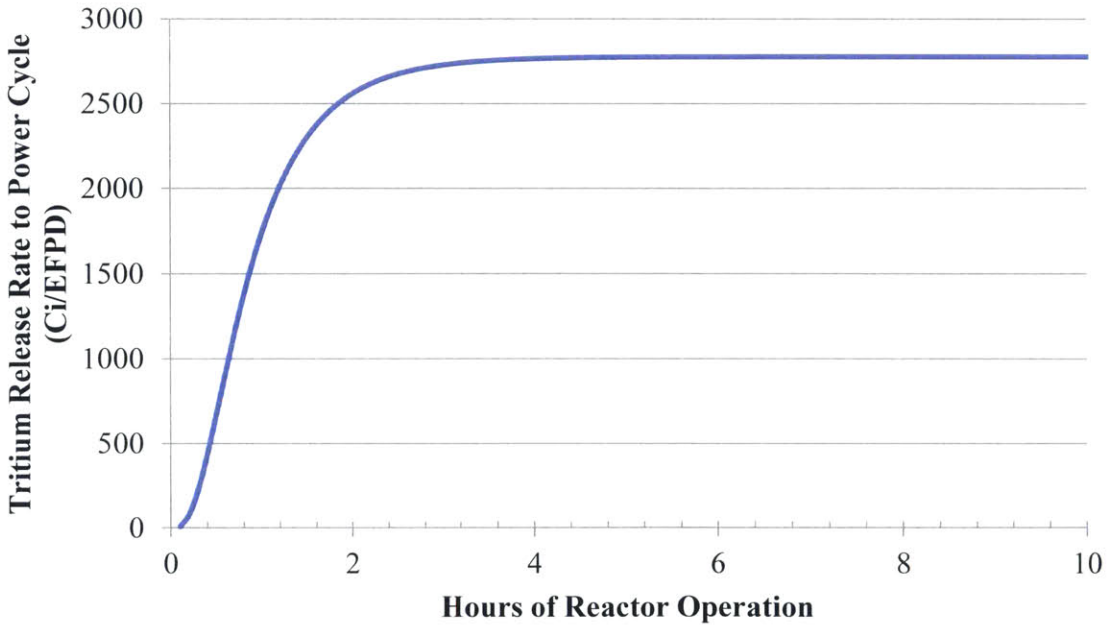

Figure 6.4: Variation of the tritium release rate to the power cycle (Ci/EFPD) with reactor operating time. Calculated with TRIDENT.

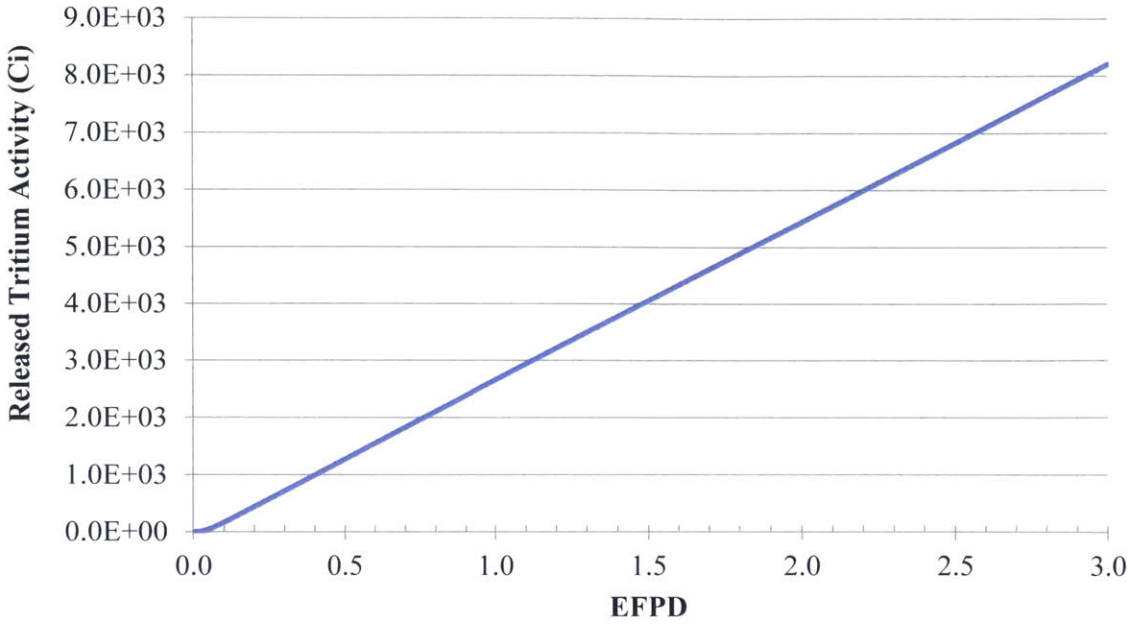

Figure 6.5: Total activity (Ci) of tritium released to the power cycle from 0 to 3 EFPD. Calculated with TRIDENT.

The simulation run from above was repeated, but this time, the input option `Tritiumproductionflag` was set to 2. (All other options and input parameters were carried over from the previous simulation, and graphite capture of tritium was not accounted for). This means that the system was analyzed for the equilibrium tritium production rate. Recall that as the initial 0.005 wt% Li-6 is burned out and additional Li-6 is born from transmutation in Be-9, the rate of tritium production will vary with time according to Eq (2.6) and as plotted in Figure 2.2. Therefore, the equilibrium tritium production rate in an FHR which was initially filled with flibe enriched to 99.995 wt% Li-7 will be considerably lower than the production rate when the reactor first starts up.[9] Table 6.5 summarizes the most important parameters from this equilibrium calculation. It shows that the equilibrium tritium release rate is more than a factor of 3 lower than the release rate at the beginning of life. For a PB-FHR filled with flibe initially enriched to 99.995 wt % Li-7, it takes about 25 effective full power years (EFPY) for the production rate to decrease to this equilibrium level.

[9] The variation in the tritium production rate is dependent on the initial Li-7 enrichment of the flibe and may not always decrease with time. This will be discussed in Section 6.5.

Table 6.5: Equilibrium tritium behavior in Mk1 PB-FHR with TRIDENT options as defined in Table 6.4 except that here `Tritiumproductionflag` was set to 2.

	Equilibrium Value
Circulating Tritium Activity (Ci)	11.9
Tritium Release Rate (Ci/EFPD)	805.2
Tritium in HX metal tube wall (moles T)	0.0087
Equilibrium Tritium Production Rate (Ci/EFPD)	810.3

6.4.2 Standard configuration with tritium capture on graphite

In this case, the initial run is repeated; however, graphite capture of tritium in the reactor core is added to the simulation. In this simulation, refueling of the pebbles is not accounted for. The input option `Tritiumproductionflag` was set to 3 so that the tritium production rate varies with time. The relevant input options are summarized below in Table 6.6.

Table 6.6: TRIDENT input options for simulations in Section 6.4.2.

Input Options	Value (and meaning)
`Loops`	1
`Days`	100
`Hour_Fraction`	0.4
`Elements`	6
`T_uptake`	2 (On, tritium uptake on graphite is simulated)
`CoreRefuelFrac`	0 (Pebble refueling not accounted for)
`CoreGeometryAdjust`	2 (On)
`Redoxflag`	2 (TF and T_2 may exist subject to the redox option `Feedbackflag`)
`Feedbackflag`	2 (Redox potential is fixed at the baseline potential from Table 6.2)
`Oxideflag`	2 (oxide layer on air-side of HX is accounted for)
`PRFinput`	10 (permeation reduction factor)
`Corrosionflag`	1 (corrosion is not simulated)
`Core_mesh`	10
`Hot_mesh`	10
`HX_mesh`	10
`Cold_mesh`	10
`GBflag`	Not used. Meaningless when `Corrosionflag = 1`
`C_Cr_initial_ppm`	Not used. Meaningless when `Corrosionflag = 1`
`Tritiumproductionflag`	3 the tritium production rate varies with time according to Eq (2.6)

Figure 6.6 shows the early buildup of tritium in the reactor coolant and the early release rate to the power cycle. A temporary steady state develops after 4 hours. Compared to Figure 6.2 and Figure 6.4, the time to reach this temporary steady state is virtually unchanged; however both the release rate and the circulating tritium activity are much lower. This is due to capture of both T_2 and TF on the graphite in the core. This temporary steady state continues until about 250 hours of reactor operation. At this point, the graphite begins to saturate with tritium. Figure 6.7 shows the buildup of

tritium in the reactor coolant and the release rate to the power cycle as a function of EFPD. The slight roughness in the plot after about 10 days is due to the way in which the effect of tritium saturation behavior was implemented. After about 10 EFPD, the core graphite begins to saturate with tritium. This is a slow process because the graphite capacity for tritium is related to the partial pressure of tritium (T_2 and TF) over the salt according to Eq (2.8). If graphite in one part of the core saturates, additional tritium is held in the salt, which increases the partial pressure of tritium which increases the graphite capacity for tritium. A new steady state is reached after about 70 EFPD. At this point the amount of tritium in the coolant and the rate of tritium release slowly decreases due to the reduction in the tritium production rate as Li-6 is consumed through neutron transmutation in flibe until it too reaches a steady state after about 25 EFPY. Figure 6.8 shows the total amount of tritium absorbed and captured on graphite in the core throughout the simulation. Without refueling, the graphite will saturate after about 70 EFPD.

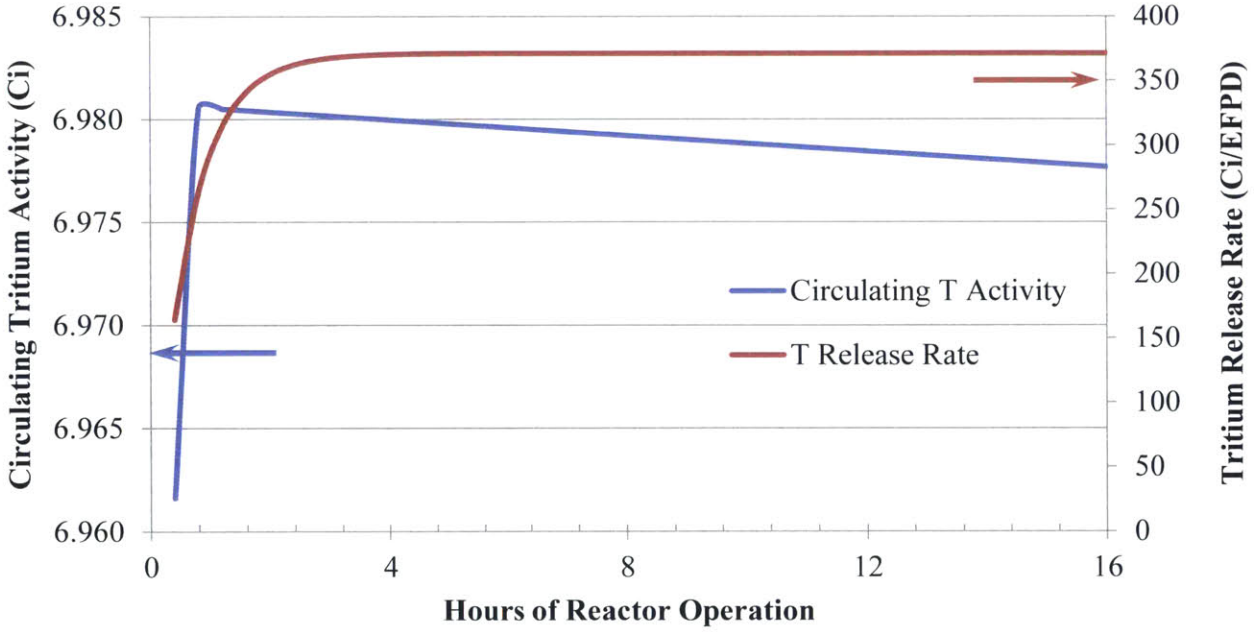

Figure 6.6: Plot of tritium activity circulating in the salt (left axis) and the tritium release rate (right axis) shortly after startup. Calculated with TRIDENT.

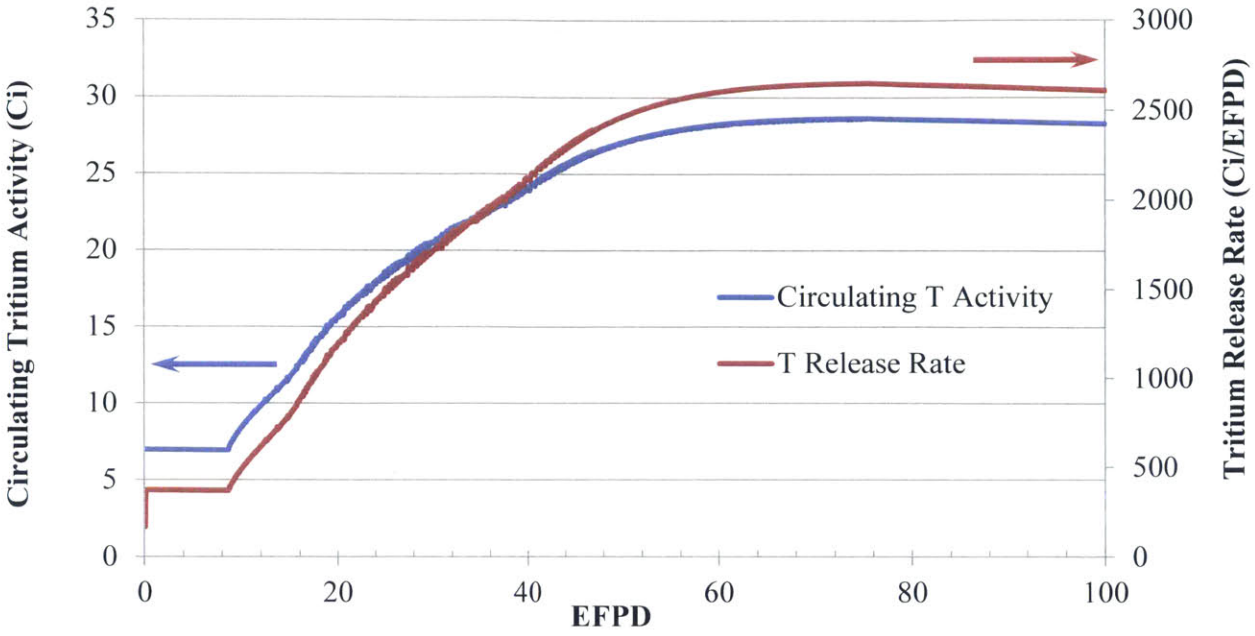

Figure 6.7: Tritium activity in the coolant salt (left axis) and tritium release rate to the power cycle (right axis) versus EFPD. Calculated with TRIDENT.

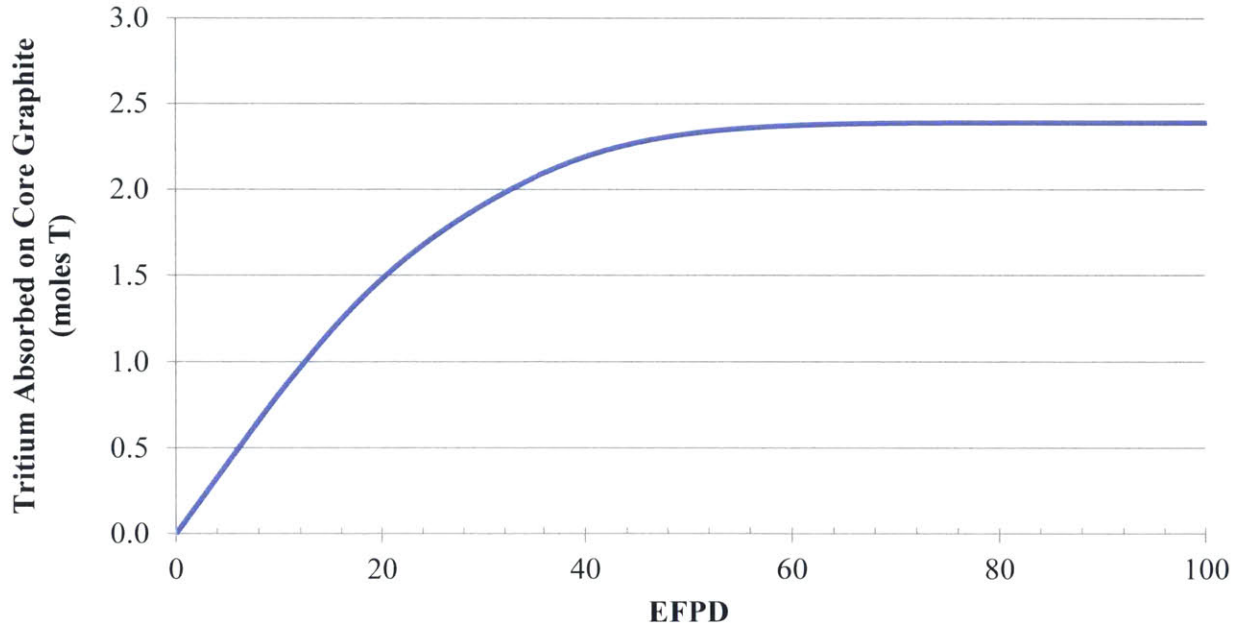

Figure 6.8: Total moles of tritium atoms captured on graphite in the core. Calculated with TRIDENT.

6.4.3 Standard configuration with tritium capture and refueling

The Mk1 PB-FHR features online refueling where pebbles move from the bottom of the core to the top (due to the positive buoyancy of the pebbles in flibe) on a 30 day cycle. Each pebble will experience 10 to 12 30 day cycles before being discarded. At the end of each cycle, the burnup of the pebble is checked. Since the pebble graphite will be a significant sink for tritium, it may be possible to drive the tritium off of each pebble between cycles by heating the pebbles to a temperature of about 1000 °C. In order to simulate this, the `CoreRefuelFrac` option can be activated in TRIDENT by specifying the fraction of the core that is refueled per day. TRIDENT then assumes that all of the tritium present on a given pebble is driven off between each cycle by heating the pebbles. The input options for this simulation are summarized in Table 6.7.

Figure 6.9 compares the tritium activity circulating in the coolant when pebble refueling is and is not accounted for. When each pebble is circulated every 30 days, the steady state tritium activity in the coolant is only slightly reduced compared to a case with no refueling. The roughness in the plot between about 10 days and 55 days is due to the combined effect of graphite saturation behavior[10] and online refueling of the pebble fuel. Reducing the cycle length would mean that the pebbles cycle through the core more frequently, which would further reduce the activity of tritium circulating in the coolant. Figure 6.10 compares the tritium release rate (Ci/EFPD) when refueling is on and off. When steady state is reached after about 70 days, the case where refueling is accounted for has a tritium release rate of about 2410 Ci/EFPD compared to about 2640 Ci/EFPD when refueling is not simulated. Figure 6.11 shows the amount of tritium captured on core graphite as a function of EFPD for cases with and without simulated refueling. Since the pebbles are cleared of tritium between cycles, tritium is continually captured on graphite, and the rate of tritium capture becomes proportional to the rate of refueling. If refueling is not simulated, tritium capture ceases after about 70 days when the graphite has become saturated.

Once the equilibrium level of tritium generation has been reached (which takes about 25 EFPY in the baseline configuration), then the equilibrium behavior is characterized by significantly lower release rates. The equilibrium quantities are summarized in Table 6.8.

[10] An increase in tritium partial pressure increases the graphite capacity for tritium, allowing the graphite to absorb additional tritium. However, the absorption of additional tritium reduces the partial pressure and the graphite capacity for tritium. This balance creates some roughness in the plots due to the method of implementation of this phenomenon in the model.

Table 6.7: Input options for TRIDENT simulation of tritium transport including tritium capture on core graphite and fuel pebble online refueling.

Input Options	Value (and meaning)
Loops	1
Days	80
Hour_Fraction	0.1
Elements	6
T_uptake	2 (On, tritium uptake on graphite is simulated)
CoreRefuelFrac	1/30 (Pebble refueling is accounted for with a 30 day cycle)
CoreGeometryAdjust	2 (On)
Redoxflag	2 (TF and T_2 may exist subject to the redox option Feedbackflag)
Feedbackflag	2 (Redox potential is fixed at the baseline potential from Table 6.2)
Oxideflag	2 (oxide layer on air-side of HX is accounted for)
PRFinput	10 (permeation reduction factor)
Corrosionflag	1 (corrosion is not simulated)
Core_mesh	10
Hot_mesh	10
HX_mesh	10
Cold_mesh	10
GBflag	Not used. Meaningless when Corrosionflag = 1
C_Cr_initial_ppm	Not used. Meaningless when Corrosionflag = 1
Tritiumproductionflag	3 the tritium production rate varies with time according to Eq (2.6)

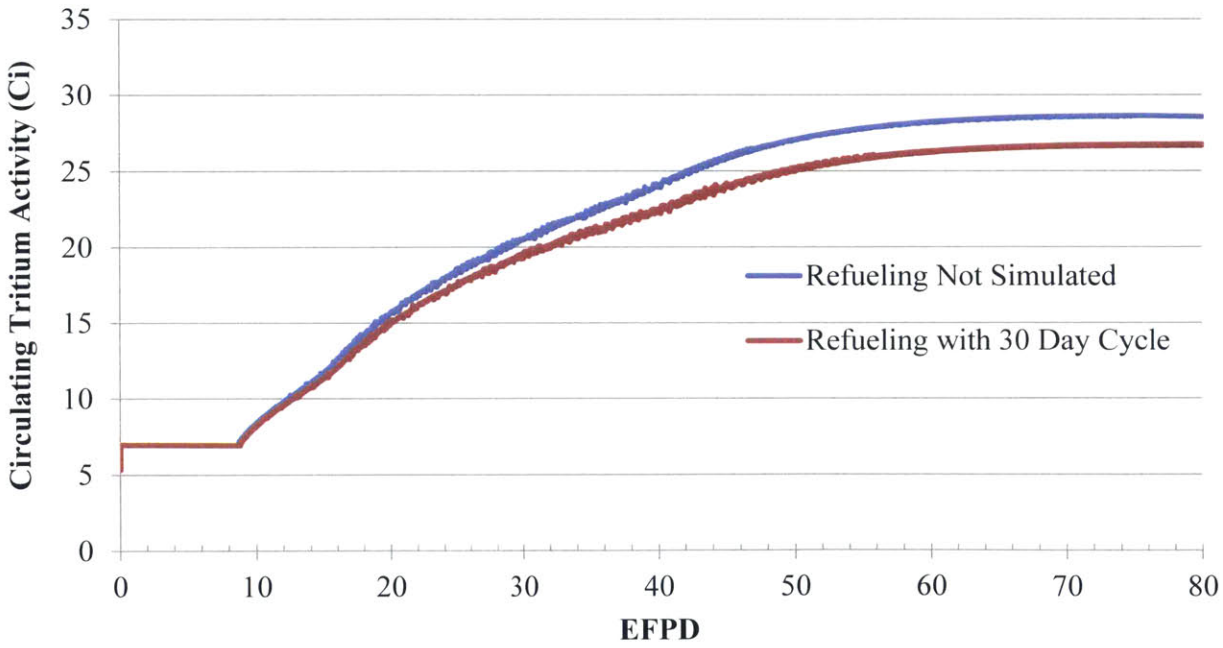

Figure 6.9: Comparison of the tritium activity in the salt when pebble refueling is and is not accounted for. Calculated with TRIDENT.

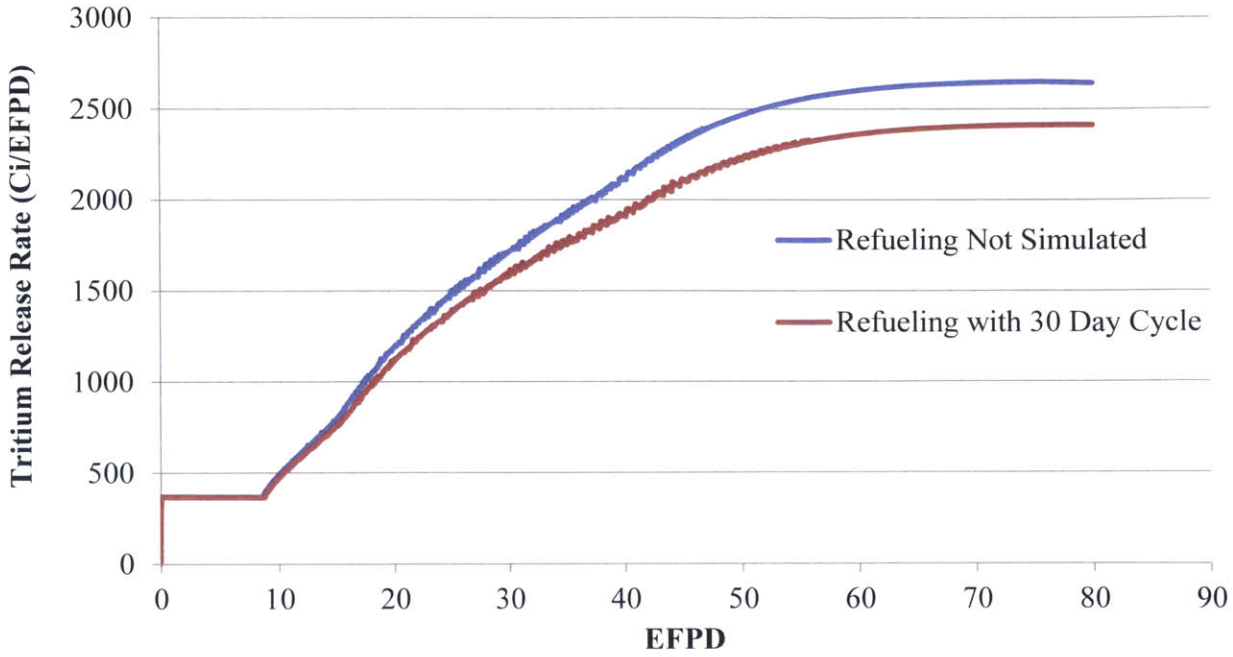

Figure 6.10: Comparison of the tritium release rate (Ci/EFPD) when pebble refueling is and is not accounted for. Calculated with TRIDENT.

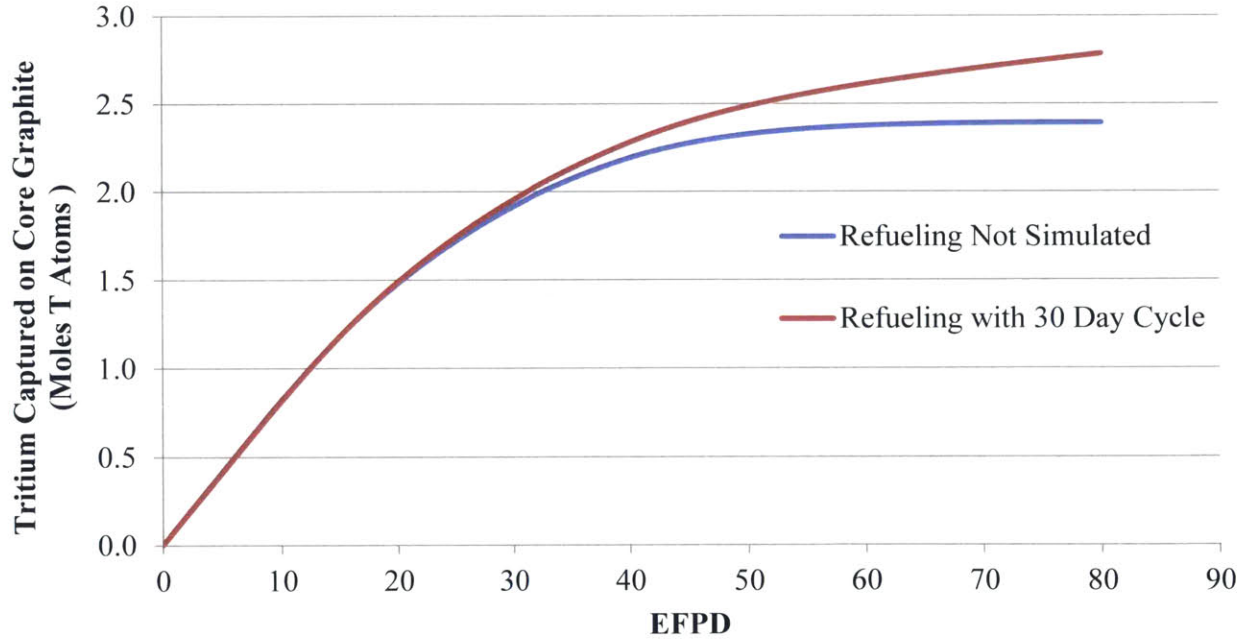

Figure 6.11: Comparison of the total amount of tritium capture by core graphite with and without the effects of pebble refueling. Calculated with TRIDENT.

Table 6.8: Tritium activity in the coolant, release rate, and content in the HX tube wall. Calculated with TRIDENT using the same input as in Table 6.7 except that `Tritiumproductionflag` was set to 2 for equilibrium tritium production.

	Equilibrium Value
Circulating Tritium Activity (Ci)	10.4
Tritium Release Rate (Ci/EFPD)	668.6
Tritium in HX metal tube wall (moles T)	0.0072
Equilibrium Tritium Production Rate (Ci/EFPD)	810.3

6.4.4 Standard configuration with tritium capture, refueling, and corrosion

As has been discussed, the chemical form of tritium can alternate between T_2 and TF depending on the redox potential and/or corrosion reactions. This section retains the same conditions as the preceding section, but now it adds the effect of corrosion reactions between TF and Cr in Type 316L stainless steel. The relevant input options and input values used in this TRIDENT simulation are summarized in Table 6.9.

With the redox potential fixed at the baseline potential, there is virtually no difference between the tritium transport results of this simulation (with corrosion effects) and the previous simulation (without corrosion effects) from Section 6.4.3. For example, Figure 6.12 shows that the tritium release rate to the power cycle is unchanged.

Table 6.9: Simulation options and input required for modeling corrosion reactions in TRIDENT.

Input Options	Value (and meaning)
`Loops`	1
`Days`	200
`Hour_Fraction`	0.2
`Elements`	6
`T_uptake`	2 (On, tritium uptake on graphite is simulated)
`CoreRefuelFrac`	1/30 (Pebble refueling is accounted for with a 30 day cycle)
`CoreGeometryAdjust`	2 (On)
`Redoxflag`	2 (TF and T_2 may exist subject to the redox option `Feedbackflag`)
`Feedbackflag`	2 (Redox potential is fixed at the baseline potential from Table 6.2)
`Oxideflag`	2 (oxide layer on air-side of HX is accounted for)
`PRFinput`	10 (permeation reduction factor)
`Corrosionflag`	2 (corrosion is simulated)
`Core_mesh`	10
`Hot_mesh`	10
`HX_mesh`	10
`Cold_mesh`	10
`GBflag`	2 (grain boundary corrosion is activated)
`C_Cr_initial_ppm`	25
`GB_diameter`	31.8 μm

Table 6.9 continued from previous page	
GB_width	10 nm
Lattice_param	0.3596 nm
Ratio_TF_T2	9.2×10^{-5} (MSRE standard redox potential used in the previous simulations)
Tritiumproductionflag	3 the tritium production rate varies with time according to Eq (2.6)

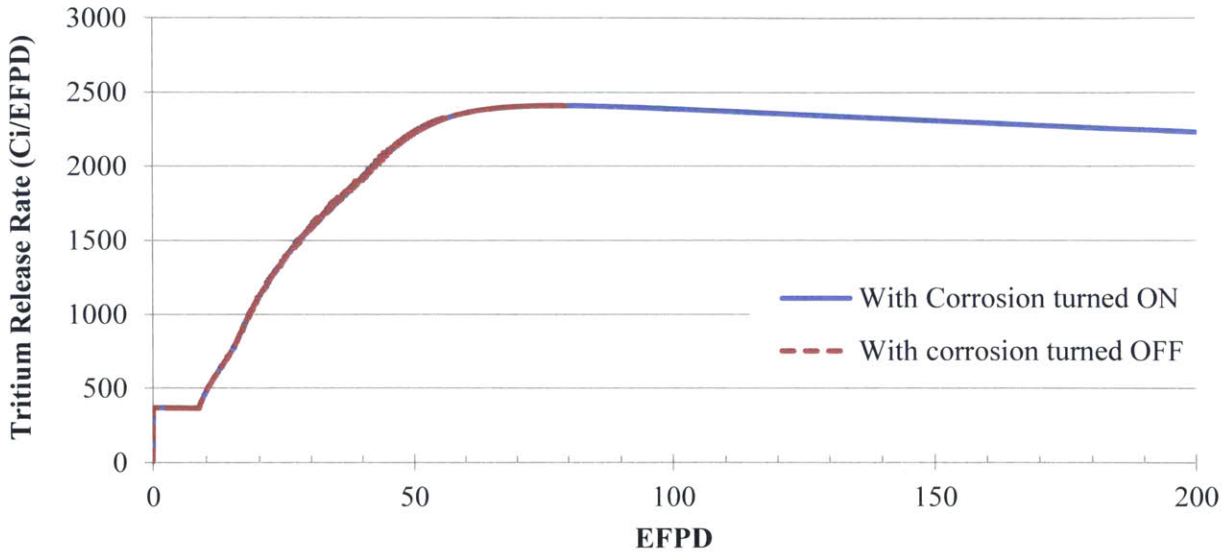

Figure 6.12: Tritium release rate comparison between calculations with and without the effects of corrosion. Simulated with TRIDENT.

Activation of the corrosion model tracks Cr throughout the system. Figure 6.13 shows the buildup of Cr in the coolant as a function of time. The Cr concentration begins at the specified value of 25 ppm. As the tritium concentration builds up in the coolant, the concentration of dissolved Cr begins to increase. After about 80 EFPD, the Cr concentration levels off at 39 ppm because the equilibrium concentration of Cr in the salt at the specified redox potential is 39 ppm.

Figure 6.14 shows the gross weight gain throughout the reactor coolant loop after 200 EFPD of operation. The majority of the Cr is deposited in the hot leg. Very little Cr is deposited anywhere else in the loop. Chromium deposition occurs when the local Cr concentration in the coolant exceeds the equilibrium concentration of Cr at that location. The rate of Cr deposition is determined by the mass transfer relations described in Section 5.8.2. Unlike many corrosion reactions, the reaction between TF and Cr is an exothermic reaction which has a more negative Gibbs reaction free energy as temperature decreases. This means that more corrosion occurs in the cold section of the loop than in the hot section of the loop. Figure 6.15 shows that the gross corrosion (in terms of mg of Cr lost per cm^2 in a particular loop section) occurs in the heat exchanger and in the cold leg. Thus TRIDENT results demonstrate that mass transfer occurs from the cold leg to the hot leg when TF is the principle oxidant. This possibility was first acknowledged by Evans, Koger, and DeVan [133]. Conversely, the corrosion reactions between UF_4 or FeF_2 and Cr are endothermic, and result in the

more familiar mass transfer of Cr from the hot leg to the cold leg. Figure 6.16 shows the net weight change due to Cr corrosion and deposition throughout the coolant loop after 200 EFPD. Net weight gain occurs in the hot leg, and net weight loss occurs in the heat exchanger and cold leg.

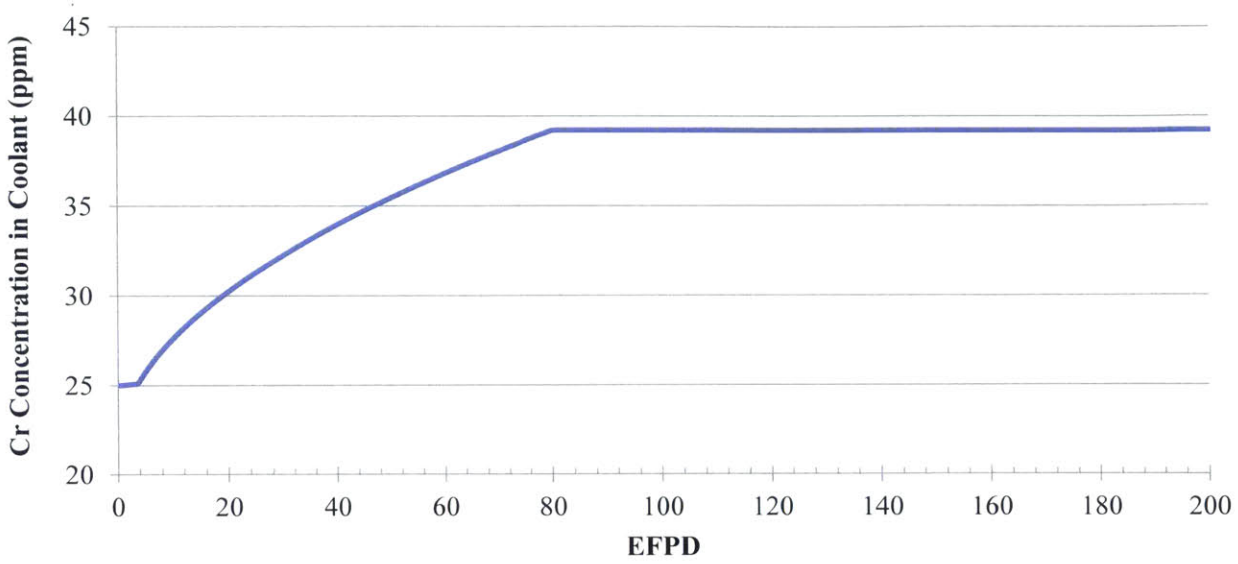

Figure 6.13: Cr concentration in the coolant as function of EFPD. Simulated with TRIDENT.

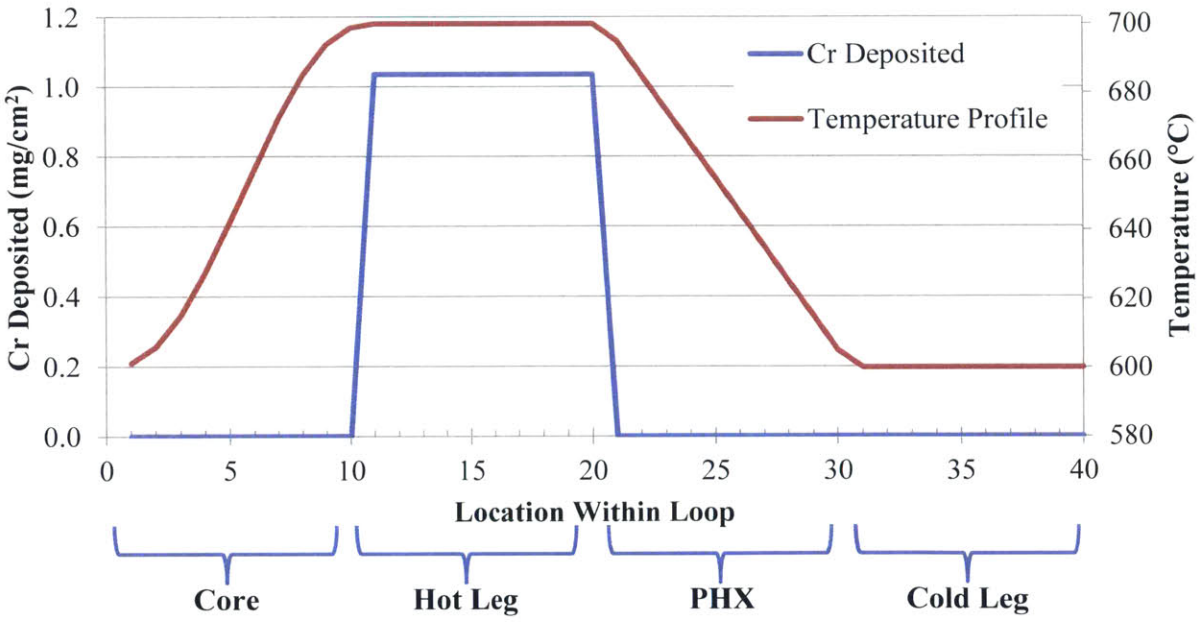

Figure 6.14: Mass of Cr deposited at various locations throughout the reactor coolant loop after 200 EFPD. Simulated with TRIDENT.

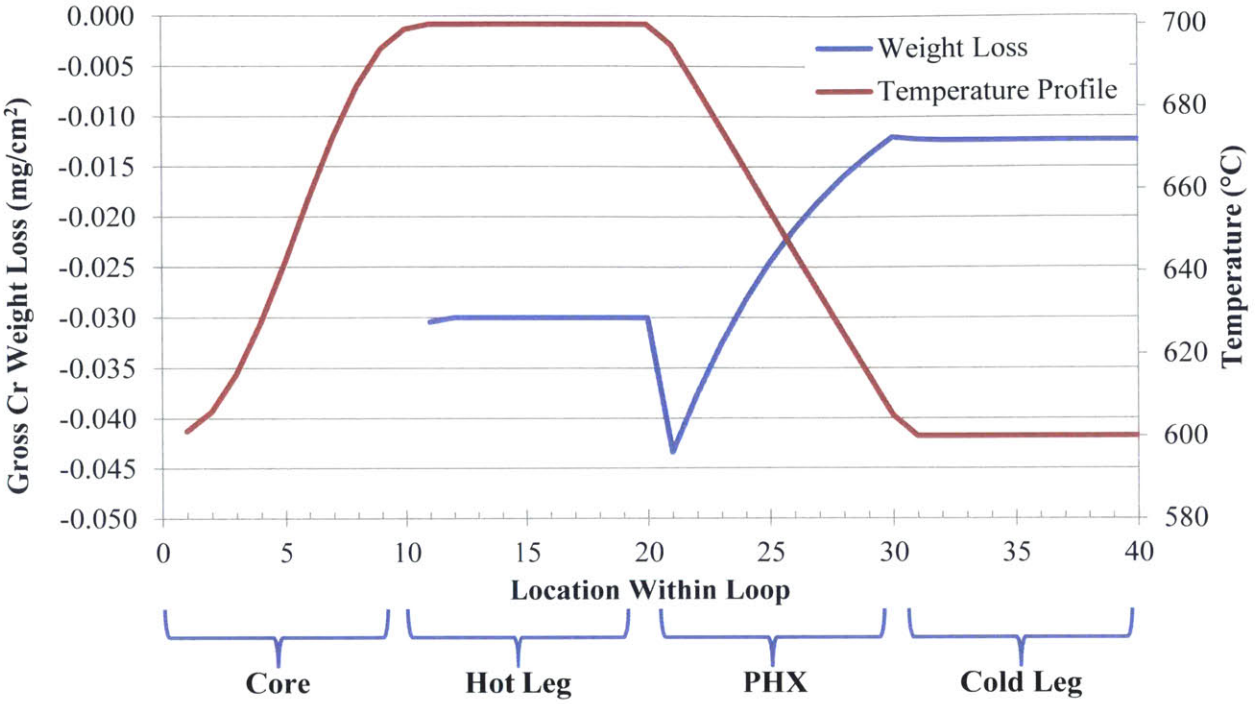

Figure 6.15: Gross mass of Cr lost from various sections of the reactor coolant loop after 200 EFPD. Simulated with TRIDENT.

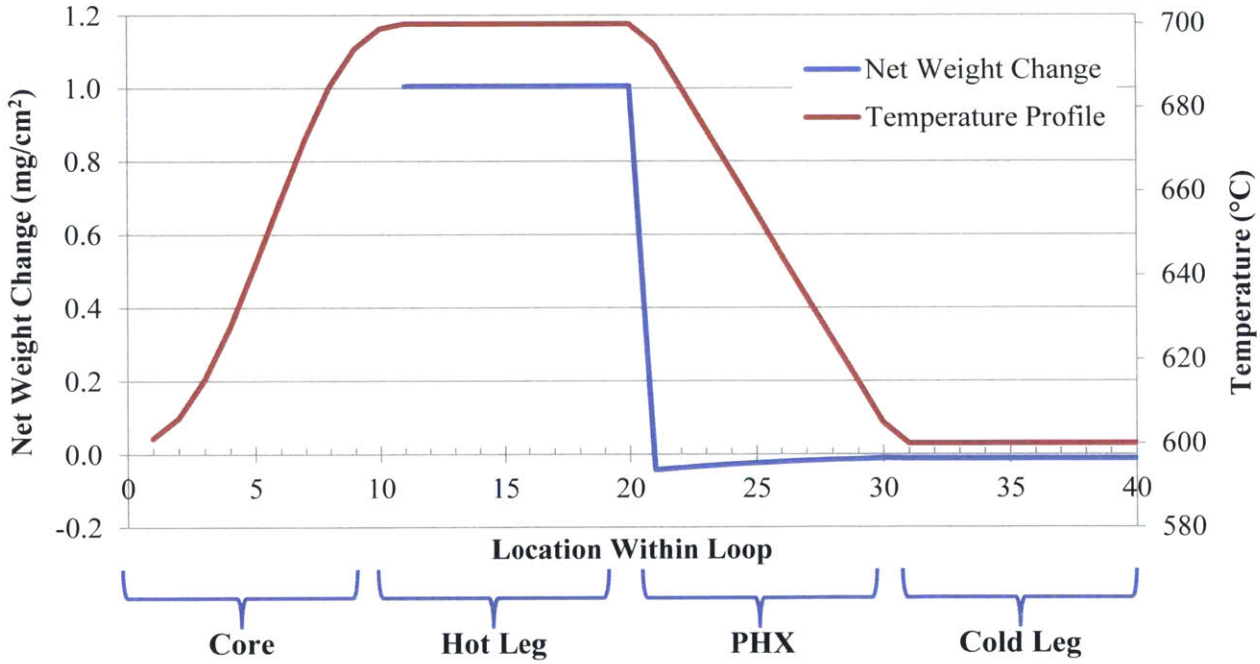

Figure 6.16: Net weight change due to Cr deposition and corrosion throughout the reactor coolant loop after 200 EFPD. Simulated with TRIDENT.

Figure 6.17 shows the bulk Cr concentration profile within the pipe wall after 200 EFPD for three locations in the coolant loop. The reason the Cr concentration is higher in the section of the HX at 675 °C than in the section at 695 °C is that the concentration of tritium in the coolant decreases along the HX due to diffusion of T_2 through the HX walls. Thus even though the ratio $[P_{TF}]/[P_{T2}]^{0.5}$ is held constant, the concentration of each species decreases from the HX entrance to the HX exit. The site of greatest Cr loss is toward the entrance of the HX at 695 °C. At this point, some chromium depletion was calculated down to a depth of about 2.5 μm after 200 EFPD. This corresponds to a Cr depletion rate of about 4.5 μm per year in the bulk metal. Greater Cr loss would be expected in the vicinity of grain boundaries. A 9.2 year loop corrosion test of Hastelloy-N in MSRE fuel salt observed voids (due to selective Cr attack) at depths ranging from 50 μm to 100 μm [35]. This corresponds to a Cr depletion rate of between 5.5 and 11 μm per year, and was deemed sustainable for use in the MSRs [35]. This indicates that the simulated Cr depletion in Type 316L stainless steel in the FHR may also be sustainable. The caveat in comparing Hastelloy-N to Type 316L SS is that Hastelloy-N has less than half the Cr content of Type 316L SS, and void production is more difficult in Hastelloy-N [35,126]. It was noted that in otherwise comparable loops, void formation in a Type 304L SS sample after 0.65 years was roughly equal to the void formation in Hastelloy-N after 9 years [35]. Experiments which include the effect of mass transfer in corrosion and/or a more sophisticated corrosion model would be required in order to prove that excessive void formation does not occur in Type 316L SS under FHR conditions.

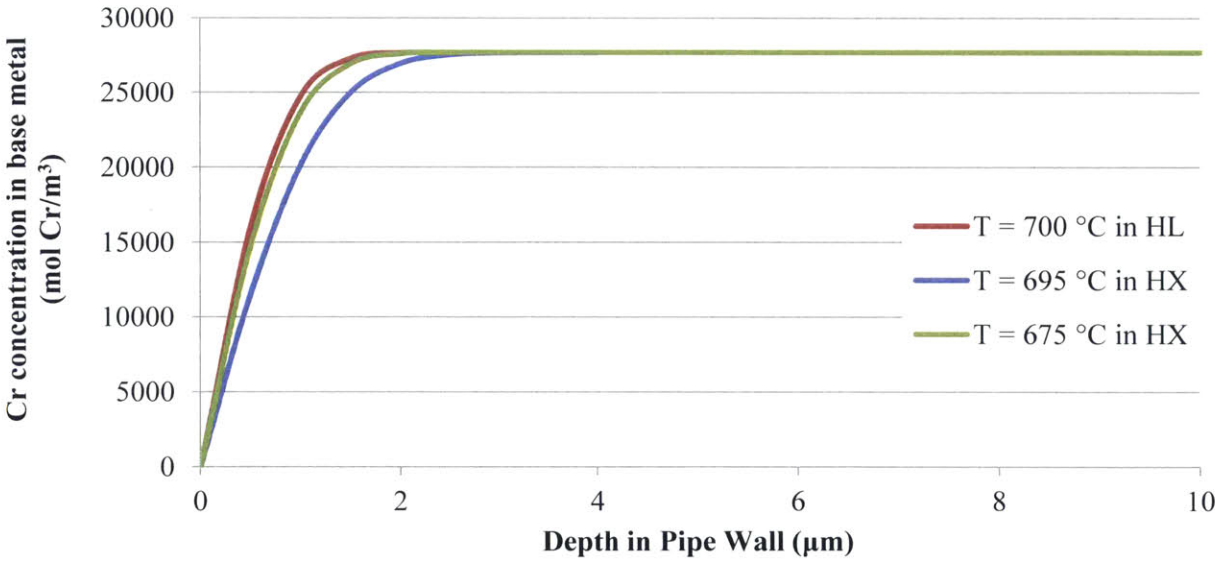

Figure 6.17: Chromium concentration in the pipe wall at one location in the hot leg (HL) and two locations in the heat exchanger (HX) after 200 EFPD. Simulated with TRIDENT.

6.5 Effect of redox potential on tritium transport and corrosion in FHRs

This section explores the effects of the redox potential on corrosion and tritium transport in an FHR. The coolant redox potential determines the chemical form of tritium and the extent of

corrosion. Tritium existing as TF is an oxidant capable of corroding structural metals, particularly Cr. Tritium existing as T_2 is notable for its high permeability in structural metals and relatively low solubility in the salt. In Section 3.2, Figure 3.15 shows that as the redox potential increases (becomes more corrosive), the ratio of TF to T_2 increases. If the redox potential is decreased (made more reducing) the ratio of TF to T_2 decreases. Figure 3.16 shows the equilibrium concentration of Cr^{2+} dissolved in flibe contacting Type 316L stainless steel at 650 °C. The top horizontal axis shows the fluorine potential and the bottom horizontal axis shows the corresponding ratio of $[P_{HF}]^2$:$[P_{H2}]$. As the fraction of TF increases, the redox potential increases, the salt becomes more oxidizing, and a greater amount of Cr^{2+} is corroded.

Four cases were simulated in TRIDENT: baseline, reducing redox, corrosive redox, and floating redox. The baseline redox potential is defined as a fluorine potential of -700.5 kJ/mol F_2 at 650 °C. The "reducing" and "corrosive" labels are defined relative to the baseline redox potential. Thus the "reducing" redox case uses a redox potential that is more reducing than the baseline redox potential, and the "corrosive" redox case uses a redox potential that is more corrosive than the baseline redox potential. The "corrosive redox" case used a redox potential of -654.5 kJ/mol F_2 at 650 °C. The "reducing redox" case used a redox potential of -740 kJ/mol F_2 at 650 °C. The "floating redox" case did not control the redox potential. In this case, tritium was born as TF and only corrosion reactions converted TF to T_2. Thus the redox potential was allowed to drift throughout the simulation. All other variables and input parameters are the same as those used in Section 6.4.4 and Table 6.9.

6.5.1 Tritium transport results

Figure 6.18 through Figure 6.20 summarize the tritium transport results. Figure 6.18 shows the circulating activity in the reactor coolant as a function of reactor operating time for each of the four redox cases. By maintaining a corrosive redox potential, a greater fraction of tritium exists as TF. Because TF cannot diffuse through the heat exchanger, and it has a higher solubility in flibe than T_2, the case with the more corrosive potential maintains a greater radiological activity of tritium in the coolant. Conversely, the case with the more reducing potential sees tritium exist in a greater fraction as T_2, which results in less tritium being retained in the coolant. In Figure 6.19, the amount of tritium captured on graphite in the reactor core varies in a similar fashion in that the cases with higher circulating tritium activities also see greater amounts of tritium absorption on graphite. Figure 6.20 shows the variation in the tritium release rate to the power cycle as a function of EFPD for each of the four redox cases. The case of the corrosive potential sees lower release rates because more of the tritium is forced into the non-diffusing TF form. The case of the more reducing potential sees a greater fraction of tritium as T_2 which results in higher release rates, especially at early times. The case of floating redox results in sharper variations in the release rate before attaining a release rate similar to that of the baseline potential. These variations are due to a number of factors: corrosion rate, tritium sorption rate on graphite, tritium solid-state diffusion rate, and a redox potential that varies throughout the loop.

This section has shown that the tritium release rates can be affected by the redox potential in the salt. This is due to the fact that the redox potential determines the chemical form of tritium (T_2 or TF). A more reducing potential increases the fraction of tritium existing as T_2 which is capable of diffusing through metal. Figure 6.20 shows that relative to the baseline potential, the "reducing redox" case simulated here increased the tritium release rate by a factor of 2 at early times, but once the pseudo steady state was achieved after about 60 EFPD, the release rate was only about 50 Ci/EFPD higher than in the baseline case. Specifying a potential more corrosive than the baseline potential increases the fraction of tritium existing as TF. This greatly reduces the tritium release rate at times less than 150 EFPD and results in a greater amount of tritium absorbed on graphite. Before 50 EFPD the more corrosive potential reduces tritium release rates by more than about 2000 Ci/EFPD compared to the baseline case. After 150 EFPD, a pseudo steady state is reached and the release rate for the more corrosive case is about 500 Ci/EFPD less than the baseline case. Allowing the redox potential to "float" results in pseudo-steady state tritium release rates comparable to those of the baseline case. The early release rates for the case of floating redox vary sharply as tritium born as TF reacts with Cr to generate T_2. Of the four cases analyzed in this section, the "baseline" and "corrosive" redox cases have the lower tritium release rates. The next section will analyze the corrosion implications of these redox choices.

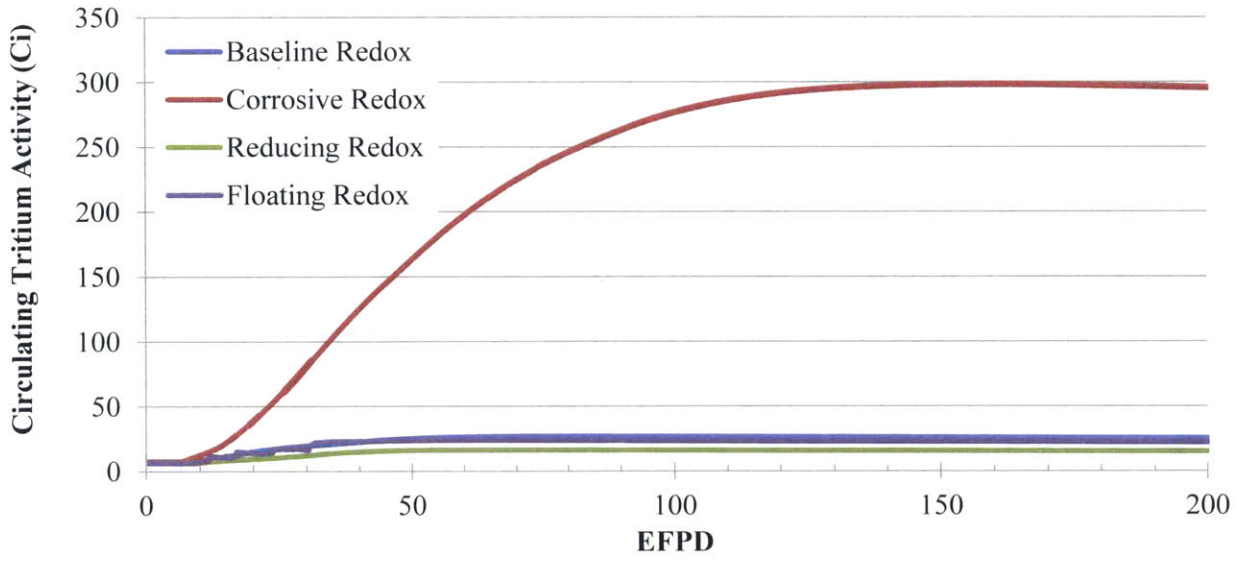

Figure 6.18: Circulating tritium activity for the four different redox cases. Simulated with TRIDENT.

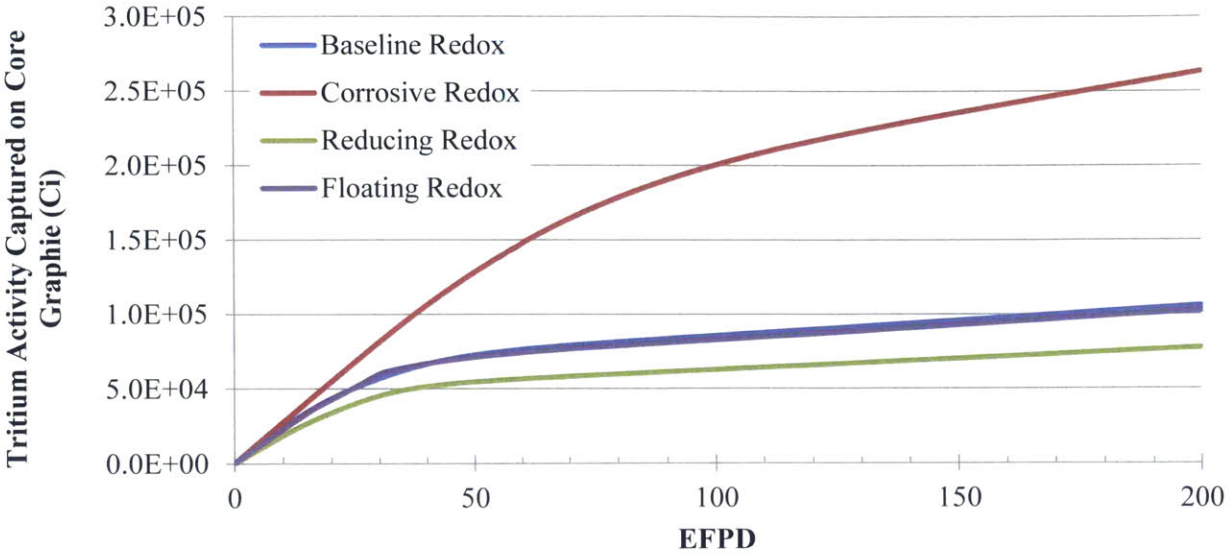

Figure 6.19: Tritium activity captured on core graphite. Simulated with TRIDENT.

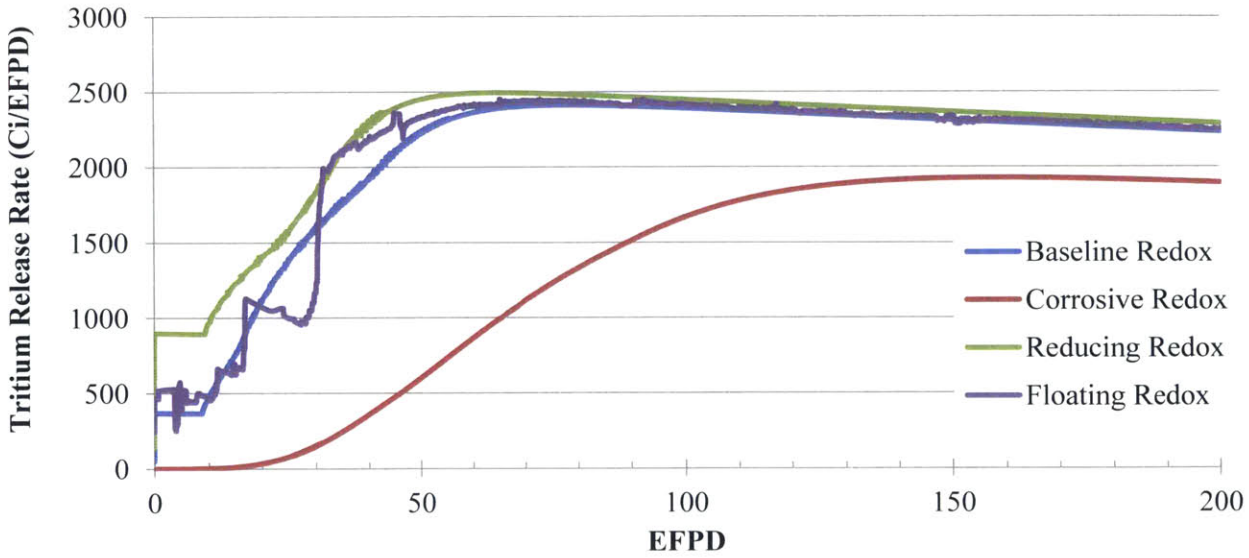

Figure 6.20: Tritium release rates to the power cycle (Ci/EFPD). Simulated with TRIDENT.

6.5.2 Corrosion results

Figure 6.21 shows the variation of the redox potential for the case of "floating" redox. In the other three cases, the redox potential was held constant throughout the calculation. When the redox potential is held constant at a particular value in these calculations, it is assumed that this potential is maintained via the use of a redox control method such as an applied voltage, gas-phase control, dissolved redox buffer, or sacrificial anode such as were mentioned in Section 3.2. Except for early spikes of high redox potential, the floating redox potential attains virtually the same potential as the

baseline. This happens because the TF/Cr reaction becomes the couple which is controlling the redox potential in the floating case. If a Be sacrificial anode was used, the TF/Be couple would be controlling the redox potential and would set a value more reducing than the TF/Cr couple. The problem of letting the TF/Cr couple set the redox potential is that the Cr in the structural metals effectively becomes the sacrificial anode and selective Cr corrosion is the result. Figure 6.22 shows the gross weight loss due to corrosion of Cr normalized by the metal surface area in each loop segment for each of the four cases after 200 EFPD. The case of the floating redox saw the largest gross weight loss. There is no coolant-facing metal in the core, thus weight loss is not possible in the core. The sharp jumps at the "20" and "30" locations in the loop occur because the metal surface area in the heat exchanger is three orders of magnitude higher than that in the hot and cold legs. Thus the absolute (not normalized by surface area) gross weight loss in the heat exchanger is much higher than that in the hot leg and cold leg. It is interesting to note that in the case of the floating and corrosive redox conditions, higher surface-normalized gross weight loss occurs in the hot leg than in the cold leg. This is opposite of the gross weight loss observed for the baseline and reducing redox conditions.[11]

At all locations in the coolant loop, the surface-normalized gross weight loss is greater (more weight is lost) as the redox potential becomes more oxidizing. However, the effect is greater at higher temperatures for two reasons: 1.) for a fixed p_{TF}^2:p_{T2} ratio, the fluorine potential increases with temperature and 2.) the chromium diffusivity in the metal (which is the rate determining step in the selective attack of Cr) is greater at higher temperatures. This effect is also observed in the chromium concentration profile calculated for each redox case. Figure 6.23 shows the chromium concentration calculated at the exit of the hot leg for each of the four redox cases after 200 EFPD. Beyond the surface Cr that was oxidized, no Cr is lost from this location in the loop for the case with the very reducing potential. The case with the baseline redox potential experiences additional Cr oxidation. The corrosive and floating redox cases experience the greatest amount of Cr oxidation and demonstrate Cr depletion down to a depth of about 3 μm after 200 EFPD. This corresponds to a Cr depletion rate of about 5.5 μm/yr (compared to 3.6 μm/yr at this loop location in the baseline case). Although the "corrosive redox" case appears to be identical to the "floating redox" case, the Cr depletion is slightly higher in the "floating redox" case. For example, at a depth of 0.5 μm, the Cr concentration in the "floating redox" case is 10888 mol Cr/m^3 and the Cr concentration in the "corrosive redox" case is 10905 mol Cr/m^3.

Figure 6.24 shows the gross weight gain due to Cr deposition after 200 EFPD. Only the case of the "reducing redox" potential predicts weight gain in the core region. The amount of Cr deposited in the core is small: 0.004 mg/cm^2 at the core outlet and 0.0002 mg/cm^2 at the core inlet after 200 EFPD. Chromium deposition in the core could be a concern because chromium carbides can form with the graphite. The stability of chromium carbides versus chromium fluorides was analyzed by setting up three reactions of three chromium carbide stoichiometries and calculating the Gibbs

[11] Note that this is only talking about gross weight loss. Net weight change is discussed with Figure 6.26.

reaction free energies. The Gibbs reaction free energies are plotted in Figure 6.25 along with the baseline redox potential in units of kJ/mol-F_2. This plot shows that Cr carbides are stable at the operating temperatures and baseline redox potential of the FHR. This means that chromium carbides may form not only after Cr metal is deposited on graphite surfaces, but also anytime dissolved chromium fluoride is in contact with graphite. This suggests that it is beneficial to keep the dissolved Cr concentration low.

Returning to Figure 6.24, the reducing redox case causes some degree of gross Cr deposition at all parts of the loop. In contrast, the corrosive redox case does not result in deposition at any part of the loop after 200 EFPD. A much longer calculation would be necessary to show Cr deposition because the more corrosive potential will support an equilibrium Cr concentration in the coolant of greater than 1400 ppm, and it will take longer to see the Cr concentration build up to that level. The baseline redox potential only sees Cr deposition in the hot leg. The floating redox potential sees gross Cr deposition in the hot leg and heat exchanger.

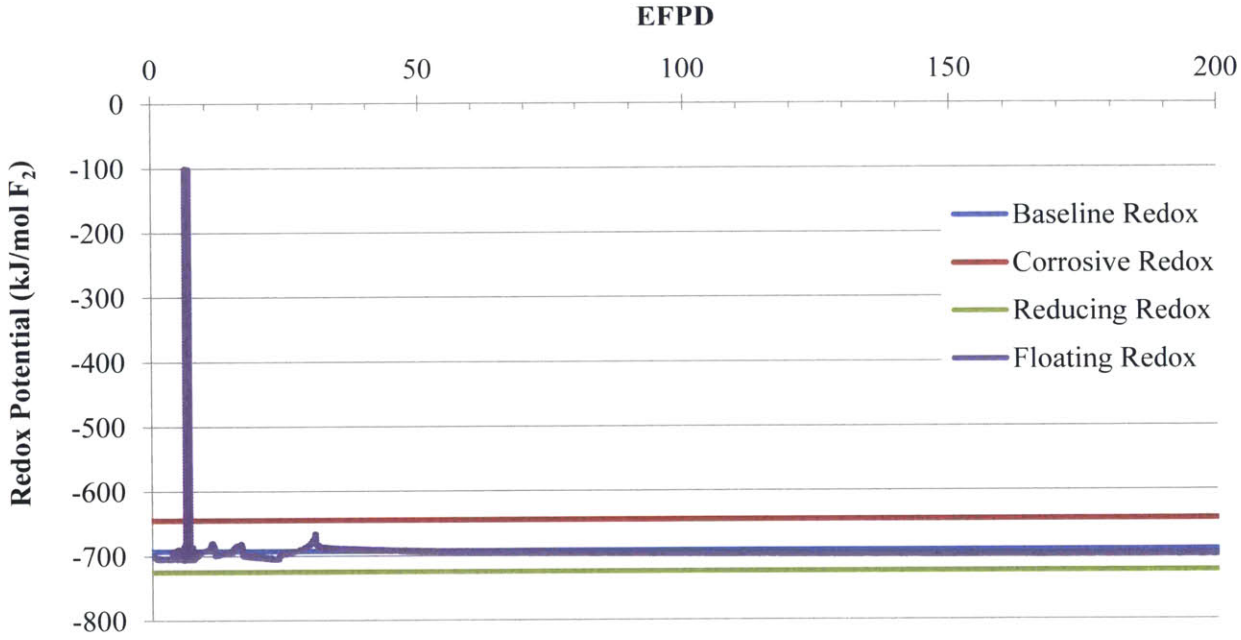

Figure 6.21: Redox potential versus operating time. Except for the "Floating Redox" case, the redox potentials were held constant throughout the simulation.

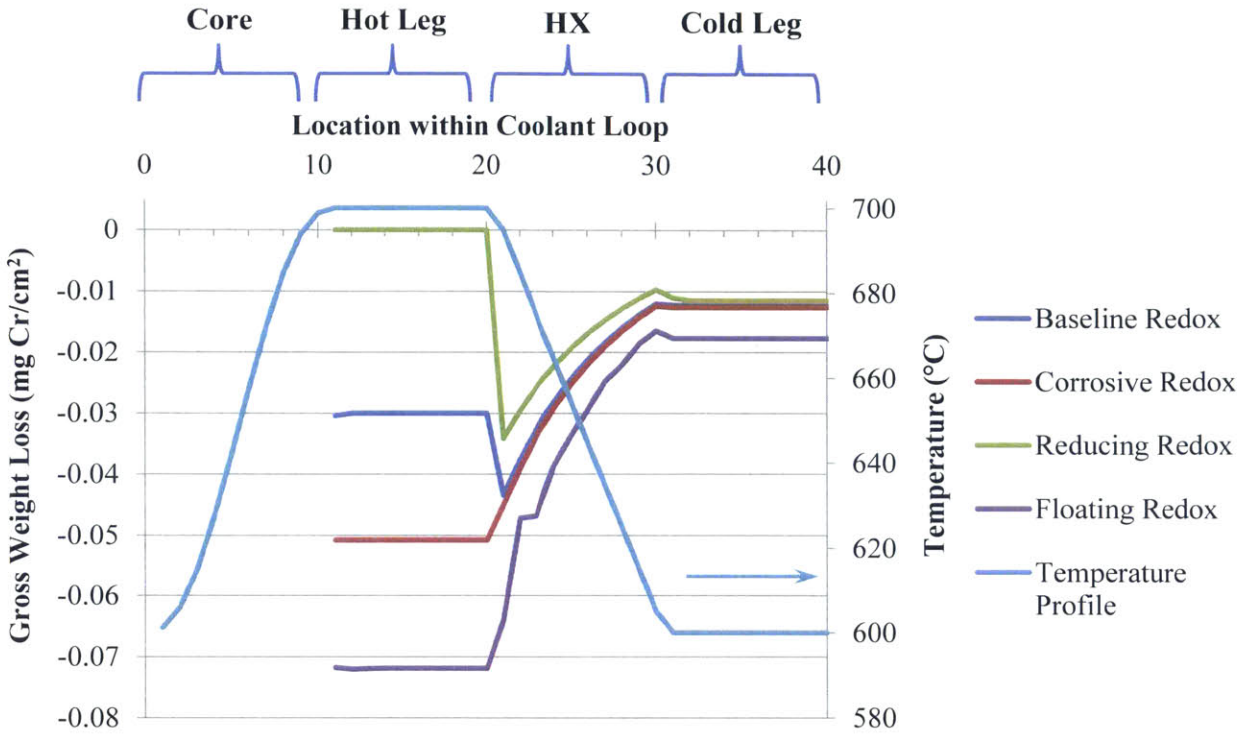

Figure 6.22: Gross weight loss due to corrosion of Cr after 200 EFPD. Simulated with TRIDENT.

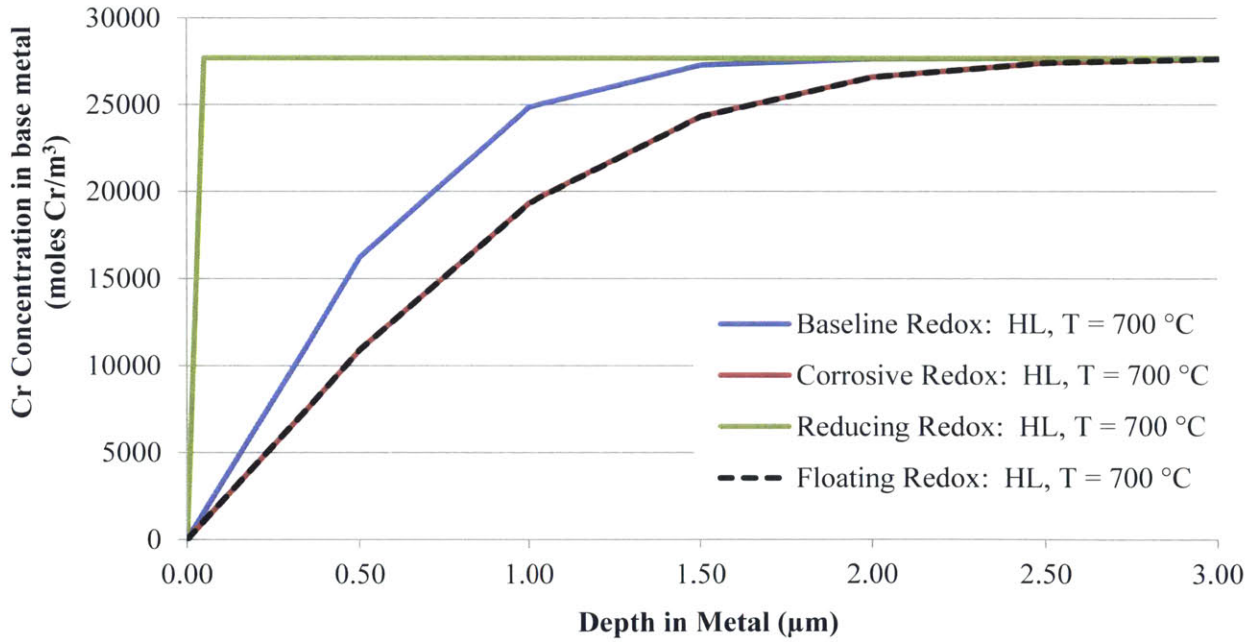

Figure 6.23: Cr concentration profile in the base metal after 200 EFPD at the exit of the hot leg for four different redox cases. Simulated with TRIDENT.

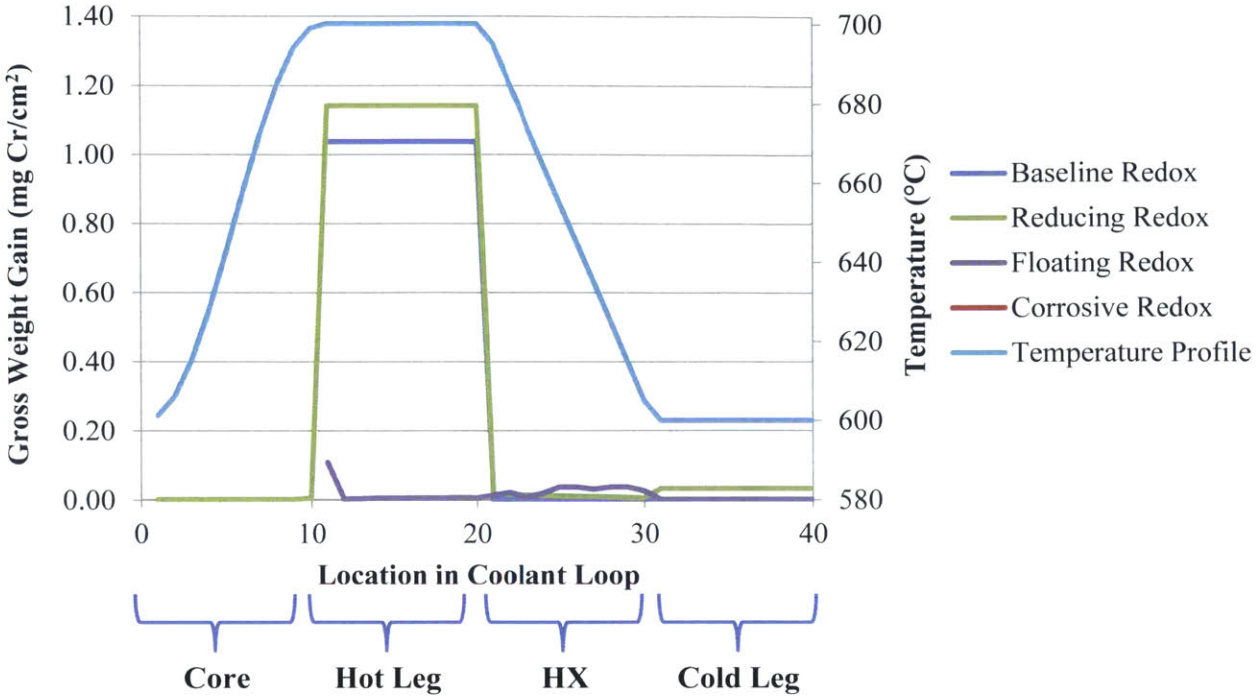

Figure 6.24: Gross weight gain due to Cr deposition at various points in the coolant loop after 200 EFPD. Simulated with TRIDENT.

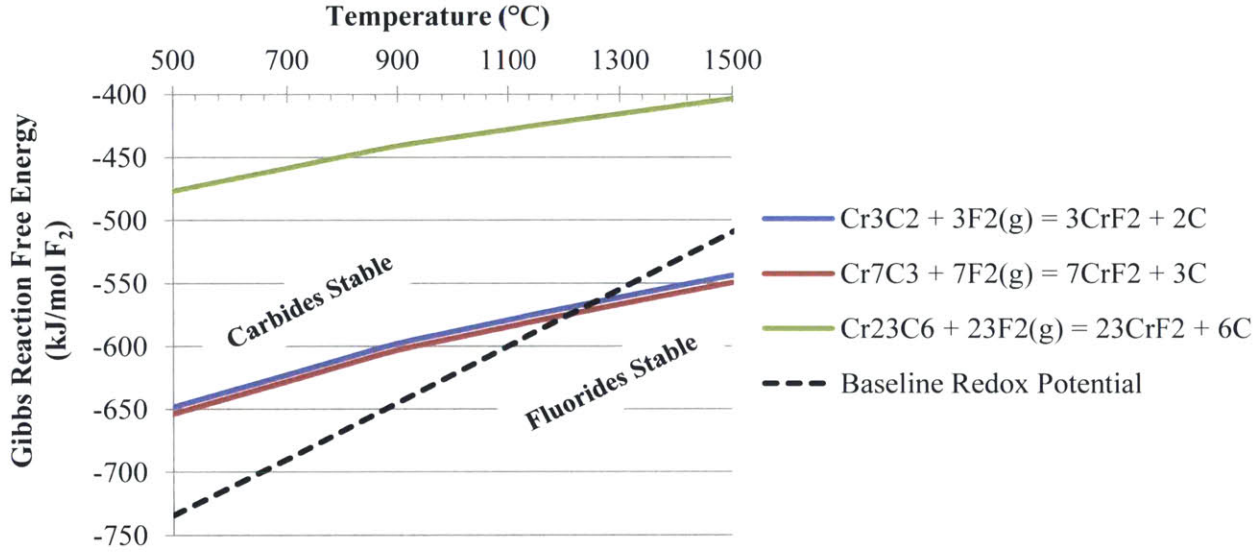

Figure 6.25: Gibbs reaction free energy for the reaction of chromium carbides with fluorine. Carbides are stable above the redox line. Fluorides are stable below the redox line. Calculated with HSC Chemistry v7.

Figure 6.26 shows the net weight change throughout the coolant loop after 200 EFPD due to the combined effects of Cr corrosion and deposition. The reducing redox case saw slight net weight gain in the core (< 0.004 mg/cm^2) due to Cr deposition on the core graphite. The baseline and reducing redox potentials saw net weight gain in the hot leg. The case of the corrosive and floating redox potentials saw net weight loss in the hot leg. The baseline, reducing, and corrosive cases all saw net weight loss in the heat exchanger. The floating redox case saw some net weight gain and some net weight loss in the heat exchanger. In this case, the net weight loss occurred in the hotter half of the HX while the net weight gain occurred in the cooler half. In the cold leg, the baseline, corrosive, and floating redox cases saw net weight loss, but the reducing case saw net weight gain in the cold leg. It is interesting to note that net weight loss occurred in both the hot leg and the cold leg in the case of the floating redox potential. The only location where net weight gain occurred in the floating redox case was in the cooler half of the HX. This demonstrates some mass transfer from a hot section to a cool section. This suggests that the direction of mass transfer depends not only on the reaction enthalpy of the corrosion reaction (whether it is endothermic or exothermic) but also whether or not the redox potential is actively controlled.

Figure 6.27 shows the chromium concentration profile at the point of greatest gross weight loss. The corrosive and floating cases saw greatest corrosion in the middle of the hot leg. The reducing and baseline cases saw the greatest corrosion in the middle of the heat exchanger. From each of these locations, the Cr concentration profile is plotted as a function of the depth in the metal. The metal-salt interface is at 0 on the x-axis. Greater amounts of Cr were lost in the corrosive and floating cases which show nearly identical concentration profiles, with the floating case losing slightly more Cr than the corrosive case. The baseline case lost slightly more Cr than the reducing case at the point of greatest corrosion. At the point of greatest Cr oxidation, the Cr depletion rate for the baseline and reducing redox cases is about 4.5 μm/yr, and for the floating and corrosive redox cases, this rate is about 5.5 μm/yr.

Figure 6.28 shows the dissolved chromium concentration in the reactor coolant (ppm) as a function of operating time. Recall that in each case, the initial Cr concentration in the coolant was 25 ppm. The reducing potential shows that it is so reducing that less than 0.5 ppm Cr is dissolved in the salt after the initial startup of the reactor. The Cr concentration in the coolant in the baseline case increases until it reaches the equilibrium Cr concentration in the coolant (at this particular redox potential) of 39 ppm. At this point, corrosion reactions continue, but the amount of Cr in the coolant is constant because the rate of corrosion is matched by the rate of deposition. In the corrosive case, the redox potential is so corrosive (-654.5 kJ/mol-F_2) that the Cr concentration in the salt will continue until it reaches the solubility limit for Cr in flibe.[12] The dissolved Cr concentration in the case of the floating redox potential increases more gradually due to a more balanced rate of corrosion versus deposition. In the absence of applied redox controls, the TF/Cr couple sets the redox

[12] To visualize this, refer to Figure 3.16 which shows that any redox potential more positive than -682 kJ/mol-F_2 will result in a solution saturated in dissolved Cr.

potential, which Figure 6.21 shows is near the baseline potential. Thus the Cr concentration from the floating case should increase until reaching roughly 39 ppm.

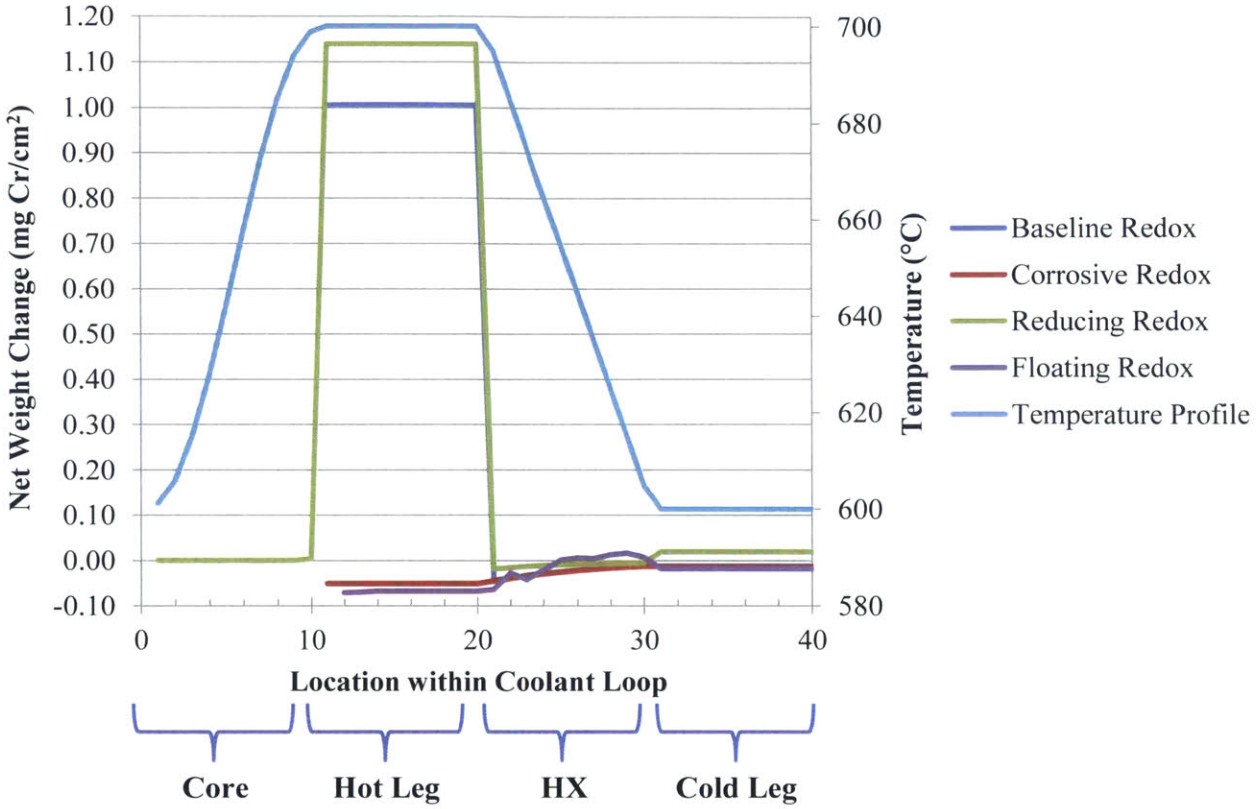

Figure 6.26: Net weight change due to the combined effects of Cr corrosion and deposition after 200 EFPD. Simulated with TRIDENT.

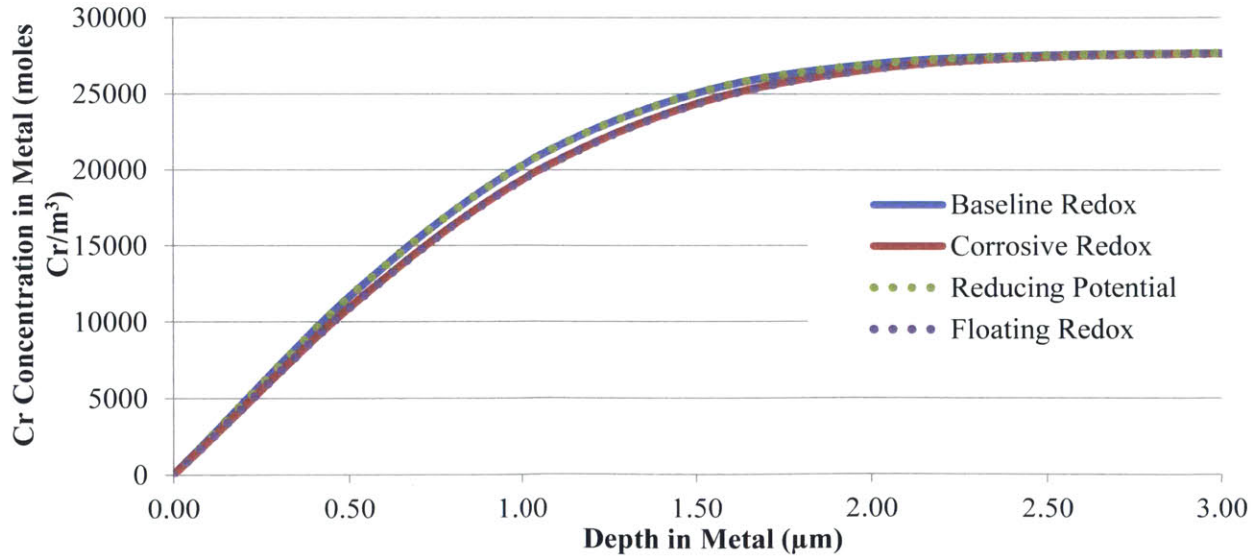

Figure 6.27: Concentration profile of Cr at the point of the loop with the highest corrosion weight loss after 300 EFPD. Simulated with TRIDENT.

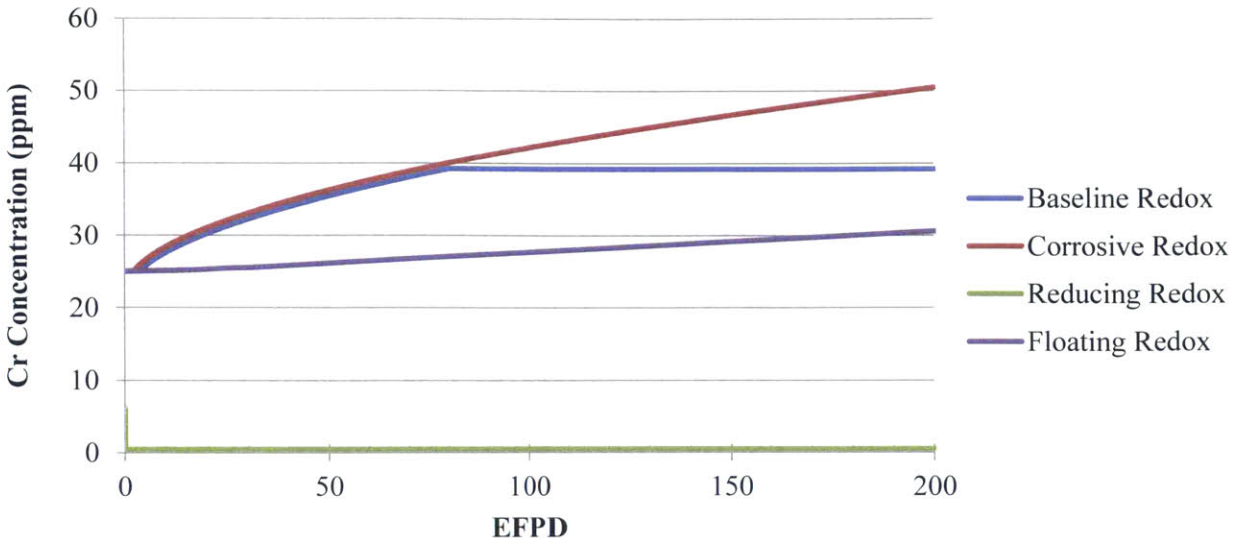

Figure 6.28: Concentration of Cr dissolved in the coolant. Simulated with TRIDENT.

This section (Section 6.5) has shown that the tritium release rates can be affected by the chosen redox potential in the salt and that there are corrosion implications of these redox choices. A more corrosive redox potential reduces tritium release rates, but incurs greater corrosion rates and higher dissolved Cr concentrations in the coolant. Given that the tritium release rate reduction from the more corrosive redox potential is only 50 Ci/EFPD lower than the baseline case, but the corrosion rates are substantially higher, it would seem that the baseline redox potential is still the best option.

6.6 TRIDENT Simulations to Evaluate Methods for Tritium Mitigation

Section 6.4, evaluated the baseline Mk1 PB-FHR configuration. The current section (Section 6.6) will propose methods and systems which could be used to modify the Mk1 PB-FHR in order to mitigate tritium releases. Due to the high fraction of tritium that permeates through the heat exchanger tube walls in a single coolant pass, these mitigation systems should be placed between the core exit and the heat exchanger entrance. Additionally, it will be shown that sufficient tritium removal cannot be achieved via a side-stream process where only a fraction of the coolant is diverted into an engineered system for tritium capture.

6.6.1 Investigation of the effect of PRF and HX material

The permeation reduction factor (PRF) is the ratio of the permeability of a material *without* a permeation barrier to the permeability of a material *with* a permeation barrier. Metal oxides are known to reduce hydrogen permeation through metals; however, they are generally unstable in fluoride salts. Thus, a metal oxide permeation barrier could only be applied on the air-facing side of the heat exchangers. The type of metal used for the heat exchanger also affects tritium mobility through the heat exchanger (HX) tube wall. For example, the hydrogen permeability in tungsten is

about four orders of magnitude less than that in Type 316 SS (refer to Table 2.8). Hydrogen diffusivity in tungsten is similar to that in Type 316 SS; however, the solubility of hydrogen in tungsten is about 5000 times less than in Type 316 SS. Table 2.9 summarizes the PRF gained from several types of oxide layers over their base metals. TRIDENT accounts for the effect of an oxide layer on the baseline Type 316 SS heat exchangers. The baseline PRF applied for this purpose is 10 for Cr oxide on Type 316 SS, suggested by Table 2.9. Other oxides may have higher PRFs. The SNAP program developed oxide coatings (comprised mainly of SiO_2, BaO, TiO_2, and ZrO_2) specifically for retaining hydrogen in uranium-zirconium-hydride fuel (see Section 2.6). In order to investigate the effect of PRF on the tritium release behavior from the Mk1 PB-FHR, a series of simulations were run with PRFs of 1, 10, 100, 500, and 1000. A simulation which specified tungsten as the HX material was also performed in order to determine the effects of using a lower permeability metal in the HX. Graphite uptake of tritium and refueling were accounted for. All other baseline parameters (see Table 6.1 and Table 6.2) were retained. The TRIDENT input options for the runs with various PRFs are summarized in Table 6.10. The same options were used for the simulation using a tungsten HX except that the PRF was set to 1, the HX metal hydrogen diffusivity came from Table 2.8, and the HX metal hydrogen solubility also came from Table 2.8.

Figure 6.29 through Figure 6.33 compare the simulations run with a range of PRF from 1 to 1000 applied to the heat exchanger between the salt coolant and the air-Brayton power cycle. Figure 6.29 shows the variation in the tritium release rate (Ci/EFPD) with time over a range of PRFs. The difference between a PRF of 1 and a PRF of 10 is not detectable on this plot. As the PRF is increased, the time required to reach the steady state is increased; however, the steady state release rate is unchanged. The pseudo-steady state reached prior to 10 days occurs when the rate of tritium release, birth, and capture on graphite are balanced. After 10 days, some amount of graphite saturation is occurring. Even though refueling is being simulated, the rate of pebble removal is lower than the rate at which tritium begins to saturate the graphite. The release rate slowly increases as tritium birth, release, and capture come to a final steady state after about 70 to 80 EFPD. Figure 6.30 shows the total activity of tritium (Ci) released to the power cycle. After 80 days, the total activity of tritium released with a PRF of 10 is 8300 Ci higher than that with a PRF of 1000. Figure 6.31 shows the circulating tritium activity in the coolant. There is a barely perceptible increase in the amount of tritium in the coolant when the PRF is 1000. After 80 EFPD, the circulating tritium activity for a case where the PRF = 10 is 26.7 Ci compared to 27.1 Ci for the case where the PRF is 1000. Figure 6.32 shows the total moles of tritium captured on the core graphite. Again, the difference between each case is difficult to discern. After 80 EFPD, with a PRF = 10, 2.78 moles of tritium atoms were captured on core graphite. After 80 EFPD, with a PRF = 1000, 2.80 moles of tritium atoms were captured on core graphite.

Figure 6.33 shows the amount of tritium retained within the tube walls of the heat exchanger. It is immediately evident that the higher the PRF, the more tritium is held within the heat exchanger tube wall. Given the small amount of change in the amount of tritium in the coolant and the amount of tritium captured on the graphite, the differences seen in the tritium release rates (Figure 6.29) are

due mostly to the fact that a higher PRF traps more tritium within the metal tubing of the heat exchangers. In fact, the amount of tritium in the HX tube walls differs by factors of the PRF in each case. With an oxide permeation barrier only on the air-facing side of the HX, there is no difference in the solubility and diffusivity of tritium at the salt-metal interface. Thus, tritium builds up in the metal due to the oxide layer on the downstream surface which slows tritium permeation out of the HX tube wall. Increasing the PRF reduces the permeability by a factor of the PRF; however, when the oxide layer only exists downstream of the tritium gradient, the tritium concentration in the HX metal tubing increases by the same factor. This means that the same release rate is attained with a PRF of 1 as with a PRF of 1000. The major difference is that it takes longer to reach this steady state with a larger PRF.

Because the boundary condition at the salt/metal interface considers the solubility of tritium, both in the metal and in the salt at the interface, the amount of tritium dissolved in the metal is never allowed to exceed the solubility for tritium in the metal. Thus, the formation of tritium bubbles in the metal should not occur. The solubility of tritium in flibe could be exceeded if sufficient tritium buildup occurred, however. Helium bubbles due to tritium decay in the metal could form if the tritium residence time in the metal were long enough. However, TRIDENT predicts that the residence time of a tritium atom in the metal is about 6 hours for a PRF of 10, 2 days for a PRF of 100, and about 16 days for a PRF of 1000.

Decay heat generated in the HX tube walls due to the radioactive decay of tritium dissolved in the HX metal will not be a problem. The decay heat from tritium is 0.32 watts/g [187]. With a PRF of 10, the equilibrium amount of tritium in the heat exchanger tube walls is 0.078 g and the total tritium decay energy throughout the entire HX is 0.025 watts. With a PRF of 1000, the equilibrium amount of tritium in the heat exchanger tube walls is 7.8 g, and the total decay energy throughout the entire HX is 2.5 watts.

Table 6.10: Input options for evaluating the effect of PRF on tritium releases from the Mk1 PB-FHR. Five simulations were run with five different PRFs. The same input was used for the simulation with a HX made of tungsten except that a PRF of 1 was used in that case and the hydrogen diffusivity and solubility in tungsten were used place of values for Type 316 SS.

Input Options	Value (and meaning)
`Loops`	1
`Days`	80
`Hour_Fraction`	0.1
`Elements`	6
`T_uptake`	2 (On, tritium uptake on graphite is simulated)
`CoreRefuelFrac`	1/30 (Pebble refueling is accounted for with a 30 day cycle)
`CoreGeometryAdjust`	2 (On)
`Redoxflag`	2 (TF and T_2 may exist subject to the redox option `Feedbackflag`)
`Feedbackflag`	2 (Redox potential is fixed at the baseline potential from Table 6.2)
`Oxideflag`	2 (oxide layer on air-side of HX is accounted for)
`PRFinput`	1, 10, 100, 500, and 1000
`Corrosionflag`	1 (corrosion is not simulated)
`Core_mesh`	10
`Hot_mesh`	10
`HX_mesh`	10
`Cold_mesh`	10
`GBflag`	Not used. Meaningless when `Corrosionflag = 1`
`C_Cr_initial_ppm`	Not used. Meaningless when `Corrosionflag = 1`
`Tritiumproductionflag`	3 the tritium production rate varies with time according to Eq (2.6)

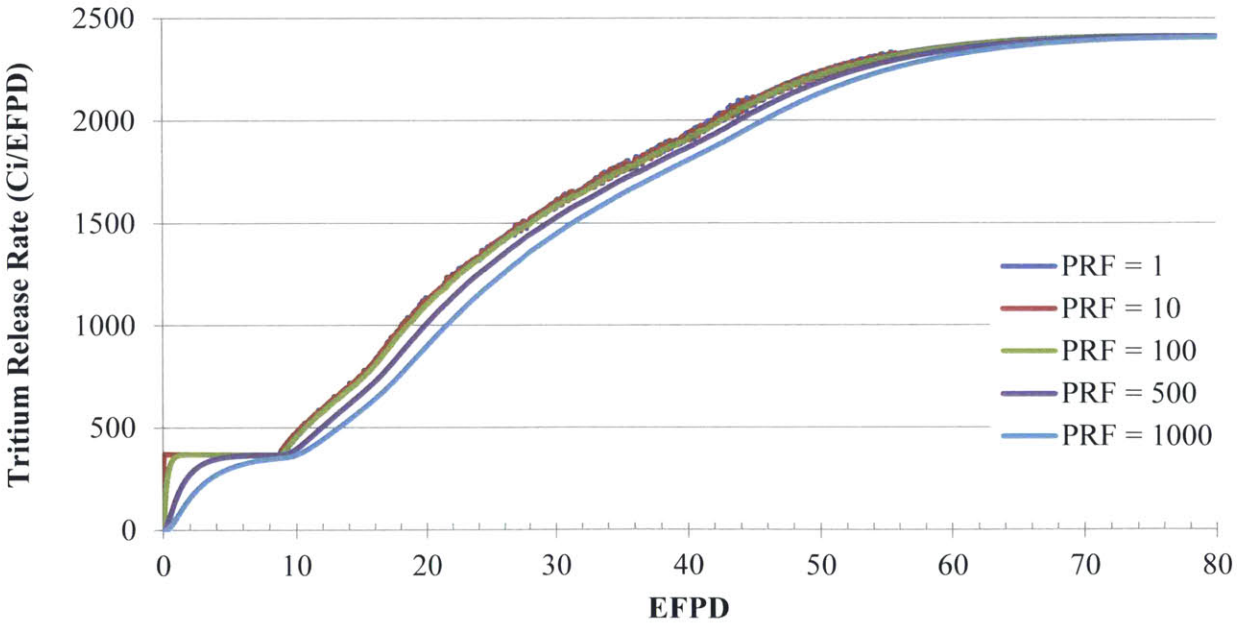

Figure 6.29: Tritium release rate (Ci/EFPD) for various PRF from 1 to 1000 from 0 to 80 EFPD. The baseline PRF is assumed to be 10. Calculated with TRIDENT.

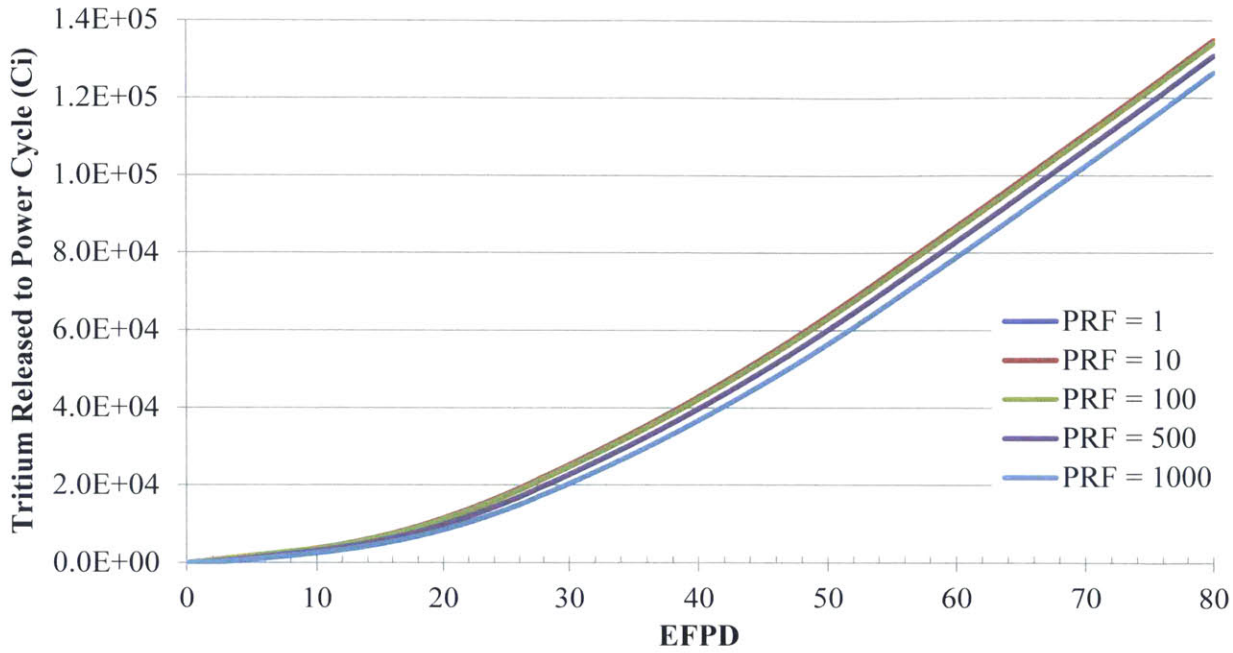

Figure 6.30: Tritium activity (Ci) released to the power cycle. Calculated with TRIDENT.

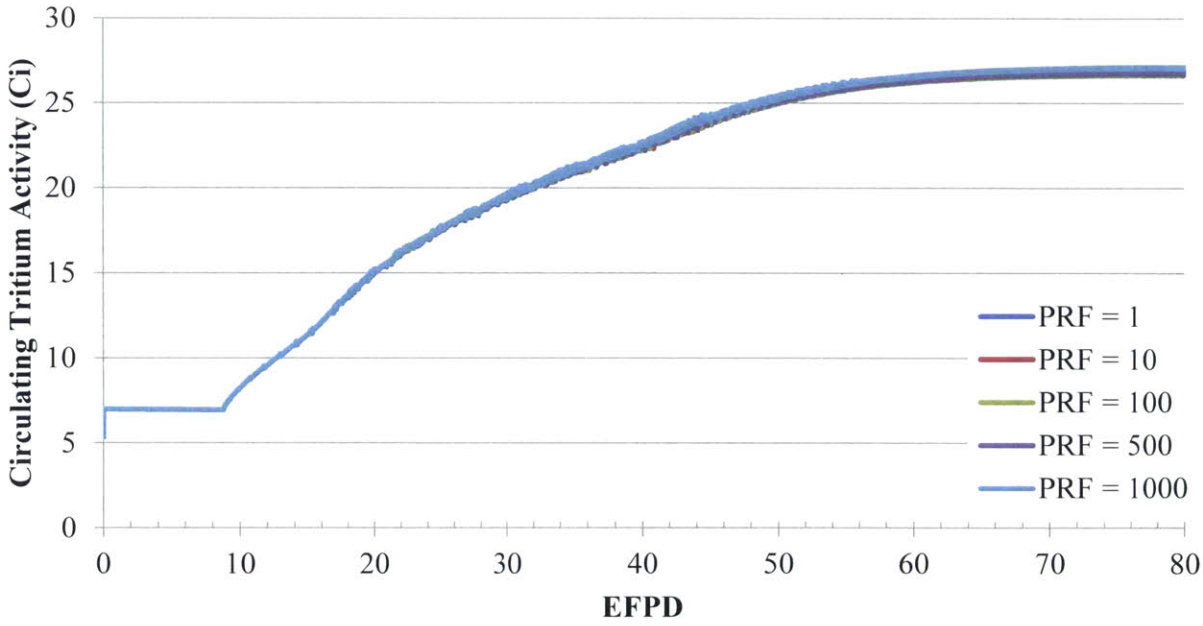

Figure 6.31: Tritium activity circulating in the salt coolant for various PRFs. Calculated with TRIDENT.

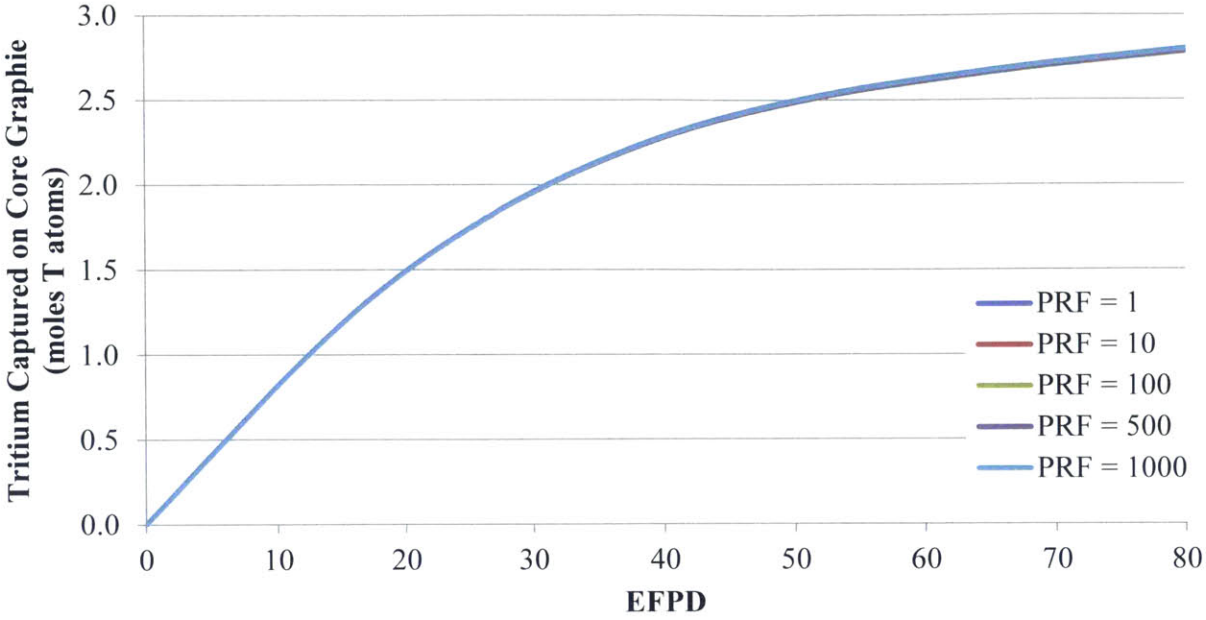

Figure 6.32: Moles of tritium atoms captured on core graphite vs EFPD. Calculated with TRIDENT.

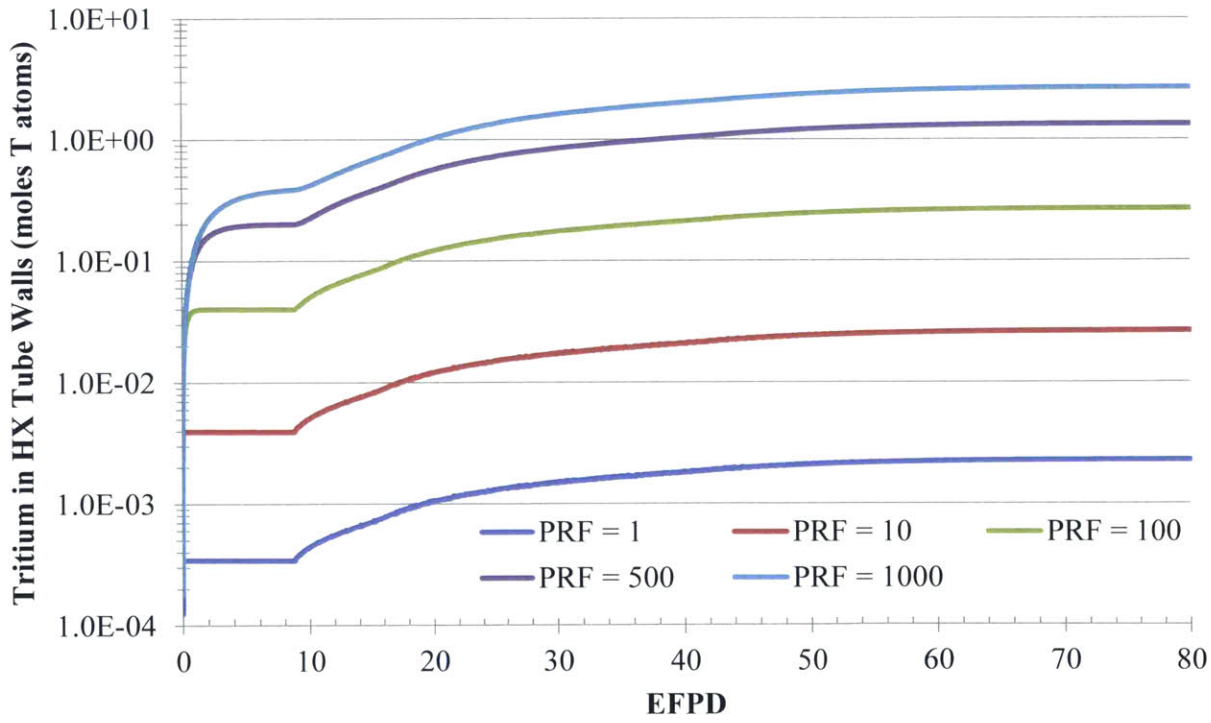

Figure 6.33: Moles of tritium atoms retained in the tube walls of the heat exchangers. Calculated with TRIDENT.

Above, it was shown that tritium builds up in the metal due to the oxide layer on the downstream surface which slows tritium permeation out of the air-facing side of the HX tube wall. When the oxide layer only exists downstream of the tritium gradient, the tritium concentration in the HX metal tubing increases by a factor of the PRF. This means that the same steady state release rate is ultimately attained with a PRF of 1 as with a PRF of 1000. Because structural metal oxides are not chemically stable in fluoride salts, they cannot be used for reducing tritium permeation on the flibe-facing surface of the HX tube wall. In order to reduce tritium permeation from the salt into the HX tube wall, a material which is chemically stable in flibe and which possesses a lower hydrogen permeability would be required. Tungsten has a lower permeability than Type 316 SS and is stable in flibe. (Calculations with HSC indicate that the stability of tungsten metal in flibe should be similar to that of nickel.) A simulation was carried out using the same Mk1 PB-FHR baseline conditions used in Section 6.4.3.[13] Graphite uptake of tritium and online refueling were accounted for. The only difference is that the PRF was set to 1 (in order to neglect the effect of any oxide layer) and the HX metal properties for tungsten were used in place of those for Type 316 SS. All other baseline parameters (see Table 6.1 and Table 6.2) were retained.

Figure 6.34 through Figure 6.37 compare the baseline case to a case utilizing a tungsten HX. Figure 6.34 shows that the tritium release rate is considerably lower when a W HX is used, and the time it takes to reach steady-state is considerably longer. The peak tritium release rate with the tungsten HX will be less than that in the baseline case because tritium permeability is much lower in tungsten and the tritium production rate from neutron transmutation will be lower by the time the peak rate is achieved (see Section 2.2 for an explanation). After 80 EFPD the release rate in the baseline case is 2410 Ci/EFPD. At 80 EFPD in the case with a W HX, steady state has not yet been achieved, and the release rate is 1440 Ci/EFPD. Figure 6.35 shows that the amount of tritium dissolved in the W HX is much less than in the baseline case. This is due to the lower solubility of tritium in tungsten. Figure 6.36 shows that since less tritium is going into the W HX, the amount of tritium circulating in the reactor coolant is greater. Because a greater amount of tritium is retained within the coolant system, the partial pressure of tritium in the coolant will increase and the graphite capacity for tritium will increase (see Section 2.4.2.2). Figure 6.37 shows that the result of this is that a greater amount of tritium is captured on the core graphite in the case using a W HX. By retaining more tritium in the primary system, more tritium could be removed and captured in a controlled manner using the systems discussed in Sections 6.6.2 through 6.6.4.

Due to cost and weight, tungsten is not likely to be a viable material for the HX. However, a tungsten (or similar low-permeability material) coating on the flibe-facing side of a Type 316 SS heat exchanger would be expected to provide similar benefits by greatly reducing the amount of tritium that enters the HX tube walls from the coolant. Because tungsten forms stable carbides, the Type 316 SS could first be coated with nickel and then a tungsten coating could be applied. This would

[13] The combination of tungsten and flibe requires that the (10 times slower) fsolve scheme be used for solving tritium transport at the salt/metal interface in TRIDENT. See Section 5.7.1 for a discussion of the two solution schemes employed by TRIDENT.

prevent tungsten from forming carbides with carbon from the stainless steel. This coating would also prevent TF and other impurities in flibe from selectively oxidizing Cr from the stainless steel.

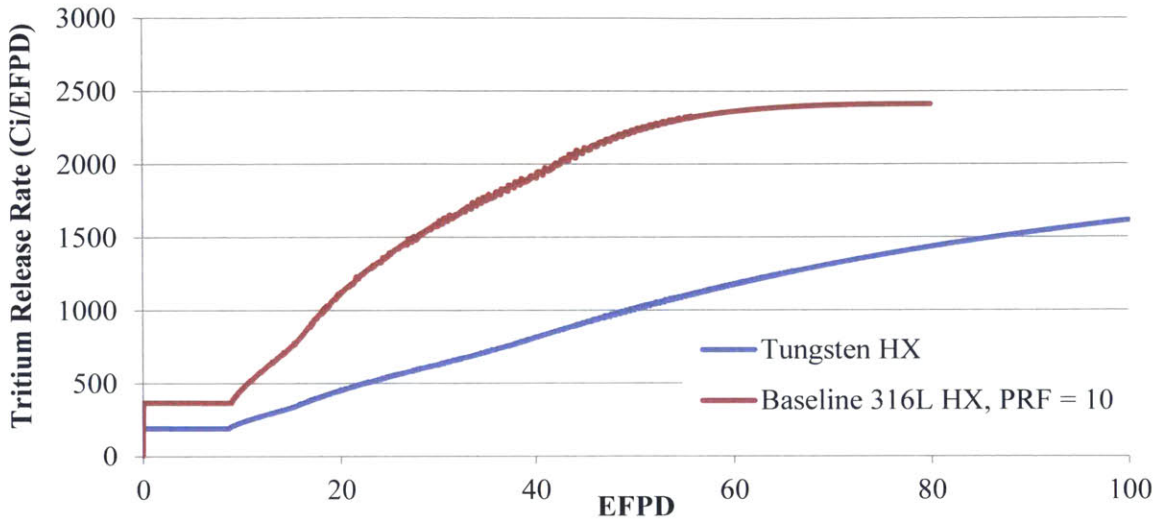

Figure 6.34: Tritium release rate for the baseline Mk1 PB-FHR compared to a case with a tungsten HX which is otherwise identical to the Mk1 PB-FHR case. Simulated with TRIDENT.

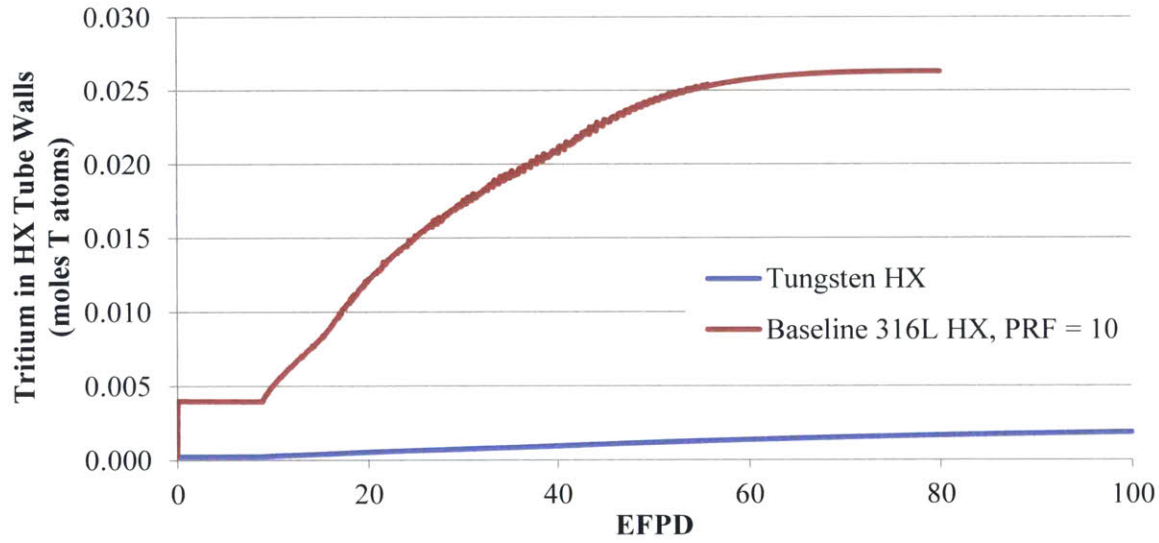

Figure 6.35: Comparison of the amount of tritium in the HX tube walls between the baseline case and the case with a tungsten HX. Simulated with TRIDENT.

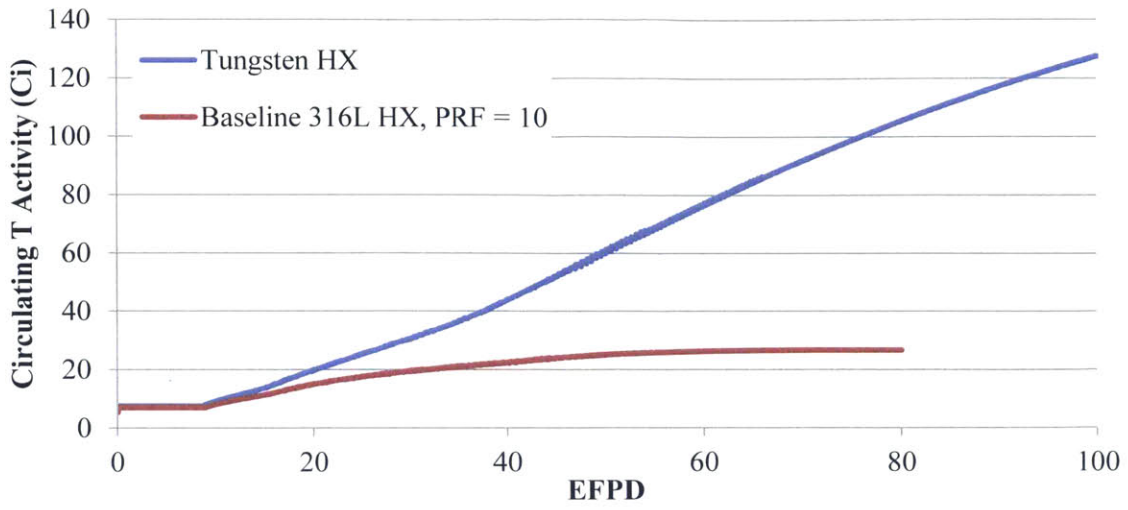

Figure 6.36: Comparison of the circulating tritium activity in the reactor coolant for the baseline case and the case with a tungsten HX. Simulated with TRIDENT.

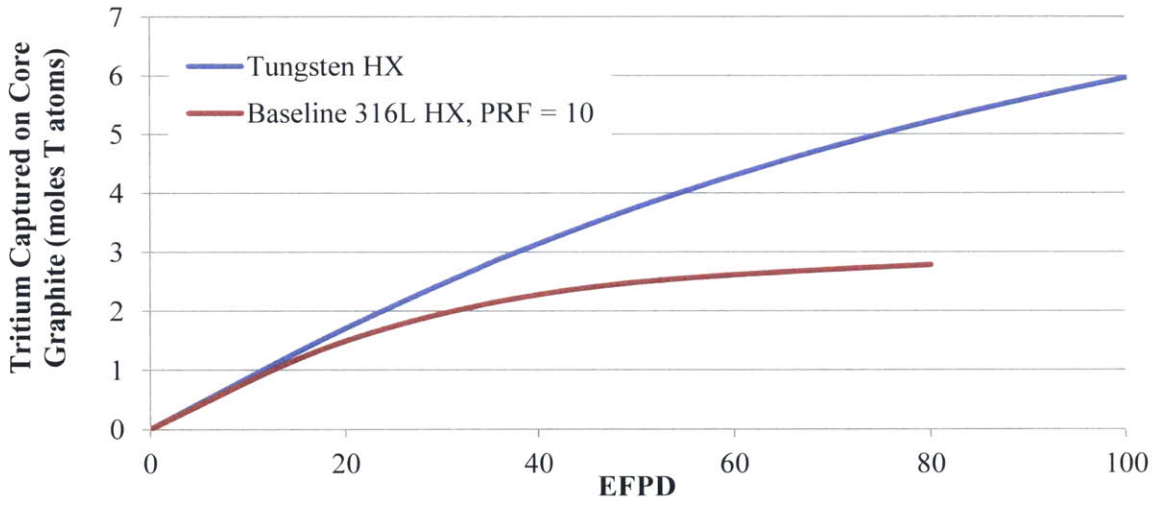

Figure 6.37: Comparison of the amount of tritium captured on core graphite for the baseline case and the case with a tungsten HX. Simulated with TRIDENT.

6.6.2 Tritium removal from coolant via permeation window

Permeation windows can be used for removing tritium from the coolant by passing tritium-laden coolant through tubing constructed from metal having a high permeability to hydrogen. Table 6.11 compares the hydrogen permeability of Type 316 SS with that of Ni and Pd. The coolant would flow through the inside of the tubing while a sweep gas (such as helium) would flow around the outside of the tubing in order to remove the permeated tritium for capture on a charcoal bed. The sweep gas

and the coolant never come into contact. Figure 6.38 is a schematic showing the placement of a proposed permeator within the FHR system. The permeator governing equations, mass balances, boundary conditions, and diffusion through the permeator tube walls are treated in the same way as they were in the heat exchanger (see Sections 5.6.2 and 5.7) except that there is no oxide layer on the permeator tubes.

Table 6.12 describes the input options that are required to simulate a permeation window in TRIDENT. Table 6.13 lists the specific values of the input options used for this simulation. In this case, the permeator specifications use the same tube outer diameter and tube wall thickness as the tubes in the heat exchanger. The total surface area of the permeator was specified to be twice the surface area of the heat exchanger. The total number of tubes in the permeator is the same as the total number of tubes in the heat exchanger. This means that the flow area in the permeator is the same as the flow area inside the heat exchanger. The only difference is that the length of tubing in the permeator is twice as long as the length of tubing in the heat exchanger. For this simulation, the permeator tubing is made of nickel instead of Type 316L SS. Nickel may not have the proper mechanical properties (its yield strength is less than half of that of Type 316L SS) and would be quite expensive, but it was chosen in order to test the performance of a permeator made of a metal having a higher permeability than Type 316 SS. Due to the availability of data, the diffusivity of tritium in Ni is assumed to be the same as the diffusivity of hydrogen in Ni. (The diffusivity of hydrogen in Ni could be modified to account for the kinetic isotope effect that would be expected with tritium; however, for conservativeness, this was not done.) The diffusivity of hydrogen in Ni is given by Eq (2.18), and the solubility (Sievert's law constant) of hydrogen in Ni is given by Eq (2.19). The constants used in these equations are listed in Table 2.6.

Table 6.11: Permeability of 316 SS, Ni, and Pd at 873 K.

Metal	Permeability (mol H_2/m-s-$MPa^{0.5}$) at 873 K	Reference
316 SS	5.5×10^{-8}	[110]
Ni	3.7×10^{-7}	[110]
Pd	2.5×10^{-5}	[111]

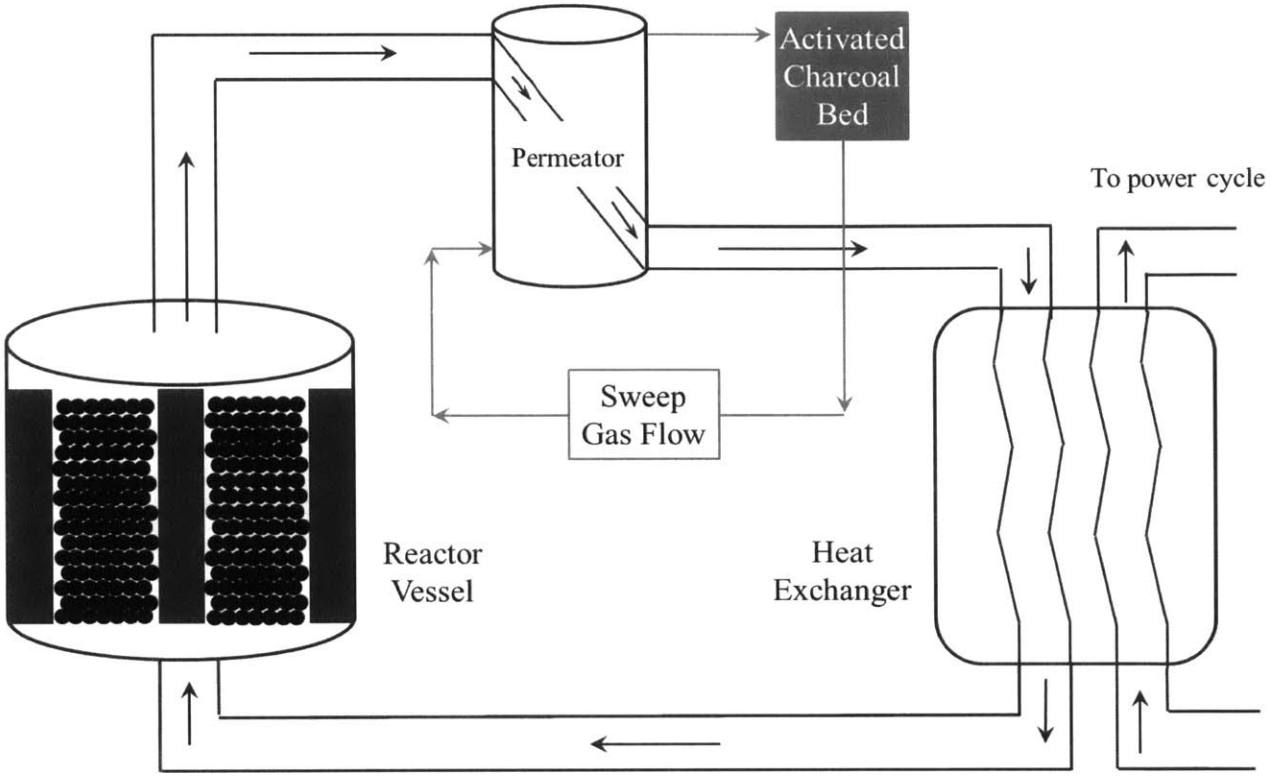

Figure 6.38: Schematic representation of proposed permeator (permeation window) for tritium removal from reactor coolant.

Table 6.12: Description of input options required to simulate a tritium permeation window in the reactor primary coolant in TRIDENT.

Input Option or Variable Name	Description/Meaning
PermeationFlag_primary	1 = off 2 = on, permeation window in the primary coolant is modeled
WindowArea_p	Surface area of primary system permeation window (m^2)
WindowThick_p	Thickness of primary system permeation window tube walls (m)
Permp_tube_od	Primary permeator tube outer diameter (m)
NumPermptubes_opt	1 = off, TRIDENT determines the number of permeator tubes such that the flow area in the permeator is equal to the flow area of the pipe feeding the permeator 2 = on, user specifies number of tubes in permeator
NumberofPermeatorTubes	Number of tubes in the permeator
PermElements	Number of radial elements for the finite difference diffusion solver

Table 6.13: Specific values used to simulate permeation window in the Mk1 PB-FHR using TRIDENT.

Input Option or Variable Name	Value (and meaning)
PermeationFlag_primary	2 (on, permeation window in the primary coolant is modeled)
WindowArea_p	20164 (Surface area of permeation window [m^2])
WindowThick_p	8.89×10^{-4} (Thickness permeation window tube walls [m])
Permp_tube_od	0.00635 (permeator tube outer diameter [m])
NumPermptubes_opt	2 (on, user specifies number of tubes in permeator)
NumberofPermeatorTubes	27360 (Number of tubes in the permeator)
PermElements	6 (Number of elements for the finite difference diffusion solver)

Figure 6.39 shows the tritium activity removed from the coolant via the permeator and the total tritium activity captured on the core graphite. Initially, tritium capture in the graphite has a high rate. Once the graphite begins to saturate around 16 EFPD, the rate of tritium removal through the permeator increases. Figure 6.40 shows the tritium release rates to the power cycle for the Mk1 PB-FHR without a permeator (with specifications described in Section 6.4.3) compared to a Mk1 PB-FHR with a permeator (having a surface area twice that of the heat exchanger) whose specifications were described above and summarized in Table 6.13. The tritium release rate for a permeator with a surface area equal to that of the heat exchanger is also plotted for comparison in Figure 6.40. By incorporating a permeator between the core outlet and the inlet to the heat exchanger, the peak tritium release rate is reduced from 2410 Ci/EFPD to 800 Ci/EFPD. This is a significant improvement, but not enough to reduce tritium release rates to LWR or HWR levels. Other tritium mitigation systems will be proposed and simulated in the following sections.

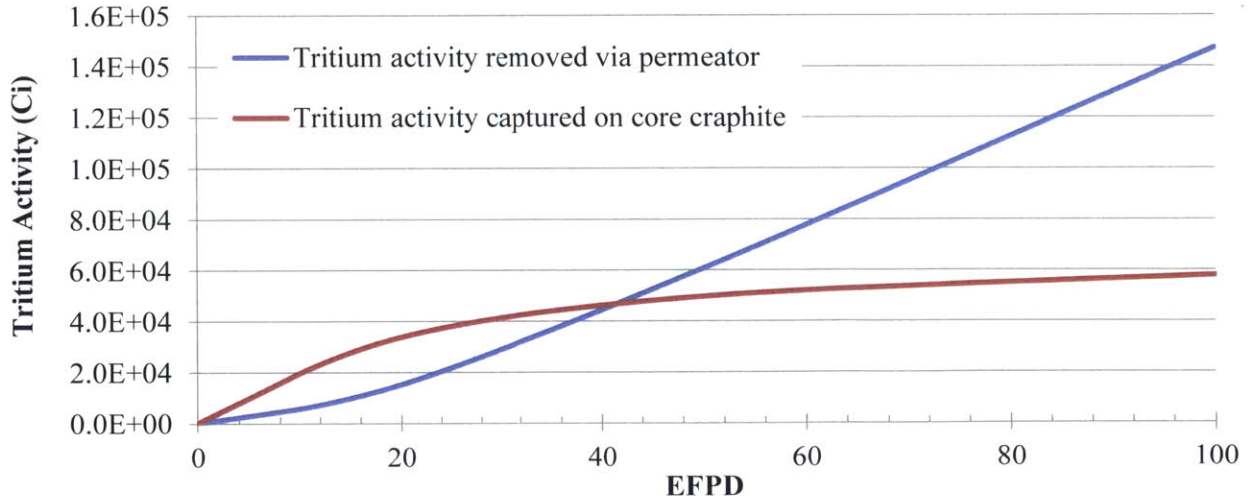

Figure 6.39: Total tritium activity removed from the coolant through the permeator and captured on core graphite. Simulated with TRIDENT.

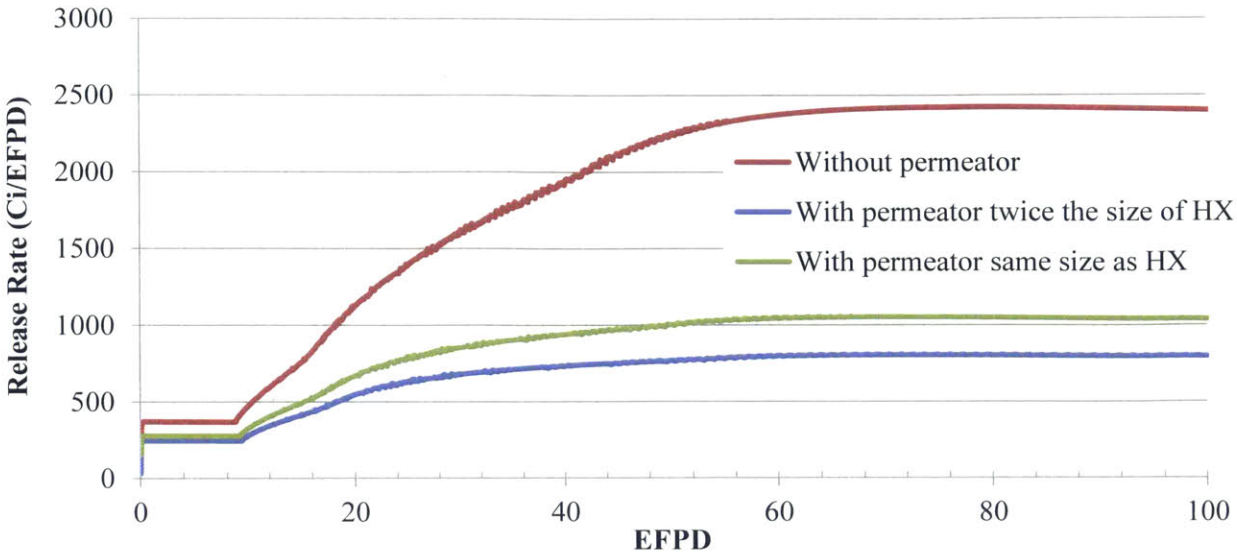

Figure 6.40: Tritium release rates to power cycle with and without a Ni permeator. Simulated with TRIDENT.

6.6.3 Tritium removal from coolant with gas stripping

Counter-current gas stripping is a common process in chemical processing. As depicted in Figure 6.41, a liquid (flibe) laden with a dissolved gas (tritium as TF and T_2) enters the top of the stripper. A stripping gas with zero or near-zero solubility in the liquid (such as helium) enters at the bottom of the stripper. In a series of stages, the dissolved gas (T_2 and some TF) is removed from the liquid into the gas stream which exits the stripper separate from the liquid stream. Due to a greater solubility in flibe, less TF than T_2 is removed from the salt via gas stripping. This type of system could be employed in the FHR for removing tritium from the coolant and trapping it for disposal. A schematic representation of this is given in Figure 6.42. Under certain circumstances, these systems have an analytical solution, but under other circumstances, algebraic or numerical solutions are required. Fortunately, a counter-current gas stripping system in the FHR lends itself to a relatively simple solution as an "equilibrium staged separation". Equilibrium staged separations are treated with the following assumptions [188]:

1. The solution is dilute. The concentration of tritium in the gas and liquid flows through the stripper are less than 1 mole %.
2. The gas stripper system is isothermal
3. The gas stripper system is isobaric
4. There is a negligible heat of absorption for TF and T_2 in flibe
5. The equilibrium line is straight, meaning that the energy balance is satisfied by #2 and #4.
6. The liquid (flibe in this case) is non-volatile

7. The stripping gas is insoluble
8. The total flow rate of solute and gas are constant

With these assumptions, the Kremser equations as presented by Wankat and reproduced in Eq (6.1) and Eq (6.2) can be used [188]. In these equations, N represents the number of stripping stages, V represents the stripping gas flow rate (mol/s), L represents the salt flow rate (mol/s), m is the inverse of the Henry's law constant (in units of mol T_2 or TF/mol flibe-atm) for TF or T_2 in the salt. The variable x_N is the concentration of T_2 or TF in the salt (mole TF or T_2 per mole salt) exiting the final stage of the stripper. The variable x_N^o is the concentration of T_2 or TF in the salt (mole TF or T_2 per mole salt) entering the first stage of the stripper. In Eq (6.2), y_{N+1} is the concentration of T_2 or TF in the gas stream entering the stripper (mole T_2 or TF per mole gas). If it is assumed that the gas entering the stripper is free of tritium (*i.e.* all tritium is removed from the gas stream after it exits the top of the stripper prior to the gas returning to the stripper entrance), then y_{N+1} is set to zero, as is common practice. The MSRE captured fission products from the helium sparge gas using a bed of activated charcoal [66]. A similar approach could be used here as illustrated in Figure 6.42. The variable b is the intercept of the equilibrium line for the stripper, which is commonly taken as zero [188]. Thus, x_N^* is zero for this analysis. One other assumption that is made is that T_2 and TF do not interact, meaning each component (T_2 and TF) can be treated separately, and calculations for each can be done in-series rather than simultaneously [188]. A mass balance around the stripper is used to account for the amount of tritium flowing into the stripper in the salt and the amount of tritium exiting the stripper in the salt. Assuming that the stripper operates at equilibrium within each time step, the difference between x_N^o and x_N can be calculated with Eq (6.1). When the difference between x_N^o and x_N is multiplied by the coolant molar flow rate (L), the rate of tritium removal from the salt is given (mol T_2 or TF/s). The amount of tritium in the salt exiting the stripper is then updated accordingly.

In order to simulate gas stripping, TRIDENT requires certain input options and specifications for the stripper. The options and specifications required to model a counter current gas stripper in TRIDENT are described in Table 6.14 and the specific values used for the simulation are given in Table 6.15. Except for the addition of the gas stripping system described in Table 6.14 and Table 6.15, the other input options are the same as those used for the simulation of the standard Mk1 PB-FHR configuration in Section 6.4.3.

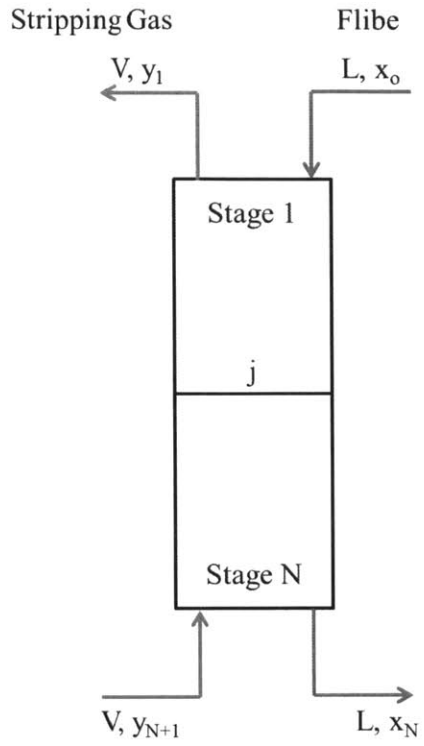

Figure 6.41: Schematic of multi-stage counter-current gas stripping.

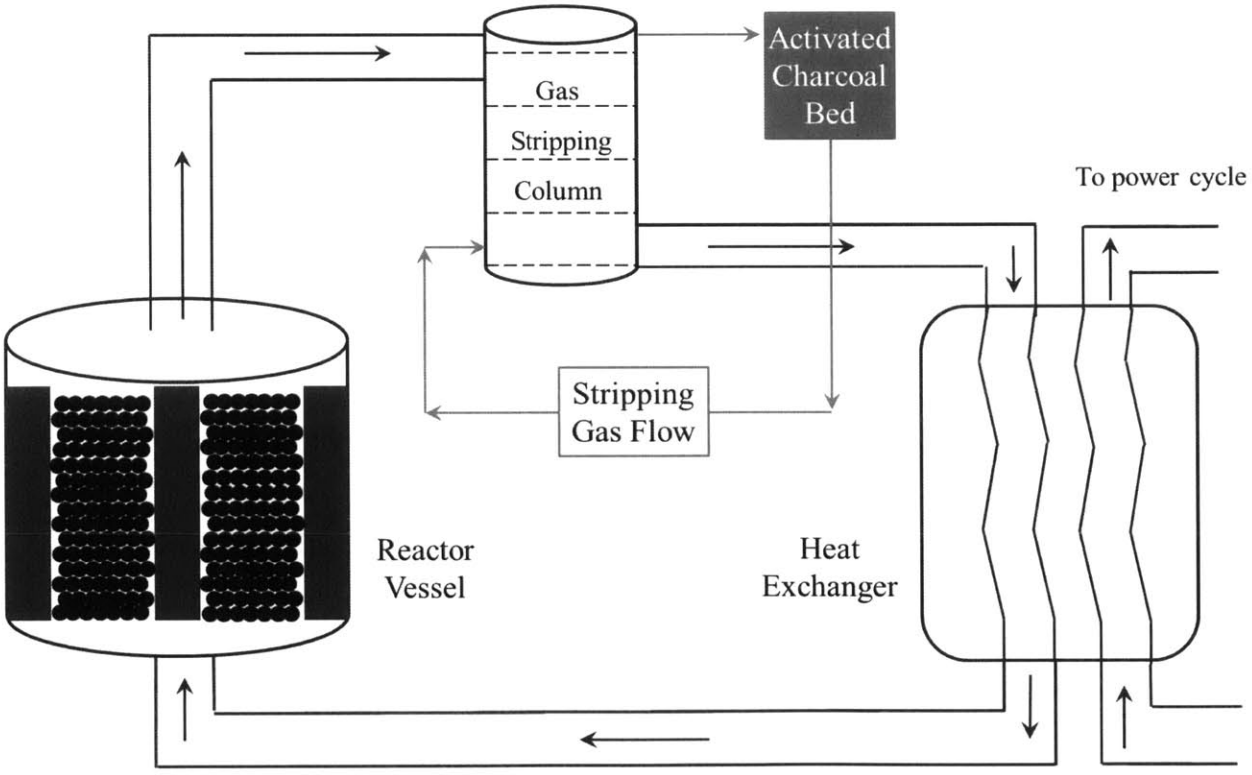

Figure 6.42: Schematic of a PB-FHR with a multi-stage countercurrent gas stripper and charcoal bed for removing tritium from the stripping gas.

$$\frac{x_N - x_N^*}{x_o - x_N^*} = \frac{1-\left(mV/L\right)}{1-\left(mV/L\right)^{N+1}} \tag{6.1}$$

$$x_N^* = \frac{y_{N+1} - b}{m} \tag{6.2}$$

Table 6.14: Options and specifications for gas stripping of tritium from the coolant.

Input Option or Variable Name	Description/Meaning
GasStrippingFlag	Turn on/off countercurrent gas stripping. 1 = off 2 = gas stripping simulated in the primary coolant only 3 = gas stripping is simulated in the secondary coolant only (if Loops= 2) 4 = gas stripping is simulated in both the primary and secondary coolant (if Loops= 2)
StrippingFlowFraction_p	Fraction of the primary coolant that is diverted to the gas stripper. If 1, all coolant flow goes through the stripper. If 0.1, only 10% of the coolant flow passes through the stripper
StrippingFlowFraction_s	Fraction of the secondary coolant (if Loops= 2) that is diverted to the gas stripper. If 1, all coolant flow goes through the stripper. If 0.1, only 10% of the coolant flow passes through the stripper
NStages_p	Number of stripping stages in the primary gas stripper
NStages_s	Number of stripping stages in the secondary gas stripper
Gas_hrflowrate_p	Stripping gas flow rate (L/hr at STP)
Gas_hrflowrate_s	Stripping gas flow rate (L/hr at STP)

Table 6.15: Specific values of input options used to simulate a gas-stripper in the Mk1 PB-FHR in TRIDENT.

Input Option or Variable Name	Value (and meaning)
GasStrippingFlag	2 (gas stripping simulated in the primary coolant only)
StrippingFlowFraction_p	0.5 (50% of the coolant flow passes through the stripper)
StrippingFlowFraction_s	N/A
NStages_p	10 (Number of stripping stages in the gas stripper)
NStages_s	N/A
Gas_hrflowrate_p	20000 (Stripping gas flow rate [L/hr at STP])
Gas_hrflowrate_s	N/A

As indicated in Table 6.15, the gas stripping system simulated here is a large system in which 50% of the coolant flow is diverted to the stripper. Fifty percent of the reactor coolant flow rate is 498 kg/s (250 L/s). A stripping gas flow rate of 2.0×10^4 L/hr (5.6 L/s) was specified. Increasing the number of stages and/or the stripping gas flow rate has a non-linear effect with diminishing returns. With the system as specified in Table 6.15, increasing the number of stripping stages or the stripping gas flow rate further yield very small improvements in the rate of tritium removal from the coolant.

Figure 6.43 shows the rate of tritium release to the power cycle for the base Mk1 PB-FHR system with and without the stripping gas system. The peak release rate is reduced from 2410 Ci/EFPD to 439 Ci/EFPD. Figure 6.44 shows the total activity of tritium removed from the coolant via the stripping gas system. Figure 6.45 shows the total activity of tritium captured on the graphite in the reactor core. Typical side streams used for processing coolant in LWRs might take 10% of the coolant flow. The stripping system simulated here takes 50% of the coolant flow. Given that a system this large can only reduce the peak tritium release rate to 439 Ci/EFPD, it does not appear that a gas stripping system will be feasible for an FHR.

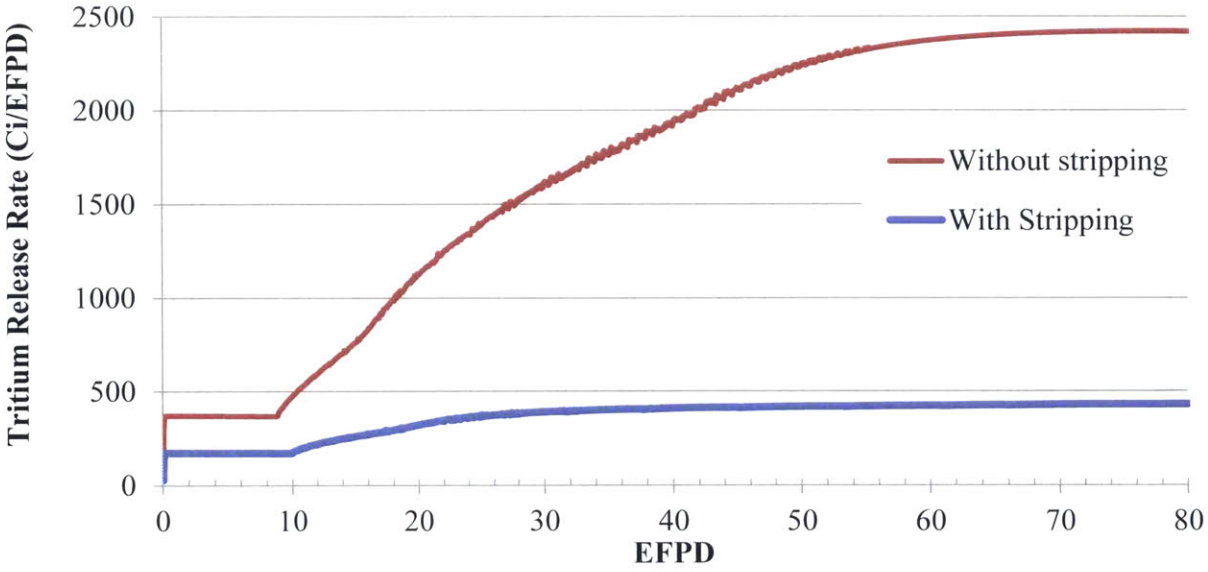

Figure 6.43: Tritium release rates to power cycle with and without a gas stripping system. Simulated with TRIDENT.

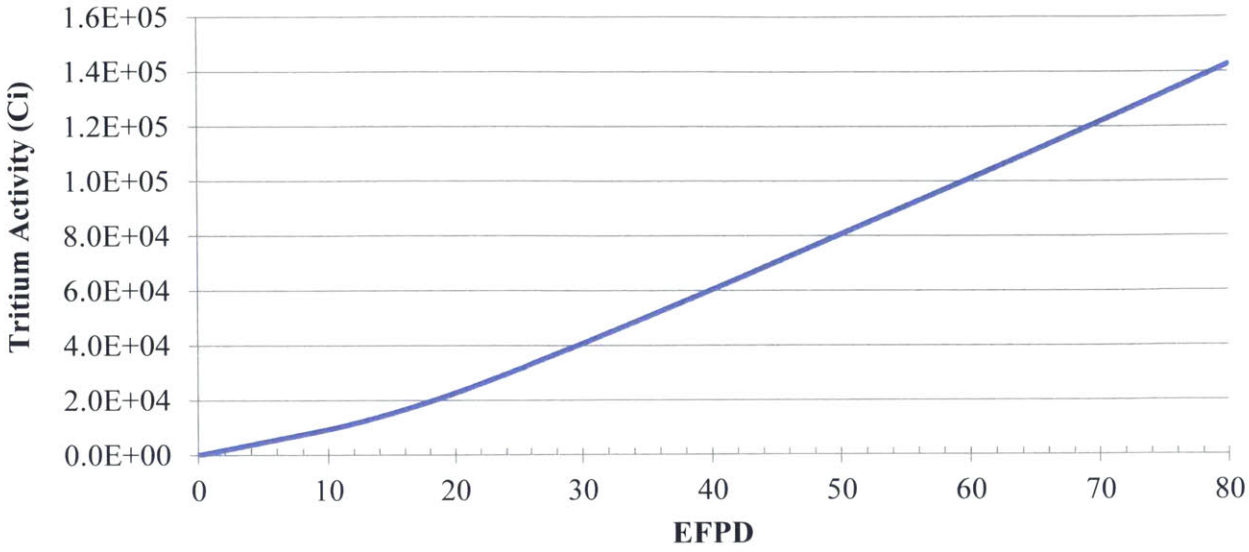

Figure 6.44: Total activity of tritium removed from the coolant via the gas stripping system. Simulated with TRIDENT.

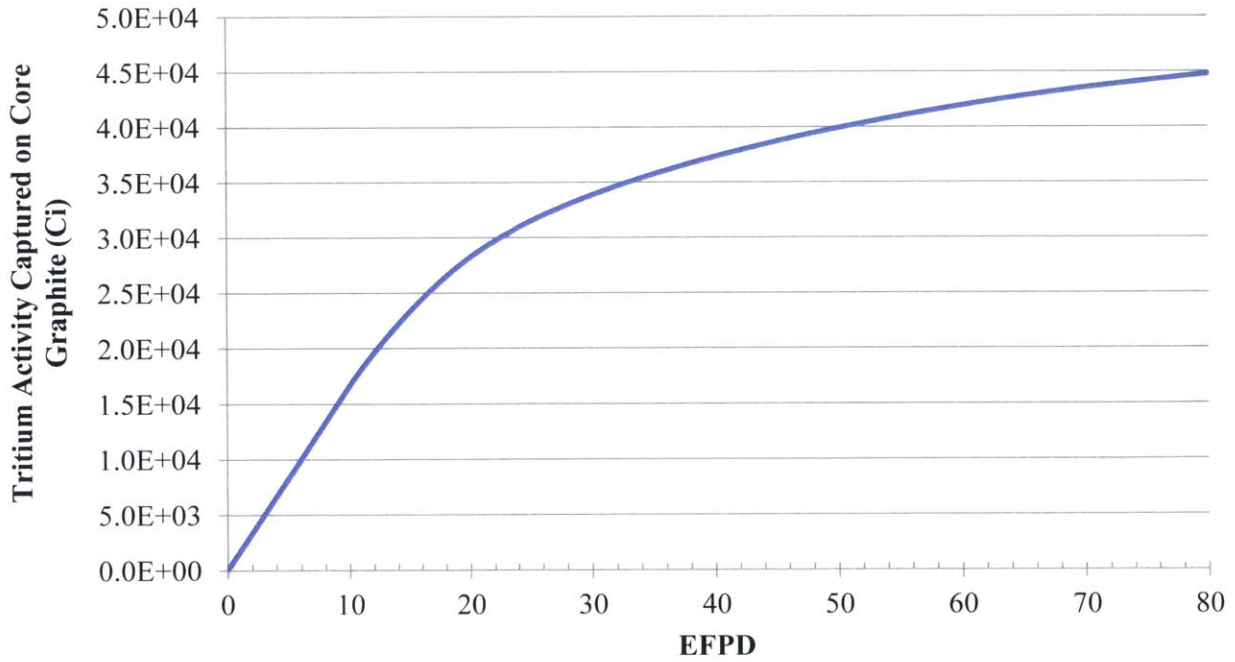

Figure 6.45: Total tritium activity (Ci) captured on core graphite when a gas stripper is incorporated in the system. Simulated with TRIDENT.

6.6.4 Tritium capture on a packed bed of graphite

It is well known that graphite is a strong sink for tritium (and hydrogen in general). Section 2.4 reviewed experimental determinations of hydrogen uptake on graphite. The MSRE found that about 15% of the total tritium produced during the lifetime of MSRE operations had been captured on the graphite moderator [66]. Both TF and T_2 can be removed from the salt via absorption on graphite

[50]. This distinguishes graphite capture of tritium from permeation windows which only remove T_2 from the salt. Section 6.4.1 used TRIDENT to simulate the operation of the Mk1 PB-FHR without the effect of tritium capture on the core graphite. Section 6.4.3 simulated operation with the effect of tritium capture on the core graphite with refueling. Comparing these two simulations, the effect of graphite capture of tritium reduces the steady state release rate from 2770 to 2410 Ci/EFPD. Furthermore, without the effect of graphite capture, the steady state is reached after about 5 hours of reactor operation. Including the effect of tritium capture on graphite delays the attainment of steady state to 70 EFPD. There is large potential for the use of graphite for capturing and storing tritium in order to manage its escape to the power cycle.

Here, a packed bed of graphite spheres is proposed for capturing tritium. Figure 6.46 provides a simple schematic of the proposed system for tritium capture. All of the coolant exiting the core would pass through this packed bed of graphite, and tritium would be captured from the coolant onto the graphite prior to the coolant entering the heat exchangers. There are a number of variables for the design of such a packed bed. Variables such as the sphere size, type of graphite, vessel height, vessel diameter, vessel orientation (vertical or horizontal) could all be altered. The vessel could even be designed to allow for online regeneration of the graphite spheres. Essentially the same mechanisms used for online refueling in the core might be applied to online regeneration of the graphite in the packed bed. The packed bed of graphite is modeled in the same manner as the graphite in the core.

A series of simulations were completed using TRIDENT in order to determine the effectiveness of a packed bed of graphite for capturing tritium and mitigating tritium escape to the power cycle. Because the graphite in this packed bed will exist outside of the core, many options exist for choosing the size of the graphite spheres and the type of graphite used in the packed bed. Smaller graphite spheres could be used in order to increase the graphite surface area. Non-nuclear grades of graphite could be attractive options for use in the packed bed. For example, the activated graphites AX-21, GX-31, and Maxsorb have high BET surface areas (up to about 4000 m^2/g) and high specific hydrogen capacities [70]. For these initial simulations, conservative choices were made, however. Graphite spheres identical in size to the fuel pebble spheres were specified. The type of graphite used in the packed bed was also specified to be the same as that used in the matrix of the fuel pebbles (IG-110U). The equation used for tritium capacity is the same as that used for the core graphite and was given in Eq (2.8) from work performed by Atsumi *et. al.* on ISO-88 graphite in reference [86]. As discussed in Section 2.4.2.2, depending on the study, ISO-88 has a specific capacity for tritium comparable to similar grades of graphite (such as IG-110U).

In order to simulate a bed of graphite for tritium capture, new input options were added to TRIDENT. The input option `Tritiumcapturebedflag` turns on/off the packed bed of graphite spheres. To turn on this feature, this variable is set to 2. To turn this feature off, this variable is set to 1. Several variables for the packed bed must also be specified. The fraction of the packed bed which is replaced online per day is specified using the input variable `Bed_frac_rep`. If `Bed_frac_rep` is set to 0, then online bed regeneration is not simulated. If this variable is set to 1/30, then $1/30^{th}$ of the bed is regenerated each day. The definition of the packed bed specifications

are summarized in Table 6.16. For the first simulation of a packed bed of graphite, the input options and packed bed specifications are summarized in Table 6.17. Graphite pebbles of 3 cm diameter (the same size as used for the fuel pebbles) were used in the absorber bed. The height of the bed is not specified. Instead, the desired graphite surface area is specified, and then TRIDENT calculates the height of the bed given the desired bed radius, packing fraction, and graphite pebble (or particle) radius. The height of the bed corresponding to the specifications in Table 6.17 is 3.58 m. The pressure drop across this bed is 0.496 atm, and the Reynolds number in the bed is 1980.

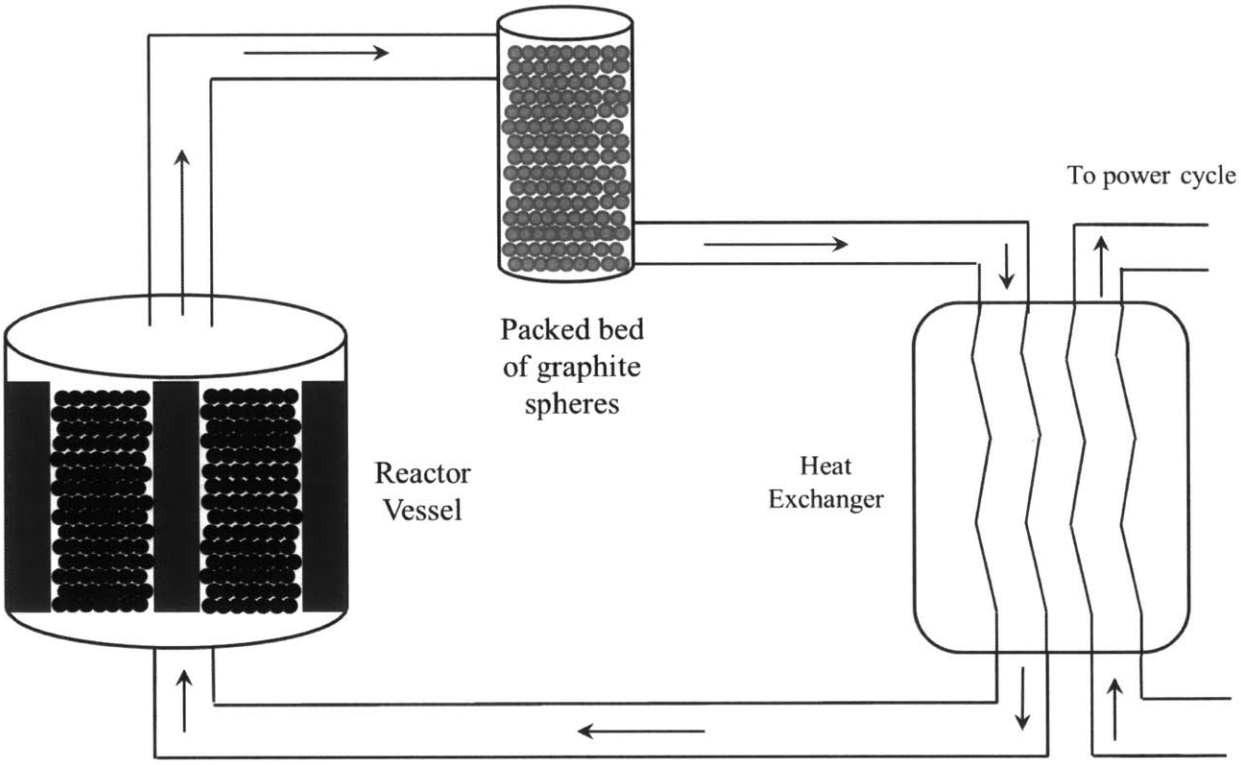

Figure 6.46: Schematic of proposed graphite bed for capturing tritium from the coolant prior to the heat exchanger.

Table 6.16: Input option and specifications required to simulate a packed bed of graphite for tritium adsorption in TRIDENT.

Input Option/Variable Name	Description/Meaning
Tritiumcapturebedflag	Turn on/off packed bed of graphite. 1 = off, 2 = on
Bed_frac_rep	Fraction of the packed bed replaced per day
Bed_vessel_radius	Inner radius of the packed bed [m]
Bed_surface_area	Total graphite surface area in the packed bed [m^2]
Particle_radius	Radius of the graphite particles in the packed bed [m]
Particle_density	Density of graphite [g/m^3]
Bed_packingfraction	Packing fraction in the bed

Table 6.17: Input options and packed bed specifications for the first packed bed simulation.

Input Options	Value (and meaning)
Loops	1
Days	500
Hour_Fraction	0.2
Elements	6
T_uptake	2 (On, tritium uptake on graphite is simulated)
CoreRefuelFrac	1/30 (Pebble refueling is accounted for with a 30 day cycle)
CoreGeometryAdjust	2 (On)
Redoxflag	2 (TF and T_2 may exist subject to the redox option Feedbackflag)
Feedbackflag	2 (Redox potential is fixed at the baseline potential from Table 6.2)
Oxideflag	2 (oxide layer on air-side of HX is accounted for)
PRFinput	10 (permeation reduction factor)
Corrosionflag	1 (corrosion is not simulated)
Core_mesh	10
Hot_mesh	10
HX_mesh	10
Cold_mesh	10
GBflag	Not used. Meaningless when Corrosionflag = 1
C_Cr_initial_ppm	Not used. Meaningless when Corrosionflag = 1
Tritiumproductionflag	3 the tritium production rate varies with time according to Eq (2.6)
Tritiumcapturebedflag	2 (on)
Bed_frac_rep	0 (no bed regeneration) and 1/30 ($1/30^{th}$ of bed regenerated per day)
Bed_vessel_radius	1.2 (Inner radius of the packed bed [m])
Bed_surface_area	1945.3 (Total graphite surface area in the packed bed [m^2])
Particle_radius	0.015 (Radius of the graphite particles in the packed bed [m])
Particle_density	1.77×10^6 (Density of graphite [g/m^3])
Bed_packingfraction	0.60 (Packing fraction in the bed)

Figure 6.47 shows the tritium release rate (Ci/EFPD) when a bed of stationary graphite spheres having the same graphite surface area as the reactor core is located between the core outlet and the entrance to the heat exchangers. At very early operating times, there is a quick increase to a release rate of about 3 Ci/EFPD. This rate is maintained for about 3 EFPD. At this point, saturation behavior begins to affect the tritium uptake rate on the graphite. There is a period from about 5 EFPD to 35 EFPD where the release rate remains relatively flat at an average of 80 Ci/EFPD. The release rate then begins to increase again until it reaches a steady state value of about 2050 Ci/EFPD at about 300 EFPD. After 300 EFPD, the release rate slowly decreases due to the consumption of the initial Li-6 loading in flibe.

Figure 6.48 shows the total amount of tritium captured on graphite in both the core and on the graphite bed. Since the fuel pebbles are refueled online in the core, tritium absorption on graphite in the core continues and does not level off. On the other hand, since the graphite in the absorber bed is fixed, it eventually reaches saturation after about 300 EFPD. At this point, the bed cannot absorb any more tritium. The same number of pebbles as in the core is used in the bed. Because the graphite

pebbles in the absorber bed are un-fueled, each un-fueled pebble has a greater mass of graphite than in an equivalently sized fuel pebble. Since tritium capacity on graphite is given in terms of a specific capacity (moles T/g graphite, see Section 2.4.2), an un-fueled pebble has a greater capacity for tritium than an equivalently sized fuel pebble.

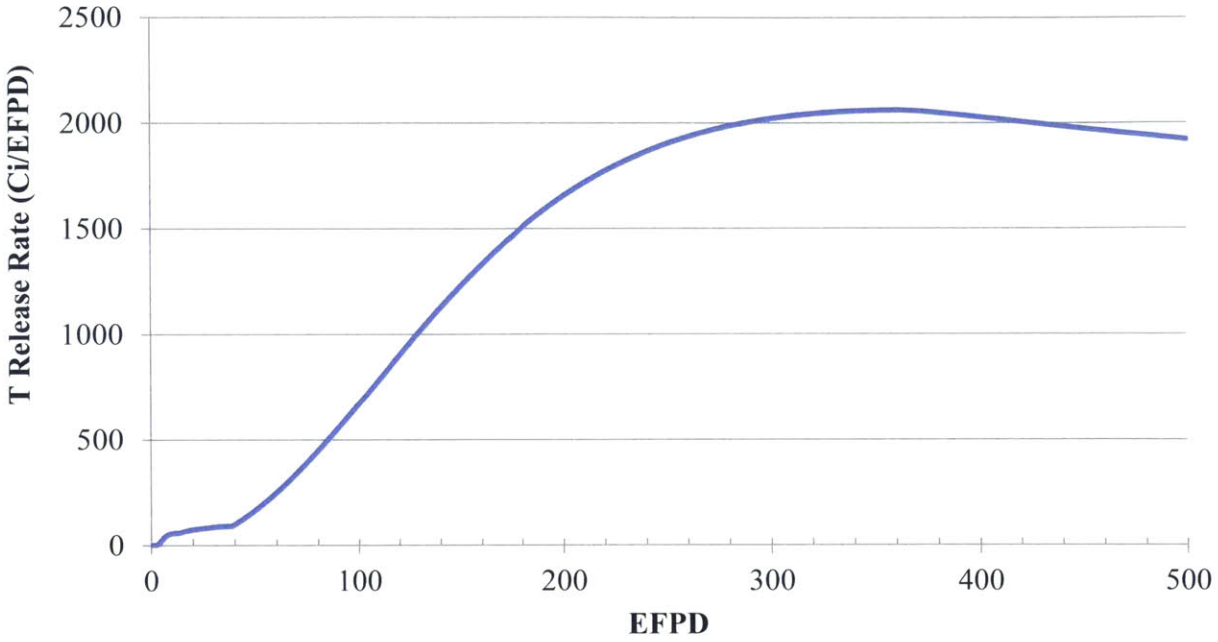

Figure 6.47: Tritium release rate (Ci/EFPD) when a bed of stationary graphite specified by Table 6.17 is placed between the reactor core and the heat exchanger. Simulated with TRIDENT.

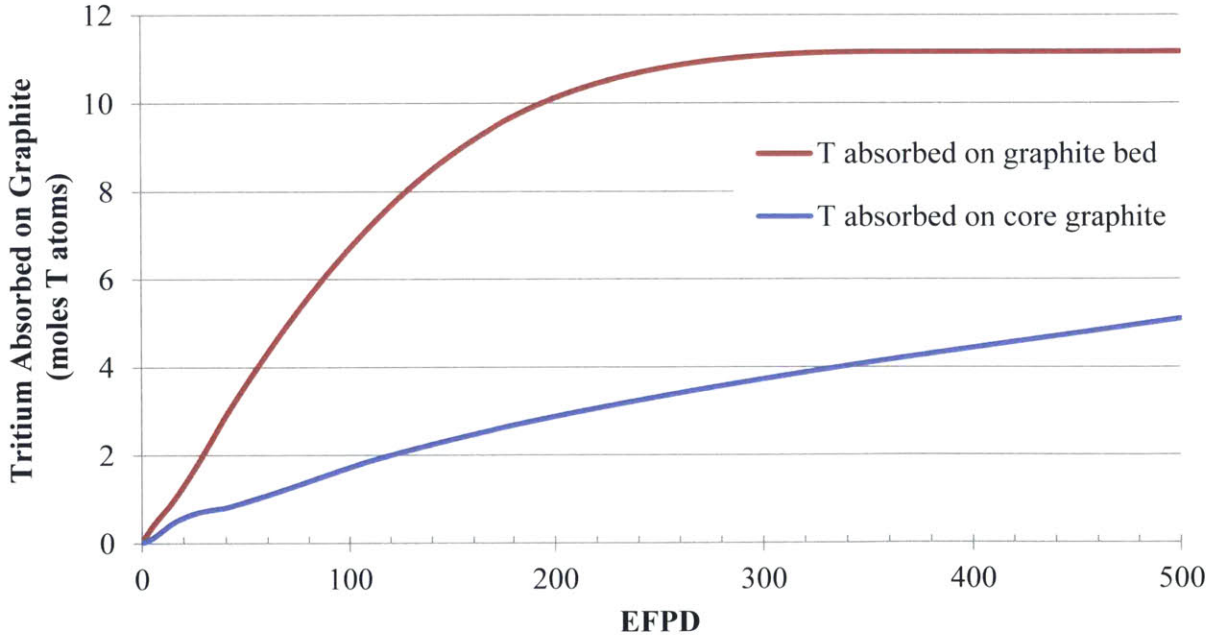

Figure 6.48: Total cumulative amount of tritium absorbed on graphite in the reactor core and on the stationary graphite spheres in the packed bed. Simulated with TRIDENT.

Next, the simulation was repeated by adding online regeneration of the graphite bed. This means that some of the graphite particles are removed from the bed, the tritium is driven off of the particles, and the particles are returned to the bed to absorb more tritium. A regeneration rate of $1/30^{th}$ was specified for this simulation by setting `Bed_frac_rep` to 1/30. This means that $1/30^{th}$ of the pebbles in the absorber bed are regenerated each day. In this case, a regeneration rate of $1/30^{th}$ equates to regenerating the same number of pebbles as are refueled in the reactor core per day. All of the other options and specifications (see Table 6.17) were retained from the previous simulation.

Figure 6.49 shows the rate of tritium release to the power cycle as a function of reactor operating time. This configuration is very effective in keeping tritium release rates low. In this case, the core graphite sees some saturation behavior, but the graphite bed does not. This means that the rate of tritium absorption on the graphite bed is limited by the rate of mass transfer of tritium to the graphite surfaces in the bed. Figure 6.50 shows the cumulative amount of tritium absorbed on the core graphite (plotted on the right vertical axis) and the graphite in the absorber bed (plotted on the left vertical axis).

This simulation shows that passing all of the coolant exiting the core through a bed of graphite pebbles (with online pebble regeneration) located between the core and the heat exchanger system is effective for reducing the rate of tritium release to the power cycle to levels comparable to those in LWRs and HWRs. This system is substantial, requires systems and equipment for online pebble regeneration, and requires that all of the reactor coolant pass through the system. Additional tritium could be captured by increasing the size of the bed, altering the graphite pebble size, or selecting a different grade of graphite. Non-nuclear grades of graphite could be attractive options for use in the packed bed. For example, the activated graphites AX-21, GX-31, and Maxsorb have high BET surface areas (up to about 4000 m^2/g) and high specific hydrogen capacities [70]. As discussed in 2.4.2.3, irradiation may increase the specific tritium capacity of graphite. One way to increase the graphite capacity for tritium would be to process the graphite with neutron or ion irradiations prior to using it in the packed bed. While irradiation has been shown to increase the graphite capacity for tritium, it may also reduce the rate of tritium uptake on graphite. Thus, irradiating graphite in order to increase tritium capacity may not produce a net benefit for tritium capture in a reactor.

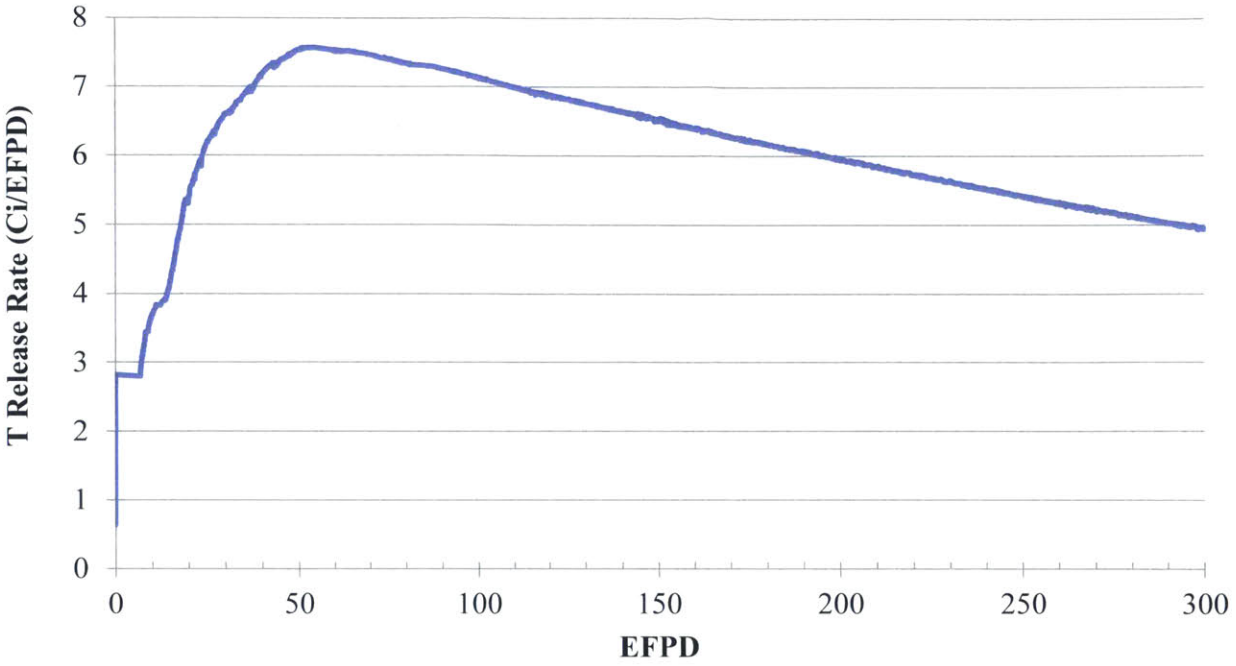

Figure 6.49: Tritium release rate when a bed of graphite placed between the reactor core and the heat exchanger is regenerated at a rate of 1/30th per day. Simulated with TRIDENT.

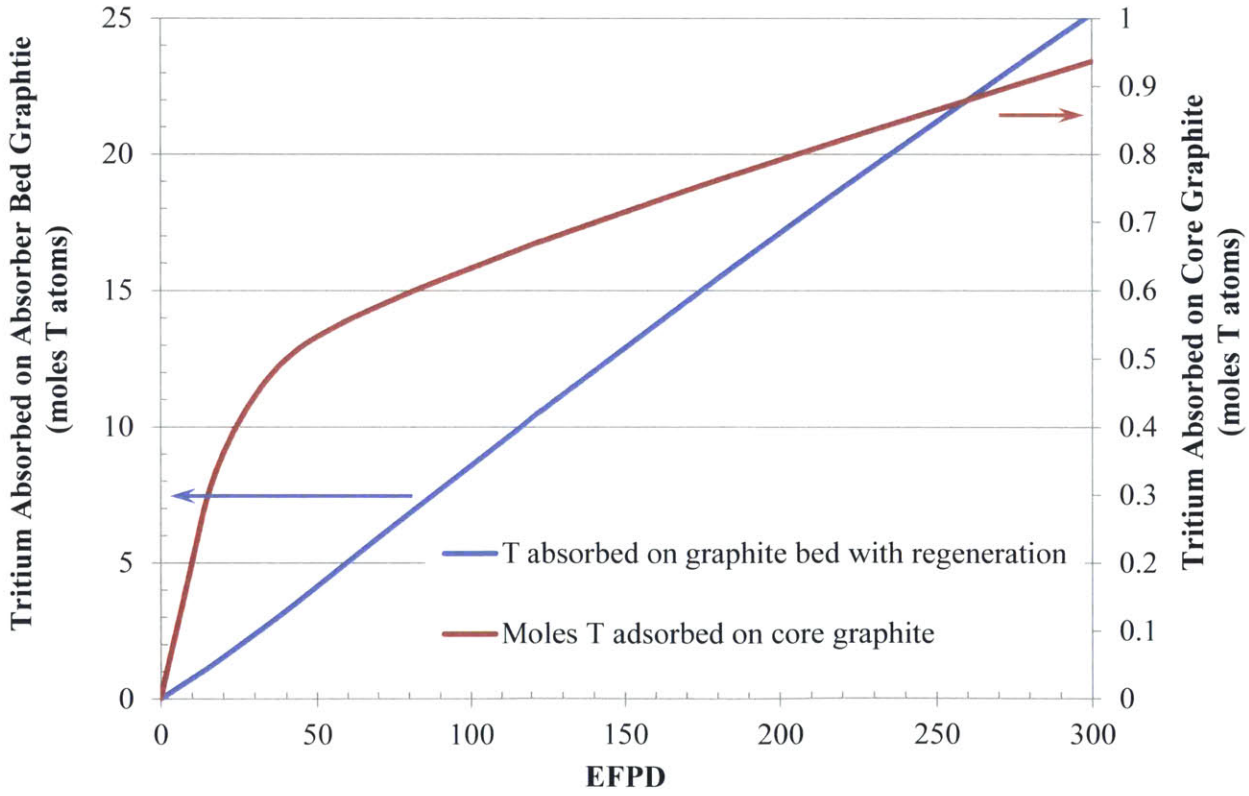

Figure 6.50: Cumulative moles of T atoms absorbed on core graphite and absorber bed graphite. Simulated with TRIDENT.

6.6.5 Tritium release rate with a flinak intermediate loop

The MSRE utilized an intermediate loop of clean flibe between the primary fuel-salt and the air-cooled heat exchanger [6]. Earlier FHR concepts proposed the use of an intermediate loop filled with flinak which would separate the primary coolant loop from the power cycle [189,190]. Flinak was suggested based on its favorable thermophysical properties and lack of toxic beryllium. This section will use TRIDENT to simulate tritium transport in a PB-FHR if a secondary (intermediate) loop of flinak is used to separate the flibe primary coolant from the air-Brayton power cycle. Figure 6.51 provides a schematic representation of a PB-FHR with a flibe primary coolant loop and a flinak intermediate loop. The system configuration simulated in Section 6.4.3 is utilized in this section as well, except that a flinak intermediate loop is now added to the system. This means that the baseline redox potential is retained, tritium capture on fuel pebbles, and the effects of online refueling are included. Options exist within TRIDENT for simulating tritium capture systems in the primary coolant, the secondary coolant, or in both the primary and secondary coolants simultaneously. For the simulations in this section, tritium mitigation systems are modeled in the secondary coolant only.

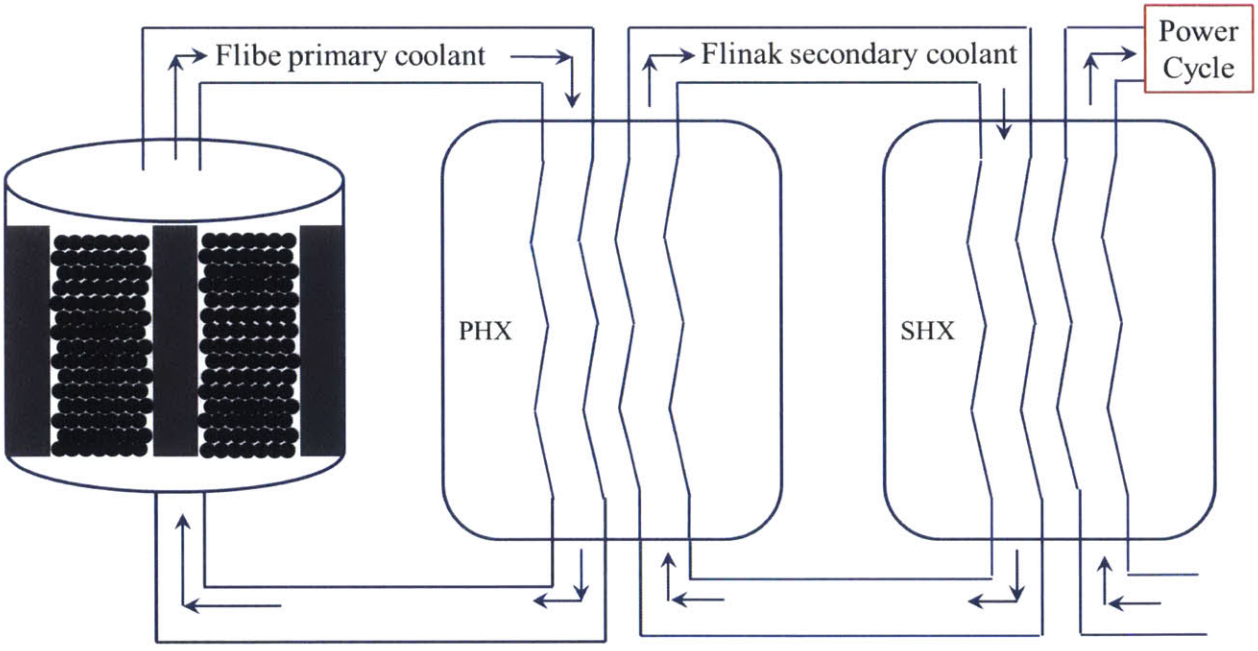

Figure 6.51: Schematic representation of a PB-FHR with a flibe primary coolant loop and a flinak secondary coolant loop.

Table 6.18 summarizes the input options for simulating an FHR with a secondary coolant loop in TRIDENT. One simulation was completed with a bare secondary loop (with no tritium mitigation systems). Input options for this bare secondary loop are summarized in Table 6.19. A second simulation was completed with a graphite bed for tritium capture in the secondary system. The specifications for the graphite bed in the secondary system are summarized in Table 6.20. A third simulation was completed with a permeation window in the secondary system. The TRIDENT

options for this permeation window are summarized in Table 6.21. Finally, a fourth simulation was completed with a gas stripping system in the secondary coolant loop. The TRIDENT options used for this gas stripping system are summarized in Table 6.22.

Table 6.18: TRIDENT input options for simulating a secondary coolant system and tritium mitigation systems within the secondary system. Note that the primary and secondary hot and cold leg pipes are assumed to have the same dimensions.

Input Option/Variable Name	Description/Meaning
Loops	Turn on/off secondary coolant loop model 1 = off, 2 = on
Tritiumcapturebedflag_s	Turn on/off packed bed of graphite for tritium sorption in the secondary loop 1 = off, 2 = on
Bed_frac_rep_s	Fraction of the secondary coolant packed bed replaced per day
Bed_vessel_radius_s	Inner radius of the packed bed in the secondary coolant system [m]
Bed_surface_area_s	Total graphite surface area in the packed bed in the secondary system [m^2]
Particle_radius_s	Radius of the graphite particles in the packed bed of the secondary system [m]
Particle_density_s	Density of graphite in the packed bed of graphite in the secondary coolant [g/m^3]
Bed_packingfraction_s	Packing fraction in the bed graphite bed in the secondary system
GasStrippingFlag	Turn on/off simulation of a gas stripping system 1 = no gas stripping 2 = gas stripping in the primary system only 3 = gas stripping in the secondary system only 4 = gas stripping in both primary and secondary systems
StrippingFlowFraction_s	Specifies the fraction of the secondary coolant mass flow rate that is diverted into the gas stripper
NStages_s	Number of stages in the secondary system gas stripper
Gas_hrflowrate_s	Stripping gas flow rate [L/hr STP] in the secondary stripping system
PermeationFlag_secondary	Turn on/off model of permeation window in the secondary system 1 = off, 2 = on
WindowArea_s	Surface area of the secondary system permeation window [m^2]
WindowThick_s	Thickness of secondary system permeation window tube wall [m]
Perms_tube_od	Tube outer diameter of secondary system permeation window
HX2tubes	Number of tubes in secondary heat exchanger
Hx_tube_od	Heat exchanger tube outer diameter [m]
Thick	Thickness of heat exchanger tube wall [m]
A2	Surface area of secondary heat exchanger [m^2]
pipe_thick1 and	Hot and cold leg pipe wall thicknesses [m]

pipe_thick2	
Table 6.18 continued from the previous page	
pipe_d and pipe_d2	Hot and cold leg pipe inner diameter [m]
pipe_l and pipe_l2	Hot and cold leg pipe length [m]

Table 6.19: TRIDENT input options selected for simulation of secondary loop without tritium capture systems in the secondary loop.

Input Option/Variable Name	Description/Meaning
Loops	2 (secondary loop is simulated)
Tritiumcapturebedflag_s	1 (capture on secondary graphite bed not simulated)
GasStrippingFlag	1 (no gas stripping simulated)
PermeationFlag_secondary	1 (no permeation windows simulated)
HX2tubes	27360 (# of tubes in secondary heat exchanger)
Hx_tube_od	0.00635 (HX tube outer diameter [m])
Thick	8.89×10^{-4} (thickness of HX tube wall [m])
A2	10820 (surface area of secondary heat exchanger [m^2])
pipe_thick1 and pipe_thick2	0.02 (hot and cold leg pipe wall thicknesses [m])
pipe_d and pipe_d2	pipe_d = 0.792 (hot leg pipe inner diameter [m]) pipe_d2 = 0.495 (cold leg pipe inner diameter [m])
pipe_l and pipe_l2	pipe_l = 29.74 (hot leg pipe length [m]) pipe_l2 = 35.44 (cold leg pipe length [m])

Table 6.20: TRIDENT input options for simulating a secondary coolant loop with a graphite bed for tritium capture.

Input Option/Variable Name	Description/Meaning
Loops	2 (secondary loop is simulated)
Tritiumcapturebedflag_s	2 (capture on secondary graphite bed is simulated)
GasStrippingFlag	1 (no gas stripping simulated)
PermeationFlag_secondary	1 (no permeation windows simulated)
Bed_frac_rep_s	1/30
Bed_vessel_radius_s	1.2 [m]
Bed_surface_area_s	1945.3 [m^2]
Particle_radius_s	0.015 [m]
Particle_density_s	1.77×10^6 [g/m^3]
Bed_packingfraction_s	0.60

Table 6.21: TRIDENT input options for simulating a permeation window in the secondary loop.

Input Option/Variable Name	Description/Meaning
Loops	2 (secondary loop is simulated)
Tritiumcapturebedflag_s	1 (capture on secondary graphite bed not simulated)
GasStrippingFlag	1 (no gas stripping simulated)
PermeationFlag_secondary	2 (permeation window is simulated)
WindowArea_s	10082 [m^2]
WindowThick_s	8.89×10^{-4} [m]
Perms_tube_od	0.00635 [m]

Table 6.22: TRIDENT input options for simulating a gas stripper in the secondary loop.

Input Option/Variable Name	Description/Meaning
Loops	2 (secondary loop is simulated)
Tritiumcapturebedflag_s	1 (capture on secondary graphite bed not simulated)
GasStrippingFlag	3 (gas stripping is simulated in secondary system only)
PermeationFlag_secondary	1 (no permeation windows simulated)
StrippingFlowFraction_s	0.50
NStages_s	10
Gas_hrflowrate_s	20000 [L/hr STP]

The tritium release rates for the four simulations using the secondary coolant loop model in TRIDENT are summarized in Figure 6.52. Also plotted in Figure 6.52 is the tritium release rate for the baseline PB-FHR (with only a flibe primary coolant loop) that was simulated in Section 6.4.3. Since any tritium diffusing from the primary system into the secondary system will recombine as T_2 at the primary heat exchanger-flinak surface, only tritium in the form of T_2 is considered to exist in the flinak secondary coolant. Compared to the baseline simulation, the simulations which incorporate a secondary loop see much lower tritium release rates up to 10 to 15 EFPD. This is due to the time it takes for tritium to distribute within the secondary system and also due to the fact that flinak has a T_2 solubility about 1000 times greater than that of flibe. Note also that the peak tritium release rate with the secondary loop is slightly higher than the peak tritium release rate predicted for the baseline case. This is because the tritium diffusion calculations at the flinak-facing heat exchanger surfaces accrued about 2.9 % error over the course of the calculation. This error could be reduced by tightening the tolerances used in the MatLab "fsolve" routine (see Section 5.7.1).

The tritium release rate for the case with the bare secondary loop and the case with the secondary loop utilizing the graphite bed are nearly identical. The right vertical axis in Figure 6.52 plots the release rate for the case with the graphite bed as a percentage of the release rate without the graphite bed. At early times, the release rate for a system with a bed of graphite in the secondary coolant loop is about 70 % of that for a bare secondary loop; however, the graphite in the secondary loop quickly begins to saturate. The graphite bed used in the secondary loop here uses the same

specifications as the graphite bed simulated in the primary coolant loop in Section 6.6.4. In this application, the effectiveness of graphite for tritium capture is reduced in flinak because flinak has a 1000 times higher solubility for T_2 than flibe. This means that the tritium partial pressure (which determines the graphite capacity for tritium, as discussed in Section 2.4) is lower in the secondary flinak coolant than it is in flibe primary coolant.

The same specifications used in Section 6.6.3 for the simulation of the gas stripping system in the flibe primary coolant were used for the simulation in the flinak secondary loop in this section. When employed in flibe, this gas stripping system reduced the peak tritium release rate from 2410 Ci/EFPD to 439 Ci/EFPD. When employed in flinak, this same system reduced the peak tritium release rate to 2170 Ci/EFPD. This reduction in the effectiveness of the stripping system is likely due to the fact that flinak has a much higher solubility for T_2, making it harder to remove from the salt via gas stripping.

A Ni permeator having a surface area equal to that of the heat exchanger was simulated in the flinak-filled secondary loop. This permeator reduced the peak tritium release rate to 1185 Ci/EFPD. The performance of this permeator is comparable to that of an identical permeator in the flibe primary loop (see the green line plotted in Figure 6.40). Despite the fact that the solubility of T_2 in flinak is 1000 times higher than that in flibe, the fact that T_2 is the only species in the flinak secondary loop results in similar permeator effectiveness in both the primary and secondary coolants. (In the primary flibe coolant, both T_2 and TF may exist due to TF production from neutron transmutation.)

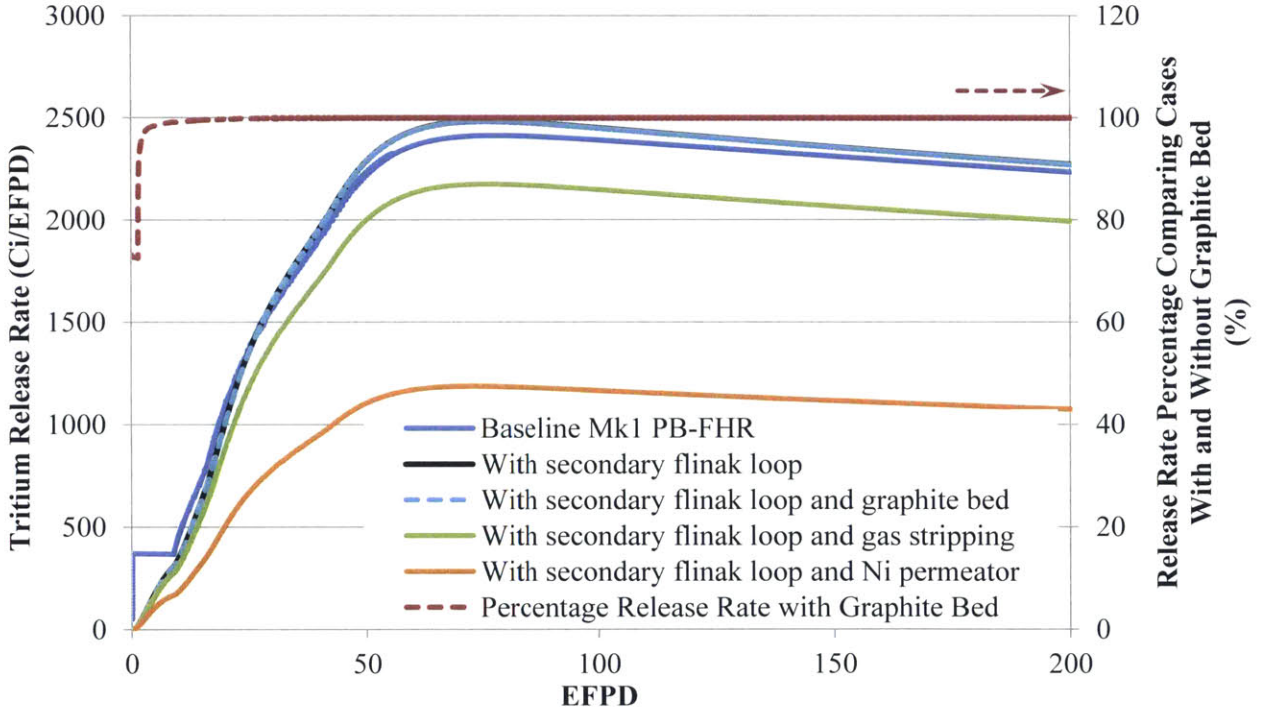

Figure 6.52: Tritium release rate with and without a secondary (intermediate) flinak loop with and without tritium capture systems. The right axis compares the tritium release rate with a secondary loop with and without a bed of graphite in the secondary loop. Simulated with TRIDENT.

6.6.6 Effects of Li-7 enrichment on tritium transport

A series of calculations were performed which show that the initial Li-7 enrichment in flibe is a significant factor in the time-dependent tritium production rate. Figure 6.53 shows a plot of the tritium production rate per GWD in a Mk1 PB-FHR type reactor as a function of EFPY and the initial Li-7 enrichment of the flibe.[14] For comparison, a plot of the tritium production rate in an alternative non-Li bearing salt (0.57NaF-0.43BeF_2) is also plotted.[15] The baseline Mk1 PB-FHR Li-7 enrichment in flibe is 99.995 wt%, which is highlighted as a dashed line in Figure 6.53. The tritium production for flibe initially 99.995 wt% in Li-7 was plotted earlier in Figure 2.2. At a Li-7 enrichment of 99.999 wt%, the tritium production rate is virtually constant with time because the rate of initial Li-6 consumption is matched by the rate of Li-6 production via transmutation in Be-9. With Li-7 enrichments less than 99.999 %, the tritium production rate decreases with time as the initial Li-6 is consumed through transmutation to tritium and as additional Li-6 is produced via transmutation in Be-9. For initial Li-7 enrichments greater than 99.999 %, the tritium production rate increases with time before reaching the same equilibrium production rate as in flibe with other enrichments. For flibe with Li-7 enrichments greater than 99.999 %, the tritium production rate is initially low due to the low Li-6 content. The production rate increases as the new Li-6 is produced from transmutation in Be-9.

For long operating times of 10 years or greater, this plot shows that there is no incentive for enriching beyond 99.999 %. At early times there is a substantial incentive to increase enrichment from 99.995 % to 99.999 % because this reduces the BOL tritium production rate from 10,000 Ci/GWD to 2900 Ci/GWD. This would also reduce the requirements for any tritium mitigation systems employed for capturing tritium.

[14] Note that natural lithium is 92.5 mole % Li-7 and 93.5 weight % Li-7.

[15] In the case of 0.57NaF-0.43BeF_2, tritium production from sodium is ignored because the n,T reaction in Na-23 has a cross section of 0 below 12.1 MeV.

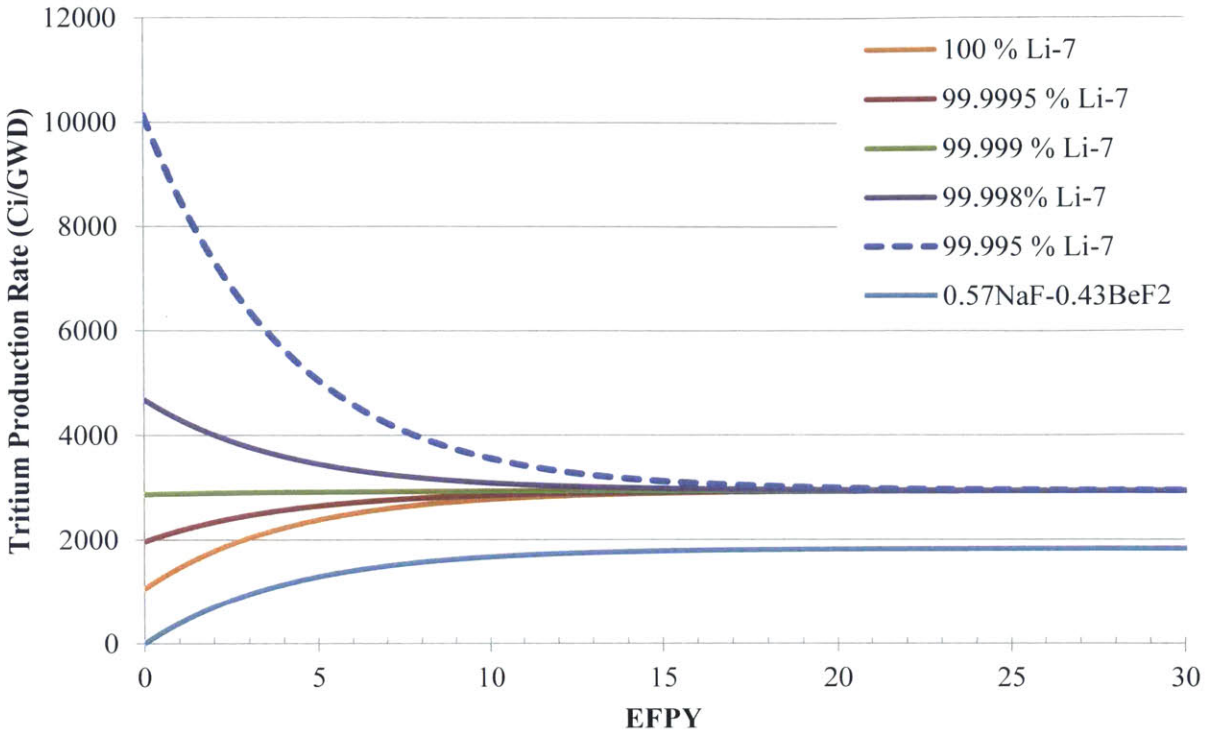

Figure 6.53: Tritium production rate in a Mk1 PB-FHR as a function of EFPY and initial Li-7 enrichment (wt %) in flibe. The tritium production rate for an alternative salt (0.57 NaF-0.43 BeF_2) is also shown. The baseline salt enrichment is highlighted by a dashed line. Calculated with Eq (2.6).

There are numerous chemical and electromagnetic methods for enriching lithium. Chemical methods include ion exchange and liquid-liquid extractions which often utilize crown ethers [191–196]. Assuming that lithium enrichment follows classical behavior, the separative work units (SWU) required to enrich lithium can be calculated with a well-known set of equations. First, the desired weight fraction of enriched Li-7 in the product (x_P) is specified. Next, the Li-7 content of the feed (x_F) is specified. Then, the Li-7 content of the waste (or tails) stream (x_W) is specified. In all cases, the waste stream was assumed to have 0.001 wt fraction Li-7. The mass of the desired enriched Li-7 product, P, was specified as 1 kg. With this initial input, the feed-to-product and waste-to-product mass ratios can be calculated according to Eq (6.3) and Eq (6.4). Knowing that $P = 1$, F and W (the feed mass and the waste mass, respectively) can be calculated. Next, the value function V is calculated for the product (P), the feed (F), and the waste (W) streams using Eq (6.5). In Eq (6.5), i can be W, P, or F. Finally, the SWU required to produce 1 kg of enriched Li-7 is calculated from Eq (6.6). Figure 6.54 shows the SWU required to produce 1 kg of enriched Li-7 as a function of the desired enrichment for two feed enrichments (natural and 96 wt %) assuming the waste stream is 0.1 wt % in Li-7.

The cost of a salt enriched to 99.999 % Li-7 would be only slightly higher than the cost of the baseline salt at 99.995 % Li-7 enrichment. The SWU/kg required to enrich Li-7 is plotted as a

function of the desired enrichment and two Li-7 feed concentrations in Figure 6.54. The x and y values of points in Figure 6.54 are also shown. Increasing the Li-7 enrichment from 99.995 to 99.999 % requires an additional 1.6 SWU/kg, an increase of a factor of 1.2. This investment in additional enrichment reduces the BOL tritium production rate by a factor of 3.5. This would also reduce the requirements for any tritium mitigation systems employed for capturing tritium.

$$\frac{F}{P} = \frac{x_P - x_W}{x_F - x_W} \tag{6.3}$$

$$\frac{W}{P} = \frac{x_P - x_F}{x_F - x_W} \tag{6.4}$$

$$V_i = (1 - 2x_i)\ln\left[\frac{1 - x_i}{x_i}\right] \tag{6.5}$$

$$SWU = P \times V_P + W \times V_W - F \times V_F \tag{6.6}$$

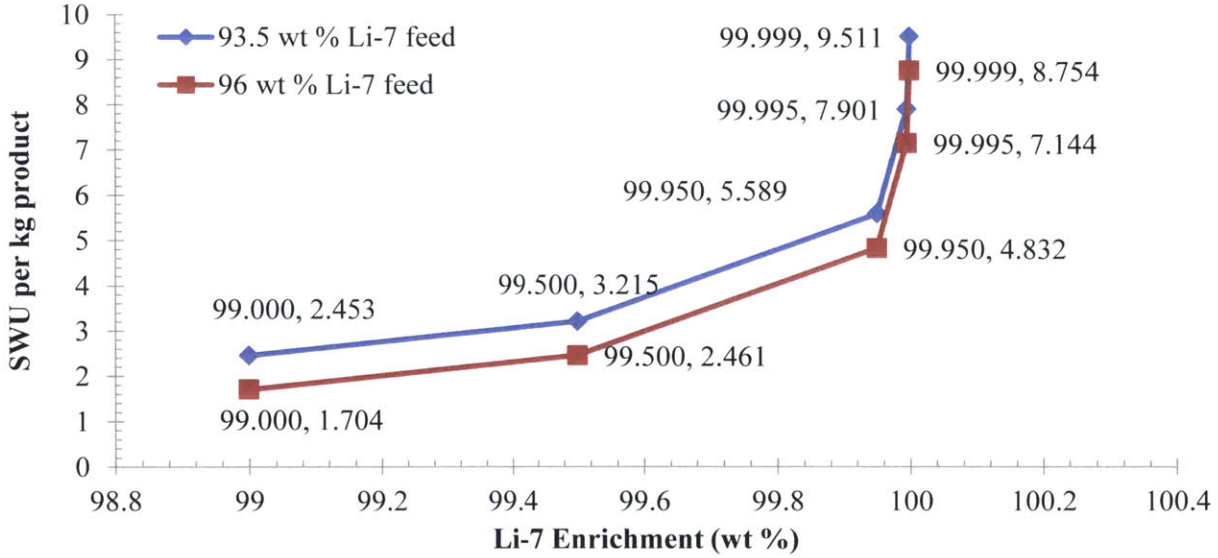

Figure 6.54: SWU per kg enriched Li-7 as a function of product Li-7 enrichment and two feed concentrations. Natural lithium is 93.5 wt % (92.5 mole %) Li-7.

Figure 6.54 also showed the SWU required to enrich a lithium feed that is 96 wt % in Li-7. Due to thermonuclear weapons production, which desired enriched Li-6, stocks of tails (depleted in Li-6 but enriched in Li-7) exist. At the Y-12 facility in Oak Ridge, Tennessee, between 1954 and 1963, the United States produced 442.4 metric tons of enriched lithium-6 [197]. In the process of producing enriched Li-6, vast amounts of tails enriched in Li-7 (depleted in Li-6) were generated. Summarized in Table 2.1, the stores of these tails are located at the Portsmouth Gaseous Diffusion Plant in Portsmouth, Ohio and the Y-12 plant. Amounts of natural Li stored at each site are also summarized in Table 2.1. The tails and the unused Li are stored as lithium hydroxide monohydrate ($LiOH\text{-}H_2O$). Work is ongoing at ORNL in order to better characterize the Li isotopic concentration

in these inventories [198]. Much of the unused and tails lithium was recently sold by the Department of Energy (DOE) and is being transferred to the buyers [3]. While the tails compositions may not be 99.995 % Li-7, some of them are at least 99 wt% Li-7. Additional separations could be performed on the tails in order to achieve the desired Li-7 enrichment. Because the tails are already enriched in Li-7, the work required for enrichment would be less than if one were to start with natural lithium.

Table 6.23: Summary of tails (depleted in Li-6) enriched in Li-7 and natural Li in the United States. Both tails and unused Li are stored as $LiOH-H_2O$. Compiled from [197].

Location	Mass of Tails (metric tons)	Approximate Tails Composition (wt % Li-7)	Mass of unused natural Li (metric tons)
Portsmouth, OH	30,909	96-99 %	-
K-25	-	-	10,455
Y-12	8	96-99%	12

Four simulations were carried out in TRIDENT using an enrichment of 99.999 wt% Li-7 in order to compare the results with the baseline Li-7 enrichment of 99.995 wt% Li-7 and in order to determine the effects of increased Li-7 enrichment on the effectiveness of three tritium mitigation methods. The "Baseline Mk1 PB-FHR" reactor input to TRIDENT is the same as that used in Section 6.4.3. The other runs in Figure 6.55 use this same input as well except that the Li-7 enrichment was increased to 99.999 wt% and three instances of tritium mitigation methods were evaluated. Figure 6.55 shows the tritium release rate results from these simulations. Compared to the baseline Mk1 PB-FHR (at 99.995 wt% Li-7 enrichment), the higher Li-7 enrichment (99.999 wt %) reduces the pseudo steady state release rate from about 2130 Ci/EFPD to 650 Ci/EFPD without the use of any tritium mitigation methods.

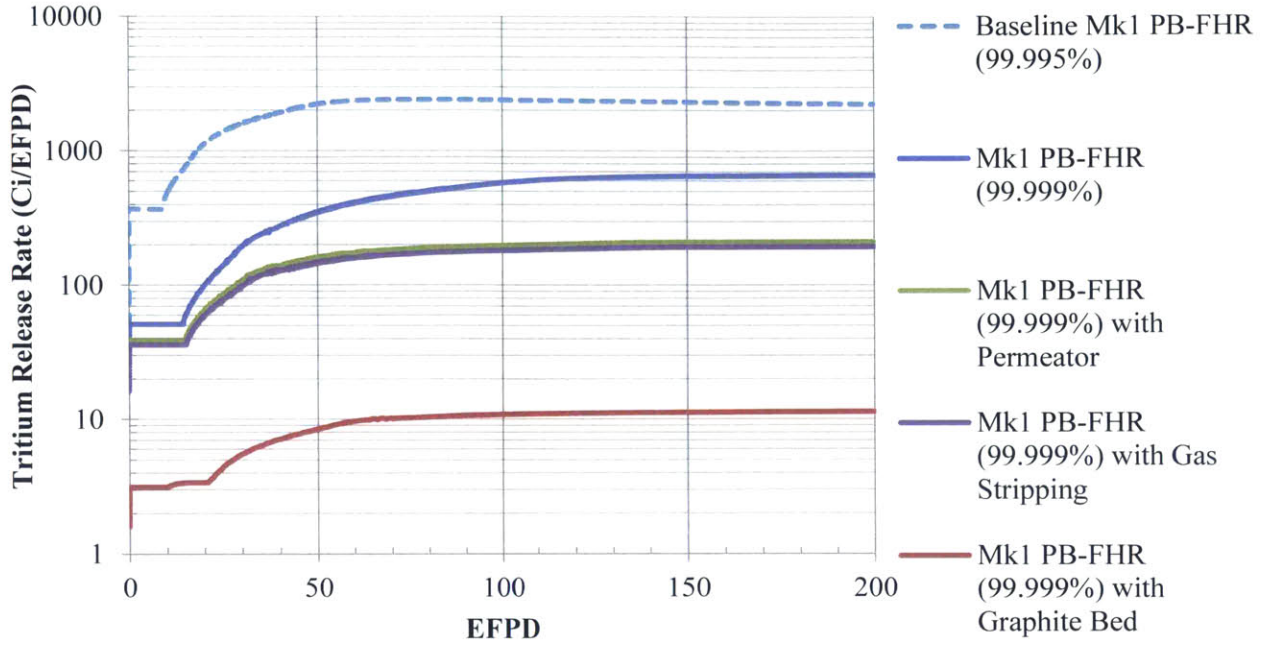

Figure 6.55: Tritium release rate for Li-7 enrichments in flibe of 99.995 wt % (baseline) and 99.999 wt %. Three tritium mitigation systems were analyzed at this higher Li-7 enrichment. Simulated with TRIDENT.

A nickel permeator was simulated with the higher Li-7 enrichment. The concept and specifications of this permeator are the same as those from Section 6.6.2. Compared to Section 6.6.2, the tritium release rate with the permeator is now 200 Ci/EFPD instead of 800 Ci/EFPD because the higher Li-7 enrichment reduces the tritium production rate. This permeator still has a surface area twice that of the heat exchanger and requires that all of the coolant flow pass through it. Thus, even with the lower tritium production rate, a permeator does not reduce tritium release rates to LWR or HWR levels.

Next, a gas stripping system similar to that in Section 6.6.3 was simulated for flibe with the higher Li-7 enrichment. In this case, the size of the gas stripping system was reduced from 50 to 25 % of the total coolant flow and the stripping gas flow rate was reduced from 20000 L/hr to 10000 L/hr. Table 6.24 summarizes the input values for the gas stripper simulated in this section. In this case, the tritium release rate is reduced from 493 Ci/EFPD in Section 6.6.3 (with the baseline Li-7 enrichment and the larger gas stripper) to 193 Ci/EFPD with a Li-7 enrichment of 99.999 wt % and a smaller gas stripper. With the higher Li-7 enrichment, the size of the stripper can be cut in half and the tritium releases are still reduced compared to the baseline Li-7 enrichment case.

Finally, a packed bed of graphite for tritium capture was simulated with the higher Li-7 enrichment in flibe. The concept of this packed bed is the same as that in Section 6.6.4, except that the lower tritium production rate (due to the increased Li-7 enrichment) allows a smaller bed to be used. The graphite bed input parameters are summarized in Table 6.25. With the higher Li-7 enrichment, the size of the packed bed of graphite was reduced by a factor of 4 compared to the size

of the bed used in Section 6.6.4 and the tritium release rate is still reduced to 11 Ci/EFPD. The radius of the bed was held constant, but the number of graphite pebbles in the packed bed (and the height of the bed) was reduced by a factor of 4. This reduces the pressure drop across the bed to 0.12 atm and reduces the volume of graphite pebbles that must be processed online by a factor of 4. Thus, increased Li-7 enrichment may incur higher salt costs, but the smaller tritium mitigation systems may offset this expense.

Table 6.24: Input options for simulation of gas stripping system for tritium removal with flibe at 99.999 wt% Li-7 enrichment.

Input Option or Variable Name	Value (and meaning)
GasStrippingFlag	2 (gas stripping simulated in the primary coolant only)
StrippingFlowFraction_p	0.25 (50% of the coolant flow passes through the stripper)
StrippingFlowFraction_s	N/A
NStages_p	10 (Number of stripping stages in the gas stripper)
NStages_s	N/A
Gas_hrflowrate_p	10000 (Stripping gas flow rate [L/hr at STP])
Gas_hrflowrate_s	N/A

Table 6.25: Input options for simulation of packed bed of graphite for tritium absorption with flibe at 99.999 wt % Li-7 enrichment.

Input Options	Value (and meaning)
Loops	1
Days	200
Hour_Fraction	0.4
Elements	6
T_uptake	2 (On, tritium uptake on graphite is simulated)
CoreRefuelFrac	1/30 (Pebble refueling is accounted for with a 30 day cycle)
CoreGeometryAdjust	2 (On)
Redoxflag	2 (TF and T_2 may exist subject to the redox option Feedbackflag)
Feedbackflag	2 (Redox potential is fixed at the baseline potential from Table 6.2)
Oxideflag	2 (oxide layer on air-side of HX is accounted for)
PRFinput	10 (permeation reduction factor)
Corrosionflag	1 (corrosion is not simulated)
Core_mesh	10
Hot_mesh	10
HX_mesh	10
Cold_mesh	10

(Table 6.25 continued) Input Options	Value (and meaning)
GBflag	Not used. Meaningless when Corrosionflag = 1
C_Cr_initial_ppm	Not used. Meaningless when Corrosionflag = 1
Tritiumproductionflag	3 the tritium production rate varies with time according to Eq (2.6)
Tritiumcapturebedflag	2 (on)
Bed_frac_rep	1/30 (fraction of bed regenerated per day)
Bed_vessel_radius	1.2 (Inner radius of the packed bed [m])
Bed_surface_area	486.325 (Total graphite surface area in the packed bed [m^2])
Particle_radius	0.015 (Radius of the graphite particles in the packed bed [m])
Particle_density	1.77×10^6 (Density of graphite [g/m^3])
Bed_packingfraction	0.60 (Packing fraction in the bed)

6.7 System response to rapid tritium desorption

In temperature programmed desorption (TPD) a surface is first "charged" with a gas for a specific period of time under a specific temperature and pressure. Then the temperature is increased at a specific rate in order to desorb the gas from the surface. This allows a determination of the capacity of the surface for a gas under the experimental conditions at which the surface was first charged [199]. If the temperature of the FHR coolant and fuel were to increase, such as in an accident, this could cause tritium to desorb from the graphite in the reactor. This would increase the amount of tritium in the coolant for two reasons. First, the previously captured tritium would be released into the coolant. Second, the graphite would no longer be absorbing tritium.

Tritium sorption on a given grade of graphite is a function of temperature, time, and the partial pressure of tritium over the graphite. Similarly, tritium desorption is a function of temperature, time, the prevailing partial pressure, and also the conditions (temperature and partial pressure) at which the graphite initially absorbed the tritium [199]. Desorption rates can decrease as the pressure at which the hydrogen was initially absorbed is decreased. Additionally, the temperature at which the maximum desorption rate is achieved may increase as the pressure at which the hydrogen was initially absorbed is decreased [199]. Thus, tritium absorption and desorption is a function of more than four variables, and data do not exist for cases of simultaneously varying time, pressure, and temperatures. Hydrogen desorption rate data are also limited for the type of graphite and low tritium partial pressure relevant to FHRs. For example, the T_2 partial pressure at steady-state in the study carried out in Section 6.4.3 is 20 Pa. For the case simulated in Section 6.6.6, the steady-state T_2 partial pressure above flibe is 0.1 Pa.

This section analyzes a case where an FHR had operated for 200 days and a pseudo–steady state had been achieved. Then, the coolant temperature is spontaneously increased to 1000 °C for a duration of 15 days and tritium is desorbed from the tritium inventory on the reactor graphite. For the purposes of this exercise it is assumed that the reactor continues operating, tritium production from transmutation in flibe continues, and that the coolant continues to flow. Then, after 15 days of

operation at 1000 °C with no tritium absorption on graphite, the normal temperature conditions are restored and graphite sorption is resumed. During the period of time at 1000 °C, whatever tritium that had been absorbed on the graphite is desorbed and further tritium absorption does not occur until normal temperatures and operations are resumed.

In Section 6.6.6, a Mk1 PB-FHR with 99.999 wt% enriched Li-7 in flibe was modeled with a packed bed of graphite (with bed parameters defined by Table 6.2) for tritium absorption. This case will be used for this analysis. Desorption rates were measured for ISO-880U graphite for charging pressures down to 83 Pa [199]. At 1000 °C, the desorption rate is about $3x10^{13}$ molecules of D_2 per gram of graphite per second [199]. After 200 days for this particular configuration of FHR, the tritium inventory on the core graphite is 0.3963 moles T (11597 Ci), and the tritium inventory on the packed bed of graphite is 0.0758 moles T. Assuming that the tritium desorption rate would be the same as the deuterium desorption rate from the experiment ($3x10^{13}$ molecules D_2/g-s or $6x10^{13}$ atoms D/g-s), and knowing that the total system graphite mass is $2.04x10^7$ g, it would take only 232 seconds to desorb all of the tritium from the graphite in the system at 1000 °C. This desorption rate is used for this analysis.

Figure 6.56 shows the tritium release rate for a Mk1 PB-FHR operating with flibe that is 99.999 wt% Li-7, utilizing the baseline redox potential, accounting for tritium uptake on core graphite (including the effects of refueling), and with a bed of graphite between the core exit and the heat exchanger entrance. The parameters specific to this run were summarized in Table 6.25. The data in Figure 6.56 are the same data plotted in red in Figure 6.55.

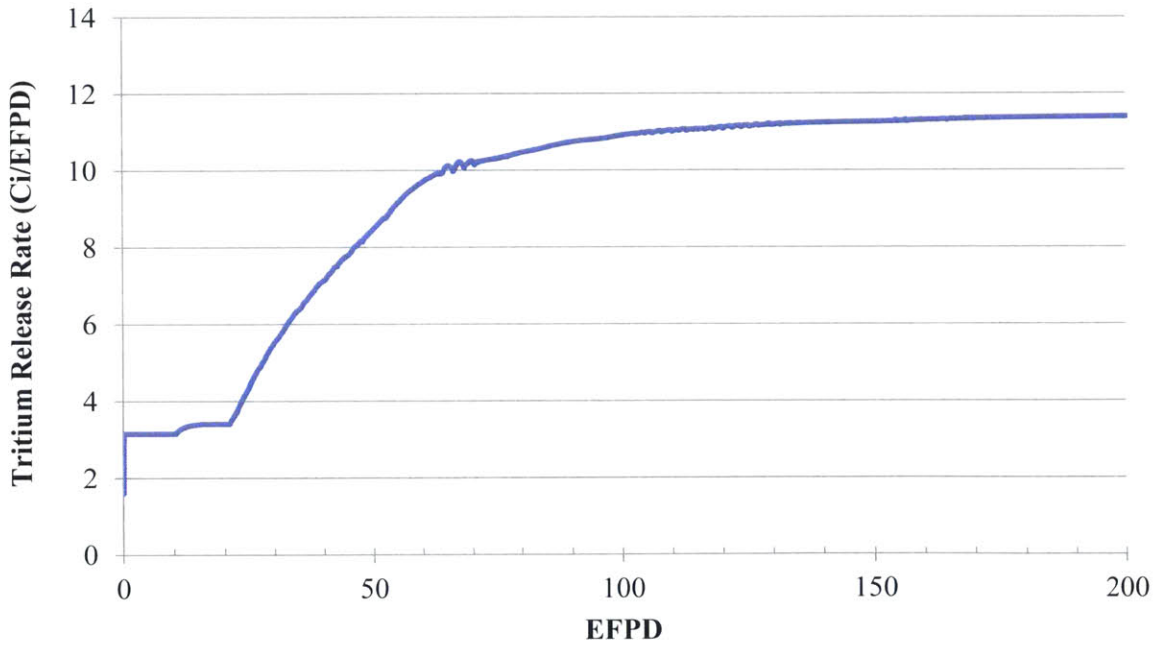

Figure 6.56: Tritium release rate for the case with parameters summarized in Table 6.25. Prior to high-temperature transient. Simulated with TRIDENT.

Next, at exactly 200 EFPD, the system inlet and outlet temperatures were each increased by 300 °C, tritium absorption on graphite was turned off, and a tritium desorption rate from the graphite of $6x10^{13}$ atoms T/g-s was specified. The tritium desorption rate was added to the normal tritium production rate from neutron transmutation in flibe by setting the `Tritiumproductionflag` option in TRIDENT equal to 4 and inserting criteria specific to this simulation. This tritium desorption rate was held constant for 232 seconds, at which point the tritium inventory on the graphite was depleted. The response of the system throughout this transient is plotted in Figure 6.57 in terms of the tritium release rate (Ci/EFPD). Prior to 200 EFPD, the system is at a steady state. The achievement of this steady state was shown in Figure 6.56. The transient begins at 200 EPFD when the system inlet and outlet temperatures were each increased by 300 °C, tritium absorption on graphite was turned off, and a tritium desorption rate from the graphite of $6x10^{13}$ atoms T/g-s was specified in addition to the normal tritium production from neutron transmutation in flibe. In 232 seconds 11597 Ci of tritium is desorbed from the system graphite. This release accounts for the sharp spike just after 200 EFPD. After this desorbed tritium has escaped the system, the release rate decreases such that the rate of tritium release equals the rate of tritium production. This state is maintained until 215 EFPD.

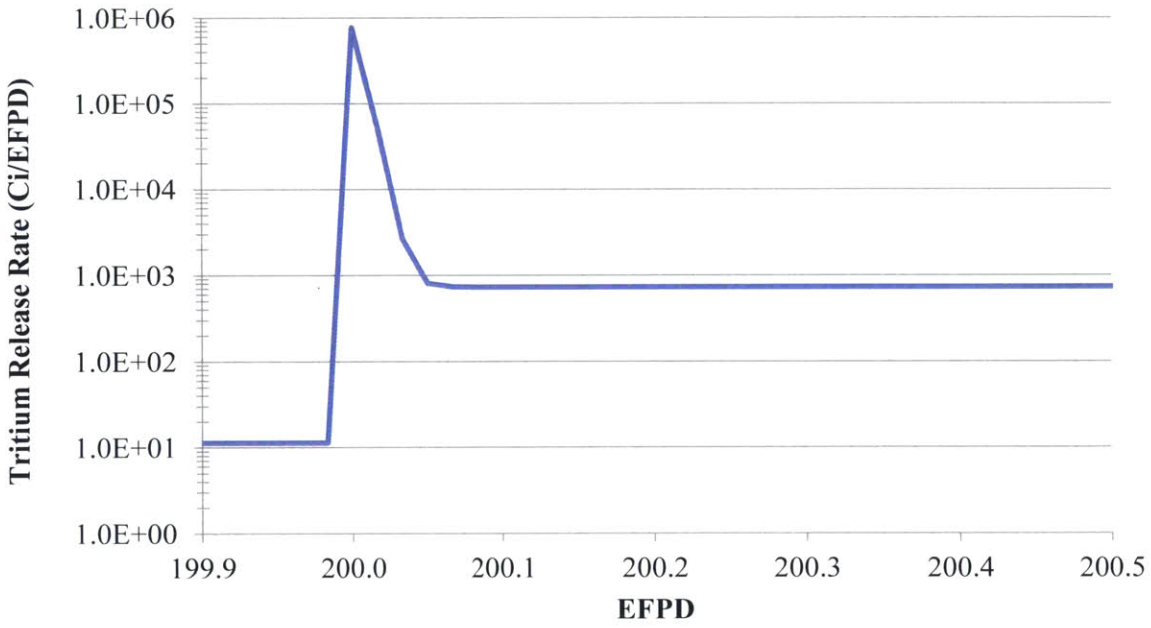

Figure 6.57: System response to instantaneous system-wide temperature jump of 300 °C at 200 EFPD with simultaneous desorption of tritium from system graphite. Simulated with TRIDENT.

At 215 EFPD, the system temperatures are instantaneously lowered back to normal (with core inlet and outlet temperatures of 600 °C and 700 °C, respectively). Simultaneously, the absorption of tritium on graphite is resumed. Figure 6.58 shows the initial system response immediately after normal conditions are resumed at 215 EFPD. Since all of the tritium originally on the system

graphite prior to 200 EFPD has been desorbed, the graphite is able to rapidly absorb tritium again now that temperatures have been reduced and absorption has resumed. This results in a sharp decrease in the tritium release rate down to levels first seen prior to 10 EFPD in Figure 6.56. Figure 6.59 shows the long-term reattainment of the original steady-state conditions seen prior to 200 EFPD. Tritium is rapidly absorbed from the system until 236 EFPD, at which point saturation of the graphite begins to occur and the release rate increases gently until leveling off. Because the amount of tritium in the system is higher after the high-temperature transient than it was at 0 EFPD, the graphite saturates more quickly. Figure 6.56 through Figure 6.59 have shown the transient behavior one segment at a time, the entire simulation from beginning to end is shown in Figure 6.60.

In this section, the system response to a stepwise increase in temperature with desorption of the system inventory of tritium from graphite was simulated. This simulation showed that there is potential for rapid tritium desorption and release at high temperatures characteristic of accidents. More than 11000 Ci of tritium was released in a matter of minutes. Realistically, the release would be more gradual given that it would take some time for the system to heat up and for desorption to begin. Nevertheless, this gives incentive for maintaining low system tritium inventories. If the inventory is low (where tritium is continually removed and not allowed to build up) then the potential for tritium release due to high-temperature transients will be low. After a period of time at high temperatures, the system was instantaneously restored to nominal conditions and tritium absorption on graphite was resumed. This demonstrated that the system can respond quickly if nominal conditions are restored. Once nominal conditions were restored, the tritium release rate was reduced from 700 Ci/EFPD to 3.5 Ci/EFPD in a matter of 3.5 hours.

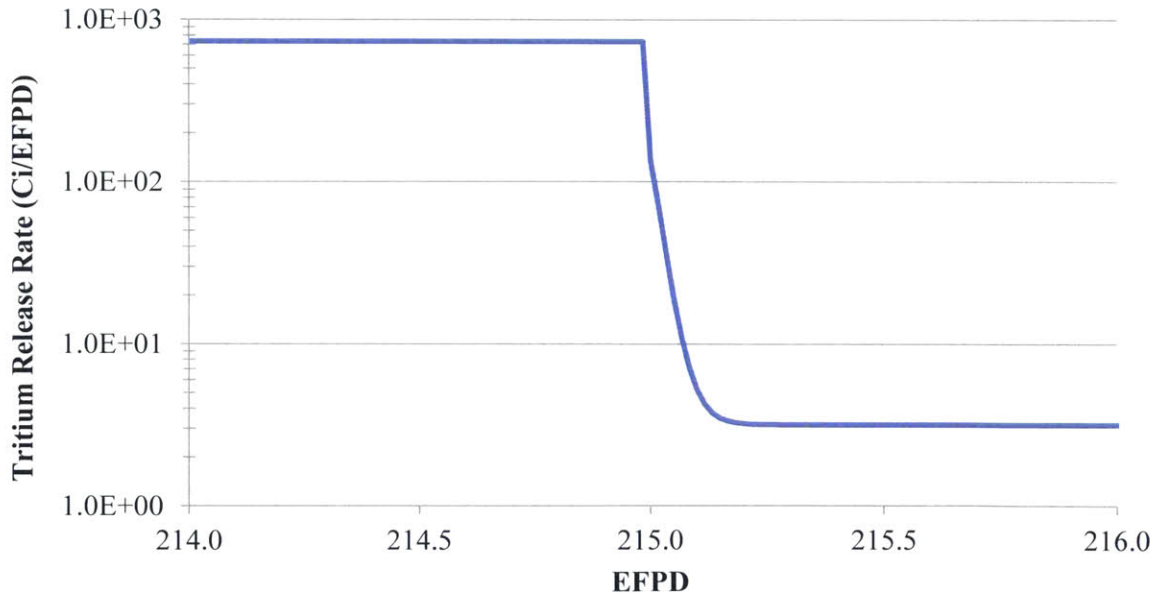

Figure 6.58: After 15 days with elevated system temperatures and no graphite sorption of tritium, plot of system response to instantaneous system-wide temperature decrease by 300 °C (back to normal operating temperatures) with simultaneous resumption of tritium uptake on graphite. Simulated with TRIDENT.

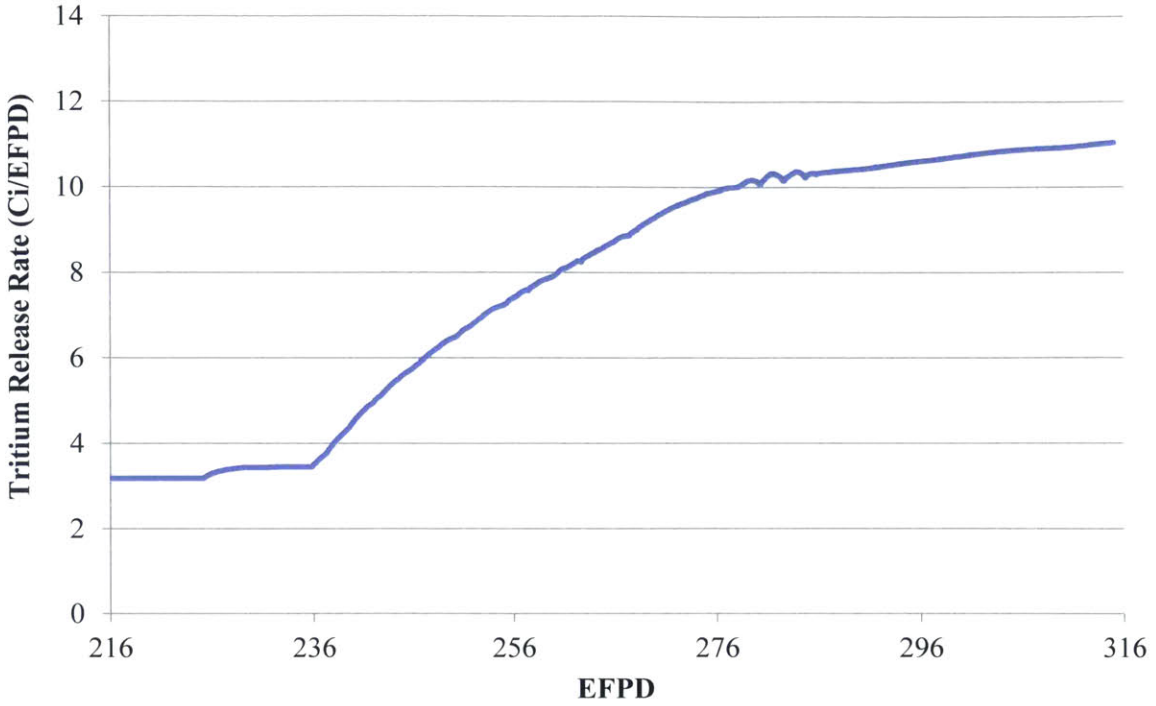

Figure 6.59: System reattainment of original steady-state condition upon return to nominal operating conditions. Simulated with TRIDENT.

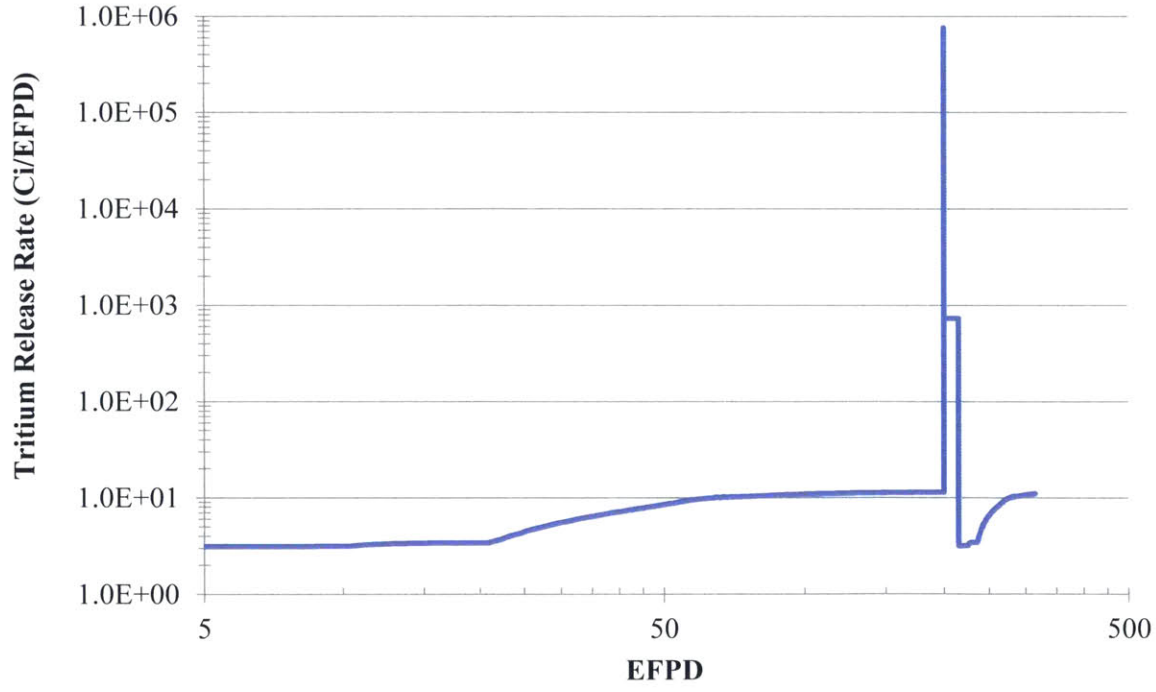

Figure 6.60: Summary of the entire simulation from 5 EFPD to 315 EFPD.

6.8 Chapter summary of TRIDENT simulations of the FHR

The reactor, reactor systems, material properties, and simulation options for TRIDENT were introduced. A systematic study of the tritium transport and corrosion behavior of the Mk1 PB-FHR was completed using TRIDENT. The initial simulations focused on the baseline Mk1 PB-FHR using only the baseline reactor specifications and material properties. It was shown that tritium uptake on graphite in the reactor core (accounting for fuel pebble refueling) delays the time it takes to reach a pseudo steady state rate of tritium release from a mere 5 hours (if graphite uptake is neglected) to 70 EFPD. Additionally, this pseudo steady state release rate (when tritium sorption on graphite is accounted) for is 2410 Ci/EFPD compared to about 2710 Ci/EFPD without the effects of tritium sorption on graphite.

The effects of the redox potential on corrosion and tritium transport in an FHR were simulated with TRIDENT. The coolant redox potential determines the chemical form of tritium and the extent of corrosion. Tritium existing as TF is an oxidant capable of corroding structural metals, particularly Cr. Tritium existing as T_2 is notable for its high permeability in structural metals and relatively low solubility in the salt. The simulations show that tritium release rates can be affected by the chosen redox potential in the salt and that there are corrosion implications of these redox choices. A more corrosive redox potential reduces tritium release rates, but incurs greater corrosion rates and higher dissolved Cr concentrations in the coolant. Given that the tritium release rate reduction from the more corrosive redox potential is only 50 Ci/EFPD lower than the baseline case, and that the corrosion rates are substantially higher at the more corrosive potential, these simulations suggest that the baseline redox potential used during the MSRE is the preferred option for the FHR.

A series of tritium mitigation systems were proposed and analyzed in TRIDENT. It was shown that a low-permeability oxide layer on the air-side of the heat exchanger delays tritium release, but ultimately the same tritium release rates are obtained regardless of the permeability reduction factor (PRF) of that oxide layer. With an oxide layer on the air-facing side of the HX, the tritium concentration in the HX metal tubing increases by a factor of the PRF. This means that the same steady state release rate is attained with a PRF of 1 as with a PRF. In order to prevent tritium from entering the HX tube wall from the coolant, a low permeability material is required. Metal oxides are not chemically stable in flibe, but tungsten is. An FHR using a tungsten HX was simulated. Tungsten reduced the peak tritium release rate and increased the amount of tritium retained in the coolant system and captured by graphite in the reactor core. By retaining more tritium in the primary system, more tritium could be removed and captured in a controlled manner using engineered systems. Due to cost and weight, tungsten is not likely to be a viable material for the HX. It was proposed that a tungsten (or similar low-permeability material) be used as a coating on the Type 316 SS heat exchangers.

A permeation window constructed of Ni, having a surface area twice that of the heat exchanger, and requiring that 100% of the coolant flow through it (not a side stream operation) reduced the tritium release rate from 2410 Ci/EFPD to 800 Ci/EFPD. A gas stripping system passing 50% of the

coolant flow through 10 stripping stages with a stripping gas flow rate of 20000 L/hr reduced tritium release rates from 2410 Ci/EFPD to 439 Ci/EFPD. A packed bed of graphite spheres having the same surface area as the pebbles in the reactor core and featuring online regeneration was effective for reducing peak tritium release rates from 2410 Ci/EFPD to 7.5 Ci/EFPD. Because the graphite in this packed bed will exist outside of the core, many options exist for choosing the size of the graphite spheres and the type of graphite used in the packed bed. Smaller graphite spheres could be used in order to increase the graphite surface area. Non-nuclear grades of graphite could be attractive options for use in the packed bed.

A secondary (intermediate) coolant loop filled with flinak was simulated for separating the primary coolant from the power cycle. The rate of tritium release was much lower for the first 10 to 15 EFPD with an intermediate loop. Beyond 15 EFPD, the tritium release rate for a system with a secondary loop is similar to that of a system with only a primary loop. The effectiveness of gas stripping and capture by graphite for removing tritium from the secondary flinak coolant is less than the effectiveness of identical systems in the flibe primary coolant because flinak has a 1000 times higher solubility for T_2 than flibe does. The effectiveness of permeation windows in the flinak secondary loop was comparable to the effectiveness in flibe.

The effect of varying the initial Li-7 enrichment in flibe was analyzed. By increasing the Li-7 enrichment from 99.995 wt% to 99.999 wt%, the tritium generation rate remains constant with time and the peak tritium release rate without tritium mitigation systems is reduced from 2410 Ci/EFPD to 645 Ci/EFPD. When a packed bed of graphite is used for tritium absorption in this case, its size can be reduced by a factor of 4 (compared to the case with Li-7 enrichment of 99.995 wt%) and the peak tritium release rate is 11 Ci/EFPD.

Finally, the system response to a stepwise increase in temperature with desorption of the system inventory of tritium from graphite was simulated. This simulation showed that there is potential for rapid tritium desorption and release at high temperatures characteristic of accidents. More than 11000 Ci of tritium was released in a matter of minutes. Realistically, the release would be more gradual given that it would take some time for the system to heat up and for desorption to begin. Nevertheless, this gives incentive for maintaining low system tritium inventories. If the inventory is low (where tritium is continually removed and not allowed to build up) then the potential for tritium release due to high-temperature transients will be low. After a period of time at high temperatures, the system was instantaneously restored to nominal conditions and tritium absorption on graphite was resumed. This demonstrated that the system can respond quickly if nominal conditions are restored. Once nominal conditions were restored, the tritium release rate was reduced from 700 Ci/EFPD to 3.5 Ci/EFPD in a matter of 3.5 hours.

7 Fuel performance modeling in the FHR

FHRs will operate with higher power densities, but overall, lower fuel temperatures compared to gas-cooled reactors. This is due to the high volumetric heat capacity of flibe compared to helium. However, the temperature gradient within the fuel is expected to be higher in FHRs than in gas-cooled reactors. Figure 7.1 compares the projected FHR fuel operating envelope with the available TRISO fuel experimental experience. The German TRISO particle experience stems primarily from particles with UO_2 kernels fabricated and irradiated between 1981 and the early 1990s [13]. The US Very High Temperature Reactor (VHTR), previously known as the Next Generation Nuclear Plant (NGNP), refers to a project which is currently developing and qualifying TRISO fuel (with a UCO kernel) for high temperature gas-cooled reactors [16,200]. The first two phases of fuel irradiations in the US VHTR program (called AGR-1/2 and AGR-3/4) have already been completed [16,200,201]. This same generation of fuel may be used in FHRs. The DOE "Deep Burn" project was initiated in order to investigate the use of TRISO fuel (with a mixed-oxide kernel) for consuming transuranic elements from LWR spent nuclear fuel (SNF) [202,203]. In the Deep Burn concept, burnups may reach 60 % fissions per initial metal atom (FIMA) in a single irradiation. The FHR power density in the active fuel region is higher than that of gas-cooled reactors. The particle packing fraction in the pebbles is specified at 40%, which is at the limits of current experience and fabricability. In terms of temperature, burnup, and fast fluence the FHR fuel operating regime is within existing data. Table 7.1 summarizes the average power densities in the Mk1 PB-FHR, a gas-cooled pebble-bed reactor concept called the MPBR1, and the US Very High Temperature Reactor (VHTR), a prismatic block gas-cooled reactor. Because of these differences in FHR fuel specifications and available irradiations data, a fuel performance code called TIMCOAT was used to evaluate TRISO fuel performance in an FHR.

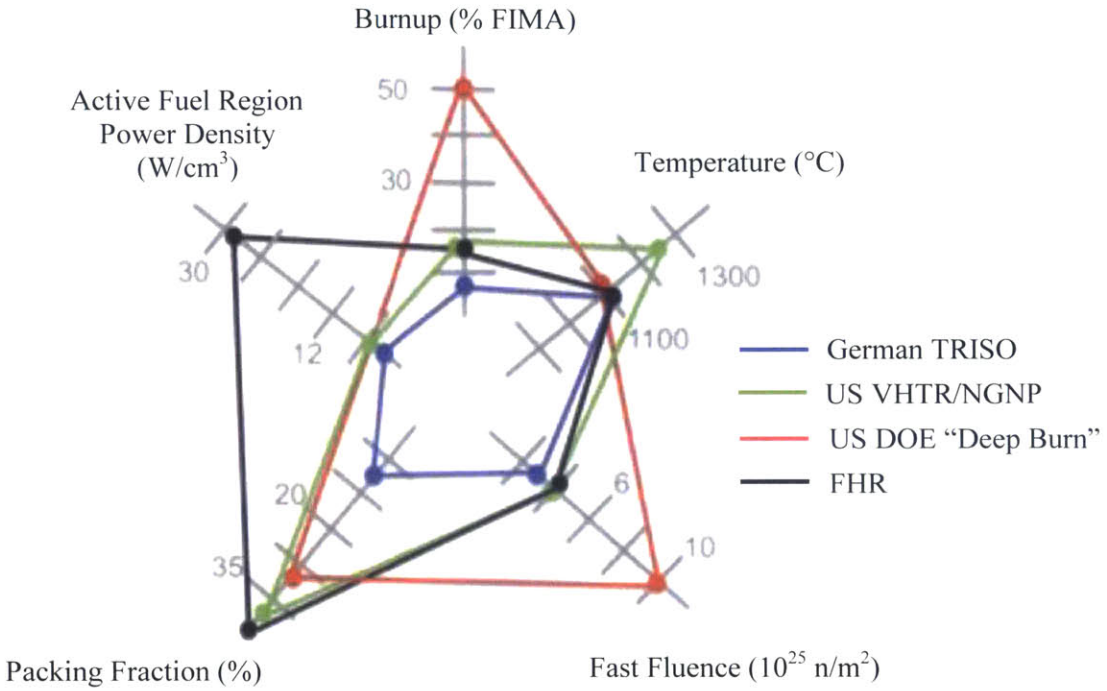

Figure 7.1: Comparison of TRISO fuel operating and experimental envelopes among different reactors. From [3].

Table 7.1: Average fuel and reactor power densities. Mk1 PB-FHR values calculated from data in reference [8]. MPBR1 is a gas-cooled reactor concept. MPBR1 values calculated from data in reference [18]. US VHTR data from reference [204].

Average Power Densities	Mk1 PB-FHR	MPBR1	US VHTR
Active Fuel Region Power Density (MWt/m^3)	22.69	3.65	6.0
Core Active Fuel Region Volume (m^3)	10.4	67.9	-
W/pebble	533	694	-
mW/particle	112.7	63.1	50
W/cm^3 in a particle	404.0	160.0	2230.0

7.1 Introduction to TIMCOAT

The fuel performance code "TIMCOAT" was written at MIT in 2004 [18,205]. TIMCOAT is an integrated probabilistic fuel performance model for TRISO coated-particle fuel. It is capable of modeling fuel histories for both pebble-bed and prismatic fuel cores. For the pebble-bed core, pebble refueling is simulated to account for the non-uniform environment in the core. Because of the SiC and pyrocarbon coatings and the inherent variations in the dimensions and geometries of the

particles, TIMCOAT uses Monte Carlo methods to sample material properties from a distribution in order to capture the statistical nature of material properties and the pebble-bed refueling process. TIMCOAT can analyze for a number of different failure modes. Microscopic cracking can be simulated from a Weibull flaw distribution. A feature that sets TIMCOAT apart from other TRISO codes, such as PARFUME, is that TIMCOAT utilizes a pyrocarbon crack-induced failure model based on probabilistic fracture mechanics in order to simulate the effects from macroscopic cracking in the pyrocarbon and how this may affect the SiC layer. The mechanical model developed in TIMCOAT includes the effects of anisotropic irradiation-induced dimensional changes, isotropic irradiation-induced creep, and fluence-dependent Poisson ratio in irradiation creep. TIMCOAT also includes a chemical model to account for chemical attack of the SiC layer (due to Pd penetration and corrosion by rare-earth fission products) and kernel migration (amoeba effect). A flow chart illustrating the operation of TIMCOAT is shown in Figure 7.2.

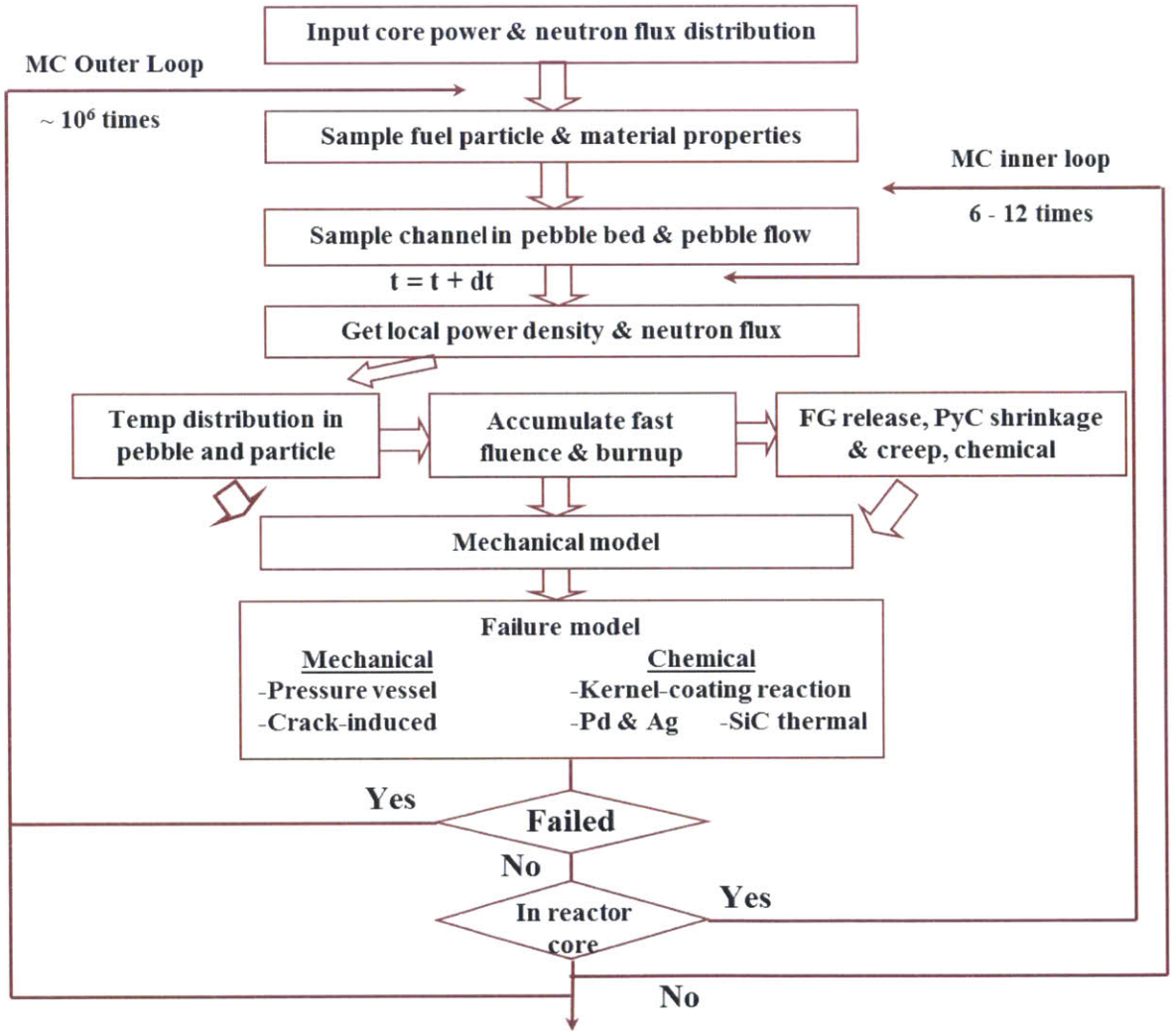

Figure 7.2: TIMCOAT operation flow chart. From [18].

7.2 Verification of current TIMCOAT

TIMCOAT has previously been benchmarked successfully against other codes and irradiations data [18,205,206]. Prior to the current work, TIMCOAT was last used in 2006, and changes had been made to the material library since the original TIMCOAT version was completed in 2004. Due to compatibility issues, (perhaps due to newer compilers), a different random number generator is now used, and the use of the Intel IMSL library has been replaced with RogueWave© IMSL libraries. In order to verify that TIMCOAT was operating correctly for this thesis work, several comparisons were made. In two different cases, the tangential stresses at the IPyC inner surfaces were calculated using the current version of TIMCOAT and compared to the those calculated by Wang in reference [18]. The input parameters for this comparison are given in Table 7.2. Each case was run with TIMCOAT in its steady-state irradiation mode (selected with TIMCOAT option PSWITCH = 3). Figure 7.3 plots the tangential stress at the IPyC inner surface for the current TIMCOAT version overlaid on the original "Figure 3-5" from reference [18]. The calculation was performed twice: once with the Poissons ratio for irradiation creep in pyrocarbon (NUc) fixed at 0.5 and once when this ratio is allowed to vary. The label "MIT, NUc" denotes the original TIMCOAT version. The label "INEEL" refers to the value calculated by the Idaho National Environmental and Engineering Laboratory (now the Idaho National Laboratory) in a comparison performed in reference [18]. Figure 7.4 plots the tangential stress at the IPyC inner surface calculated with the current version of TIMCOAT overlaid on the original "Figure 3-6" from reference [18]. In each case, reasonably close agreement is achieved.

Next, the TRISO particle failure probability functionality from the current version of TIMCOAT was compared with a study from reference [207]. Two types of Modular Pebble Bed Reactors (MPBRs) were simulated using TRISO fuel in the "design specification" (DS) and the as-fabricated specifications (AS). These simulations consider the non-uniform nature of the pebble refueling process and the statistical variation in the as-fabricated TRISO particle layer dimensions. The two sets of MPBR parameters are listed in Table 7.3. The power density is the power density in the active fuel zone of the reactor. VSOP is a reactor physics model developed for pebble-bed reactors [208]. A model of MPBR-type reactors was developed in VSOP in order to provide power and flux distributions to TIMCOAT [18]. In both MPBR1 and MPBR2, the reactor model in VSOP is divided into blocks and channels as depicted in Figure 7.5. The two fuel specifications used in the comparison are listed in Table 7.4. The comparison between the current version of TIMCOAT and the previous "v.2" version is given in Table 7.5. In TIMCOAT, the particle specifications used in the calculations are sampled from a statistical variation about the mean (input) values and the pebble refueling schemes are also sampled from a distribution of likely scenarios. Considering that the current version of TIMCOAT and the "v.2" version use different random number generators and slightly different mathematics libraries, the results are reasonably consistent between the two.

Table 7.2: Parameters for comparison of the current TIMCOAT version with a previous version. From reference [18].

Parameter	Case 1	Case 2
Fuel Type	UCO	UCO
Carbon to Uranium ratio	0.36	0.36
Oxygen to Uranium ratio	1.51	1.51
U235 Enrichment (%)	93.15	93.15
End-of-life Burnup (%FIMA)	70.0	70.0
End-of-life Fluence (10^{21}n/cm^2)	3.0	3.0
Irradiation Temperature (°C)	1032	1200
Irradiation Time (EFPD)	1095	1095
Ambient Pressure (MPa)	6.38	6.38
Kernel Density (g/cm^3)	10.52	10.50
Buffer Density (g/cm^3)	0.958	0.958
IPyC/OPyC Density (g/cm^3)	1.96	1.90
IPyC/OPyC BAF0	1.0	1.16
Kernel Diameter (μm)	200	195
Buffer Thickness (μm)	102	100
IPyC Thickness (μm)	53	40
SiC Thickness (μm)	35	35
OPyC Thickness (μm)	39	43

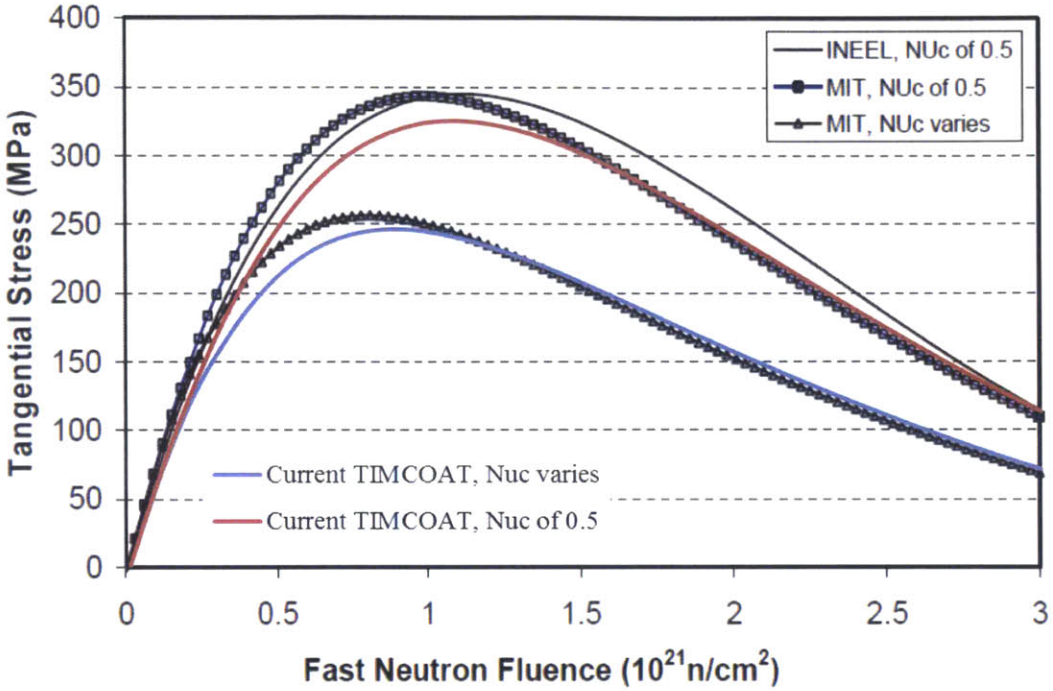

Figure 7.3: Comparison of the tangential stress at the IPyC inner surface from the current version of TIMCOAT with the original version using "Case 1" parameters from Table 7.2. Current version plotted in blue and red. Original black lines from reference [18].

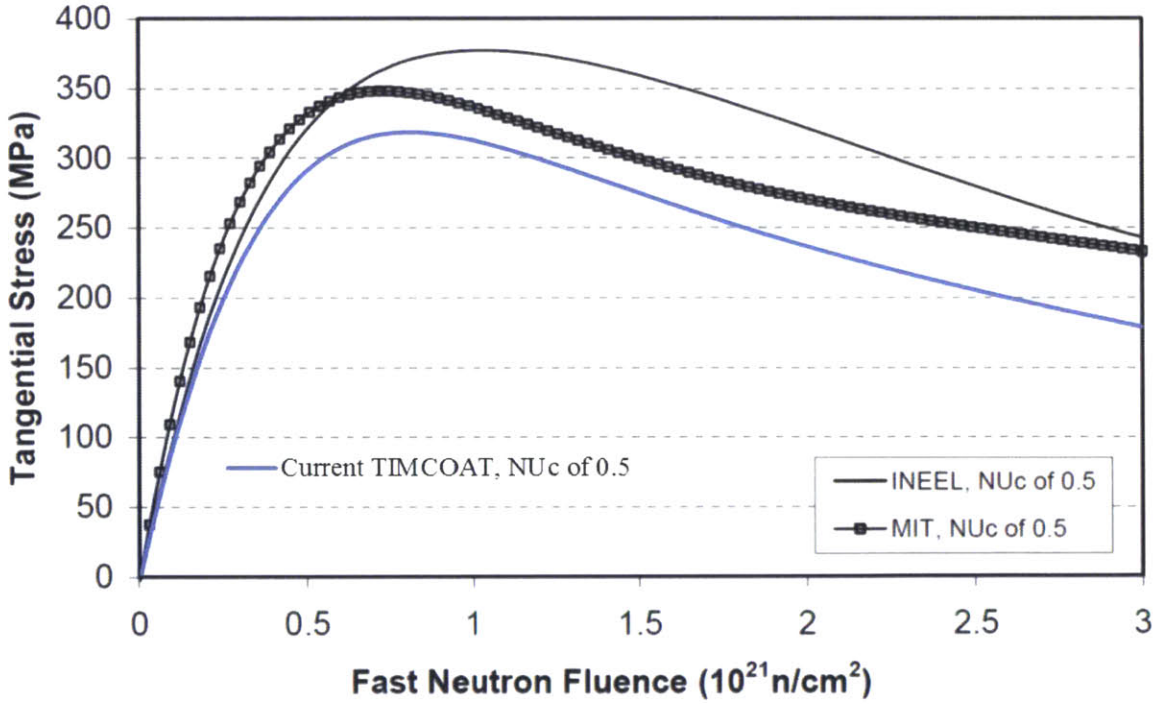

Figure 7.4: Comparison of the tangential stress at the IPyC inner surface from the current version of TIMCOAT with the original version using "Case 2" parameters from Table 7.2. Current version is plotted in blue. Original black lines from reference [18].

Table 7.3: MPBR1 and MPBR2 parameters for past and current TIMCOAT comparisons. From reference [207].

Parameter	MPBR1	MPBR2
Core Height (m)	10.0	11.0
Core Radius (m)	1.75	1.85
Thermal Power (MW)	250	400
Coolant	Helium	Helium
Core Inlet Temperature (°C)	450	500
Core Outlet Temperature (°C)	850	900
Average Power Density (MW/m^3)	3.652	4.777
Max. Power Peaking Factor	5.27	2.74
Min. Power Peaking Factor	4.44E-5	2.70E-5
Coolant Mass Flow Rate (kg/s)	118.0	154.6
Number of Pebbles in Core	360,000	451,600
Number of Particles per Pebble	11,000	15,000
Pebble Cycling Times	10	6
Number of VSOP Blocks	57	93
Number of VSOP Batches per Block	11 (10 effective*)	7 (6 effective*)
Pebble Fuel Zone Radius (mm)	25.0	25.0
Pebble Radius (mm)	30.0	30.0

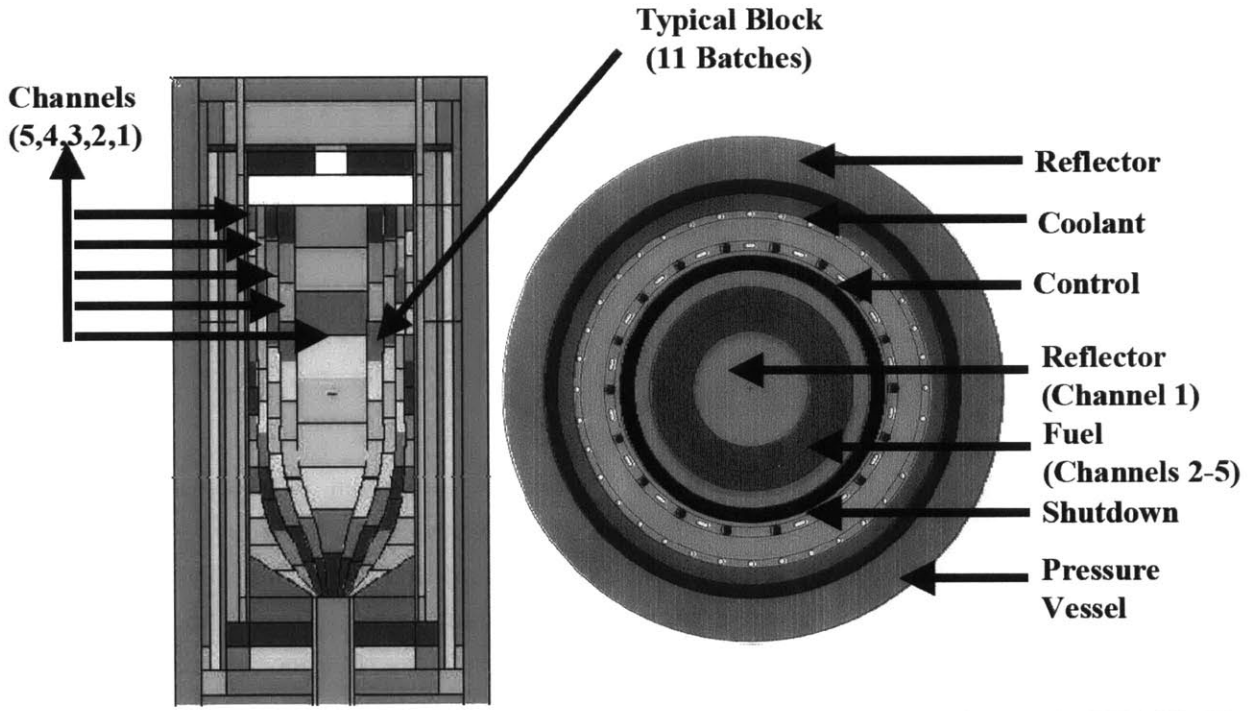

Figure 7.5: VSOP reactor physics model of a pebble bed reactor (MPBR1) for use in TIMCOAT. Image from reference [18].

Table 7.4: TRISO fuel specification for MPBR comparisons. From [209].

Parameter	Design Specifications (DS)	As-Fabricated Specifications (AS)
Fuel Type	UO_2	UO_2
U^{235} Enrichment (%)	7.8 ± 0.1	†
Kernel Diameter (μm)	500 ± 20	497 ± 14.1
Kernel Density (g/cm^3)	≥ 10.4	10.81 ± 0.01
Buffer Thickness (μm)	90 ± 18	94 ± 10.3
Buffer Density (g/cm^3)	≤ 1.05	1.00 ± 0.05
IPyC Thickness (μm)	40 ± 10	41 ± 4.0
IPyC Density (g/cm^3)	1.90 ± 0.1	Not Measured
SiC Thickness (μm)	35 ± 4.0	36 ± 1.7
SiC Density (g/cm^3)	≥ 3.18	3.20
OPyC Thickness (μm)	40 ± 10	40 ± 2.2
OPyC Density (g/cm^3)	1.90 ± 0.1	1.88
IPyC/OPyC BAF0	1.058 ± 0.00543	1.058 ± 0.00543

Table 7.5: TRISO particle failure probabilities comparison.

	TRISO Particle Failure Probability Current TIMCOAT	TRISO Particle Failure Probability TIMCOAT "v.2" from [207]
DS-MPBR1	0.0147	0.0142
AF-MPBR1	0.0146	0.0123
DS-MPBR2	0.0305	0.0279
AF-MPBR2	0.0308	0.0290

7.3 TIMCOAT comparison with PARFUME

The stress evolution during a steady-state irradiation simulation was compared between TIMCOAT and PARFUME (a TRISO fuel performance model developed at INL [210]). A sample calculation with PARFUME (from reference [211]) was compared with the TIMCOAT results obtained using the same input. The input parameters are summarized in Table 7.6. In this case, PARFUME simulated a pebble fuel element. In PARFUME the element surface temperature is set at a constant value, and then the temperature profile is calculated throughout the pebble and into the particles. In the steady-state irradiation mode of TIMCOAT, the irradiation temperature is constant in time and space. Thus a flat temperature profile is assumed through the particle layers. In order to

account for this difference in operation between TIMCOAT and PARFUME, the input irradiation temperature for TIMCOAT was set to 950 °C so that this temperature was close to the average particle temperature (evident from "Figure 6-7" in reference [211]) in the PARFUME simulation.

Two other points must be highlighted. First, PARUME uses a Poisson's ratio fixed at 0.5 for irradiation creep of pyrocarbon. TIMCOAT allows this value to decrease down to 0.4 with irradiation. For the comparison in Figure 7.6, the TIMCOAT Poisson's ratio was fixed at 0.5 in order to match PARFUME. Second, PARFUME uses an input variable called "CREEPAMP" whose default value multiplies the steady state irradiation creep coefficient in pyrocarbon by a factor of 2. TIMCOAT does not use this type of factor; however, for the purposes of the comparison in Figure 7.6, the steady state irradiation creep coefficient in pyrocarbon was also multiplied by a factor of 2 in TIMCOAT. Figure 7.6 compares the tangential (t) and radial (r) stresses in the different layers between a simulation with PARFUME and a simulation with the current version of TIMCOAT. In the legend, "t" stands for tangential, "r" stands for radial, "i" stands for the inner surface of a layer and "o" stands for outer surface of a layer. In this case, the stresses calculated with TIMCOAT (with the two alterations mentioned above) are very close to those calculated with PARFUME. All of the PyC tangential stresses are tensile (positive) all of the SiC tangential stresses are compressive (negative). The radial stress at the SiC outer surface is compressive, and the radial stress at the SiC inner surface is tensile.

Figure 7.7 compares the tangential (t) and radial (r) stresses in the different layers between a simulation with PARFUME and a simulation with the current version of TIMCOAT without the alterations to the creep coefficient and the Poisson's ratio made for Figure 7.6. In Figure 7.7, because the creep coefficient is *not* multiplied by 2 (as is done in PARFUME and was done in TIMCOAT for Figure 7.6) the stresses are exaggerated. That is, tensile stresses are more tensile, and compressive stresses are more compressive.

The purpose of this comparison was not necessarily to distinguish one code as "correct" and the other as "incorrect". Instead, it was to note two differences between the models which result in significant differences in the calculations and to make the reader and future model-users aware of these differences. To summarize, PARUME uses a Poisson's ratio fixed at 0.5 for irradiation creep of pyrocarbon. TIMCOAT allows this value to decrease down to 0.4 with irradiation. PARFUME uses an input variable called "CREEPAMP" whose default value multiplies the steady state irradiation creep coefficient in pyrocarbon by a factor of 2. TIMCOAT does not use this type of factor. In Figure 7.7, compared to PARFUME, TIMCOAT calculates compressive stresses which are more compressive and tensile stresses which are more tensile. If TIMCOAT is altered to mimic PARFUME with a fixed Poisson's ratio and a creep multiplication factor of 2, then Figure 7.6 shows that the TIMCOAT calculations are comparable to those of PARFUME.

Table 7.6: Fuel and irradiation input parameters for PARFUME/TIMCOAT comparison. EOL = end-of-life. From [211].

Parameter	Value
Fuel Element Surface Temperature (°C)	840.05
Irradiation Time (days)	351
EOL Fast Fluence (n/m^2, $E > 0.18$ MeV)	$5x10^{25}$
Fuel Type	UO_2
Oxygen-to-Uranium Ratio	2
Carbon-to-Uranium Ratio	0
Kernel Density (g/cm^3)	10.81
Buffer Density (g/cm^3)	1.0
IPyC Density (g/cm^3)	1.9
OPyC Density (g/cm^3)	1.88
IPyC BAF	1.053
OPyC BAF	1.019
IPyC Weibull Modulus	9.5
SiC Weibull Modulus	8.02
Poisson's Ratio	0.5
Creep Amplification Factor	2.0
Kernel Diameter (μm)	497
Buffer Thickness (μm)	94
IPyC Thickness (μm)	41
SiC Thickness (μm)	36
OPyC Thickness (μm)	40

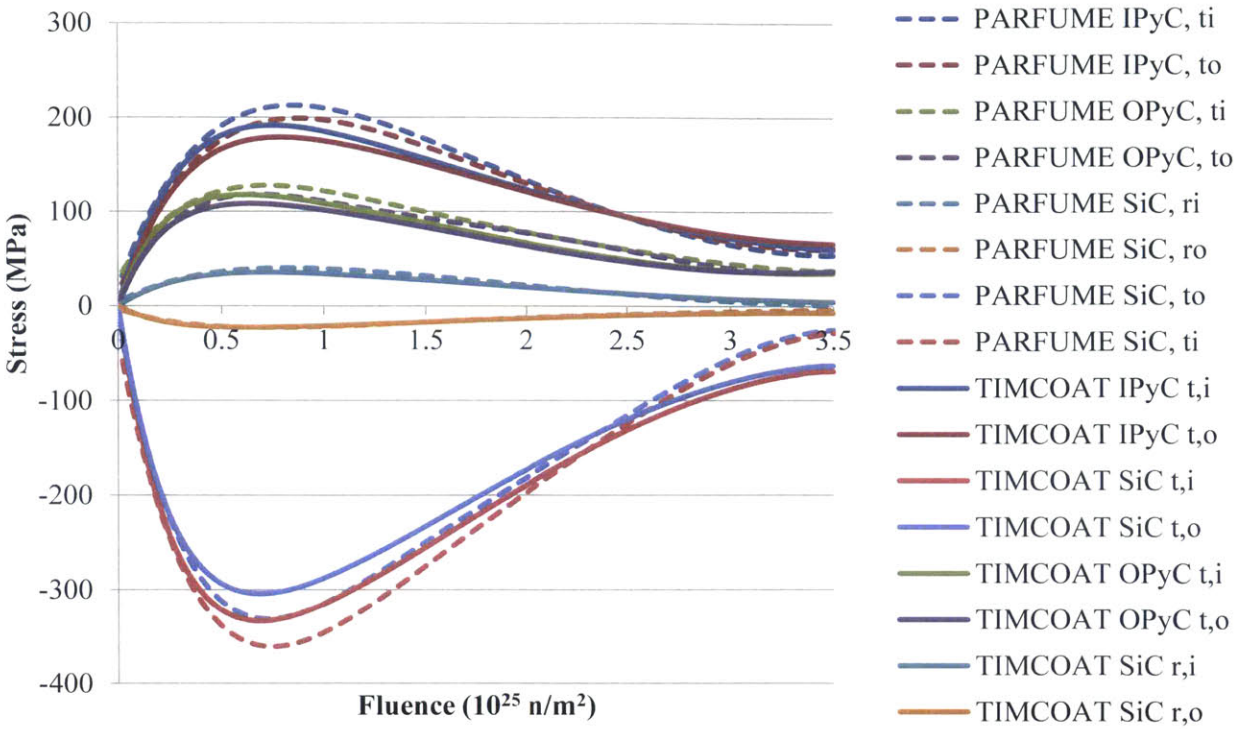

Figure 7.6: Comparison between TIMCOAT and PARFUME. PARFUME data from reference [211]. In this case TIMCOAT was altered such that the creep Poisson's ratio was fixed at 0.5 and the steady state creep coefficient was multiplied by 2. These are two things that PARFUME does.

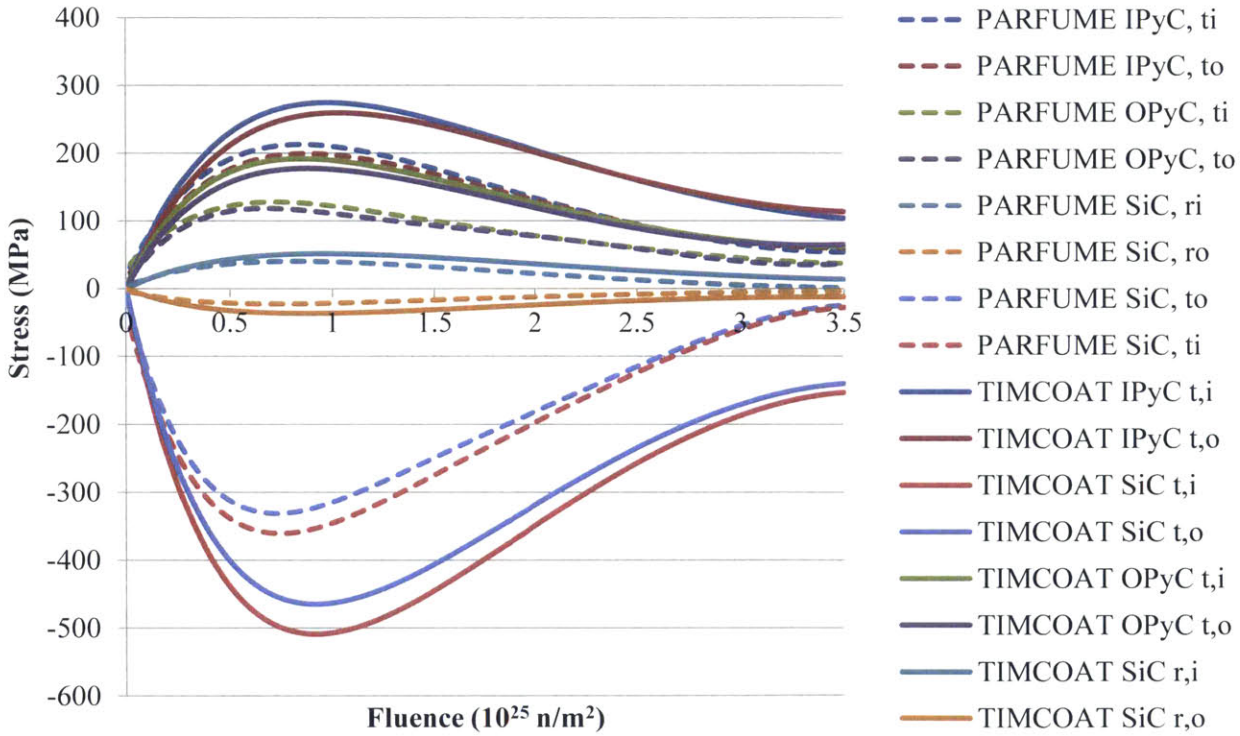

Figure 7.7: Comparison between TIMCOAT and PARFUME. PARFUME data from reference [211]. In this case TIMCOAT was NOT altered in any way from its native format.

7.4 TIMCOAT comparison with AGR-1 irradiation

The preceding sections in this chapter focused on the stress calculations within TIMCOAT. In this section, particle failure probabilities calculated with TIMCOAT are compared to particle failure probabilities calculated with PARFUME using input from the AGR-1 irradiation. The TIMCOAT TRISO particle failure probability calculations have previously been benchmarked favorably against the NPR series of irradiations and others [18,205,206]. There are many different effects (fission gas release, statistical variations in layer densities/dimensions, $CO_{(g)}$ production, chemical reactions, etc.) which can be turned on or off in TIMCOAT and PARFUME, and these effects impact the calculated particle failure rates. A brief comparison between the AGR-1 irradiation, a PARFUME simulation, and a TIMCOAT simulation will be made here in order to provide a new comparison of TIMCOAT with a recent irradiation. The AGR-1 irradiation was the first of 8 planned TRISO fuel irradiations at INL for the Advanced Gas Reactor (AGR) fuel development and qualification program [16]. It was completed in 2009. The AGR-1 experiment consisted of numerous capsules, each filled with several stacks of several graphite compacts (similar to those illustrated in Figure 1.8) with embedded AGR-1 specification TRISO particles.

The AGR-1 baseline fuel specifications used for the PARFUME simulations are given in Table 7.7. Except for a few parameters which are not used by TIMCOAT, these same specifications are also used in the TIMCOAT simulations. Additional parameters required by TIMCOAT are summarized in Table 7.8. Aside from the coating rates in Table 7.8, the other parameters were taken from reference [18], and most of these parameters originated in reference [212], which is also used by PARFUME [210]. The irradiation conditions for the simulations are summarized in Table 7.9. Although there were 13 cycles of the Advanced Test Reactor (ATR) during the AGR-1 irradiation, the PARFUME simulation was carried out using steady-state, constant temperature conditions where the accumulation of fast-fluence and burnup was assumed to be linear [213]. The irradiation temperature in Table 7.9 is the time-averaged-volume-averaged (TAVA) temperature in compact 3-3-1. In PARFUME, the OPyC surface temperature is held constant at this TAVA temperature and a temperature profile is calculated between the OPyC and the kernel center. In the steady-state irradiation mode in TIMCOAT the irradiation temperature is constant throughout the particle thickness, *i.e.* the temperature profile is flat in the particle. It is reported that the kernel temperature can be 40 to 60 °C higher than the OPyC temperature [213]. In order to take this difference into consideration, TIMCOAT steady-state irradiations were run with temperatures of 1051 °C and 1100 °C. Although both PARFUME and TIMCOAT can account for statistical variations in material properties, the PARFUME simulation only accounted for statistical variations in coating thicknesses; thus the same simplification was used in the TIMCOAT simulation. Additionally, the $CO_{(g)}$ production model and Pd attack of SiC were not activated in the PARFUME simulation. Correspondingly, the chemical model in TIMCOAT was also turned off for certain runs.

Table 7.10 summarizes the particle failure[16] probabilities for AGR-1 baseline particles in compact 3-3-1 as calculated by TIMCOAT and PARFUME. In each TIMCOAT run, 1 million particles were simulated. PIE from the AGR-1 irradiations showed that no particles failed during the irradiations [16]. A total of 297,744 particles were irradiated in the entire AGR-1 experiment [16]. Compact 3-3-1 contained 4154 particles, and none of these were found to have failed [16]. Thus, the experimental data do not allow calculation of a failure probability. Given that none of the 4154 particles in Compact 3-3-1 failed, the TIMCOAT runs which calculated particle failure rates of 1.1×10^{-4} and 9.3×10^{-5} are plausible, but the other TIMCOAT runs predict conservative failure rates. PARFUME predicts particle failure rates a couple orders of magnitude lower than TIMCOAT. The predicted IPyC failure rates are about one order of magnitude higher in the TIMCOAT simulation than in the PARFUME simulation. In both TIMCOAT and PARFUME, the models determined that all of the simulated failures were induced by IPyC cracking and not by any other mechanisms.

Table 7.7: TRISO particle specifications for AGR-1 baseline particles used in AGR-1 compact 3-3-1. From [16,213].

	Parameter	± Standard Deviation	Used in TIMCOAT?	Used in PARFUME?
Fuel Type	UCO		X	X
U-235 Enrichment (wt %)	19.736	0.047	X	X
O/U (atomic ratio)	1.3613		X	X
C/U (atomic ratio)	0.3253		X	X
Uranium contamination fraction	3.64×10^{-7}			X
Kernel diameter (μm)	349.7	9.0	X	X
Buffer thickness (μm)	103.5	8.2	X	X
IPyC thickness(μm)	39.4	2.3	X	X
SiC thickness (μm)	35.3	1.3	X	X
OPyC thickness (μm)	41.0	2.1	X	X
Particle aspect ratio at SiC layer	1.040			X
IPyC Weibull modulus	9.5		X	X
SiC Weibull modulus	6.0		X	X
OPyC Weibull modulus	9.5		X	X
PyC Poisson's ratio in creep[17]	0.5			X
PyC creep coefficient amplifier	2.0			X
Kernel density (g/cm^3)	10.924	0.015	X	X
Buffer density (g/cm^3)	1.10	0.04	X	X
IPyC density (g/cm^3)	1.904	0.014	X	X
OPyC density (g/cm^3)	1.907	0.008	X	X
IPyC BAF	1.022	0.002	X	X
OPyC BAF	1.019	0.003	X	X
Ambient pressure (MPa)	0.1		X	X

[16] Particle failure is defined as cracking in the three structural layers: IPyC, SiC, and OPyC.
[17] TIMCOAT utilizes a Poisson's ratio in PyC creep; however it is calculated to vary between 0.5 and 0.4. It is not an input parameter.

Table 7.8: Additional parameters required by TIMCOAT which were not reported for the AGR-1 TRISO particles.

Parameter	Value	Reference
IPyC coating rate (μm/min)	3.0	[214]
OPyC coating rate (μm/min)	3.0	[214]
PyC crystallite length (μm)	29.98	[18]
PyC characteristic strength (MPa-m^3/modulus)	24.0	[18]
SiC characteristic strength (MPa-m^3/modulus)	9.0	[18]
SiC fracture toughness (MPa-$\mu m^{0.5}$)	3500	[18]
Standard deviation in SiC fracture toughness (MPa-$\mu m^{0.5}$)	± 530.72	[18]

Table 7.9: Irradiation conditions for AGR-1 compact 3-3-1 simulation in PARFUME and TIMCOAT. From [213].

Burnup (% FIMA)	Fluence (n/m^2, E > 0.18 MeV)	Irradiation Time (days)	Temperature (°C)
19.00	$4.23x10^{25}$	620.2	1051

Table 7.10: Summary of failure probabilities calculated for particles in AGR-1 compact 3-3-1 calculated with TIMCOAT compared to those reported from a PARFUME calculation in reference [213]. *In steady-state mode, TIMCOAT uses a flat temperature profile in the particle.

Code	Failure Probability	Probability of IPyC Cracking	Temperature (°C)	Property Sampling	Fission Gas Model	Chemical Model
TIMCOAT	$3.2x10^{-3}$	$5.7x10^{-1}$	1051*	Dimensions only	Off	Off
TIMCOAT	$7.2x10^{-4}$	$3.6x10^{-1}$	1100*	Dimensions only	Off	Off
TIMCOAT	$1.1x10^{-4}$	$3.7x10^{-1}$	1100*	Dimensions only	On	Off
TIMCOAT	$7.1x10^{-3}$	$3.7x10^{-1}$	1100*	Dimensions only	On	On
TIMCOAT	$9.3x10^{-5}$	$3.7x10^{-1}$	1100*	All	On	Off
PARFUME	$7.15x10^{-7}$	$4.01x10^{-2}$	1051	Dimensions only	On	Off

7.5 TIMCOAT modifications for FHR simulations

Figure 1.7 shows that the Mk1-PB-FHR fuel pebble is different from previous fuel pebble concepts. This pebble is an annular pebble consisting of a fuel zone in the pebble which surrounds a

center graphite annulus. TIMCOAT was modified in order to enable simulation of this type of pebble. Two input options were created: "ANNULAR_PEBBLE" is a flag turning on or off the simulation of an annular pebble, and "PFZINRADIUS" is the inner radius of the fuel zone in the annular pebble.

Since TIMCOAT calculates the coolant temperature throughout the reactor and then calculates the fuel temperature using the coolant temperature as a boundary condition, TIMCOAT was modified with the necessary flibe coolant properties and heat transfer correlations. The correlation for the Nusselt number in a packed bed with Reynolds numbers from 250 to 500,000 is given by Eq (7.1) [172,173]. The Reynolds number is given by Eq (7.2), where ρ is the flibe density given by Eq (2.11), v_s is the superficial velocity of flibe in the core, d_{pebble} is the fuel pebble diameter, μ is the flibe viscosity given by Eq (5.24), and P_f is the pebble packing fraction in the core. The Prandtl number is given by Eq (7.3) where c_p is the heat capacity of flibe (2390 J/kg-K,) and k is the thermal conductivity of flibe given by Eq (7.4). In Eq (7.4), k is given in units of W/m-K, T is temperature in Kelvin, and M is the formula mass of the salt (for flibe M = 33.0 g/mol) [40]. Finally, the heat transfer coefficient from the coolant to the pebble surface is given by Eq (7.5).

$$\mathrm{Nu} = \mathrm{Pr}^{1/3}\left[\left(1.18\mathrm{Re}^{0.58}\right)^4 + \left(0.23\mathrm{Re}^{0.75}\right)^4\right]^{0.25} \tag{7.1}$$

$$\mathrm{Re} = \frac{\rho v_S d_{pebble}}{\mu P_f} \tag{7.2}$$

$$\mathrm{Pr} = \frac{c_p \mu}{k} \tag{7.3}$$

$$k = 5.0\times10^{-4}T + {}^{32.0}\!/_{M} - 0.34 \tag{7.4}$$

$$h = \frac{k\,\mathrm{Nu}}{d_{pebble}} \tag{7.5}$$

7.6 FHR full core simulation in TIMCOAT

TIMCOAT has two existing pebble-bed reactor models which derive reactor power and flux distributions from pebble-bed models made in the VSOP code (see Section 7.2 and Figure 7.5). Because an FHR reactor model for TIMCOAT was not available, the existing VSOP models were used. This is believed to be a reasonable approach since the neutronics in a PB-FHR will be similar to those in a gas-cooled pebble-bed reactor. The input to TIMCOAT was selected in order to match the Mk1 PB-FHR power densities, fuel specifications, and core inlet and outlet temperatures. The VSOP model for the MPBR1 reactor was used for the FHR simulations. The MPBR1 core model in VSOP was shown in Figure 7.5. The core height and radius are 10.0 m and 1.75 m, respectively. The core active fuel region has a volume of 67.9 m^3. Assuming a pebble packing fraction of 0.60 in the core, the volume of fuel pebbles in the MPBR1 core is 40.715 m^3. The Mk1 PB-FHR uses a fuel

pebble having diameter of 3 cm. The volume of one Mk1-PB-FHR pebble is 1.414×10^{-5} m^3; thus, an MPBR1 core model in TIMCOAT will hold 2879997 Mk1-PB-FHR pebbles. Table 7.1 gives the thermal power per pebble in the Mk1-PB-FHR at 533 W/pebble. At 533 W/pebble, a pebble-bed FHR using the VSOP MPBR1 model in TIMCOAT will have a thermal power of 1535 MWt. With core inlet and outlet temperatures of 600 and 700 °C, respectively, this reactor would have a coolant mass flow rate of 6422.6 kg/s. With these specifications, this model FHR matches the Mk1-PB-FHR active fuel region power density of 22.6 MW/m^3. The reactor parameters for simulating an FHR-type reactor (which will be called "FHR-T1") using the MPBR1 model in TIMCOAT are summarized in Table 7.11. The fuel specifications are summarized in Table 7.12. Mk1-PB-FHR fuel parameters were used except for parameters that are required but which were not specified in the Mk1-PB-FHR report. The layer coating rates and characteristic strengths for this simulation are from Table 7.8.

There are some significant limitations to using the existing VSOP MPBR1 model in TIMCOAT for FHR analysis. First, the VSOP MPBR1 model only allows exactly 10 refueling cycles for a total pebble in-core time of about 300 days. Second, this model only allows burnup to 0.10 FIMA. The actual projected burnup for the Mk1 PB-FHR is 180 MWd/kg HM (or about 0.18 FIMA) [8]. The current model limitations compared to Mk1 PB-FHR specifications are summarized in Table 7.13. Since the Mk1 PB-FHR TRISO specifications are different from the AGR specifications being qualified at INL, the FHR-T1 simulations carried out here should provide some indication of the performance of this fuel specification relative to the AGR-1 specifications.

Table 7.11: Parameters for FHR-T1 simulation in TIMCOAT.

Parameter	Value
Core Height (m)	10.0
Core Radius (m)	1.75
Core Power (MWt)	1535
Average Power Density in Active Fuel Region (MWt/m^3)	22.6
Coolant inlet temperature (°C)	600
Coolant outlet temperature (°C)	700
Coolant mass flow rate (kg/s)	6422.6
Fuel Pebble Radius (m)	0.0150
Fuel Pebble fuel zone outer radius (m)	0.0140
Fuel Pebble inner annulus radius (m)	0.0125
Number of fuel pebbles in core	2879997
Number of particles per pebble	4730

Table 7.12: TRISO fuel specifications for FHR-T1 simulation in TIMCOAT. Where possible, parameters were taken from the Mk1-PB-FHR report [8]. Other parameters required by TIMCOAT were taken from the AGR-1 baseline fuel specifications.

	Parameter	References for Parameters	± Standard Deviation	References for Std Dev
Fuel Type	UCO	[8]		
U-235 Enrichment (wt %)	19.90	[8]	0.047	[16]
O/U (atomic ratio)	0.5	[8]		
C/U (atomic ratio)	1.5	[8]		
Kernel diameter (μm)	400	[8]	9.0	[16]
Buffer thickness (μm)	100	[8]	8.2	[16]
IPyC thickness(μm)	35.0	[8]	2.3	[16]
SiC thickness (μm)	35.0	[8]	1.3	[16]
OPyC thickness (μm)	35.0	[8]	2.1	[16]
IPyC Weibull modulus	9.5	[213]		
SiC Weibull modulus	6.0	[213]		
OPyC Weibull modulus	9.5	[213]		
Kernel density (g/cm^3)	10.924	[213]	0.015	[16]
Buffer density (g/cm^3)	1.10	[213]	0.04	[16]
IPyC density (g/cm^3)	1.904	[213]	0.014	[16]
OPyC density (g/cm^3)	1.907	[213]	0.008	[16]
IPyC BAF	1.022	[213]	0.002	[16]
OPyC BAF	1.019	[213]	0.003	[16]
Ambient pressure (MPa)	0.1			

Table 7.13: Quantities which cannot be changed in the current VSOP model in TIMCOAT compared to Mk1 PB-FHR values.

	VSOP MPBR1 model used in TIMCOAT for FHR-T1 simulation	Mk1 PB-FHR
EOL Burnup (FIMA)	0.10	0.18
Core Residence Time	Variable based on refueling simulation up to about 300 days	1 year or more
Refueling cycles per pebble	10	12

Table 7.14 summarizes the failure rates for five different simulations. Two simulations were run with Monte Carlo sampling of material properties turned on. These properties are sampled based the standard deviations of the properties about the mean values specified in the input file. The Mk1-PB-FHR report does not specify the standard deviation for coating thicknesses, densities, strengths, etc. Thus, for the two cases where the properties were sampled, the standard deviations in the property values were taken from the AGR-1 fuel specifications and other references as summarized in Table 7.8 and Table 7.12. In the two cases where properties were not sampled, the mean particle values were used. Without property sampling, this means that all of the particles were identical and the only difference is the irradiation history for each particle based on its circulation through the reactor core.

Additionally, cases were run with and without the chemical model in TIMCOAT which accounts for thinning of the SiC layer due to corrosion with Pd and other fission products and kernel migration (also known as the amoeba effect). Kernel migration is the process by which the fuel kernel moves up the temperature gradient within the particle. Most fuel performance models assume that the SiC layer fails if the kernel migrates to the point that it comes into contact with the SiC layer. Kernel migration occurs due to carbon dissolution at the hot side of the kernel and graphite deposition at the cold side of the kernel. Migration increases with time, temperature, thermal gradient, and carbon monoxide production [13]. Historically, kernel migration is only significant in oxide fuel (UO_2 kernel), whereas UCO kernels significantly reduce or completely eliminate kernel migration [13].

Table 7.14 shows high failure rates for all of the cases using the Mk1 PB-FHR specification of TRISO particle. The two cases utilizing nominal particle specifications (without property sampling) had failure rates considerably lower. In all cases the failure rates are dominated by initiation from IPyC cracking. Overpressure failures and kernel migration failures (amoeba effect) did not occur.

The simulation was repeated using the AGR-1 TRISO particle specifications instead of the Mk1 PB-FHR TRISO particle specifications. The AGR-1 specifications were summarized in Table 7.7 and Table 7.8. For this simulation, the AGR-1 enrichment was increased from 19.7 to 19.9 wt % U-235 in accordance with Mk1 PB-FHR specification on enrichment. Because the AGR-1 particle is smaller than the Mk1 PB-FHR particle, the number of AGR-1 particles in a single Mkl PB-FHR pebble would be 5136 in order to retain the same total volume of TRISO particles per pebble. Using the AGR-1 specification of fuel reduced the particle failure rate by a factor of 20 to 30. It is not clear how the Mk1 PB-FHR TRISO specifications were chosen, but the AGR-1 particles clearly exhibit better performance in the simulations. AGR-1 particles have a carefully selected UCO stoichiometry, significantly different from the Mk1 PB-FHR particles. The AGR-1 particles also have a smaller kernel while utilizing a slightly larger buffer than the Mk1 PB-FHR particle. Additionally, the IPyC and OPyC layers are thicker in the AGR-1 particle. The confluence of these differences results in improved performance.

Table 7.14: Failure probabilities simulated with TIMCOAT for a burnup of 0.10 FIMA (~100 MWd/kg) for the FHR-T1 case with and without property sampling and the chemical model.

TRISO Specification	Property Sampling	Chemical Model	Particle Failure Probability	IPyC Layer Failure Probability	Probability of failure induced by IPyC cracking
Mk1 PB-FHR	On	Off	0.3120	0.9943	0.3120
Mk1 PB-FHR	On	On	0.3206	0.9944	0.3206
Mk1 PB-FHR	Off	Off	0.1901	0.9958	0.1901
Mk1 PB-FHR	Off	On	0.2227	0.9958	0.2227
AGR-1	Off	On	0.0107	0.9977	0.0107

7.7 Summary of fuel performance modeling

The FHR power density in the active fuel region is higher than that of gas-cooled reactors. The particle packing fraction in the pebbles is specified at 40%, which is at the limits of current experience and fabricability. Because of these differences in FHR fuel specifications and available irradiations data, a fuel performance code called TIMCOAT was used for an initial evaluation of TRISO fuel performance in an FHR.

After nearly 10 years since its last use, the TIMCOAT fuel performance code developed at MIT was revived for use on the pebble-bed FHR concept. TIMCOAT has previously been benchmarked successfully against other codes and irradiations data [18,205,206]. Some changes had been made to the material library since its original version in 2004, and TIMCOAT was last used in 2006. Due to compatibility issues (with the available compilers), a different random number generator is now used, and the use of Intel IMSL libraries has been replaced with RogueWave© IMSL libraries. In order to verify that TIMCOAT is operating correctly, several comparisons were made. The code comparisons with previous TIMCOAT results show good agreement.

The stress evolution during a steady-state irradiation simulation was compared between TIMCOAT and PARFUME (a TRISO fuel performance model developed at INL). The purpose of this comparison was not necessarily to distinguish one code as "correct" and the other as "incorrect". Instead, it was to note two differences between the models which result in significant differences in the calculations and to make the reader and future model-users aware of these differences. To summarize, PARUME uses a Poisson's ratio fixed at 0.5 for irradiation creep of pyrocarbon. TIMCOAT allows this value to decrease down to 0.4 with irradiation. PARFUME uses an input variable called "CREEPAMP" whose default value multiplies the steady state irradiation creep coefficient in pyrocarbon by a factor of 2. TIMCOAT does not use this type of factor. In its native format, TIMCOAT calculates compressive stresses which are more compressive and tensile stresses which are more tensile than PARFUME. If TIMCOAT is altered to mimic PARFUME with a fixed Poisson's ratio and a creep multiplication factor of 2, then the TIMCOAT calculations are comparable to those of PARFUME.

The TIMCOAT TRISO particle failure probability calculations have previously been benchmarked favorably against the NPR series of irradiations and others. A brief comparison between the AGR-1 irradiation, a PARFUME simulation, and a TIMCOAT simulation was made here in order to provide a new comparison of TIMCOAT with a recent irradiation. Given that none of the 4154 particles in Compact 3-3-1 failed, the two TIMCOAT runs which calculated particle failure rates of 1.1×10^{-4} and 9.3×10^{-5} are plausible, but the other TIMCOAT runs over predict the failure rates. PARFUME predicts particle failure rates a couple orders of magnitude lower than TIMCOAT.

Several options were added to TIMCOAT to enable simulation of a pebbled bed FHR. The Mk1-PB-FHR fuel pebble is different from previous fuel pebble concepts. This pebble is an annular pebble consisting of a fuel zone in the pebble which surrounds a center graphite annulus. TIMCOAT

was modified in order to enable simulation of this type of pebble. Two input options were created: "ANNULAR_PEBBLE" is a flag turning on or off the simulation of an annular pebble, and "PFZINRADIUS" is the inner radius of the fuel zone in the annular pebble. Next, because TIMCOAT calculates the coolant temperature throughout the reactor and then calculates the fuel temperature using the coolant temperature as a boundary condition, TIMCOAT was modified with the flibe coolant properties and heat transfer correlations necessary for these calculations.

A series of full reactor simulations were performed using the modified TIMCOAT code. Because an FHR reactor model for TIMCOAT was not available, the existing VSOP reactor physics model in TIMCOAT was used. This is believed to be a reasonable approach since the neutronics in a PB-FHR will be similar to those in a gas-cooled pebble-bed reactor. The input to TIMCOAT was selected in order to match the Mk1 PB-FHR power densities, fuel specifications, and core inlet and outlet temperatures. Failure rates for all of the cases run using the TRISO specification listed in the Mk1 PB-FHR design report were between 20 and 30%. Switching the fuel specification to the AGR-1 parameters reduced the failure rate to 1%.

8 Summary, conclusions, and future work

8.1 TRIDENT original contribution

A major original contribution of this work is the development of the TRIDENT tritium transport and corrosion model for the FHR. TRIDENT is the only model which integrates a time-dependent model of tritium transport with a time-dependent model of corrosion of structural metals in a fluoride salt reactor coolant system. TRIDENT can simulate both tritium transport and corrosion with or without a specific redox state being specified. This allows simulation of a reactor system where strict redox control maintains a fixed redox potential which, in turn, maintains a constant ratio of the corrosive species (TF) to the diffusive species (T_2). Alternatively, TRIDENT can simulate systems where the relative amounts of TF and T_2 are allowed to drift due to competing phenomena such as the following: TF production from neutron transmutation in flibe; corrosion reactions which consume TF and produce T_2; TF and T_2 sorption on graphite; T_2 diffusion out of the salt; or removal of T_2 and/or TF from the salt via gas stripping, permeation windows, or sorption on graphite. The studies performed with TRIDENT represent the first ever analysis of tritium transport and corrosion in an FHR. The first simulation of the tritium transport response of an FHR system to a high-temperature transient was performed. This study is the first to propose, provide specifications, and analyze measures for mitigating tritium releases in FHRs. The results indicate that although permeation windows and gas stripping are able to significantly reduce tritium release rates, only tritium capture from flibe on a continuously regenerated bed of graphite is capable of reducing tritium release rates to LWR or HWR levels.

While other models of tritium transport have been developed previously, they have had a different focus (such as gas-cooled reactors or fusion reactors) and they do not couple the same phenomena that are coupled in TRIDENT. Table 8.1 compares and contrasts major features of different tritium transport models and a fluoride salt corrosion model. In report "ORNL-4575" a "quasi-steady-state" model of corrosion and corrosion product mass transport in simple "harp" loops was developed [133]. This model was limited to the Hastelloy-N/flibe system, did not couple to tritium transport, lacked true time-dependence, and could only work with simple loop temperature profiles and uniform geometries. Models of corrosion in liquid metal systems (such as lead-bismuth-eutectic and sodium) have been developed. However, the coolant chemistry is different from that in fluoride salts, and there is no need to couple the corrosion models to tritium transport in these reactors [180].

In 1975, a model for the steady-state tritium distribution in a Molten Salt Breeder Reactor was developed in report ORNL-TM-4804 [64]. This model lacked dynamic time-dependence, treated the coolant in 0D (assuming the coolant was homogeneous throughout), and did not couple to corrosion reactions. Codes such as THYTAN (reference [215]) and TPAC (reference [60]) have detailed system-level models for tritium transport in helium-cooled reactors which couple to hydrogen

production. The TPC-SFR and TPC-FUS codes consider tritium transport in sodium-cooled fast-reactors (SFR) and fusion (FUS) reactors with a Pb-Li breeder blanket [216,217]. While THYTAN, TPAC, and TPC-SFR/FUS use simplified steady state permeation approximations, TMAP and TRIDENT use more accurate finite difference diffusion solutions for tritium permeation through metals. TMAP is a tritium analysis code originally written for tritium safety analyses in fusion applications [218,219]. While TMAP does not appear to have any built-in coolant loops or systems, TMAP allows the user to specify different systems (called "enclosures") and to define various reactions or phenomena which may occur in those enclosures. A number of tritium transport studies using TMAP have been carried out for tritium transport in gases, fluoride salts, and liquid metals, including several studies which used TMAP on a systems level for fusion applications [220–222]. However, none of these studies coupled tritium transport behavior with tritium redox and corrosion reactions in a fluoride salt with tritium sorption on fuel pebbles in a pebble bed reactor with a variety of tritium capture systems as is done in TRIDENT.

Table 8.1 Comparison of TRIDENT features critical for FHR analysis with features of other codes.

	TRIDENT	TMAP4/7	ORNL-4575	TPAC	ORNL-TM-4804	SFR/FUS-TPC	THYTAN
Time-dependence	X	X		X		X	X
T Transport	X	X		X	X	X	X
T production model in flibe	X						
Other T production (ternary fission etc.)		User must define		X		X	X
Reactor system-level model	X	User may build		X	X	X	X
Reactor Coolants	flibe/flinak	flibe/He/ Pb/Pb-Li	flibe	He	flibe	Na/Pb-Li	He
Redox Dependence	X		X		X		
Isotope Exchange		X		X	X	X	X
Corrosion Reactions	X		X				
Corrosion Product Mass Transport	X		X				
Model of T sorption on graphite	X				X		
Online pebble refueling effects	X						
T permeator	X						

system model							
Table 8.1 continued	**TRIDENT**	**TMAP4/7**	**ORNL-4575**	**TPAC**	**ORNL-TM-4804**	**SFR/FUS-TPC**	**THYTAN**
T removal to purge gas	X	User may define			X	X	
Counter-current gas stripping	X						
Secondary loop model	X			X	X		X

8.2 TRIDENT summary and conclusions

The model TRItium Diffusion EvolutioN and Transport (TRIDENT) was developed and benchmarked. The equations governing the tritium transport and diffusion phenomena were presented in Chapter 5. TRIDENT considers one dimensional fluid transport and diffusion. The coolant is segmented into volume elements for applying the conservation equations, and the coolant loop is segmented into elements in order to apply a temperature profile and define specific locations in the loop where reactions such as corrosion, tritium absorption, or tritium diffusion may occur. Tritium diffusion through the heat exchanger walls is treated by a finite difference diffusion solution in the metal. The boundary conditions are specified by enforcing an equilibrium (determined by Henry's law in the salt and Sievert's law in the metal) at the salt-metal boundary and by conserving the mass flux to the metal surface with the mass flux into the metal surface. Both the tritium diffusion and corrosion models were benchmarked.

While data from a forced-convection polythermal loop of molten salt containing tritium do not exist for comparison, TRIDENT can be compared to data from static salt diffusion tests. Two such tests were used for benchmarking here. One test involves tritium diffusion through Ni and flibe, and the other test involves tritium diffusion through Ni and flinak. In each case, TRIDENT matched the transient and steady-state behavior of these tritium diffusion experiments.

The corrosion model in TRIDENT was compared against the natural convection flow-loop experiments at ORNL from the 1960s and early 1970s which used MSRE fuel salt containing UF_4. Despite the lack of data required by TRIDENT for modeling the loops, some reasonable results were obtained. The TRIDENT corrosion rates follow the experimentally observed dependence on the square root of the product of the Cr diffusion coefficient with time. Additionally the TRIDENT model shows mass transfer of corrosion products from the hot to the cold leg (as was observed in the experiments). Improvements to the corrosion model must recognize that bulk diffusion and grain boundary diffusion of Cr can be related due to the existence of 3D networks of grain boundaries in real materials. Flow loop corrosion experiments may be required along with an investigation of the deposition kinetics (inverse of the corrosion reaction) in order to improve the corrosion model.

The reactor, reactor systems, material properties, and simulation options for TRIDENT were introduced. A systematic study of the tritium transport and corrosion behavior of the Mk1 PB-FHR

was completed using TRIDENT. The initial simulations focused on the baseline Mk1 PB-FHR using only the baseline reactor specifications and material properties. It was shown that tritium uptake on graphite in the reactor core (accounting for on-line refueling) delays the time it takes to reach a pseudo steady state rate of tritium release from a mere to 5 hours (if graphite uptake is neglected) to 70 EFPD. Additionally, this pseudo steady state release rate when tritium sorption on graphite is accounted for is 2410 Ci/EFPD compared to about 2710 Ci/EFPD without the tritium sorption effects.

The effects of the redox potential on corrosion and tritium transport in an FHR were simulated with TRIDENT. The coolant redox potential determines the chemical form of tritium and the extent of corrosion. Tritium existing as TF is an oxidant capable of corroding structural metals, particularly Cr. Tritium existing as T_2 is notable for its high permeability in structural metals and relatively low solubility in the salt. The simulations show that the tritium release rates can be affected by the chosen redox potential in the salt and that there are corrosion implications of these redox choices. A more corrosive redox potential reduces tritium release rates, but incurs greater corrosion rates and higher dissolved Cr concentrations in the coolant. Given that the tritium release rate reduction with the more corrosive redox potential is only 50 Ci/EFPD lower than the baseline case, and that the corrosion rates are substantially higher at the more corrosive potential, these simulations suggest that the baseline redox potential used during the MSRE is the preferred option for the FHR.

A series of tritium mitigation systems were proposed and analyzed in TRIDENT. It was shown that a low-permeability oxide layer on the air-side of the heat exchanger delays tritium release, but ultimately the same tritium release rates are obtained regardless of the permeability reduction factor (PRF) of that oxide layer. With an oxide layer on the air-facing side of the HX, the tritium concentration in the HX metal tubing increases by a factor of the PRF. This means that the same steady state release rate is attained with a PRF of 1 as with a PRF. In order to prevent tritium from entering the HX tube wall from the coolant, a low permeability material is required. Metal oxides are not chemically stable in flibe, but tungsten is. An FHR using a tungsten HX was simulated. Tungsten reduced the peak tritium release rate and increased the amount of tritium retained in the coolant system and captured by graphite in the reactor core. By retaining more tritium in the primary system, more tritium could be captured in a controlled manner using engineered systems. Due to cost and weight, tungsten is not likely to be a viable material for the HX. It was proposed that a tungsten (or a similar low-permeability material) be used as a coating on the Type 316 SS heat exchangers.

A permeation window constructed of Ni, having a surface area twice that of the heat exchanger, and requiring that 100% of the coolant flow through it (not a side stream operation) reduced the tritium release rate from 2410 Ci/EFPD to 800 Ci/EFPD. A gas stripping system passing 50% of the coolant flow through 10 stripping stages with a stripping gas flow rate of 20000 L/hr reduced tritium release rates from 2410 Ci/EFPD to 439 Ci/EFPD. A packed bed of graphite spheres having the same surface area as the pebbles in the reactor core and featuring online regeneration was effective for reducing peak tritium release rates from 2410 Ci/EFPD to 7.5 Ci/EFPD. Because the graphite in

this packed bed will exist outside of the core, many options exist for choosing the size of the graphite spheres and the type of graphite used in the packed bed. Smaller graphite spheres could be used in order to increase the graphite surface area. Non-nuclear grades of graphite could be attractive options for use as well.

A secondary (intermediate) coolant loop filled with flinak was simulated for separating the primary coolant from the power cycle. The rate of tritium release was much lower for the first 10 to 15 EFPD with an intermediate loop. Beyond 15 EFPD, the tritium release rate for a system with a secondary loop is similar to that of a system with only a primary loop. The effectiveness of gas stripping and capture by graphite for removing tritium from the secondary flinak coolant is less than the effectiveness of identical systems in the flibe primary coolant because flinak has a 1000 times higher solubility for T_2 than does flibe. The effectiveness of permeation windows in the flinak secondary loop was comparable to the effectiveness in flibe.

The effects of varying the initial Li-7 enrichment in flibe were analyzed. By increasing the Li-7 enrichment from 99.995 wt% to 99.999 wt%, the tritium generation rate remains constant with time and the peak tritium release rate without tritium mitigation systems is reduced from 2410 Ci/EFPD to 645 Ci/EFPD. When a packed bed of graphite is used to capture tritium from the salt in this case, its size can be reduced by a factor of 4 (compared to the case with a Li-7 enrichment of 99.995 wt%) and the peak tritium release rate is 11 Ci/EFPD. This is less than the tritium release rate of a large heavy water reactor (HWR). Calculations show only a small requirement for additional SWU in order to achieve this higher Li-7 enrichment.

Finally, the system response to a stepwise increase in temperature with desorption of the system inventory of tritium from graphite was simulated. This simulation showed that there is potential for rapid tritium desorption and release at high temperatures characteristic of accidents. More than 11000 Ci of tritium was released in a matter of minutes. Realistically, the release would be more gradual given that it would take some time for the system to heat up and for desorption to begin. Nevertheless, this gives incentive for maintaining low system tritium inventories. If the inventory is low (where tritium is continually removed and not allowed to build up in the coolant) then the potential for tritium release due to high-temperature transients will be low. After a period of time at high temperatures, the system was instantaneously restored to nominal conditions and tritium absorption on graphite was resumed. Once nominal conditions were restored, the tritium release rate was reduced from 700 Ci/EFPD to 3.5 Ci/EFPD in a matter of 3.5 hours. This demonstrated that the system can respond quickly to absorb tritium if nominal conditions are restored.

8.3 TRIDENT future work

TRIDENT could be used for a number of future studies or modified to incorporate new phenomena. TRIDENT could be used to optimize systems for tritium removal and capture from the coolant. Further systems optimization could reduce tritium releases further and/or reduce the size

and complexity of the tritium capture systems. For example, a packed bed of graphite located between the core exit and the HX entrance has a number of available options. Smaller graphite spheres could be used in order to increase the graphite surface area, and non-nuclear grades of graphite could be attractive for tritium capture. Activated graphites such as AX-21, GX-31, and Maxsorb have high BET surface areas (up to about 4000 m^2/g) and high specific hydrogen capacities. The transient analysis showed that there is potential for rapid tritium desorption at high temperatures characteristic of accidents. Designing systems that minimize the reactor inventory of tritium would be beneficial. TRIDENT could be modified to account for isotopic exchange. The current formulation of TRIDENT does not account for isotopic exchange. This was done in order to simplify the model and is believed to provide more conservative calculations of tritium release rates (especially when a fixed redox condition is specified). Tritium isotopic exchange could be modeled if hydrogen gas were deliberately added to the salt for purposes of redox control, or if tritium permeation into another system containing moisture or hydrogen were modeled. Tritium isotopic exchange with hydrogen (H_2) and water could allow formation of HT and HTO, respectively. TRIDENT could also be used to determine the effects of different coolants. For example, the use of a salt with a high or low solubility for tritium might be desired in an intermediate loop. With a high solubility for tritium, more tritium would be dissolved in the salt. With a low solubility for tritium, it would be easier to remove tritium from the salt.

Other areas for future work concern issues of data availability. Tritium solubilities and material properties for salts other than flibe or flinak are very limited. TRIDENT tritium transport calculations within static salt were compared with data from experiments; however, there were no available data for comparing the tritium transport calculations in TRIDENT with actual tritium transport measurements in *flowing* salt. Next, graphite is a critical sink for tritium, and while data do exist for graphite capacities for tritium, specific studies using the exact graphite used in the reactor should be pursued. Hydrogen uptake experiments on graphite have been conducted using gas-phase hydrogen, but hydrogen uptake on graphite in salt (with varying redox potentials) should be explored. Data exist for cases of hydrogen uptake on graphite at fixed temperatures and/or pressures, but in a real reactor system, the temperature and pressure will vary with time. This creates some uncertainty when data obtained under isothermal or isobaric conditions are used for modeling systems with time-variant temperatures or partial pressures.

Another feature which could be added to TRIDENT, and investigated experimentally, is the effect of neutron irradiation on tritium behavior on graphite. Experiments have shown that irradiation increases the number of hydrogen trapping sites in graphite. This increases the graphite capacity for hydrogen. A fit to experimental data was carried out in Section 2.4.2.3 for predicting the evolution of the number of trapping sites with neutron dose. However, radiation damage in graphite may also decrease the rate at which hydrogen is absorbed on graphite.

The corrosion model in TRIDENT could also be improved. The calculated average weight losses may seem reasonable, but localized losses (such as on grain boundaries due to void formation) may be high. This void formation is not captured in the TRIDENT model. Grain boundaries are 3D

networks, which the current model treats in a 1D fashion where grain boundary diffusion is treated as a separate phenomenon which has no coupling to bulk diffusion. In reality, the grain boundaries can receive new Cr due to chromium from the bulk of the metal diffusing into a grain boundary. This Cr can then diffuse down the grain boundary, which may have intersections with other grain boundaries. Thus, improvements to the corrosion model must recognize that bulk diffusion and grain boundary diffusion of Cr can be related. Flow loop corrosion experiments (with controlled ratios of HF to H_2) may be required along with an investigation of the deposition kinetics (inverse of the corrosion reaction) in order to improve the corrosion model. In Section 3.2.1, aluminum major-metal redox control was suggested as an option for enforcing a reducing potential in flibe. This could also be investigated with loop and static salt experiments.

While this thesis took a broad look at systems and materials for controlling tritium transport, many unexplored options still exist. For example, tritium capture and mitigation systems were simulated individually, but it is possible to employ two or more such systems at the same time. The size and characteristics of the graphite bed for capturing tritium could be optimized. The type of graphite used in the bed for capturing graphite could be engineered specifically for this purpose. A tungsten coating was suggested, but other materials could be investigated as coatings for use on the flibe-facing side of system piping and heat exchangers in order to prevent tritium permeation.

8.4 Chemical stabilities and TRISO fuel PIE in support of BDBA analysis: summary and future work

The chemical stability of fission products and concrete in FHRs was analyzed by calculating the Gibbs free energies of formation and Gibbs reaction free energies for specific reactions. All of this was done in the context of a specific baseline redox potential for the FHR. It is important to consider the redox potential because the stability of various fission products will vary with redox potential. This was the first fission product analysis to consider TRISO fuels in a liquid fluoride salt environment. This was also the first look at the stability of concrete in contact with a fluoride salt under severe accident conditions.

The chemical stability of fission products has been previously analyzed in MSRs (where the fuel is dissolved in the coolant and all of the fission products are generated in the coolant) and in TRISO fuels separately, but the fission product stability as a function of redox potential in a system utilizing both a fluoride salt and TRISO fuel has never been performed until now. The available data for fission product behavior in the MSRE and in TRISO fuels were combined in order to help establish a general framework for fission product stability in the FHR. Calculations were performed in order to determine the stability of fission products in reference to the redox potential in the coolant for a severe case where a UCO TRISO kernel is exposed to the salt.

If fission products are released from the fuel pebble, they will encounter the flibe coolant in the FHR. The chemical redox potential of the coolant will determine whether these fission products will be stable fluorides dissolved in the coolant, or volatile forms liable to escape the coolant. For TRISO

particles with intact SiC layers, only Ag, Eu, and Pd are able to escape, and the Gibbs formation free energies show that at the reference redox potential, Ag and Pd will form metals, but Eu will form a salt-soluble fluoride. If TRISO layers are damaged (such as at high temperatures > 1600 °C), Cs, Ce, I, Kr, Sr, and Xe may escape the particles. It was shown that at the reference redox potential, Cs, Ce, and Sr will form stable fluorides. The noble gases (Kr and Xe) will be released to the off-gas system. At extreme temperatures, CsF will have reduced stability and some Cs may be volatilized from the metallic state. Additionally, if the redox potential is significantly more reducing than that used in the MSRE, CsF stability will be reduced and some Cs may exist in metallic form. Strontium appears to form a stable fluoride under any possible coolant temperature. In the MSRE, iodine was often found to remain in the salt with no evidence of deposition on metal or graphite surfaces. At the reference redox potential of the MSRE, iodine existed in the salt as the iodide ion or as iodides (e.g. CsI), and less than 0.1% was stripped from the salt as I_2 gas [66]. If the salt were to be increasingly oxidizing, a greater portion of the iodine would be in the I_2 gas form.

The stability of fission product carbides, oxides, and fluorides was analyzed by comparing a set of Gibbs reaction free energies. The significance of these results is that if the kernel were to be exposed to the salt, most elements of interest should remain as immobile oxides or carbides in the kernel or as soluble fluorides in the melt. This helps contain radioactivity in the event of a severe accident.

In the event of a coolant leak where liquid salt contacts concrete, concrete chemical stability is important. Most concretes are composed of metal oxides. The Gibbs reaction free energies for the reactions of metal oxides with BeF_2 were evaluated for all of the major metal oxide constituents of the various types of concrete. Many types of thermal insulation are composed of metal oxides. Thus, this analysis is applicable in both cases. The results were normalized by the number of moles of BeF_2 required to balance the equations. The reaction free energies were compared against the BeF_2 potential in flibe which shows that none of the metal oxides are truly stable in the salt. This is an assertion that is well supported by experiments from other researchers which show that liquid fluoride salts dissolve metal oxides. While this analysis determined chemical stabilities, it did not discuss reaction kinetics. Experimental observations by other researchers indicate that reactions of fluoride salts with metal oxides are relatively fast. If metal oxides must be used in locations where they may come into contact with salt, then the most stable of the metal oxides should be chosen. This may require new formulations of concrete, or it may require that critical concrete structures can never come in contact with liquid salt even during an accident. Based on their reaction free energies being near the BeF_2 potential, nickel, chromium, iron and aluminum oxides (though still unstable) are more stable compared to other metal oxides. Calcium, magnesium, potassium, and titanium oxides are the least stable metal oxides in flibe.

It is also important to know whether these reactions are exothermic (generate heat) or endothermic (absorb heat). The reaction enthalpy for each reaction was calculated and used to determine the increase (from exothermic reactions) or decrease (from endothermic reactions) in the coolant temperature due to a chemical reaction between BeF_2 and metal oxides. Whether an

exothermic or endothermic reaction is desirable depends on the situation. If the salt is cooled by an endothermic reaction, this cooling may aid the freezing of the salt, which could plug leaks. If the salt were to freeze on contact with the concrete, this would reduce or eliminate salt-concrete chemical reactions. On the other hand, freezing might block desirable salt coolant flow. Exothermic reactions might heat the salt further, weakening structural materials and changing the chemical stability of any dissolved fission products. Thus, it may be beneficial to select materials with the smallest absolute value of reaction enthalpy. In locations where a salt leak is possible, aluminum, iron, and nickel oxides have better stability than some metal oxides and have small effects on coolant temperature in the event that chemical reactions do occur.

Future work in this area might investigate pathways for the possible mobilization of fission products (such as if the redox potential were suddenly made more reducing). Regarding salt-concrete chemical interactions, experiments could be designed which could test chemical compatibilities and determine if freezing of the salt is sufficient to prevent chemical reactions with concrete. Additionally, new concrete formulations could be explored.

TRISO particles from batch ZrO2-500-AK2 having different exposure histories were examined. Particles in the as-fabricated condition showed no defects of any of the layers. Particles which had been exposed for 3000 hours to flibe at 700 °C in the absence of a neutron field showed no signs of outer degradation and no signs of inner degradation after mounting and polishing. Under normal circumstances, TRISO particles should never come into contact with salt because they are embedded in fuel pebbles. If severe fuel damage were to occur during a BDBA, salt-TRISO contact might occur. By performing a series of freeze-thaw tests in flibe, it was determined that the OPyC layer of irradiated particles is susceptible to cracking in flibe if the salt is allowed to freeze around the particles. This indicates that preventing the salt from freezing around any low-density graphite structures will be important. Future work will involve irradiations of newer TRISO particles fabricated using more established parameters in accordance with the AGR TRISO fuel specifications. The effects of flibe freezing after irradiation of other relevant low-density graphite samples should also be investigated.

8.5 FHR fuel performance modeling summary and future work

The FHR power density in the active fuel region is higher than that of gas-cooled reactors. The particle packing fraction in the pebbles is specified at 40%, which is at the limits of current experience and fabricability. Because of these differences in FHR fuel specifications and available irradiations data, a fuel performance code called TIMCOAT was used for an initial evaluation of TRISO fuel performance in an FHR.

After nearly 10 years since its last use, the TIMCOAT fuel performance code developed at MIT was revived for use on the pebble-bed FHR concept. TIMCOAT has previously been benchmarked successfully against other codes and irradiations data [18,205,206]. Some changes had been made to

the material library since its original version in 2004, and TIMCOAT was last used in 2006. Due to compatibility issues (with the available compilers), a different random number generator is now used, and the use of Intel IMSL libraries has been replaced with RogueWave© IMSL libraries. In order to verify that TIMCOAT is operating correctly, several comparisons were made. The code comparisons with previous TIMCOAT results show good agreement.

The stress evolution during a steady-state irradiation simulation was compared between TIMCOAT and PARFUME (a TRISO fuel performance model developed at INL). The purpose of this comparison was not necessarily to distinguish one code as "correct" and the other as "incorrect". Instead, it was to note two differences between the models which result in significant differences in the calculations and to make the reader and future model-users aware of these differences. To summarize, PARUME uses a Poisson's ratio fixed at 0.5 for irradiation creep of pyrocarbon. TIMCOAT allows this value to decrease down to 0.4 with irradiation. PARFUME uses an input variable called "CREEPAMP" whose default value multiplies the steady state irradiation creep coefficient in pyrocarbon by a factor of 2. TIMCOAT does not use this type of factor. In its native format, TIMCOAT calculates compressive stresses which are more compressive and tensile stresses which are more tensile than PARFUME. If TIMCOAT is altered to mimic PARFUME with a fixed Poisson's ratio and a creep multiplication factor of 2, then the TIMCOAT calculations are comparable to those of PARFUME.

The TIMCOAT TRISO particle failure probability calculations have previously been benchmarked favorably against the NPR series of irradiations and others. A brief comparison between the AGR-1 irradiation, a PARFUME simulation, and a TIMCOAT simulation was made here in order to provide a new comparison of TIMCOAT with a recent irradiation. Given that none of the 4154 particles in Compact 3-3-1 failed, the two TIMCOAT runs which calculated particle failure rates of 1.1×10^{-4} and 9.3×10^{-5} are plausible, but the other TIMCOAT runs over predict the failure rates. PARFUME predicts particle failure rates a couple orders of magnitude lower than TIMCOAT.

Several options were added to TIMCOAT to enable simulation of a pebbled bed FHR. The Mk1-PB-FHR fuel pebble is different from previous fuel pebble concepts. This pebble is an annular pebble consisting of a fuel zone in the pebble which surrounds a center graphite annulus. TIMCOAT was modified in order to enable simulation of this type of pebble. Next, because TIMCOAT calculates the coolant temperature throughout the reactor and then calculates the fuel temperature using the coolant temperature as a boundary condition, TIMCOAT was modified with the flibe coolant properties and heat transfer correlations necessary for these calculations.

A series of full reactor simulations were performed using the modified TIMCOAT code. Because an FHR reactor model for TIMCOAT was not available, the existing VSOP reactor physics model in TIMCOAT was used. This was believed to be a reasonable approach since the neutronics in a PB-FHR will be similar to those in a gas-cooled pebble-bed reactor. The input to TIMCOAT was selected in order to match the Mk1 PB-FHR power densities, fuel specifications, and core inlet and outlet temperatures. Failure rates for all of the cases run using the TRISO fuel specification

listed in the Mk1 PB-FHR design report were between 20 and 30% depending on whether the chemical model was activated in TIMCOAT. Switching the fuel specification to the AGR-1 parameters reduced the failure rate to 1%.

Future fuel performance modeling work will involve the development of an FHR-specific reactor physics model for TIMCOAT which incorporates the baseline commercial FHR annular core geometry and the higher burnups targeted by commercial FHRs.

References

[1] FORSBERG, C., PETERSON, P.F., PICKARD, P.S., "Molten-Salt-Cooled Advanced High-Temperature Reactor for Production of Hydrogen and Electricity," *Nuclear Technology*. **144**, 289–302 (2003).

[2] HOLCOMB, D.E., FLANAGAN, G.F., MAYS, G.T., POINTER, W.D., ROBB, K.R., YODER, JR., G.L., "Fluoride Salt-Cooled High-Temperature Reactor Technology Development and Demonstration Roadmap," ORNL/TM-2013/401, Oak Ridge National Laboratory, (2013).

[3] FORSBERG, C.W., HU, L., PETERSON, P.F., SRIDHARAN, K., "Fluoride-Salt-Cooled High-Temperature Reactors (FHRs) for Base-Load and Peak Electricity, Grid Stabilization, and Process Heat," MIT-ANP-TR-147, Massachusetts Institute of Technology: Center for Advanced Energy Systems, (2013).

[4] FORSBERG, C.W., "Commercialization Approaches and Challenges for Fluoride-Salt-Cooled High-Temperature Reactors (FHRs)," *Transactions of the American Nuclear Society*, **109**, Washington, D. C., November 10, 2013, pp.1088–1091.

[5] FORSBERG, C.W., HU, L., PETERSON, P.F., SRIDHARAN, K., "Fluoride-Salt-Cooled High Temperature Reactor (FHR) for Power and Process Heat Final Project Report," MIT-ANP-TR-157, Center for Advanced Nuclear Energy Systems, Massahusetts Institute of Technology, (2014).

[6] HAUBENREICH, P.N., ENGEL, J.R., "Experience with the Molten-Salt Reactor Experiment," *Nuclear Applications & Technology*. **8**, 118–136 (1970).

[7] KEISER, J.R., DEVAN, J.H., MANNING, D.L., "The Corrosion Resistance of Type 316 Stainless Steel to Li2BeF4," ORNL/TM-5782, Oak Ridge National Laboratory, (1977).

[8] ANDREADES, C., CISNEROS, A.T., CHOI, J.K., CHONG, Y.K., FRATONI, M., HONG, S., ET AL., "Technical Description of the 'Mark 1' Pebble-Bed Fluoride-Salt-Cooled High-Temperature Reactor (PB-FHR) Power Plant," UCBTH-14-002, University of California-Berkeley, (2014).

[9] CURTIS, D., FORSBERG, C.W., "Market Performance of the Mark 1 Pebble-Bed Fluoride-Salt-Cooled High-Temperature Reactor," *Transactions of the American Nuclear Society*, **110**, Reno, NV, June 15, 2014, pp.397–400.

[10] FORSBERG, C.W., "Market for Hot Air from Salt-Cooled Reactors with Air-Brayton Power Cycles," *Transactions of the American Nuclear Society*, **110**, Reno, NV, June 15, 2014, pp.394–396.

[11] TODREAS, N.E., KAZIMI, M.S., "Nuclear Systems Volume I: Thermal Hydraulic Fundamentals, Second Edition," 2 edition, CRC Press, Boca Raton, FL, 2011.

[12] FORSBERG, C.W., STEMPIEN, J.D., MINCK, M.J., MARAGH, A., BALLINGER, R.G., "Eliminating Major Radionuclide Releases in Fluoride-salt-cooled High-Temperature Reactor Severe Accidents," *Nuclear Technology*. **inpress**, inpress (inpress).

[13] PETTI, D.A., DEMKOWICZ, P.A., MAKI, J.T., HOBBINS, R.R., *3.07 - TRISO-Coated Particle Fuel Performance*, in: "Comprehensive Nuclear Materials," Elsevier, Oxford, 2012: pp. 151–213.

[14] KOK, K., ED., "Nuclear Engineering Handbook," CRC Press, Boca Raton, 2009.

[15] HOMAN, F.J., LINDEMER, T.B., LONG, E.L., "Stoichiometric Effects on Performance of High-Temperature Gas-Cooled Reactor Fuels from the U-C-O System," *Nuclear Technology*. **35**, 428–441 (1977).

[16] COLLIN, B.P., "AGR-1 Irradiation Test Final As-Run Report," INL/EXT-10-18097, Idaho National Laboratory, (2012).

[17] SAWA, K., *3.06 - TRISO Fuel Production*, in: "Comprehensive Nuclear Materials," Elsevier, Oxford, 2012: pp. 143–149.
[18] WANG, J., "An Integrated Performance Model for High Temperature Gas Cooled Reactor Coated Particle Fuel," PhD, Massachusetts Institute of Technology, 2004.
[19] BELL, G.L., PAPPANO, P.J., HUNN, J.D., "FHR TRISO Fuel Development," (2010).
[20] HUNN, J.D., "Module 7b TRISO Fuel Manufacturing – Fabrication and Quality Control," (2010).
[21] "Fuel Performance and Fission Produce Behaviour in Gas Cooled Reactors," IAEA-TECDOC-978, International Atomic Energy Agency, (1997).
[22] VARMA, V.K., HOLCOMB, D.E., PERETZ, F.J., BRADLEY, E.C., ILAS, D., QUALLS, A.L., ET AL., "AHTR Mechanical, Structural, and Neutronic Preconceptual Design," ORNL/TM-2012/320, Oak Ridge National Laboratory, (2012).
[23] ROSENTHAL, M.W., BRIGGS, R.B., KASTEN, P.R., "Molten-Salt Reactor Program Semiannual Progress Report," ORNL-4548, Oak Ridge National Laboratory, (1970).
[24] ROBERTSON, R.C., "MSRE Design and Operations Report Part I: Description of Reactor Design," ORNL-TM-728, Oak Ridge National Laboratory, (1965).
[25] ROSENTHAL, M.W., "An Account of Oak Ridge National Laboratory's Thirteen Nuclear Reactors," ORNL/TM-2009/181, Oak Ridge National Laboratory, (2010).
[26] "Giving Wings to the Atom: Chronological History of NEP Nuclear Energy for Propulsion of Aircraft and GE-ANP General Electricl Nuclear Propulsion Program," General Electric Aircraft Nuclear Propulsion Department, (1996).
[27] THORNTON, G., BLUMBERG, B., "ANP HTREs Fulfill Test Goals," *Nucleonics*. **19**, 45–51 (1961).
[28] BETTIS, E.S., SCHROEDER, R.W., CRISTY, G.A., SAVAGE, H.W., AFFEL, R.G., HEMPHILL, L.F., "The Aircraft Reactor Experiment—Design and Construction," *Nuclear Science and Engineering*. **2**, 804–825 (1957).
[29] BETTIS, E.S., COTTRELL, W.B., MANN, E.R., MEEM, J.L., WHITMAN, G.D., "The Aircraft Reactor Experiment—Operation," *Nuclear Science and Engineering*. **2**, 841–853 (1957).
[30] COTTRELL, W.B., "Aircraft Nuclear Propulsion Project Quarterly Progress Report," ORNL-1515, Oak Ridge National Laboratory, (1953).
[31] "Aircraft Nuclear Propulsion Project Quarterly Progress Report," ORNL-1947, Oak Ridge National Laboratory, (1955).
[32] ROSENTHAL, M.W., KASTEN, P.R., BRIGGS, R.B., "Molten-Salt Reactors: History, Status, and Potential," *Nuclear Applications & Technology*. **8**, 107–117 (1970).
[33] GRIMES, W.R., "Reactor Chemistry Division Annual Progress Report," ORNL-3789, Oak Ridge National Laboratory, (1965).
[34] BRIGGS, R.B., "Molten-Salt Reactor Program Semiannual Progress Report," ORNL-3626, Oak Ridge National Laboratory, (1964).
[35] KOGER, J.W., "Evaluation of Hastelloy N Alloys After Nine Years Exposure to Both a Molten Fluorided Salt and Air at Temperatures from 700 to 560 C," ORNL-TM-4189, Oak Ridge National Laboratory, (1972).
[36] KEISER, J.R., "Status of Tellurium-Hastelloy N Studies in Molten Fluoride Salts," ORNL/TM-6002, Oak Ridge National Laboratory, (1977).
[37] "Molten-Salt Reactor Experiment," *Wikipedia, the Free Encyclopedia*. (2014).
[38] HAUBENREICH, P.N., ENGEL, J.., PRINCE, B.E., CLAIBORNE, H.C., "MSRE Design and Operations Report Part III. Nuclear Analysis," ORNL-TM-730, Oak Ridge National Laboratory, (1964).
[39] GRIMES, W.R., "Chemical Research and Development for Molten-Salt Breeder Reactors," ORNL-TM-1853, Oak Ridge National Laboratory, (1967).

[40] WILLIAMS, D.F., TOTH, L.M., CLARNO, K.T., "Assessment of Candidate Molten Salt Coolants for the Advanced High-Temperature Reactor (AHTR)," ORNL/TM-2006/12, Oak Ridge National Laboratory, (2006).

[41] INGERSOLL, D.T., FORSBERG, C., OTT, L.J., WILLIAMS, D.F., RENIER, J.P., WILSON, D.F., ET AL., "Status of Preconceptual Design of the Advanced High-Temperature Reactor (AHTR)," ORNL/TM-2004/104, Oak Ridge National Laboratory, (2004).

[42] BENEŠ, O., KONINGS, R.J.M., *3.13 - Molten Salt Reactor Fuel and Coolant*, in: "Comprehensive Nuclear Materials," Elsevier, Oxford, 2012: pp. 359–389.

[43] "Lithium fluoride," *Wikipedia, the Free Encyclopedia*. (2014).

[44] MATHEWS, A.L., BAES, C.F., "Oxide chemistry and thermodynamics of molten lithium fluoride-beryllium fluoride solutions," *Journal of Inorganic Chemistry*. **7**, 373–382 (1968).

[45] SOHAL, M.S., EBNER, M.A., SABHARWALL, P., SHARPE, P., "Engineering Database of Liquid Salt Thermophysical and Thermochemical Properties," INL/EXT-10-18297, Idaho National Laboratory, (2010).

[46] GRIMES, W.R., "Molten-Salt Reactor Chemistry," *Nuclear Applications & Technology*. **8**, 137–155 (1970).

[47] JACOBS, D.G., "Sources of Tritium and Its Behavior Upon Release to the Environment," ORNL/NSIC-37,(1968).

[48] "DOE Handbook: Tritium Handling and Safe Storage," DOE-HDBK-1129-2008, U.S. Department of Energy, (2008).

[49] DELACROIX, D., GUERRE, J.P., LEBLANC, P., HICKMAN, C., "Radionuclide and Radiation Protection Data Handbook 2002," *Radiation Protection Dosimetry*. **98**, 21 (2002).

[50] BRIGGS, R.B., "Tritium in Molten-Salt Reactors," *Reactor Technology*. **14**, 335 (1971).

[51] SUZUKI, A., TERAI, T., TANAKA, S., "Tritium release behavior from Li2BeF4 molten salt by permeation through structural materials," *Fusion Engineering and Design*. **51–52**, 863–868 (2000).

[52] SHAPIRO, M.D., REED, C.M., "Removal of Tritium from the Molten Salt Breeder Reactor Fuel," ORNL-MIT-117, Oak Ridge National Laboratory, (1970).

[53] ANDERL, R.., FUKADA, S., SMOLIK, G.., PAWELKO, R.., SCHUETZ, S.., SHARPE, J.., ET AL., "Deuterium/tritium behavior in Flibe and Flibe-facing materials," *Journal of Nuclear Materials*. **329–333, Part B**, 1327–1331 (2004).

[54] FUKADA, S., MORISAKI, A., SAGARA, A., TERAI, T., "Control of tritium in FFHR-2 self-cooled Flibe blanket," *Fusion Engineering and Design*. **81**, 477–483 (2006).

[55] SUZUKI, A., TERAI, T., TANAKA, S., "Change of tritium species in Li2BeF4 molten salt breeder under neutron irradiation at elevated temperature," *Journal of Nuclear Materials*. **258–263, Part 1**, 519–524 (1998).

[56] CALDERONI, P., SHARPE, P., NISHIMURA, H., TERAI, T., "Control of molten salt corrosion of fusion structural materials by metallic beryllium," *Journal of Nuclear Materials*. **386–388**, 1102–1106 (2009).

[57] FIELD, P.E., SHAFFER, J.H., "The solubilities of hydrogen fluoride and deuterium fluoride in molten fluorides," *J. Phys. Chem.* **71**, 3218–3222 (1967).

[58] WICHNER, R.P., DYER, F.., "Distribution and Transport of Tritium in the Peach Bottom HTGR," ORNL-5497, Oak Ridge National Laboratory, (1979).

[59] "Engineering Services for the Next Generation Nuclear Plant (NGNP) with Hydrogen Production - Technical Basis for NGNP Fuel Performance and Quality Requirements (GA Project 30302)," 911168, General Atomics, (2009).

[60] OH, C.H., KIM, E.S., "Development and Verification of Tritium Analyses Code for a Very High Temperature Reactor," INL/EXT-09-16743, Idaho National Laboratory, (2009).

[61] THOMA, R.E., "Chemical Aspects of MSRE Operations," ORNL-4658, Oak Ridge National Laboratory, (1971).
[62] CISNEROS, A.T., "Pebble Bed Reactors Design Optimization Methods and Their Application to the Pebble Bed Fluoride Salt Cooled High Temperature Reactor (PB-FHR)," PhD, University of California, Berkeley, 2013.
[63] "Management of Waste Containing Tritium and Carbon-14," Technical Reports Series No. 421, International Atomic Energy Agency, (2004).
[64] BRIGGS, R.B., NESTOR, C.W., "A Method for Calculating the Steady State Distribution of Tritium in a Molten Salt Breeder Reactor Plant," ORNL-TM-4804, Oak Ridge National Laboratory, (1975).
[65] SHERMAN, S.R., ADAMS, T.M., "Tritium Barrier Materials and Separation Systems for the NGNP," WRSC-STI-2008000358, Rev. 1, Savannah River National Laboratory, (2008).
[66] COMPERE, E.L., "Fission Product Behavior in the Molten Salt Reactor Experiment," ORNL-4865, Oak Ridge National Laboratory, (1975).
[67] ROSENTHAL, M.W., BRIGGS, R.B., KASTEN, P.R., "Molten Salt Reactor Program Semiannual Progress Report," ORNL-4548, Oak Ridge National Laboratory, (1970).
[68] MCNEESE, L.E., "Program Plan for Development of Molten-Salt Breeder Reactors," ORNL-5018, Oak Ridge National Laboratory, (1974).
[69] MACPHERSON, H.G., "The Molten Salt Reactor Adventure," *Nuclear Science and Engineering*. **90**, 374–380 (1985).
[70] WANG, L., STUCKERT, N.R., YANG, R.T., "Unique Hydrogen Adsorption Properties of Graphene," *AIChE Journal*. **57**, 2902–2908 (2011).
[71] CAUSEY, R.A., KARNESKY, R.A., SAN MARCHI, C., *4.16 - Tritium Barriers and Tritium Diffusion in Fusion Reactors*, in: Konings, R.J.M. (Ed.), "Comprehensive Nuclear Materials," Elsevier, Oxford, 2012: pp. 511–549.
[72] SMOLIK, G.R., ANDERL, R.A., PAWELKO, R.J., CARMACK, W.J., HEMBREE, P.B., OATES, M.A., "BET Surface Area Measurements of Materials for Fusion Safety Studies," *Fusion Engineering, 1997. 17th IEEE/NPSS Symposium*, **1**, October 1997, pp.183–187 vol.1.
[73] "Tritium Distribution in the MHTGR," DOE-HTGR-88098, General Atomics, (1998).
[74] REDMOND, J.P., WALKER, P.L., "HYDROGEN SORPTION ON GRAPHITE AT ELEVATED TEMPERATURES1,2," *The Journal of Physical Chemistry*. **64**, 1093–1099 (1960).
[75] TSETSKHLADZE, T.V., CHERKEZISHVILI, L.I., CHIKHLADZE, L.A., "Interaction of Tritium with Graphite," *Soviet Atomic Energy*. **64**, 254–258 (1988).
[76] CAUSEY, R.A., "The interaction of tritium with graphite and its impact on tokamak operations," *Journal of Nuclear Materials*. **162–164**, 151–161 (1989).
[77] XU, W.-C., TAKAHASHI, K., MATSUO, Y., HATTORI, Y., KUMAGAI, M., ISHIYAMA, S., ET AL., "Investigation of hydrogen storage capacity of various carbon materials," *International Journal of Hydrogen Energy*. **32**, 2504–2512 (2007).
[78] KIYOSHI, T., NAMBA, T., YAMAWAKI, M., "Hydrogen permeation through graphite," *Journal of Nuclear Materials*. **155–157, Part 1**, 230–233 (1988).
[79] STREHLOW, R.A., "Chemisorption of tritium on graphite at elevated temperatures," *Journal of Vacuum Science and Technology A*. **4**, 1183 (1986).
[80] YANG, R.T., DUAN, R.Z., "Kinetics and mechanism of gas-carbon reactions: Conformation of etch pits, hydrogen inhibition and anisotropy in reactivity," *Carbon*. **23**, 325–331 (1985).
[81] YANG, R.T., YANG, K.L., "Kinetics and mechanisms of the carbon-steam reaction on the monolayer and multilayer edges of graphite," *Carbon*. **23**, 537–547 (1985).

[82] ATSUMI, H., ISEKI, M., SHIKAMA, T., "Traping and detrapping of hydrogen in carbon-based materials exposed to hydrogen gas," *Journal of Nuclear Materials*. **212-215**, 1478–1482 (1994).

[83] CAUSEY, R.A., ELLEMAN, T.S., VERGHESE, K., "Hydrogen diffusion and solubility in pyrolytic carbon," *Carbon*. **17**, 323–328 (1979).

[84] CAUSEY, R.A., WILSON, K.L., "Retention of deuterium and tritium in Papyex graphite," *Journal of Nuclear Materials*. **138**, 57–64 (1986).

[85] CAUSEY, R.A., BASKES, M.I., WILSON, K.L., "The retention of deuterium and tritium in POCO AXF-5Q graphite," *Journal of Vacuum Science & Technology A*. **4**, 1189–1192 (1986).

[86] ATSUMI, H., TOKURA, S., MIYAKE, M., "Absorption and desorption of deuterium on graphite at elevated temperatures," *Journal of Nuclear Materials*. **155–157, Part 1**, 241–245 (1988).

[87] TANABE, T., ATSUMI, H., "Bulk Hydrogen Retention in Graphite at Elevated Tempertaure," *Journal of Nuclear Materials*. **209**, 109–112 (1994).

[88] ATSUMI, H., ISEKI, M., "Hydrogen absorption process into graphite and carbon materials," *Journal of Nuclear Materials*. **283–287, Part 2**, 1053–1056 (2000).

[89] "Property Data | Special Graphite | Toyo Tanso Co., Ltd Products website," (n.d.).

[90] ATSUMI, H., ISEKI, M., SHIKAMA, T., "Hydrogen behavior in carbon-based materials and its neutron irradiation effect," *Journal of Nuclear Materials*. **233–237, Part 2**, 1128–1132 (1996).

[91] CAUSEY, R.A., WILSON, K.L., WAMPLER, W.R., DOYLE, B.L., "The Effects of Neutron Irradiation on the Trapping of Tritium in Graphite," *Fusion Science and Technology*. **19**, 1585–1588 (1991).

[92] ATSUMI, H., TANABE, T., SHIKAMA, T., "Bulk hydrogen retention in neutron-irradiated graphite at elevated temperatures," *Journal of Nuclear Materials*. **390–391**, 581–584 (2009).

[93] ATSUMI, H., TANABE, T., SHIKAMA, T., "Hydrogen behavior in carbon and graphite before and after neutron irradiation – Trapping, diffusion and the simulation of bulk retention–," *Journal of Nuclear Materials*. **417**, 633–636 (2011).

[94] ATSUMI, H., "Hydrogen bulk retention in graphiet and kinetics of diffusion," *Journal of Nuclear Materials*. **307-311**, 1466–1470 (2002).

[95] MASAKATSU SAEKI, "Influence of radiation damage on diffusivity of tritium in graphite," *The International Journal of Applied Radiation and Isotopes*. **34**, 739–742 (1983).

[96] SUZUKI, A., TERAI, T., TANAKA, S., "In-situ HT release behavior from molten Li2BeF4 salt," *Fusion Engineering and Design*. **39–40**, 781–785 (1998).

[97] SUZUKI, A., TERAI, T., TANAKA, S., "Mechanism on Change of Tritium Species in Li2BeF4 Molten Salt Breeder Under Neutron Irradiation at Elevated Temperature," *Fusion Technology*. **34**, 526–530 (1998).

[98] MALINAUSKAS, A.P., RICHARDSON, D.M., "The Solubilities of Hydrogen, Deuterium, and Helium in Molten Li2BeF4," *Industrial & Engineering Chemistry Fundamentals*. **13**, 242–245 (1974).

[99] FUKADA, S., MORISAKI, A., "Hydrogen permeability through a mixed molten salt of LiF, NaF and KF (Flinak) as a heat-transfer fluid," *Journal of Nuclear Materials*. **358**, 235–242 (2006).

[100] CALDERONI, P., SHARPE, P., HARA, M., OYA, Y., "Measurement of tritium permeation in flibe (2LiF–BeF2)," *Fusion Engineering and Design*. **83**, 1331–1334 (2008).

[101] FUKADA, S., ANDERL, R.A., SAGARA, A., NISHIKAWA, M., "Diffusion Coefficient of Tritium Through Molten Salt Flibe and Rate of Tritium Leak from Fusion Reactor System," *Fusion Science and Technology*. **48**, 666–669 (2005).

[102] KATSUTA, H., FURUKAWA, K., "Hydrogen Behavior in Molten Fluoride Mixtures (LiF-NaF-KF)," *Revue de Chimie Minerale*. **15**, 49–58 (1978).
[103] HOLCOMB, D.E., CETINER, S.M., "An Overview of Liquid-Fluoride-Salt Heat Transport Systems," ORNL/TM-2010/156, Oak Ridge National Laboratory, (2010).
[104] FUKADA, S., KATAYAMA, K., TERAI, T., SAGARA, A., "Recovery of Tritium from Flibe Blanket in Fusion Reactor," *Fusion Science and Technology*. **52**, 677–681 (2007).
[105] OISHI, J., MORIYAMA, H., MAEDA, S., ASAOKA, Y., "Tritium recovery from molten LiF-BeF2 salt," *Fusion Engineering and Design*. **8**, 317–321 (1989).
[106] MALINAUSKAS, A.P., RICHARDSON, D.M., SAVOLAINEN, J.E., SHAFFER, J.H., "Apparatus for the Determination of the Solubility of Hydrogen in Molten Salts," *Industrial & Engineering Chemistry Fundamentals*. **11**, 584–586 (1972).
[107] QUICK, N.R., JOHNSON, H.H., "Permeation and diffusion of hydrogen and deuterium in 310 stainless steel, 472 K to 779 K," *Metallurgical Transactions A*. **10**, 67–70 (1979).
[108] SCHMIDT, A.S., VERFUSS, F., WICKE, E., "Studies on the permeation of hydrogen and tritium through heat resistant alloys," *Journal of Nuclear Materials*. **131**, 247–260 (1985).
[109] KATSUTA, H., FURUKAWA, K., "Hydrogen and Deuterium Transport through Type 304 Stainless Steel at Elevated Temperatures," *Journal of Nuclear Science and Technology*. **18**, 143–151 (1981).
[110] TANABE, T., YAMANISHI, Y., SAWADA, K., IMOTO, S., "Hydrogen Transport in Stainless Steels," *Journal of Nuclear Materials*. **122 & 123**, 1568–1572 (1984).
[111] STEWARD, S.A., "Review of Hydrogen Isotope Permeability Through Materials," UCRL-53441, Lawrence Livermore National Laboratory, (1983).
[112] HOLLENBERG, G.., SIMONEN, E.., KALININ, G., TERLAIN, A., "Tritium/hydrogen barrier development," *Fusion Engineering and Design*. **28**, 190–208 (1995).
[113] OYA, Y., KOBAYASHI, M., OSUO, J., SUZUKI, M., HAMADA, A., MATSUOKA, K., ET AL., "Effect of surface oxide layer on deuterium permeation behaviors through a type 316 stainless steel," *Fusion Engineering and Design*. **87**, 580–583 (2012).
[114] CARPENTER, H.W., "Observations on the Properties and Behavior of Early SNAP 8 Hydrogen Permeation Barriers," NAA-SR-10027, Atomics International a Division of North American Aviation, Inc., (1965).
[115] WEBB, R.W., "SNAP 8 Experimental Reactor (S8ER) Hydrogen Barrier Coating Development," NAA-SR-9618, Atomics International a Division of North American Aviation, Inc., (1964).
[116] VOSS, S.S., "SNAP Reactor Overview," AFWL-TN-84-14, Air Force Weapons Laboratory, (1984).
[117] KISHIMOTO, N., TANABE, T., SUZUKI, T., YOSHIDA, H., "Hydrogen diffusion and solution at high temperatures in 316L stainless steel and nickel-base heat-resistant alloys," *Journal of Nuclear Materials*. **127**, 1–9 (1985).
[118] BAES JR., C.F., "Symposium on Reprocessing of Nuclear Fuels: The Chemistry and Thermodynamics of Molten Salt Reactor Fuels," *Nuclear Metallurgy*. **15**, 617–644 (1969).
[119] BAES JR., C.F., "The chemistry and thermodynamics of molten salt reactor fuels," *Journal of Nuclear Materials*. **51**, 149–162 (1974).
[120] DEVAN, J.H., EVANS III, R.B., "Corrosion Behavior of Reactor Materials in Fluoride Salt Mixtures," ORNL-TM-328, Oak Ridge National Laboratory, (1962).
[121] CANTOR, S., GRIMES, W.R., "Fused-Salt Corrosion and Its Control in Fusion Reactors," *Nuclear Technology*. **22**, 120–126 (1974).
[122] NISHIMURA, H., TERAI, T., YAMAWAKI, M., TANAKA, S., SAGARA, A., MOTOJIMA, O., "Compatibility of ferritic steels with Li2BeF4 molten salt breeder," *Journal of Nuclear Materials*. **307–311, Part 2**, 1355–1359 (2002).

[123] SHAFFER, J.H., "Preparation and Handling of Salt Mixtures for the Molten Salt Reactor Experiment," ORNL-4616, Oak Ridge National Laboratory, (1971).
[124] KEISER, J.R., "Compatibility Studies of Potential Molten-Salt Breeder Reactor Materials in Molten Fluoride Salts," ORNL/TM-5783, Oak Ridge National Laboratory, (1977).
[125] SUZUKI, T., MUTOH, I., YAGI, T., IKENAGA, Y., "Sodium corrosion behavior of austenitic alloys and selective dissolution of chromium and nickel," *Journal of Nuclear Materials*. **139**, 97–105 (1986).
[126] KOGER, J.W., "Alloy Compatibility with LiF-BeF2 Salts Containing ThF4 and UF4," ORNL-TM-4286, Oak Ridge National Laboratory, (1972).
[127] EVANS III, R.B., DEVAN, J.H., WATSON, G.M., "Self-Diffusion of Chromium in Nickel-Base Alloys," ORNL-2982, Oak Ridge National Laboratory, (1961).
[128] IGNATIEV, V., SURENKOV, A., *5.10 - Material Performance in Molten Salts*, in: Rudy J.M. Konings (Ed.), "Comprehensive Nuclear Materials," Elsevier, Oxford, 2012: pp. 221–250.
[129] KONDO, M., NAGASAKA, T., SAGARA, A., NODA, N., MUROGA, T., XU, Q., ET AL., "Metallurgical study on corrosion of austenitic steels in molten salt LiF–BeF2 (Flibe)," *Journal of Nuclear Materials*. **386–388**, 685–688 (2009).
[130] KONDO, M., NAGASAKA, T., XU, Q., MUROGA, T., SAGARA, A., NODA, N., ET AL., "Corrosion characteristics of reduced activation ferritic steel, JLF-1 (8.92Cr–2W) in molten salts Flibe and Flinak," *Fusion Engineering and Design*. **84**, 1081–1085 (2009).
[131] MIZOUCHI, M., YAMAZAKI, Y., IIJIMA, Y., ARIOKA, K., "Low Temperature Grain Boundary Diffusion of Chromium in SUS 316 and 316L Stainless Steels," *Materials Transactions*. **45**, 2945–2950 (2004).
[132] GRIMES, W.R., MACDUFFIE, H.F., "Reactor Chemistry Division Annual Progress Report," ORNL-2931, Oak Ridge National Laboratory, (1960).
[133] EVANS III, R.B., KOGER, J.W., DEVAN, J.H., "Corrosion in Polythermal Loop Systems II. A Solid-State Diffusion Mechanism with and without Liquid Film Effects," ORNL-4575, Vol 2, Oak Ridge National Laboratory, (1971).
[134] KEISER, J.R., DEVAN, J.H., LAWRENCE, E.J., "Compatibility of molten salts with type 316 stainless steel and lithium," *Journal of Nuclear Materials*. **85–86, Part 1**, 295–298 (1979).
[135] "NGNP High Temperature Materials White Paper," INL/EXT-09-17187, Idaho National Laboratory, (2010).
[136] HILL III, R.S., "Section III - Component Design and Construction," (2008).
[137] "Stainless Steels - Stainless 316 Properties, Fabrication and Applications, Supplier Data by Aalco," *AZO Materials*. (2014).
[138] AK STEEL, "Product Data Bulletin: 316/316L Stainless Steel," 316/316L-B-08-01-07,(n.d.).
[139] MANLY, W.D., ADAMSON, JR., G.M., COOBS, J.H., DE VAN, J.H., "Aircraft Reactor Experiment: Metallurgical Aspects," ORNL-2349, Oak Ridge National Laboratory, (1957).
[140] OLANDER, D., "Redox condition in molten fluoride salts: Definition and control," *Journal of Nuclear Materials*. **300**, 270–272 (2002).
[141] ENGEL, J.R., BAUMAN, H.F., DEARING, J.F., GRIMES, W.R., MCCOY, E.H., RHOADES, W.A., "Conceptual Design Characteristics of a Denatured Molten-Salt Reactor with Once-Through Fueling," ORNL/TM-7207, Oak Ridge National Laboratory, (1978).
[142] TOTH, L.M., GILPATRICK, L.O., "The Equilibrium of Dilute UF3 Solutions Contained in Graphite," ORNL-TM-4056, Oak Ridge National Laboratory, (1972).
[143] TOTH, L.M., CUL, G.D.D., DAI, S., METCALF, D.H., "Molten Fluoride Fuel Salt Chemistry," *AIP Conference Proceedings*, **346**, September 15, 1995, pp.617–626.
[144] DEL CUL, G.D., WILLIAMS, D.F., TOTH, L.M., CAJA, J., "Redox Potential of Novel Electrochemical Buffers Useful for Corrosion Prevention in Molten Fluorides," *Proceedings of the Thirteenth International Symposium on Molten Salts*, Philadelphia, PA, May 2002, .

[145] BARTON, C.J., "Solubility of plutonium trifluoride in fused-alkali fluoride-beryllium fluoride mixtures," *The Journal of Physical Chemistry*. **64**, 306–309 (1960).
[146] MELLORS, G.W., SENDEROFF, S., "Electrodeposition of Coherent Deposits of Refractory Metals: III. Zirconium," *Journal of the Electrochemical Society*. **113**, 60–66 (1966).
[147] SIMPSON, M.F., SMOLIK, G.R., SHARPE, J.P., ANDERL, R.A., PETTI, D.A., HATANO, Y., ET AL., "Quantitative measurement of beryllium-controlled redox of hydrogen fluoride in molten Flibe," *Fusion Engineering and Design*. **81**, 541–547 (2006).
[148] WILLIAMS, D.F., TOTH, L.M., CLARNO, K.T., "Assessment of Candidate Molten Salt Coolants for the Advanced High Temperature Reactor (AHTR)," ORNL/TM-2006/12, Oak Ridge National Laboratory, (2006).
[149] FUKADA, S., SIMPSON, M.F., ANDERL, R.A., SHARPE, J.P., KATAYAMA, K., SMOLIK, G.R., ET AL., "Reaction rate of beryllium with fluorine ion for Flibe redox control," *Journal of Nuclear Materials*. **367–370, Part B**, 1190–1196 (2007).
[150] TOTH, L.M., GILPATRICK, L.O., "Equilibria of uranium carbides in the molten fluoride solutions of UF3 and UF4 contained in graphite at 850°K," *Journal of Inorganic and Nuclear Chemistry*. **35**, 1509–1513 (1973).
[151] STULL, D.R., "Vapor Pressure of Pure Substances. Organic and Inorganic Compounds," *Industrial & Engineering Chemistry*. **39**, 517–540 (1947).
[152] OLANDER, D., FUKADA, G.F., BAES JR., C.F., "Equilibrium Pressures Over BeF2/LiF (FLIBE) Molten Mixtures," *Fusion Sceince and Technology*. **41**, 141–150 (2002).
[153] STURM, B.J., THOMA, R.E., GUINN, E.H., INSLEY, H., MCVAY, T.N., *24. Solvents for Fluoride Volatility Process*, in: "Reactor Chemistry Division Annual Progress Report for Period Ending January 31, 1964," ORNL-3591, Oak Ridge National Laboratory, 1964.
[154] THOMA, R.E., BOLES, R.L., FRIEDMAN, H.A., STURM, B.J., HEBERT, G.M., GUINN, E.H., *28. Molten Fluoride Mixtures as Possible Fuel Reprocessing Solvents*, in: "Reactor Chemistry Division Annual Progress Report for Period Ending January 31, 1963," ORNL-3417, Oak Ridge National Laboratory, 1963.
[155] ROBINSON, P.J., "Chemical Potentials and the Gibbs-Duhem Equation," *Journal of Chemical Education*. **47**, 160–161 (1970).
[156] SANDELL, L., "A Review of Radionuclide Release from HTGR Cores During Normal Operations," 1009382, EPRI, (2004).
[157] SCHENK, W., PITZER, D., NABIELEK, H., "Fission Product Release Profiles from Spherical HTR Fuel Elements at Accident Temperatures," JUL-2234, KFA Juelich, (1988).
[158] DEMKOWICZ, P.A., "Preliminary Results of Post-Irradiation Examination of the AGR-1 TRISO Fuel Compacts, Paper HTR2012-3-021," *Proceedings of the HTR 2012*, Tokyo, October 28 - November 1, .
[159] "Advances in High Temperature Gas Cooled Reactor Fuel Technology," IAEA-TECDOC-1674, International Atomic Energy Agency, (2012).
[160] "Fuel Performance and Fission Product Behavior in Gas Cooled Reactors," IAEA-TECDOC-978, International Atomic Energy Agency, (1997).
[161] SCHENK, W., POTT, G., NABIELEK, H., "Fuel accident performance testing for small HTRs," *Journal of Nuclear Materials*. **171**, 19–30 (1990).
[162] ROSENTHAL, M.W., BRIGGS, R.B., KASTEN, P.R., "Molten-Salt Reactor Program Semiannual Progress Report," ORNL-4254, Oak Ridge National Laboratory, (1968).
[163] NMAI, C.K., "Cementitious Materials for Concrete," ACI Education Bulletin E3-01, American Concrete Institute, (2001).
[164] SEVON, T., "Molten Core-Concrete Interactions in Nuclear Accidents: Theory and Design of an Experimental Facility," VTT Research Notes 2311, VTT Processes, (2005).

[165] SELLERS, R.S., ANDERSON, M.H., SRIDHARAN, K., ALLEN, T.R., "Failure analysis of 316L stainless steel crucible by molten fluoride salt interaction with clay bonded silicon carbide," *Engineering Failure Analysis*. **42**, 38–44 (2014).

[166] OLSON, L.C., "Materials Corrosion in Molten LiF-NaF-KF Eutectic Salt," PhD, University of Wisconsin-Madison, 2009.

[167] KERCHER, A.K., HUNN, J.D., "Results from ORNL Characterization of ZrO2-500-AK2 Surrogate TRISO Material," ORNL/CF-05/12, Oak Ridge National Laboratory, (2005).

[168] BALLINGER, R.G., HEJZLAR, P., KAZIMI, M.S., KOHSE, G., OSTROVSKY, Y., STAHLE, P.W., ET AL., "A New Facility for Irradiation of Materials at Very High Temperatures," *Proceedings of ICAPP '06*, Reno, NV, June 4, 2006, .

[169] CISNEROS, A.T., SCARLAT, R.O., LAUFER, M.R., GREENSPAN, E., PETERSON, P.F., "Pebble Fuel Design for the PB-FHR," *Proceedings of ICAPP '12*, Chicago, USA, June 24, 2012, pp.900–910.

[170] HONG, R., HUBER, S., LEE, K., PURCELL, P., MARGOSSIAN, S., SEELIG, J.D., "Reactor Safety and Mechanical Design for the Annular Pebble-Bed Advanced High Temperature Reactor," UCBTH09-001, University of California-Berkeley, (2009).

[171] WHITAKER, S., "Forced convection heat transfer correlations for flow in pipes, past flat plates, single cylinders, single spheres, and for flow in packed beds and tube bundles," *AIChE Journal*. **18**, 361–371 (1972).

[172] DOBRANICH, D., "Heat Transfer and Thermal Stress Analyses of the Multilayered Spherical Fuel Particles of a Particle Bed Space Nuclear Reactor," SAND90-1032, Sandia National Laboratories, (1991).

[173] ACHENBACH, E., "Heat and flow characteristics of packed beds," *Experimental Thermal and Fluid Science*. **10**, 17–27 (1995).

[174] DIXON, A.G., LABUA, L.A., "Wall-to-fluid coefficients for fixed bed heat and mass transfer," *International Journal of Heat and Mass Transfer*. **28**, 879–881 (1985).

[175] BALBAUD-CÉLÉRIER, F., BARBIER, F., "Investigation of models to predict the corrosion of steels in flowing liquid lead alloys," *Journal of Nuclear Materials*. **289**, 227–242 (2001).

[176] ZHANG, J., LI, N., "Parametric study of a corrosion model applied to lead–bismuth flow systems," *Journal of Nuclear Materials*. **321**, 184–191 (2003).

[177] THOENES, D., *Section 4.4 Principles of mass transfer between two phases and Section 5.3 Mass transfer and chemical reaction in series*, in: "Chemical Reactor Development from Laboratory Synthesis to Industrial Production," 1st ed., Springer Netherlands, 1994: pp. 83–87 and 138–139.

[178] FUKADA, S., ANDERL, R.A., HATANO, Y., SCHUETZ, S.T., PAWELKO, R.J., PETTI, D.A., ET AL., "Initial studies of tritium behavior in flibe and flibe-facing material," *Fusion Engineering and Design*. **61–62**, 783–788 (2002).

[179] SEADER, J.D., HENLEY, E.J., ROPER, D.K., "Separation Process Principles, 3rd Edition," 3 edition, John Wiley & Sons, Inc., 2010.

[180] ZHANG, J., HOSEMANN, P., MALOY, S., "Models of liquid metal corrosion," *Journal of Nuclear Materials*. **404**, 82–96 (2010).

[181] FUKADA, S., EDAO, Y., KATEKARI, K., OKITSU, H., HATACHI, Y., OKADA, M., ET AL., "Tritium Recovery from Liquid Blanket Systems for Fusion Reactor," *Transactions of Fusion Science and Technology*. **61**, 58–63 (2012).

[182] ROSENTHAL, M.W., BRIGGS, R.B., HAUBENREICH, P.N., "Molten-Salt Reactor Program Semiannual Progress Report," ORNL-4676, Oak Ridge National Laboratory, (1971).

[183] ABUZAID, W., ORAL, A., SEHITOGLU, H., LAMBROS, J., MAIER, H.J., "Fatigue crack initiation in Hastelloy X – the role of boundaries," *Fatigue & Fracture of Engineering Materials & Structures*. **36**, 809–826 (2013).

[184] GEHLBACH, R.E., MCCOY, H.E., "Phase Instability in Hastelloy N," *International Symposium on Structural Stability in Superalloys*, **11**, Seven Springs, PA, 1968, pp.346–366.
[185] DARUVALA, H.S., BUBE, K.R., "Tracer diffusion of chromium in 304 stainless steel," *Materials Science and Engineering*. **41**, 293–295 (1979).
[186] PINEDO, C.E., TSCHIPTSCHIN, A.P., "Low temperature plasma carburizing of AISI 316L austenitic stainless steel and AISI F51 duplex stainless steel," *Rem: Revista Escola de Minas*. **66**, 209–214 (2013).
[187] PILLINGER, W.L., HENTGES, J.J., BLAIR, J.A., "Tritium Decay Energy," *Physical Review*. **121**, 232–233 (1961).
[188] WANKAT, P.C., "Equilibrium-Staged Separations: Separations in Chemical Engineering," Elsevier Science Ltd, New York, 1988.
[189] FORSBERG, C., HU, L., PETERSON, P.F., ALLEN, T., "Fluoride-Salt-Cooled High-Temperature Reactors (FHRs) for Power and Process Heat," MIT-ANP-143, Massachusetts Institute of Technology, (2012).
[190] GREENE, S.R., GEHIN, J.C., HOLCOMB, D.E., CARBAJO, J.J., ILAS, D., CISNEROS, A.T., ET AL., "Pre-Conceptual Design of a Fluoride-Salt-Cooled Small Modular Advanced High-Temperature Reactor (SmAHTR)," ORNL/TM-2010/199, Oak Ridge National Laboratory, (2010).
[191] LEE, D.A., BEGUN, G.M., "The Enrichment of Lithium Isotopes by Ion-exchange Chromatography. I. The Influence of the Degree of Crosslinking on the Separation Factor," *Journal of the American Chemical Society*. **81**, 2332–2335 (1959).
[192] LEE, D.A., "The Enrichment of Lithium Isotopes by Ion-Exchange Chromatography.1 II. The Influence of Temperature on the Separation Factor," *The Journal of Physical Chemistry*. **64**, 187–188 (1960).
[193] LEE, D.A., "Enrichment of Lithium Isotopes by Ion Exchange Chromatography.," *Journal of Chemical & Engineering Data*. **6**, 565–566 (1961).
[194] LEE, D.A., *The Enrichment of Lithium Isotopes by Extraction Chromatography*, in: "Isotope Effects in Chemical Processes," 1969: pp. 57–64.
[195] HEUMANN, K., *Isotopic separation in systems with crown ethers and cryptands*, in: "Organic Chemistry," Springer Berlin / Heidelberg, 1985: pp. 77–132.
[196] NISHIZAWA, K., TAKANO, T., IKEDA, I., OKAHARA, M., "Extractive Separation of Lithium Isotopes by Crown Ethers," *Separation Science and Technology*. **23**, 333–345 (1988).
[197] "Declassification of the Quantity of Enriched Lithium Produced at the Y-12 Plant in Oak Ridge, Tennessee," *Department of Energy (DOE) OpenNet Documents*. (2012).
[198] GROGAN, B., "Identification of Lithium Isotopes Using Time-Tagged Neutron Scattering," Oak Ridge National Laboratory, 53rd Annual Meeting of the INMM, Orlando, FL, (2012).
[199] ATSUMI, H., TAKEMURA, Y., KONISHI, T., TANABE, T., SHIKAMA, T., "Thermal desorption of hydrogen from carbon and graphite at elevated temperatures," *Journal of Nuclear Materials*. **438**, S963–S966 (2013).
[200] SIMONDS, J., PETTI, D.A., "Technical Program Plan for the Next Generation Nuclear Plant/Advanced Gas Reactor Fuel Development and Qualification Program," PLN-3636, Idaho National Laboratory, (2010).
[201] COLLIN, B.P., HUMRICKHOUSE, P.W., "AGR-3/4 Irradiation Experiment Test Plan," PLN-3867, Idaho National Laboratory, (2011).
[202] RODRIGUEZ, C., BAXTER, A., MCEACHERN, D., FIKANI, M., VENNERI, F., "Deep-Burn: making nuclear waste transmutation practical," *Nuclear Engineering and Design*. **222**, 299–317 (2003).

[203] BESMANN, T.M., STOLLER, R.E., SAMOLYUK, G., SCHUCK, P.C., GOLUBOV, S.I., RUDIN, S.P., ET AL., "Modeling Deep Burn TRISO particle nuclear fuel," *Journal of Nuclear Materials.* **430**, 181–189 (2012).

[204] MAKI, J.T., PETTI, D.A., KNUDSON, D.L., MILLER, G.K., "The challenges associated with high burnup, high temperature and accelerated irradiation for TRISO-coated particle fuel," *Journal of Nuclear Materials.* **371**, 270–280 (2007).

[205] WANG, J., BALLINGER, R.G., MACLEAN, H.J., "TIMCOAT: An Integrated Fuel Performance Model for Coated Particle Fuel," *Nuclear Technology.* **148**, 68–96 (2004).

[206] STAWICKI, M.A., "Benchmarking of the MIT High Temperature Gas-Cooled Reactor TRISO-Coated Particle Fuel Performance Model," Master's Thesis, Massachusetts Institute of Technology, 2006.

[207] DIECKER, J.T., "Development of a High Temperature Gas-Cooled Reactor TRISO-Coated Particle Fuel Chemistry Model," Master's Thesis, Massachusetts Institute of Technology, 2005.

[208] RUTTEN, H.J., HAAS, K.A., BROCKMANN, H., OHLIG, U., POHL, C., SCHERER, W., "V.S.O.P (99/09): Computer Code System for Reactor Physic and Fuel Cycle Simulation; Version 2009," Jul-4326, Institut für Energieforschung (IEF) Sicherheitsforschung und Reaktortechnik (IEF-6), (2010).

[209] SOONTRAPA, C., "Design Optimization and Analysis of Coated Particle Fuel Using Advanced Fuel Performance Modeling Tecniques," Master's Thesis, Massachusetts Institute of Technology, 2005.

[210] MILLER, G.K., PETTI, D.A., MAKI, J.T., KNUDSON, D.L., "PARFUME Theory and Model Basis Report," INL/EXT-08-14497, Idaho National Laboratory, (2009).

[211] PARFUME DEVELOPMENT TEAM, "PARFUME User's Guide," INL/EXT-10-18317, Idaho National Laboratory, (2010).

[212] CEGA CORPORATION, "Material Models of Pycrocarbon and Pyrolytic Silicon Carbide," CEGA-002820, Rev. 1,(1993).

[213] COLLIN, B.P., "AGR-1 Safety Test Predictions Using the PARFUME Code," INL/EXT-12-26014, Idaho National Laboratory, (2012).

[214] HUNN, J.D., MORRIS, R.N., MILLER, J.H., HUNT, R.D., "Overview of Key Issues and Guidelines for Regulatory Oversight and Inspection of High Temperature Gas Reactor Fuel Fabricatoin and Quality Control Activities," ORNL/TM-2009/041, Oak Ridge National Laboratory, (2009).

[215] OHASHI, H., SHERMAN, S.R., "Tritium Movement and Accumulation in the NGNP System Interface and Hydrogen Plant," INL/EXT-07-12746, Idaho National Laboratory, (2007).

[216] FRANZA, F., CIAMPICHETTI, A., RICAPITO, I., ZUCCHETTI, M., "A model for tritium transport in fusion reactor components: The FUS-TPC code," *Fusion Engineering and Design.* **87**, 299–302 (2012).

[217] FRANZA, F., BOCCACCINI, L.V., CIAMPICHETTI, A., ZUCCHETTI, M., "Tritium transport analysis in HCPB DEMO blanket with the FUS-TPC code," *Fusion Engineering and Design.* **88**, 2444–2447 (2013).

[218] LONGHURST, G., HOLLAND, D.F., JONES, J.L., MERRILL, B.., "TMAP4 User's Manual," EGG-FSP-10315, Idaho National Engineering Laboratory, (1992).

[219] LONGHURST, G.R., "TMAP7 User Manual," INEEL/EXT-04-02352, Idaho National Engineering and Environmental Laboratory, (2004).

[220] NYGREN, R.E., ROGNLIEN, T.D., RENSINK, M.E., SMOLENTSEV, S.S., YOUSSEF, M.Z., SAWAN, M.E., ET AL., "A fusion reactor design with a liquid first wall and divertor," *Fusion Engineering and Design.* **72**, 181–221 (2004).

[221] WONG, C.P.C., MALANG, S., SAWAN, M., DAGHER, M., SMOLENTSEV, S., MERRILL, B., ET AL., "An overview of dual coolant Pb–17Li breeder first wall and blanket concept development for the US ITER-TBM design," *Fusion Engineering and Design*. **81**, 461–467 (2006).

[222] MERRILL, B.J., SAWAN, M., WONG, C.P.C., NYGREN, R.E., CADWALLADER, L.C., MALANG, S., ET AL., "Safety assessment of two advanced ferritic steel molten salt blanket design concepts," *Fusion Engineering and Design*. **72**, 277–306 (2004).

[223] HUNN, J.D., LOWDEN, R.A., "Data Compilation for AGR-1 Baseline Coated Particle Composite LEU01-46T," ORNL/TM-2006/019, Oak Ridge National Laboratory, (2006).

[224] HUNN, J.D., BALDWIN, C.A., SILVA, C.M., GERCZAK, T.J., MONTGOMERY, F.C., MORRIS, R.N., "Detection and Analysis of Particles with Abnormal Fission Product Retention," VHTR 6th Annual FY13 Technical Review Meeting, Idaho Falls, ID, (2013).

[225] PLOGER, S.A., DEMKOWICZ, P.A., HUNN, J.D., KEHN, J.S., "Microscopic Analysis of Irradiated AGR-1 Coated Particle Fuel Compacts," Proceedings of the HTR 2012, Paper HTR2012-3-020,(2012).

Appendix A: TRISO Fuel Post-Irradiation Examination (PIE)

Surrogate TRISO particles (containing a ZrO_2 kernel in place of a UCO or UO_2 kernel) were irradiated both in and out of flibe at the MIT research reactor. While irradiations were carried out at MIT, parallel tests were carried out at UW-Madison which matched the MIT irradiation conditions except that the UW tests did not have any neutron exposure. TRISO particles irradiated in a helium atmosphere were also analyzed. Thus TRISO particles from the same batch with four different histories could be compared:

- As-fabricated
- Exposed to molten salt only (no neutron exposure)
- Simultaneously exposed to neutron flux and molten salt
- Simultaneously exposed to neutron flux and inert helium gas

Comparing as-fabricated particles to particles irradiated in a helium atmosphere to particles irradiated in flibe to particles exposed to flibe in the absence of neutrons allows for the determination of irradiation effects, combined radiation/chemical effects, and chemical effects.

A.1 PIE of Surrogate TRISO Particles Irradiated in $He_{(g)}$

Before post-irradiation examination (PIE) could be performed on the surrogate TRISO particles irradiated in helium, the particles had to be retrieved from the sample capsule. Once the particles were retrieved, sample preparation and the modification of sample preparation techniques could commence.

The high-temperature irradiation facility (HTIF) was designed and constructed at MIT in 2005 [168]. The first HTIF irradiation campaign spanned three months, ending in March 2006. A schematic representation of the HTIF rig is shown in Figure A. 1, and a picture of the rig during initial assembly is shown in Figure A. 2. The stack of sample capsules fits inside a dummy fuel element which fits into a fuel assembly location in the MIT research reactor (MITR).

A series of samples relevant to high-temperature reactor technologies was irradiated. This includes the surrogate TRISO fuel particles analyzed in this report. Thermal diffusivity samples, bend-bar samples, and tensile specimens of graphite, SiC composites, and monolithic SiC were also irradiated at various temperatures and fast fluxes ($E > 0.1$ MeV). Gamma heating and a variable He/Ne gas mixture were used to obtain temperatures between 1000 and 1400 °C in the HTIF rig. An axial temperature profile for the samples is shown in Figure A. 3.

Two capsules (#12 and #8) were loaded with surrogate TRISO fuel particles from batch ZrO2-500-AK2 fabricated at Oak Ridge National Laboratory (ORNL). These particles feature a ZrO2 kernel in place of a UCO or UO2 kernel [167]. The as-fabricated dimensions and properties of the

particles are summarized in Table A. 1. Kercher and Hunn reported the kernel radius/density and thicknesses/densities for the IPyC, SiC, and OPyC layers [167]. The densities for the buffer and IPyC layers were taken from AGR-1 baseline specifications [223]. Particle overall radius and density were calculated from the data in the two sources mentioned in the preceding two sentences. Only the particles from capsule 12 have been analyzed at this time. The capsule 12 particles investigated here were irradiated for 3 months at 1000 °C in a $He_{(g)}$ atmosphere. The fast flux (E > 0.1MeV) in capsule 12 was $4.8x10^{13}$ n/cm^2-s. Analysis of capsule 8 TRISO particles will be carried out in the near future. Capsule 8 particles were irradiated for 3 months at 1300 °C in a fast flux of $1.1x10^{14}$ n/cm^2-s.

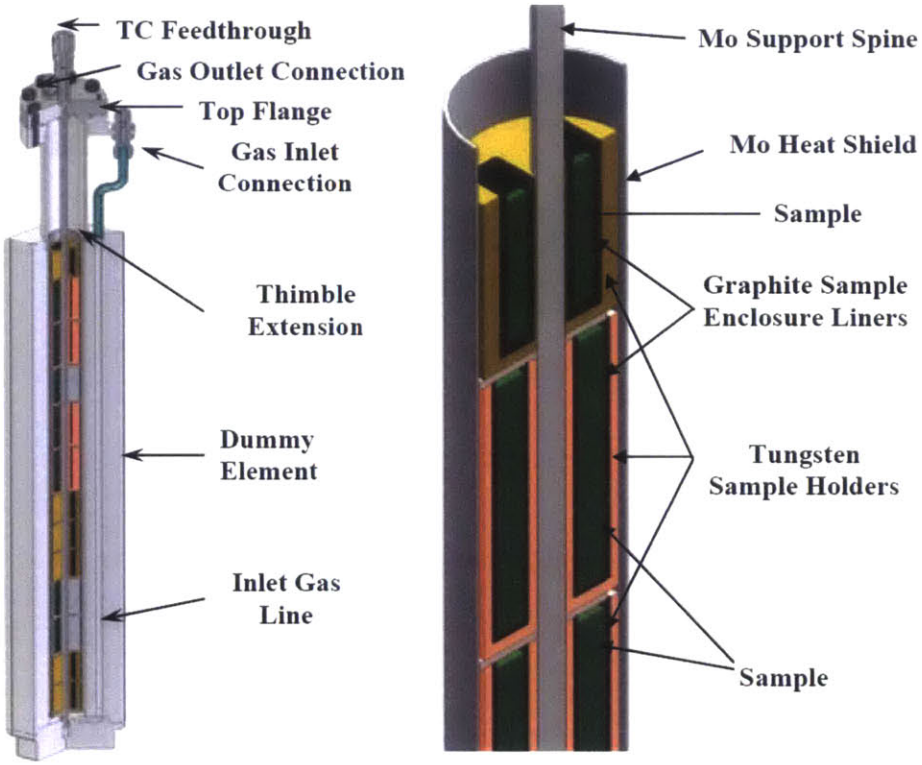

Figure A. 1: HTIF schematic. From [168].

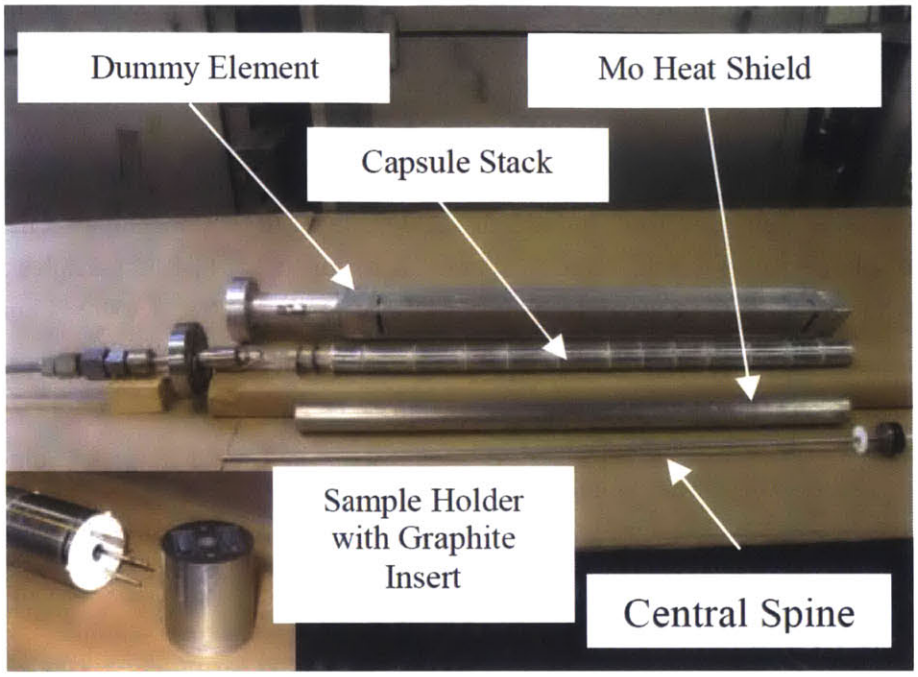

Figure A. 2: HTIF during assembly. From [168].

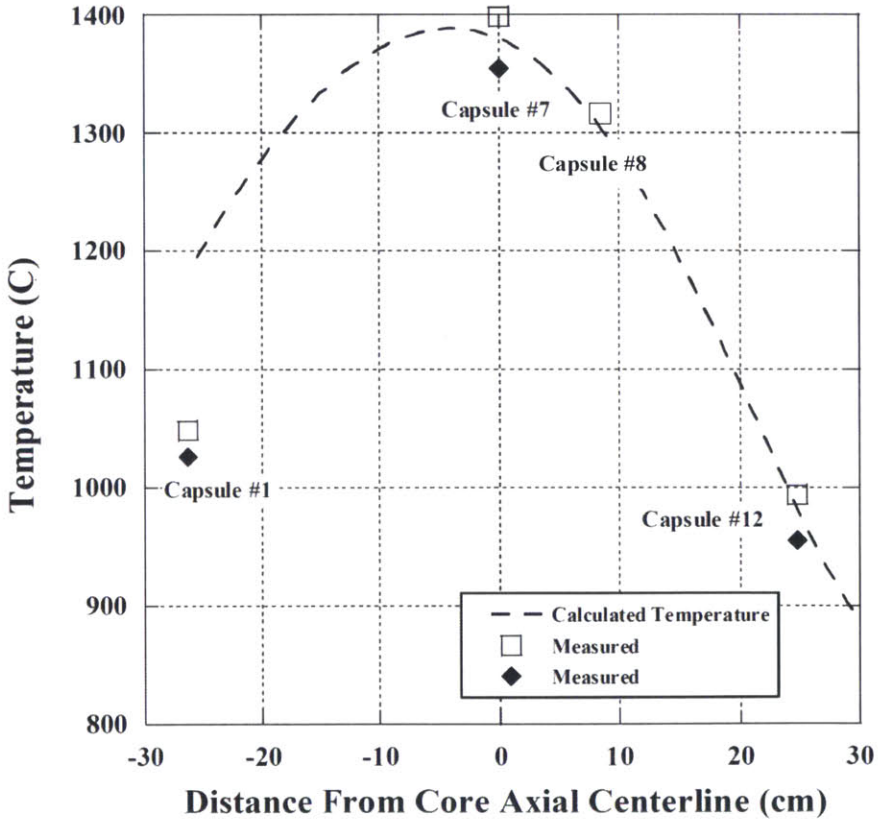

Figure A. 3: Axial temperature profile for HTIF sample capsules at a reactor power of 4.0 MW. From [168].

Table A. 1: As-fabricated properties for surrogate TRISO particles from batch ZrO_2-500-AK2.

	Thickness (μm)	Thickness SD (± μm)	Radius (μm)	Radius SD	Density (g/cm^3)
Particle Overall	-	-	458	11.729	2.734
Kernel	-	-	265	9	6.04
Buffer	85	7	-	-	1.1
IPyC	41	2	-	-	1.904
SiC	31	1	-	-	3.205
OPyC	36	1.6	-	-	2.012

A.1.1 HTIF removal from MITR spent fuel pool and transfer to hot cell

After its irradiation had been completed, the HTIF rig was stored in an upper section of the MITR spent fuel pool. The HTIF had a six foot long section of 0.5-inch tubing, used for instrumentation, extending from the top of the dummy fuel element. Figure A. 4 shows the HTIF rig suspended in the spent fuel pool during underwater dose rate measurements. While the circumferential profile of the HTIF fits within that of a normal MITR fuel element, the six feet of tubing on top made it much longer, and therefore it could not be handled using normal transfer tools.

The goal in transporting the HTIF to the hot cell was to minimize personnel exposure by using a straightforward cask loading and unloading procedure. A team of research scientists at the MITR coordinated the retrieval of the HTIF and its transfer to a hot cell. A cask (at left in Figure A. 5), with top plug and bottom shutter removed, was set on a bridge that runs over the center of the pool (at right in Figure A. 5), and a rope threaded through the cask was attached to the top of the HTIF. The HTIF was then pulled up into the cask and secured in place with as much of the assembly in the cask as possible. After some drying time, the cask was lifted to the top of the hot cell using a 3-ton polar crane, and the HTIF was immediately lowered to the hot cell floor so that the cask could be removed. The HTIF remained attached to the lifting rope, and in a subsequent operation, the upper three feet of 0.5-inch tubing was removed to allow disassembly on the hot cell work surface.

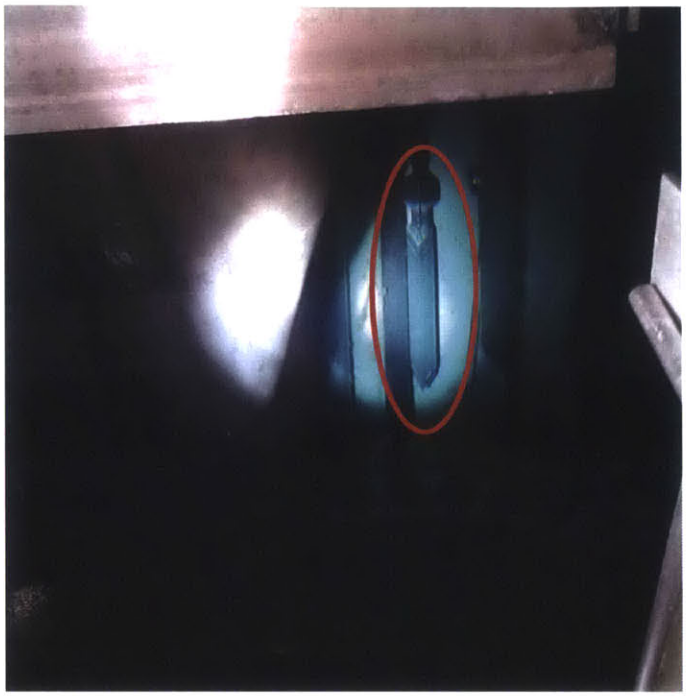

Figure A. 4: HTIF rig (highlighted in red) in MITR spent fuel pool.

Figure A. 5: At Left, the cask used to transfer the HTI. At Right, the cask being raised from the spent fuel pool bridge.

A.1.2 HTIF disassembly in hot cell

Once in the hot cell, the HTIF could be disassembled in order to access the sample capsules. Figure A. 6 shows the HTIF rig being lowered into a vise in the hot cell. The lowest portion of the rig is the dummy fuel element which housed the samples. The small line exiting the top right of the dummy element contained thermocouples, and the line exiting the top left was the gas line which carried the neon gas used to adjust the temperature of the samples. Capsule 12 containing the irradiated TRISO particles is shown in the center of Figure A. 7, and all of the sample capsules from the HTIF rig are shown in Figure A. 8. Capsule 8 also contains TRISO particles, but capsule 8 has not been moved to the fume hood for disassembly yet. Additional photos of the disassembly process are available in Appendix B.

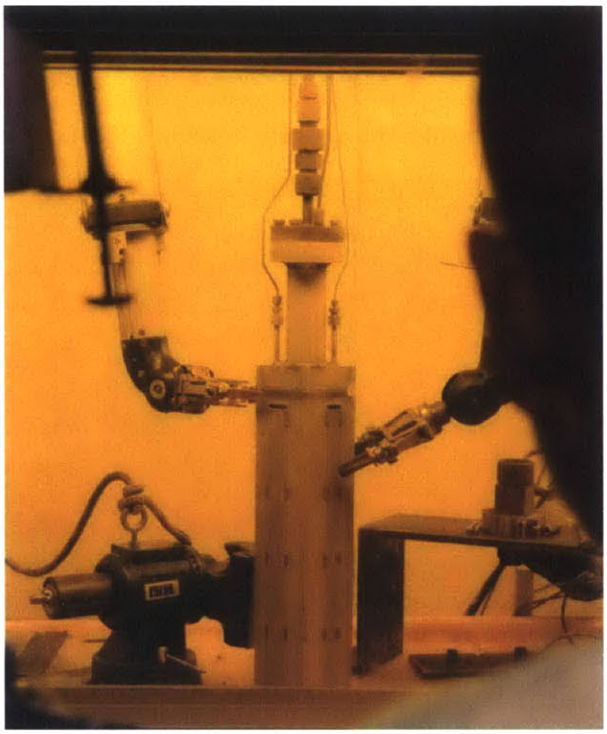

Figure A. 6: HTIF rig in hot-cell at MITR-II containment building.

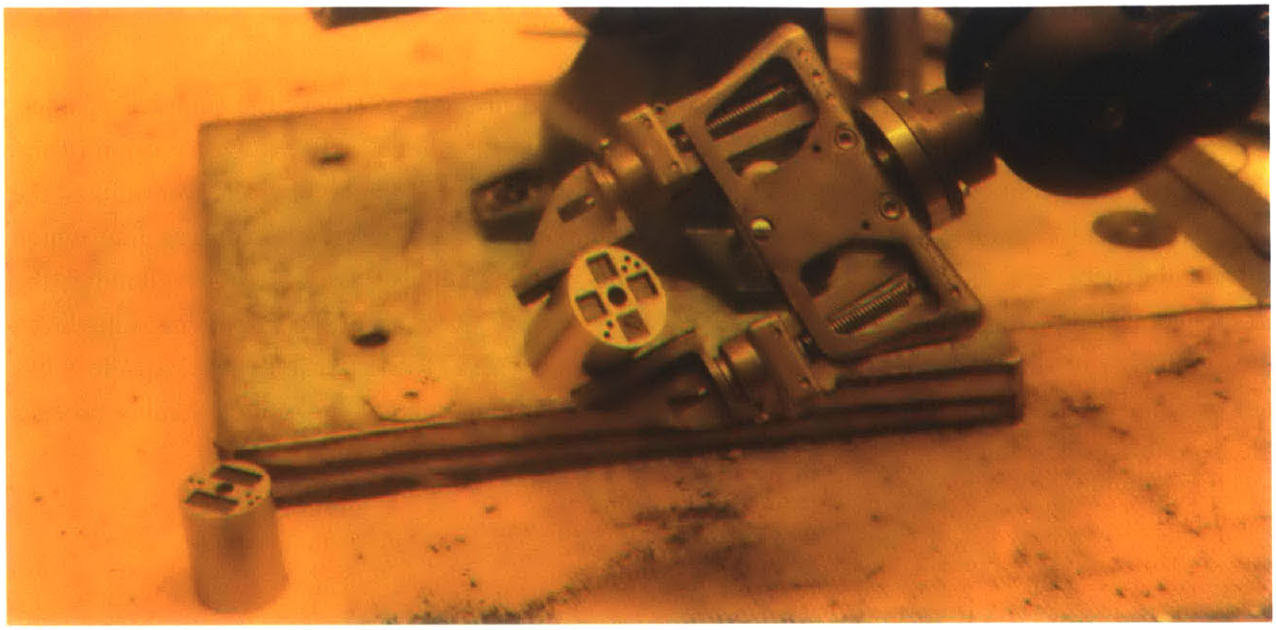

Figure A. 7: Sample #12 capsule holding TRISO samples.

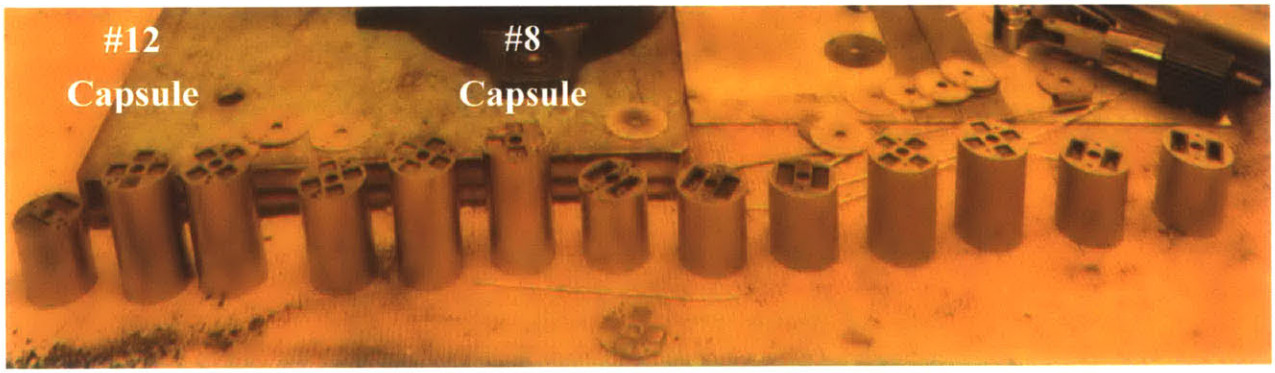

Figure A. 8: Thirteen sample capsules from the HTIF rig. Capsules are numbered 13 to 1, from left to right. #12 has TRISO irradiated at 1000 °C. #8 has TRISO irradiated at 1300 °C. Only #12 has been retrieved thus far.

A.1.3 Disassembly of sample capsule in fume hood

The #12 sample capsule containing the TRISO samples was removed from the hot-cell after radiation protection personnel at the MITR determined that the capsule radioactivity was appropriate for removal. This allowed disassembly of the sample capsule in a fume hood. The disassembled sample #12 capsule and the extracted TRISO particles are shown in Figure A. 9. The #8 capsule has not been disassembled yet.

A.1.4 Measured weights and dose-rates of TRISO particles

The irradiated particles were weighed on a Mettler Toledo XS150 analytical balance which had been calibrated in July 2013. First, all TRISO particles from the HTIF were weighed. Then, in order to obtain an average particle mass, 40 particles were weighed at the same time, and the result was divided by 40. The average particle mass was obtained in the same fashion for as-fabricated particles. Table A. 2 shows the total mass of all TRISO particles from the HTIF irradiation as well as a single-particle average mass. Table A. 3 shows the measured average mass for a single as-fabricated particle as well as a calculated mass based on material properties from the ORNL characterization report on TRISO batch ZrO2-500-AK2. A hand-held Eberline Ion Chamber Model RO-2 was used in order to determine the dose rate from the irradiated particles. The gamma and beta dose rates are shown in Table A. 4.

Figure A. 9: At left, irradiated surrogate TRISO particles from the HTIF sample capsule. At right, HTIF sample capsule and graphite specimens from that capsule.

Table A. 2: Masses of TRISO particles from HTIF and the average mass from weighing 40 particles.

TRISO irradiated in HTIF	Mass (g)	Std Dev
Total mass of TRISOs from HTIF	1.52058	2.09E-05
Single Particle Average	0.001110	3.33E-07

Table A. 3: Single particle measured and calculated masses for as-fabricated TRISO particles. The calculated mass is based on layer thicknesses and layer densities from the ORNL characterization report for the batch ZrO2-500-AK2 [167].

As-Fabricated TRISO	Mass (g)	Std Dev
Measured Single Particle Average	0.001106	6.30E-07
Calculated Single Particle	0.001100	-

Table A. 4: Dose rate for entire HTIF TRISO particle inventory. Measured with hand-held detector.

Dose rate on-contact for entire HTIF Irradiated TRISO inventory	
Gamma	0.15 mR/h
Beta	0.85 mR/h

A.1.5 Sample preparation for metallography

Dr. John Hunn and Dr. Tyler Gerczak, both of ORNL, shared their methodologies and assisted in establishing a mounting, grinding, and polishing procedure. Both irradiated and as-fabricated TRISO particles were mounted in epoxy, and through a series of grinding and polishing steps, they were prepared for optical and scanning electron microscopy (SEM). Both the irradiated and as-fabricated TRISO particles are from batch ZrO2-500-AK2 which was fabricated at ORNL in [167].

A.1.5.1 Epoxy mounting

Several batches of particles were mounted. In some batches, only four particles were in an individual mount. In other batches, more than four particles were affixed in the same mount. Both irradiated and as-fabricated particles were mounted for comparison. First, the selected particles are placed in the bottom of a two-piece, 1.25 inch diameter mounting cup. Then, a small amount of Crystal Bond 509 was dissolved in an excess of acetone. A couple drops of this mixture were dropped onto the particles in the mounting cup. The surface tension helped to draw the particles together into contact. Once the acetone evaporated away, the crystal bond precipitated, leaving a thin film which held the particles to the bottom of the mounting cup. The samples were ready for epoxy after the Crystal Bond had hardened. EpoFix epoxy was mixed as 25 parts resin with 3 parts hardener by weight. Then, the epoxy was poured into the mounting cup under vacuum. This technique prevents air bubbles from being trapped around the TRISO particles. Images pertaining to mounting TRISO particles can be found in Figure B. 7 through Figure B. 12.

A.1.5.2 Grinding epoxy mounts

After mounting in epoxy, the TRISO particles were ground to near mid-plane and polished using a Buehler MiniMet, pictured in Figure A. 10. In order to follow the progress of grinding and polishing, the particles were periodically observed in a Nikon SMZ-10 optical microscope with an Amscope MT1000 digital camera (Figure A. 11). In the first grinding step, using a Buehler UltraPrep 6 μm metal-bonded diamond disc, the TRISO were ground until the kernel was just visible. Figure A. 12 through Figure A. 15 show the evolution of the TRISO particle surfaces as grinding progressed. Figure A. 12 shows the second mount of irradiated TRISO particles, called "I2", prior to grinding. The particles are at slightly different depths in the epoxy. The particle at the top right is closest to the epoxy surface. Figure A. 13 shows the I2 mount after 15 minutes of grinding. In Figure A. 13, the OPyC, SiC, and IPyC layers are visible, and the buffer layer is barely visible in several particles as well. In Figure A. 14, the kernel is exposed in several particles after a total of 45 minutes of grinding. In Figure A. 15, the kernel is exposed in all particles after 58 minutes of grinding. At this point, the sample was back-potted with epoxy using the vacuum impregnation system. This was done in order to fix the kernel in the buffer by infiltrating any gaps or pores between the buffer and the kernel with epoxy. Additionally, this would fill any gaps between layers and support the layers as the mid-plane is approached by subsequent grinding. After the epoxy hardened from the first back-potting procedure, additional grinding removed more material and further exposed the kernel. The sample was then back-potted a second time. After the second back-potting, the samples were ground to just-above mid-plane. After a total of 6 mounts had been made, it was determined that a single back-potting was sufficient. Subsequent samples will be prepared with only a single back-pot.

Figure A. 10: Buehler MiniMet in fume hood certified for work with radioactive samples.

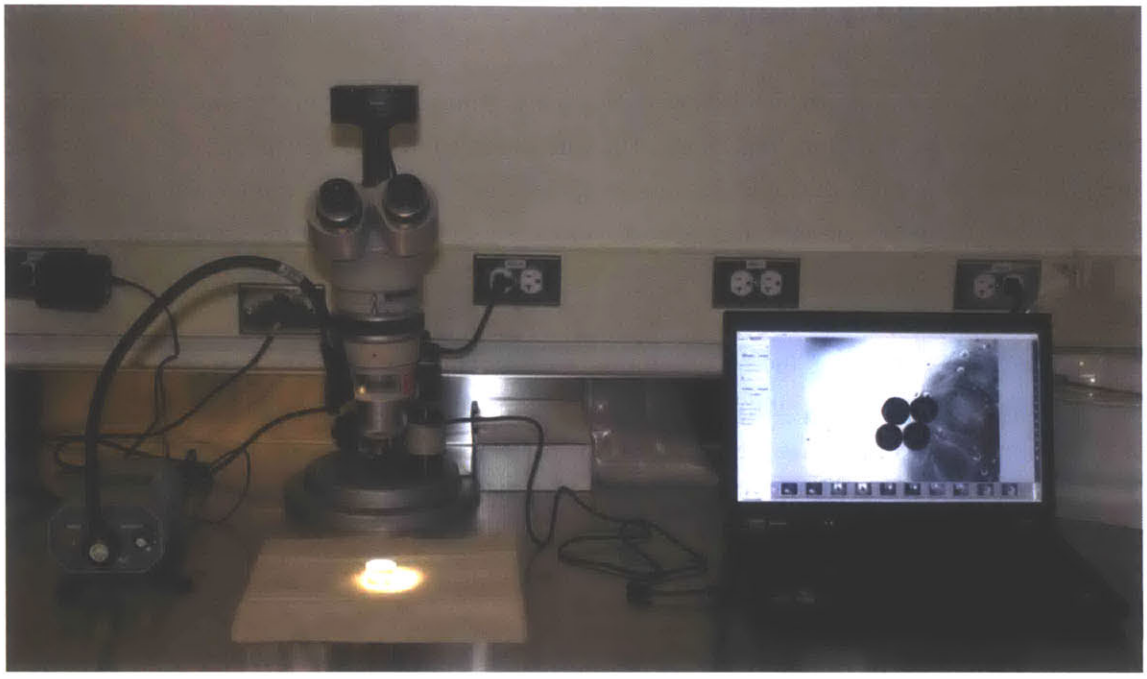

Figure A. 11: Nikon SMZ-10 microscope with Amscope MT1000 camera used for observing particles during grinding and polishing steps.

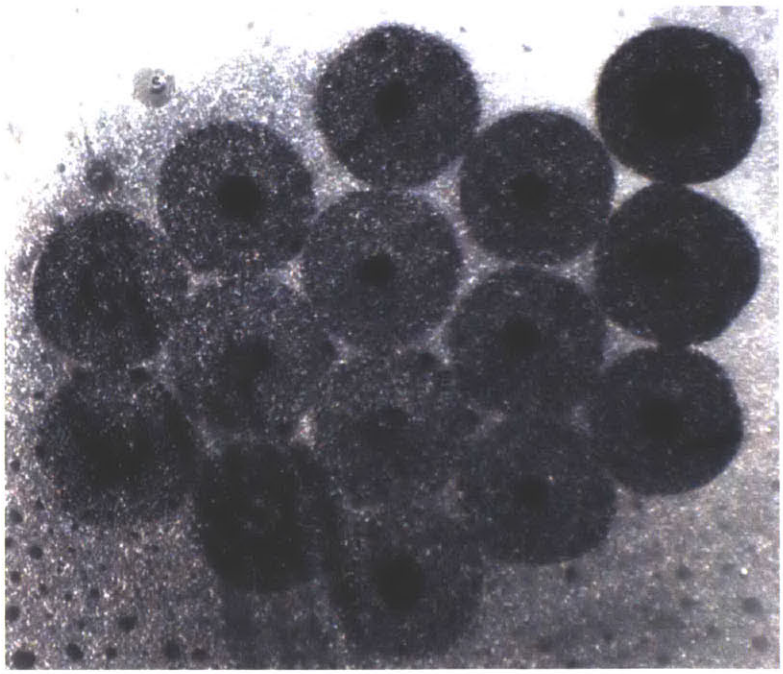

Figure A. 12: As-mounted irradiated TRISO particles (mount I2) prior to grinding.

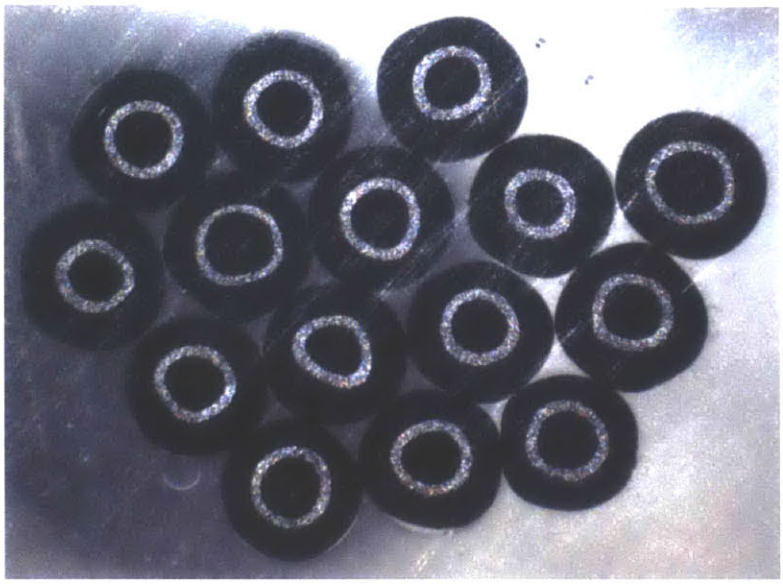

Figure A. 13: Irradiated TRISO particles (mount I2) after 15 minutes of grinding with 6 µm UltraPrep disc.

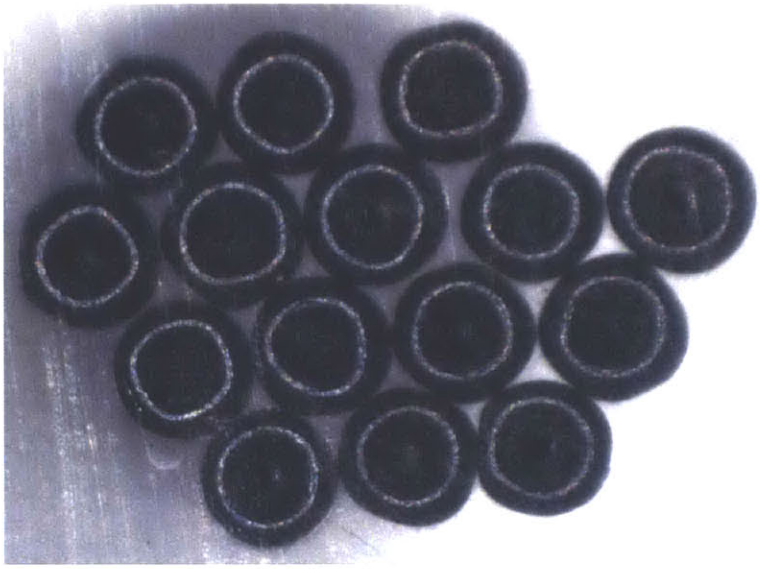

Figure A. 14: Irradiated TRISO (mount I2) after 45 minutes grinding with 6 µm UltraPrep disc.

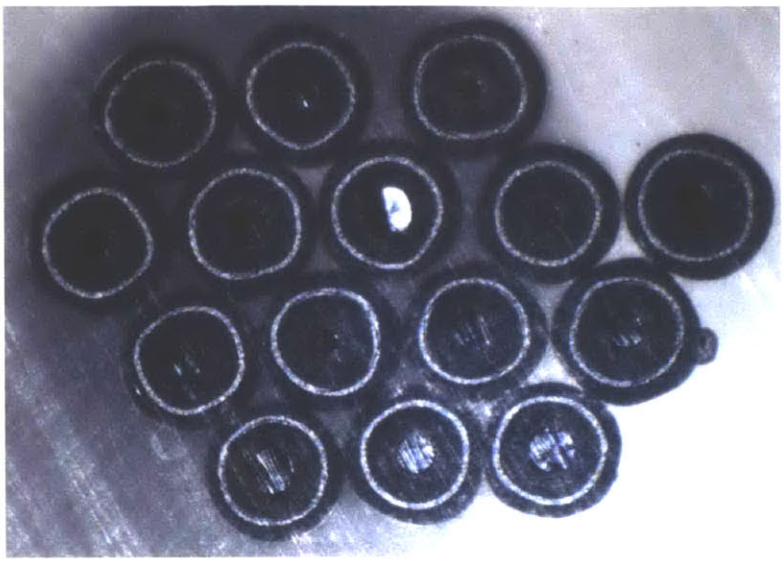

Figure A. 15: Irradiated TRISO (mount I2) particles after 58 minutes of grinding with 6 μm UltraPrep disc.

A.1.5.3 Polishing TRISO in epoxy mounts

After grinding to just-above mid-plane with the 6 μm metal bonded diamond disc, the samples were polished using progressively finer media in the MiniMet. Diamond lapping films in 3, 1, 0.5, and 0.1 micron grits were used (in that order) with de-ionized water as a lubricant. The final polish was done using Struers OP-S colloidal silica (at 0.04 micron and pH 9.8) on a Struers OP-Chem neoprene pad. Figure A. 16 shows the particles from mount I2 after the 0.1 micron polish, and Figure A. 17 shows the same particles after the final polish. For comparison, un-irradiated particles from mount U2 are shown in Figure A. 18. The images indicate that there is color difference between the kernels in the irradiated and un-irradiated samples. This is due to the automatic color temperature adjustment on the microscope camera. Higher magnification images taken with a different microscope and camera show no color difference between the irradiated and un-irradiated particles.

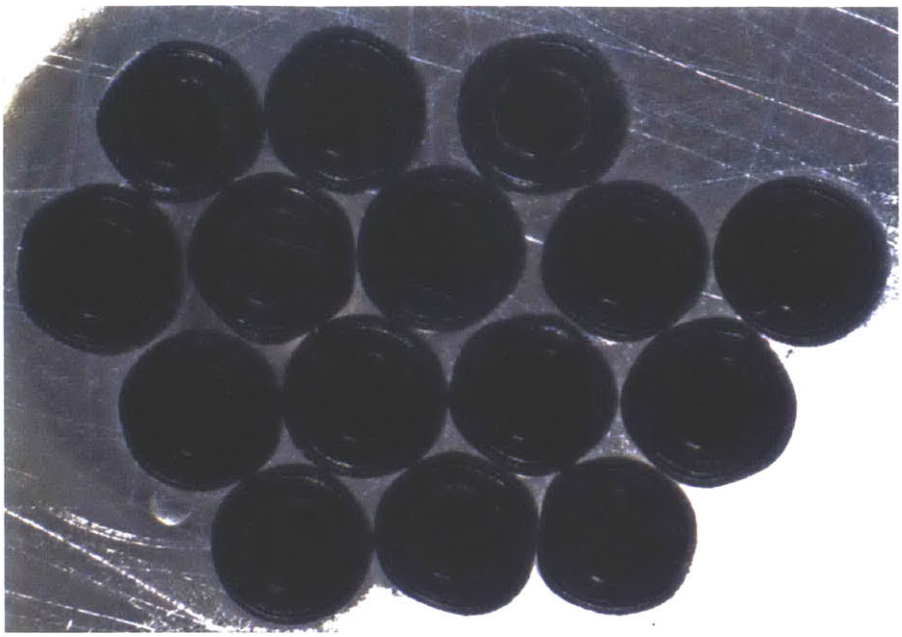

Figure A. 16: Irradiated TRISO (mount I2) after 0.1 micron polish.

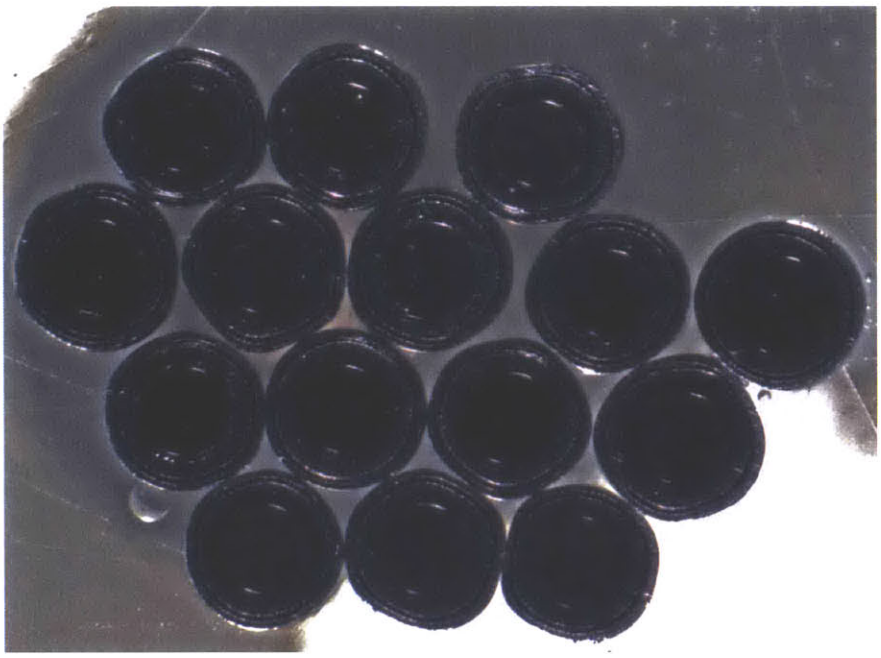

Figure A. 17: Irradiated TRISO (mount I2) after 0.04 micron final polish. White spots are SiO¬2 particles from colloidal silica polish.

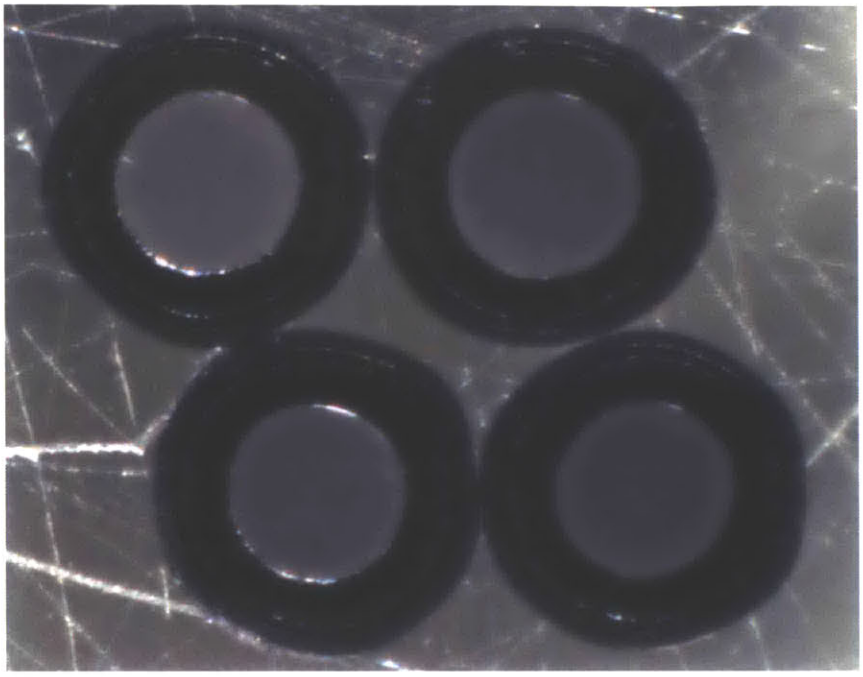

Figure A. 18: Unirradiated TRISO (mount U2) after final polish.

A.1.6 Microscopy of HTIF-irradiated and as-fabricated particles

A series of both irradiated and unirradiated (as-fabricated) TRISO particles were mounted and analyzed with optical microscopy and SEM techniques. Because many images were taken, only the highlights will be shown here. Optical microscopy was carried out first because SEM analysis required a thin layer of gold coating be applied to the samples in order to avoid charging. Optical microscopy was better suited for identifying cracks than the SEM. Because the TRISO particles are surrogates, no fission products existed in the particles and the SEM did not provide additional information. Thus, most samples were only observed in an optical microscope.

Two Zeiss optical microscopes were used. The first, pictured in Figure A. 19, has 2.5x magnification and was used with the Amscope MT1000 camera or with a Zeiss AxioCam MR camera. The second Zeiss optical microscope, pictured in Figure A. 20, has 50, 100, 200, and 500x capability, and was used with the AxioCam MR camera.

A Topcon ABT-150S SEM, pictured in Figure A. 21, was used for electron microscopy. In order to prevent charging in the SEM, a thin layer of gold was applied using a Denton Vacuum DV-502A pictured in Figure A. 22. Care must be taken not to use too much gold, as it can occlude surface details on the TRISO particles, particularly the buffer/IPyC interface. In the future, particles will be mounted in epoxy mixed with graphite powder so that gold coating is not required.

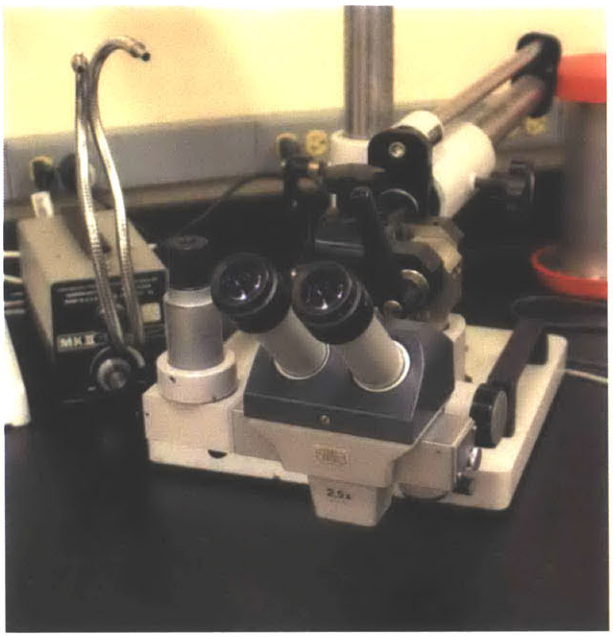

Figure A. 19: Zeiss 2.5x microscope. Light source is shown at left in the background.

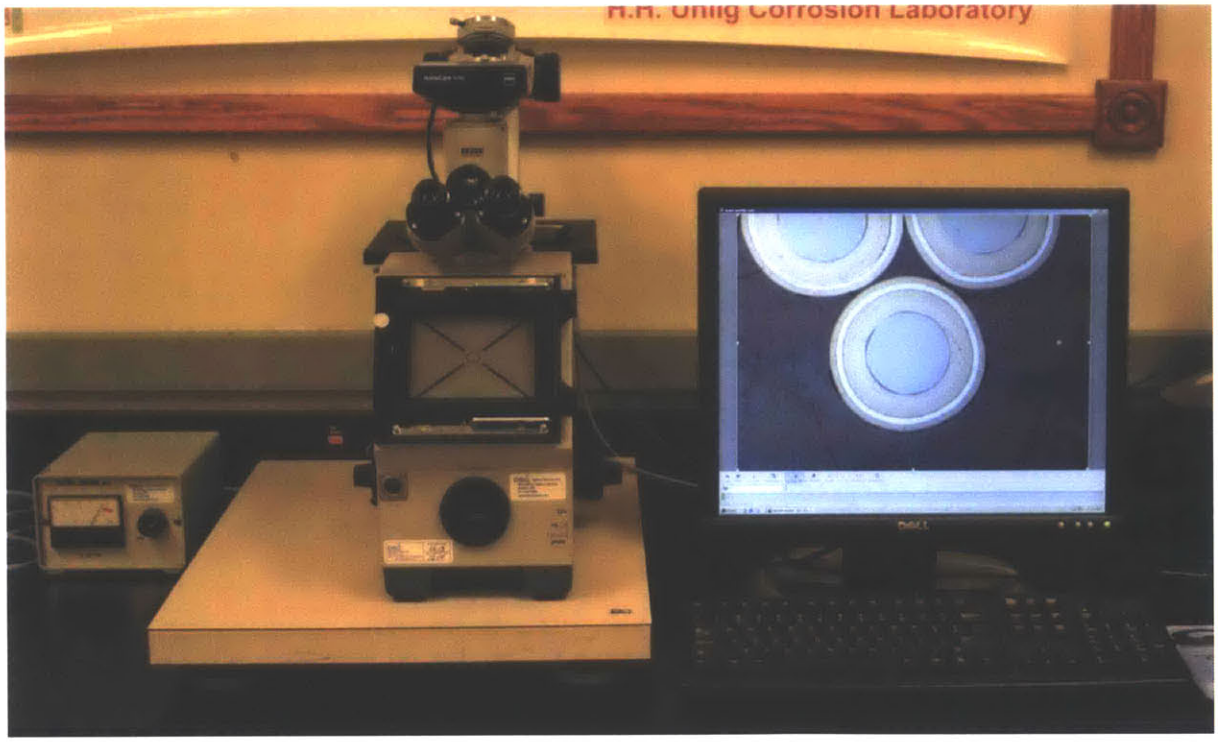

Figure A. 20: Zeiss inverted microscope with 50, 100, 200, and 500x capabilities.

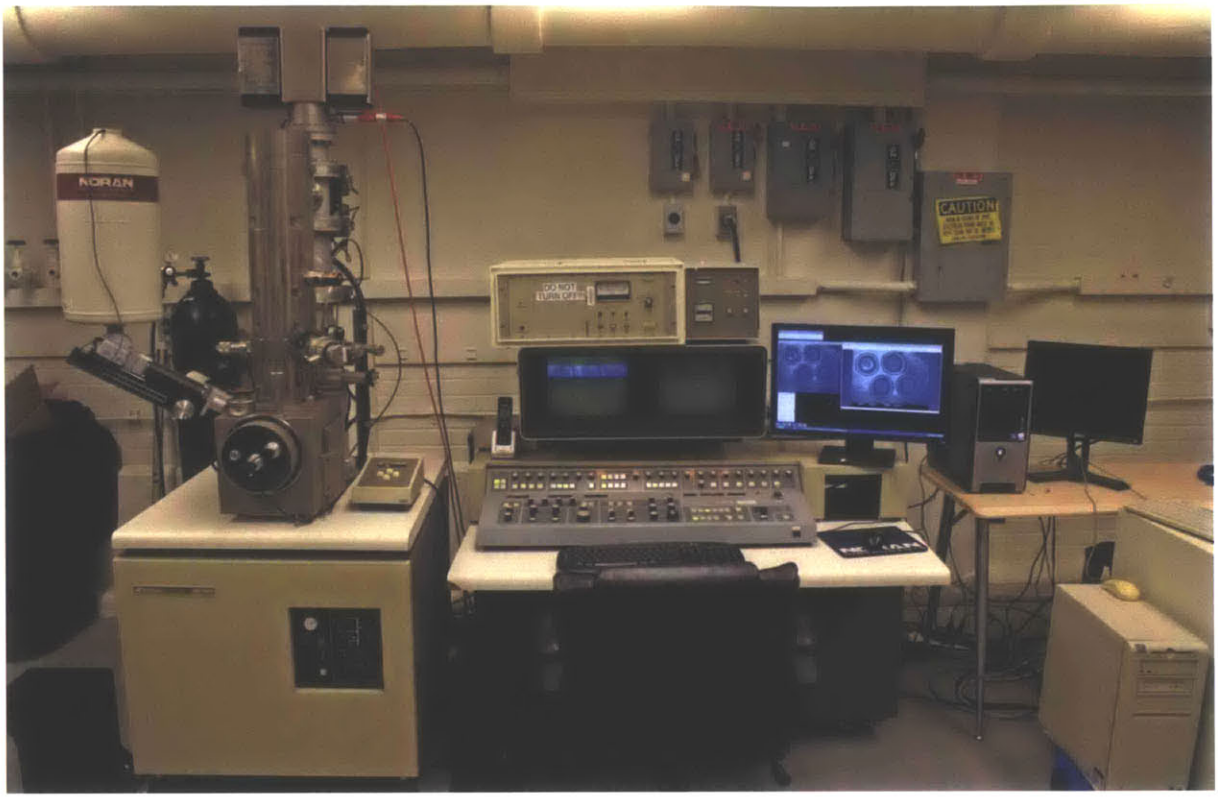

Figure A. 21: Topcon ABT-150S SEM.

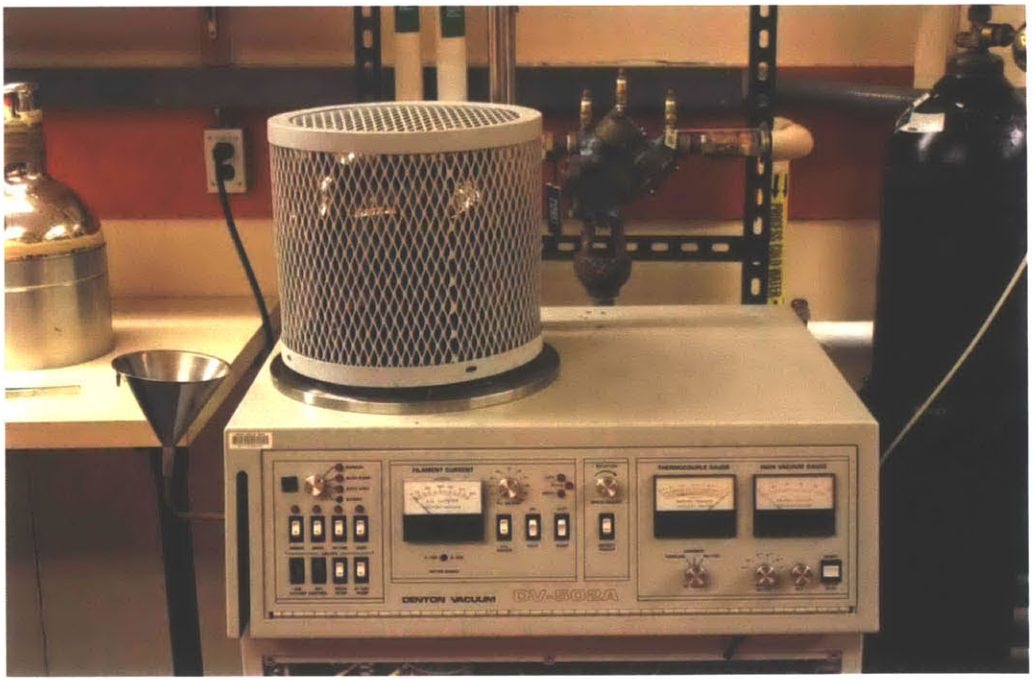

Figure A. 22: Denton Vacuum DV-502A used for gold-coating samples.

A.1.6.1 Microscopy of as-fabricated particles

Figure A. 23 shows an optical micrograph of 4 unirradiated, as-fabricated particles. This was the first sample mounted, polished, and analyzed. Based on lessons learned from this mount, improvements were made in subsequent mounts. This image was obtained using the Zeiss 2.5x microscope with the Amscope MT1000 camera. No cracks were apparent, but the magnification was low. Subsequent mounts utilized the inverted Ziess microscope at a minimum magnification of 50x. This image was calibrated, and measurements were made using the Amscope software. SiC layer thickness ranged from 0.030 to 0.035 mm, and buffer thickness ranged from 0.0839 to 0.1022 mm. The measured kernel diameter ranged from 0.37 to 0.38 mm. This is smaller than the published as-fabricated kernel diameter of 0.530 mm. This indicated that the particles were not ground as close to mid-plane as was thought.

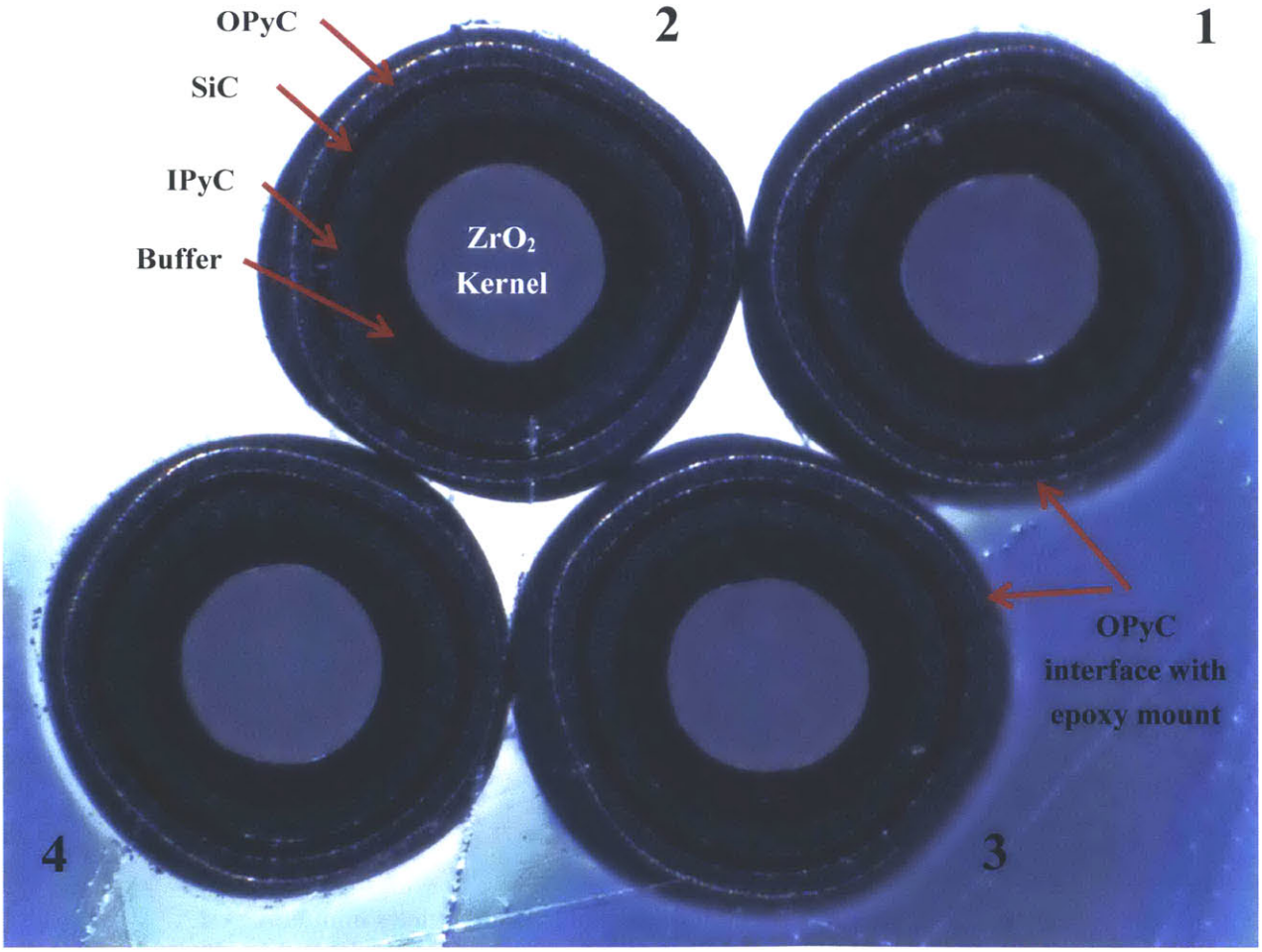

Figure A. 23: Mount "U1" optical micrograph. Each particle was numbered.

Figure A. 24 shows a 2.5x micrograph of the unirradiated, as-fabricated particles in mount "U2". U2 was the second mount produced in the analyses. Figure A. 25 shows 50x optical micrographs of each of the four particles in mount U2. The dark diagonal lines going from top left to bottom right are scratches from sample preparation. The layers are intact on all particles except for particle 3. Figure A. 26 and Figure A. 27 show 100x and 200x images, respectively, for particle 3. There are cracks in the buffer, IPyC, SiC, and OPyC. These cracks are likely to have been introduced during sample preparation. Figure A. 27 shows that the thick, dark lines in the right side of Figure A. 26 appear to be surface discolorations and not cracks. SEM micrographs of these particles are available in Appendix C.1.

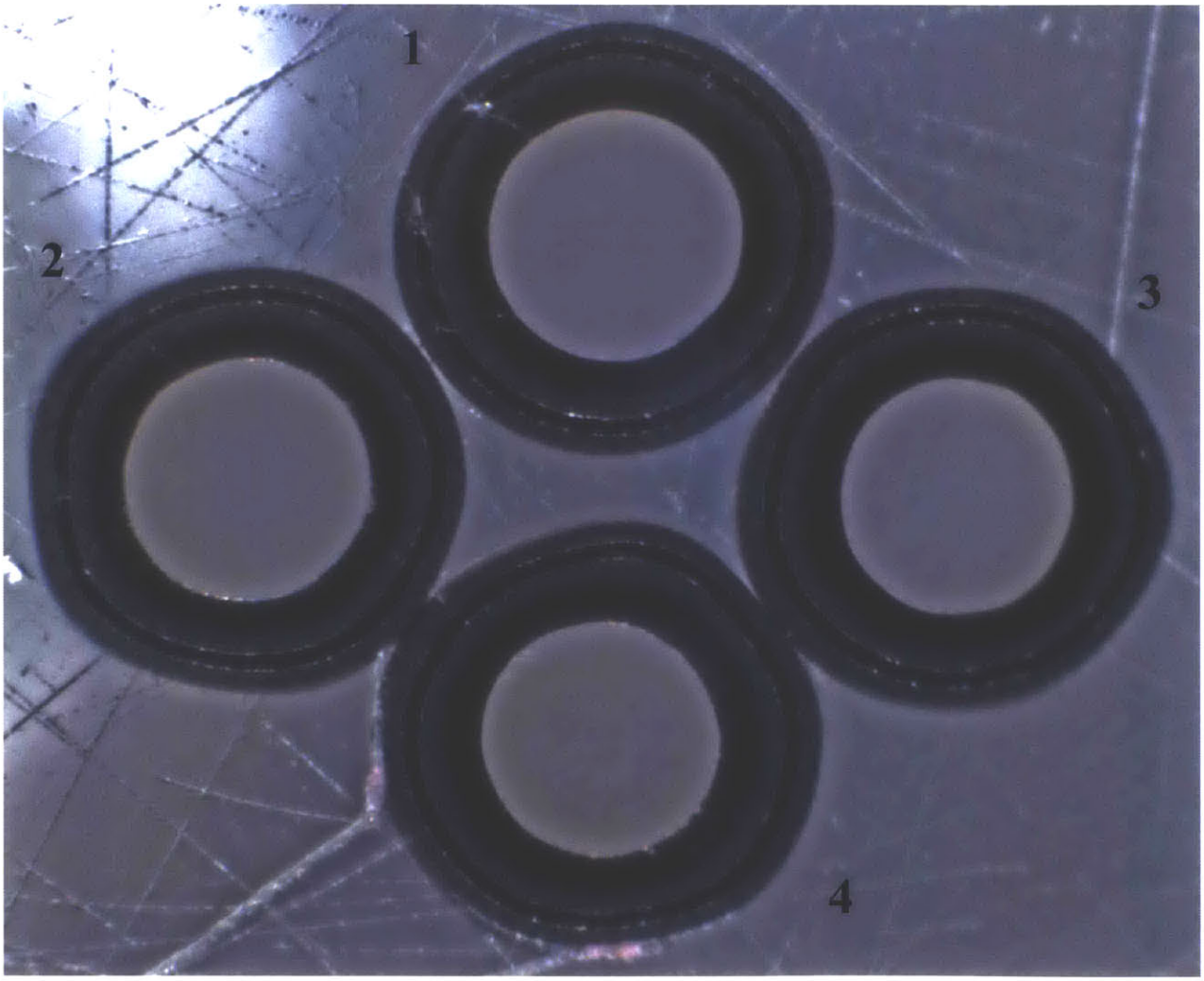

Figure A. 24: 2.5x micrograph of as-fabricated particles in mount "U2".

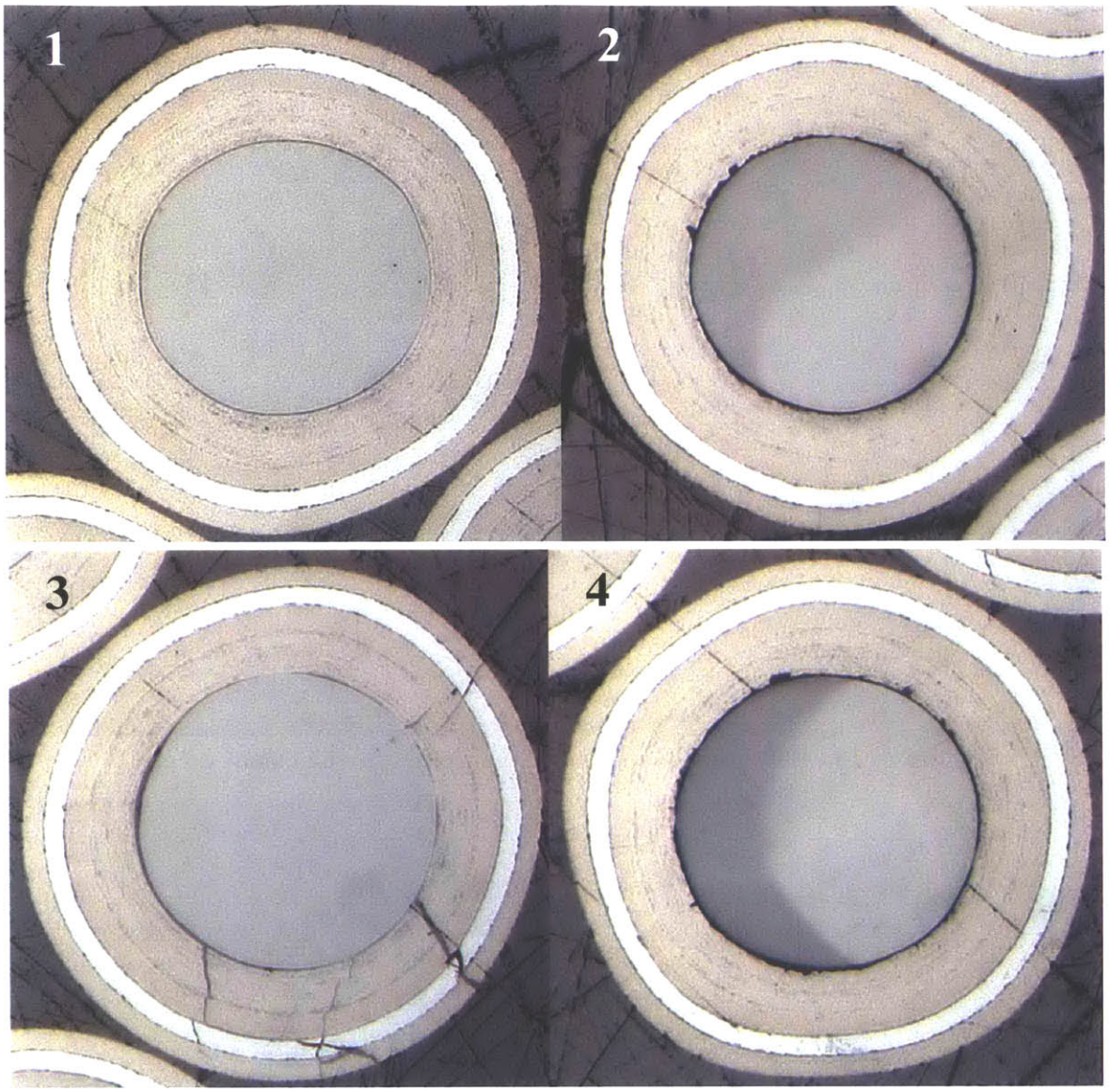

Figure A. 25: 50x optical images of mount U2 particles 1 through 4.

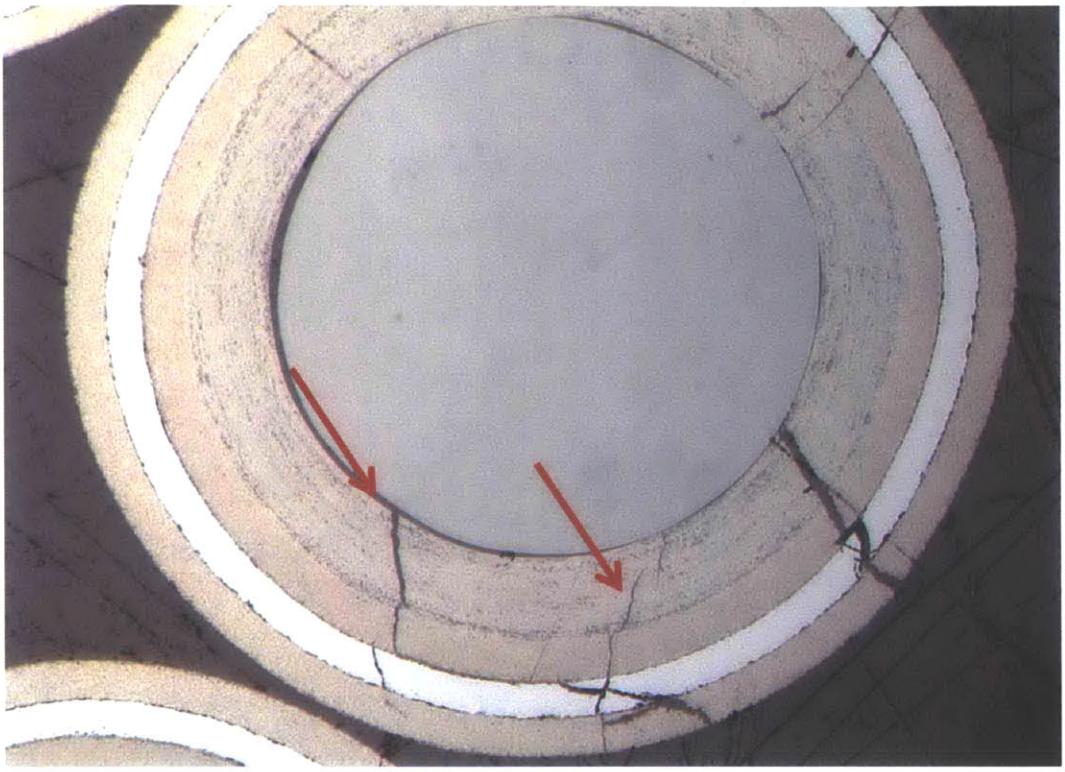

Figure A. 26: 100x optical image of U2 particle 3. Arrows show cracks.

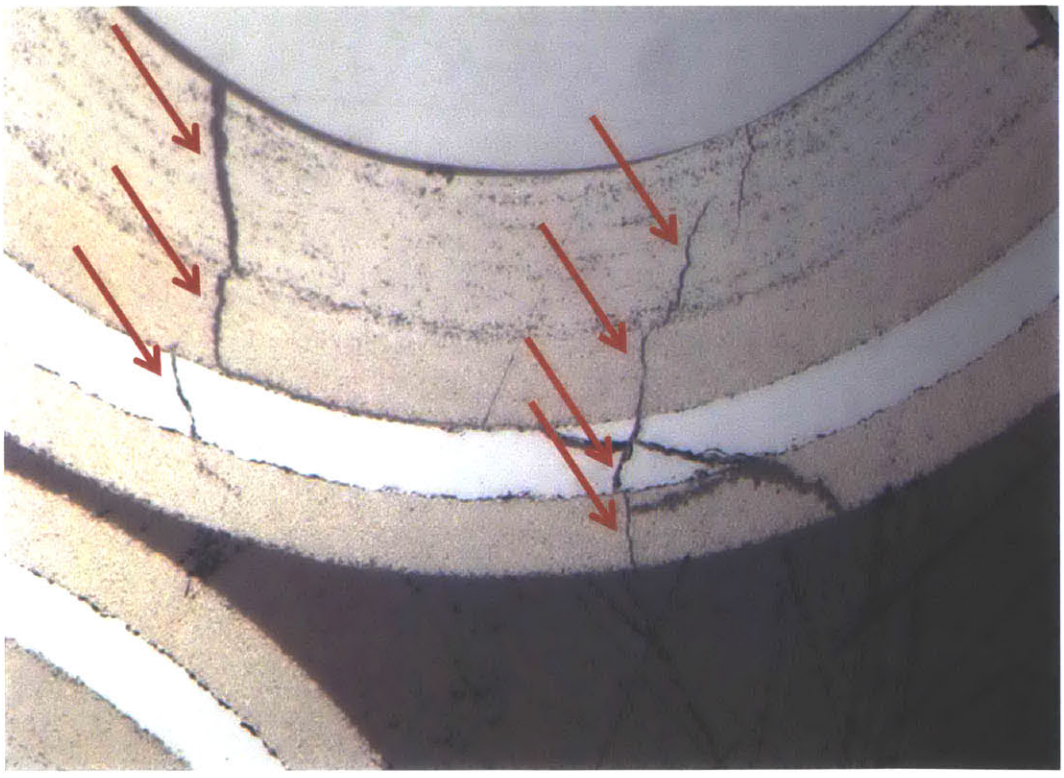

Figure A. 27: 200x optical image of U2 particle 3. Arrows show cracks.

Optical micrographs of as-fabricated particles in the third mount in this project, "U3", are shown in below in Figure A. 28. In this mount all of the particles appear to be in pristine condition. The OPyC layers are intact and appear to be well adhered to the SiC layer. In the bottom left image, there are a series of light scratches which would be removed with additional polishing. There is also one dark surface scratch in the IPyC that would also be removed with additional polishing. In the bottom right image, there is another dark surface scratch which would be removed with a longer polishing step.

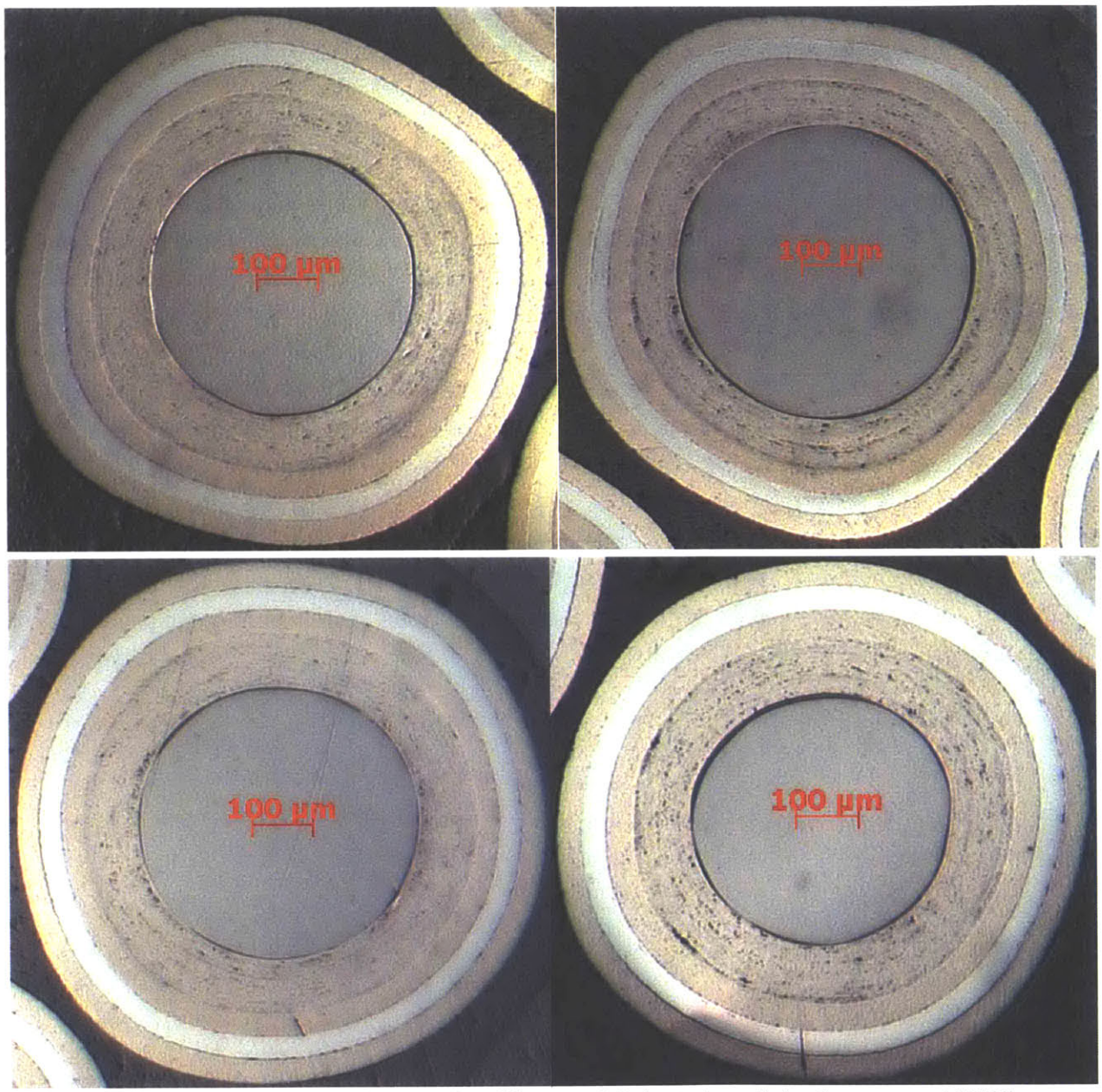

Figure A. 28: Optical micrographs of four as-fabricated particles from mount "U3".

A.1.6.2 Microscopy of TRISO particles irradiated in helium

Mount "I1" features four particles irradiated at 1000 °C in capsule 12 of the HTIF rig. Figure A. 29 shows 50x optical micrographs of the four particles in mount I1. None of the particles had OPyC cracks visible from the outside of the particle prior to mounting. All particles exhibit radial cracks in the OPyC layer after mounting. Particles 1 and 2 have long circumferential cracks in the SiC layer. Particle 3 has much shorter cracks extending circumferentially in the SiC layer. Particle 4 has only a few small flaws in the SiC layer in the vicinity of the 3 o'clock position. Particle 1 has clearly visible cracks in the buffer layer which extend to the IPyC. The cracks from the IPyC in particle 1 extend to the SiC layer, and cracks in the SiC layer seem to begin at or near the intersection of IPyC cracks with the SiC layer.

Figure A. 30 through Figure A. 37 show 100x and 200x optical micrographs of particles 1 through 4 from mount I1. It is possible that the SiC cracks were introduced during sample preparation, but these crack morphologies were not observed in any unirradiated particles prepared using identical methods. Figure A. 38 shows micrographs taken during the initial grinding with the 6 micron metal-bonded diamond disc. Large black circumferential cracks are visible at left in Figure A. 38. As mid-plane is approached, the cracks appear thinner at right in Figure A. 38. This apparent crack thickness difference is simply a geometric effect as mid-plane is approached, but it also indicates that the cracks continue throughout the layers and are not confined only to the surfaces visible in the higher magnification images. As the SiC layer is penetrated, it is very thin in the center of the particle. This is the point where the SiC layer would be most susceptible to cracking during grinding. No radial SiC cracks or through-cracks were observed in any of the particles. Figure A. 39 shows an SEM micrograph of particle 1 in mount U1. This image shows how thin the SiC cracks are and that they appear to originate at the IPyC/SiC interface. Additional SEM micrographs of mount I1 particles are available in Appendix C.2.

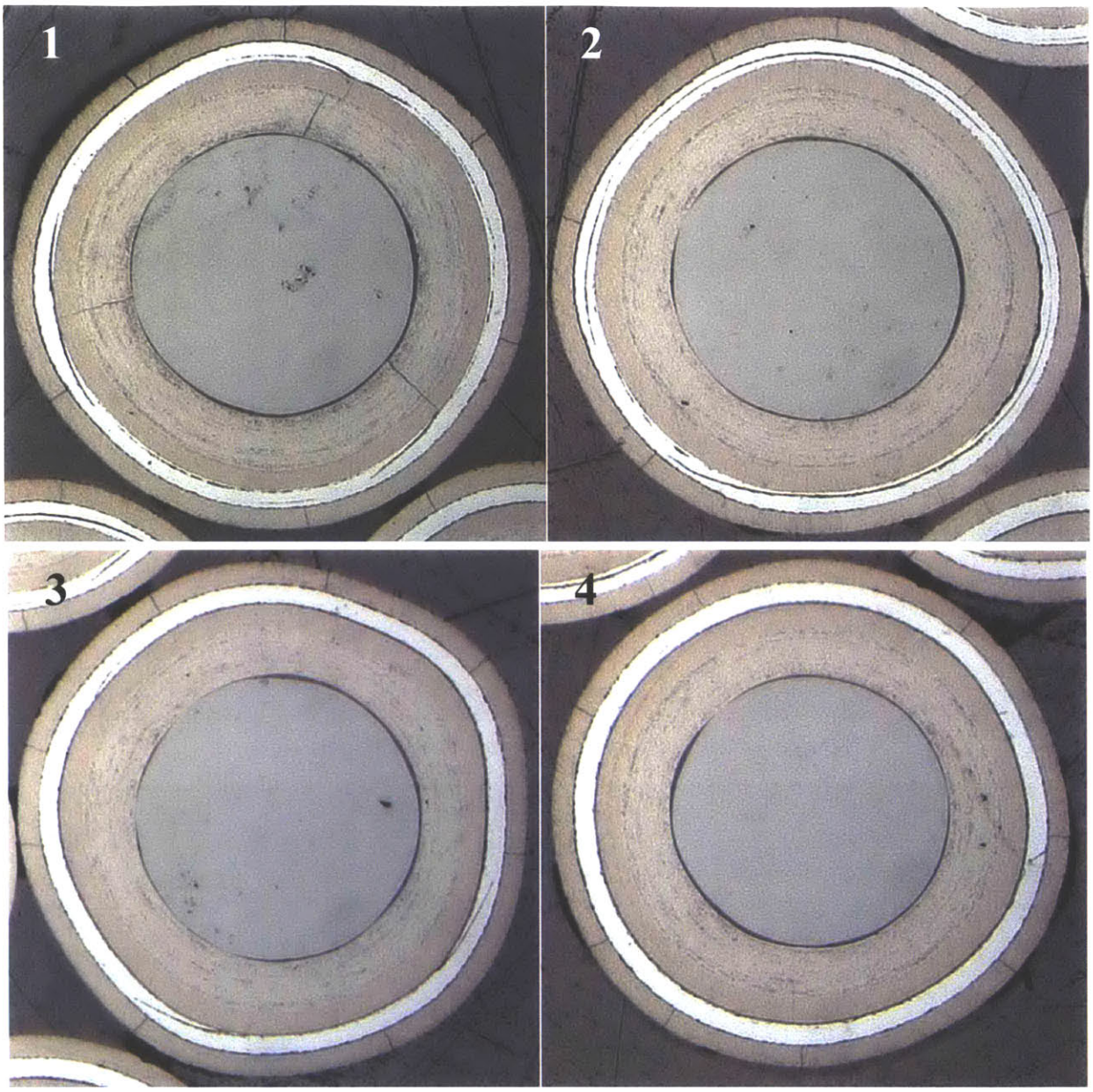

Figure A. 29: 50x Optical micrographs of the four irradiated particles in mount I1.

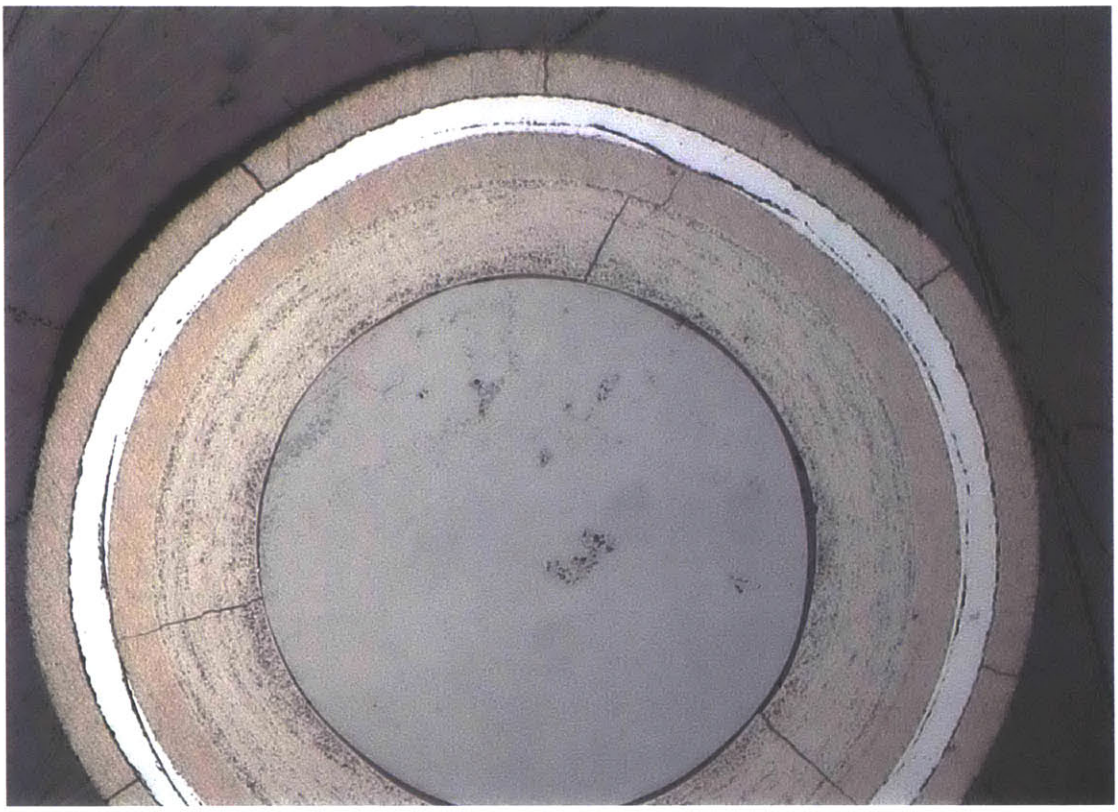

Figure A. 30: 100x optical micrograph of I1 particle 1.

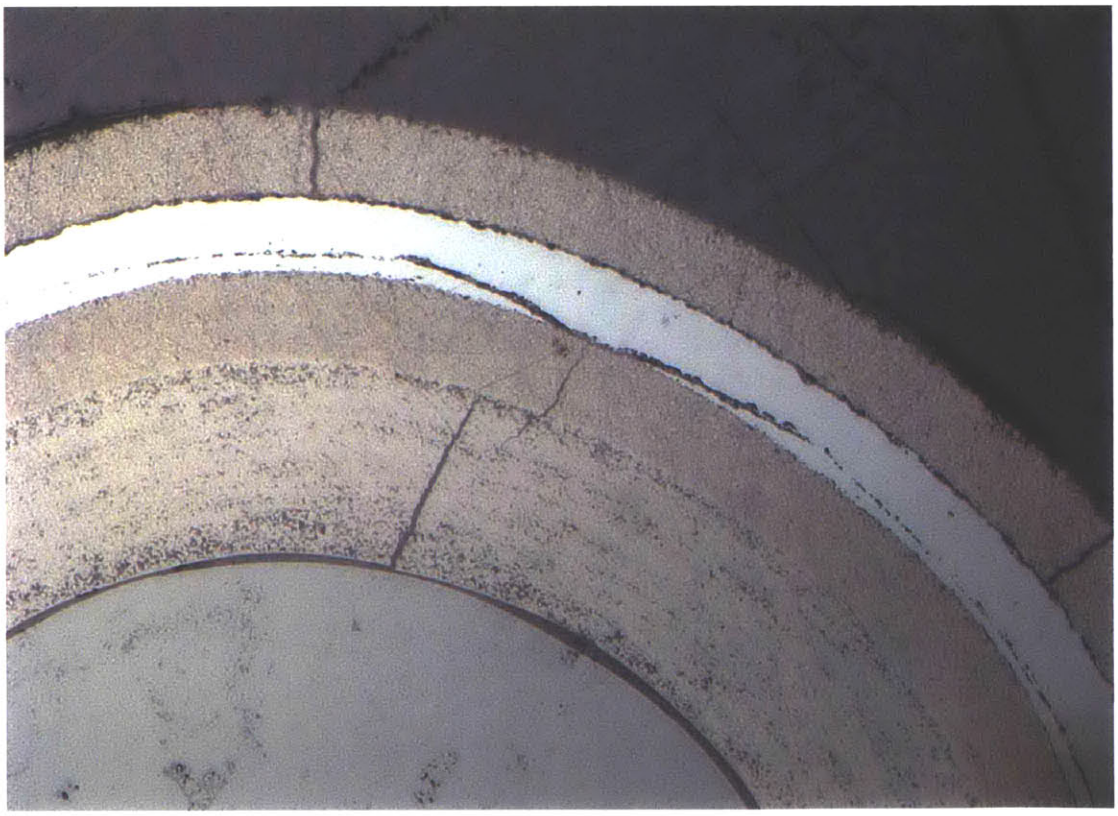

Figure A. 31: 200x optical micrograph of I1 particle 1.

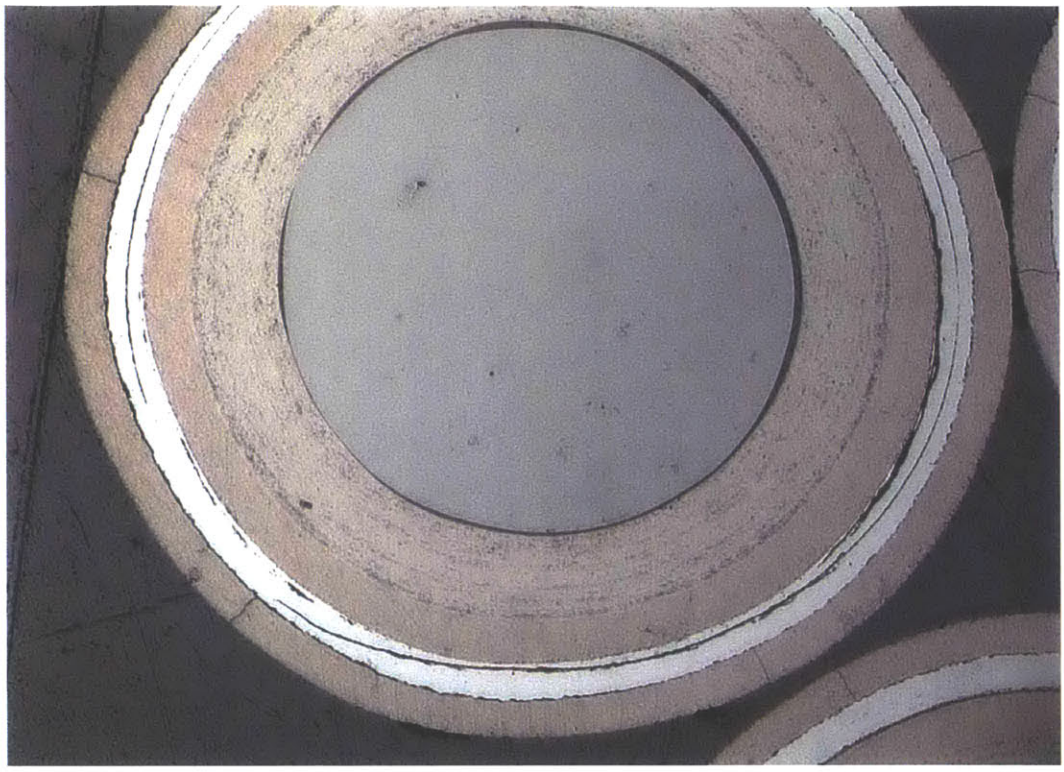

Figure A. 32: 100x optical micrograph of I1 particle 2.

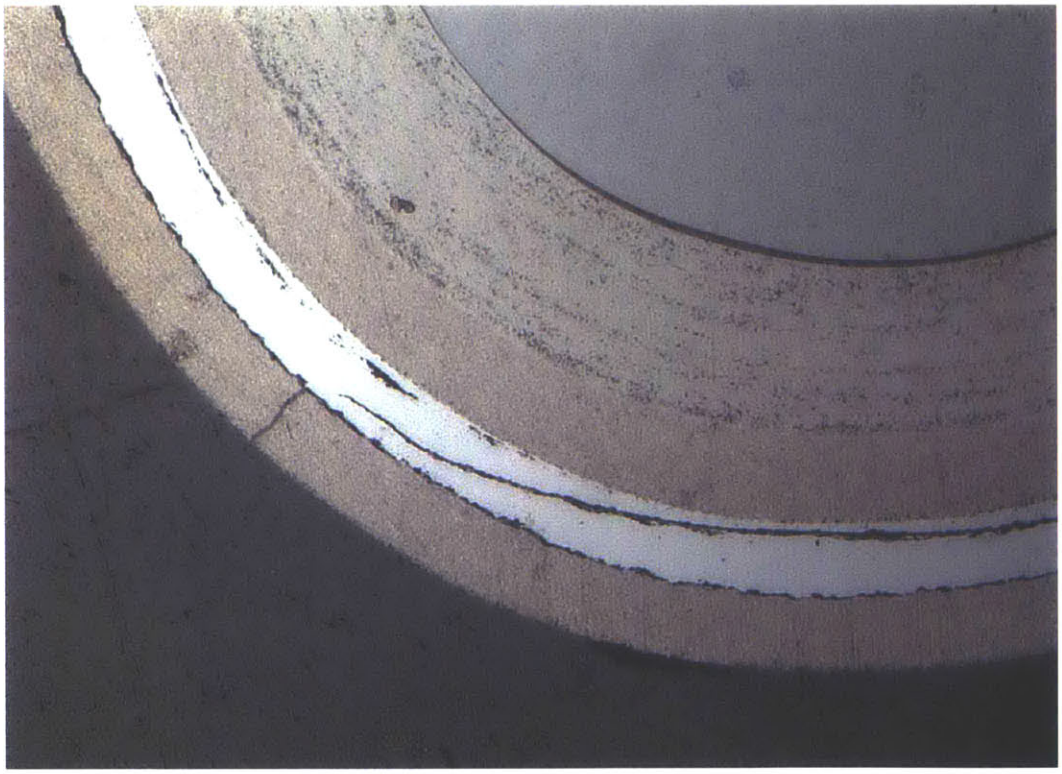

Figure A. 33: 200x optical micrograph of I1 particle 2.

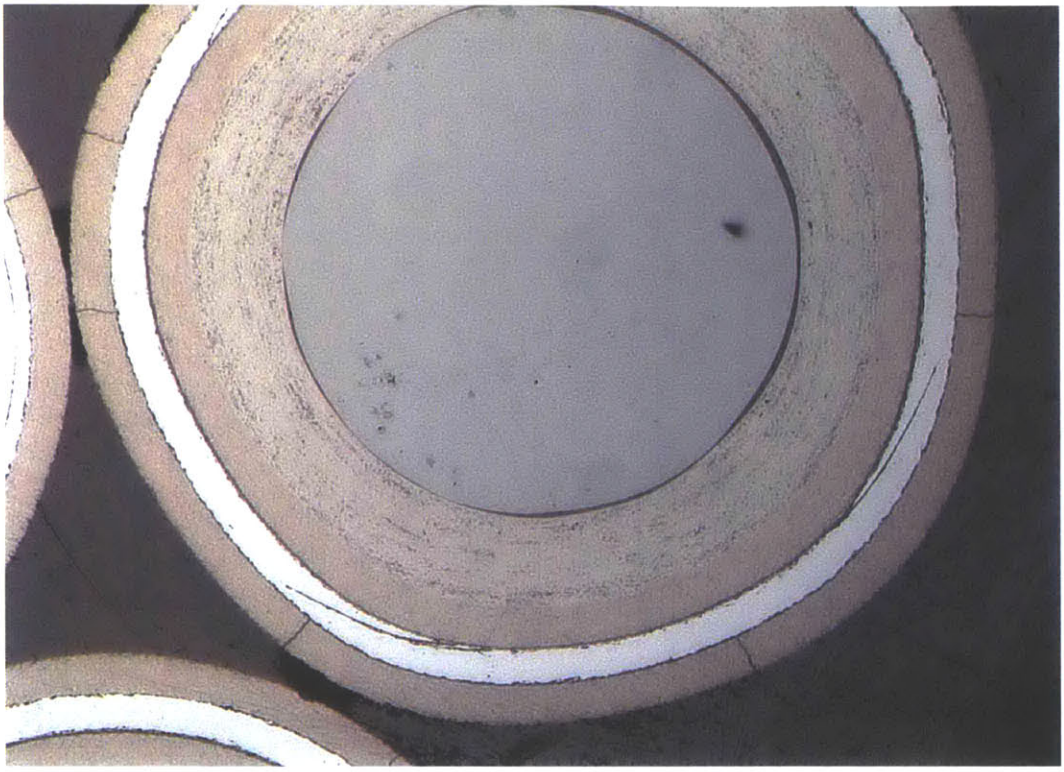

Figure A. 34: 100x optical micrograph of I1 particle 3.

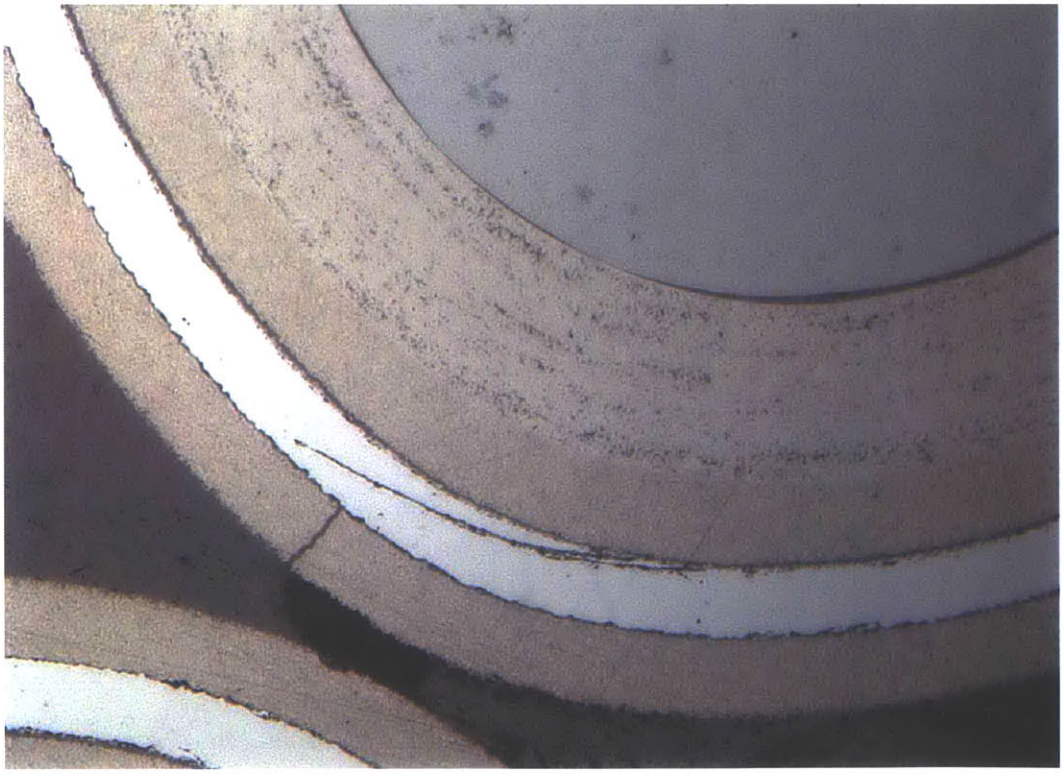

Figure A. 35: 200x optical micrograph of I1 particle 3.

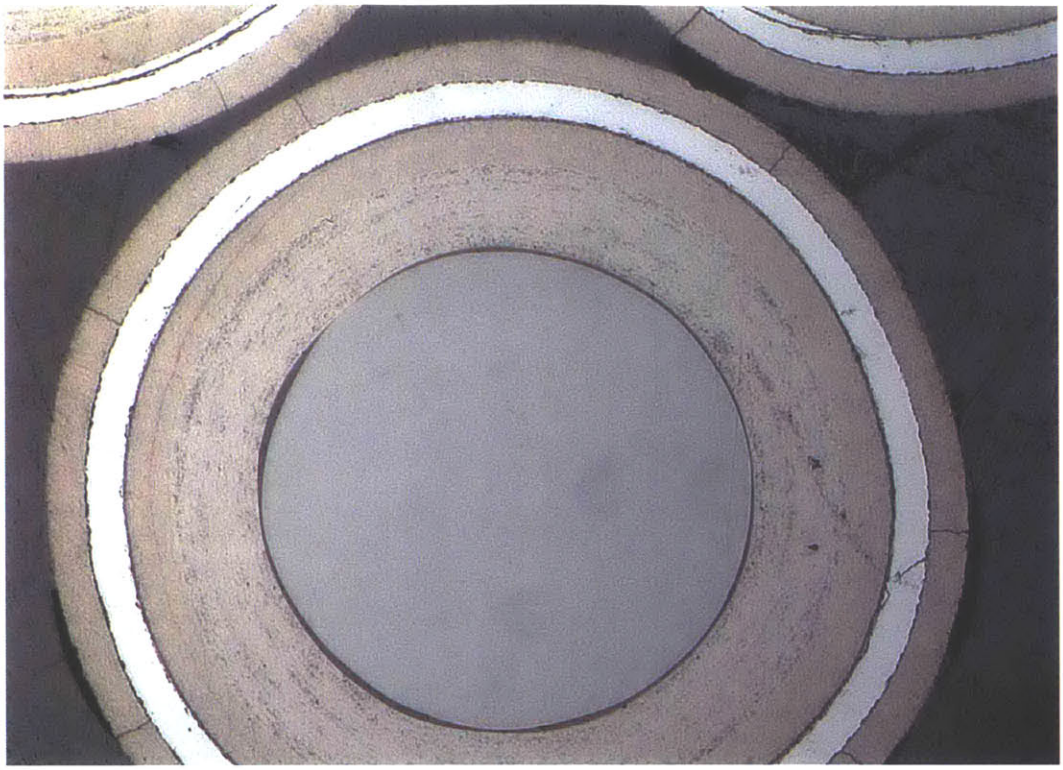

Figure A. 36: 100x optical micrograph of I1 particle 4.

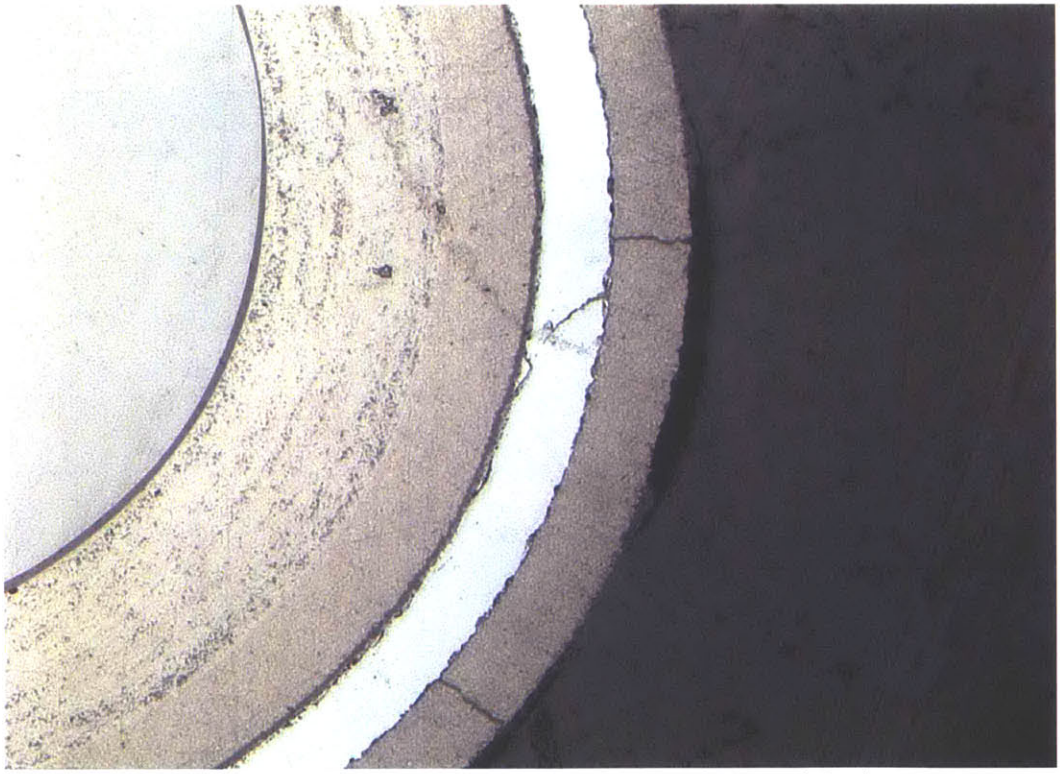

Figure A. 37: 200x optical micrograph of I1 particle 4.

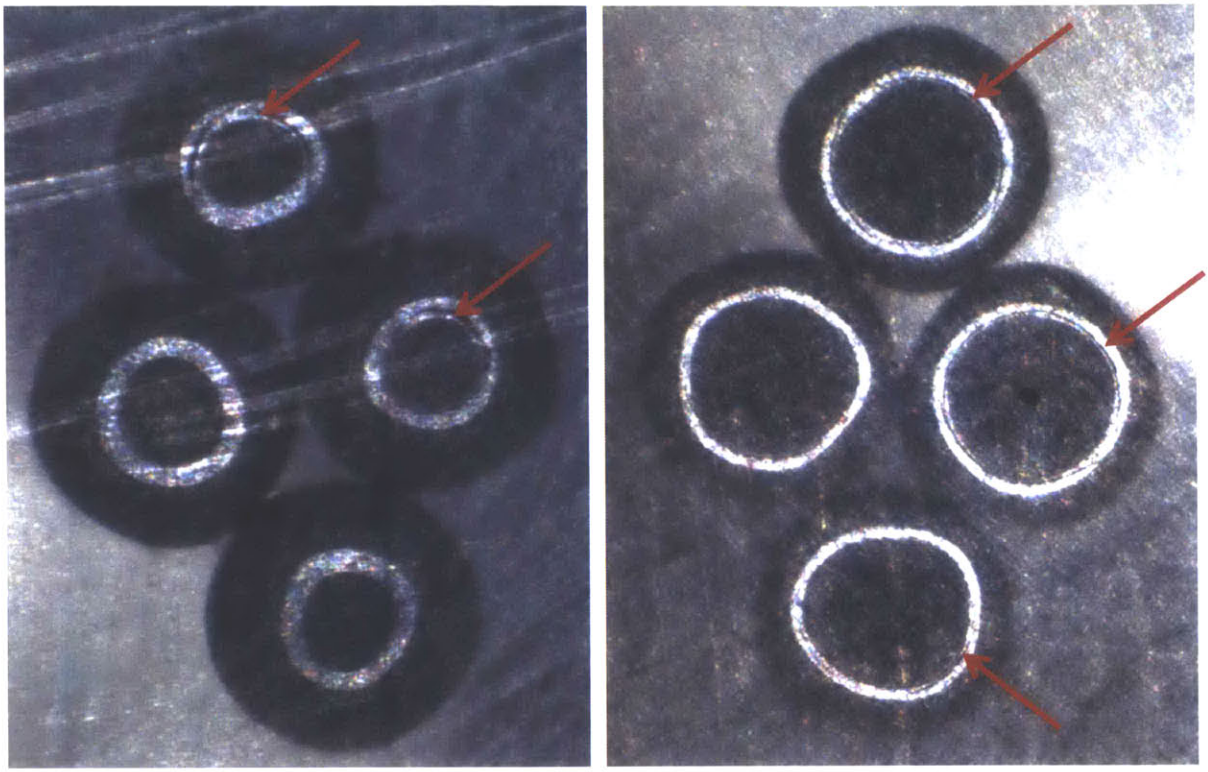

Figure A. 38: 2x optical image of mount I1 during 6 micron grind toward mid-plane. At left, OPyC, and SiC are visible. Notice cracks in SiC layer highlighted with red arrows. At right, OPyC, SiC, IPyC, and buffer layers are visible. Cracks appear thinner as mid-plane is approached.

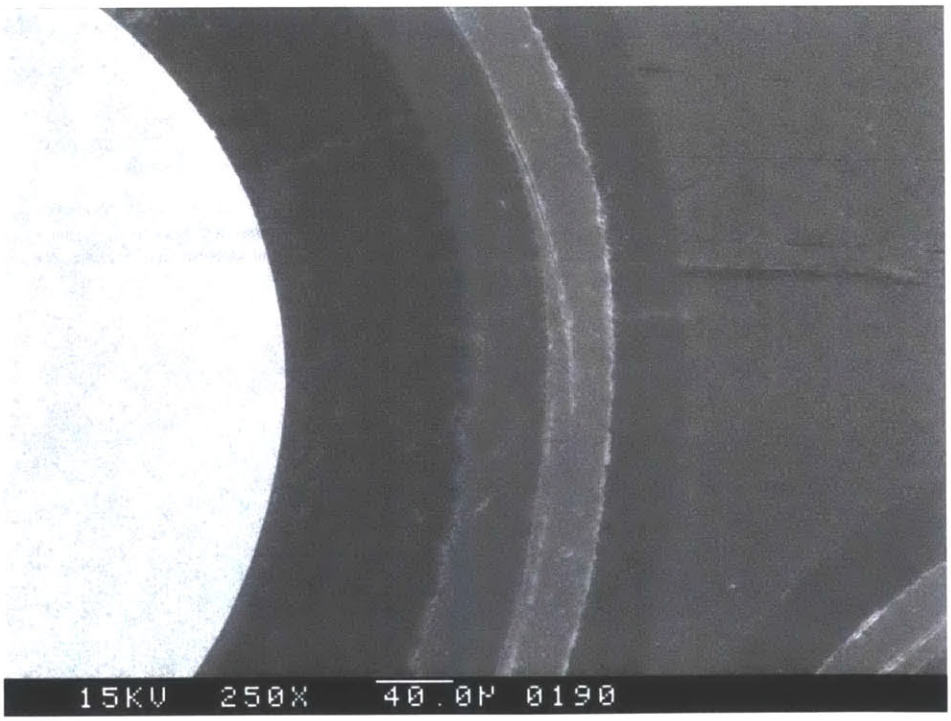

Figure A. 39: 250x SEM micrograph of I1 particle 1.

A second mount of particles irradiated in helium was prepared. As depicted in Figure A. 40, mount I2 consists of 15 particles irradiated at 1000 °C in helium at the MITR. Additional micrographs were taken for each particle at 50, 100, and 200x magnification. Only selected 50x micrographs are included here in this section. SEM micrographs of particles in mount I2 tend to provide less detail than the optical micrographs. The SEM micrographs from mount I2 can be found in Appendix C.2. Of the 15 particles mounted in I2, only particle numbers 8 and 15 showed pristine SiC layers. Particle numbers 4, 5, 6, and 14 showed very slight circumferential cracks in the SiC layer. Particles 1-3, 7, 9, and 10-13 exhibit circumferential cracks that span a significant portion of the circumference of the SiC layer. All particles exhibit radial cracks in the OPyC layer. Some of these OPyC cracks occur in areas where there may be a gap between the epoxy and OPyC. If there was a gap between the epoxy and the OPyC, then the OPyC would not have been supported during grinding, and it may have been cracked during sample preparation. Since other OPyC cracks occur in areas where there is no discernible gap, and OPyC cracking was not observed in unirradiated samples, it is suggested that the OPyC layer is susceptible to cracking after irradiation. The majority of particles have intact IPyC and buffer layers. Particles, 5, 8, 12, 13, and 15 exhibit radial cracks through the buffer and IPyC layers. Particle 9 exhibits only slight cracking of the IPyC layer. Once again, no radial SiC cracks or through-cracks were observed in any of the particles.

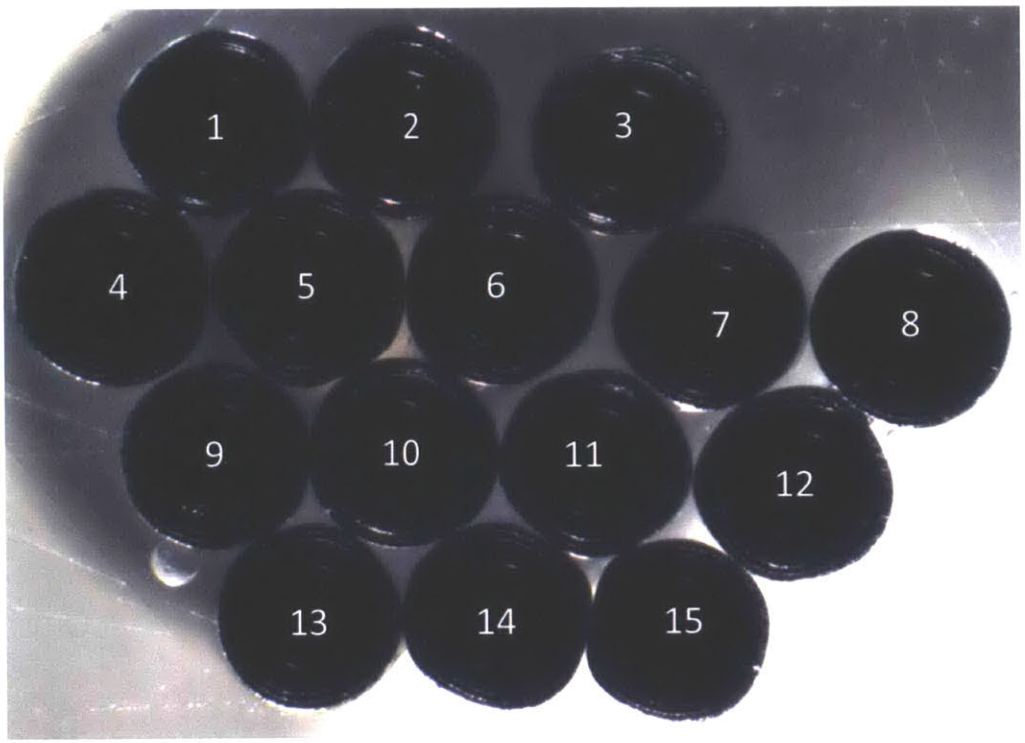

Figure A. 40: 2x optical micrograph of mount I2.

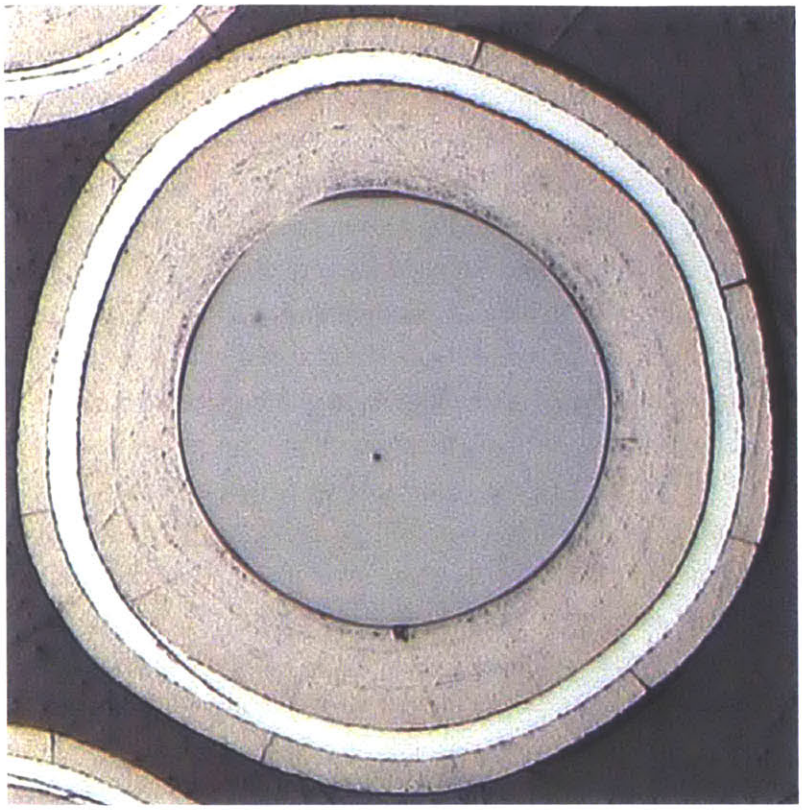

Figure A. 41: 50x optical micrograph of I2 particle 4.

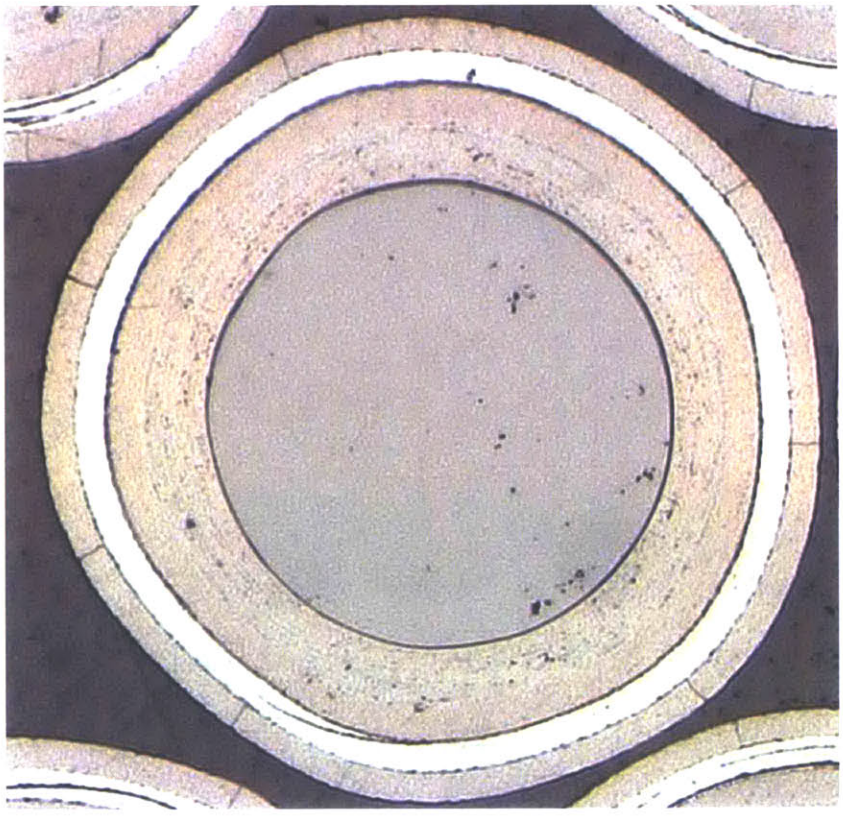

Figure A. 42: 50x optical micrograph of I2 particle 6.

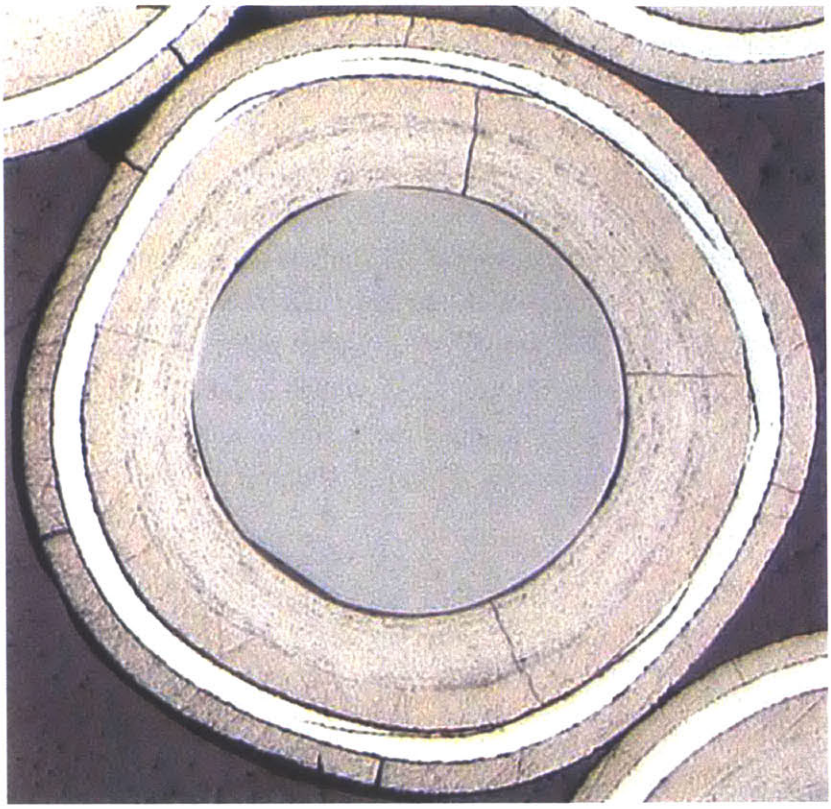

Figure A. 43: 50x optical micrograph of I2 particle 12.

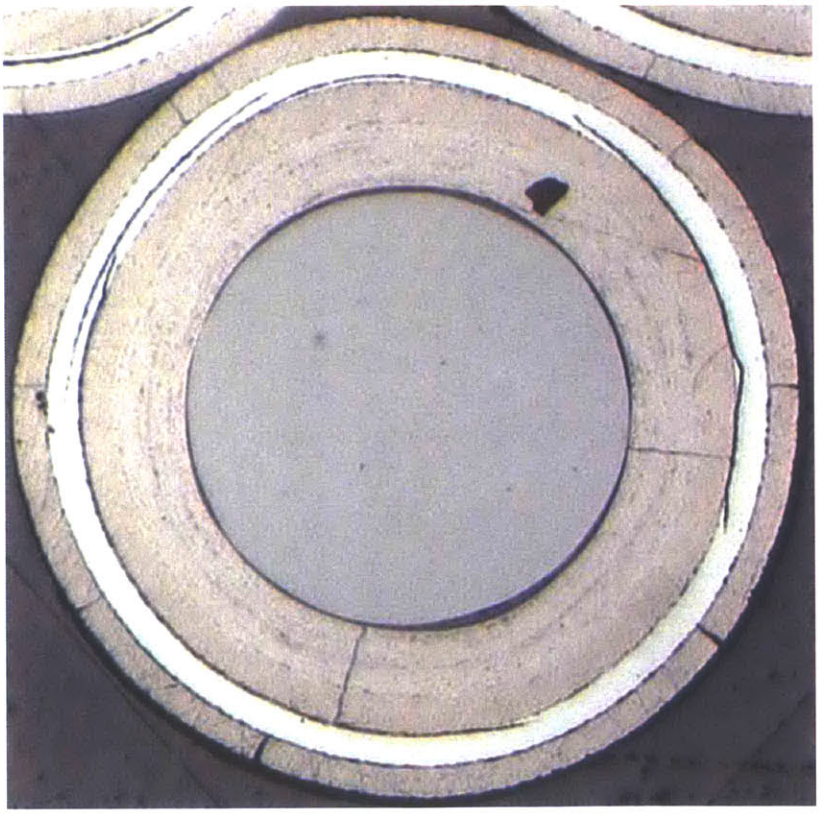

Figure A. 44: 50x optical micrograph of I2 particle 13.

A third mount of particles which had been irradiated in helium was prepared. Figure A. 45 shows optical micrographs of the four particles from mount "I3". The top left particle has intact layers except for the OPyC which has a series of radial cracks. The top right particle has radial cracks in the buffer, IPyC, and OPyC. There also a few small radial cracks in the SiC layer. The bottom left particle shows radial cracks in the buffer, IPyC, and OPyC. The SiC layer exhibits circumferential cracks. The kernel of the bottom left particle shows signs of faceting (evidenced by the flat surface at the 8 o'clock position) which can occur if the kernel moves within the buffer at any point in the grinding or polishing. The smooth ZrO_2 kernel will come loose from the buffer during grinding unless it is backpotted with epoxy. This kernel could have moved if it had not been completely backpotted with epoxy. The SiC layer in the bottom right image shows no cracks, but the buffer, IPyC, and OPyC exhibit radial cracks. Mount I1 had four particles with one of them having a nearly pristine SiC layer.

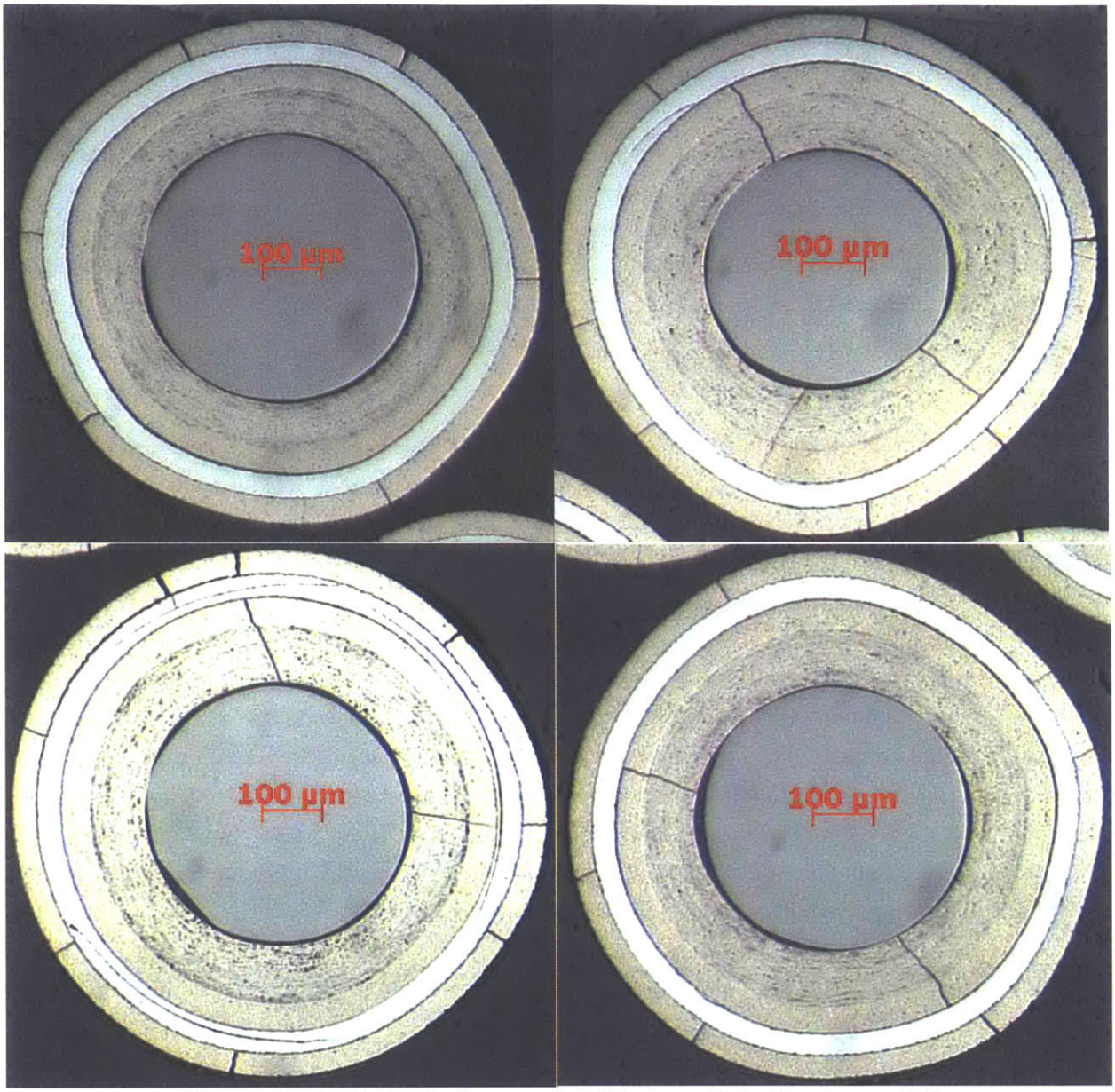

Figure A. 45: Optical micrographs of four particles from mount I3.

A.1.6.3 Determination of cause of cracking in particles irradiated in helium

Except for a few scratches which could be removed with additional polishing, the as fabricated particles were generally in pristine condition. The particles irradiated in helium, on the other hand, exhibited a number of defects after mounting and polishing. Table A. 5 summarizes the frequency of cracking from the three mounts of particles irradiated in helium in the HTIF. None of the SiC cracks

penetrated all the way through the SiC; thus, even if these cracks are purely due to irradiation effects and not sample preparation, they would not be classified as SiC layer failures.

Table A. 5: Percentage of particles with layer cracks in each mount of helium-irradiated particles.

Mount #	Buffer Crack (%)	IPyC Crack (%)	SiC Crack (%)	OPyC Crack (%)
I1	25	25	75	100
I2	36	36	86	100
I3	75	75	50	100
Overall	41	41	77	100

These circumferential and tangential cracks in the SiC layers of these surrogate particles are unusual, but similar types of cracks have been observed in fueled particles irradiated at the Advanced Test Reactor (ATR) at the Idaho National Laboratory (INL). Figure A. 46 shows some circumferential defects in the SiC layer of an AGR-1 specification particle, and Figure A. 47 shows tangential SiC layer cracks. In Figure A. 46, a circumferential defect is visible. Here this feature is termed a "defect" rather than a crack because the authors note that there is fission product penetration into the SiC layer which causes corrosion of the SiC. Thus, this defect may not be purely a crack. Figure A. 47 shows tangential SiC cracks which are located on either side of radial buffer-OPyC fractures in a fueled particle. The tangential cracks observed in the surrogate particles do not seem to form only in the vicinity of buffer-IPyC cracks. For example, the tangential SiC cracks in Figure A. 43 and Figure A. 44 do seem to be located on either side of buffer-IPyC cracks, but Figure A. 41 and Figure A. 42 have tangential SiC cracks with no buffer or IPyC cracks. The image at the bottom right of Figure A. 45 shows buffer and IPyC cracks but no SiC cracks.

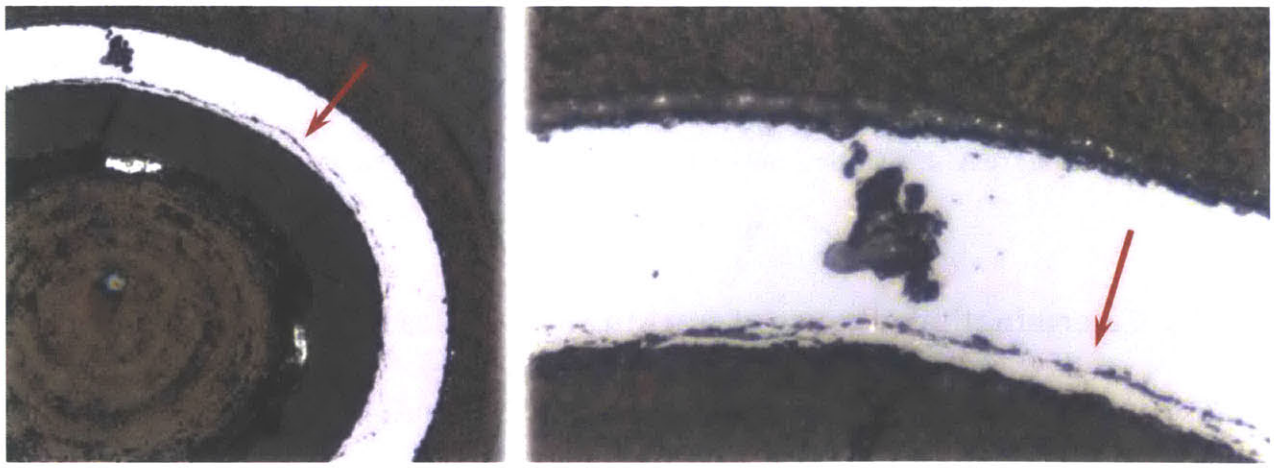

Figure A. 46: Optical micrograph of a fueled AGR-1 specification TRISO particle found to be low in Cs. From [224]. Arrows added to highlight circumferential defects in the SiC layer.

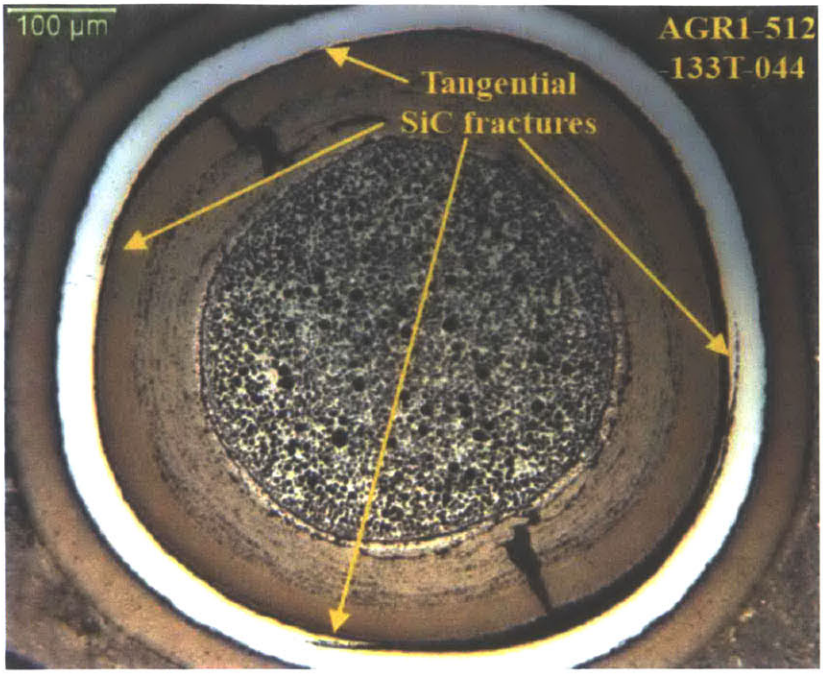

Figure A. 47: Optical micrograph of a fueled particle from the AGR-1 irradiations INL. Arrows are original to the image from [225].

In order to help determine the cause of the cracking observed in the irradiated surrogate TRISO particles after mounting and polishing, five as-fabricated particles and five particles irradiated in helium at MIT were sent to Dr. John Hunn at ORNL for additional analysis. This batch of surrogate particles (ZrO2-500-AK2) was an early ORNL fuel development batch fabricated in 2005, and several of the fabrication parameters used for this surrogate batch are different from those used in the AGR series of TRISO fuel qualification irradiations. For example, buffer deposition for the ZrO2-500-AK2 surrogates was done at 1250 °C instead of the AGR specification of 1450 °C.[18]

The five intact irradiated particles were analyzed via x-ray radiographs with tomographic reconstruction at ORNL. No layer cracks or defects were observed in any of the particles. Figure A. 48 shows a representative image from the x-ray tomography. There is some ghosting in the top left due to the reconstruction, but no cracks or defects were observed. This indicates that any cracking observed in the micrographs of the irradiated particles in Section A.1.6.2 was due to the grinding and polishing steps.

Next, the particles sent to ORNL were prepared for metallographic analysis at ORNL using the same methods employed in Section A.1.5 except that a hot press epoxy was used for the initial potting instead of the EpoFix. The un-irradiated particles showed pristine layers with no cracks, but the irradiated particles exhibited the same types of cracks after grinding and polishing. shows optical micrographs for two of the irradiated particles after grinding and polishing at ORNL. The particle at

[18] Likewise, the SiC deposition parameters were "significantly different" for the surrogate particles according to Dr. Hunn.

left in Figure A. 49 shows the same types of circumferential and tangential cracks in the SiC as were observed in mounts I1, I2, and I3 in Section A.1.6.2. Two sets of buffer and IPyC radial cracks are also visible, but there appear to be no OPyC cracks in the particle at left in Figure A. 49. The particle at right in Figure A. 49 was the second particle to be mounted and polished by Dr. Hunn at ORNL. In this mount, the particle was backpotted earlier which eliminated cracking in the buffer, IPyC, and SiC layers. Two radial cracks in the OPyC layer are visible, however.

In summary, the as-fabricated particles present pristine layers, even after metallography. Particles that had been irradiated in helium have pristine OPyC outer surfaces prior to mounting, but after mounting and polishing, radial through-cracks of the OPyC layer are evident. Optical micrographs of three separate mounts of particles irradiated in helium at MIT showed some degree of cracking in all layers as summarized in Table A. 5. Both as-fabricated and irradiated particles were sent to ORNL for x-ray tomography. X-ray tomography prior to mounting and polishing the particles showed no evidence of layer cracks or defects in the as-fabricated and irradiated particles. At ORNL, mounting and polishing of the irradiated particles showed the same crack morphologies as those observed at MIT (reported in Section A.1.6.2). Earlier and more frequent backpotting reduced this cracking. All of this information supports the conclusion that the cracking observed in the particles irradiated in helium is due to the mounting and polishing process and that these cracks did not occur during irradiation. Since no cracking of any of the mounted and polished as-fabricated particles was observed, it is clear that irradiation embrittles the layers, making them susceptible to cracking during PIE.

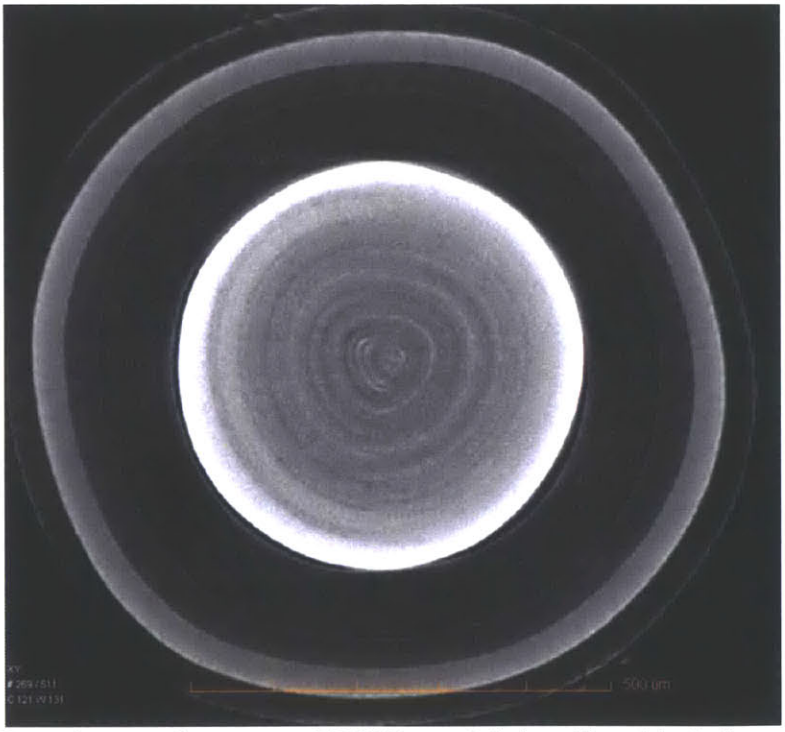

Figure A. 48: X-ray image of surrogate TRISO particle irradiated in helium at MIT. Image obtained at ORNL by John Hunn.

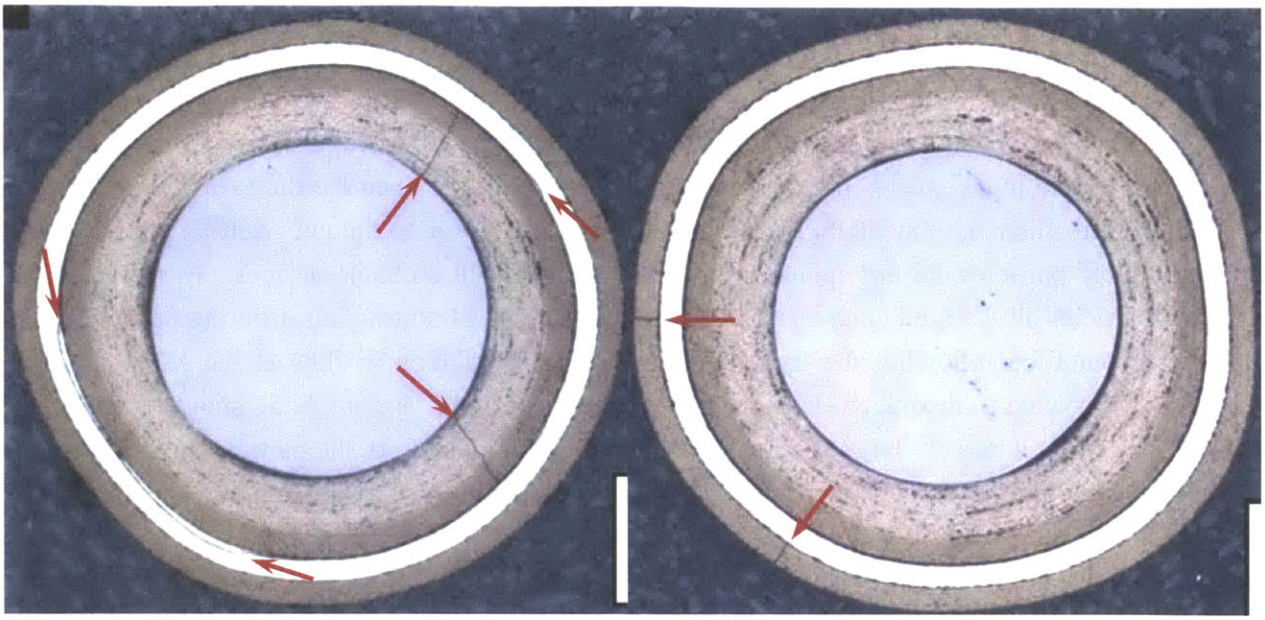

Figure A. 49: Optical micrographs of two surrogate TRISO particles irradiated at MIT in helium. Metallographic preparation and analysis performed at ORNL by John Hunn. Arrows highlight cracks.

A.2 Examination of TRISO particles exposed to flibe

Several hundred surrogate TRISO particles from the batch ZrO2-500-AK2 were irradiated in flibe in the MITR at 700 °C for 3000 hours to a fast fluence of 1.24×10^{21} n/cm^2 (E > 0.1 MeV). In a parallel test, several hundred TRISO particles were also exposed to flibe in a capsule at 700 °C for 3000 hours at the University of Wisconsin-Madison. This test was designed to mirror the conditions of the flibe irradiations at MIT except that the UW test would not have any neutron exposure. Prior to irradiation in flibe, the exterior of these particles was in the as-fabricated condition depicted in Figure A. 50.

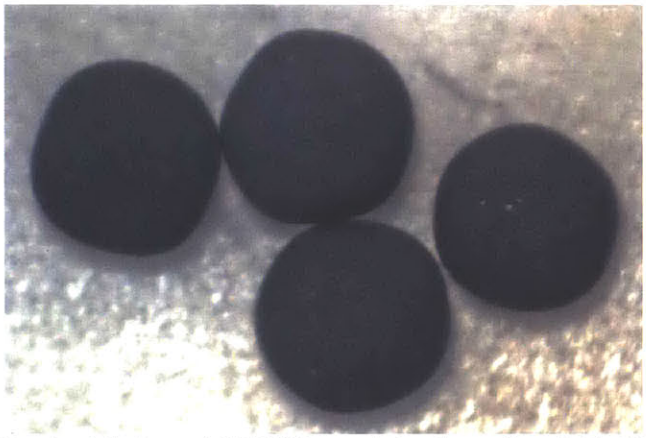

Figure A. 50: As-fabricated TRISO particles from batch ZrO2-500-AK2.

A.2.1 PIE of TRISO particles irradiated in flibe at MIT

After irradiation, the sample capsule containing flibe and the TRISO particles was moved to a glove box at the MIT nuclear reactor laboratory. Because the flibe was frozen at this point, the capsule was heated in an oven to 600 °C in order to melt the flibe. Then the flibe was poured over a mesh in order to filter out the TRISO particles. In most cases, due to the non-wetting nature of the salt, the filtered particles did not appear to have any residual salt on their surfaces. However, these extracted particles all featured cracked OPyC layers. Figure A. 51 shows four different particles after extraction from flibe following the end of the 3000 hour irradiation in flibe at the MITR. Some particles were soaked in deionized (DI) water for 24 hours or more. Figure A. 52 shows one particle after soaking in DI water. A large section of the OPyC came loose from the particle during soaking. This is evidence that liquid flibe had entered the cracks in the OPyC layer. Soaking the particle in water dissolved the frozen flibe from the crack and allowed the OPyC layer to come loose from the particle.

The four particles from Figure A. 51 were mounted and polished using the same procedure outlined in Section A.1.5. Figure A. 53 shows optical micrographs (at 100x magnification) of four particles from the irradiation in flibe after mounting and polishing. The same types of tangential and circumferential cracks observed in the SiC layers of the particles irradiated in helium (see Section A.1.6.2) are observed here as well. The particle at the bottoms left in Figure A. 53 also exhibits a pair of buffer and IPyC cracks similar to those observed in some of the particles irradiated in helium. In Section0 A.1.6.3, it was determined that the layer cracks in the particles irradiated in helium were due to mounting and polishing and that the cracks did not occur during the irradiation itself. Irradiation embrittlement of the layers made them susceptible to cracking during mechanical polishing. The most obvious differen between the particles irradiated in flibe and the particles irradiated in helium is that the particles from the irradiation in flibe have large (wide) radial OPyC cracks and large OPyC-SiC gaps. There is one other difference between the SiC cracking in the helium-irradiated particles and the SiC cracking in the flibe-irradiated particles, however. Becaue of the large OPyC-SiC gap in the particles irradiated in flibe, the circumferential cracks in the SiC layers progress radially outward before terminating on the outside of the SiC layer. The SiC cracks in the case of the helium-irradiated particles terminated within the SiC layer. For the particles from the irradiation in flibe, in places where there is no longer OPyC-SiC contact, any compressive influence that the OPyC would have had on the outside of the SiC layer during grinding and polishing is now gone.

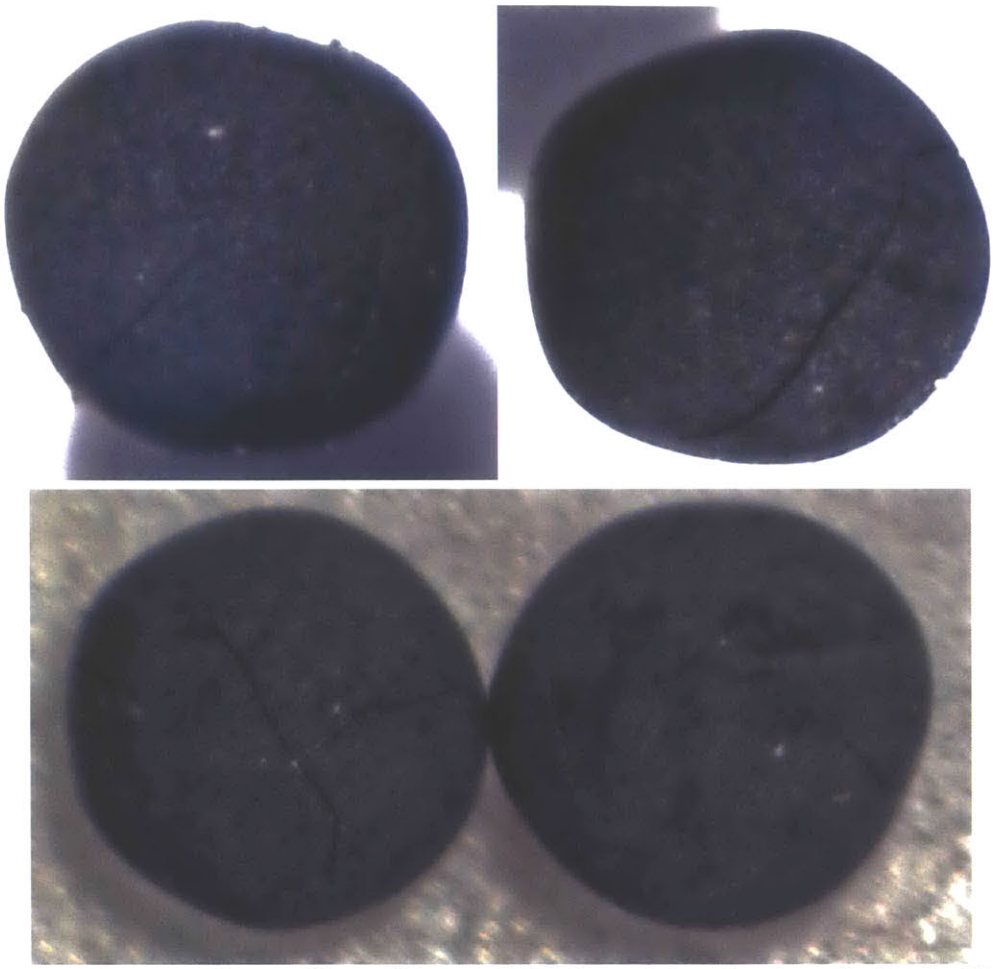

Figure A. 51: Outer surfaces of four different TRISO particles after irradiation in flibe shows significant OPyC cracks.

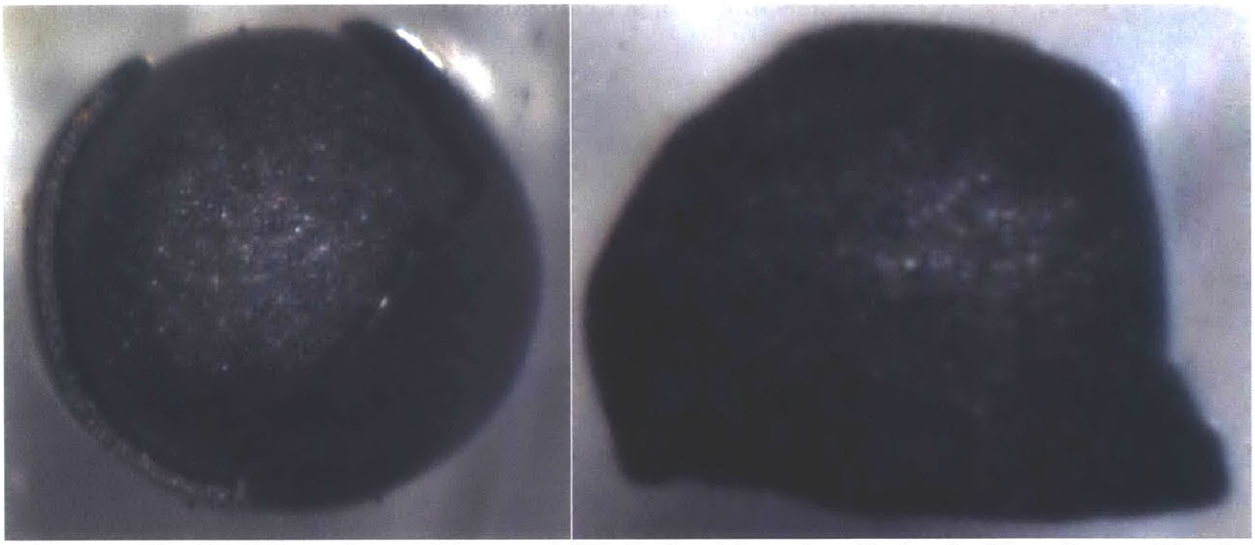

Figure A. 52: TRISO particle and loosened OPyC shard from irradiation in flibe after soaking in deionized water for 24 hours.

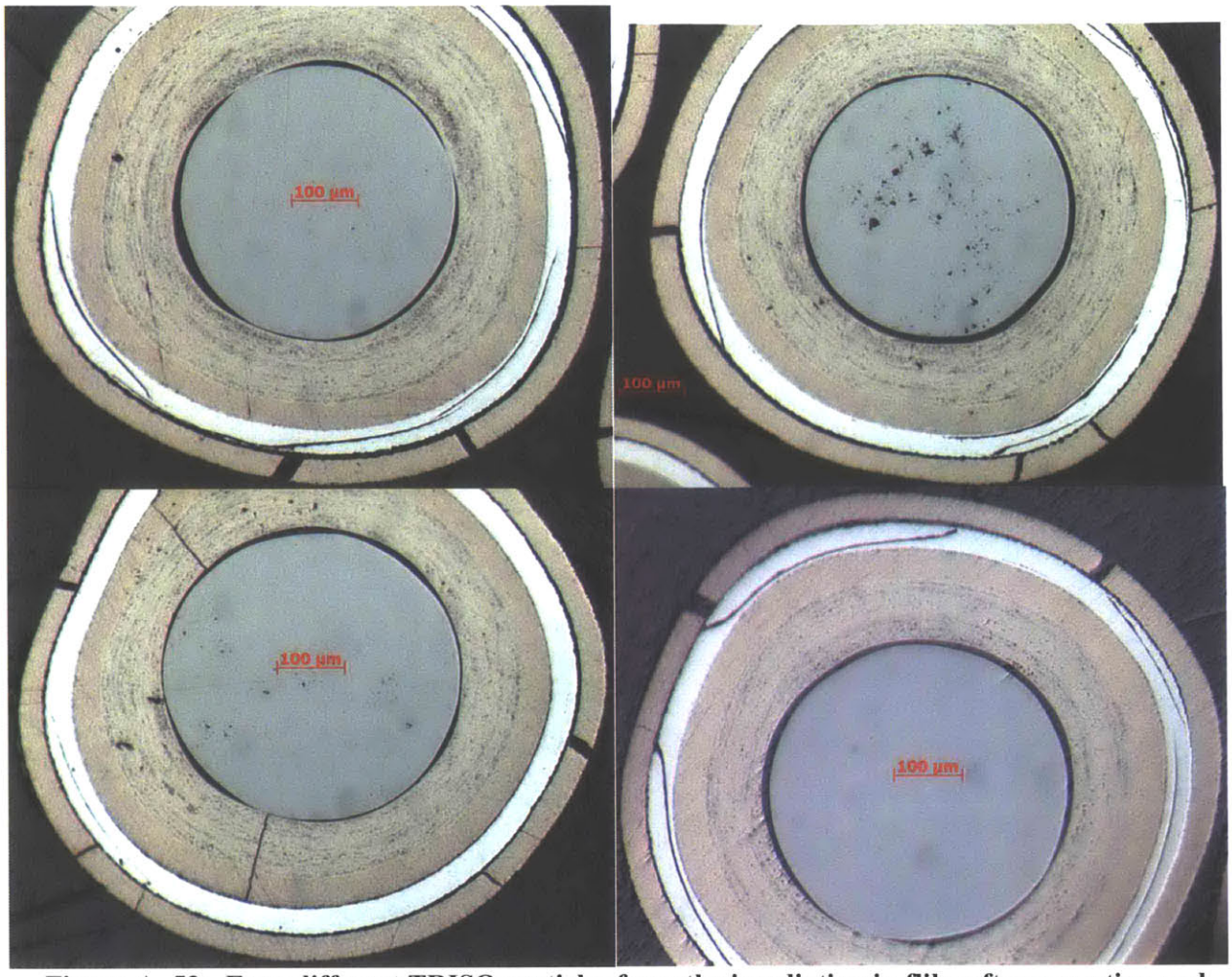

Figure A. 53: Four different TRISO particles from the irradiation in flibe after mounting and polishing. Magnification is 100x.

A.2.2 Examination of TRISO particles exposured to flibe at UW

In order to compare the particles irradiated in flibe to the particles exposed to flibe only (with no neutron exposure), particles from the 3000 hour test in flibe were obtained from UW. Figure A. 54 shows two of the UW particles prior to mounting and polishing following the procedure outline in Section A.1.5. All of the particles exhibited pristine outer surfaces which matched those in the as-fabricated condition. Figure A. 55 shows optical micrographs of these particles after mounting and polishing. No layer cracks or defects of any kind were observed. Thus, in the absence of a neutron flux, the TRISO particles exposed to flibe for 3000 hours show no signs of degradation.

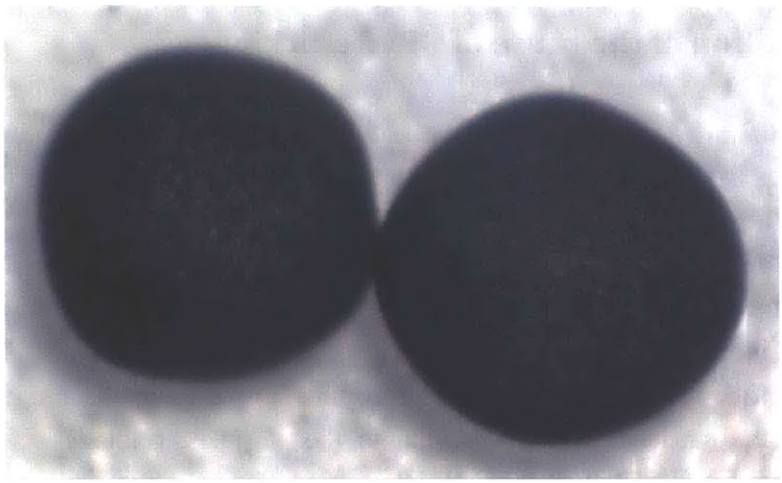

Figure A. 54: Particles from 3000 hour exposure to flibe (with no neutron exposure) at UW prior to mounting.

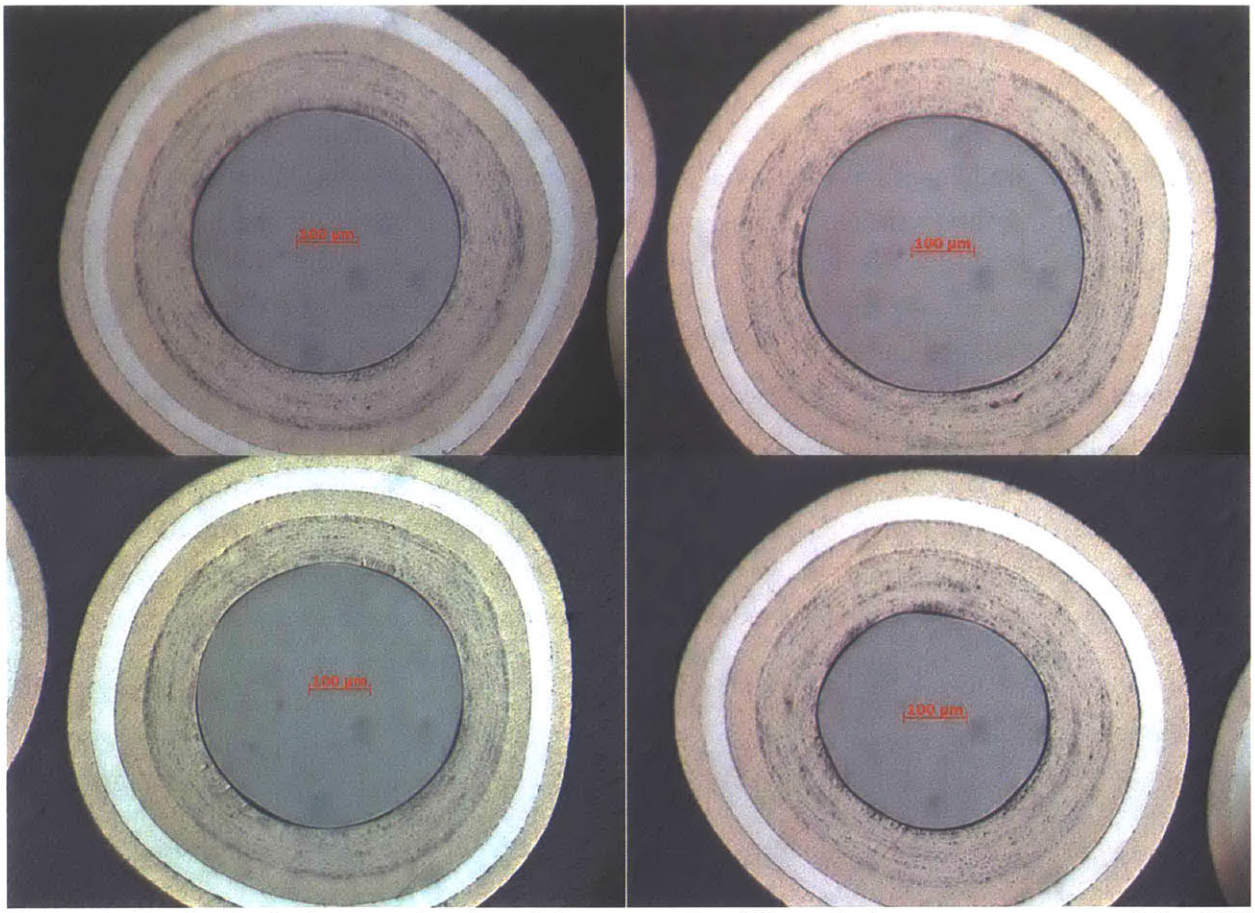

Figure A. 55: Optical micrographs of particles exposed to flibe only (no neutron exposure) for 3000 hours at UW.

A.2.3 Determination of the cause of OPyC cracking

In Section A.1.6.3, it was determined that all of the cracking in the OPyC, SiC, IPyC, and buffer layers of the particles irradiated in helium was due to grinding and polishing of the particles and the particular susceptibility of the irradiation-embrittled layers to cracking. For the particles irradiated in flibe, it is believed that the buffer, IPyC, and SiC cracking are due to this same mechanism. For the OPyC layer of the particles irradiated in flibe however, cracking was observed before the particles were even mounted in epoxy (see Figure A. 51). In comparison, Section A.2.2 showed that TRISO particles exposed to flibe in the absence of a neutron field experience no degradation of any kind. In order to determine the cause of OPyC cracking in the particles irradiated in flibe, as-fabricated particles, particles irradiated in helium, and particles exposed to flibe in the absence of neutrons were put in flibe and the flibe was allowed to free and thaw. After the freezing and thawing cycles, the particles were compared.

Figure A. 56 shows a set of as-fabricated particles prior to the freezing and thawing tests in flibe. Figure A. 57 shows the same set of as-fabricated particles after several cycles of freezing and thawing in flibe. No cracking or degradation of the OPyC layer was observed in these as-fabricated particles after exposure in flibe. Figure A. 54 showed a couple of flawless particles obtained after exposure in flibe for 3000 hours at UW. In order to extract these particles from flibe at UW, they had already been through several freezing and thawing cycles in flibe before they were sent to MIT. Figure A. 58 shows these particles remain pristine after additional freezing and thawing cycles in flibe. Figure A. 59 shows that the outer surface of the OPyC layer on the particles irradiated in helium is pristine prior to the freezing and thawing tests in flibe. Figure A. 60 shows the results of exposing helium-irradiated particles to freezing and thawing cycles in flibe. Four different particles are depicted in Figure A. 60. All of these particles experienced OPyC cracking as a result of freezing and thawing in flibe. In the case of the top right and middle left particles, the OPyC fractured and came apart from the particle. The middle right image is the OPyC shard that broke away from the particle in the middle left image. This test proves conclusively that irradiation embrittles the OPyC layer of these surrogate TRISO particles and that the surface tension and freezing/thawing forces imparted on the OPyC layer from flibe are enough to rupture the layer and separate it from the rest of the particle. Table A. 6 summarizes the findings of TRISO exposures to freezing and thawing in flibe.

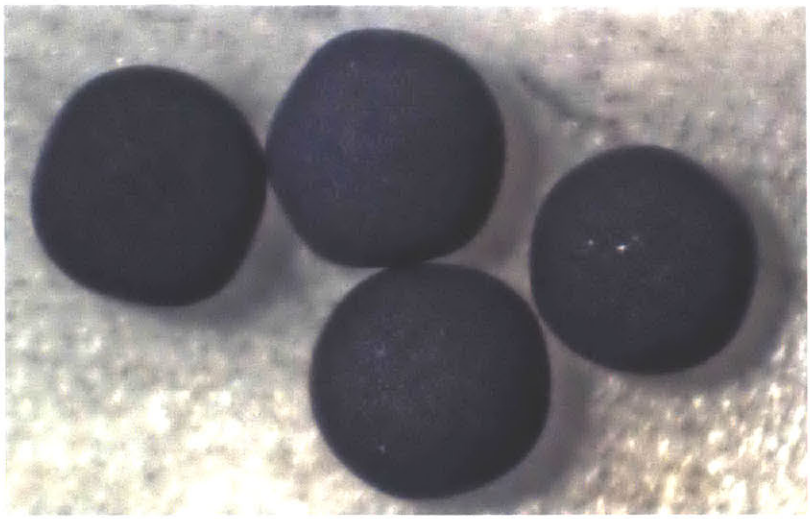

Figure A. 56: As-fabricated particles prior to freezing and thawing in flibe.

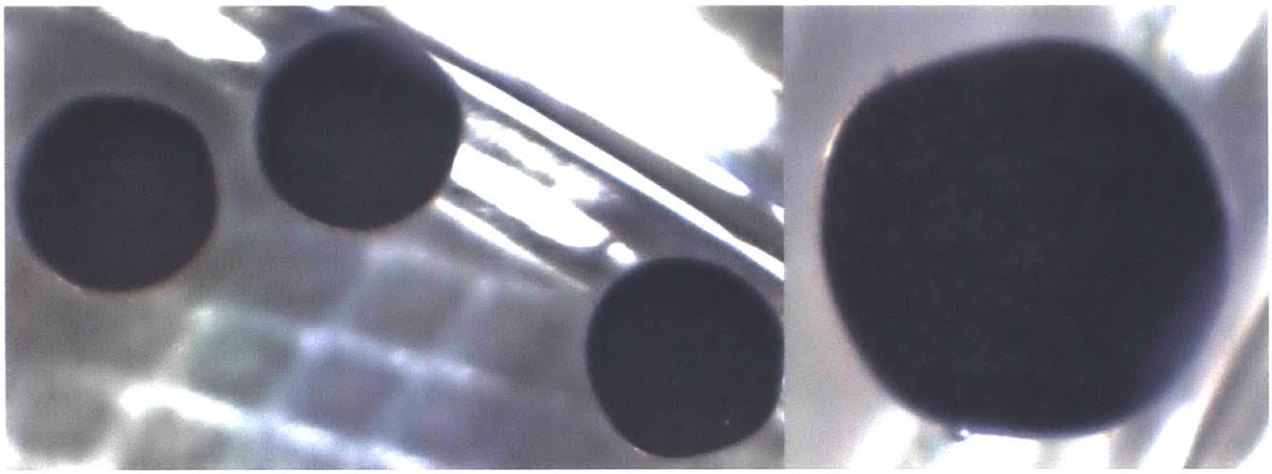

Figure A. 57: As-fabricated particles after several freeze-thaw cycles in flibe.

Figure A. 58: Particles from UW test in flibe after additional freezing and thawing cycles in flibe at MIT.

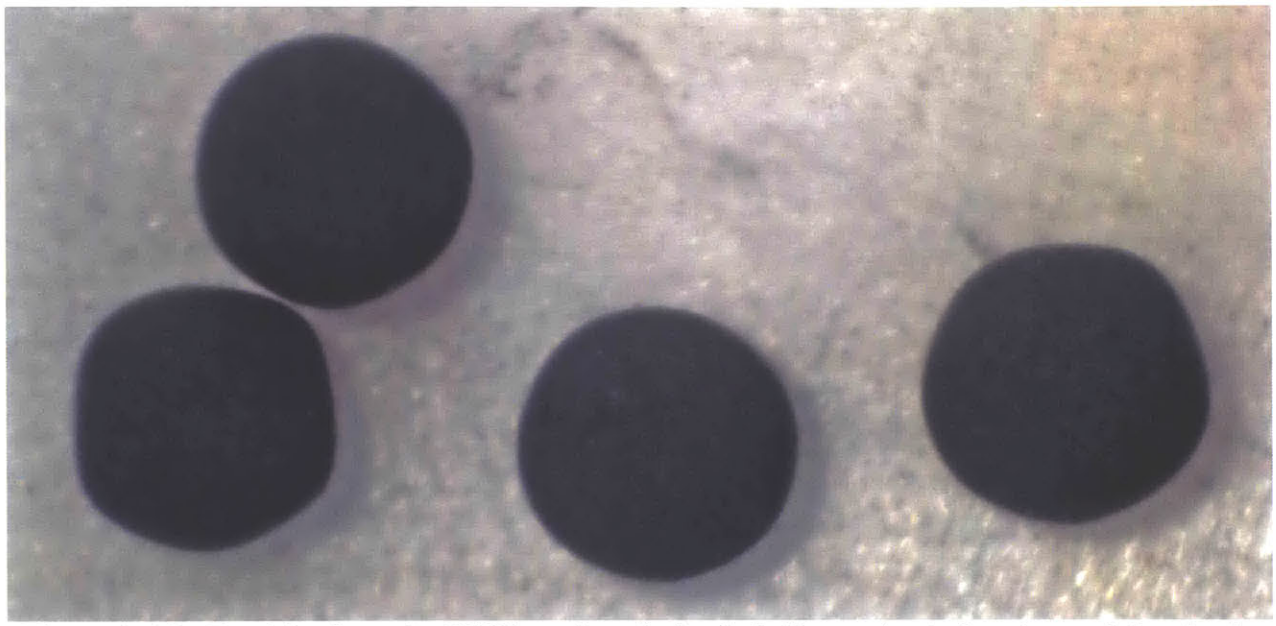

Figure A. 59: Particles from the 3000 hour irradiation in helium prior to freezing and thawing in flibe.

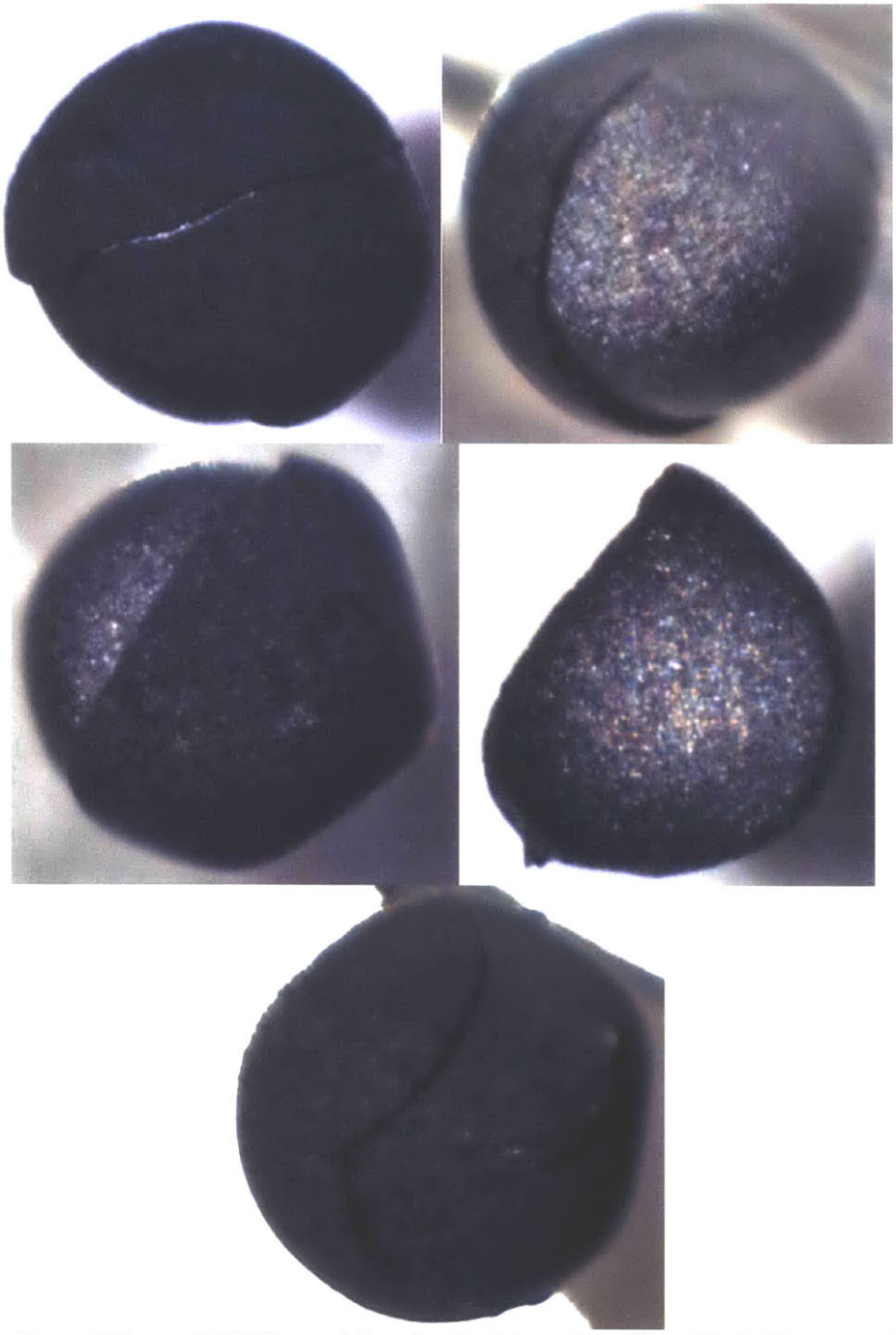

Figure A. 60: Four different TRISO particles that had been irradiated in helium are pictured after going through several freeze-thaw cycles in flibe. One OPyC shard belonging to the middle left particle is also shown.

Table A. 6: Summary of OPyC after exposure to flibe for TRISO particles with different histories.

TRISO History	Fast Neutron Fluence (n/cm^2, E > 0.1 MeV)	OPyC cracking after exposure to flibe?
As-fabricated	0	No
Exposed to flibe for 3000 hours	0	No
Irradiated in $He_{(g)}$ for 2200 hours	$3.7x10^{20}$	Yes
Irradiated in flibe for 3000 hours	$1.25x10^{21}$	Yes

A.3 Summary of TRISO particle PIE

TRISO particles from batch ZrO2-500-AK2 having different exposure histories were examined. Particles in the as-fabricated condition showed no defects of any of the layers. Particles which had been exposed for 3000 hours to flibe at 700 °C in the absence of a neutron field showed no signs of outer degradation and no signs of inner degradation after mounting and polising. No OPyC cracks were observed in the particles irradiated in helium prior to mounting and polishing. OPyC cracks were evident in particles irradiated in flibe prior to mounting. OPyC, SiC, IPyC, and buffer cracking was observed in TRISO particles irradiated in helium and irradiated in flibe after mounting and polishing. Five TRISO particles irradiated in helium were sent to ORNL for x-ray tomography which showed no cracking or degradation of these particles. This leads to the conclusion that the buffer, IPyC, SiC, and OPyC cracking observed in the particles irradiated in helium is due to the mounting and polishing process and that these cracks did not occur during irradiation. The irradiation embrittled the layers, making them susceptible to cracking during metallographic preparation. A different mechanism appeared to be responsible for the OPyC cracking observed in the particles irradiated in flibe prior to metallographic preparation. By performing a series of freeze-thaw tests in flibe, it was determined that the OPyC layer of irradiated particles is susceptible to cracking in flibe if the salt is allowed to freeze around the particles. This indicates that preventing the salt from freezing around any low-density graphite structures will be important.

Appendix B: HTIF capsule disassembly in hot cell and metallographic preparation

The HTIF sample capsule was disassembled in a hot cell at the MIT nuclear reactor laboratory. As pictured in Figure B. 1, the bolts in the flange were loosened using a wrench. Once the bolts had been loosened, they were removed by use of an electric socket drive, pictured in Figure B. 2. Once the bolts and thermocouples had been loosened, the flange and sample train could be separated from the dummy fuel element, as shown in Figure B. 3. In Figure B. 4, a pipe cutter was used to separate the flange from the sample train, which hung below the flange. Next, the Mo heat shield was slid off to expose the sample capsules (see Figure B. 5). With the shield removed, sample capsules could be removed from the top of the central spine (see Figure B. 6).

Figure B. 8 through Figure B. 12 show the epoxy mounting system used for mounting TRISO particles prior to grinding and polishing. The loose TRISO particles were placed at the bottom of the mounting cup. A small amount of CrystalBond was dissolved in an excess of acetone. A drop of the CrystlaBond/acetone mixture was deposited on the loose particles in the cup, and the acetone was allowed to evaporate. A thin layer of CrystalBond then held TRISO particles in place. The epoxy was then poured over the particles under vaccum, and the expoxy was allowed to cure.

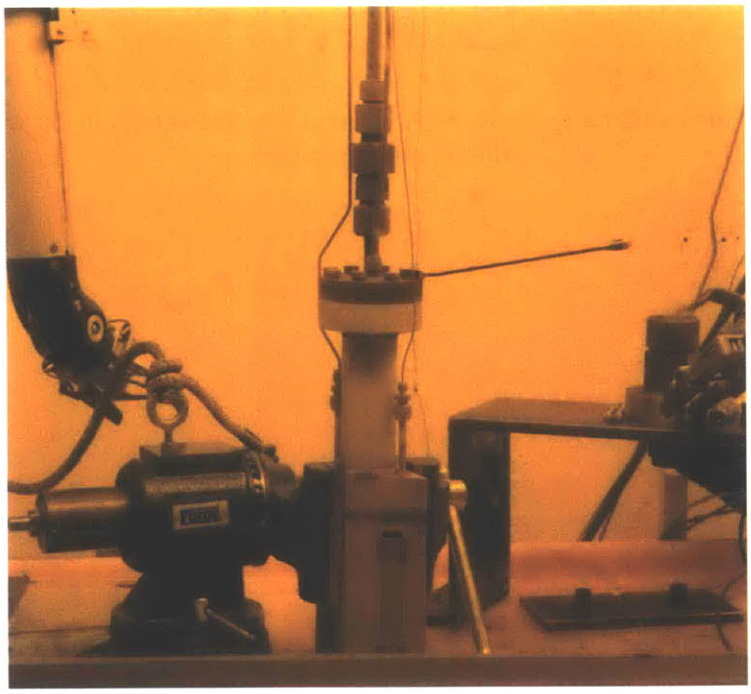

Figure B. 1: Flange bolts were loosened with a wrench.

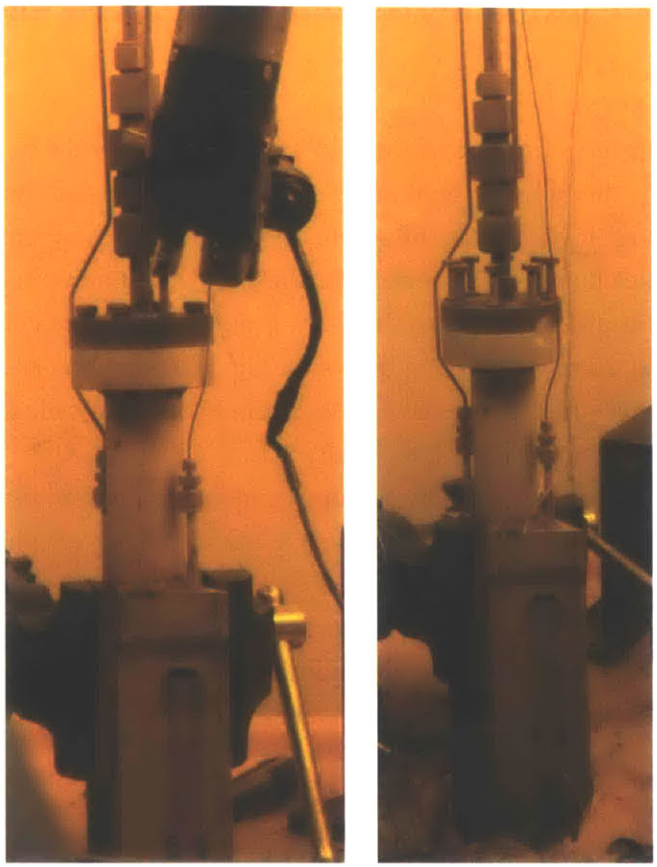

Figure B. 2: Left: loosened flange bolts were removed with electric socket wrench. Right: All flange bolts loosened.

Figure B. 3: Left: With all bolts, thermocouples, and gas lines loose, the flange can be removed from the dummy element. Right: Sample train fully extracted from dummy element.

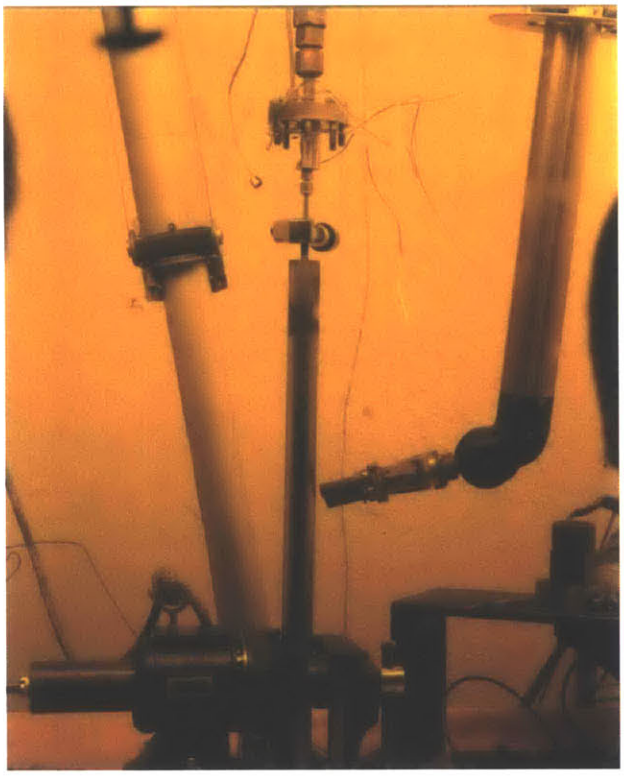

Figure B. 4: Pipe cutter used to separate the sample train from the flange.

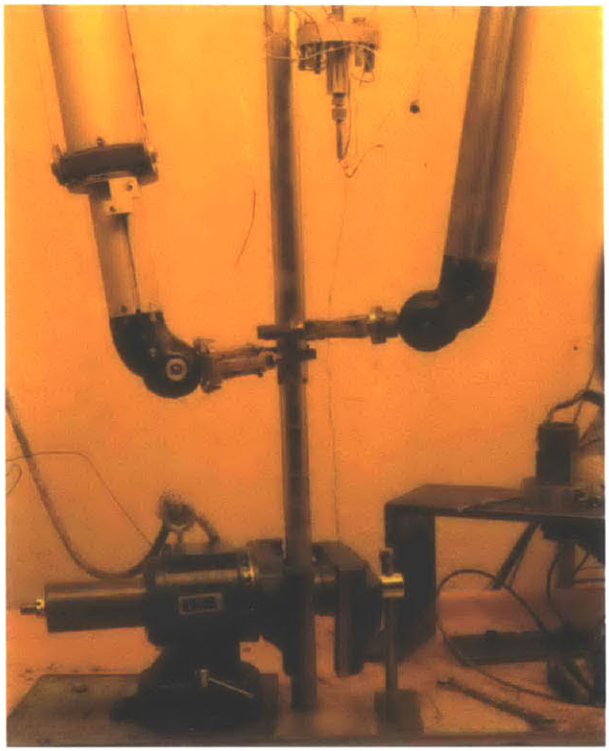

Figure B. 5: Shield was removed to reveal the sample stack. Each segment is a separate sample capsule.

Figure B. 6: Sample capsules removed from top of sample spine one-by-one.

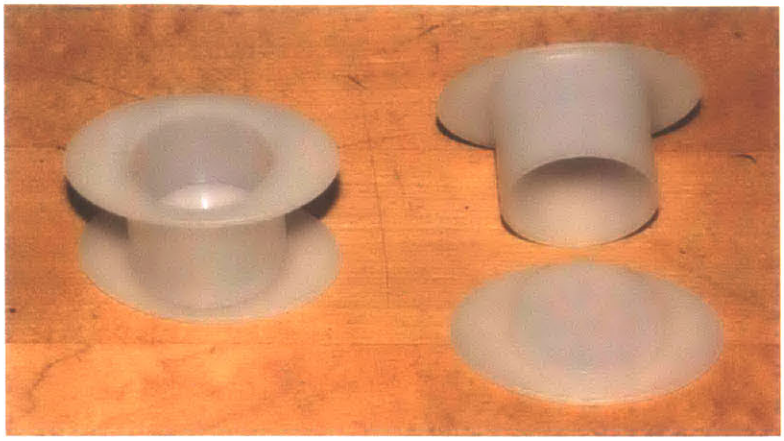

Figure B. 7: Two-piece, 1.25 inch diameter mounting cup.

Figure B. 8: Crystal Bond 509 used to affix TRISO particles to bottom of mounting cup.

Figure B. 9: Four as-fabricated TRISO particles affixed to the bottom of a mounting cup with a thin film of Crystal Bond.

Figure B. 10: Struers EpoFix epoxy system used to mount TRISO particles.

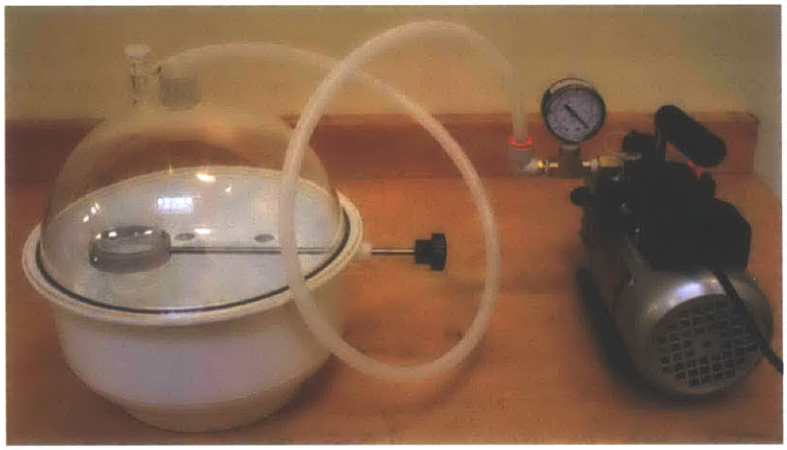

Figure B. 11: Vacuum impregnation system for pouring epoxy into the mounting cup.

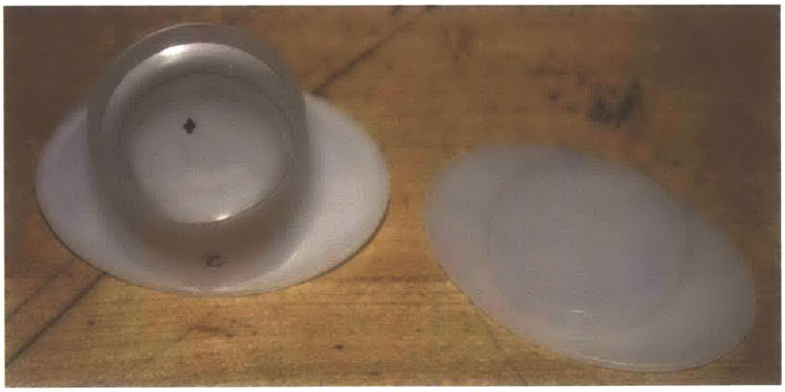

Figure B. 12: Four as-fabricated TRISO particles mounted in epoxy.

Appendix C: Additional micrographs of surrogate TRISO particles

C.1: SEM micrographs of as-fabricated particles

Mount U1 (unirradiated, as-fabricated) was gold-coated and observed in the SEM in SEI mode. Figure C. 1 shows 50x micrographs of all 4 particles in mount U1. Note that too much gold was deposited on the samples, and the buffer-IPyC interface is difficult to distinguish. Several scratches (such as the dark streak across particle 1) from sample preparation are also evident. Additional micrographs were taken at higher magnification, and dimensional measurements were made on particle features. Figure C. 2 shows a 100x SEM image of particle 2. Two particle diameters were measured: 0.867 mm and 0.862 mm. These are less than the as-fabricated value of 0.916 mm and indicate that the particles were ground to above mid-plane. Figure C. 3 shows a 200x SEM image of particle 1, with thickness measurements on the SiC and OPyC layers. The measurements are a few microns larger than the as-fabricated averages. Again, this is due to the fact that the particle was ground to a level above mid-plane. Figure C. 4 shows a 750x SEM image of particle 4 with measurements of IPyC, SiC, and OPyC thicknesses.

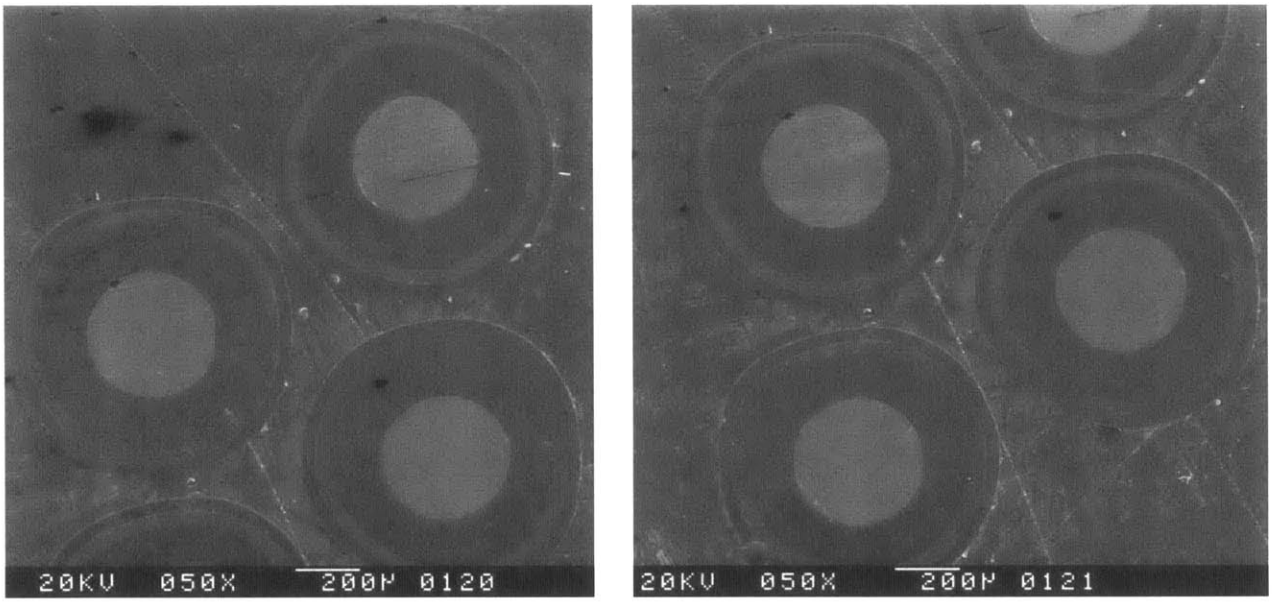

Figure C. 1: 50x SEM micrograph of mount U1. At left shows particles 1 through 3. At right shows particles 2 through 4.

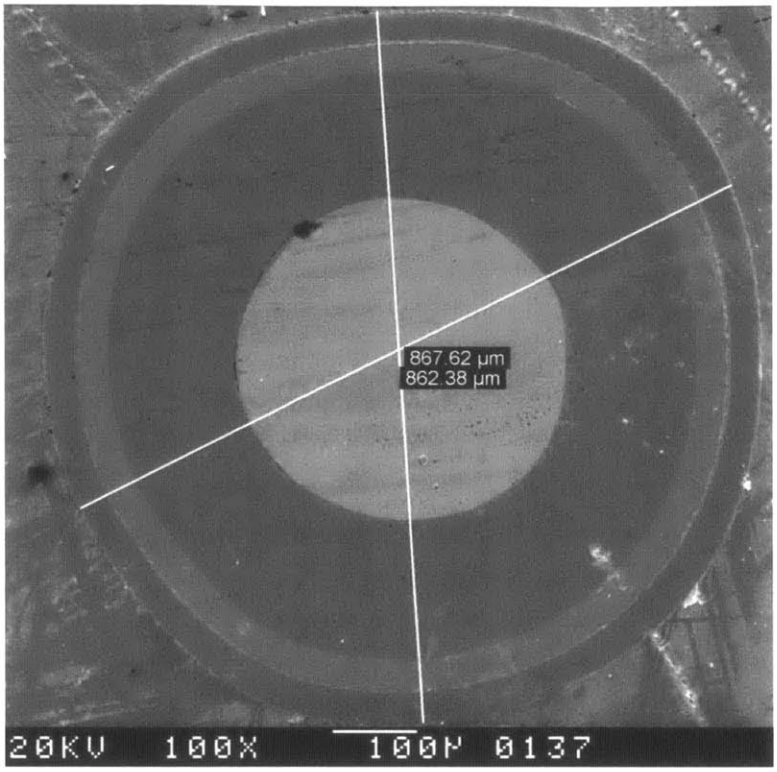

Figure C. 2: 100x SEM micrograph of U1 particle number 2.

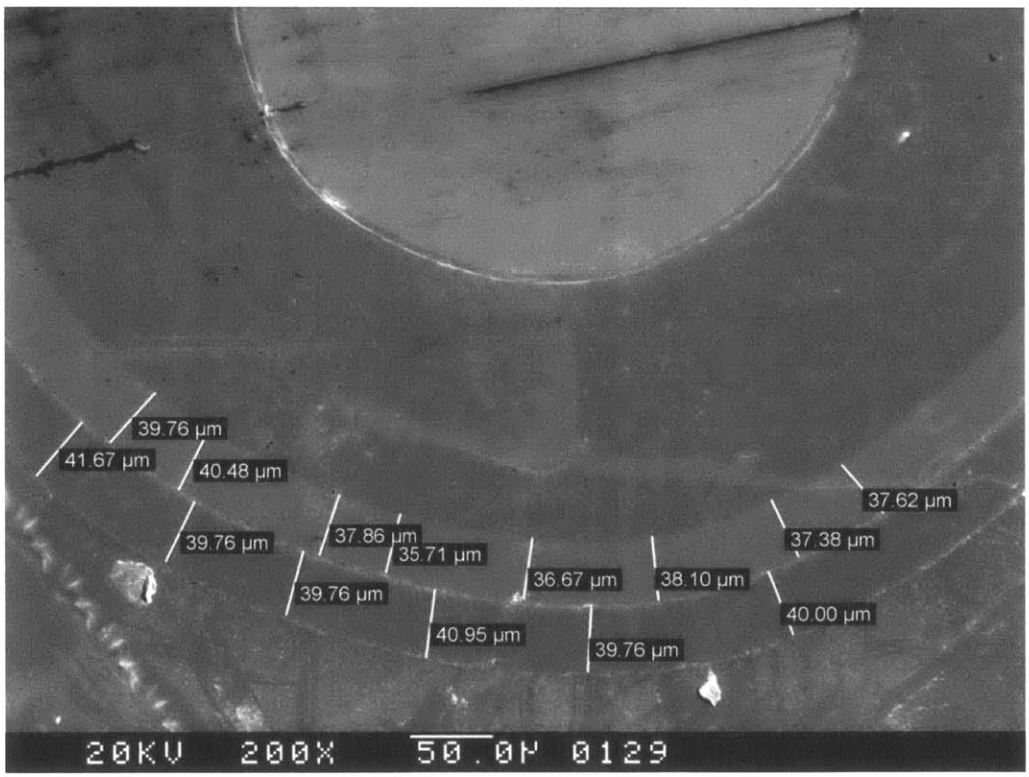

Figure C. 3: 200x SEM image of U1 particle number 1. Showing SiC and OPyC measurements.

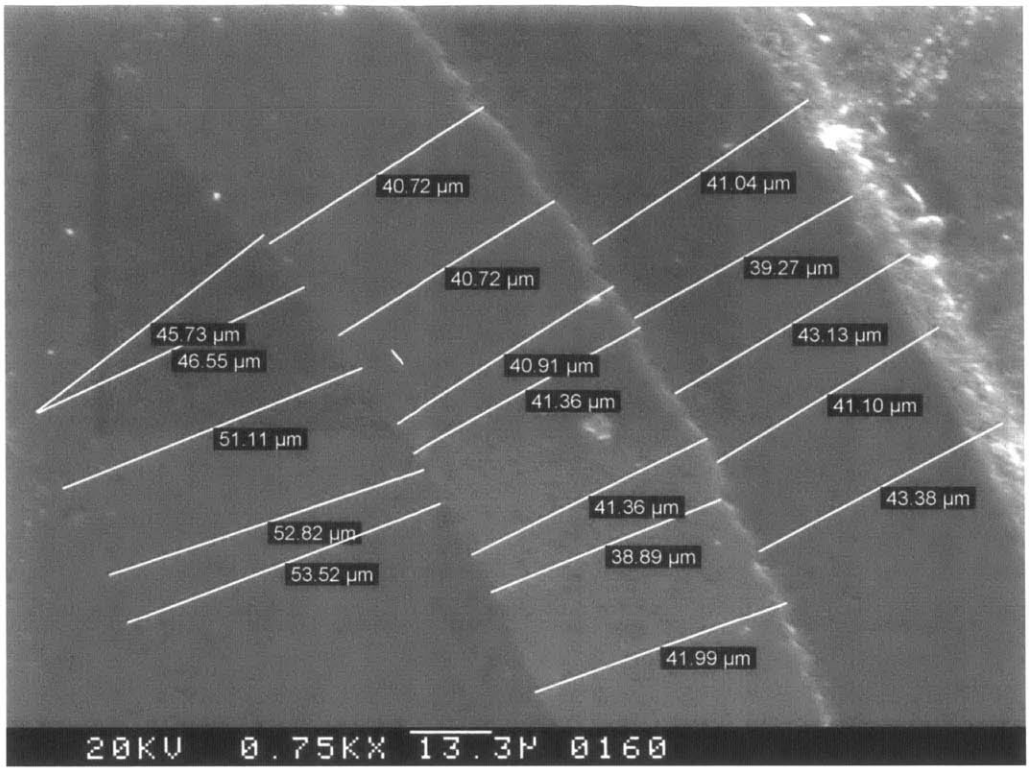

Figure C. 4: 750x micrograph of U1 particle number 4. Showing IPyC, SiC, and OPyC measurements from left to right.

Figure C. 5 through Figure C. 12 show SEM micrographs at 100x and 350x for particles 1 through 4 of mount U2. A thin gold coating was applied to these particles in order to make them conductive for SEM analysis. The coating was thin enough that the IPyC-buffer interface was clearly visible for all particles. Generally, the same features evident in the optical micrographs are evident in these SEM micrographs as well. The exception is that cracks in the buffer, IPyC, and SiC layers of particle 3 are visible in the optical micrograph, but not visible in the SEM. This is due to the fact that the gold coating can obscure the cracks. In order to avoid the gold-coating step, ultrafine graphite powder could be mixed with the epoxy prior to mounting the TRISO particles.

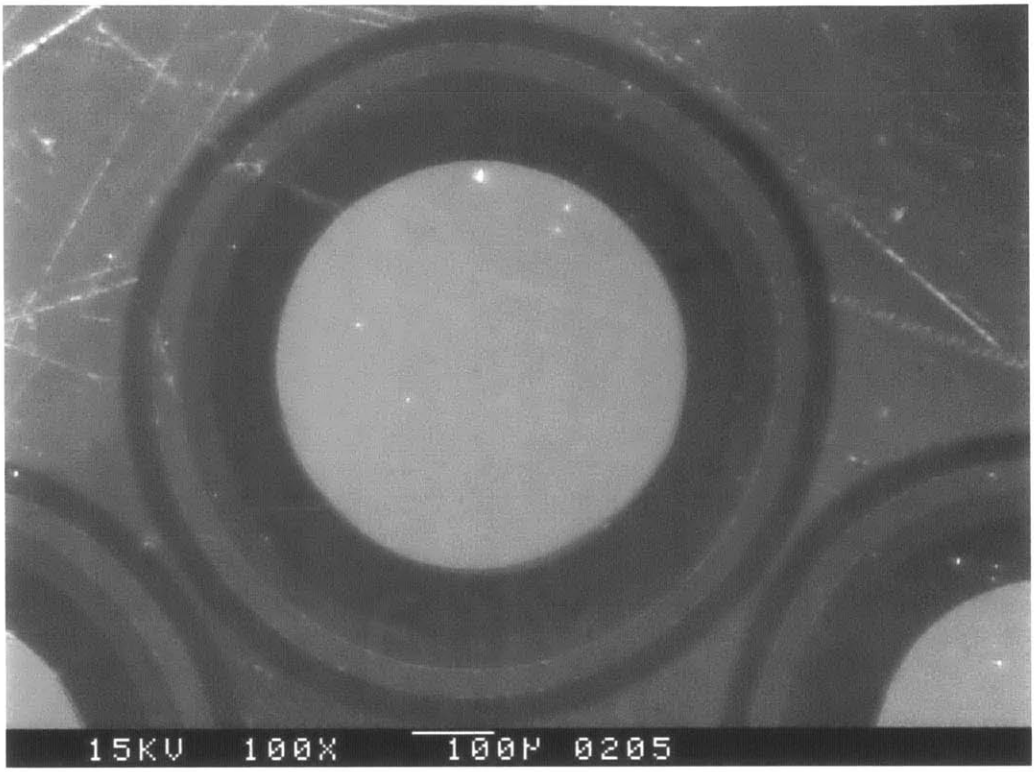

Figure C. 5: 100x SEM micrograph of mount U2 particle 1.

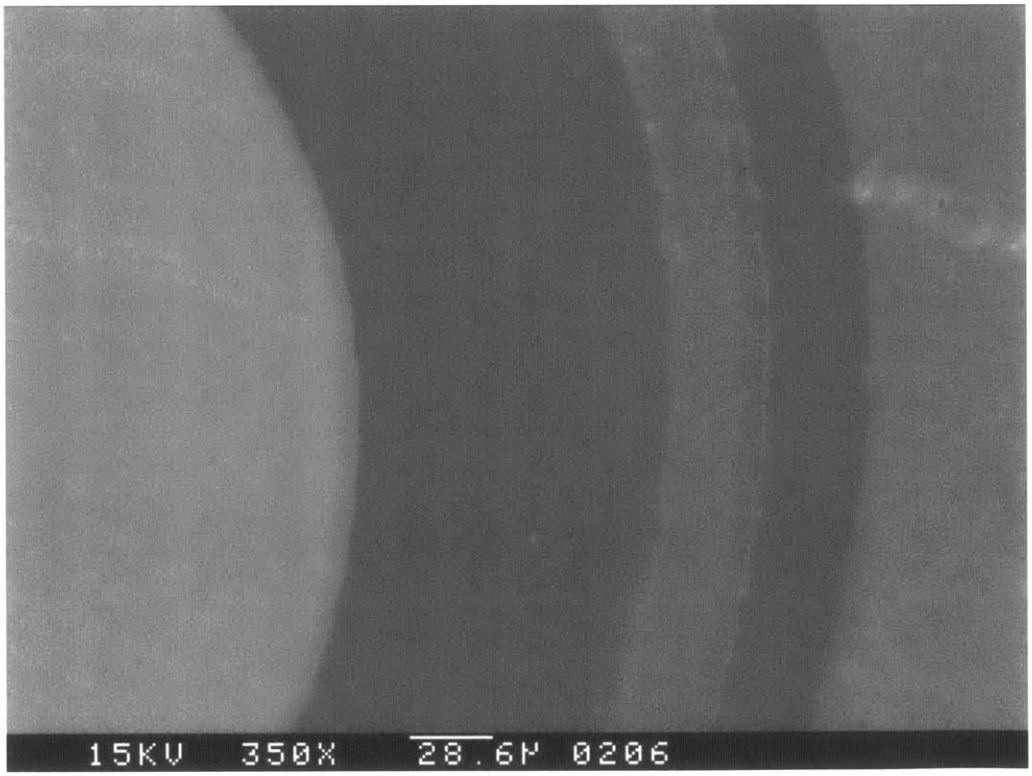

Figure C. 6: 350x SEM micrograph of mount U2 particle 1.

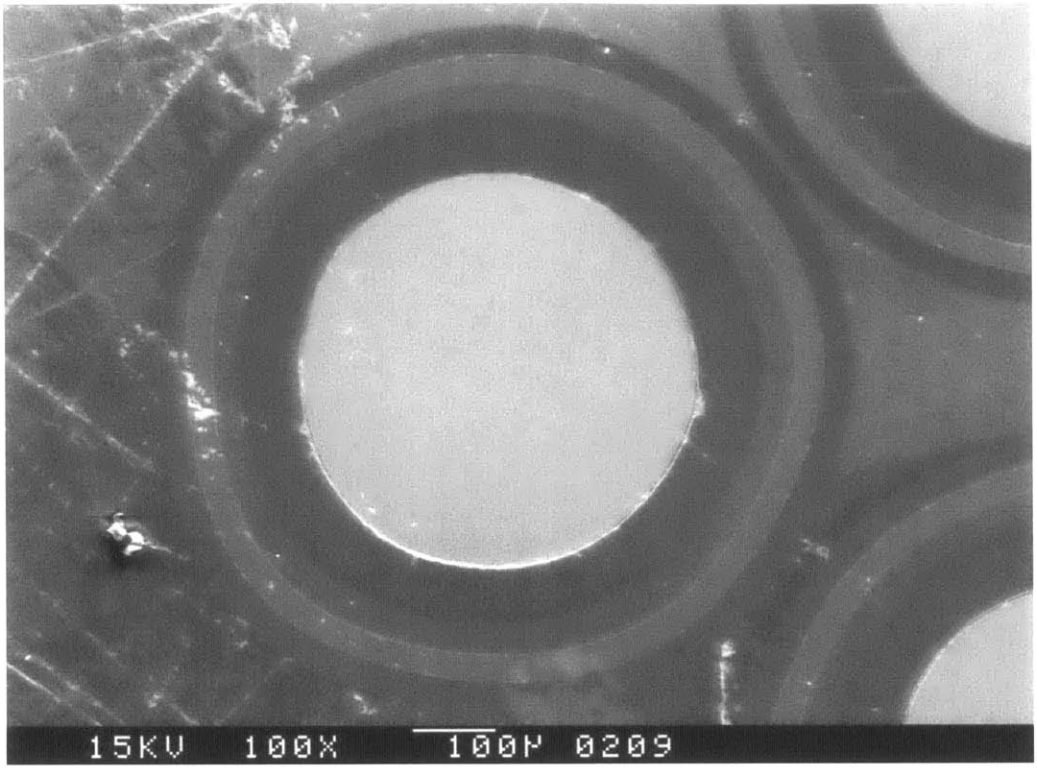

Figure C. 7: 100x SEM micrograph of mount U2 particle 2.

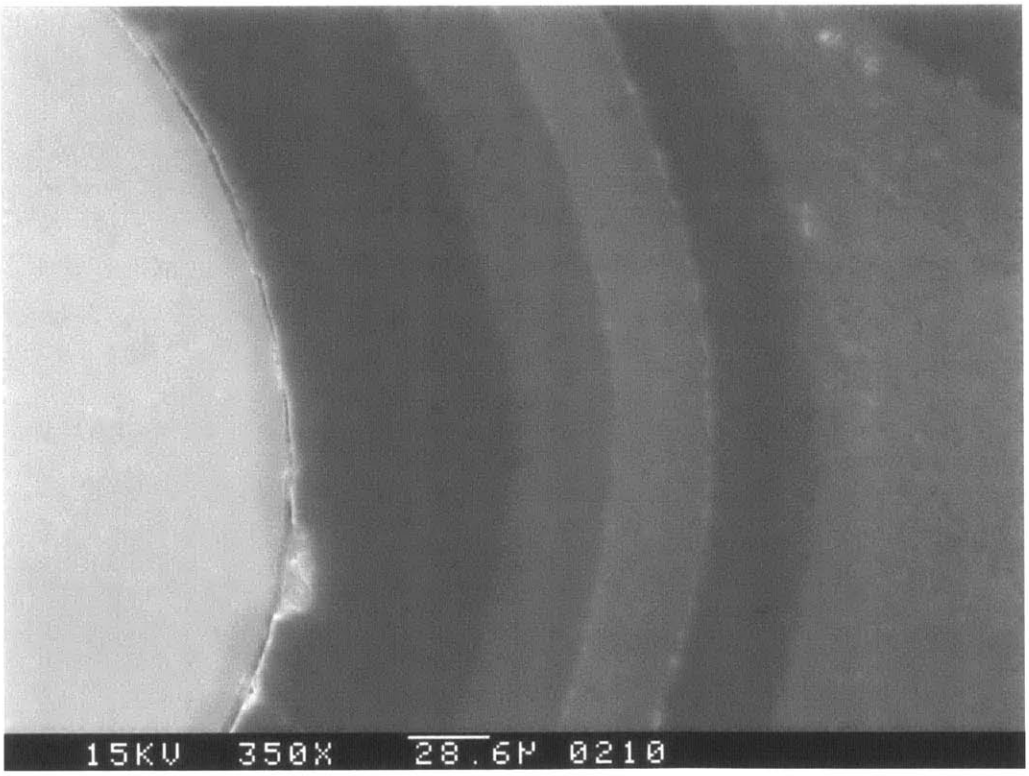

Figure C. 8: 350x SEM micrograph of mount U2 particle 2.

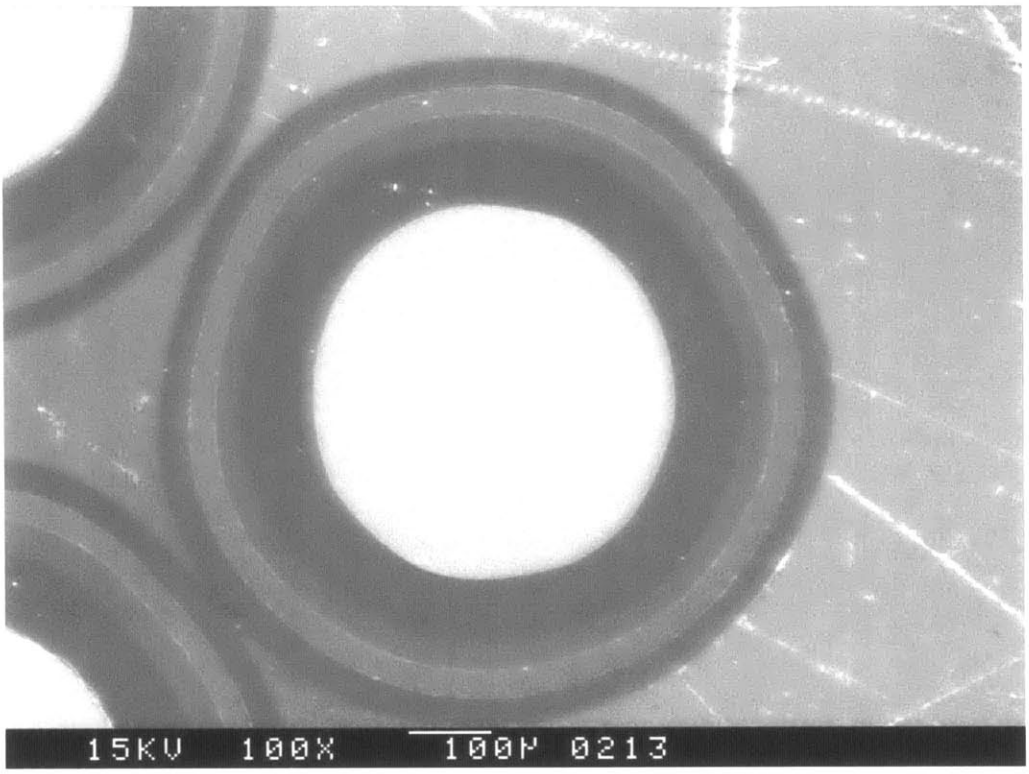

Figure C. 9: 100x SEM micrograph of mount U2 particle 3.

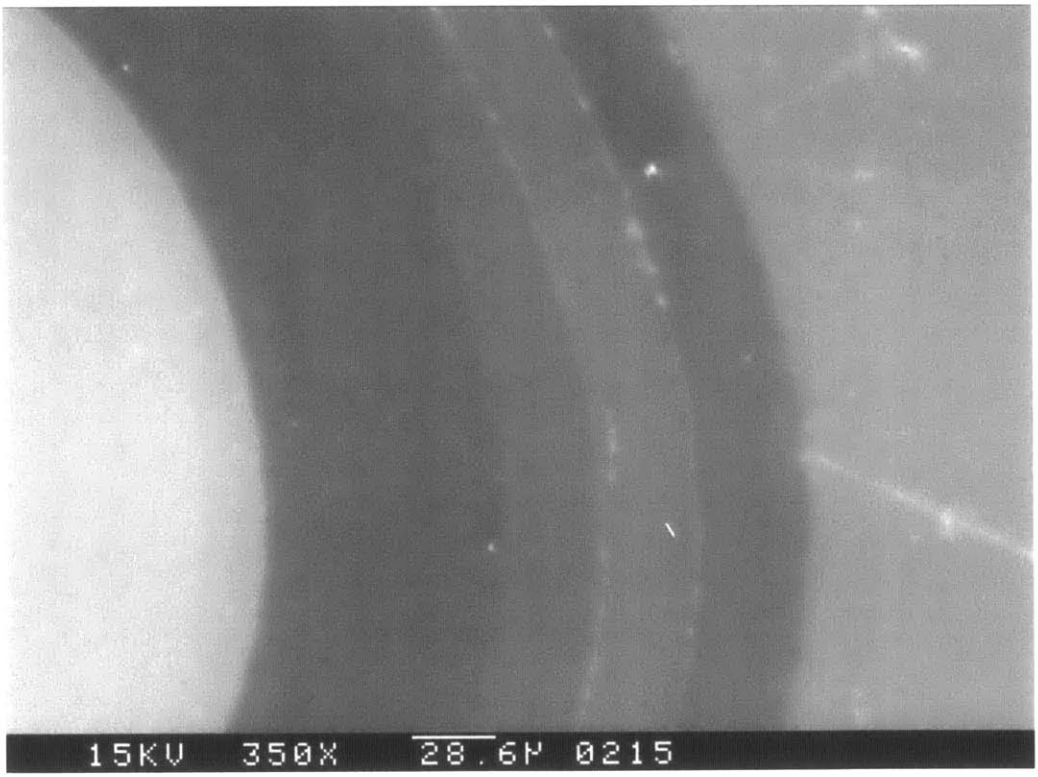

Figure C. 10: 350x SEM micrograph of mount U2 particle 3.

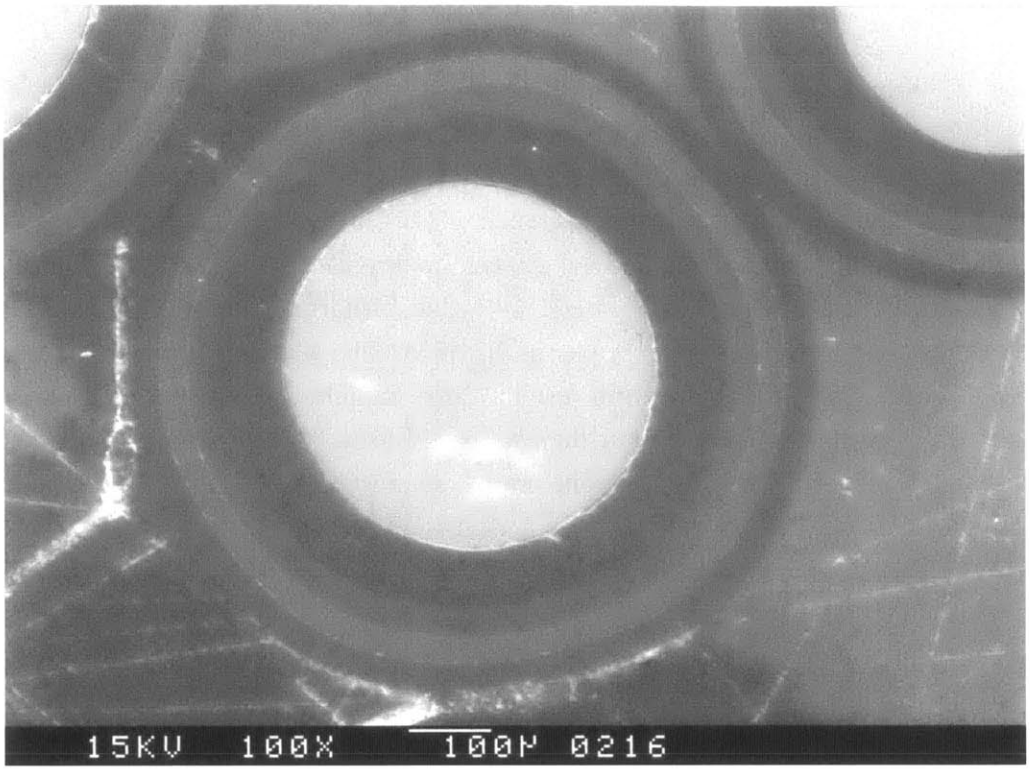

Figure C. 11: 100x SEM micrograph of mount U2 particle 4.

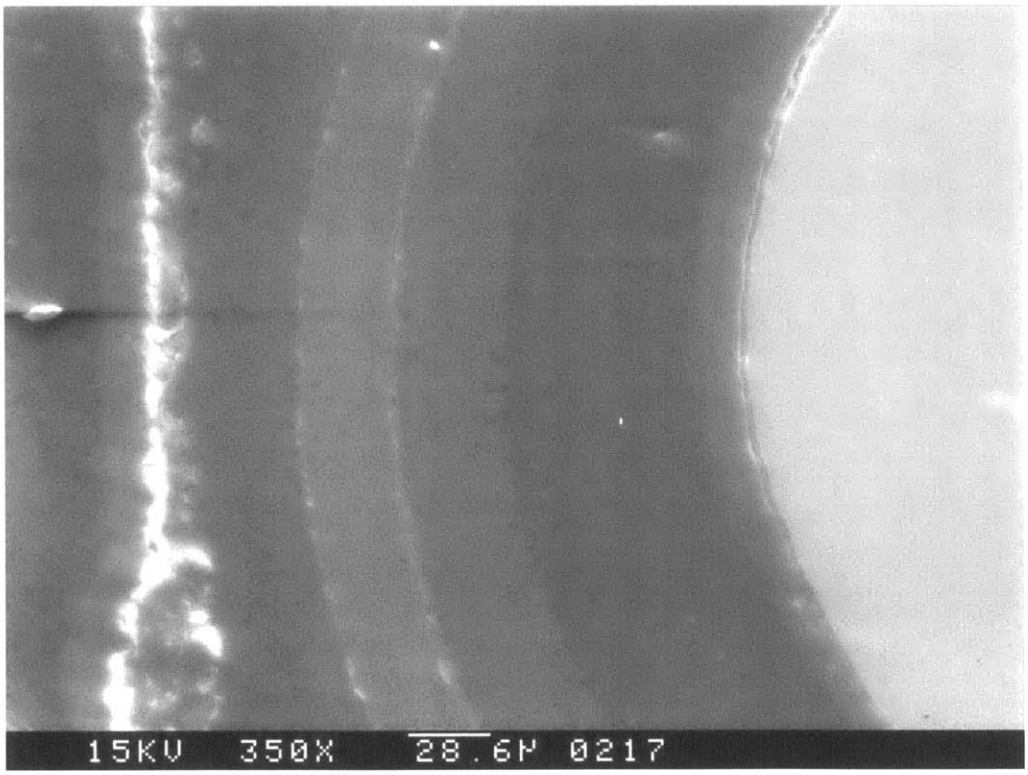

Figure C. 12: 350x SEM micrograph of mount U2 particle 4.

C.2: Additional PIE of surrogate TRISO particles irradiated in helium

Figure C. 13 through Figure C. 19 show 100x and 250x SEM micrographs of irradiated particles 1 through 4 from mount I1. These samples were gold coated with a thin layer of gold so that the IPyC-buffer interface is clearly visible. The cracks are also visible, but they are harder to see in the SEM micrographs than in the optical micrographs. The 250x SEM micrographs give a good indication of how thin the cracks are and how they seem to originate at the IPyC-SiC interface.

The dark shadowing at the right in Figure C. 14 is due to charging on the adhesive of the copper tape used to affix mount I1 to the sample holder in the SEM. The white spots visible on the kernel in Figure C. 13 through Figure C. 16 are from residual SiO_2 particles used in the final polishing step. Despite vigorously rinsing the sample after the final polish, some silica particles remained. In the future, ultrasonic cleaning in water may be done prior to microscopy.

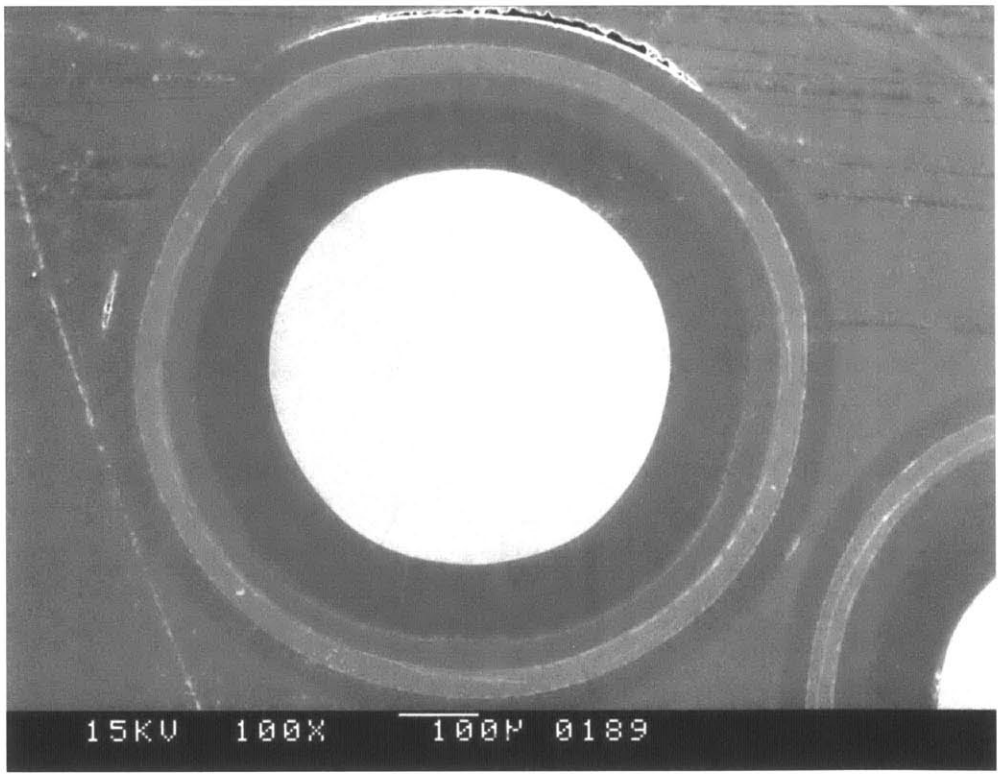

Figure C. 13: 100x SEM micrograph of I1 particle 1. Orientation is 180 degrees opposite of the earlier optical micrographs.

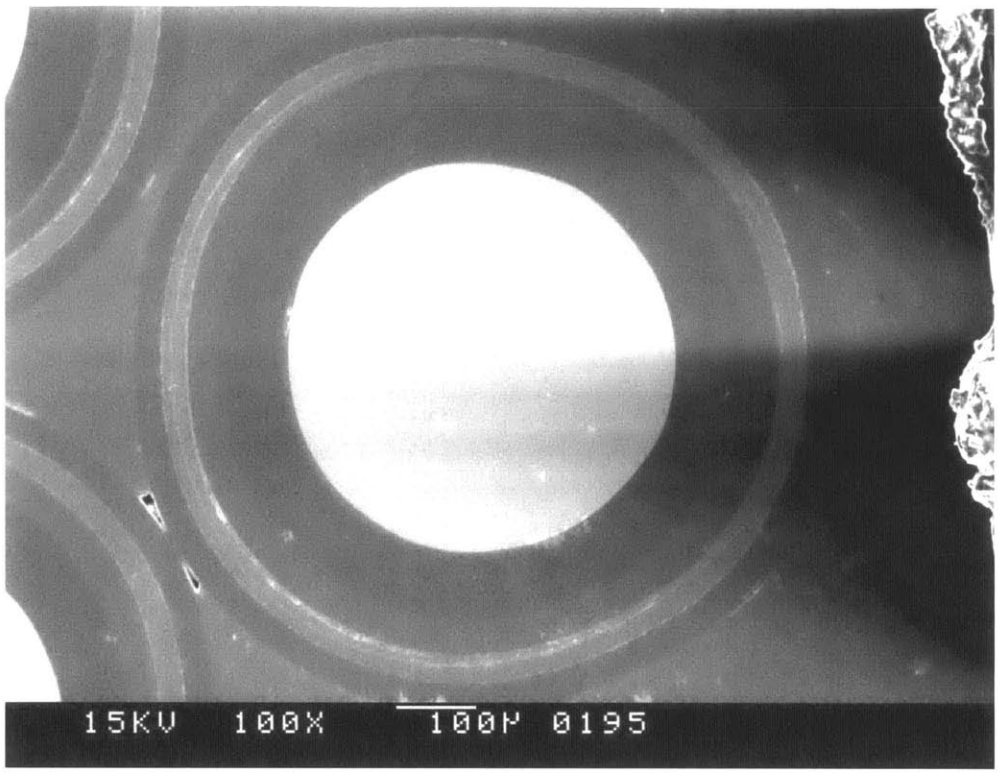

Figure C. 14: 100x SEM micrograph of I1 particle 2. Orientation is 180 degrees opposite of the earlier optical micrographs.

Figure C. 15: 250x SEM micrograph of I1 particle 2.

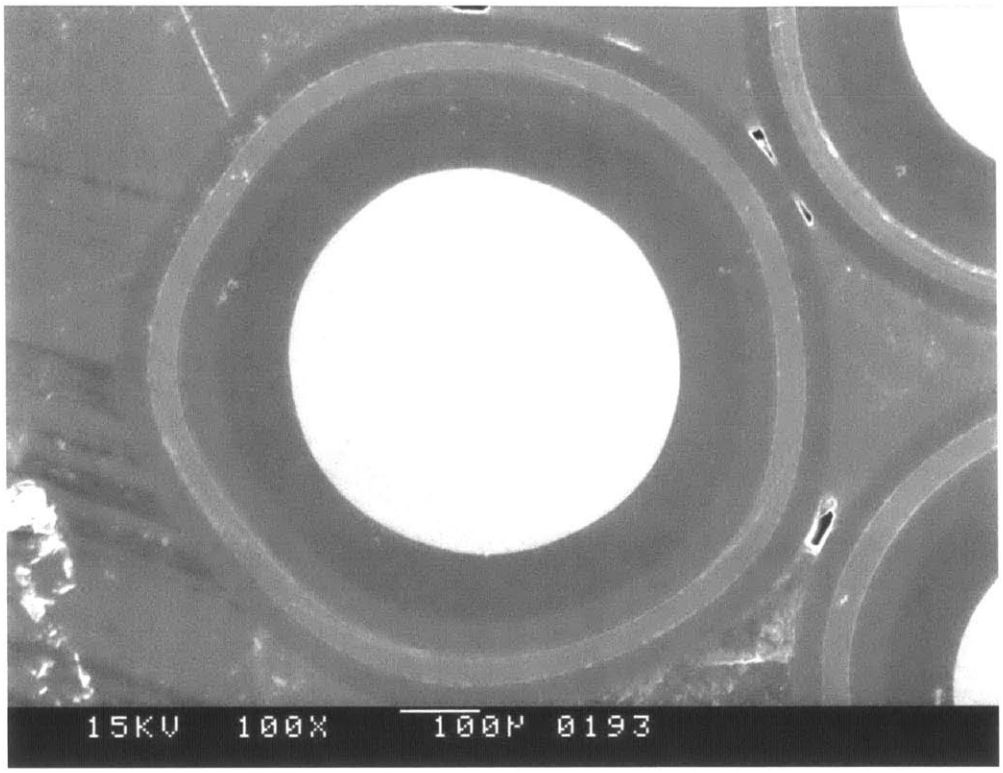

Figure C. 16: 100x SEM micrograph of I1 particle 3. Orientation is 180 degrees opposite of the earlier optical micrographs.

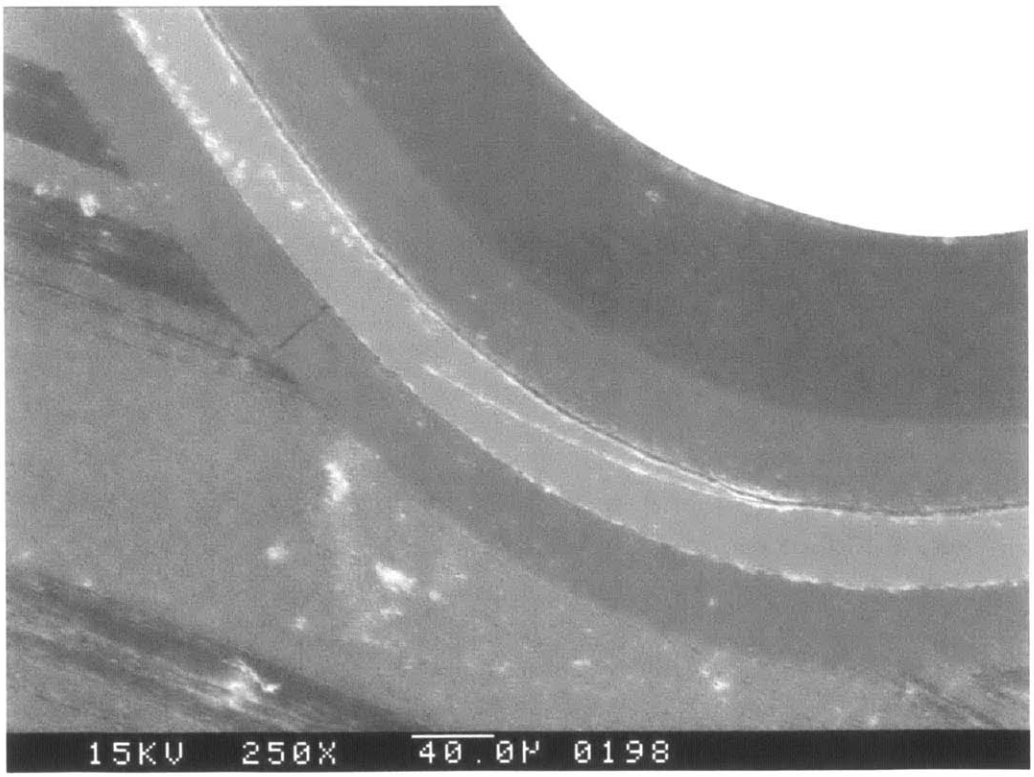

Figure C. 17: 250x SEM micrograph of I1 particle 3.

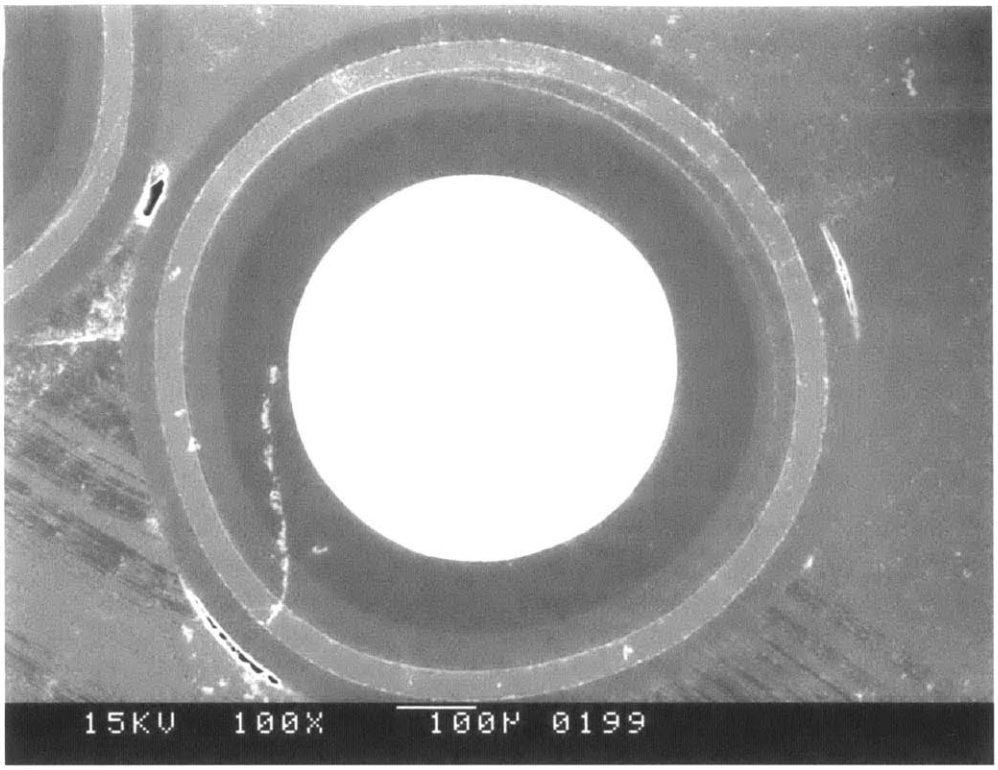

Figure C. 18: 100x SEM micrograph of I1 particle 4. Orientation is 180 degrees opposite of the earlier optical micrographs.

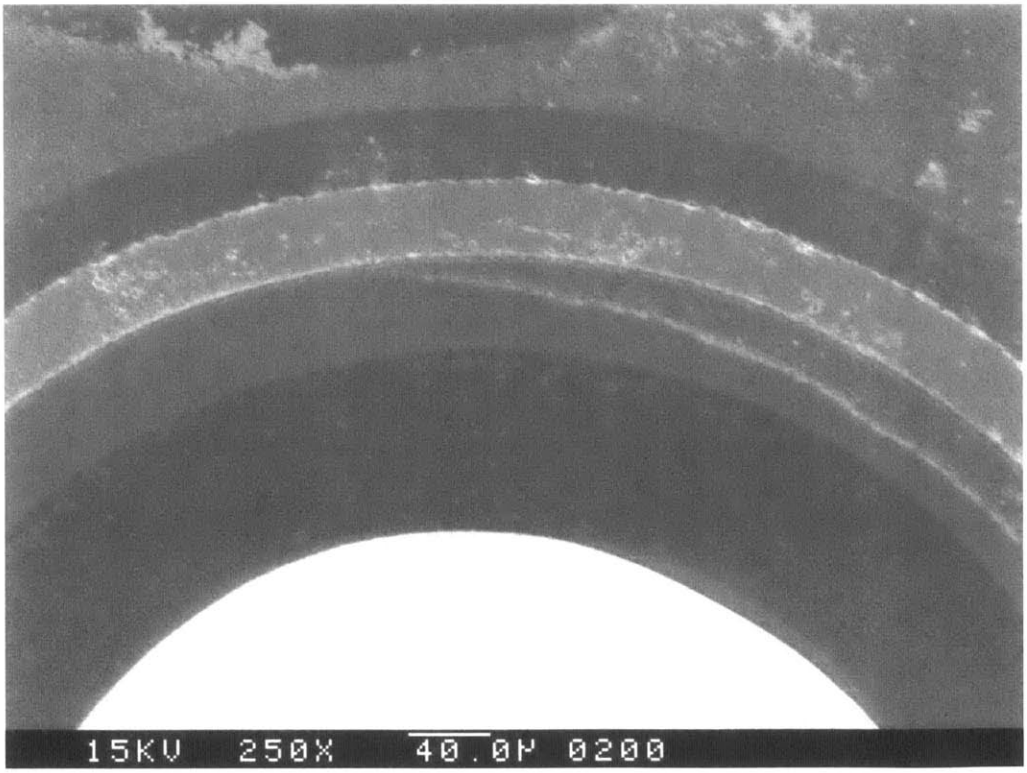

Figure C. 19: 250x SEM micrograph of I1 particle 4.

Figure C. 20 through Figure C. 30 show optical micrographs of particles not previously shown in Section A.1.6.2. Of the 15 particles mounted in I2, only particle numbers 8 and 15 showed pristine SiC layers. Particle numbers 4, 5, 6, and 14 showed very slight circumferential cracks in the SiC layer. Particles 1-3, 7, 9, and 10-13 exhibit circumferential cracks that span a significant portion of the circumference of the SiC layer. All particles exhibit radial cracks in the OPyC layer. Some of these OPyC cracks occur in areas where there may be a gap between the epoxy and OPyC. If there was a gap between the epoxy and the OPyC, then the OPyC would not have been supported during grinding, and it may have been cracked during sample preparation. Since other OPyC cracks occur in areas where there is no discernible gap, and OPyC cracking was not observed in unirradiated samples, it is suggested that the OPyC layer is susceptible to cracking after irradiation. The majority of particles have intact IPyC and buffer layers. Particles, 5, 8, 12, 13, and 15 exhibit radial cracks through the buffer and IPyC layers. Particle 9 exhibits only slight cracking of the IPyC layer. Once again, no radial SiC cracks or through-cracks were observed in any of the particles.

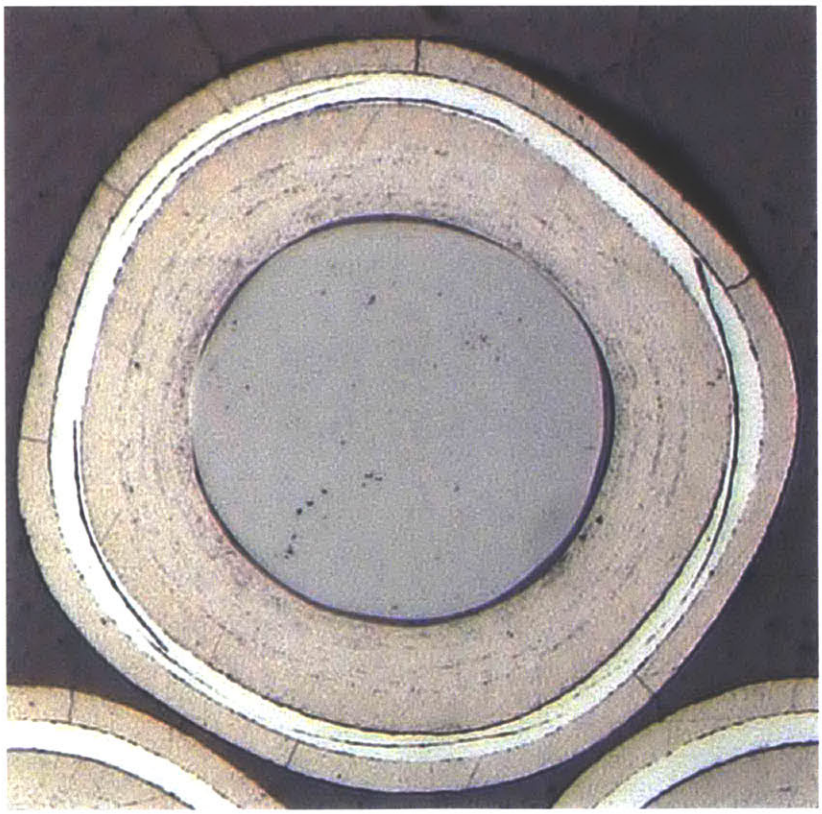

Figure C. 20: 50x optical micrograph of I2 particle 1.

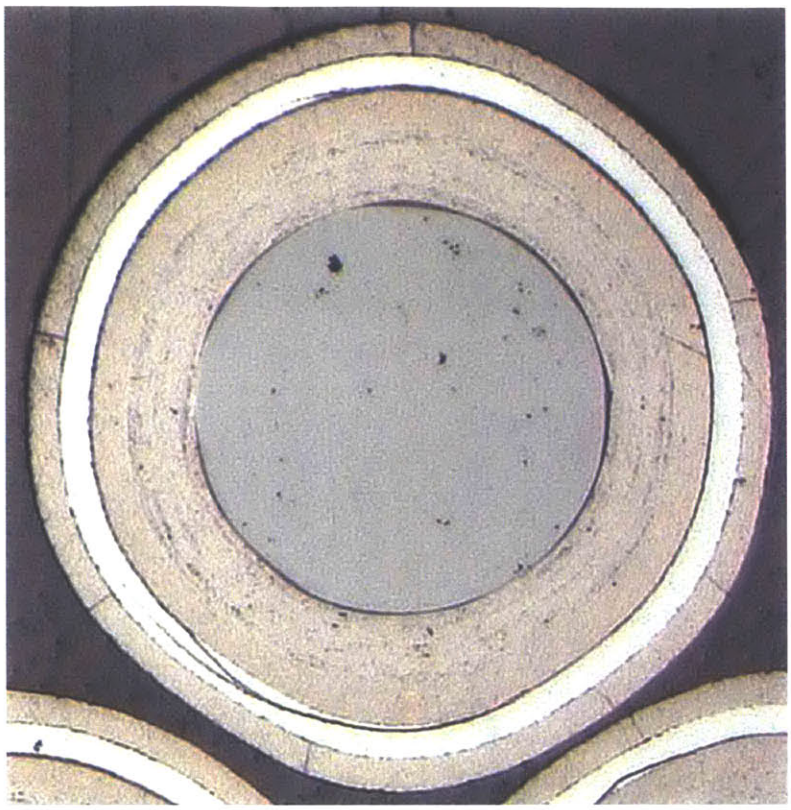

Figure C. 21: 50x optical micrograph of I2 particle 2.

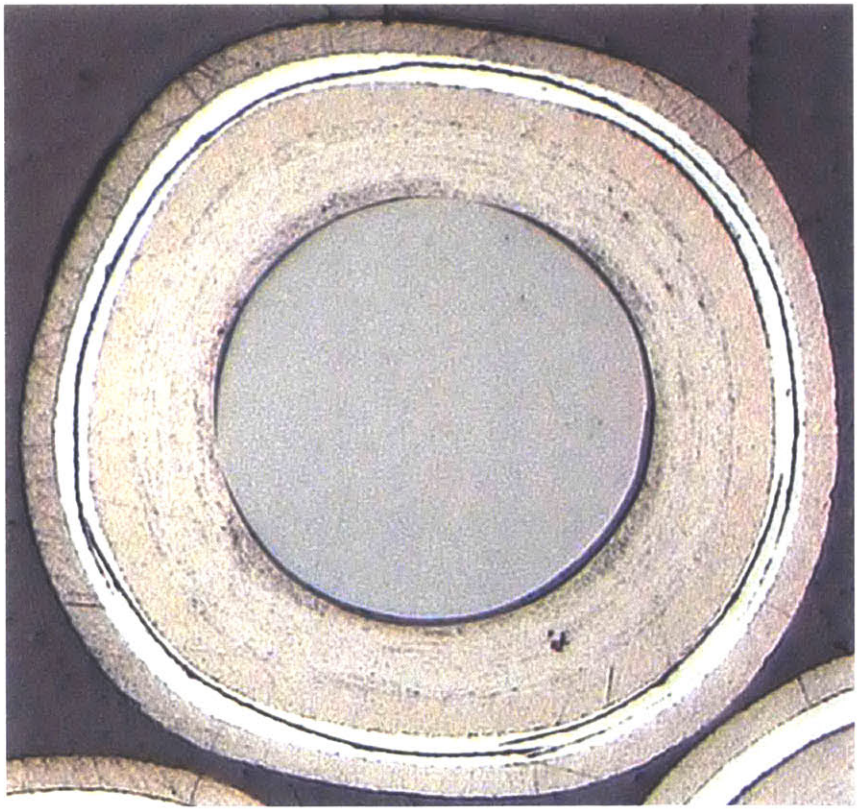

Figure C. 22: 50x optical micrograph of I2 particle 3.

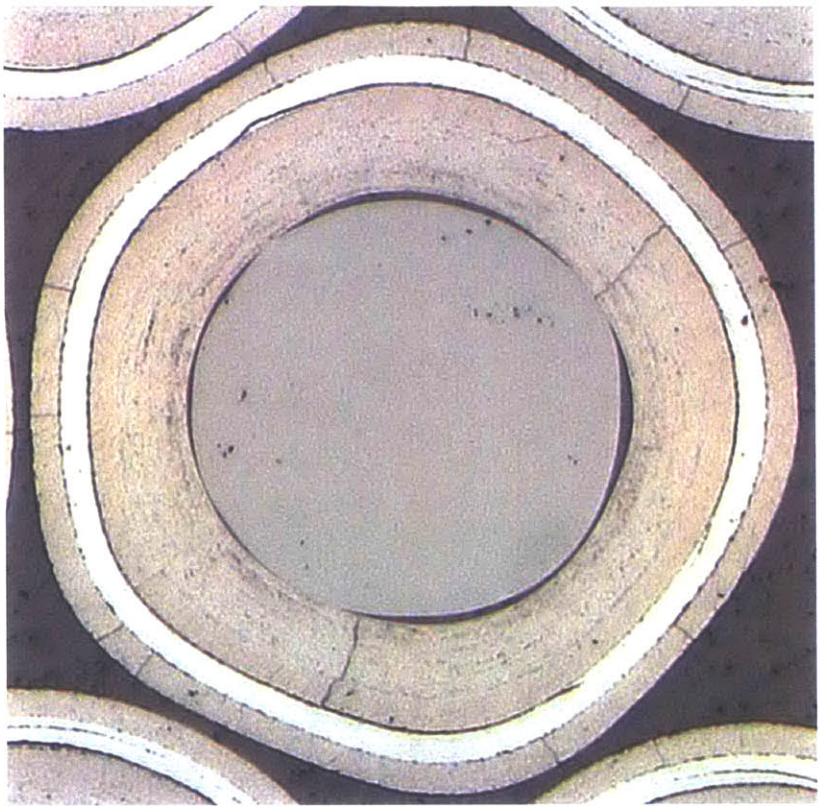

Figure C. 23: Optical micrograph of I2 particle 5.

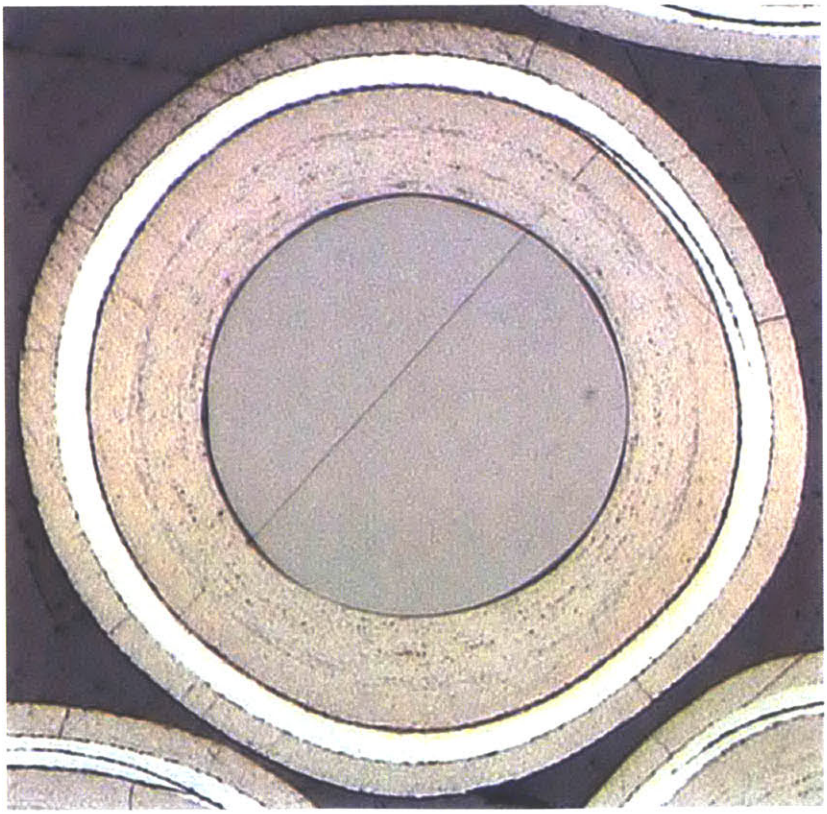

Figure C. 24: 50x optical micrograph of I2 particle 7. Diagonal line is a scratch from polishing.

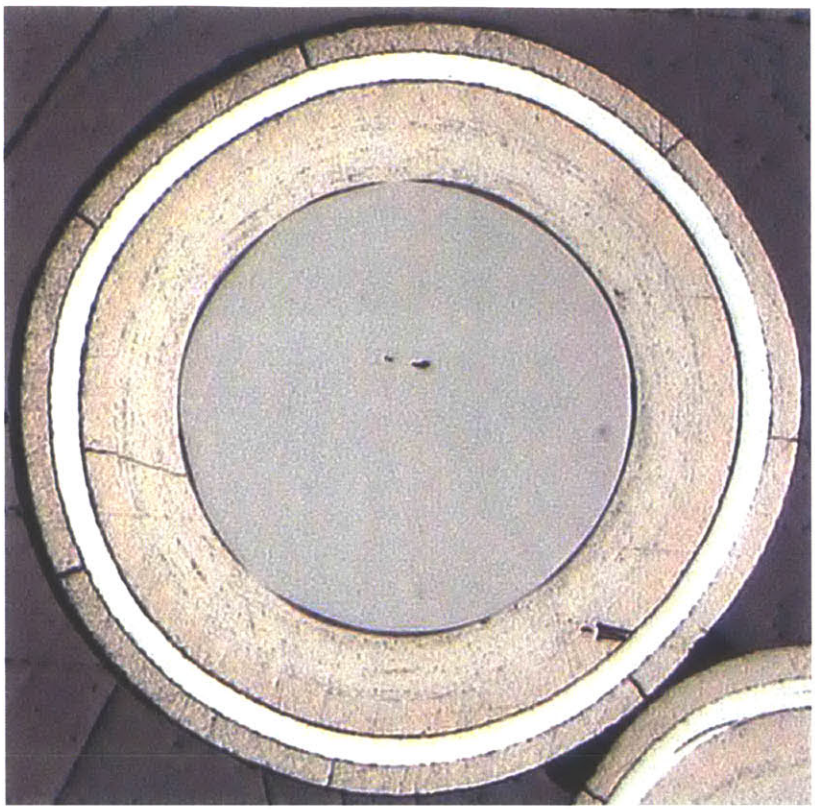

Figure C. 25: 50x optical micrograph of I2 particle 8.

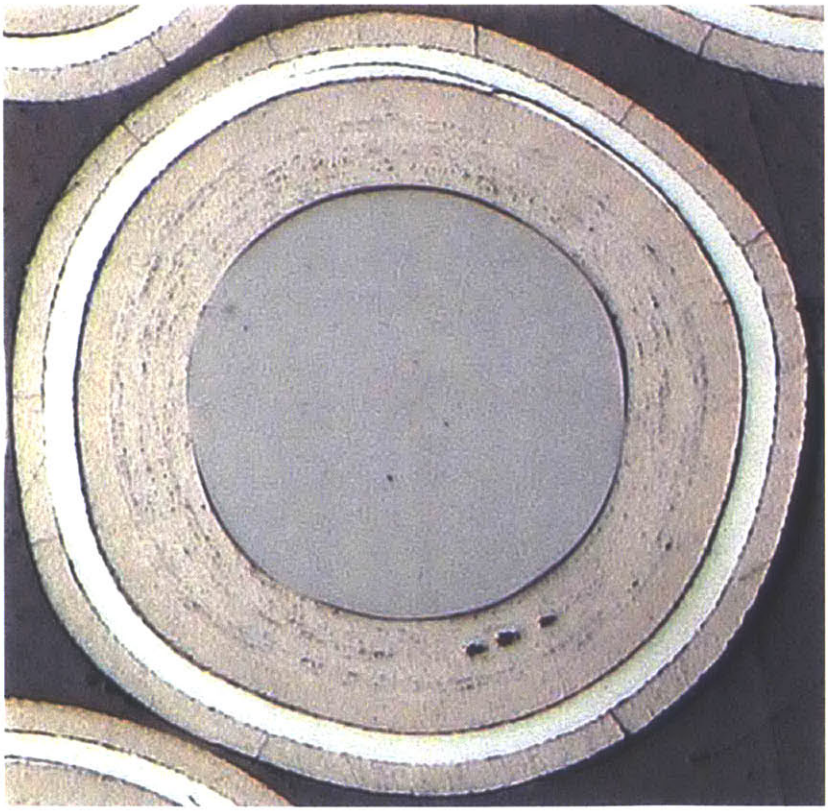

Figure C. 26: 50x optical micrograph of I2 particle 9.

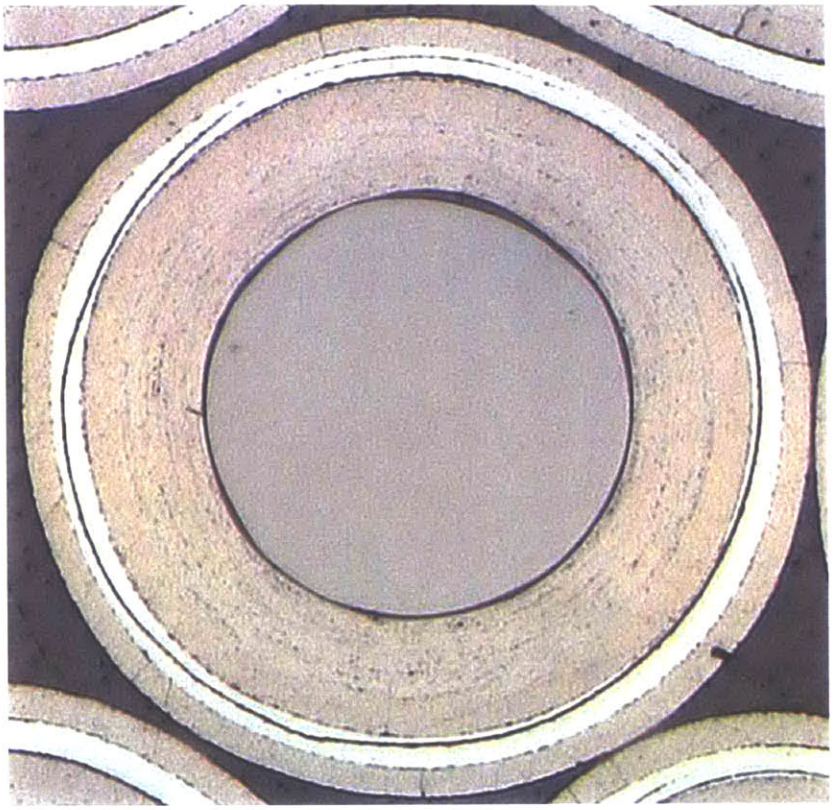

Figure C. 27: 50x optical micrograph of I2 particle 10.

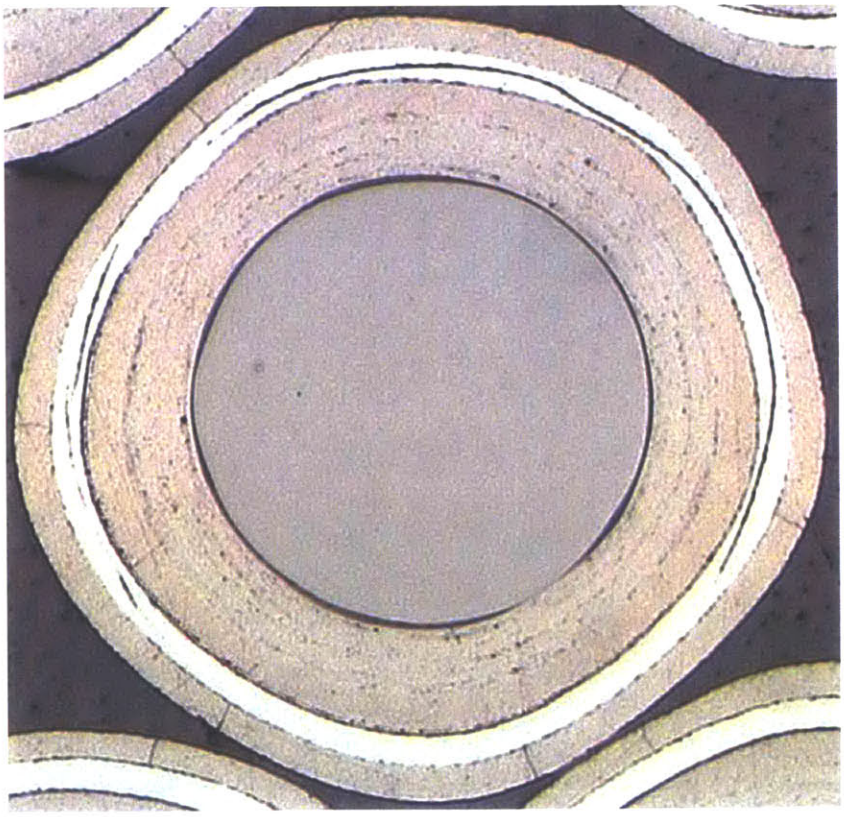

Figure C. 28: 50x optical micrograph of I2 particle 11.

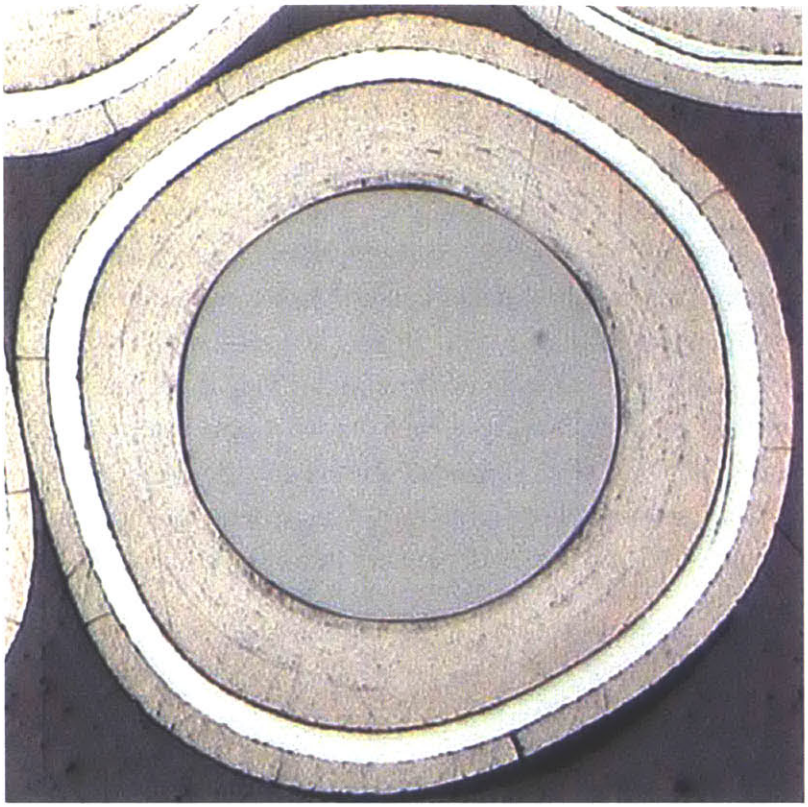

Figure C. 29: 50x optical micrograph of I2 particle 14.

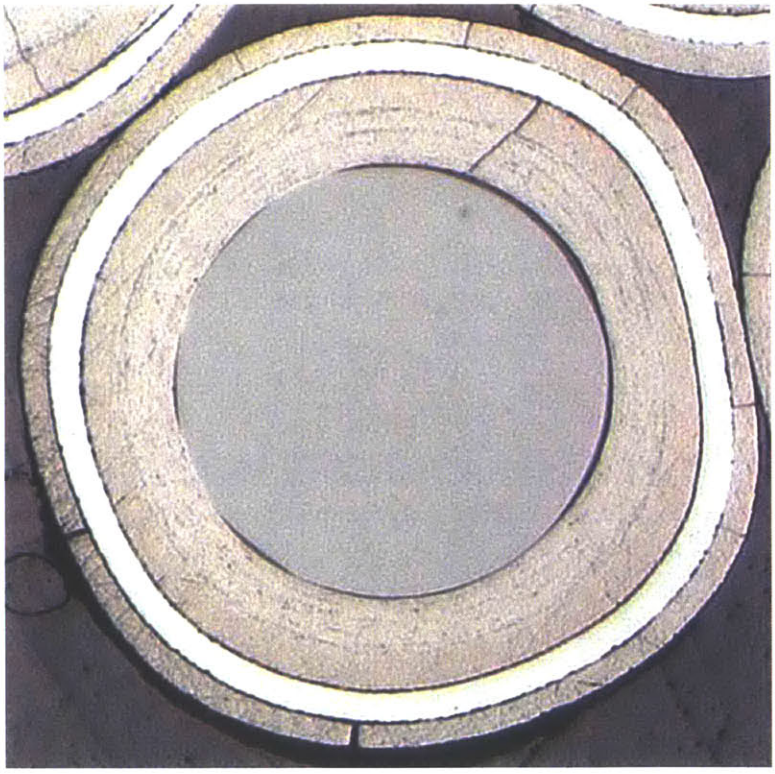

Figure C. 30: 50x optical micrograph of I2 particle 15.

Figure C. 31 through Figure C. 40 show SEM micrographs for particles from mount I2. SEM micrographs of particles in mount I2 tend to provide less detail than the optical micrographs. The IPyC-buffer interface is difficult to discern, and cracks visible in the optical micrographs may be difficult or impossible to identify in the SEM micrographs. Again, this can be attributed to the application of a gold coating after the optical micrographs had been obtained. The gold coating was necessary in order to make the sample surfaces conductive for use in the SEM, but the gold coating also makes crack identification more difficult. In several cases, a gap between the epoxy and the OPyC was observed. Often OPyC cracking occurred in the vicinity of a gap between the epoxy and the OPyC, and this type of cracking may have been caused during sample preparation. At this gap, the OPyC would not have been well supported during grinding and polishing. In the optical micrographs, OPyC cracks are also observed in areas where there is no discernible gap between the OPyC and the epoxy, suggesting that irradiation makes the OPyC susceptible to cracking.

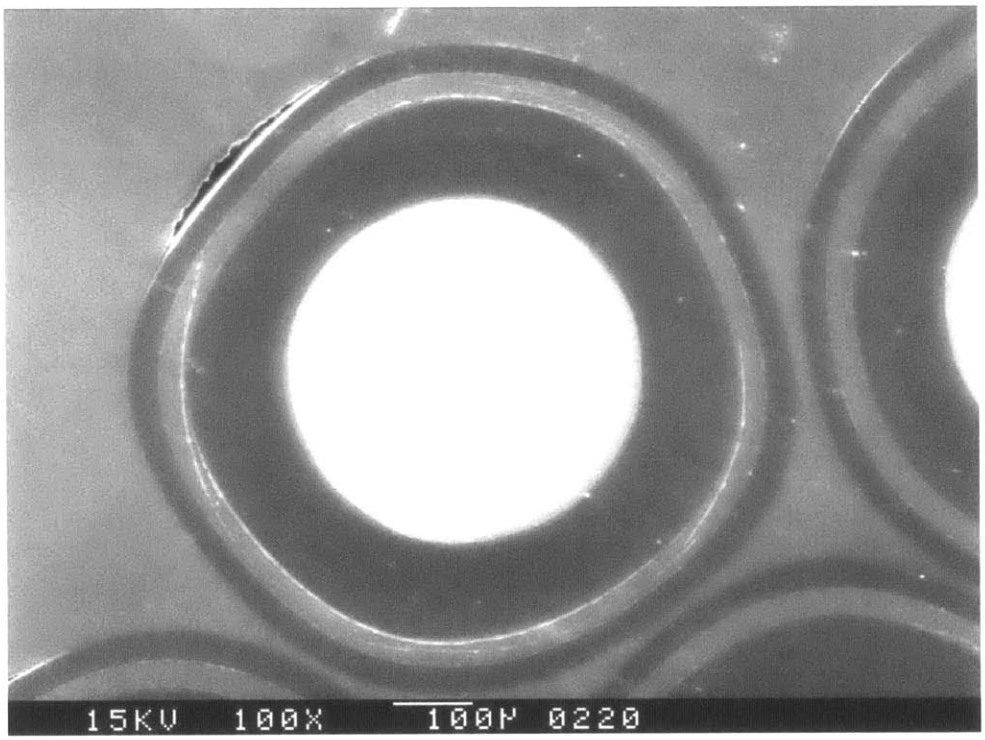

Figure C. 31: 100x SEM micrograph of mount I2 particle 1.

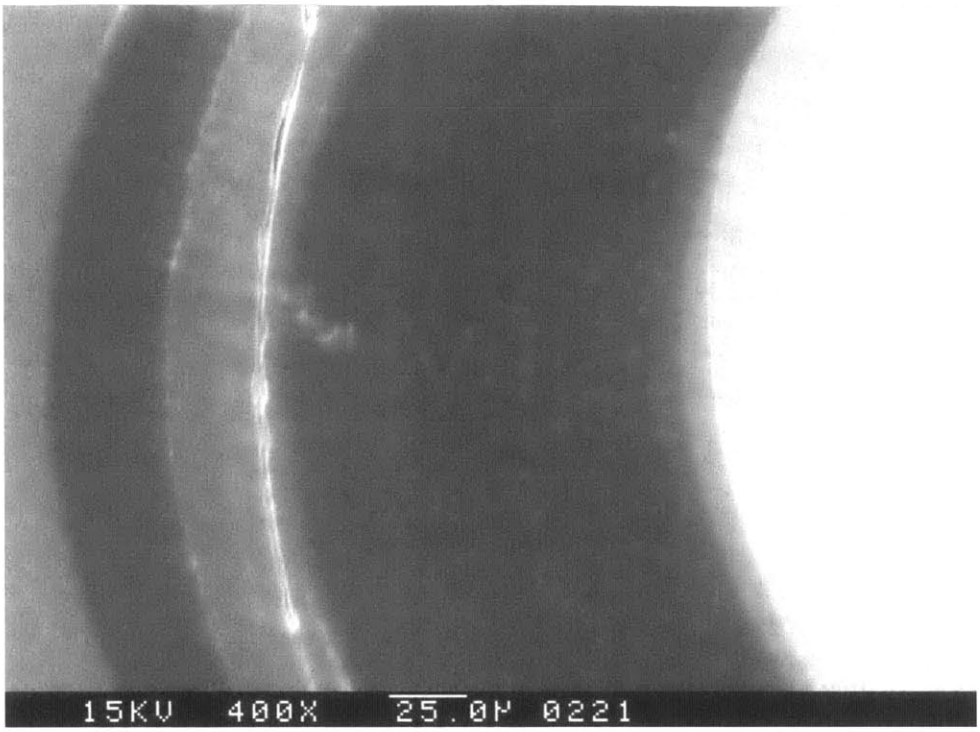

Figure C. 32: 400x SEM micrograph of mount I2 particle 1.

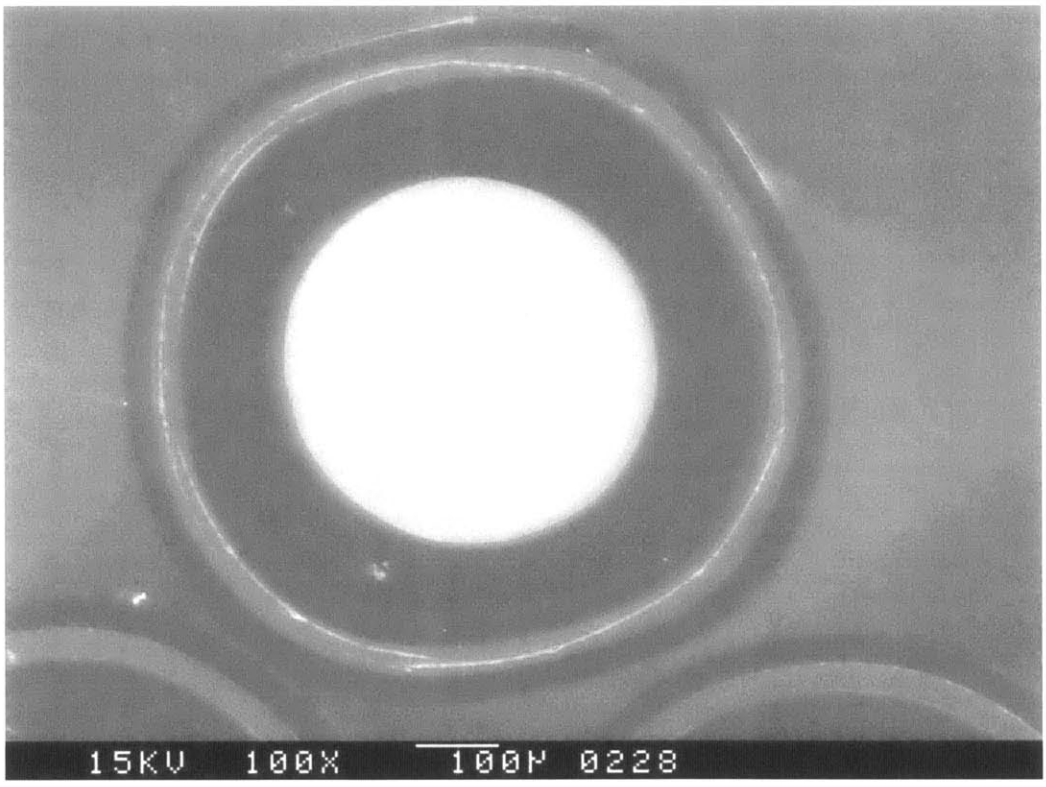

Figure C. 33: 100x SEM micrograph of mount I2 particle 3.

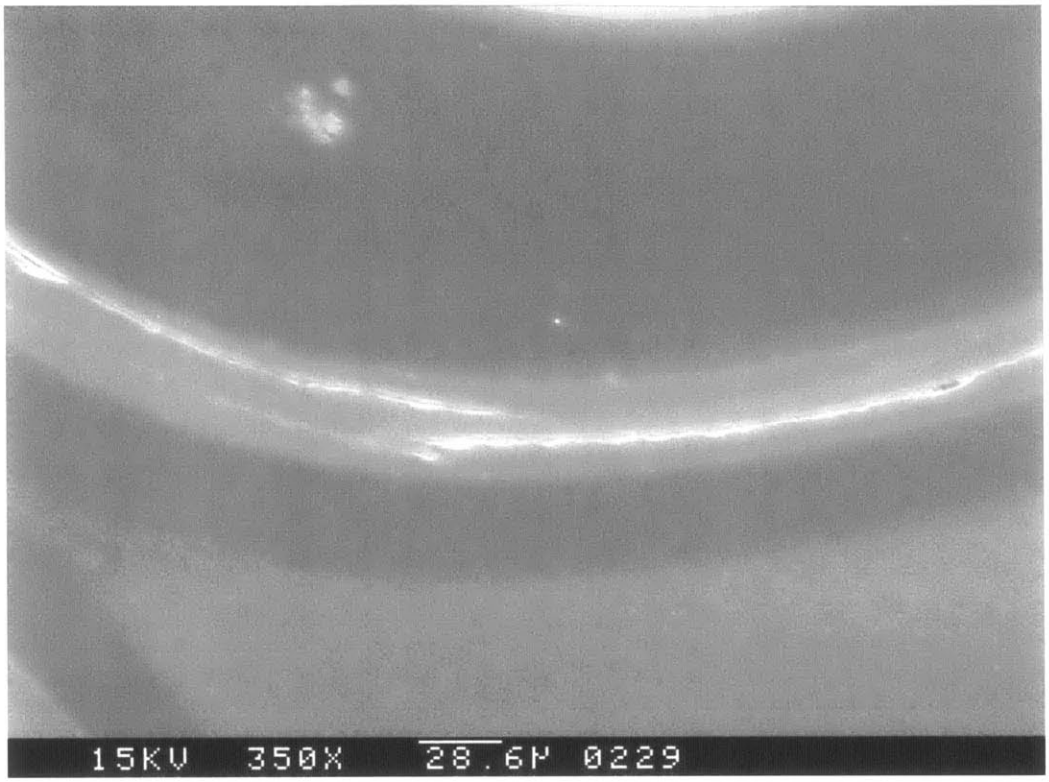

Figure C. 34: 350x SEM micrograph of mount I2 particle 3.

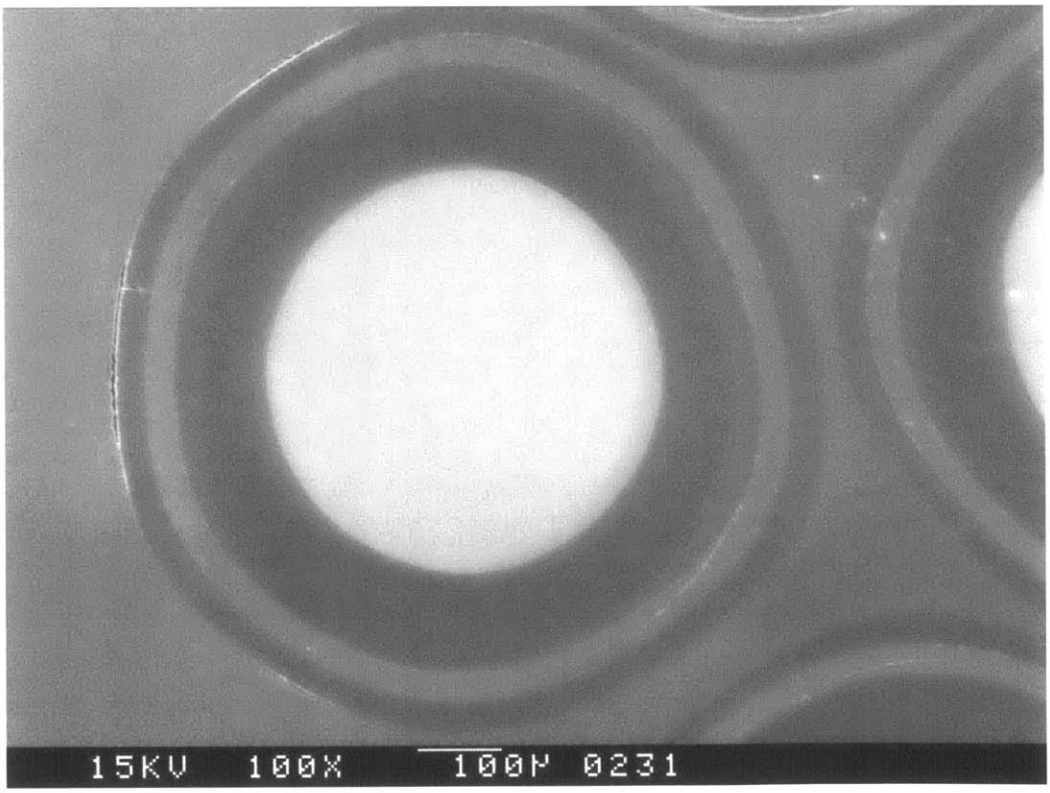

Figure C. 35: 100x SEM micrograph of mount I2 particle 4.

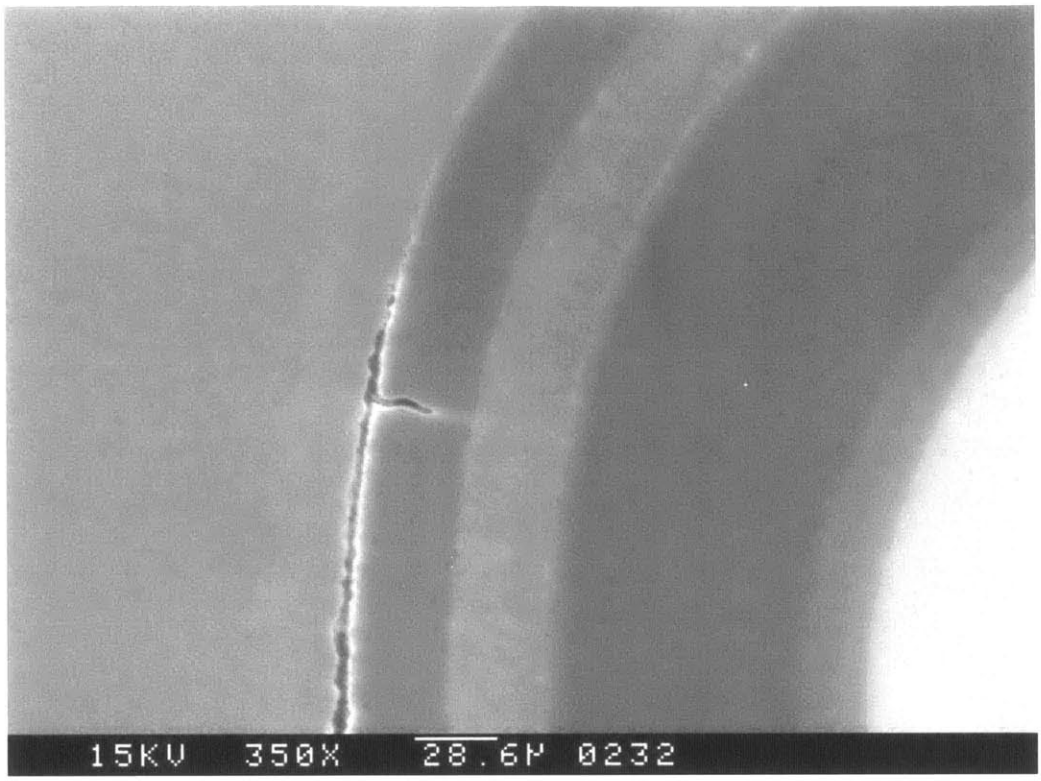

Figure C. 36: 350x SEM micrograph of mount I2 particle 4 showing OPyC crack and gap between epoxy and OPyC.

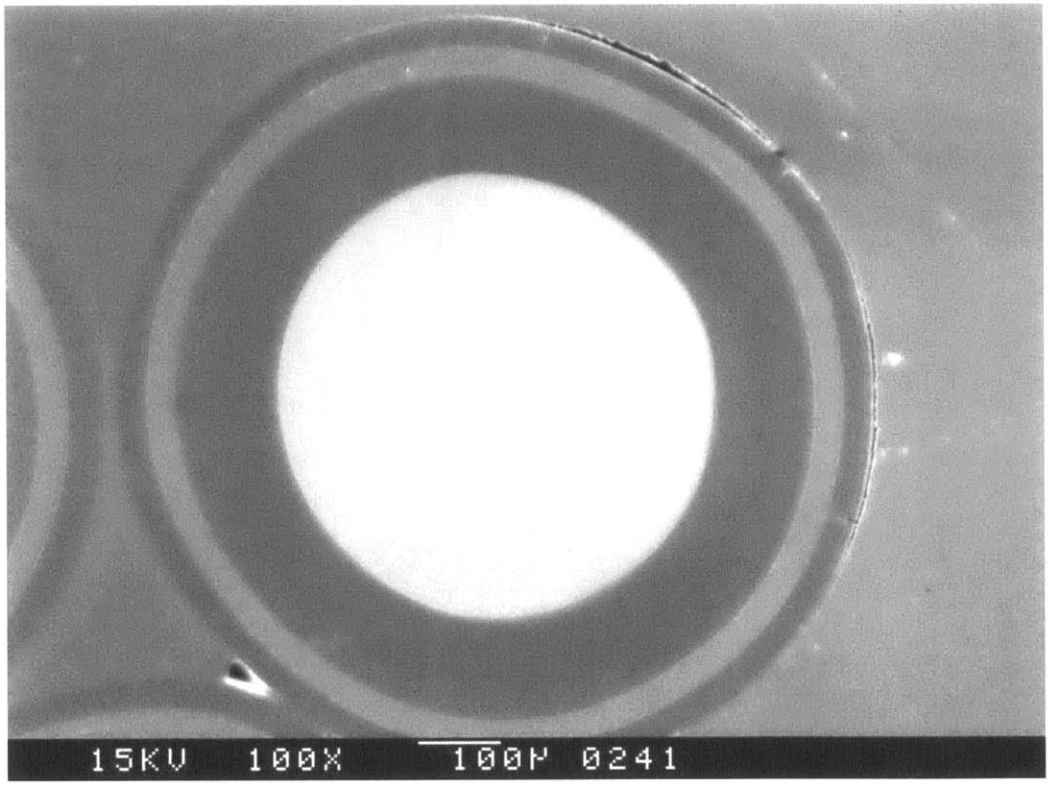

Figure C. 37: 100x SEM micrograph of mount I2 particle 8.

Figure C. 38: 344x SEM micrograph of mount I2 particle 8. Arrow indicates buffer and IPyC crack.

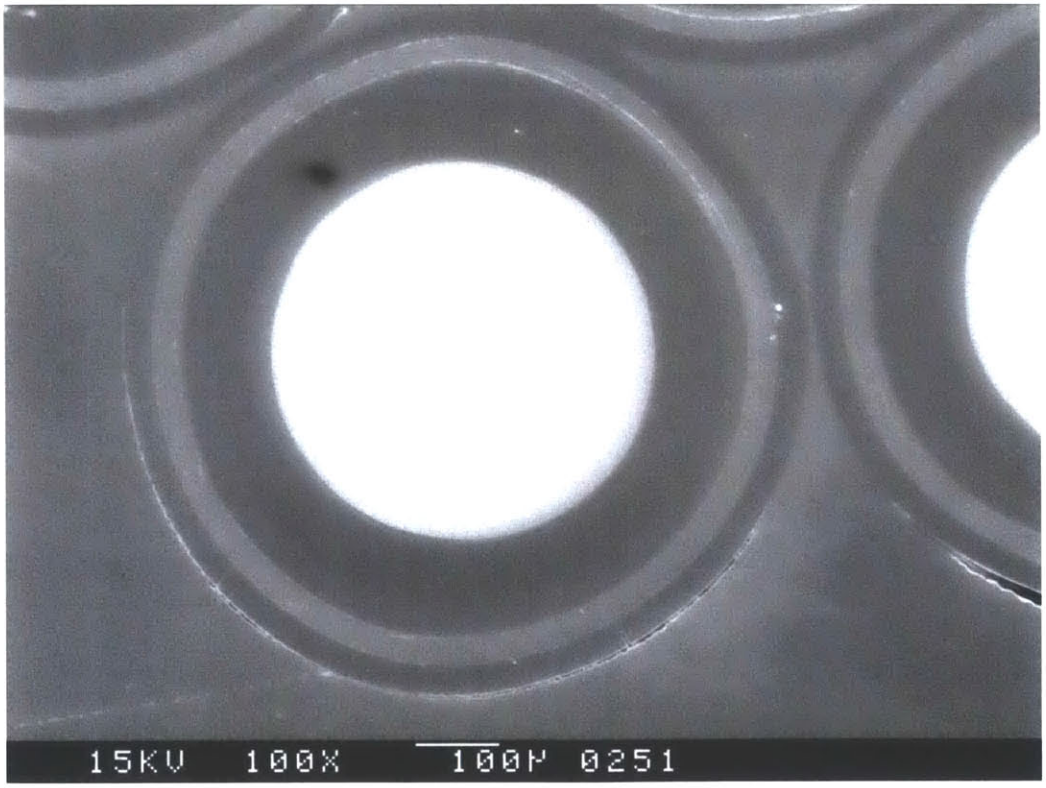

Figure C. 39: 100x SEM micrograph of mount I2 particle 13.

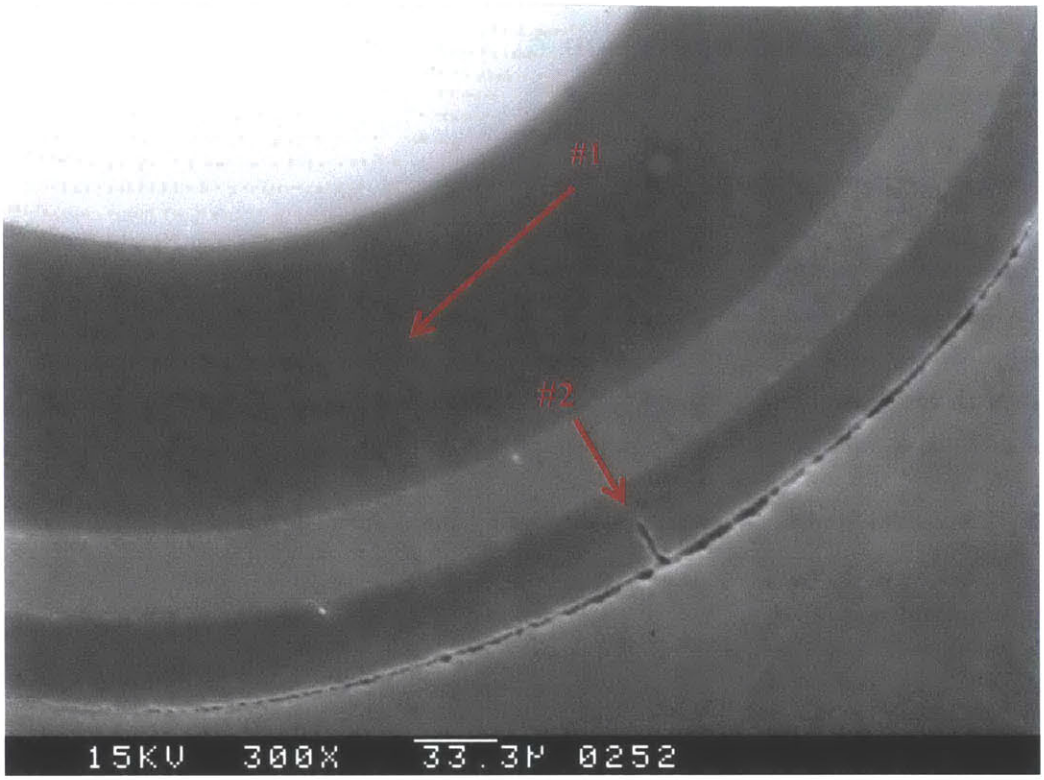

Figure C. 40: 300x SEM micrograph of mount I2 particle 13. Arrow #1 indicates buffer and IPyC crack. Arrow #2 shows OPyC crack and gap between epoxy and OPyC.

Appendix D: Notes on operation of TRIDENT, example input file, and description of TRIDENT output.

D.1: Files required for running TRIDENT

TRIDENT was developed in MATLAB R2013a. In order to run TRIDENT, a number of TRIDENT "functions" must all exist in the same directory (folder). The names and brief descriptions of each TRIDENT function are summarized in Table D. 1. An example of a TRIDENT input file is provided immediately following this table. A description of important TRIDENT output variables is given following the example input file.

Table D. 1: TRIDENT main program and supporting functions required for TRIDENT operation.

Function name and file extention (case sensitive)	Short Description
TRIDENT.m	TRIDENT main program
Example name "nominalfhr_example.m"	Input file for specifying a simulation in TRIDENT
TritiumProductionCalculation.m	Calculates the time-dependent tritium production rate from neutron transmutation in flibe
temperatureprofile.m	Constructs a system temperature profile based on parameters in the input file
temperature_dependent_polythermal.m	Calculates and stores vectors of temperature dependent properties based on the temperature profile in the system
polythermal.m	Calculates tritium transport and mass transfer throughout the system. Handles coolant chemistry. Calls out to corrosion module and gas stripping modules. Calculates tritium uptake on graphite and diffusion through heat exchanger. Contains tritium mitigation system calculations (absorption on graphite and removal in permeation window).
CorrosionModule.m	In hot and cold leg, models early corrosion limited by TF transport/concentration. Models long-term corrosion limited by solid-state Cr diffusion in base metal.
permentr_primary.m	System of equations for using the `fsolve` feature in MatLab to solve tritium transport into the permeator tube wall on upstream side of primary system permeation window
GasStrippingModule.m	Models gas stripping of TF and T_2 from the salt via an inert gas in a counter-current gas stripping equilibrium stage separation
HX1entr.m	System of equations for using the `fsolve` feature in MatLab to solve tritium transport from the coolant into the heat exchanger tube wall on the upstream side of the primary system heat exchanger
HX1exit.m	Sets up a system of equations to solve for the transport of tritium out of the primary system heat exchanger and into the secondary (intermediate) system coolant.

Table continued from previous page.	
CorrosionModuleHX.m	In heat exchanger, models early corrosion limited by TF transport/concentration. Models long-term corrosion limited by solid-state Cr diffusion in base metal.
permentr_secondary.m	System of equations for using the `fsolve` feature in MatLab to solve tritium transport into the permeator tube wall on upstream side of secondary system permeation window
HX2entr.m	System of equations for using the `fsolve` feature in MatLab to solve tritium transport from the secondary (intermediate) coolant into the heat exchanger tube wall on the upstream side of the secondary system heat exchanger

The TRIDENT input file is actually a MatLab function. The name of the function ('nominalfhr_example' for example) must be the same as the filename ('nominalfhr_example.m') used to save the function. Additionally, this function name must appear in TRIDENT as highlighted by the red box below.

```
%                              \\|||//
%                               \|||/
%                                |||
%                                |||
%                                |||
%                                |||
%                                |||
%                                |||
%                                |||
%  #######  ########     #######  #######     #######  ##     #  #######
%     #     #       #       #     #      #    #        ##     #     #
%     #     #       #       #     #       #   #        # #    #     #
%     #     ########        #     #        #  ######   #  #   #     #
%     #     #      #        #     #        #  #        #   #  #     #
%     #     #       #       #     #       #   #        #    # #     #
%     #     #        #      #     #      #    #        #     ##     #
%     #     #        ##  #######  #######     ########  #    ##     #
%
%                  TRItium Diffusion EvolutioN and Transport
%                                     by
%                               John D. Stempien
%              MIT, Department of Nuclear Science and Engineering
%                               Completed May 2015
%%%%%%%%%%%%%%%%%%%%%%%%%%%%%%%%%%%%%%%%%%%%%%%%%%%%%%%%%%%%%%%%%%%%%%%%%%%%
%  Code Description:  Calculates tritium birth rates and concentrations in
%  the coolant loops of the FHR.  Simulates corrosion reactions of TF with
%  Cr and selective leaching of Cr from the structural metals in the
%  system.  Options exist to simulate tritium removal systems.
%%%%%%%%%%%%%%%%%%%%%%%%%%%%%%%%%%%%%%%%%%%%%%%%%%%%%%%%%%%%%%%%%%%%%%%%%%%%

clear;
clc;
tic
%Read in input parameters and calculation options from input function
[Density_metal, MM, Wtfrac, Lattice_param, T_out, T_in, Rx_power, qo, T_avg, Days, Elements, Corrosionflag, T_uptake, Redoxflag, Feedbackflag, Oxideflag, ...
    Kernel_d, Buffer_t, IPyC_t, SiC_t, OPyC_t, TRISOperPebble, Pebble_radius, Core_height, Core_mesh, CentralRef_radius, ...
    OuterRef_outradius, OuterRef_inradius, Fuelzone_innerradius, Fuelzone_outerradius, pipe_d, pipe_1, Hot_mesh, pipe_d2, pipe_12, Cold_mesh, ...
    Hx_mesh, Hx_tube_od, Thick, A1, A2, C_Cr_initial_ppm, pipe_thick1, pipe_thick2, pipe_zone1, pipe_zone2, slices1, slices2, slice_thick1, ...
    slice_thick2, depth_inwall, flux, Tritiumproductionflag, GBflag, GasStrippingFlag, NStages_p, NStages_s, G_s, G_p, Hour_Fraction, Birth_User, ...
    StrippingFlowFraction_p, StrippingFlowFraction_s, PermeationFlag_primary, WindowArea_p, WindowThick_p, Vac_p, PermeationFlag_secondary, ...
    WindowArea_s, WindowThick_s, Vac_s, PermElements, Permp_tube_od, Perms_tube_od, Tritiumcapturebedflag, Bed_vessel_radius, Bed_surface_area, ...
    Particle_radius, Particle_density, Bed_packingfraction, Bed_frac_rep, Restart, Restartfilename, Savefilename, Loops, PRFinput, PF, TubeNumber, ...
    Hx1tubes, Hx2tubes, CoreGeometryAdjust, N_CoreFuelPebbles, N_CoreGrapPebbles, CoreRefuelFrac, NumPermptubes_opt, NumberofPermeatorTubes, ...
    Ratio_TF_T2, Surf_area_gb, Li7_enrichment, Tritiumcapturebedflag_s, Bed_frac_rep_s, Bed_vessel_radius_s, Bed_surface_area_s, Particle_radius_s, ...
    Particle_density_s, Bed_packingfraction_s] = nominalfhr_example;
```

TRIDENT example input file 'nominalfhr_example.m'

```
function [Density_metal, MM, Wtfrac, Lattice_param, T_out, T_in, Rx_power, qo, T_avg,
Days, Elements, Corrosionflag, T_uptake, Redoxflag, Feedbackflag, Oxideflag, ...
          Kernel_d, Buffer_t, IPyC_t, SiC_t, OPyC_t, TRISOperPebble, Pebble_radius,
Core_height, Core_mesh, CentralRef_radius, ...
          OuterRef_outradius, OuterRef_inradius, Fuelzone_innerradius,
Fuelzone_outerradius, pipe_d, pipe_l, Hot_mesh, pipe_d2, pipe_l2, Cold_mesh, ...
          Hx_mesh, Hx_tube_od, Thick, A1, A2, C_Cr_initial_ppm, pipe_thick1,
pipe_thick2, pipe_zone1, pipe_zone2, slices1, slices2, slice_thick1, ...
          slice_thick2, depth_inwall, flux, Tritiumproductionflag, GBflag,
GasStrippingFlag, NStages_p, NStages_s, G_s, G_p, Hour_Fraction, Birth_User, ...
          StrippingFlowFraction_p, StrippingFlowFraction_s, PermeationFlag_primary,
WindowArea_p, WindowThick_p, Vac_p, PermeationFlag_secondary, ...
          WindowArea_s, WindowThick_s, Vac_s, PermElements, Permp_tube_od,
Perms_tube_od, Tritiumcapturebedflag, Bed_vessel_radius, Bed_surface_area, ...
          Particle_radius, Particle_density, Bed_packingfraction, Bed_frac_rep,
Restart, Restartfilename, Savefilename, Loops, PRFinput, PF, TubeNumber, ...
          Hx1tubes, Hx2tubes, CoreGeometryAdjust, N_CoreFuelPebbles,
N_CoreGrapPebbles, CoreRefuelFrac, NumPermptubes_opt, NumberofPermeatorTubes, ...
          Ratio_TF_T2, Surf_area_gb, Li7_enrichment, Tritiumcapturebedflag_s,
Bed_frac_rep_s, Bed_vessel_radius_s, Bed_surface_area_s, Particle_radius_s, ...
          Particle_density_s, Bed_packingfraction_s] = nominalfhr_example


Restart = 1;  %If restarting a previous calculation, turn ON Restart = 2
              %If Restart = 1, restart is NOT used.  A fresh caclulation is performed
if Restart == 1
    Restartfilename = 'nothing';  %Only provide a file name to restart a calculation
if Restart = 2
elseif Restart == 2
    clear all
    Restart = 2;
    Restartfilename = 'nominalfhr_example_restart.mat';  %Provide a file name to
restart from if Restart = 2
end

Savefilename = 'nominalfhr_example.mat';  %Provide a file name for saving the current
run

%Reactor Temperature, time, time step, calculation model, and output options:
T_in = 873.15;   %Core inlet temperature [K]
T_out = 973.15;  %Core outlet temperature [K]
T_avg = 923.15;      %Core average temp in Kelvin. Used for the initial calculation of
flibe density
Rx_power = 236;      %Reactor power [MWt]
qo = 79.7221;        %Axial peak linear heat generation rate calculated from equation
in Ch. 14 of Todreas and Kazimi if core height and power are known [MWt]

Ratio_TF_T2 = 9.2E-5;  %Nominal = 9.2E-5 ratio of P_TF/Sqrt(P_T2) calculated at 650 C
for fluorine potential of -700.5 kJ/mol F2
Li7_enrichment = 99.995;  %wt % Li-7 enrichment in flibe.  Baseline is 99.995
Loops = 1;  %Number of coolant loops to simulate (options are 1 or 2).  Currently, any
secondary (intermediate loop uses the salt flinak)

Days = 365; %Total number of days of simulation

Hour_Fraction = 0.5;   %Record and store calculation results every fraction of an
hour.
```

```
                        %For example, if you want to record ouput every hour,
Hour_Fraction = 1. If you want to store output after every 30 minutes, Hour_fraction =
0.5
                        %This is useful for capturing behavior which occurs
                        %quickly.  Do not use less than 1 for long simulations.

%Calculation options
Elements = 6;       %Number of meshpoints for solving diffusion in HX.  When running
                     %finite difference, the number of Elements needs to be related
                     %to DT via the Fourier Number calculated lower down in
                     %the code

T_uptake = 2;       %Turn off/on tritium uptake on core graphite
                     %1 = off
                     %2 = on
CoreRefuelFrac = (1/30)/86400;  %Fraction of the core pebbles to "refuel" per second
                                 %Set = 0 if not simulating core refueling

CoreGeometryAdjust = 2;    %Option to correct the pebble graphite surface areas in the
                           %core to account for non-uniform geometries.  TRIDENT
                           %only models concentric cylinders in the core, but there
                           %may be chutes and other geometries in a real core
                           %1 = off
                           %2 = on
                           %TRIDENT only uses the number of pebbles below if
CoreGeometryAdjust = 2
                           %Otherwise, TRIDENT calculates the number of pebbles in the
core based on the core geometry,
                           %the pebble size, and the pebble packing fraction in the
core
N_CoreFuelPebbles = 470000;  %Number of fuel pebbles in the core from Table 2-1 of Mk1
PB-FHR Report
N_CoreGrapPebbles = 218000;  %Number of graphite-only pebbles in the core from Table
2-1 of Mk1 PB-FHR Report

Redoxflag = 2;      %Turn off/on redox control
                     %1 = off - everything is T2, there is no TF and no corrosion
                     %2 = on, the user may specify a fixed redox condition as a ratio
via "Ratio_TF_T2" or

Feedbackflag = 2;  %Turn off/on redox feedback
                     %1 = off, calculates a fixed T2 and T+ generation rate based on an
initially specified redox potential, then
                     %  applies this generation rate for the entire calculation.  When
T2 diffusion occurs, this will change the overall redox
                     %  state in the coolant, but the T2 and T+ generation rate remains
constant.  Corrosion reactions do not alter the the T2 and T+ generation rate
                     %2 = on, Fixed redox: the generation rate of atoms T per second in
the reactor remains constant, but the portion of this
                     %  which is generated at T+ and the portion generated as T2 is
varied in order to maintain a fixed redox
                     %  potential in the coolant.  Any corrosion reactions are also
taken into account if Corrosionflag == 2 below
                     %3 = pseudo feedback, all T is produced as T+, corrosion reactions
produce T2, redox potential is allowed to
                     %  drift based on buildup of T+, consumption of T+ by corrosion,
generation of T2 by corrosion and diffusion
                     %  of T2.  Redox state is calculated, but not controlled

Oxideflag = 2;      %Turn off/on oxide layer permeation reduction on air side of HX
                     %1 = off
                     %2 = on
```

```
PRFinput = 10;      %Permeation reduction factor due to an oxide layer on the air-
facing side of the heat exchanger.  Only used if Oxideflag = 2


Corrosionflag = 1;  %Turn off/on corrosion of structural metals
                      %1 = off, no corrosion
                      %2 = on, corrosion is considered
GBflag = 2;         %Turn off/on corrosion surface area adjustment based on GB. Only
meaningful if Corrosionflag = 2
                      %1 = off, use whole surface area
                      %2 = on, adjust active surface area for corrosion to
                      %only the surface area of the grain boundaries
if GBflag ==2
    GB_diameter = 31.8E-6;   %Grain boundary diameter for 316 from azom.com (spacing
between grain boundaries) [m]
    % GB_diameter = 10E-6;  %304 L stainless fine grain size
%     GB_diameter = 23E-6;  %23E-6 304 L stainless from kestenbach, 1976 springer
    %     GB_diameter = 60E-6;   %Grain boundary diameter (spacing between grain
boundaries) for Hastelloy X  88 micron from Lippold 2013 [m]
    %     GB_diameter = 24E-6;   %Grain boundary diameter (spacing between grain
boundaries) for Hastelloy X. 24 micron from Abuzaid.  88 micron from Lippold 2013 [m]
    GB_width = 10E-9;      %Grain boundary width [m]  For 10 Ni atomic distances
2.48E-9 m

    %     GB_width = 0.01E-6;      %Grain boundary width [m]  For Hastelloy N, grain
width is about 0.5 nm?
    %     Surf_area_gb =
(4*(GB_diameter*GB_width)+GB_width^2)/(2*GB_diameter+GB_width)^2;  %Multiplier with
units of m2 GB surface per m2 of metal surface.  Typically around 3E-4
    %
    Circ_radius = (2*GB_diameter+sqrt(3)*GB_width/2)/2;
    Surf_area_gb =
((3*GB_diameter*GB_width)+(sqrt(3)/4)*GB_width^2)/(pi*(Circ_radius)^2); %Multiplier
with units of m2 GB surface per m2 of metal surface.

else
    Surf_area_gb = 1;  %Surface area not adjusted for grain boundaries
end

%%% Metal material properties
% Initial elements in 316 L SS, atom densities, surface atoms, etc.
Density_metal = 8000;  %[kg/m^3] density of 316L SS from azom.com
%     Cr       Fe      Ni      C       Mn      P       S       Si      Mo      N
Molar Mass [g/mol]
MM = [51.9961; 55.845; 58.693; 12.011; 54.938; 30.974; 32.065; 28.086; 95.94; 14.007];
%  Note that the Fe wt fraction is set to 0.00 initially.  Iron is assumed to make up
the balance of SS, and is calculated separately after all the other elements are
specified
%         Cr    Fe    Ni    C       Mn    P       S       Si      Mo      N     Weight
fraction from aksteel.com for 316L SS
Wtfrac = [0.18; 0.00; 0.12; 0.0003; 0.02; 0.00045; 0.0003; 0.0075; 0.025; 0.001];
Wtfrac(2,1) = 1-sum(Wtfrac); %Iron is the balance of the 316 composition

Lattice_param = 0.359E-9;  %[m] lattice parameter for austenite in 316 L stainless
steel


C_Cr_initial_ppm = 25; %Initial Cr concentration [ppm] in the salt after processing
pipe_zone1 = 0.000254; %[m] Thickness over which corrosion calcs are done for TF
transport limited mode
```

```
pipe_zone2 = 0.000254; %[m] Thickness over which corrosion calcs are done for Cr
diffusion limited mode
slices1 = 10;  %number of slices at which to calc Cr concentration distribution
slices2 = 10;  %number of slices at which to calc Cr concentration for Cr diff limited
mode
slice_thick1 = pipe_zone1/slices1;  %[m] thickness of each slice of the pipe through-
wall thickness for TF-limited case
slice_thick2 = pipe_zone2/slices2;  %[m] thickness of each slice of the pipe through-
wall thickness for Cr diffusion-limited case
depth_inwall = (0:pipe_zone1/slices1:pipe_zone1);  %[m] depth of each slice in the
pipe wall

Tritiumproductionflag = 3;  %Turn off/on variable tritium production rate with time
                            %Tritium production rate in primary loop.  Moles of T
atoms per second
                            %1 = use BOL tritium generation rate, time variation is
OFF, BOL generation rate is used for entire calculation
                            %2 = use EOL tritium generation rate, time variation is
OFF, equilibrium production rate is used
                            %3 = variation is ON, tritium production varies
                            %as Li-6 is consumed and Be-9 is transmuted to Li-6 based
on a model from Cisneros, 2013
                            %4 = user specifies the tritium production rate in units
of [molt T/sec]
                            if Tritiumproductionflag == 4
                                Birth_User = (7.44486E-7);  %[Mole T/sec] for 900 MWt
PB-FHR based on AHTR estimates (7.44486E-7) used in ICAPP 2014 Paper
                            else
                                Birth_User = 0;  %Birth_User not used.  Use
Tritiumproduction flag 1, 2, or 3 to specify birth rate.
                            end

flux = 3.41E14;  %flux in coolant for tritium calculation (n/cm2-s).  From Cisneros,
2013

%%%%%%%%%%%%%%%%%%%%%%%%%%%%%%%%%%%%%%%%%%%%%%%%%%%%%%%%%%%%%%%%%%%%%%%%%%%%%%%
%%%  Primary Graphite bed for capture of tritium %%%
%%%%%%%%%%%%%%%%%%%%%%%%%%%%%%%%%%%%%%%%%%%%%%%%%%%%%%%%%%%%%%%%%%%%%%%%%%%%%%%
Tritiumcapturebedflag = 1;  %1 = tritium capture on separate graphite bed is turned
OFF
%2 = tritium capture on separate graphite bed is turned ON
%Model options for graphite bed
Bed_frac_rep = 1/30;      %Fraction of bed to be replaced aka replacement rate
[fraction of bed graphite/d]. If this is 0, then the bed is not replaced online
Bed_frac_rep = Bed_frac_rep*(1/86400);  %Fraction of bed being replaced per second
%Input variables for graphite absorption bed
Bed_vessel_radius = 1.2; %[m]
Bed_surface_area = 1945.3/4;  %[m2] total bed surface area.  Nominal core pebble
surface area is 1945.3 m2
Particle_radius = 0.015;  %[m] radius of particle/pebble assuming a spherical particle
Particle_density = 1.77E6;  %From Toyo Tanso density for IG-110U graphite [g/m^3];
Bed_packingfraction = 0.60;  %Packing fraction in the graphite bed. Fraction of bed
volume occupied by pebbles

%%%%%%%%%%%%%%%%%%%%%%%%%%%%%%%%%%%%%%%%%%%%%%%%%%%%%%%%%%%%%%%%%%%%%%%%%%%%%%%
%%%  Secondary Graphite bed for capture of tritium %%%
%%%%%%%%%%%%%%%%%%%%%%%%%%%%%%%%%%%%%%%%%%%%%%%%%%%%%%%%%%%%%%%%%%%%%%%%%%%%%%%
Tritiumcapturebedflag_s = 1;  %1 = tritium capture on separate graphite bed is turned
OFF
%2 = tritium capture on separate graphite bed is turned ON
%Model options for graphite bed
```

```
Bed_frac_rep_s = 1/30;      %Fraction of bed to be replaced aka replacement rate
[fraction of bed graphite/d]. If this is 0, then the bed is not replaced online
Bed_frac_rep_s = Bed_frac_rep_s*(1/86400);  %Fraction of bed being replaced per second
%Input variables for graphite absorption bed
Bed_vessel_radius_s = 1.2; %[m]
Bed_surface_area_s = 1945.3;  %[m2] total bed surface area
Particle_radius_s = 0.015;  %[m] radius of particle/pebble assuming a spherical
particle
Particle_density_s = 1.77E6;  %From Toyo Tanso density for IG-110U graphite [g/m^3];
Bed_packingfraction_s = 0.60;  %Packing fraction in the graphite bed. Fraction of bed
volume occupied by pebbles

%%% Gas Stripping Options
GasStrippingFlag = 1;  % Option for including counter current gas strippers at various
points in the system
                       % If stripping is used, strippers are located just before the
heat exchangers
                       % 1 = no gas strippers
                       % 2 = gas stripping in primary coolant system only
                       % 3 = gas stripping in secondary coolant system only
                       % 4 = gas stripping in both primary and secondary system
StrippingFlowFraction_p = 0.5;  %Put value from 0 to 1.  Specifies how much of the
primary flow rate is diverted into the gas stripper
                            %1 means that the full primary coolant flow is going
through the stripper
                            %Anything < 1 means that only a fraction of the coolant
flow is being diverted to the stripper
StrippingFlowFraction_s = 0.5; %Put value from 0 to 1.  Specifies how much of the
secondary coolant flow is diverted into the gas stripper
NStages_p = 10;  %Number of stages in primary gas stripper
NStages_s = 10;  %Number of stages in secondary gas stripper
Gas_hrflowrate_p = 20000;  %Stripping gas flow rate [L/hr] at STP in primary
G_p = (Gas_hrflowrate_p*0.987/(0.08206*273.15))*(1/3600); %Use IGL to conver stripping
gas flow rate in primary [mole/s]
Gas_hrflowrate_s = 20000;  %Stripping gas flow rate [L/hr] at STP in secondary
G_s = (Gas_hrflowrate_s*0.987/(0.08206*273.15))*(1/3600); %Use IGL to conver stripping
gas flow rate in secondary [mole/s];

%%%%%%%%%%%%%%%%%%%%%%%%%%%%%%%%
%%% Permeation Window Options %%%
%%%%%%%%%%%%%%%%%%%%%%%%%%%%%%%%

%TRIDENT assumes that the flow area in the permeators is equal to the flow
%area of the pipe flowing into the permeator
NumPermptubes_opt = 2;  %Option to specify the number of tubes in the permeator or to
have TRIDENT calculate the number of tubes based on other input
                        %1 = off
                        %2 = on, user specifies number of tubes
NumberofPermeatorTubes = 2*13680; %Number of tubes to put in the permeator
PermElements = 6;  %Number of radial finite difference elements in the primary and/or
secondary permeator(s)
%Primary System
%%%%%%%%********NOTE: need to tell TRIDENT main program what the diffusion
%%%%%%%%coefficient is for the permeator so that it can calculate an
%%%%%%%%appropriate DT size (around line 680 in main program)
PermeationFlag_primary = 1;      %1 = off
                                 %2 = on;  Permeation window is turned on in the
primary system.
WindowArea_p = 12000;   %Surface area of primary system permeation window (m^2)
WindowThick_p = 8.89E-4;  %(Hx thickness 8.89E-4 m)Thickness of primary system
permeation window tube walls (m)
Permp_tube_od = 0.00635;  %Primary permeator tube outer diameter [m]
```

```
Vac_p = 1E-6; %NOT USED -- Pressure on outside of permeation window (side opposite the
coolant flow) [Pa]
%Secondary System
PermeationFlag_secondary = 1;    %1 = off
                                 %2 = on - permeation window is turned on in the
secondary system
WindowArea_s = 10082;   %Surface area of secondary system permeation window (m^2)
WindowThick_s = 8.89E-4;  %Thickness of secondary system permeation window (m)
Perms_tube_od = 0.00635; %Secondary permeator tube outer diameter [m]
Vac_s = 1E-6;  %NOT USED -- Pressure on outside of permeation window [Pa]

%Fuel pebble and TRISO particle properties  %From PB-FHR Mk1 Report
Kernel_d = 400E-6;       %Fuel kernel diameter [m]
Buffer_t = 100E-6;       %Buffer thickness [m]
IPyC_t = 35E-6;          %IPyC thickness [m]
SiC_t = 35E-6;           %SiC layer thickness [m]
OPyC_t = 35E-6;          %OPyC thickness [m]
TRISOperPebble = 4730;     %Number of TRISO particles per pebble
Pebble_radius = 1.5/100;  %Pebble radius [m]  3cm diameter pebble
PF = 0.60;            %Pebble packing fraction

%%% Reactor Core geometry Mk1 Report p. 31 and 38
Core_height = 4.65;           %236 MWt core effective height based on Figure 2-17 in
p.61 of PB-FHR Mk1 Report [m]
Core_mesh = 10;               %Number of axial core divisions for polythermal loop
calculations
CentralRef_radius = 0.35;      %Central reflector radius [m]
OuterRef_outradius = 1.69;     %Outer reflector outer radius [m] Based on Table 1-5
OuterRef_inradius = 1.25;     %Outer refelctor inner radius [m]
Fuelzone_innerradius = 0.35;  %Fuel zone inner radius [m]
Fuelzone_outerradius = 1.05;  %Fuel zone outer radius [m]

%Reactor Hot Leg Pipe Parameters from p. 89 of Mk1 PB-FHR Report where the
%four manifold pipes are combined into a single pipe having equivalent
%inner cross sectional area
pipe_thick1 = 0.02;  %Pipe wall thickness [m]
pipe_d = 0.79196; %Pipe inner diameter [m]
pipe_l = 29.74;  %Pipe length [m]
Hot_mesh = 10;  %number of axial divisions for polythermal loop calculations

%Reactor Cold Leg pipe parameters
pipe_thick2 = 0.02;  %Pipe wall thickness [m]
pipe_d2 = 0.494975;  %Pipe inner diameter [m]
pipe_l2 = 35.443;   %Pipe length [m]
Cold_mesh = 10;  %number of axial divisions for polythermal loop calculations

%%%%%%%%%%%%%%%%%%%%%%%%%%%%%%%%%%%%%%%%%%%%%%%%%%%%%%%%%%%%%%%%%%%%%%%%%%%%%%%
%%% Heat exchanger properties, coolant volumes, from MK1-PB-FHR paper %%%
%%%%%%%%%%%%%%%%%%%%%%%%%%%%%%%%%%%%%%%%%%%%%%%%%%%%%%%%%%%%%%%%%%%%%%%%%%%%%%%
TubeNumber = 1;  %TubeNumber = 1: input number of tubes in the HX1 and HX2 if known
                 %TubeNumber = 0: number of HX tubes is calculated in
                 %TRIDENT assuming the total flow cross sectional area in
                 %the HX matches that in the hot leg pipe
Hx1tubes = 2*13680;  %Number of HX1 tubes (from Table 3-2 in Mk1 Report)
Hx2tubes = 2*13680;  %Number of Hx2 tubes

Hx_mesh = 10;  %number of axial mesh points for the primary HX for polythermal loop
calculations
Hx_tube_od = 0.00635; %[m] Heat exchanger tube outer diameter from MK1-PB-FHR paper
Thick = 8.89E-4; %Heat exchanger tube wall thickness from Mk1-PB-FHR [m]
%1.6E-3;  %Heat exchanger tube wall thickness [m] from ICAPP 2014 report
A1 = 2*5041;  %Primary heat exchanger surface area from MK1-PB-FHR paper [m^2]
```

```
A2 = 2*5041;  %Secondary heat exchanger surface area from MK1-PB-FHR paper[m^2]

end
```

D.2: TRIDENT output

TRIDENT saves the Matlab "workspace" (which includes all of the values available to the TRIDENT.m main program) at the end of each simulation day (virtual time) and again at the final completion of the calculations. The filename (including the .mat file extension) for saving this output is set using the variable "Savefilename" in the input file. For example, the sample input file above saves all of the output as follows: `Savefilename = 'nominalfhr_examplesave.mat'`. The matrix called "OutputData" is saved after a calculation has been completed in order to gather vectors of key results into a single matrix. If the calculation is suspended for any reason prior to normal completion (perhaps if the user halts the calculation using the command "ctrl-c") "OutputData" is not written; however, the data that would be in each column of the matrix OutputData are still available from the original separate vectors. Table D. 2 describes each column in the matrix "OutputData". Each column is a set of time-dependent data which correspond to the simulation time (in days or hours) in the first two columns of OutputData. Table D. 3 summarizes other important output from TRIDENT simulations. All of these values, vectors, and matrices are also saved by TRIDENT to the .mat filename specified in the input file using the "Savefilename" variable.

Table D. 2: Upon completion of a simulation, TRIDENT writes a matrix called OutputData. The information contained in OutputData is summarized below

Column in matrix "OutputData"	Original vector name	Description
1	x	Simulation days
2	x*24	Simulation hours
3	MT1_total	Total moles of tritium atoms (T) in the primary reactor coolant
4	MT1_total*29263.83	Total tritium activity (Ci) in primary reactor coolant
5	MT1_T2	Moles of tritium existing as T_2 in the primary reactor coolant
6	MT1_TF	Moles of tritium existing as TF in the primary reactor coolant
7	MT2	Total moles of tritium atoms (T) in the secondary (intermediate) coolant if the system being modeled has an intermedieate system
8	MT2*29263.83	Total tritium activity in the secondary coolant (Ci)
9	MT3	Total moles of tritium released to the power cycle
10	MT3*29263.83	Total tritium activity (Ci) released to the power cycle
11	ReleaseRate_Ci	Tritium release rate to the power cycle (Ci/day)

(Table Continued) Column in matrix "OutputData"	Original vector name	Description
12	CoreGraphiteCumulativeT_bank	Total moles of T atoms that have been absorbed on core graphite
13	HX1_T	Moles of T atoms dissolved in HX1 tube walls
14	HX2_T	Moles of T atoms dissolved in HX2 tube walls (if system is configured with a secondary heat exchanger)
15	PP_TF_coolantbank	Partial pressure (atm) of TF above the primary coolant
16	PP_T2_coolantbank	Partial pressure (atm) of T_2 above the primary coolant
17	Global_Redox	Redox potential (kJ/mol F_2) in the coolant just prior to the core inlet
18	CumulativeT_bank	Total moles of T atoms produced from transmutation during the calculation
19	TritiumBalance	Total moles of T atoms summed up throughout the system to check for conservation of tritium
20	Ratio	Ratio of TritiumBalance:CumulativeT_bank. This ratio should be 1. If it is not 1, tritium is being erroneously lost or generated.
21	Cr_coolant_conc	Concentration of dissolved Cr in the coolant mole (Cr/m^3)
22	Cr_coolant_conc converted to ppm	Concentration of dissolved Cr in the coolant (weight ppm)
23	CoreGraphiteCumulativeT_bank *29263.8	Total tritium activity (Ci) absorbed on core graphite during the calculation

Table D. 3: Other important vectors and matrices of information calculated during TRIDENT simulations are summarized below. Depending on the input options, not all of these will be calculated.

Vector or Matrix Name	Description
x	Column vector of the hours at which data from the simulation are stored
T2onbedbank	Column vector of cumulative total moles of T_2 captured on the (optional) packed bed of graphite spheres between the core exit and the HX entrance
TFonbedbank	Column vector of cumulative total moles of TF captured on the (optional) packed bed of graphite spheres between the core exit and the HX entrance
T_2onbedbank2	Column vector of cumulative total moles of T_2 captured on the (optional) packed bed of graphite spheres in the secondary (intermediate) coolant system located in the hot leg of the secondary coolant loop
mtg_T2	Moles of T_2 currently absorbed on the core graphite in the different axial segements of the core. This is overwritten at the end of each timestep
mtg_TF	Moles of TF currently absorbed on the core graphite in the different axial segements of the core. This is overwritten at the end of each timestep
mtgbed_T2	Current inventory moles of T_2 captured on the (optional) packed bed of graphite spheres between the core exit and the HX entrance. This is overwritten at the end of each timestep
mtgbed_TF	Current inventory moles of T_2 captured on the (optional) packed bed of graphite spheres between the core exit and the HX entrance. This is overwritten at the end of each timestep

Vector or Matrix Name (table continued)	Description
FinalGramsDep_persa	Column vector of the final amount of Cr corrosion products deposited throughout the system at the end of a simulation (mg Cr/cm^2). Each row represents a segment of the coolant loop
GRAMSCr_persa_new	Matrix of Cr deposition (mg Cr/cm^2). Each row corresponds to the simulation time vector "x". Each column represents a location in the coolant loop
Crcorroded_persa_new	Matrix of Cr lost from segments of the loop due to corrosion (mg Cr/cm^2). Each row corresponds to the simulation time vector "x". Each column represents a location in the coolant loop. Adding GRAMSCr_persa_new to Crcorroded_persa_new will give the net weight change throughout the loop as a function of time. Because no metal faces the coolant in the core, there is no corrosion in the core.
Cr_profile_bulk	Matrix of Cr concentration profile through the bulk of the pipe walls at different locations in the coolant loop. Each row represents a particular segment of the coolant loop. Each column represents a location in the pipe wall. The first column is the Cr concentration in the metal at the metal-coolant interface. The depth (m) corresponding to each column in Cr_profile_bulk is given by the row vector depth_bulk.
Cr_profile_gb	Matrix of Cr concentration profile along a grain boundary extending from coolant-metal interface into the depth of the metal at different locations in the coolant loop. Each row represents a particular segment of the coolant loop. Each column represents a depth along a fictitious grain boundary. The first column is the Cr concentration at a grain boundary in the metal at the metal-coolant interface. The depth (m) corresponding to each column in Cr_profile_gb is given by the row vector depth_gb.
PrimaryStripTotal_T2 or SecondaryStripTotal_T2	Column vector of the cumulative moles of T_2 removed from the coolant in the primary or secondary gas stripper. Each row corresponds to the simulation time in vector "x"
PrimaryStripTotal_TF or SecondaryStripTotal_TF	Column vector of the cumulative moles of TF removed from the coolant in the primary or secondary gas stripper. Each row corresponds to the simulation time in vector "x"
PrimaryStripTotal_T or SecondaryStripTotal_T	Column vector of the cumulative moles of T atoms removed from the coolant in the primary or secondary gas stripper. Each row corresponds to the simulation time in vector "x"
PrimaryStripActivity or SecondaryStripActivity	Column vector of the cumulative tritium activity stripped out of the salt in the primary or secondary gas stripper. Each row corresponds to the simulation time in vector "x".
PrimaryStripGas_TF_Conc or SecondaryStripGas_TF_Conc	Column vector of the TF concentration in the stripping gas exiting the stripper (mol TF/mol gas). Each row corresponds to the simulation time in vector "x".
PrimaryStripGas_T2_Conc or SecondaryStripGas_T2_Conc	Column vector of the T2 concentration in the stripping gas exiting the stripper (mol T2/mol gas). Each row corresponds to the simulation time in vector "x".
PrimaryStripCoolantExit_T2 or SecondaryStripCoolantExit_T2	Column vector of the T2 concentration in the coolant exiting the stripper (mol T2/mol salt). Each row corresponds to the simulation time in vector "x".
PrimaryStripCoolantExit_TF or SecondaryStripCoolantExit_TF	Column vector of the TF concentration in the coolant exiting the stripper (mol TF/mol salt). Each row corresponds to the simulation time in vector "x".

Vector or Matrix Name (Table continued)	Description
PrimaryPermeatorTactivity or SecondaryPermeatorTactivity	Column vector of the tritium activity (Ci) removed via the primary or secondary permator. Each row corresponds to the simulation time in vector "x".

Appendix E: Stand-alone calculations of tritium production rates and redox potentials.

Several small MatLab programs were written for quickly and easily investigating certain effects. These programs are included below.

Code for calculating the tritium production rate in flibe (or NaF-BeF$_2$) in a typical PB-FHR "Standalone_Tritium_ProductionCalculation."

```
%%%%%%%%%%%%%%%%%%%%%%%%%%%%%%%%%%%%%%%%%%%%%%%%%%%%%%%%%%%%%%%%%%%%%%%%%%%%%%%%%%%%%%%%%%%%%%%%
%This program calculates the tritium production rate due to neutron
%transmutation in flibe (or approximated for NaF-BeF2) for a typical FHR.
%Calculations are time-dependent, temperature dependent, reactor volume
%dependent, and dependent on the Li-7 enrichment specified.
%
%                            John Stempien
%                    MIT, Nuclear Science and Engineering
%                                May, 2015
%%%%%%%%%%%%%%%%%%%%%%%%%%%%%%%%%%%%%%%%%%%%%%%%%%%%%%%%%%%%%%%%%%%%%%%%%%%%%%%%%%%%%%%%%%%%%%%%

clear;
close all;

Rx_power = 0.236;  %GWt
Salt = 1;  %1 = flibe
           %2 = 0.57NaF-0.43BeF2
Li7_enrichment = 99.999; %
%Vol_1 = 46.82;  %total primary coolant volume for MK1 PB-FHR single loop design (m3)
Vol_1 = 39.8026;  %total primary coolant volume for Mk1 PB-FHR with TRIDENT geometric
approx
%Core_coolant_vol = 29.8577; %core coolant volume for 900 MWt two-loop design (m3)
%Core_coolant_vol =  7.2;  %core coolant volume for MK1 PB-FHR (m3)
Core_coolant_vol = 8.4144;  %Core coolant vol for Mk1 PB-FHR with TRIDENT geometric
approximation
T = 950 + 273.15;  %Coolant temp [K]

if Salt == 1
MoleFracLiCompound = 0.67;
MoleFracBeCompound = 0.33;
MoleFracNaCompound = 0;
elseif Salt == 2
MoleFracNaCompound = 0.57;
MoleFracBeCompound = 0.43;
MoleFracLiCompound = 0;
end

%Molar Masses
Li7_MM = 7.01600455;  %[g/mol]
Li6_MM = 6.015122795;  %[g/mol]
Na23_MM = 22.98976928; %[g/mol]
Be_MM = 9.0121831;  %[g/mol]
F_MM = 18.998403163;  %[g/mol]

Flibe_MM = 32.8931;      %Molar mass of flibe with 99.995% Li-7 [g/mol] from doing
0.67*MM_LiF + 0.33*MM_BeF2
NaFBeF2_MM = MoleFracNaCompound*(Na23_MM + F_MM)+MoleFracBeCompound*(Be_MM+2*F_MM);
```

```
dens_flibe = 2415.6-0.49072*T;          %Flibe density from Janz correlation in Sohal
2010 [kg/m^3]
dens_NaFBeF2 = 2010;  %NaF-BeF2 density from Sohal 2010 [kg/m3]
mole_dens_NaFBeF2 = dens_flibe*(1000/NaFBeF2_MM);  %Molar density of NaFBeF2 [mole
NaF-BeF2/m3]
mole_dens_flibe = dens_flibe*(1000/Flibe_MM);  %Molar density of flibe [mol flibe/m3]
if Salt ==1
    mole_dens_salt = mole_dens_flibe;
elseif Salt == 2
    mole_dens_salt = mole_dens_NaFBeF2;
end

Li7_molefrac = (Li7_enrichment/Li7_MM)/((Li7_enrichment/Li7_MM)+((100-
Li7_enrichment)/Li6_MM));  %Mole fraction of lithium in flibe that is Li-7
Li6_molefrac = ((100-Li7_enrichment)/Li6_MM)/((Li7_enrichment/Li7_MM)+((100-
Li7_enrichment)/Li6_MM));  %Mole fraction of lithium in flibe that is Li-6
mole_dens_Li_flibe = MoleFracLiCompound*mole_dens_salt;  %Molar density of total
lithium in flibe [mol Li/m3]
N_Li7 = (Li7_molefrac*mole_dens_Li_flibe*6.022E23)*10^-6;  %Number density of Li-7
atoms in flibe [atoms Li-7/cm3]
N_Li6 = (Li6_molefrac*mole_dens_Li_flibe*6.022E23)*10^-6;  %Number density of Li-6
atoms in flibe [atoms Li-6/cm3]

N_Be9 = (MoleFracBeCompound*mole_dens_salt*6.022E23)*10^-6;  %Number density of Be-9
in salt [atoms Be-9/cm3]
N_Na23 = (MoleFracNaCompound*mole_dens_salt*6.022E23)*10^-6;  %Number density of Na-23
in NaF-BeF2 salt [atoms/cm3]

flux = 3.41E14;  %flux in coolant (n/cm2s)
sig_T_Li7 = (1E-3)*10^(-24);  %(n,T) cross section in Li-7 [cm2]
sig_T_Li6 = 148.026E-24;  %(n,T) cross section in Li-6 [cm2]
sig_abs_Li6 = 148.032E-24;  %(n,abs) cross section in Li-6 [cm2]
sig_alpha_Be9 = (3.63E-3)*10^-24;  %(n,alpha) in Be-9 [cm2]
sig_T_Na23 = 0;
sig_abs_Na23 = 3.9E-24;

Years = 50;

%Setting initial values and pre-allocations
Total_seconds = Years*3.1536E7;
dNdT = zeros(1/0.2,1);
time = zeros(1/0.2,1);
derivative = zeros(1/0.2,1);
counter = 0;
cumulative_t_produced = 0; %total moles produced
fraction = 0.005;  %fraction to determine total number of steps having t seconds to
run

for t = 0:fraction*Total_seconds:Total_seconds  %t has units of seconds
    counter = counter + 1;
    if Salt == 1
        dNdT(counter,1) = (flux*sig_T_Li7*N_Li7+flux*sig_T_Li6*(N_Li6*exp((-
Core_coolant_vol/Vol_1)*flux*sig_abs_Li6*t)+((flux*sig_alpha_Be9*N_Be9) ...
            /(flux*sig_abs_Li6))*(1-exp((-
Core_coolant_vol/Vol_1)*flux*sig_abs_Li6*t))))*(Core_coolant_vol*10^6)*86400/(6.022E23
);  %[mole T/EFPD] Equation comes from Cisneros, 2013 Thesis
        derivative(counter,1) = (flux*sig_T_Li6*(N_Li6*((-
Core_coolant_vol/Vol_1)*flux*sig_abs_Li6*t)*exp((-
Core_coolant_vol/Vol_1)*flux*sig_abs_Li6*t)+((flux*sig_alpha_Be9*N_Be9) ...
            /(flux*sig_abs_Li6))*(-((-
Core_coolant_vol/Vol_1)*flux*sig_abs_Li6*t)*exp((-
```

```
Core_coolant_vol/Vol_1)*flux*sig_abs_Li6*t))))*(Core_coolant_vol*10^6)*86400/(6.022E23
);
    elseif Salt == 2
        dNdT(counter,1) = (flux*sig_T_Li6*(N_Li6*exp((-
Core_coolant_vol/Vol_1)*flux*sig_abs_Li6*t)+((flux*sig_alpha_Be9*N_Be9) ...
            /(flux*sig_abs_Li6))*(1-exp((-
Core_coolant_vol/Vol_1)*flux*sig_abs_Li6*t))))*(Core_coolant_vol*10^6)*86400/(6.022E23
);  %[mole T/EFPD] Equation comes from Cisneros, 2013 Thesis
        derivative(counter,1) = (flux*sig_T_Li6*(N_Li6*((-
Core_coolant_vol/Vol_1)*flux*sig_abs_Li6*t)*exp((-
Core_coolant_vol/Vol_1)*flux*sig_abs_Li6*t)+((flux*sig_alpha_Be9*N_Be9) ...
            /(flux*sig_abs_Li6))*(-((-
Core_coolant_vol/Vol_1)*flux*sig_abs_Li6*t)*exp((-
Core_coolant_vol/Vol_1)*flux*sig_abs_Li6*t))))*(Core_coolant_vol*10^6)*86400/(6.022E23
);

    end
    if dNdT(counter,1) == 0
        stop = t;
    end
    time(counter,1) = t/3.1536E7;  %[effective full power years]
    cumulative_t_produced = cumulative_t_produced +
dNdT(counter,1)*fraction*Total_seconds/86400;
end
dNdT_Ci = dNdT*29263.8287;  %Tritium production rate in Ci/EFPD
dNdT_grams = dNdT*3.0160492/236;  %Tritium prodcution rate g/MWt
% figure; plot(time,dNdT); xlabel('Effective Full Power Years (EFPY)'); ylabel('T
Production Rate (mol T/EFPD)');
figure; plot(time,dNdT_Ci); xlabel('Effective Full Power Years (EFPY)'); ylabel('T
Production Rate (Ci T/EFPD)');
figure; plot(time,dNdT_Ci/Rx_power); xlabel('Effective Full Power Years (EFPY)');
ylabel('T Production Rate (Ci T/GWD)');
% figure; plot(time,derivative); xlabel('Effective Full Power Years (EFPY)');
ylabel('Derivative');
```

"RedoxCalculation.m" calculates the fluorine potential associated with different ratios of UF_4:UF_3 and P_{TF2}^2:P_{T2} over a range of temperatures

```
%%%%%%%%%%%%%%%%%%%%%%%%%%%%%%%%%%%%%%%%%%%%%%%%%%%%%%%%%%%%%%%%%%%%%%%%%%%%%%%%
%Redox Calculator
%Calculates the redox potential in flibe in terms of the fluorine potential
%(kJ/mol F2) as a function of temperature and the ratio P_TF^2/P_T2 and/or
%in releation to the UF4/UF3 ratio used in the MSRE.
%
%                          John D Stempien
%                              May 2015
%                MIT, Nuclear Science and Engineering
%%%%%%%%%%%%%%%%%%%%%%%%%%%%%%%%%%%%%%%%%%%%%%%%%%%%%%%%%%%%%%%%%%%%%%%%%%%%%%%%

%Assumes total pressure is 1 atm
clear all;
%close;
R = 0.0083144621;  %Universal gas constant kJ/mol-K
% Ratio_UF4_UF3 = 100;

%Constant Temperature with variable UF4/UF3 ratios
T = 650 + 273.15;  %Temp in kelvin
%"K12" is the equilibrium constant for the reaction UF3 + TF = UF4 + 0.5T2
Log_K12 = -4.07 + 9.33*(1000/T);  %from Baes, 1969. T is in Kelvin
K12 = 10^Log_K12;
G12 = -R*T*log(K12);  %G12, kJ/mol F2.  G12 is the Gibbs reaction free energy for the
reaction UF3 + TF = UF4 + 0.5T2
G13 = -4.6976E-10*(T)^3+3.1425E-6*(T)^2-8.8612E-3*(T)-2.7305E2;  %Delta G13 from HSC
for kJ/mol F.  T in this equation must be in Kelvin
%G13 is the Gibbs reaction free energy for the reaction 0.5T2 + 0.5F2 = TF
G14 = G12 + G13;  %kJ/mol F2.  G14 is the reaction free energy for the reaction
UF3+0.5F2=UF4
for i = 1:1:1000
    Ratio_UF4_UF3(i,1) = 1 + (i-1)*10;
    G_F2_UF(i,1) = 2*R*T*log(Ratio_UF4_UF3(i,1)) + 2*G14;  %Fluorine potential [kJ/mol
F2] at specified temperature and ratio of UF4:UF3
    Ratio_T2_TF(i,1) = (exp((G_F2_UF(i,1) - 2*G13)/(2*R*T)))^2;  %ratio of (TF^2)/T2
end
figure; plot(Ratio_UF4_UF3,sqrt(Ratio_T2_TF)); xlabel('Ratio of UF_4 to UF_3');
ylabel('Ratio of TF/sqrt(T_2)');
figure; plot(Ratio_UF4_UF3,Ratio_T2_TF); xlabel('Ratio of UF_4 to UF_3');
ylabel('Ratio of TF^2/T_2');
figure; plot(Ratio_UF4_UF3,G_F2_UF); xlabel('Ratio of UF_4 to UF_3'); ylabel('Fluorine
Potential (kJ/mol F2');
figure; plot(G_F2_UF, sqrt(Ratio_T2_TF)); xlabel('Fluorine Potential (kJ/mol F_2)');
ylabel('Ratio of TF/sqrt(T_2)');

%Constant UF4/UF3 ratio with variable temperature
R = 8.314/1000;  %Universal gas constant kJ/mol-K
Ratio_UF4_UF3_fixed = 100;

T_start = 773.15;  %Set starting temp in kelvin
Temp_step_size = 25;  %Vary by a certain degree K each step

for i = 1:1:20
    T = T_start + Temp_step_size*(i-1);  %Variable temperature [K]
    Log_K21_temp = -4.07 + 9.33*(1000/T);  %from Baes, 1969. T is in Kelvin
    K12 = 10^(Log_K21_temp); %Solve for K12
    G12 = -R*T*log(K12);  %G12, kJ/mol F2
    G13 = -5E-10*T^3 + 3E-6*T^2 - 0.0089*T - 273.05; %Delta G13 from HSC for kJ/mol F.
At variable temperature (K)
```

```
    G14 = G12 + G13;  %kJ/mol F2
    G_F2_UF_temp(i,1) = 2*R*T*log(Ratio_UF4_UF3_fixed) + 2*G14;  %Fluorine potential
[kJ/mol F2] at specified temperature and ratio of UF4:UF3
    Ratio_T2_TF_temp(i,1) = (exp((G_F2_UF_temp(i,1) - 2*G13)/(2*R*T)))^2;  %ratio of
(TF^2)/T2 at a specific fluorine potential
    Temperature(i,1) = T;  %Vector of temperatures [K]
end
figure; plot(Temperature, G_F2_UF_temp); xlabel('Temperature [K]'); ylabel('Fluorine
potential [kJ/mol F_2]')
figure; plot(Temperature, Ratio_T2_TF_temp); xlabel('Temperature [K]'); ylabel('Ratio
(TF^2)/T_2')
```